

The background of the entire page is a complex, grayscale fractal pattern. It features a large, prominent spiral in the upper left quadrant, with smaller, more intricate fractal structures scattered throughout. The pattern has a high level of detail, with many small, repeating geometric shapes that create a sense of depth and complexity.

Université de Liège

Asteroseismic study of solar-like pulsators along their evolution

Martin Farnir

Thesis manuscript
Supervisor

2021

Marc-Antoine Dupret



UNIVERSITÉ DE LIÈGE
FACULTÉ DES SCIENCES
DÉPARTEMENT D'ASTROPHYSIQUE, DE GÉOPHYSIQUE ET D'OCÉANOGRAPHIE

Asteroseismic study of solar-like pulsators along their evolution

MARTIN FARNIR

Astrophysique Stellaire Théorique et Astérosismologie

Sart-Tilman
Liège, Belgique
Année Académique 2020 – 2021

Jury members:

Marc-Antoine Dupret (Supervisor), Professor

University of Liège

Margarida Cunha, Principal Researcher

University of Porto

Andrea Miglio, Professor

University of Bologna

Sébastien Deheuvels, Associate Professor

University of Toulouse III Paul Sabatier

Marie-Jo Goupil, Professor

Paris observatory

Jean-Marie Beckers, Professor

University of Liège

Valérie Van Grootel, Chercheur Qualifié du F.R.S.-FNRS

University of Liège

Dissertation submitted in partial fulfilment of the
requirements for the degree of Doctor of
Philosophy in Science.

Acknowledgements

I would like to thank my thesis supervisor, Marc-Antoine Dupret, without whom the present manuscript would not be. Marc-Antoine has overseen my work with great care, interest and kindness. This is therefore with great scientific and human skills that he helped me to develop a mature scientific mindset. Marc-Antoine has been very available throughout my PhD and we held many fruitful conversations, essential to the completion of my work.

I am also thankful to the complete ASTA team, my host team. Amongst that team, I thank Arlette, Valérie, and Sébastien who were always extremely kind and provided me with their expertise at key times. They are responsible for my successful FRIA application, which has financed my work. Furthermore, it was with great pleasure that we collaborated and I learned a great deal at their contact.

I would also like to thank the LESIA team, from the Paris Meudon observatory, especially Marie-Jo, Daniel, Rhita, and Kevin. They warmly welcomed me to collaborate, enlarging my network of collaborators. They also offered me the opportunity to present the advances in my work on two occasions. This was a great experience, which I particularly enjoyed. I also thank the Birmingham team and Josefina that also permitted me to give a seminar to a slightly different audience and further advertise my advances.

I am especially thankful of Arlette, Daniel, and Marc-Antoine who were of a great support in my post-doctoral applications as the many recommendation letters they wrote testify.

Charly and Gaël were also two notorious collaborators with whom it was a great pleasure to work but also to relax. Furthermore, their advice turned out to be very valuable in all cases and helped me to further develop my skills and knowledge.

I thank Angelo who, through his master thesis work, contributed to the present manuscript. He was also the very first student I supervised and it was a very rewarding experience. He was also extremely involved in his work, which was a pleasure to me.

I would also like to thank all my loved ones: my family, who have been present from the very start of this adventure (and before of course); my girlfriend, Sandy, who endured by my side, even by the difficult end, and gave me courage and comfort. She was also a great example of patience at times, I am grateful that we met; my friends and my colleagues, which I can call my friends, who provided me the necessary support, courage but also fun and relaxation in order to make it. Everyone played an important part. I am happy that I have so many reliable people by my side who understood the difficulties that I sometimes met in these four years of work.

I also thank Sandy and Sophie who took the time to read this manuscript in order to reduce the number of typos that I so often tend to make.

I am grateful to the jury of my thesis who agreed to read and evaluate this work. I am honoured to get the chance to share my work.

Finally, I give my thanks to the FNRS (Fonds National de la Recherche Scientifique) who financed my work and without whom this work could obviously not have been undertaken.

Following the advent of space-borne missions (e.g. CoRoT, Kepler), came a wealth of data of unprecedented quality. This enabled asteroseismology to thrive and to probe the stellar structure of a wide variety of pulsating stars. Amongst these pulsating stars is the notable category of low-mass stars. These exhibit masses below $2.3 M_{\odot}$, encompassing the case of our Sun.

Throughout their evolution, these stars exhibit a few interesting peculiarities. First, during the main-sequence phase, they display a very regular pressure-mode oscillation spectrum. However, small perturbations to that regularity may occur. Such perturbations are the result of sharp and localised variations in the stellar structure. These create an oscillating feature, as a function of the frequency, in the oscillation spectrum, the so-called glitches. These glitches are of particular interest as they allow us to probe very localised regions of the stellar interior and provide diagnoses about specific stellar features, inaccessible by other means. In main-sequence low-mass stars, we distinguish two main causes of glitches: the helium second-ionisation zone, providing information about the surface helium abundance, and the base of the envelope convection zone, constraining the mixing processes in that region. The first part of my thesis was dedicated to the development of a seismic technique, WhoSGlAd, that consistently analyses the complete oscillation spectra of main-sequence low-mass stars and robustly retrieves the glitches signatures present in these spectra. Special care was put in the definition of stringent seismic indicators as we decorrelated them as much as possible. This is done thanks to a Gram-Schmidt orthonormalisation process. The defined indicators were then used to constrain stellar models and provide a characterisation of both the 16 Cygni system and the Kepler Legacy Sample, representing the best solar-like seismic data currently available.

After the main-sequence phase, low-mass stars evolve on the subgiant and red-giant phases. Their core then contracts while their envelope expands, developing a large core-envelope density contrast. This produces the appearance of mixed-modes, presenting a twofold nature: a gravity-dominated nature in the inner radiative regions, and a pressure-dominated nature in the outer convective regions. These modes have the great advantage to propagate throughout most of the stellar interior and, therefore, to probe almost the complete stellar structure. To exploit the information these modes carry, we developed the EGGMiMoSA method. It relies on the asymptotic expression and allows us to precisely measure seismic indicators on both subgiant and red-giant stars. The method was applied to a grid of models extending from the subgiant phase to the luminosity bump. The results are excellent in regard to the asymptotic values of the seismic indicators and also qualitatively agree with observed and theoretical studies. These indicators also allow us to efficiently infer the stellar age, mass, and radius of subgiant stars and of red-giant stars with masses $\gtrsim 1.8 M_{\odot}$. Below this threshold, we noted that the central electron degeneracy impaired our diagnosis of the stellar age, mass, and radius in red-giants.

The combination of both methods should provide means to constrain the stellar structure of low-mass stars from the early main-sequence phase to the late red-giant one. This is a unique opportunity to study their structure through most of their evolution and, for example, pinpoint missing physical processes in their modelling.

Suite à l'avènement des missions spatiales (telles que CoRoT et Kepler), de larges quantités de données d'une qualité jusque là inégalées furent rassemblées. Ceci permit à l'astérosismologie de s'épanouir et de sonder tout un éventail d'étoiles pulsantes. Parmi celles-ci, nous comptons la catégorie notable des étoiles de faible masse. Ces étoiles présentent des masses inférieures à $2.3 M_{\odot}$, et comprennent ainsi le cas de notre Soleil.

Tout au long de leur évolution, ces étoiles affichent certaines particularités intéressantes. Tout d'abord, au cours de leur phase de séquence principale, elles présentent un spectre de modes de pression particulièrement régulier. Cependant, de faibles perturbations peuvent affecter cette régularité. Ces perturbations sont le résultat de variations localisées et brusques au sein de la structure stellaire. Leur conséquence est alors une signature oscillante, en fonction de la fréquence, dans le spectre d'oscillations. Ce sont les glitches. Leur intérêt est tout particulier car ils permettent le sondage précis des régions stellaires étant à leur origine. Ils fournissent ainsi des diagnostics au sujet de caractéristiques stellaires spécifiques auxquelles nous n'aurions pas accès au travers de techniques alternatives. Pour les étoiles de séquence principale, nous distinguons deux causes à ces glitches: la zone de seconde ionisation de l'hélium, nous informant quant à l'abondance en surface d'hélium, et la base de l'enveloppe convective, contraignant les processus de mélange dans cette région. La première partie de ma thèse fut consacrée au développement d'une technique de sondage sismique, WhoSGLAd, qui analyse de façon cohérente le spectre d'oscillations complet d'étoiles de séquence principale et de faible masse, tout en extractant la signature des glitches acoustiques présents dans leurs spectres. Nous avons porté une attention toute particulière à la définition d'indicateurs sismiques contraignants que nous avons décorrélés tant que possible grâce au procédé d'orthonormalisation de Gram-Schmidt. Les indicateurs ainsi définis furent alors utilisés comme contraintes pour des modèles stellaires, ce dans le but de caractériser le système 16 Cygni et l'échantillon du Kepler Legacy, qui constitue le meilleur ensemble de données sismiques d'étoiles de type solaire disponibles à ce jour.

Une fois la séquence principale achevée, les étoiles de faible masse évoluent vers les phases de sous-géante et géante rouge. Le cœur de ces étoiles se contracte alors que leur enveloppe se dilate. Le résultat est l'apparence d'un important contraste de densité entre leurs cœur et enveloppe. Ceci permet l'apparence de modes mixtes. Ceux-ci présentent une nature double: dominée par la gravité dans les régions radiatives profondes et dominée par la pression dans les régions plus superficielles et convectives. Leur grande force est qu'ils se propagent au travers de la plus grande partie de l'intérieur stellaire, permettant ainsi de sonder la presque totalité de leur structure. Afin d'exploiter l'information dont ces modes sont porteurs, nous avons développé la méthode EGGMiMoSA. Cette méthode repose sur la formulation asymptotique et permet la mesure précise d'indicateurs sismiques, tant au cours de la phase de sous-géante que de celle de géante rouge. La méthode fut appliquée à une grille de modèles s'étendant de la phase de sous-géante au 'luminosity bump'. Les résultats obtenus sont excellents, en comparaison avec les indicateurs sismiques asymptotiques, et sont en accord qualitatif avec les études théoriques et observationnelles. Ces indicateurs nous permettent d'inférer la masse, le rayon et l'âge de sous-géantes ainsi que de géantes rouges ayant une masse $\gtrsim 1.8 M_{\odot}$. En deçà de cette limite, nous avons remarqué que la dégénérescence électronique centrale nuit à notre diagnostic de la masse, du rayon et de l'âge des géantes rouges.

Combinaison des deux méthodes définies durant cette thèse devrait nous fournir les moyens de contraindre la structure d'étoiles de faibles masses, depuis les moments précoces sur la séquence principale jusqu'aux phases tardives sur la branche des géantes rouges. Ceci représente une opportunité unique d'étudier leur structure au long de la majorité de leur évolution et, par exemple, de mettre en évidence des processus physiques manquants à leur modélisation.

Contents

Acknowledgements	iii
Abstract	iv
Contents	vii
List of Figures	ix
List of Tables	xi
1 Introduction	1
1.1 From stellar variability to asteroseismology	1
1.2 Asteroseismology	1
1.3 Objectives and structure of the thesis	2
2 Theoretical framework	3
2.1 Stellar structure and evolution	3
2.2 Stellar pulsations	10
I The main sequence	23
3 The WhoSGlAd method	25
3.1 Context	25
3.2 The method	27
3.3 Advantages and limitations	47
3.4 Toy model of the first adiabatic index	49
3.5 Providing an estimate for the acoustic depth of the helium glitch	51
3.6 Conclusion	55
3.A Large frequency separation in common notations	56
3.B The case of correlated frequencies	56
3.C Brent minimisation	57
3.D Paper: Comprehensive stellar seismic analysis: New method exploiting the glitches information in solar-like pulsators	59
4 Application of the WhoSGlAd method	79
4.1 Minimisation schemes	79
4.2 Application to the 16 Cygni system	82
4.3 Application to the Kepler LEGACY sample	92
4.A Paper: Thorough characterisation of the 16 Cygni system: I. Forward seismic modelling with WhoSGlAd	101
4.B Proceeding: Determination of precise stellar parameters of Kepler LEGACY targets using the WhoSGlAd method	125

II	The subgiants and red-giants	131
5	The EGGMiMoSA method	133
5.1	Introduction	133
5.2	The method	139
5.3	Notable results	139
5.4	Improvements of the method	148
5.5	Conclusion	150
5.A	Paper: Modelling the mixed-mode patterns of subgiant and red-giant stars with EGGMiMoSA	151
6	Conclusion	173
6.1	Part I: Main-sequence solar-like stars	173
6.2	Part II: Subgiant and red-giant stars	174
6.3	General perspectives	175
	Bibliography	177

List of Figures

2.1	HR diagram of the stars observed by the CoRoT (left) and <i>Kepler</i> (right) spacecrafts presented in Chaplin & Miglio (2013, Fig. 5)	7
2.2	Propagation diagram for a solar clibrated model.	15
2.3	Schematisation of the p-cavity.	17
2.4	Echelle diagram using the frequencies for 16CygA measured by Davies et al. (2015)	17
2.5	Schematisation of the g-cavity.	18
2.6	Schematisation of the coupling between the p- and g-cavities.	20
2.7	Representation of the helium glitch retrieved 16CygA frequencies with our method, WhoSGlAd.	22
3.1	The WhoSGlAd logo.	25
3.2	First adiabatic index as a function of the reduced radius in the most superficial regions of a solar-like stellar model.	27
3.3	Visualisation of the orthonormalisation process and fitting procedure for the smooth component of the oscillation spectrum.	32
3.4	Visualisation of the orthonormalisation process and fitting procedure for the glitch component of the oscillation spectrum.	33
3.5	Evolution of the small separation ratios defined in Eq. (3.32) over a grid of models.	37
3.6	Evolution of the small separation ratios as defined in Eq. (3.30) (Roxburgh & Vorontsov 2003) over the same grid as in Fig. 3.5.	38
3.7	\hat{r}_{01} - Δ_{01} diagram for several main sequence $1.2 M_{\odot}$ tracks with different overshooting parameter values as in Farnir et al. (2019) , Fig. 3.	39
3.8	Fig. 3 of Deheuvels et al. (2016)	40
3.9	\hat{r}_{01} - Δ_{01} diagram for models adjusting the large separation, Δ , of KIC7510397 for several masses and overshooting parameter values.	40
3.10	\hat{r}_{01} - Δ_{01} diagram for models adjusting the large separation, Δ , of KIC7206837 for several masses and overshooting parameter values.	41
3.11	Evolution of $\hat{\epsilon}$ with Δ over the same grid of models as in Fig. 3.5.	42
3.12	Helium glitch amplitude evolution with the surface helium abundance at fixed $(Z/X)_0 = 0.022$ value.	44
3.13	Helium glitch amplitude evolution with the surface metals abundance at fixed $Y_0 = 0.24$ value.	44
3.14	Γ_1 toy model in the helium second-ionisation zone.	45
3.15	Evolution of the convection zone glitch amplitude with the amount of undershooting below the base of the convection zone.	46
3.16	Temperature gradients around the base of the convection zone.	46
3.17	Fitted glitches signatures to the 16CygA frequencies measured by Davies et al. (2015)	48
3.18	Evolution of the helium glitch amplitude with the surface helium abundance in the limit case ($1.25 M_{\odot}$ and $1.3 M_{\odot}$).	48
3.19	Evolution of the degrees of ionisation x of hydrogen and helium as a function of the pressure in a solar model presented in Kippenhahn et al. (2012)	51
3.20	Evolution of the acoustic depth of the helium glitch for a grid of models with masses in $[0.80M_{\odot}, 1.15M_{\odot}]$ ($0.05M_{\odot}$ step) for the initial composition $X_0 = 0.75$ and $Z_0 = 0.012$	54
3.21	Relative difference between the fitted and model acoustic depth of the helium glitch for a grid of models with masses in $[0.80M_{\odot}, 1.15M_{\odot}]$ ($0.05M_{\odot}$ step) for the initial composition $X_0 = 0.75$ and $Z_0 = 0.012$	54

3.22	Relative difference between the fitted and model acoustic depth of the helium glitch for a grid of models with masses in $[0.80M_{\odot}, 1.15M_{\odot}]$ ($0.05M_{\odot}$ step) for the initial composition $X_0 = 0.725$ and $Z_0 = 0.014$	55
4.1	Schematic modelling procedure.	82
4.2	Summary of the adjusted stellar models for 16CygA, considering it as an isolated star. . . .	87
4.3	Summary of the adjusted stellar models for 16CygB, considering it as an isolated star. . . .	88
4.4	Surface metallicity and helium abundance of the set of models presented in Fig. 4.2 compared to the reference values of Ramírez et al. (2009) (metallicity) and Verma et al. (2014).	89
4.5	Surface metallicity and helium abundance of the set of models presented in Fig. 4.3 compared to the reference values of Ramírez et al. (2009) (metallicity) and Verma et al. (2014).	89
4.6	HR diagram representing the best fit models.	98
4.7	Age (in Gyrs) as a function of the mass for the best fit models.	98
4.8	Overshooting parameter as a function of the mass for the best fit models.	99
4.9	Initial helium abundance as a function of $(Z/X)_0$ for the best fit models.	99
4.10	Surface helium abundance as a function of the surface (Z/X) ratio for the best fit models. .	100
5.1	The EGGMiMoSA logo.	133
5.2	Large frequency separation as a function of the period for a $1 M_{\odot}$, $X_0 = 0.72$, $Z_0 = 0.015$ subgiant model.	137
5.3	Period spacing as a function of the frequency for a $1 M_{\odot}$, $X_0 = 0.72$, $Z_0 = 0.015$ red-giant model.	137
5.4	Measured values of $\Delta\nu$ and $\Delta\pi_1$ for almost 1200 evolved <i>Kepler</i> stars taken from Mosser et al. (2014, Fig. 3).	138
5.5	Evolution of the coupling factor as a function of the g-dominated modes density, taken from Mosser et al. (2017, Fig. 6).	138
5.6	Evolution of $\Delta\pi_1$ as a function of $\Delta\nu_0$ for different masses.	141
5.7	Density of the helium core as a function of its mass (in solar units) for every track presented in Fig. 5.6.	142
5.8	Evolution of $\Delta\pi_{1,as}$ as a function of $\Delta\nu_0$ on the subgiant phase for the different masses considered in Fig. 5.6.	142
5.9	Evolution of the ratio of the central density over the mean stellar density with the evolution, represented by $\Delta\nu_0$	143
5.10	Evolution of $\Delta\pi_1$ as a function of $\Delta\nu_0$ for a $1 M_{\odot}$ track and different initial compositions. .	143
5.11	Evolution of $\Delta\pi_{1,as}$ as a function of $\Delta\nu_0$ on the subgiant phase for different compositions considered in Fig. 5.10.	144
5.12	Evolution of the gravity offset as a function of ν_{\max} for different masses.	145
5.13	Evolution of the gravity offset with ν_{\max} on the red-giant phase taken from Pinçon et al. (2019).	145
5.14	Propagation diagram for a $1 M_{\odot}$ young red giant between the center and a reduced radius of $r/R = 0.3$	146
5.15	Propagation diagram for a $1 M_{\odot}$ red giant, right before the luminosity bump, between the center and a reduced radius of $r/R = 0.1$	146
5.16	Evolution of the density contrast in the evanescent region as a function of \mathcal{N} for all the tracks of Fig. 5.6, with the corresponding colour code.	147
5.17	Evolution of the coupling factor with \mathcal{N} for different masses represented by the colours. . .	148
5.18	Evolution of the width of the evanescent region (Eq. (5.9)) for different masses represented by the colours.	148

List of Tables

2.1	Typical time scales for 1 M_{\odot} stars.	4
3.1	Reference stellar parameters.	34
3.2	Glitches amplitudes for 16 Cyg A and B uncorrected frequencies.	43
4.1	Summary of literature properties of the 16 Cygni system.	83
4.2	Observed seismic indicators, as in Farnir et al. (2020a)	84
4.3	Set of reference physical ingredients.	85
4.4	Accepted stellar range defined as the centroid of the extremum values for each parameter of the set of accepted models.	91
4.5	Observed effective temperature and surface metallicity of the Kepler LEGACY stars. Some of the other identifiers are gathered.	93
4.6	Values of the seismic indicators measured with WhoSGLAd for the complete LEGACY sample. When possible, we provide the value of the acoustic depth of the helium glitch.	94
4.7	Stellar parameters obtained by adjusting Δ , \hat{r}_{01} , \hat{r}_{02} , Δ_{01} , and A_{He} . The results are ordered in increasing χ^2 values. Only the 14 best models with overshooting and the nine best without are displayed.	97
4.8	Stellar parameters obtained by adjusting Δ , \hat{r}_{01} , \hat{r}_{02} , Δ_{01} , and $[\text{Fe}/\text{H}]$. The results are ordered in increasing χ^2 values. Only the 14 best models with overshooting and the nine best without are displayed.	97

CHAPTER 1

Introduction

1.1 From stellar variability to asteroseismology

As long as humans roamed the Earth, they looked at the sky for an understanding of the events occurring on Earth. The heavens held important roles in everyday life. Navigators used the positions of the stars to orient themselves. Others, studied planetary configurations to predict the fate of eminent personalities. At these times, it was believed that a change in the stars was a bad omen. One of the first manifestation of such a drastic change in the heavens was the observation of a ‘new’ star by Chinese astronomers around the year 185. This new star persisted in the sky for about eight months. It was suggested that this manifestation was in fact a type Ia supernova, RCW 86 (Clark & Stephenson 1975). Supernovae are the manifestation of stellar death, leading to a large increase in their luminosities.

Beside these intermittent phenomena, variable stars were later observed. Such stars display variations in their luminosity over time. One of which is the famous Algol star, in the Perseus constellation, known to the ancient Egyptians. Its luminosity varies with a period of approximately three days (Goodricke 1783). This leads us to the definition of the first type of variable stars, the **extrinsic variables**. The variability of such stars is caused by external factors. In the case of the Algol star, it is actually a pair of stars that orbit and partially occult one another, leading to a decrease in the apparent magnitude of the star. Such variable stars are referred to as eclipsing binaries and provide essential information through their orbital motion. Another example of extrinsic variable stars corresponds to the so-called ‘cataclysmic variables’. These stars exhibit sudden variability because of brutal physical processes. One of these is the accretion of stellar matter from one star to its companion in a close binary configuration. The arrival of new material may trigger new nuclear reactions and provoke a sudden increase in the luminosity.

There also exist stars that pulsate as a result of their intrinsic conditions. Such stars are **intrinsic variables**. The most famous examples are the very bright Cepheids which present variations in their luminosity with periods on the order of days to months. They have been observed for a long period of time now and are of particular interest as it was shown that they exhibit a period-luminosity relation (Leavitt & Pickering 1912). This relation is essential as it allows to calibrate the distance of these stars, upon which many other physical quantities rely. For example, without a measurement of the distance of an isolated star, we may not measure its absolute radius. We only retrieve the angular radius which is (approximately) the ratio of the radius of the star to its distance. The determination of stellar radii and distances, even though of essential nature, is not the only use of pulsating stars. As the pulsation periods of the excited oscillation modes are in direct correlation with the inner stellar structure, they allow us to draw inferences on the latter. This is the topic of asteroseismology, which will be further described in Sect. 2.2. There exists other types of intrinsic variables such as the rotating stars which present dark spots. As a result of their rotation, their luminosity experiences a regular modulation, the period of which being that of rotation. Finally, we may cite eruptive variables that eject coronal matter in an erratic fashion.

1.2 Asteroseismology

Because the information we collect from the Universe comes from the photons that the stars emit, our understanding of the universe strongly relies on our knowledge of stellar structure and evolution. Nevertheless, current stellar models suffer from numerous caveats (e.g. the treatment of convective regions, opacities determinations). Information about the internal stellar structure is therefore vital to constrain our models and theories. However, stars are opaque and their interior may not be observed directly. Hopefully, the asteroseismology is a powerful tool to probe stellar interiors. Indeed, it is the study of stellar pulsations and their link to the stellar structure, which relates oscillation frequencies with the

stellar structure. This therefore constitutes an efficient means to constrain the stellar structure. We distinguish two kinds of oscillation modes: the pressure modes, with the pressure gradient serving as the restoring force of the oscillations, and the gravity modes, with the buoyancy force as the restoring force.

Nevertheless, asteroseismology comes at a cost, the necessity of highly precise data. We require the ability to measure variations in luminosities averaged over the complete stellar disk on the order of one part per million. Therefore, asteroseismology was at first possible only in the case of our Sun. That specific branch of asteroseismology is the helioseismology. One notable success of helioseismology was the determination of the solar rotation profile (e.g. [Brown & Morrow 1987](#); [Schou et al. 1998](#); [Fossat et al. 2017](#)), showing a solid body rotation in the central radiative regions and a differential rotation in the outer convective regions.

But advances were not limited to our Sun. With the advent of space-borne missions, freeing observations from atmospheric perturbations and the diurnal cycle, came a boom in interest towards asteroseismology. Two of the most notable space missions may be the CoRoT ([Baglin et al. 2009](#)) and *Kepler* ([Borucki et al. 2010](#)) spacecrafts. These missions allowed for the continuous and extended observation of pulsating stars necessary to the gathering of precise data essential to asteroseismology. The precise characterisation of a wide variety of stars at different stages of evolution became possible. With rich oscillation spectra of pressure modes, main-sequence solar-like stars were extensively studied and stellar masses, radii and, ages were measured with unprecedented precision (e.g. [Miglio & Montalbán 2005](#); [Lebreton & Goupil 2014](#); [Appourchaux et al. 2015](#); [Campante et al. 2015](#)). Also on the main sequence, the γ Dor stars constitute excellent targets for asteroseismology. Due to their fast rotation ([Abt & Morrell 1995](#)), their gravity modes spectra are sufficiently perturbed to measure rotation rates (e.g. [Ouazzani et al. 2019](#)). The asteroseismic characterisation of star also extends to later phases of evolution such as the subgiant and red-giant branches. Because they present mixed-modes spectra, allowing for their deep probing, they represent essential targets to characterise the evolution of solar-like stars, providing us with an insight into the future of our Sun, for example by putting constraints on the mixing processes up to these late phases (e.g. [Beck et al. 2012](#); [Deheuvels et al. 2014](#); [Gehan et al. 2018](#)).

1.3 Objectives and structure of the thesis

The present thesis aims at precisely and accurately characterising low-mass stars throughout most of their evolution via asteroseismic means. To that end, we constructed two seismic probing techniques that take the most advantage of the highly precise data available. These two methods focus on two different evolutionary stages of solar-like stars and exploit the features their oscillation spectra present to ensure a robust and reliable adjustment of the observed seismic data. As opposed to many techniques currently available, the philosophy behind the present study is to fast and efficiently build seismic indicators that carry relevant structural information. We therefore rely on simple minimisation schemes combined with appropriate parameters estimates.

We first studied the case of main-sequence low-mass stars and defined the WhoSGlAd method to precisely measure the signature of acoustic glitches, traces of sharp variations in the stellar structure. The objective was to construct seismic indicators in such a way that they are as little correlated to each other as possible. This allows us to use these indicators to tightly constrain the stellar structure and to draw meaningful inferences. This method was applied to the case of the 16 Cygni system and to the Kepler Legacy sample.

Second, we followed stellar evolution of low-mass stars and moved on from the main-sequence to the subsequent subgiant and red-giant phases. To account for the complex mixed-modes spectra of these stars, we defined the EGGMiMoSA method. The method relies on the prior knowledge we have about the structure of these stars to estimate the optimal parameters. Not unlike the case of main-sequence stars, we defined robust seismic indicators which we demonstrated to effectively carry relevant structural information. The proposed method also aims at providing a unified sounding approach for subgiants and red giants.

After introducing the relevant theoretical concepts necessary to our work in Chap. 2, we divide this manuscript into two parts, according to the stellar stage of evolution. The first part is concerned with main-sequence stars while the second part focuses on the subgiant and red-giant stars. In the first part of the manuscript, we present the WhoSGlAd method and its application to the 16 Cyg system and Kepler Legacy sample in Chaps. 3 and 4, respectively. In the second part, we describe the EGGMiMoSA method in Chap. 5. We finally conclude the present work in Chap. 6.

CHAPTER 2

Theoretical framework

In the current chapter we recall all the theoretical notions necessary to the purpose of this thesis manuscript proper understanding. We first address the theory of stellar structure (Sect. 2.1) and consider small perturbations of this structure leading to the stellar pulsations (Sect. 2.2).

2.1 Stellar structure and evolution

Before diving into asteroseismology as a means to constrain the stellar structure, we first need to study the stellar structure theory and the equations that govern it. Furthermore, it is appropriate to highlight some of the current limitations of this theory. The present theoretical developments will mostly be based on the work presented by [Kippenhahn et al. \(2012\)](#).

2.1.1 Typical time scales

Convenient quantities, relevant to the stellar structure and its evolution, are the typical time scales over which the stellar structure might evolve in specific contexts. We consider a star of total mass M , radius R , and luminosity L .

The first time scale is the **dynamical time scale**

$$\tau_{\text{dyn}} \sim \left(\frac{R^3}{GM} \right)^{1/2} \sim (\bar{\rho}G)^{-1/2}, \quad (2.1)$$

G being the gravitational constant and $\bar{\rho} \equiv \frac{M}{4/3\pi R^3}$ the mean stellar density. It expresses the balance between the pressure and the gravitational force, which corresponds to the hydrostatic equilibrium. It gives the time over which the star reacts to a perturbation of the hydrostatic equilibrium. This is also the relevant time scale of stellar oscillations.

The second time scale represents the typical time necessary for a star to adjust to a thermal imbalance and restore the thermal equilibrium. This is the **Kelvin-Helmholtz time scale**

$$\tau_{\text{KH}} \sim \frac{GM^2}{RL}. \quad (2.2)$$

This time scale is relevant to the phases of stellar contraction during the thermal disequilibrium phases such as the pre-main sequence.

The last typical time scale is the **nuclear time scale** which represents the balance of the radiated energy by the one generated by nuclear reactions, E_{nuc} ,

$$\tau_{\text{nuc}} \sim \frac{E_{\text{nuc}}}{L}. \quad (2.3)$$

We observe that, in regular cases, the three time scales have very different orders of magnitude, and

$$\tau_{\text{dyn}} \ll \tau_{\text{KH}} \ll \tau_{\text{nuc}}. \quad (2.4)$$

This is particularly relevant to the case of stellar oscillations as we may assume, in most of the star, that the heat exchange during one oscillation cycle is negligible compared to the internal energy (as $\tau_{\text{dyn}} \ll \tau_{\text{KH}}$). The oscillations are said to be quasi-adiabatic. We provide in Table 2.1 typical values for the three time scales in different stars.

Table 2.1: Typical time scales for $1 M_{\odot}$ stars.

	$R (R_{\odot})$	$L (L_{\odot})$	τ_{dyn}	τ_{KH}	τ_{nuc}
Sun	1	1	27 min	16 Myr	10 Gyr
Red giant	100	30	18 days	5 kyr	300 Myr
White dwarf	0.02	0.01	4.5 s	80 Gyr	1000 Gyr

2.1.2 Basic equations

When modelling the stellar structure, one relies on the general equations of hydrodynamics while including additional hypotheses. We usually assume the star to be perfectly spherical. Therefore, we describe its structure in spherical coordinates, with r the radial coordinate, θ the polar coordinate and φ the azimuthal coordinate. We may assume spherical symmetry because only the gravity and pressure act on a mass element. The rotation, tidal interactions, and magnetic fields are neglected. This can, in some cases, be a limitation but this is out of the scope of the current discussion. As a result of the spherical symmetry of the star, only one spatial coordinate is necessary to describe its structure, the distance from the stellar center, r , referred to as the radius. This quantity varies from 0 at the center and reaches a value of R at its surface. To study the fluid mechanics, there usually are two approaches: the Eulerian approach, studying the physical quantities as a function of their distance to the center, and the Lagrangian approach, seeing these quantities as a function of the mass, m , contained in a concentric spherical shell. The Lagrangian approach is especially convenient when studying stellar structure, as different regions of the star may contract or expand (e.g. the contracting core and expanding envelope of giants). Therefore, a given r coordinate is not constant while (if the model assumes no mass loss) the mass coordinate remains constant. The relation between both coordinates is given by the **continuity equation**

$$\frac{\partial \rho}{\partial t} + \nabla \cdot (\rho \mathbf{v}) = 0, \quad (2.5)$$

where ρ represents the fluid density, \mathbf{v} the fluid velocity and ∇ the spatial derivative. In spherical coordinates, we write $\nabla = \nabla_r + \nabla_h = \left(\frac{\partial}{\partial r}, \frac{1}{r} \frac{\partial}{\partial \theta}, \frac{1}{r \sin \theta} \frac{\partial}{\partial \varphi} \right)$, with ∇_r and ∇_h the vertical and horizontal components of the gradient operator. In general, the r and h subscripts will represent radial and horizontal components of any vector quantity. Assuming no mass loss, which is valid for the low-mass stars considered in the present manuscript, and spherical symmetry it takes the form

$$\frac{\partial r}{\partial m} = \frac{1}{4\pi r^2 \rho}. \quad (2.6)$$

The second equation of hydrodynamics, necessary to the description of the stellar structure, is the **conservation of momentum**

$$\rho \left(\frac{\partial}{\partial t} \mathbf{v} \cdot \nabla \right) \mathbf{v} = \rho \mathbf{f} - \nabla P - \rho \nabla \phi + \nabla \cdot \zeta, \quad (2.7)$$

with \mathbf{f} being the sum of the external forces, P the pressure, ϕ the gravitational potential, and ζ the viscous stress tensor. Because of sphericity and neglecting viscous stresses, which are generally small in stellar interior, the only forces acting on a mass element are the pressure gradient and gravity. As the stars are in a stable state during most of their lives, these forces should balance each other. We have the **hydrostatic equilibrium**.

$$\frac{\partial P}{\partial m} = - \frac{Gm}{4\pi r^4}. \quad (2.8)$$

To obtain Eq. (2.8), we used **Poisson's equation** relating the gravitational potential and the distribution of matter

$$\nabla^2 \phi = 4\pi G \rho, \quad (2.9)$$

where ∇^2 is the Laplacian operator

The last hydrodynamics equation to consider is the **conservation of energy**

$$\rho T \left(\frac{\partial}{\partial t} \mathbf{v} \cdot \nabla \right) S = \rho (\epsilon_{\text{nuc}} + \epsilon_v) - \nabla \cdot \mathbf{F}_R, \quad (2.10)$$

where T , S , ϵ_{nuc} , ϵ_v and F_R represent the temperature, the entropy, the nuclear energy generation rate, the heat generation rate by viscous stresses, which is neglected, and, the radiative energy flux, respectively.

We now need equations to describe the energy transport and generation. We define $l(r)$ as the energy traversing a sphere of radius r . This is the local luminosity. Its extremal values are 0 at the center and L , the total luminosity at the surface. Considering the star to be in hydrostatic and thermodynamic equilibrium, energy is only produced through nuclear reactions or contraction. The rate of energy production per unit mass, decomposed in both contributions, is $\epsilon = \epsilon_{\text{nuc}} + \epsilon_g$. Therefore, the variation dl in the l function is only due to nuclear reactions and we obtain the **simplified conservation of energy**

$$\frac{dl}{dm} = \epsilon. \quad (2.11)$$

We now consider the **transport of energy** in the stellar interior. The two main transport mechanisms are the *radiation* and the *convection*. The total energy flux is thus the sum of both contributions: $\vec{F} = \vec{F}_{\text{rad}} + \vec{F}_{\text{conv}}$. Let us first consider the energy transport by radiation. Because stellar interiors are very opaque (typically the mean free path of photons is on the order of the centimetre in the Sun's interior: $\ell_{\text{ph}} = 1/\kappa\rho$, with a typical mean absorption coefficient, $\kappa \sim 1 \text{ cm}^2 \text{ g}^{-1}$, and $\rho \sim 1.4 \text{ g cm}^{-3}$), we consider the transport of energy by the photons to be a diffusive process. This does not hold close to the surface where the density decreases and the mean free path of photons significantly increases. But this greatly complicates the picture and we stick in the current discussion to the diffusive approximation. In that case, the radiative transport of energy is given by

$$\frac{\partial T}{\partial m} = -\frac{3}{64\pi^2 ac} \frac{\kappa l}{r^4 T^3}, \quad (2.12)$$

with the radiation density constant $a = 7.57 \cdot 10^{-15} \text{ erg cm}^{-3} \text{ K}^{-4}$, the speed of light $c = 3.00 \cdot 10^{10} \text{ cm s}^{-1}$, and the mean stellar opacity κ . A convenient form of the radiative flux is

$$F_{\text{rad}} = \frac{4acG}{3} \frac{T^4 m}{\kappa P r^2} \nabla_{\text{rad}}, \quad (2.13)$$

with ∇_{rad} the temperature gradient necessary for the energy flux to be completely transported by the radiation

$$\nabla_{\text{rad}} \equiv \left. \frac{d \ln T}{d \ln P} \right|_{\text{rad}}. \quad (2.14)$$

Whenever the real temperature stratification

$$\nabla \equiv \frac{d \ln T}{d \ln P} \quad (2.15)$$

is not sufficient to transport all the energy via radiation, the energy is transported by the motion of matter, the convection. In the case of the transport of energy by convection, the picture is more complex. The energy is transported by mass elements of a finite size which exchange energy with their environment in dynamically unstable regions. This process can be very efficient in stellar interiors, due to the very large enthalpy. As part of the energy is carried by convection, the actual temperature gradient $\nabla \equiv \frac{d \ln T}{d \ln P}$ is smaller than the radiative one ∇_{rad} and the radiative flux is

$$F_{\text{rad}} = \frac{4acG}{3} \frac{T^4 m}{\kappa P r^2} \nabla, \quad (2.16)$$

and the temperature stratification

$$\frac{\partial T}{\partial m} = -\frac{GmT}{4\pi r^4 P} \nabla. \quad (2.17)$$

The actual gradient is unknown and has to be determined. The complexity of the problem mainly arises from the very short time scales of the dynamical motions of the convective elements of matter compared to stellar evolution time scales. Following the movement of individual blobs of matter, evolving over time scales on the order of the dynamical time scale, and over the whole stellar evolution, which is on the order of the nuclear time scale, is completely impossible because of the large difference in magnitude between the two time scales (see Table 2.1). Therefore, a simplified description is in order. The most commonly used in stellar evolution theory and models is the mixing-length theory, which assumes the convective elements to have a mean free path, the mixing-length. This mixing-length is often treated as a free parameter that has to be adjusted to match observations. An alternative approach, is to interpolate between grid

points of 3D hydrodynamical simulations. This approach has been applied by Jørgensen et al. (2021) who implemented it in the CLES evolution code (Code Liégeois d'Evolution Stellaire Scuflaire et al. 2008a).

It is also interesting to be able to recognise regions where the energy will be efficiently transported by radiation from regions where convection will be necessary. To do so, one may remember that it is the buoyancy force that sets blobs of matter in motion. Therefore, comparing the density of this blob with its surrounding can provide us with such a criterion. To do so, we consider an element of matter displaced upwards in the stellar interior, where its surroundings are cooler. If the element is lighter than its surroundings, it will be pushed further upwards by buoyancy. The layer is therefore unstable towards convection. Conversely, an element heavier than its surroundings and which is pushed upwards will be pushed back downwards. The layer is therefore convectionally stable. These considerations, after some manipulations and assuming there are no changes in the chemical composition (see Kippenhahn et al. 2012, Chap. 6), lead to the famous Schwarzschild criterion. A layer is stable against convection when

$$\nabla_{\text{rad}} < \nabla_{\text{ad}}, \quad (2.18)$$

with the adiabatic temperature gradient

$$\nabla_{\text{ad}} \equiv \left. \frac{\partial \ln T}{\partial \ln P} \right|_S \quad (2.19)$$

and S the entropy.

All the previous equations only present spatial variations. Nevertheless, to compute stellar evolution, a temporal variation remains necessary. This happens through changes in the chemical composition, via nuclear reactions, that in turn impact the stellar structure. Defining X_i the mass abundance of the element labelled i and $r_{j,k}$ the rates of transformation from a species j into another k , the **evolution of composition** is

$$\frac{\partial X_i}{\partial t} = \frac{m_i}{\rho} \left(\sum_j r_{j,i} - \sum_k r_{i,k} \right), i = 1, \dots, I, \quad (2.20)$$

with I being the number of considered species and m_i the mass of the nuclei labelled i . Before the phases of helium combustion, which are considered in this thesis, it is customary in stellar models to consider only three species, the hydrogen, denoted X , the helium, Y , and the combination of all the other species, Z , referred to as ‘metals’. This is justified by the fact that stellar abundances are mostly dominated by that of hydrogen and helium. As the species heavier than helium are gathered, a reference for their relative abundance is necessary. This has been a subject to many debates (see the numerous references such as Asplund et al. 2009).

Finally, to sum up, when considering the star to be in complete equilibrium, that is in hydrodynamic and thermal equilibrium, we have 5 differential equations to solve in order to compute the stellar structure and evolution:

$$\frac{\partial r}{\partial m} = \frac{1}{4\pi r^2 \rho}, \quad (2.21)$$

$$\frac{\partial P}{\partial m} = -\frac{Gm}{4\pi r^4}, \quad (2.22)$$

$$\frac{dl}{dm} = \epsilon, \quad (2.23)$$

$$\frac{\partial T}{\partial m} = -\frac{GmT}{4\pi r^4 P} \nabla, \quad (2.24)$$

$$\frac{\partial X_i}{\partial t} = \frac{m_i}{\rho} \left(\sum_j r_{j,i} - \sum_k r_{i,k} \right), i = 1, \dots, I. \quad (2.25)$$

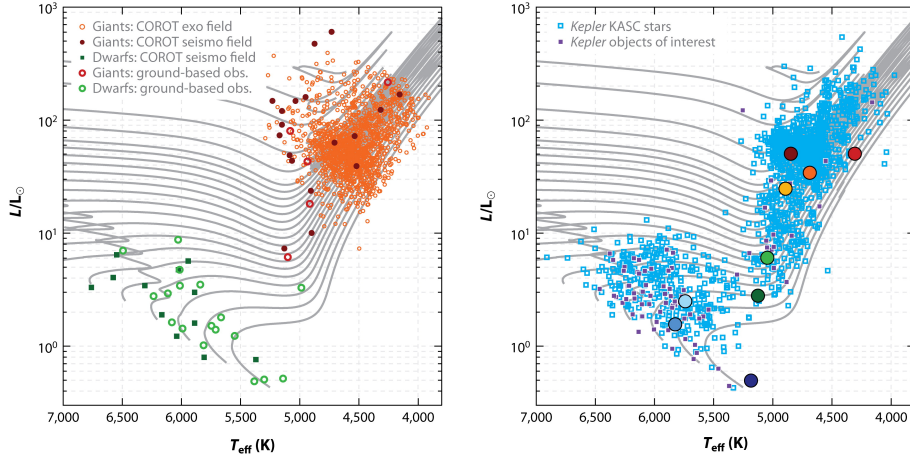
The independent variables are the mass m and the time t . Assuming the equation of state

$$\rho = \rho(P, T, X_i) \quad (2.26)$$

and the rates of nuclear reactions

$$r_{j,k} = r_{j,k}(P, T, X_i) \quad (2.27)$$

to be known and with the knowledge of appropriate boundary conditions, we may solve these 5 differential equations to obtain the functions $r(m)$, $P(m)$, $l(m)$, $T(m)$, and $X_i(m, t)$ for $0 \leq m \leq M$ and $t_0 \leq t, t_0$



A Chaplin WJ, Miglio A. 2013.
Annu. Rev. Astron. Astrophys. 51:353–92

Figure 2.1: HR diagram of the stars observed by the CoRoT (left) and *Kepler* (right) spacecrafts presented in Chaplin & Miglio (2013, Fig. 5).

being the time at which stellar evolution begins. These constitute what is referred to as a stellar model. Because of the complete equilibrium, spatial and temporal variations are separated in these equations. The complete equilibrium hypothesis is met during several stellar evolution phases such as the main sequence, and the subgiant and red-giant phases for low-mass stars such as considered here. At each time step of the evolution, it is then possible to solve the temporal variation of the composition and then the structural evolution of the other free variables, as a function of the composition at the current time step.

2.1.3 Evolution on the main sequence phase

The first phase, relevant to the present study is the main sequence phase. This corresponds to the phase during which stars spend most of their lifetime. It can easily be recognised in a Hertzsprung-Russell (HR) diagram, which represents the logarithmic stellar luminosity (expressed in solar units) over the reversed logarithmic effective temperature (in K). Indeed, the main sequence corresponds to a dense diagonal strip of stars extending (roughly) from the bottom right of the HR diagram to its top left. To illustrate this, we provide in Fig. 2.1 the figure presented by Chaplin & Miglio (2013, Fig. 5) which represents the stars observed by the CoRoT (Baglin et al. 2009) and *Kepler* (Borucki et al. 2010) satellites. CoRoT targets are showed on the left panel while *Kepler* targets are on the right panel. The clump of stars extending from the lower right to the middle left of both panels correspond to main sequence stars. We also distinctly observe the red-giant branch (RGB) extending upwards in an almost vertical fashion (these stars are discussed in the subsequent section).

Nuclear burning of hydrogen

The main sequence is composed of stars that are in complete equilibrium and burn hydrogen in their central region. This phase extends until the central hydrogen is completely depleted. We may estimate the duration of this phase as the ratio between the energy generation by hydrogen burning and the rate of energy loss by radiation, the stellar luminosity. This corresponds to the nuclear time scale of hydrogen burning (Eq. (2.3)). We roughly assume for any star that the same fraction of the total stellar mass serves to the nuclear burning. The energy generation rate by hydrogen burning is then proportional to the total mass, that is to say $E_H \sim M$. Then, from homology relations, the total luminosity is proportional to some power η of the stellar mass, such that $L \sim M^\eta$. More information regarding the latter relation is to be found in Kippenhahn et al. (2012, Chaps. 20 and 22). We retrieve

$$\tau_H \sim M^{1-\eta}. \quad (2.28)$$

With a typical value for η of 3.5, we obtain $\tau_H \sim M^{-2.5}$. Therefore, the duration of the main sequence is expected to strongly decrease with the stellar mass, which is what we observe in practice.

The nuclear burning of hydrogen into helium, which is initiated for a temperature of about 5×10^6 K, happens through two different channels: the pp-chain and the CNO-cycle. The first channel, the pp-chain, is the successive recombination of two protons into deuterium atoms, then of this newly formed deuterium atom with another proton to form the light helium isotope ^3He . The formation of the final ^4He happens in various reactions that may involve a second ^3He atom, ^7Be , ^7Li or ^8B . The second channel is the CNO cycle. As implied by its name, C, N, and O atoms, which may readily be available at the formation of the star, are required as catalysts to form the ^4He . These reactions may only happen in a given range around specific temperatures. The width of such ranges is referred to as the temperature sensitivity of the thermonuclear reactions. It represents the exponent ν of the power-law representation of the energy generation by the considered nuclear reaction ϵ

$$\nu \equiv \left. \frac{\partial \ln \epsilon}{\partial \ln T} \right|_{\rho}. \quad (2.29)$$

The first reaction series, the pp-chain, displays a temperature sensitivity of about six, while the CNO-cycle has a temperature sensitivity of about 23. This has the consequence that the pp-chain dominates over the CNO-cycle to burn hydrogen atoms until $T \gtrsim 15 \times 10^6$ K, where the CNO-cycle takes over as the dominant source. As the central temperature is greatly dependent on the stellar mass, less massive stars will mostly produce hydrogen through the pp-chain while the more massive ones (above $\sim 1.6 M_{\odot}$) will be dominated by the CNO-cycle.

Another consequence of this important temperature sensitivity of the nuclear reactions is the highly concentrated generation of energy towards the center. Overall, in a $1 M_{\odot}$ mass star, all the nuclear energy that is produced by the pp-chain is done so within approximately the inner 20% of the stellar mass. In the case of the CNO-cycle, due to the higher temperature sensitivity, energy production is even more concentrated, within 10% of the stellar mass. In stars where the CNO-cycle starts to participate to the energy generation ($\gtrsim 1.2 M_{\odot}$), because of this large concentration of power by the CNO-cycle, $L/m \sim \epsilon$ is very large near the center, so that the radiative gradient, ∇_{rad} , which proportional to it, is larger than the adiabatic gradient, ∇_{ad} , and a central convective region starts to develop (see the Schwarzschild criterion, Eq. (2.18)). This transition is of great importance as it defines two stellar regimes. The low-mass stars ($0.5 M_{\odot} \lesssim M \lesssim 1.2 M_{\odot}$) which have a radiative core and a convective envelope, which dives deeper with decreasing mass ($M \simeq 0.5 M_{\odot}$ is the approximate limit for a fully convective star), and the intermediate mass stars ($1.2 M_{\odot} \lesssim M \lesssim 8 M_{\odot}$) with a convective core and a radiative envelope. Because of their structural differences, these stars evolve differently.

Uncertainties

The extent of convective regions is a source of uncertainties in current stellar models. First, because of the treatment of convection itself, often described in one dimension via the mixing-length theory, relying over a single parameter to depict the complex convective motions. The mixing-length theory (Prandtl 1925) assumes that a convective element will move a given distance, the mixing-length, before dissolving in its surroundings and losing its identity. However, there is no physical ground that can help determine the mixing-length parameter, α_{MLT} , often expressed in terms of the pressure-scale height, $H_P = -\frac{dr}{d \ln P}$. Hence, that quantity must be calibrated in stellar models. There exist several studies that rely on 3D hydrodynamical simulations of the outer layers of stars to connect the calibrated value of the mixing length parameter with the global parameters of the atmosphere: effective temperature, surface gravity, and metallicity of the star (e.g. Magic et al. 2015).

Second, there exist uncertainties concerning the exact boundaries of convective regions. Indeed, the Schwarzschild criterion for stability against convective motions provides the limit where the acceleration of the convective blob of matter does not experience any acceleration. Nevertheless, it is not stopped on the spot, as this would require an efficient braking. Therefore, the element penetrates the radiative region where it is decelerated. This is the phenomenon called overshooting, which extends convective regions past the Schwarzschild limit. In the present manuscript, we will refer to overshooting above central convective regions as ‘overshooting’, and to the overshooting below convective envelopes as ‘undershooting’. The description of the overshooting requires another ‘ad-hoc’ parameter which has to be measured or calibrated (written α_{ov} , in the case of overshooting, and α_{un} , in the case of undershooting). Nevertheless, the inclusion of overshooting may be required as it was shown that its inclusion allows us to properly reproduce the shape of the end of the main sequence in a colour - magnitude diagram (Pietrinferni et al. 2004). The uncertain nature and amount of overshooting may propagate to later phases of evolution. Indeed, Khan et al. (2018) also showed the necessity to include undershoot in order to accurately reproduce the luminosity bump of red giants.

Finally, the last complication related to convection is the semiconvection. When deriving a criterion for convective stability, we neglected the possibility that a blob of matter may cross regions with different compositions. The molecular weight gradient,

$$\nabla_\mu \equiv \frac{d \ln \mu}{d \ln P}, \quad (2.30)$$

μ being the mean molecular weight, is therefore non-zero and must be accounted for in our criterion. This is what Ledoux did in deriving his criterion. A layer is stable when

$$\nabla_{\text{rad}} < \nabla_{\text{ad}} + \frac{\phi}{\delta} \nabla_\mu, \quad (2.31)$$

with $\delta \equiv -\left(\frac{d \ln \rho}{d \ln T}\right)$ and $\phi \equiv \left(\frac{d \ln \rho}{d \ln \mu}\right)$. The complication arises whenever the layer is unstable against the Schwarzschild criterion but ∇_μ stabilises the layer and the layer is stable against the Ledoux criterion:

$$\nabla_{\text{ad}} < \nabla_{\text{rad}} < \nabla_{\text{ad}} + \frac{\phi}{\delta} \nabla_\mu. \quad (2.32)$$

The layer is said vibrationally unstable (while it is dynamically stable) and a displaced element of matter will oscillate slowly with increasing amplitude and will produce a slow mixing. This is the semiconvection. The treatment of semiconvection is difficult as it is expected to have a noticeable impact on the chemical stratification.

2.1.4 Evolution on the subgiant and red-giant branches

After the end of the main sequence, when central hydrogen has been depleted, the star may proceed towards the subgiant branch and the red-giant branch. At this stage, low-mass stars have a condensed quasi-isothermal helium core and a diluted envelope. As the central hydrogen abundance has dropped and the temperature of the core has risen, hydrogen burning now takes place in a shell above the helium core because of its large temperature sensitivity. While the burning of hydrogen proceeds, the shell moves upwards, in mass, increasing the core's mass. The evolution continues with the contraction of the core and the expansion of the envelope.

A peculiarity of the low mass stars is that they have small or no convective cores. Hence, the helium core smoothly grows from zero mass. Furthermore, as their cores are highly condensed, the electron degeneracy is non-negligible. This degeneracy is a direct consequence of the Pauli's principle stating that two fermions cannot occupy the same quantum state. This has the consequence, in highly condensed stellar cores, such as the ones exhibited by low-mass post-main sequence stars, that individual electrons must gain in momentum, consequently energy, to occupy available quantum states. The pressure in the core is dominated by the electronic pressure which is quasi-insensitive to temperature. Consequently, there is a relation between the mass and radius of the core, which resembles the structure of a white dwarf, except that such stars are composed of helium.

Because of the important density contrast between the core and the envelope, it is possible to show via simple homology considerations that the properties in the shell solely depend on those of the core. We present here a small demonstration based on the works of [Refsdal & Weigert \(1970\)](#) and [Kippenhahn et al. \(2012\)](#). We consider an homogeneous and isothermal helium core of mass M_c and radius R_c and assume homology relations of the form

$$\rho(r/R_c) \sim M_c^{\phi_1} R_c^{\phi_2}, \quad (2.33)$$

$$T(r/R_c) \sim M_c^{\psi_1} R_c^{\psi_2}, \quad (2.34)$$

$$P(r/R_c) \sim M_c^{\tau_1} R_c^{\tau_2}, \quad (2.35)$$

$$l(r/R_c) \sim M_c^{\sigma_1} R_c^{\sigma_2}, \quad (2.36)$$

the exponents ($\phi_1, \phi_2, \psi_1, \psi_2, \tau_1, \tau_2, \sigma_1$, and σ_2) have to be determined from the structural equations (Eqs. (2.21) - (2.24)). When comparing two models with different core masses M_c and M'_c , and radii R_c and R'_c , all homologous points, such that $r/R_c = r'/R'_c$ will be connected by these relations. We may

then obtain

$$P(r) \sim \frac{GM_c}{R_c} \int_{r_s/R_c}^{r/R_c} \rho(r/R_c) d(r/R_c), \quad (2.37)$$

$$T(r) \sim \mu \frac{M_c}{R_c}, \quad (2.38)$$

$$L(r) \sim (M_c \mu)^{4+\frac{\nu-4}{3}} R_c^{\frac{6-\nu}{3}-3}, \quad (2.39)$$

with r_s the radius at the top of the shell and ν the temperature sensitivity of nuclear reactions (Eq. (2.29)). At fixed composition, we see from Eqs. (2.37) to (2.39) that the properties of the shell only depend on the mass and radius of the core. Furthermore, as the core is degenerate, there is a relation between the mass and radius of the core. For a non-relativistic degenerate gas, we have

$$R_c \sim M_c^{-1/3}. \quad (2.40)$$

Therefore, the properties of the shell depend only on the mass of the helium core. As a consequence, the luminosity and temperature in the shell will be determined by the core mass. Indeed, the luminosity is constant above the shell because of the thermal equilibrium. Consequently, the total luminosity is also a function of the core's mass only, independently of the total mass. Finally, as the shell processes the layer above the core and produces helium, it increases the mass of the core and we observe from Eq. (2.40) that the core must contract. Furthermore, the temperature in the shell must increase with increasing core mass and the luminosity also increases strongly (Eqs. (2.38) and (2.39)). Thus, after the star has approached the Hayashi line, corresponding to the locus of fully convective models in the HR diagram, it climbs the red-giant branch and proceeds almost vertically in the HR diagram. The effective temperature varies little and, because the radius, luminosity, and effective temperature are related through Stefan-Boltzmann relation

$$sT_{\text{eff}}^4 = \frac{L}{4\pi R^2}, \quad (2.41)$$

with s Stefan-Boltzmann's constant, the radius is also function of the core's mass.

From Eq. (2.39), we note a dependency of the luminosity on the composition. For energy generated through the CNO cycle and for fixed M_c and R_c , $\nu = 13$ and $L \sim \mu^7$. A decrease in the molecular weight is expected to strongly decrease the luminosity. This is exactly what happens on the RGB-bump. As the shell moves upwards, it may reach the region where the outer convective layer has penetrated the deepest. At this point, there is a composition discontinuity between the central helium-rich region and the outer hydrogen-rich region. This results in a sudden drop in mean molecular weight and, therefore, luminosity.

After the bump, as the star continues its climb along the RGB-branch, the central temperature can reach that of helium burning ($\sim 10^8$ K). As a consequence of the central degeneracy, this happens for a core mass of $0.47 M_\odot$, regardless of the total stellar mass. Furthermore, because of the degeneracy, the ignition of helium burning happens in a rather violent way. The core is unstable with respect to a thermal perturbation, which tends to greatly increase. Indeed, because of the central electron degeneracy, the volume of the core is fixed and the energy generated by nuclear reactions is entirely converted into kinetic energy. The result is a thermal runaway, strongly increasing the core temperature at constant density. The power excess is completely converted into internal energy, increasing the luminosity of the core to orders of $10^{11} L_\odot$. However, this luminosity excess is almost completely absorbed by the work of the expanding overlying layers. Finally, the increase in the central temperature allows the degeneracy to be lifted, the core may expand with increasing temperature, thus preventing further increase in the central temperature, and the helium burning is stabilised. Because the core increases in size while maintaining a constant mass, the luminosity must decrease again (Eq. (2.39)). The star finally settles on the horizontal branch where it quietly burns helium.

2.2 Stellar pulsations

In this section, we discuss and present the basic principle of the theory of stellar pulsations. All developments follow the work of [Unno et al. \(1989\)](#).

2.2.1 Linear adiabatic oscillations equations

In Sect. 2.1.1, we provided typical time scales of physical phenomena in stellar interiors, two of them being relevant to the present discussion, the dynamical time scale (Eq. (2.1)) on the same order of magnitude

as the travel time of a sound wave from the center to the surface, and the Kelvin-Helmoltz time scale (Eq. (2.2)) representative of the exchanges of heat. As $\tau_{\text{dyn}} \ll \tau_{\text{HK}}$ in most of the stellar interior, there is no heat exchange during the travel of the sound wave, the oscillations are considered quasi-adiabatic. We will work under this hypothesis. However, this hypothesis falls apart in the outermost regions of the star, where both time scales are comparable and the exchange of heat has to be accounted for. These complications are part of the problem referred to as the ‘surface effects’, which are poorly represented by oscillation codes. These surface effects are the consequences of the poor modelling of the superficial layers (e.g. convection, energetics) on the computed frequencies. Several empirical corrections have been proposed to tackle these issues (e.g. Kjeldsen et al. 2008; Ball & Gizon 2014; Sonoi et al. 2015).

As briefly discussed in Sect. 2.1.2, the stellar structure may be analysed in two different frames, the Eulerian and Lagrangian frames. The former considers stellar quantities at fixed positions while the latter follows fluid elements. It follows that, in defining perturbations of the physical quantities, one may either define the Eulerian perturbation, usually denoted by a prime, or the Lagrangian perturbation, denoted by the δ symbol. A departure from the equilibrium value of a given physical quantity, f , symbolised by the subscript 0 is then expressed either as

$$f(\mathbf{r}, t) = f_0(\mathbf{r}) + f'(\mathbf{r}, t), \quad (2.42)$$

or

$$f(\mathbf{r}, t) = f_0(\mathbf{r}_0) + \delta f(\mathbf{r}_0, t). \quad (2.43)$$

This corresponds to linearised perturbations of small amplitudes. The two perturbations are linked through the relation

$$\delta f(\mathbf{r}, t) = f'(\mathbf{r}, t) + \boldsymbol{\xi} \cdot \nabla f_0(\mathbf{r}), \quad (2.44)$$

with $\boldsymbol{\xi} \equiv \mathbf{r} - \mathbf{r}_0$ the first order displacement with respect to the Lagrangian equilibrium position and \cdot symbolising the scalar product.

Time variations are then written $d\delta f(\mathbf{r}, t)/dt$ and $\partial f'(\mathbf{r}, t)/\partial t$. Both operators are related via

$$\frac{d}{dt} = \frac{\partial}{\partial t} + \mathbf{v} \cdot \nabla. \quad (2.45)$$

Perturbing the equations of structure (Eqs. (2.5), (2.7), and (2.10)) in the Eulerian frame while neglecting non-adiabatic terms (involving either variations in entropy or energy fluxes and generation), we retrieve the three adiabatic oscillation equations

$$\frac{1}{\rho} \left(\frac{\partial}{\partial r} + \frac{\rho g}{\Gamma_1 P} \right) P' - (\sigma^2 + gA) \xi_r + \frac{\partial \phi'}{\partial r} = 0, \quad (2.46)$$

$$\frac{1}{r^2} \frac{\partial}{\partial r} (r^2 \xi_r) + \frac{1}{\Gamma_1} \frac{d \ln P}{dr} \xi_r + \left(\frac{\rho}{\Gamma_1 P} + \frac{\nabla_h^2}{\sigma^2} \right) \frac{P'}{\rho} + \frac{1}{\sigma^2} \nabla_h^2 \phi' = 0, \quad (2.47)$$

$$\left(\frac{1}{r^2} \frac{\partial}{\partial r} r^2 \frac{\partial}{\partial r} + \nabla_h^2 \right) \phi' - 4\pi \rho G \left(\frac{P'}{\Gamma_1 P} - A \xi_r \right) = 0, \quad (2.48)$$

where $g = Gm/r^2$ is the local gravitational acceleration. These are linear equations in the perturbations of the radial position ξ_r , pressure P' , and gravitational potential ϕ' . We have dropped the zero subscript of equilibrium quantities, for the sake of clarity. We have introduced the Schwarzschild discriminant

$$A \equiv \frac{d \ln \rho}{dr} - \frac{1}{\Gamma_1} \frac{d \ln P}{dr}, \quad (2.49)$$

the sign of which provides a criterion for convective stability; and the first adiabatic exponent

$$\Gamma_1 \equiv \left. \frac{\partial \ln P}{\partial \ln \rho} \right|_S, \quad (2.50)$$

where $|_S$ means that the first adiabatic index is evaluated at constant entropy. Furthermore, as the temporal and spatial variation are well separated, all variables are assumed to be proportional to $e^{i\sigma t}$, with σ the angular frequency. It is related to the linear frequency via the relation

$$\sigma = 2\pi\nu. \quad (2.51)$$

2. Theoretical framework

All the coefficients of Eqs. (2.46) to (2.48) depend only on r and the radial derivatives are well distinct from the horizontal ones. Furthermore, the horizontal derivatives appear within the same operator, the Legendrian

$$\mathcal{L}^2 = -r^2 \nabla_h^2. \quad (2.52)$$

Thus, the horizontal variation may be separated from the vertical one, with the radial dependency of the functions often being left out. And the functions take the form

$$f'(t, r, \theta, \varphi) = f'(r) Y_l^m(\theta, \varphi) e^{i\sigma t}, \quad (2.53)$$

with the spherical harmonics Y_l^m of **azimuthal order**, m , and **spherical degree**, l . This stems from the fact that the spherical harmonics are eigenfunctions of the Legendrian:

$$\mathcal{L}^2 Y_l^m = l(l+1) Y_l^m. \quad (2.54)$$

With this separation of variables, Eqs. (2.46) to (2.48) take the form

$$\frac{1}{\rho} \frac{dP'}{dr} + \frac{g}{\rho c^2} P' + (N^2 - \sigma^2) \xi_r + \frac{d\phi'}{dr} = 0, \quad (2.55)$$

$$\frac{1}{r^2} \frac{d}{dr} (r^2 \xi_r) + \frac{1}{\Gamma_1} \frac{d \ln P}{dr} \xi_r + \left(1 - \frac{L_l^2}{\sigma^2}\right) \frac{P'}{\rho c^2} - \frac{l(l+1)}{\sigma^2 r^2} \phi' = 0, \quad (2.56)$$

$$\frac{1}{r^2} \frac{d}{dr} \left(r^2 \frac{d\phi'}{dr} \right) - \frac{l(l+1)}{r^2} \phi' - 4\pi \rho G \left(\frac{P'}{\rho c^2} + \frac{N^2}{g} \right) \xi_r = 0. \quad (2.57)$$

In these equations, we have introduced the adiabatic sound speed¹

$$c \equiv \sqrt{\left. \frac{\partial P}{\partial \rho} \right|_S} = \sqrt{\Gamma_1 \frac{P}{\rho}}, \quad (2.58)$$

the squared Lamb frequency

$$L_l^2 \equiv \frac{l(l+1)c^2}{r^2}, \quad (2.59)$$

and the squared Brunt-Väisälä frequency, also referred to as the buoyancy frequency,

$$N^2 \equiv -gA = g \left(\frac{d \ln \rho}{dr} - \frac{1}{\Gamma_1} \frac{d \ln P}{dr} \right). \quad (2.60)$$

Both frequencies are the typical frequencies of two different types of oscillating modes, respectively the **pressure modes** (henceforth p-modes), animated by the pressure gradient, and the **gravity modes** (g-modes), animated by the buoyancy force. Equations (2.55) to (2.57) are the linear adiabatic oscillation equations and constitute an eigenvalue problem, in which σ^2 is the eigenvalue and the perturbed quantities are the eigenfunctions. Solving for σ^2 provides the eigenmodes of the problem. Finally, this problem requires boundary conditions. As ϕ' , ξ_r , and $(P'/\rho + \phi')$ must be regular at the center we have the two conditions

$$\frac{d\phi'}{dr} - \frac{l\phi'}{r} = 0 \quad \text{for } r \rightarrow 0, \quad (2.61)$$

$$\xi_r - \frac{l}{\sigma^2 r} \left(\frac{P'}{\rho} + \phi' \right) = 0 \quad \text{for } r \rightarrow 0. \quad (2.62)$$

We also need boundary conditions at the surface. The most obvious one is to require the pressure perturbation to vanish

$$\delta P = 0 \quad \text{for } r \rightarrow R. \quad (2.63)$$

¹Which is not to be mistaken with the speed of light, introduced earlier.

2.2.2 Radial oscillations and the Sturm-Liouville problem

The first step to grasp the physics of stellar oscillations is to study their radial component. This corresponds to modes associated with a spherical degree $l = 0$. The adiabatic linear oscillations equations (Eqs. (2.55) to (2.57)) can then be reduced and recombined into a simple form

$$\frac{d}{dr} \left[\Gamma_1 P r^4 \frac{d}{dr} \left(\frac{\xi_r}{r} \right) \right] + \left\{ \sigma^2 \rho r^4 + r^3 \frac{d}{dr} [(3\Gamma_1 - 4) P] \right\} \frac{\xi_r}{r} = 0. \quad (2.64)$$

This is a Sturm-Liouville eigenvalue problem, with the eigenvalue σ^2 . Such a problem has very convenient properties:

1. The problem has an infinite number of eigenvalues σ_n^2 and of eigenfunctions $\xi_{r,n}$. n is called the **radial order**;
2. The eigenvalues are real and can be ordered: $\sigma_0^2 < \sigma_1^2 < \dots$, with $\sigma_n^2 \rightarrow \infty$ for $n \rightarrow \infty$;
3. The solutions are interlaced, that is to say, with increasing radial order, the eigenfunctions $\xi_{r,n}$ present an increasing number of nodes. These nodes are placed between the nodes of the previous eigenfunction $\xi_{r,n-1}$. The eigenmode associated with the lowest radial order $n = 0$ is called the **fundamental mode** and has no node in the cavity $0 \leq r \leq R$;
4. The eigenfunctions are orthonormal to one another.

Another useful property of the Sturm-Liouville problem is the variational principle, which allows us to study the reaction of the solutions to a small perturbation of the equilibrium structure. This is particularly interesting for the inverse seismic techniques as well as to investigate structural glitches. This will be dealt with in later sections (see Sect. 2.2.5).

In general, the eigenmodes, solutions of the general adiabatic non-radial oscillations equations are characterised by three ‘quantum’ numbers: the radial order n , the spherical degree l , and the azimuthal order m .

2.2.3 Pressure, gravity and mixed-modes

To simplify the picture while preserving the general picture, we may neglect the perturbation to the gravitational potential, thus setting $\phi' = 0$. This is the Cowling approximation (Cowling 1941). This means that Eq. (2.57) can be integrated to provide a solution for the gravitational potential.

Cowling’s approximation is acceptable for large values of n (i.e. large numbers of radial nodes in the propagation cavity, thus short wavelengths) and large l values. Assuming short wavelengths also implies that the function derivatives dominate. Consequently, in Eqs. (2.55) and (2.56), $\frac{g \rho P'}{c^2}$ is negligible in front of $\frac{1}{\rho} \frac{dP'}{dr}$ and $\left(\frac{g}{c^2} - \frac{2}{r} \right) \xi_r$ is negligible in comparison with $\frac{d\xi_r}{dr}$. Equations (2.55) and (2.56) therefore become

$$\frac{1}{\rho} \frac{dP'}{dr} + (N^2 - \sigma^2) \xi_r \simeq 0, \quad (2.65)$$

$$\frac{d\xi_r}{dr} + \left(1 - \frac{L_l^2}{\sigma^2} \right) \frac{P'}{\rho c^2} \simeq 0. \quad (2.66)$$

Differentiating Eq. (2.65) with respect to r , combining the result with Eq. (2.66), and neglecting P' in front of $\frac{dP'}{dr}$, we obtain

$$\frac{d^2 \xi_r}{dr^2} + k_r^2(r) \xi_r \simeq 0, \quad (2.67)$$

with the radial wavenumber k_r given by the dispersion relation

$$k_r^2 = \left(1 - \frac{L_l^2}{\sigma^2} \right) \left(1 - \frac{N^2}{\sigma^2} \right) \frac{\sigma^2}{c^2}. \quad (2.68)$$

The last equation (2.68) is essential as it provides a condition on the wave radial propagation. Indeed, under the JWKB (Jeffreys 1925; Wentzel 1926; Kramers 1926; Brillouin 1926) approximation, the eigenfunction is assumed to be the combination of two plane waves with opposite directions

$$\xi_r \simeq A_+ \exp \left(i \int k_r dr \right) + A_- \exp \left(-i \int k_r dr \right), \quad (2.69)$$

2. Theoretical framework

with A_+ and A_- the amplitudes of the plane waves in the prograde and retrograde directions, respectively. The sign of k_r^2 dictates the behaviour of the wave, as it is the argument of an imaginary exponential (Eq. (2.69)). Whenever k_r^2 is positive, that is for $\sigma^2 < L_l^2, N^2$ or $\sigma^2 > L_l^2, N^2$, the wavenumber k_r is real and the mode can propagate radially. Equation (2.69) then becomes

$$\xi_r \simeq \frac{A}{\sqrt{k_r}} \cos \left(\int k_r dr \right), \quad (2.70)$$

with A being the amplitude of the wave. Conversely, for $L_l^2 < \sigma^2 < N^2$ or $L_l^2 > \sigma^2 > N^2$, $k_r^2 < 0$ and k_r is imaginary. Thus, Eq. (2.69) yields

$$\xi_r \simeq \frac{A}{\sqrt{k_r}} \exp \left(\int |k_r| dr \right). \quad (2.71)$$

A region of imaginary wavenumber is called evanescent. These conditions on k_r define three types of regions in the stellar interior:

1. Regions where $\sigma^2 < L_l^2$ and $\sigma^2 < N^2$ and where the buoyancy force acts as the restoring force of the oscillation are referred to as **gravity cavities** (g-cavities). The modes propagating in these regions are called **gravity modes** (g-modes);
2. Regions where $\sigma^2 > L_l^2$ and $\sigma^2 > N^2$ and where the pressure gradient acts as the restoring force of the oscillation are referred to as **pressure cavities** (p-cavities). The modes propagating in these regions are called **pressure modes** (p-modes);
3. Regions where $L_l^2 < \sigma^2 < N^2$ or $L_l^2 > \sigma^2 > N^2$ and the eigenfunctions are the combination of an increasing and decreasing exponential in the asymptotic limit (see next section), are called **evanescent**.

It is important to note that both the Lamb and Brunt-Väisälä frequencies (Eqs. (2.59) and (2.60)) play the role of critical frequencies, determining the behaviour of the mode throughout the stellar interior. Another important consequence comes from the existence of propagation regions separated by evanescent regions. In main-sequence solar-like pulsators, the p- and g-cavities are well separated, probing distinct regions of the stellar interior (outermost and innermost regions, respectively). To illustrate this, we represent in Fig. 2.2 the run of the two critical frequencies throughout the interior of a solar calibrated model.² Such a diagram is called a propagation diagram. We indicate the p- and g-cavities associated to two modes of arbitrary frequencies with the double-sided arrows. In low-mass main-sequence stars, due to the faint amplitudes of the g-modes, only p-modes are detected and only informations about the outermost layers of the star can be retrieved. However, for more evolved stars, such as the subgiants and red giants, the important density contrast between the core and envelope allows for the pressure and gravity cavities to couple through the evanescent region. This allows these modes to exhibit a mixed nature and to propagate through most of the stellar interior. These are the **mixed-modes**.

2.2.4 The asymptotic treatment

In the previous section, and under the Cowling approximation, we have seen that there exist regions in the stellar interior where the modes propagate, p- and g-cavities, and regions where modes fade away. In the present section, we study the properties of the modes when either entirely trapped in the p-cavity, in the g-cavity or when both cavities interact, through the evanescent region. To determine those properties, a common and very informative approach is the asymptotic treatment (Shibahashi 1979; Tassoul 1980; Gough 1986). Similarly to the Cowling approximation, the asymptotic expansion is valid for high-order modes. This corresponds to either high-frequency modes in the p-cavity or low-frequency modes in the g-cavity. This allows us to regard waves as plane waves under the JWKB approximation. We retrieve simplified solutions for pressure modes, gravity modes and mixed modes. The mathematical developments we propose are similar to the works presented in Takata (2016b) and are valid at first order.

²Solar calibrated models refer to models that have been adjusted to reproduce the solar radius, luminosity, and surface metallicity while fixing the age at the known solar value, 4.57 Gyr. The composition and mixing-length parameter are the free parameters.

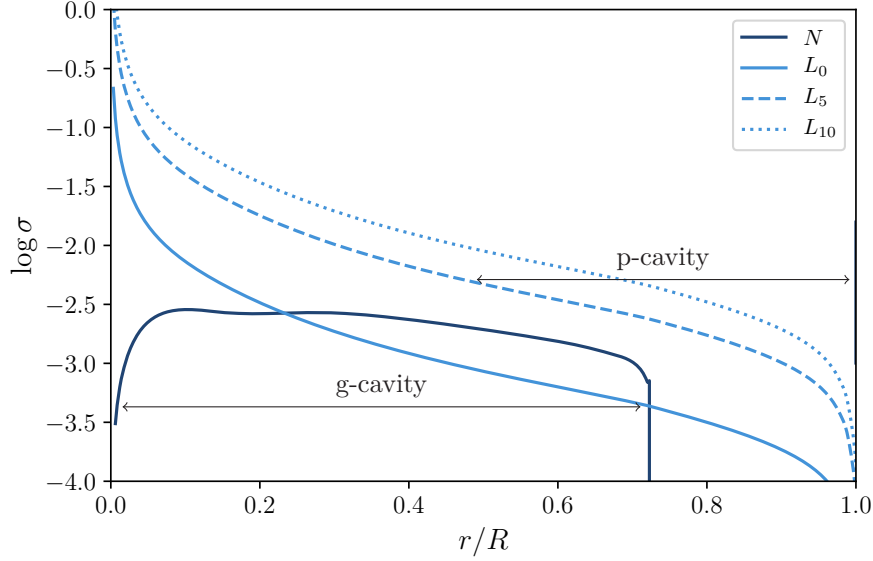


Figure 2.2: Propagation diagram for a solar calibrated model, representing the angular frequency as a function of the reduced radius. The Brunt-Väisälä frequency is shown in dark blue while the Lamb frequency is shown in light blue. We show the Lamb frequency associated with the spherical degree $l = 0$ with a continuous line, the one for $l = 5$ with a dashed line, and that of spherical degree $l = 10$ with a dotted line. The double-sided arrows indicate the propagation regions associated with p- and g-modes of arbitrary frequencies.

Acoustic modes

We consider only the resonant p-cavity, in which pressure modes propagate. As we consider high frequency modes, we have $\sigma \gg L_l, N$. In that cavity, we define a coordinate x representing the phase difference with the lower bound of the cavity. It takes the value of $x = 0$ and $x = \theta_p = \int_{\text{p-cavity}} k_r dr$ at the lower and upper bounds of the cavity, respectively. This simplified representation is illustrated in Fig. 2.3.

The wave solution is

$$\psi(x) = \alpha^{\rightarrow} e^{ix} + \alpha^{\leftarrow} e^{-ix}, \quad (2.72)$$

where the first term is the prograde contribution and the second one is the retrograde contribution. α^{\rightarrow} and α^{\leftarrow} are the amplitudes in both directions.

We now need to impose boundary conditions. The first and essential condition is to require a total reflection at the boundaries of the cavity. At the lower and upper boundaries, phase lags of Δ_L and Δ_U are introduced, respectively. We also require that the amplitude of the wave is conserved at both reflections. This translates into, at the lower boundary,

$$x = 0 : \quad \alpha^{\leftarrow} = \alpha^{\rightarrow} e^{i\Delta_L}, \quad (2.73)$$

and, at the upper boundary,

$$x = \theta_p : \quad \alpha^{\rightarrow} e^{i\theta_p} = \alpha^{\leftarrow} e^{-i\theta_p + i\Delta_U}. \quad (2.74)$$

In both equations, the left term corresponds to the incident wave and the right term corresponds to the reflected wave.

Eliminating the amplitude in one direction, we obtain

$$e^{i(\Delta_L + \Delta_U - 2\theta_p)} = 1, \quad (2.75)$$

which yields

$$2\theta_p = \Delta_L + \Delta_U + n_p \pi, \quad n_p \in \mathbb{N}. \quad (2.76)$$

Because we consider high frequency modes, that is modes with $\sigma^2 \gg L_l^2, N^2$ the dispersion relation (Eq. (2.68)) simplifies to

$$k_r^2 \simeq \frac{\sigma^2}{c^2}. \quad (2.77)$$

The phase difference between the lower and upper edges of the p-cavity becomes

$$\theta_p = \int_{\text{p-cavity}} k_r dr \simeq \sigma \int_{\text{p-cavity}} \frac{dr}{c}, \quad (2.78)$$

and, using Eq. (2.51), Eq. (2.76) becomes

$$2\pi\nu_{n_p,l} \simeq (\Delta_L + \Delta_U + n_p\pi) \left[\int_{\text{p-cavity}} \frac{dr}{c} \right]^{-1}. \quad (2.79)$$

The exact values of the phase lags Δ_L and Δ_U are determined by the boundary conditions of the problem.

At first order, this corresponds to the famous asymptotic solution for pressure modes of spherical degree l and radial order n_p (Tassoul 1980; Gough 1986)

$$\nu_{n_p,l} \simeq \left(n_p + \frac{l}{2} + \epsilon \right) \Delta\nu, \quad (2.80)$$

with ϵ a constant mostly resulting from the contribution of the outermost layers, the large separation

$$\Delta\nu = \left(2 \int_0^{R_*} \frac{dr}{c(r)} \right)^{-1}, \quad (2.81)$$

and R_* being the radius at the photosphere. We denoted the radial order of p-modes with the subscript p to make the distinction with g-modes.

The first consequence of this formulation is the equidistance of oscillation frequencies of identical spherical degree and subsequent radial order. These modes are separated by one large separation, $\nu(n_p + 1, l) - \nu(n_p, l) \simeq \Delta\nu$, which is a proxy of the mean stellar density (Ulrich 1986). This equidistance is therefore convenient to infer the mean stellar density and also to provide an identification, n_p and l values, of p-modes. This is the first example of a seismic indicator. The quasi equidistance of modes with successive radial order is clearly visible in the so-called *échelle* diagram, introduced by Grec et al. (1983). In such diagrams, the frequencies are represented as a function of themselves modulo their large separation. As a consequence, frequencies associated with a common spherical degree align themselves vertically, forming ridges. We represent the *échelle* diagram with the frequencies of 16CygA measured by Davies et al. (2015) in Fig. 2.4. We observe four separated ridges as modes with degrees $l = 0, 1, 2$, and 3 have been measured. We also note that subsequent modes over a given ridge are separated by one large separation. We may also note that the separation between two ridges also bears some information. Indeed, from Eq. (2.80) we would expect that two modes with n_p, l and $n_p + 1, l + 2$ would produce the same frequency. Therefore, the two ridges would align. This is not the case, indicating a necessary refinement of the asymptotic description. The difference $\nu_{n_p+1,l+2} - \nu_{n_p,l}$ is known as the small frequency difference and has often been used as a constrain to the stellar evolutionary stage (e.g. Christensen-Dalsgaard 1988). Finally, we show in Fig. 2.4 the approximation of the frequencies by a second order expansion in n_p as a blue line and a refined representation, in which the remainder is approximated by an oscillating function, as a red line. This oscillating contribution is in fact the result of acoustic glitches which will be introduced in Sect. 2.2.5 and extensively discussed throughout the present manuscript.

Gravity modes

Similarly to the p-modes, an asymptotic expansion can be obtained for the g-modes. In the g-cavity, represented in Fig. 2.5, for the low frequency modes, we have $\sigma \ll L_l, N$. The dispersion relation (Eq. (2.68)) becomes

$$k_r \simeq \frac{L_l N}{\sigma c} \simeq \frac{\sqrt{l(l+1)} N}{\sigma r}. \quad (2.82)$$

Following the same reasoning as in the previous section we may obtain a relation for the period of g-modes of spherical degree l and radial order n_g . One must however pay attention that the phase velocity and group velocity have opposite signs for g-modes. As we follow the energy propagation, therefore the group velocity, our phase coordinate is reverted. We thus write the phase difference at the lower boundary

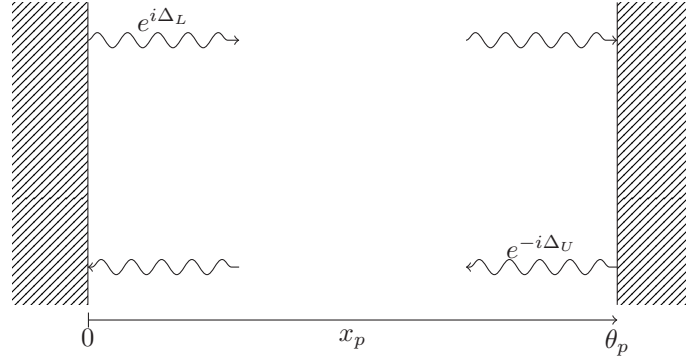


Figure 2.3: Schematisation of the p-cavity.

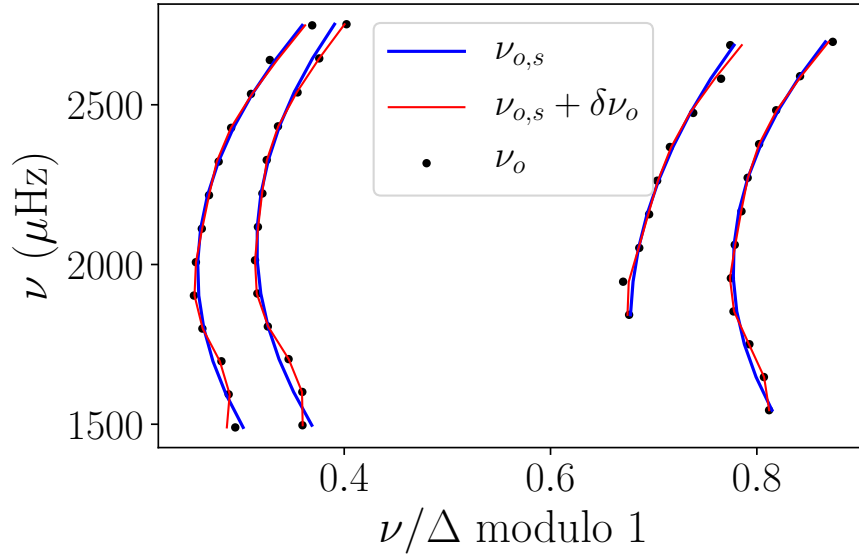


Figure 2.4: Echelle diagram using the frequencies for 16CygA measured by [Davies et al. \(2015\)](#). The circles correspond to the frequencies, the blue line to a second order representation of the frequencies, and the red line to a representation including the contribution of acoustic glitches.

of the cavity $x = \theta_g = \int_{g\text{-cavity}} k_r dr$. With these considerations, we obtain the relation

$$P_{n_g, l}/\pi \simeq (\Delta_L + \Delta_U + n_g \pi) \left[\sqrt{l(l+1)} \int_{g\text{-cavity}} \frac{N}{r} dr \right]^{-1}. \quad (2.83)$$

In the case of dipolar modes, this expression again corresponds to the widely used expression ([Tassoul 1980](#); [Mosser et al. 2012c](#))

$$1/\nu(n_g, l) = P(n_g, l) \simeq (|n_g| + \alpha) \Delta \pi_1, \quad (2.84)$$

with the gravity radial order defined negative, such that $P(n_g, l) < P(n_g - 1, l)$, α a constant, and

$$\Delta \pi_l = 2\pi^2 \sqrt{l(l+1)} \left(\int_{g\text{-cavity}} \frac{N}{r} dr \right)^{-1}, \quad (2.85)$$

the period spacing of modes of degree l . From Eq. (2.84), we note that the g-modes are equidistant in period. This again provides valuable insight with regard to the stellar structure as the period spacing of dipolar modes is a proxy of the mean density of the core ([Montalbán et al. 2013](#)). We also observe from Eq. (2.83) that radial gravity modes cannot exist.

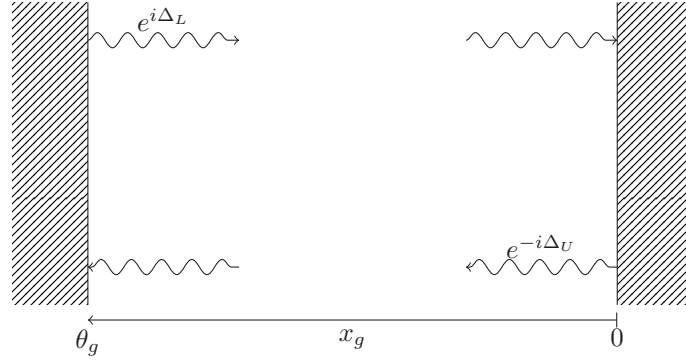


Figure 2.5: Schematisation of the g-cavity.

Mixed modes

Finally, as seen in Sect. 2.1.4, when low-mass stars evolve on the subgiant and red-giant branches, their cores contract while their envelopes expand. This results in a large density contrast between the two regions and renders the evanescent region significantly thinner than on the main sequence. Furthermore, the frequency of g-modes increases while that of p-modes decreases as the star evolves. As a consequence, the frequencies of both types of modes approach one another and may couple. This results in a mode sharing both characters, a so-called mixed mode, and propagating throughout most of the stellar interior. An expression for these modes is given by (Shibahashi 1979; Tassoul 1980; Takata 2016a)

$$\tan \theta_p = q \tan \theta_g, \quad (2.86)$$

where θ_p is the contribution of the pressure cavity, the pressure phase, to the mode, θ_g is the contribution of the gravity cavity, gravity phase, and q is the coupling factor. These three terms depend on the frequency. Solving this implicit relation then provides the eigenfrequencies.

Proceeding in a similar way as in the previous sections and following the work of Takata (2016b), we may derive this expression. We now consider two cavities: the g-cavity (as in Sect. 2.2.4) in the inner regions and the p-cavity (as in Sect. 2.2.4) in the outer regions. These two cavities are separated by an evanescent region which allows the waves to be partially transmitted and reflected. In the g-cavity, we define the phase coordinate, x_g , which varies between θ_g and 0 at the lower and upper edges of the cavity, respectively. The upper edge of the cavity coincides with the lower edge of the evanescent region. Similarly, the phase coordinate, x_p , varies in the p-cavity from 0 to θ_p at the lower and upper edges of the cavity, respectively. The upper edge of the evanescent region corresponds to the lower edge of the p-cavity. This configuration is represented in Fig. 2.6. The partial transmission and reflection are characterised by the coefficients T and R , respectively. They describe the wave amplitude change after interaction with the evanescent region. The energy conservation requires that we have conservation of the wave amplitude, which translates into

$$R^2 + T^2 = 1. \quad (2.87)$$

When reflected by the evanescent region, an additional phase lag occurs. Takata (2016b) showed that the phase lag occurring at a partial reflection on the left of the evanescent region, δ , and the one occurring on the right, δ' , are related by

$$\delta + \delta' = \pi. \quad (2.88)$$

In each cavity, the standing wave is a superposition of a prograde and a retrograde wave. We thus have, in the g-cavity,

$$\psi_g(x) = \alpha^{\rightarrow} e^{ix_g} + \alpha^{\leftarrow} e^{-ix_g} \quad (2.89)$$

and, in the p-cavity,

$$\psi_p(x) = \beta^{\rightarrow} e^{ix_p} + \beta^{\leftarrow} e^{-ix_p}. \quad (2.90)$$

We now have to set the boundary conditions. First, let us consider the total reflections, occurring at $x_g = \theta_g$ and $x_p = \theta_p$. Conservation of energy requires

$$x_G = \theta_g : \quad \alpha^{\rightarrow} e^{i\theta_g} = \alpha^{\leftarrow} e^{-i\theta_g + i\Delta_L}, \quad (2.91)$$

$$x_P = \theta_p : \quad \beta^{\leftarrow} e^{-i\theta_p} = \beta^{\rightarrow} e^{i\theta_p + i\Delta_U}, \quad (2.92)$$

where Δ_L and Δ_U are the phase lags introduced by the reflections at $x_g = \theta_g$ and $x_p = \theta_p$, respectively.

We also need conditions for the partial transmission and reflection of the waves by the evanescent region. For the transmission from the g-cavity to the p-cavity, we have

$$x_p = 0 : \quad \beta^{\rightarrow} = T\alpha^{\rightarrow} + R\beta^{\leftarrow} e^{i\delta'}, \quad (2.93)$$

and for the transmission from the p-cavity to the g-cavity

$$x_g = 0 : \quad \alpha^{\leftarrow} = T\beta^{\leftarrow} + R\alpha^{\rightarrow} e^{i\delta}. \quad (2.94)$$

Equations (2.91) to (2.94) constitute a system of four equations with four unknowns: the amplitudes α^{\leftarrow} , α^{\rightarrow} , β^{\leftarrow} , and β^{\rightarrow} . Two of them, α^{\leftarrow} and β^{\leftarrow} are easily substituted, thanks to the total reflection conditions (Eqs. (2.91) and (2.92)), reducing the problem to a two-equations and two-unknowns system. A solution is found when the determinant of the system vanishes. This is given by the following expression

$$\left[e^{-i(2\theta_g - \Delta_L)} - R e^{i\delta} \right] \left[1 - R e^{i(2\theta_p + \Delta_U + \delta')} \right] - T^2 e^{i(2\theta_p + \Delta_U)} = 0. \quad (2.95)$$

Defining the new pair of variables

$$2\vartheta_p = 2\theta_p + \Delta_U - \delta + \pi, \quad (2.96)$$

$$2\vartheta_g = 2\theta_g - \Delta_L - \delta + \pi, \quad (2.97)$$

representing the phase contributions of the p- and g-cavities, respectively, and using the relations (2.87) and (2.88), we find the resonance condition of mixed-modes

$$\sin(\vartheta_p - \vartheta_g) = -R \sin(\vartheta_p + \vartheta_g). \quad (2.98)$$

We found the expression given by (Takata 2016b, Eq. 17).

Finally, using elementary trigonometric relations, Eq. (2.98) becomes

$$\tan \vartheta_p = q \tan \vartheta_g, \quad (2.99)$$

where we identify

$$q = \frac{1 - R}{1 + R}, \quad (2.100)$$

the coupling factor which represents the strength of the coupling between both cavities. Originally, Shibahashi (1979) only allowed for this coupling to reach a maximum value of 1/4. This is referred to as the weak coupling. The later study by Takata (2016b), on which the presented developments are based, demonstrated that it remains valid even for greater values of the coupling factor, typical of subgiant stars. Indeed, Eq. (2.100) allows q to take values in the $[0, 1]$ range. The case $q = 0$ and $R = 1$ corresponds to a complete reflection of the wave by the evanescent region, therefore the absence of coupling, while the case $q = 1$ and $R = 0$ corresponds to a complete transmission of the wave, where both cavities are fused. Expressions for the individual phases, ϑ_p and ϑ_g , will be provided later in the present manuscript (Chap. 5).

2.2.5 Variational principle and structural glitches

A useful property of the adiabatic non-radial oscillations equations is that they obey a variational principle. This allows us to compute the effect of a small perturbation in the stellar structure on the eigenmodes. Solving Poisson's equation (Eq. (2.9)) for the Eulerian perturbation of the gravitational potential

$$\phi'(\mathbf{r}) = -G \int_V \frac{\rho'(\mathbf{x}) d^3\mathbf{x}}{|\mathbf{x} - \mathbf{r}|}, \quad (2.101)$$

V being the volume of the star, we may rewrite the perturbed equation of motion (Eq. (2.46)) as

$$\sigma^2 \boldsymbol{\xi} = \mathcal{L}(\boldsymbol{\xi}), \quad (2.102)$$

where

$$\begin{aligned} \mathcal{L}(\boldsymbol{\xi}) \equiv & \frac{1}{\rho^2} (\nabla P) \nabla \cdot (\rho \boldsymbol{\xi}) - \frac{1}{\rho} \nabla (\boldsymbol{\xi} \cdot \nabla P) - \frac{1}{\rho} \nabla (c^2 \rho \nabla \cdot \boldsymbol{\xi}) \\ & + \nabla \left\{ G \int \frac{\nabla_{\mathbf{x}} \cdot [\rho(\mathbf{x}) \boldsymbol{\xi}(\mathbf{x})] d^3\mathbf{x}}{|\mathbf{x} - \mathbf{r}|} \right\} \end{aligned} \quad (2.103)$$

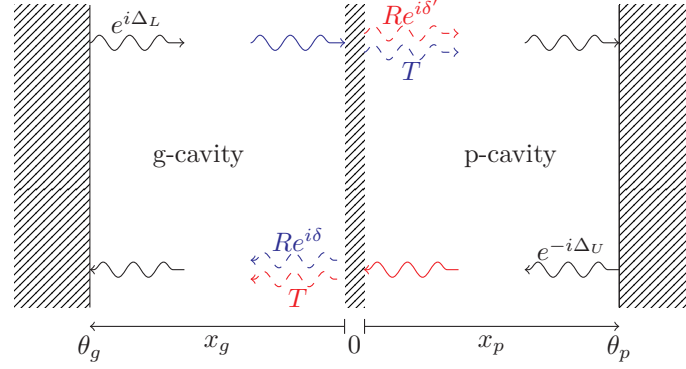


Figure 2.6: Schematisation of the coupling between the p- and g-cavities.

is a linear and hermitian operator.

Defining the scalar product of two eigenfunctions, ξ and η , of Eq. (2.102)

$$\langle \xi | \eta \rangle = \int_V \xi \cdot \eta \rho dV, \quad (2.104)$$

with V the volume of the star and the \cdot symbol representing the usual scalar product; and because of the linearity and hermiticity of the operator, we may write the effect of a small perturbation of the structure, translated in a small perturbation of the operator \mathcal{L} , $\Delta\mathcal{L}$, on the frequencies as

$$\Delta\sigma^2 = \frac{\langle \xi | \Delta\mathcal{L}(\xi) \rangle}{\langle \xi | \xi \rangle}. \quad (2.105)$$

The great advantage of Eq. (2.105) is that we do not need to solve the oscillation equations once again as the variational principle predicts the change in the frequencies from the eigenfunction of the unperturbed structure.

An application of this principle comes with structural glitches. Such glitches occur when the stellar structure locally varies sharply, when compared to the wavelength of eigenmodes. As the variation is comparable to the wavelength of the mode, the asymptotic theory becomes locally invalid. The result is an oscillation in the measured frequencies as a function of the frequency. The main two causes of such glitches are the depression of the first adiabatic index in the second-ionisation zone of helium, the helium glitch, and the discontinuity of the sound speed derivative at the base of the envelope convective zone, the convective zone glitch. What makes the glitches interesting is that they allow us to retrieve localised diagnoses and may help lift degeneracies in the stellar modelling. From the variational principle (Eq. (2.105)) an expression for the glitch may be retrieved. In the simplified case of a half-opened organ pipe, we obtain the following simple wave equation

$$\frac{d}{dr} \left(\Gamma_1 P \frac{d\xi_r}{dr} \right) + \sigma^2 \rho \xi_r = 0. \quad (2.106)$$

Considering a sharp perturbation of the sound speed $\Delta c^2(r) = c^2(r_0) \delta(r - r_0)$. The localised character of the sharp feature at r_0 is represented by the Dirac function, δ . The variational principle then yields

$$\Delta\sigma_n^2 = \frac{\int_0^M \Delta c^2(r) \left(\frac{d\xi_r(r)}{dr} \right)^2 dM_r}{\int_0^M \xi_r^2 dM_r} \quad (2.107)$$

$$= \frac{\Delta c^2(r_0) \left(\frac{d\xi_r(r_0)}{dr} \right)^2 M}{\int_0^M \xi_r^2 dM_r}. \quad (2.108)$$

Under the JWKB approximation, valid for large values of n , we may approximate the radial displacement by the function $\xi_r = A c^{1/2} \cos \left(\sigma_n \int_r^R \frac{dr'}{c} \right)$. Equation (2.108) then becomes

$$\Delta \sigma_n^2 \simeq \frac{\Delta c^2(r_0) A^2 M \sigma_n^2 \left[1 + \cos \left(\sigma_n \int_{r_0}^R \frac{dr}{c} \right) \right]}{c(r_0) A^2 M \int_0^M c(r) \left[1 - \cos \left(\sigma_n \int_{r_0}^R \frac{dr}{c} \right) \right] dM_r}. \quad (2.109)$$

Because we consider high frequencies, the cosine function presents a large number of nodes from the center to the surface and is expected to contribute little to the denominator integral, compared to unity. With this final simplification, we obtain

$$\frac{\Delta \nu_n}{\nu_n} = \frac{1}{\pi} \frac{\Delta \sigma_n^2}{\sigma_n^2} \simeq \frac{\Delta c^2(r_0) \left[1 + \cos \left(4\pi \nu_n \int_{r_0}^R \frac{dr}{c} \right) \right]}{c(r_0) \int_0^M c(r) dM_r}. \quad (2.110)$$

We indeed note from Eq. (2.110) that the glitch signature is expected to be an oscillation of the frequencies as a function of the frequency. This formulation remains however very approximate. A more accurate formulation for the helium glitch has been derived by [Houdek & Gough \(2007\)](#)

$$\Delta \nu_{n,l} \simeq A_{\text{He}} \nu_{n,l} e^{-c_2 \nu_{n,l}^2} \sin(4\pi \tau_{\text{He}} + \phi_{\text{He}}). \quad (2.111)$$

In this equation, we observe that the signal is expected to be independent of the spherical degree and exponentially decreases in amplitude with the frequency. The amplitude of the signal is symbolised by A_{He} , which is a proxy of the sharpness of the feature causing the glitch, and

$$\tau_{\text{He}} = \int_{r_{\text{He}}}^R \frac{dr}{c(r)} \quad (2.112)$$

is the acoustic depth of this feature, with r_{He} its radial position, and ϕ_{He} its phase. We may already point to the fact that this formulation for the glitch is highly non-linear and implicit in the frequency. Fitting the glitch signature therefore requires non-linear minimisation techniques, which can be costly, in terms of computational resources, and may introduce correlations between the fitted data. A portion of the present work was to provide a linearised formulation for the glitch and avoid resorting to non-linear techniques. We present in Fig. 2.7 the signature of the helium glitch retrieved with our method, WhoSGIAd that will be presented in Chap. 3, in the 16CygA frequencies measured by [Davies et al. \(2015\)](#). The observed glitch is represented by the errorbars and the fitted glitch by the continuous line. We also schematically represent the glitch amplitude in red and its acoustic depth in blue.

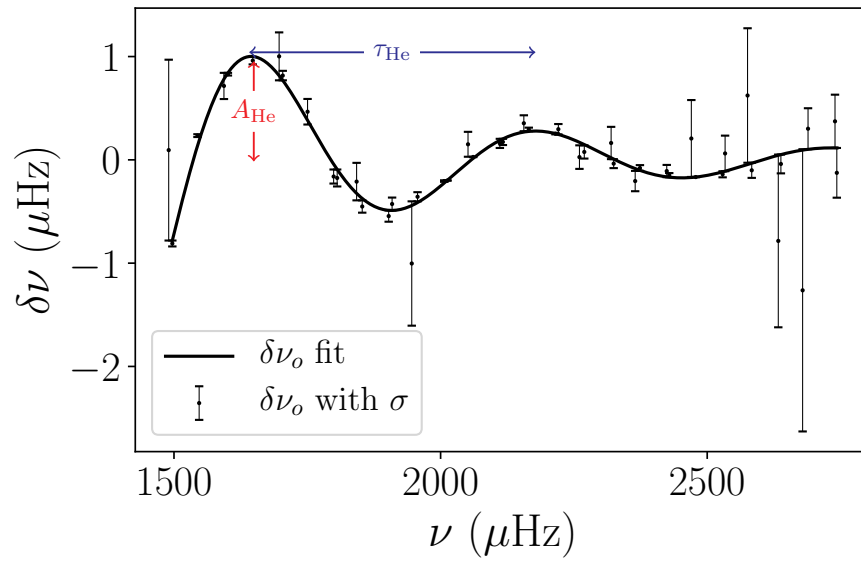


Figure 2.7: Representation of the helium glitch retrieved 16CygA frequencies with our method, WhoSGlAd. We show the observed signature of the glitch as errorbars and the adjusted signature as a continuous line. The red and blue arrows schematically represent the glitch amplitude and acoustic depth, respectively.

PART I

The main sequence

CHAPTER 3

The WhoSGLAd method

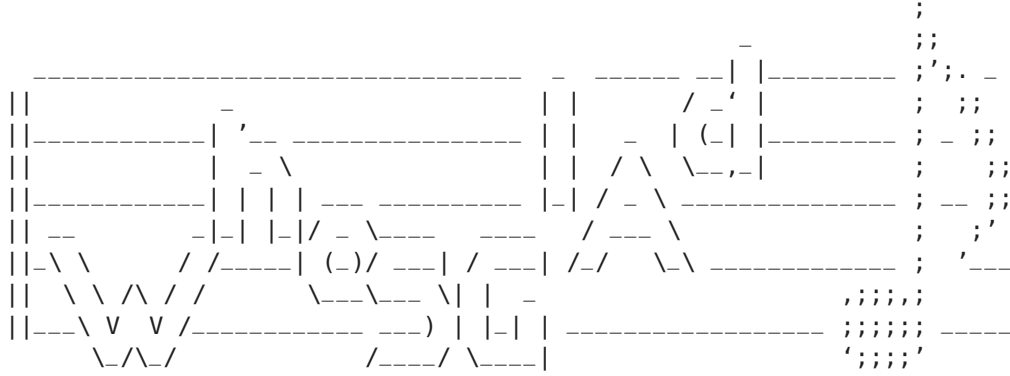


Figure 3.1: The WhoSGLAd logo.

The present chapter describes the WhoSGLAd (**W**hole **S**pectrum and **G**litches **A**djustment) method that provides the numerical means to carry a robust and fast adjustment of the oscillation spectra of main-sequence low-mass stars. This method was presented in an article (Farnir et al. 2019, see also Sect. 3.D). We here provide a slightly different and more detailed approach to the presentation of the method. The application of the method to observed stars will be detailed in the next chapter (Chap. 4).

3.1 Context

3.1.1 Motivation

Up to recent years, quality seismic data were only available for our Sun, owing to its proximity. Many programs were indeed dedicated to its observation (e.g. GONG Harvey et al. 1988, BiSON Brookes et al. 1978, SOHO Domingo et al. 1995). A wealth of pulsation modes were observed (over a thousand) that allowed us to put tight constraints on the solar structure and to raise relevant questions concerning theories of stellar structure and evolution (for a review, see for example Buldgen et al. 2019). Such data provided the scientific community with the means necessary to test the models at hand.

Lately, thanks to the CoRoT (Baglin et al. 2009) and Kepler (Borucki et al. 2010) space telescopes, seismic data of unprecedented quality has been made available for a large sample of stars, allowing asteroseismology to thrive. Some asteroseismic studies use a very classical approach, constraining stellar models in the forward modelling scheme via individual oscillation frequencies or frequency separations (e.g. Miglio & Montalbán 2005; Deheuvels et al. 2016). Others use inversion techniques to provide precise constraints on the variations of physical quantities (e.g. density, entropy,...) along the whole depth of the star (e.g. Elliott 1996; Buldgen et al. 2016a). This enables them to stray from the parameter space of models and constrain the missing physical ingredients. Finally, some account for the signatures of acoustic glitches (e.g. Monteiro et al. 2000; Basu et al. 2004; Mazumdar et al. 2014; Verma et al. 2014; Farnir et al. 2019). This is another way to pinpoint the shortcomings of stellar models. An acoustic glitch is the faint signature left in the oscillation spectrum by a sharp variation – compared to the wavelength of the oscillating mode – in the stellar structure. Such glitches mainly carry two pieces of information: their amplitude, which is directly linked to the strength of the sharp variation in the stellar structure, and their period, which is proportional to the acoustic depth at which it occurs. Because of their low amplitude,

the analysis of acoustic glitches has only been made possible by the advent of space telescopes such as we mentioned before.

Moreover, with data of such quality came the necessity to improve modelling techniques in order to exploit them at best. From the several studies exploiting the glitches information, we may cite [Verma et al. \(2014\)](#), which served as a basis to the construction of our technique. Their technique is one of the first using the helium acoustic glitch, caused by a depression in the first adiabatic index ($\Gamma_1 = \frac{d \ln P}{d \ln \rho} \Big|_S$ with P the pressure, ρ the density and S the entropy) in the helium second-ionisation zone, to calibrate the surface helium content (inaccessible by other means such as spectroscopy in solar-like stars) in stars other than the Sun. However, several flaws remained in their approach. Namely, they separated the glitch contribution from the slowly varying trend in the oscillation spectrum (referred to as the ‘smooth part’). The smooth part is then regarded as a parasite and discarded, along with the useful information it carries. Moreover, treating both components this way may lead to unnecessary correlations which impact the quality of the modelling and make it difficult to carry statistical inferences. For those reasons, we developed the WhoSGLAd method ([Farnir et al. 2019](#)) that tackles these issues and carries out a simultaneous adjustment of the complete oscillation spectrum, while combining oscillation frequencies in a clever way to build seismic indicators as little correlated as possible and representative of the stellar structure.

3.1.2 Glitches in solar-like stars

Before moving on to the method itself, a small word about acoustic glitches is in order. Usually, we may separate the oscillation spectrum of solar-like stars into two contributions: the slowly varying trend, well approximated by the asymptotic theory of stellar oscillations ([Tassoul 1980](#); [Gough 1986](#)) and an oscillating component due to a sharp variation in the stellar structure, the acoustic glitch. Acoustic glitches in solar-like pulsators have two main causes: the discontinuity in the sound-speed gradient derivative at the base of the envelope convection zone, referred to as the convection zone (BCZ) glitch, and the depression in Γ_1 in the helium second-ionisation zone, the helium glitch. They both provide valuable and localised information. The former provides us with clues about the exact extent of the envelope convection zone as well as the mixing processes that could explain such an extent and the sharpness of the transition between the radiative and convective zones. The latter gives us means to calibrate the surface helium content. Indeed, the magnitude of the depression in the first adiabatic index is in direct correlation with the helium content, as well as the exact location of the helium second-ionisation zone (e.g. [Basu et al. 2004](#); [Farnir et al. 2019](#)).

In partial ionisation zones, a local increase in the density, say by contraction of the star, leads to a reduced increase in the pressure due to the portion of energy that is used to ionise the helium atoms instead. This translates into a depression in the first adiabatic index which represents the variation of the pressure with density, at constant entropy ($\Gamma_1 \equiv \frac{\partial \ln P}{\partial \ln \rho} \Big|_S$, Eq. (2.50)). This is represented in Fig. 3.2 in a solar-like stellar model for two values of the initial helium mass fractions, 0.24 (solid line) and 0.27 (dot-dashed line). There we plot the evolution of Γ_1 in the most superficial layers of the star. In green is highlighted the rough region where the second ionisation of helium happens. At this point, we may already point out that a greater helium mass fraction leads to a more prominent depression in the first adiabatic index, as illustrated in Fig. 3.2 with the two initial helium abundance values. This constitutes a preliminary illustration of the correlation between helium mass fraction and helium glitch amplitude.

To my knowledge, the first representation of a periodic signal in frequencies was given by [Hill & Rosenwald \(1986\)](#) who clearly demonstrated the existence of such a signal in solar $l = 0, \dots, 6$ modes and already attributed it to the transition between radiative and convective regions. The usefulness of these signals (not yet referred to as ‘glitches’) has also been pointed out early on by [Vorontsov \(1988\)](#) and [Gough \(1990\)](#) who showed that the glitches signature could be extracted from frequencies or second frequency differences.

Many studies then followed these precursory works. [Monteiro et al. \(1994\)](#) proposed a method exploiting the convection zone glitch to locate the base of the solar convective envelope. They determined that models without overshooting are favoured. Using a grid of stellar models, the work of [Monteiro et al. \(2000\)](#) further assessed the possibility to detect the convection zone glitch in oscillation frequencies of $0.85 M_\odot$ to $1.20 M_\odot$ models. They demonstrated that with at least 10 modes for each spherical degree up to $l = 2$ and with sufficient precision on these modes, $\sigma(\nu) \leq 0.1 \mu\text{Hz}$, the signal can be detected. Such a precision is reached in the case of the 16 Cygni system but not for any Kepler stars. They also showed that the glitch amplitude and acoustic depth can be retrieved. While the acoustic depth can be precisely retrieved (with a relative precision ranging from $\sim 0.3\%$ to $\sim 4.3\%$), it is not the case of the

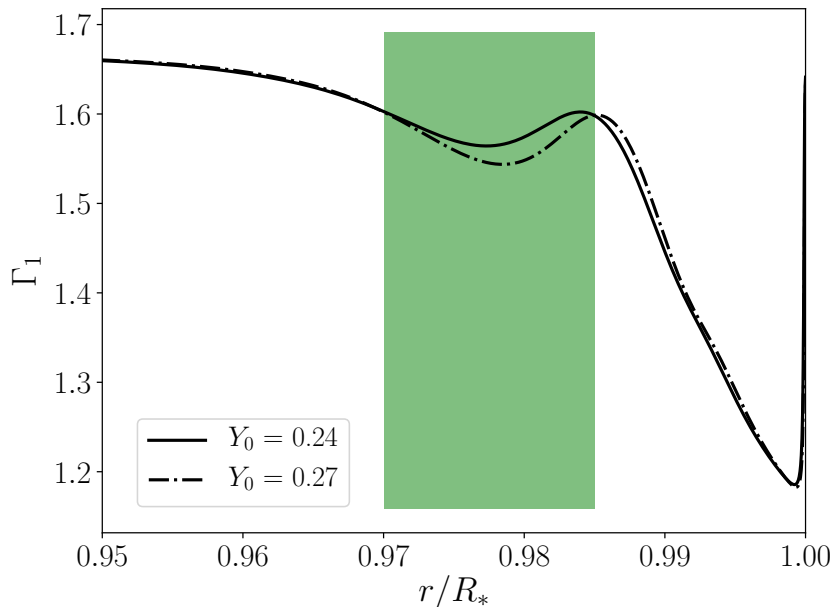


Figure 3.2: First adiabatic index as a function of the reduced radius in the most superficial regions of a solar-like stellar model ($M = 1.052 M_{\odot}$, $X = 0.75$) for two values of the initial helium abundance: 0.24, solid line, and 0.27, dot-dashed line. The green region roughly highlights the helium second-ionisation zone.

glitch amplitude (with a relative precision of $\sim 5\%$, in favourable cases, to $\sim 40\%$, in the worst cases). Ballot et al. (2004) later attempted to retrieve the convection zone glitch signature in 150 days time series of the VIRGO experiment, part of the SOHO mission (Fröhlich et al. 1995). Considering only frequencies for $l = 0, 1, 2$ modes, they managed to locate the base of the convection zone within 100 s accuracy, for what is expected to be typical solar-like data.

Focusing on the helium glitch, Monteiro & Thompson (1998) showed that we should be able to detect the signature of the helium glitch in low-degree modes of solar-like stars, which are the ones we observe. A correlation between the helium amplitude and the helium abundance in the helium second-ionisation zone was then established by Basu et al. (2004) over a grid of low-mass stellar models. Later on, Houdek & Gough (2007) provided a formulation for the glitch oscillatory contribution, which is the basis for several studies including ours (see Eq. (2.111)). We refer to Sect. 2.2.5 for a way to derive a simple formulation for the glitch. Taking advantage of this formulation, Verma et al. (2014) provided a technique to adjust the glitches signatures of both the convection zone and helium second-ionisation zone in solar-like stars and applied it to the 16 Cygni system, estimating the helium content in these stars. They went on by applying their method to the Kepler LEGACY sample (Verma et al. 2017) and provided the location of the base of the convection zone and helium second-ionisation zone in these stars.

Following their footsteps, we developed a new method to account for these glitches. It provides a simultaneous (often not the case with other techniques) and robust adjustment of the smooth part as well as of both glitches. Unfortunately, in solar-like stars, the convection zone glitch signature is often too faint to be exploited. For example, we measured that its amplitude is only three times larger than its typical standard deviation in 16 Cygni A, a benchmark solar-like pulsator. As a consequence, we will focus mainly on the helium glitch.

3.2 The method

3.2.1 Mathematical principle

The present section lays the mathematical grounds necessary to the rigorous construction of our method.

Notations

Here we define the mathematical notations that are used.

- Vectors are represented by a bold symbol: \mathbf{x} . When individual components are explicitly written, indexes of each component are given and the symbol is shown with a regular font: x_i .
- A basis of vectors over a given N -dimensional Euclidean vector space is represented by curly brackets: $\{\mathbf{x}_1 \dots \mathbf{x}_N\}$. We will conveniently write such basis in a shorthand form $\{\mathbf{x}\}$ when there will be no possibility of confusion.
- The scalar product of two vectors \mathbf{x} and \mathbf{y} is represented as $\langle \mathbf{x} | \mathbf{y} \rangle$. Its definition will be given when appropriate.
- The norm of a vector is: $\|\mathbf{x}\| = \sqrt{\langle \mathbf{x} | \mathbf{x} \rangle}$.
- We note the weighted mean of a vector quantity as $\bar{\mathbf{x}}$. We will provide its definition when appropriate.

Gram-Schmidt orthonormalisation

The method we developed relies on the Gram-Schmidt orthonormalisation process. Given a N -dimensional Euclidean vector space, this process allows us to build an orthonormal basis (i.e. all its components are normal to each other and of unit length) from any given basis.

Given the ordinary basis of vector $\{\mathbf{p}_1 \dots \mathbf{p}_N\}$, we may construct the orthonormal basis $\{\mathbf{q}_1 \dots \mathbf{q}_N\}$ as follows:

1. Starting from any basis vector, we normalise this vector.¹

$$\mathbf{q}_1 = \frac{\mathbf{p}_1}{\|\mathbf{p}_1\|}. \quad (3.1)$$

2. Working in succession, we remove from the current basis element, \mathbf{p}_i , its projection on all the previously normalised basis elements, $\sum_{j=1}^{i-1} \langle \mathbf{p}_i | \mathbf{q}_j \rangle \mathbf{q}_j$. We get the orthogonal (but not unit) vector

$$\mathbf{u}_i = \mathbf{p}_i - \sum_{j=1}^{i-1} \langle \mathbf{p}_i | \mathbf{q}_j \rangle \mathbf{q}_j. \quad (3.2)$$

3. Finally, we normalise the resulting vector.

$$\mathbf{q}_i = \frac{\mathbf{u}_i}{\|\mathbf{u}_i\|} \quad (3.3)$$

In a matrix representation, we have:

$$\mathbf{q}_i = \sum_{j=1}^i R_{i,j}^{-1} \mathbf{p}_j, \quad (3.4)$$

with $R_{i,j}$ the i -th and j -th element of the transformation matrix. Considering the scalar product to be positive definite (as will be the case), the orthonormal basis is unique. Furthermore, the ordering plays a crucial role in the definition of seismic indicators. This is further discussed in Sect. 3.2.3.

3.2.2 Adjusting the frequencies

Representation of the frequencies

For a given solar-like pulsator with N observed frequencies $\nu_{\text{obs},i}$, the associated errors σ_i , spherical degrees l_i and radial orders n_i , we define the Euclidian vector space of frequencies of dimension N , with the associated scalar product between two vector quantities $\boldsymbol{\nu}_1$ and $\boldsymbol{\nu}_2$,

$$\langle \boldsymbol{\nu}_1 | \boldsymbol{\nu}_2 \rangle = \sum_{i=1}^N \frac{\nu_{1,n_i} \nu_{2,n_i}}{\sigma_i^2}. \quad (3.5)$$

¹Usually, when working with polynomial, we start with the zero order polynomial.

We may already note that, given the definition of the scalar product, the set of orthonormal basis elements used depends on the set of observed frequencies (number of modes and uncertainties). Two notable functions are the identity, $\mathbf{1}$, and linear function of the radial order, $\mathbf{n}_l = (n_{l,1}, \dots, n_{l,N})$.

The functions used to describe the frequencies are separated into two contributions: the slowly varying trend, given by a second order polynomial in n , and the glitch part, represented by oscillating functions of the frequencies. These functions form a basis over the Euclidean subspace. Then, via the Gram-Schmidt orthonormalisation process, we build an orthonormal basis of functions, $\{\mathbf{q}\}$. The least-square fitting coefficients, a_k , are then simply given by projection of the frequencies over the basis elements, that is

$$a_k = \langle \boldsymbol{\nu}_{\text{obs}} | \mathbf{q}_k \rangle, \quad (3.6)$$

and the fitted frequencies, $\boldsymbol{\nu}_{\text{fit}}$, are then given by

$$\boldsymbol{\nu}_{\text{fit}} = \sum_{k=1}^K a_k \mathbf{q}_k, \quad (3.7)$$

where we sum over the K orthonormal basis elements \mathbf{q}_k .

The great advantage of such an approach is that, if the frequencies are independent of each other, the fitting coefficients, a_k , are also completely independent of one another and have unit standard deviations, that is to say

$$\sigma(a_k) = \|\mathbf{q}_k\| = 1. \quad (3.8)$$

This stems from the orthonormality of the basis functions. We demonstrate this as follows: As the coefficients a_k are linear combinations of the frequencies (see Eqs. (3.5) and (3.6)), we may write the covariance between two coefficients, a_k and a_l , as

$$\text{cov}(a_k, a_l) = \sum_{i,j} \frac{q_{k,i} q_{l,j}}{\sigma_i^2 \sigma_j^2} \text{cov}(\nu_{\text{obs},i}, \nu_{\text{obs},j}). \quad (3.9)$$

If we assume the individual frequencies to be independent, which is usually the case,

$$\text{cov}(\nu_{\text{obs},i}, \nu_{\text{obs},j}) = \delta_{ij} \sigma_i^2, \quad (3.10)$$

and, since the \mathbf{q}_k are orthonormal, we obtain

$$\text{cov}(a_k, a_l) = \delta_{kl}. \quad (3.11)$$

This property will allow us to build seismic indicators that are as little correlated as possible. They will serve as stringent constraints on the stellar structure with reduced standard deviations, compared to classical indicators (see Sect. 3.2.3).

Finally, the squared distance between reference frequencies $\boldsymbol{\nu}_{\text{obs}}$ and fitted frequencies $\boldsymbol{\nu}_{\text{fit}}$, given by

$$\chi^2 = \|\boldsymbol{\nu}_{\text{obs}} - \boldsymbol{\nu}_{\text{fit}}\|^2 = \sum_i \frac{(\nu_{\text{obs},i} - \nu_{\text{fit},i})^2}{\sigma_i^2}, \quad (3.12)$$

represents the quality of the fit.

Basis elements

As we mostly observe high radial order modes, we may approximate the smooth component by the first order asymptotic formulation of the frequencies as in [Tassoul \(1980\)](#) and [Gough \(1986\)](#),

$$\nu(n, l) \simeq \left(n + \frac{l}{2} + \epsilon \right) \Delta\nu, \quad (3.13)$$

where ϵ is a constant offset mainly affected by the most superficial layers and $\Delta\nu$ is the asymptotic large separation given by

$$\Delta\nu = \left(2 \int_0^{R_*} \frac{dr}{c(r)} \right)^{-1}, \quad (3.14)$$

with R_* the radius at the photosphere and $c(r)$ the adiabatic sound speed. To be more thorough and account for higher order variations, we actually depict the smooth component with second order polynomials,

$$p^k = n^k, \quad (3.15)$$

with $k = \{0, 1, 2\}$.

The method uses a linearised formulation for the glitch contribution adapted from Verma et al. (2014, Eq. 5):

$$\delta\nu_{g,\text{Verma}} = \mathcal{A}_{\text{He}}\nu e^{-c_2\nu^2} \sin(4\pi\tau_{\text{He}}\nu + \phi_{\text{He}}) + \frac{\mathcal{A}_{\text{CZ}}}{\nu^2} \sin(4\pi\tau_{\text{CZ}}\nu + \phi_{\text{CZ}}), \quad (3.16)$$

where ν is the frequency at which the glitch is evaluated, \mathcal{A}_\bullet the amplitude of the glitch (either the helium, He subscript, or convection zone glitch, CZ), τ_\bullet its acoustic depth, ϕ_\bullet its phase, and c_2 the rate of decrease in amplitude. To provide a value for the glitch contribution, we would need to adjust the fitting parameters (amplitudes, acoustic depths, phases, and rate of decrease) to the observed frequencies. However, we note that this formulation is not linear, both in the fitting parameters and in the frequency at which it is evaluated. Moreover, the formulation is implicit as the frequency is function of itself. Therefore, a non-linear approach is necessary. However, by replacing the frequency by its first order approximation from Eq. (3.13), $\nu \simeq (n + l/2)\Delta\nu$, the formulation becomes explicit. Furthermore, we managed to provide a linearised expression that properly accounts for the glitches. It is the following:

$$\begin{aligned} \delta\nu_g &= \sum_{k=5}^4 [s_{\text{He},k} \sin(4\pi T_{\text{He}}\tilde{n}) + c_{\text{He},k} \cos(4\pi T_{\text{He}}\tilde{n})] \tilde{n}^{-k} \\ &+ [s_{\text{CZ}} \sin(4\pi T_{\text{CZ}}\tilde{n}) + c_{\text{CZ}} \cos(4\pi T_{\text{CZ}}\tilde{n})] \tilde{n}^{-2}. \end{aligned} \quad (3.17)$$

The first line corresponds to the helium glitch contribution and the second line corresponds to the convective zone contribution, where we define $T_\bullet = \tau_\bullet\Delta\nu$ and $\tilde{n} = n + l/2$. We point out that the reverse order of the sum in the helium term reflects the order in which the basis elements are defined. The coefficients to be adjusted are $s_{\text{He},k}$, $c_{\text{He},k}$, s_{CZ} , and c_{CZ} . The phase term present in Eq. (3.16) is now accounted for through the separation in sine and cosine functions. The only remaining parameter which is not linear is the period of the glitch, the T_\bullet parameter. Nevertheless, using a proper estimate for it is sufficient and leaves us with a simple linear formulation of the glitch. We showed that a misestimate of its value by 10% still yields correct values for the glitch amplitude. This estimation is carried via a stellar model, accounting for the smooth component of the considered spectrum, by computation (via integration) of the acoustic depth at which the glitch occurs. This may be seen as a limitation of the technique as it requires to provide a first stellar model reproducing the smooth seismic indicators of an observed star. As a consequence, the development of a model independent estimation of τ_{He} was the subject of the master thesis of one of our students, Angelo Valentino. This will be discussed in Sect. 3.5.

The complete set of functions used to represent the oscillation spectrum, before orthonormalisation, is made of:

- The smooth component,

$$\nu_{\text{smooth},l}(n) = \sum_{k=0}^2 c_{k,l} n^k, \quad (3.18)$$

with $c_{k,l}$ some fitting coefficients. We note the dependency on the spherical degree as the smooth part of the spectrum is affected by deep layers of the stars that impact differently the several spherical degrees. This is not the case for the glitch component which is mostly affected by the outer layers of the stars. Also, we explicitly wrote the dependency of ν on n to insist on the fact that the basis elements are function of the radial order. When it is more convenient, we switch to a subscript notation, that is to say $\nu_{l,n}$;

- The helium glitch contribution,

$$\delta\nu_{\text{He}}(\tilde{n}) = \sum_{k=5}^4 [s_{\text{He},k} \sin(4\pi T_{\text{He}}\tilde{n}) + c_{\text{He},k} \cos(4\pi T_{\text{He}}\tilde{n})] \tilde{n}^{-k}; \quad (3.19)$$

- And the convection zone glitch contribution,

$$\delta\nu_{\text{CZ}}(\tilde{n}) = [s_{\text{CZ}} \sin(4\pi T_{\text{CZ}}\tilde{n}) + c_{\text{CZ}} \cos(4\pi T_{\text{CZ}}\tilde{n})] \tilde{n}^{-2}. \quad (3.20)$$

We observe that, for a star with modes observed in L different spherical degrees, as 3 different basis elements are defined for the smooth part, 3 individual modes have to be observed per spherical degree to be able to fit the smooth component. Then, for the glitches, the helium contribution requires to adjust 4 more parameters and the convection zone contribution requires 2 parameters. Overall, at least $3 \times L + 6$ modes are necessary to be able to account for both the smooth and glitches contributions.

We must add that, up to now, the convection zone glitches we measured were of very low amplitude and bore little information. It was therefore never used as relevant information to constrain stellar models. It may however happen that we encounter data with a more pronounced convection zone glitch.

We do not provide the analytical form of the orthonormal basis elements here as they are unnecessarily complex and dependent on the set of reference data, through the scalar product (Eq. (3.5)). However, we represent in Figs. 3.3 and 3.4 the orthonormalisation and fitting processes with data representative of 16 Cyg A for which we artificially amplified the convection zone glitch signal. The top panel of Fig. 3.3 shows the reference frequencies with their uncertainties, compared to their first order approximation as a solid line. We note that, this is already an excellent approximation. Nevertheless, faint signatures still remain to be retrieved. The second order approximation of the frequencies is represented in the bottom panel of the same figure. We display the residuals of the first order approximation, $\delta\nu = \nu - \nu_{\text{lin}}$ with ν_{lin} the linear approximation, as the second order contribution is about two orders of magnitudes smaller than the first order. We observe an oscillating departure of the reference data with respect to the fitted curve. This corresponds to the glitch.

The top panel of Fig. 3.4 shows the residuals of the fitting of the smooth part of the spectrum for all the spherical degrees² as a function of $\tilde{n} = n + l/2$. The dominant contribution is the helium glitch signature, represented by the continuous line. We observe that the signal is one order of magnitude smaller than the second order representation of the frequencies. This clearly demonstrates the necessity to acquire precise data and use techniques able to take the most advantage of such data. Finally, we display the helium glitch fitting residual in the bottom panel of Fig. 3.4. Even though we artificially amplified this signal to be visible, it remains extremely faint in the case of 16 Cyg A and may not be exploited. This will be further discussed later (see for example Sect. 3.2.3 and Table 3.2).

To conclude this section, we add that we tested other possibilities for the smooth basis elements, in an iterative way, but that the selected basis turned out to be the most appropriate and stable. For example, inspired by the second term in the higher order asymptotic expansion (Tassoul 1980; Gough 1986),

$$\nu(n, l) \simeq \left(n + \frac{l}{2} + \epsilon \right) \Delta\nu - A (L_l^2 - \delta) \frac{\Delta\nu^2}{\nu(n, l)}, \quad (3.21)$$

with L_l the Lamb frequency (Eq. (2.59)), δ a constant of the equilibrium, and

$$A = \frac{1}{4\pi^2 \Delta\nu} \left[\frac{c(R)}{R} - \int_0^R \frac{1}{r} \frac{dc}{dr} \right], \quad (3.22)$$

we tested a polynomial basis element in n^{-1} . However, the quadratic polynomial yielded better results.

²We recall that the glitch fitting is carried out simultaneously for all spherical degrees as its signature is expected to be independent of the spherical degree.

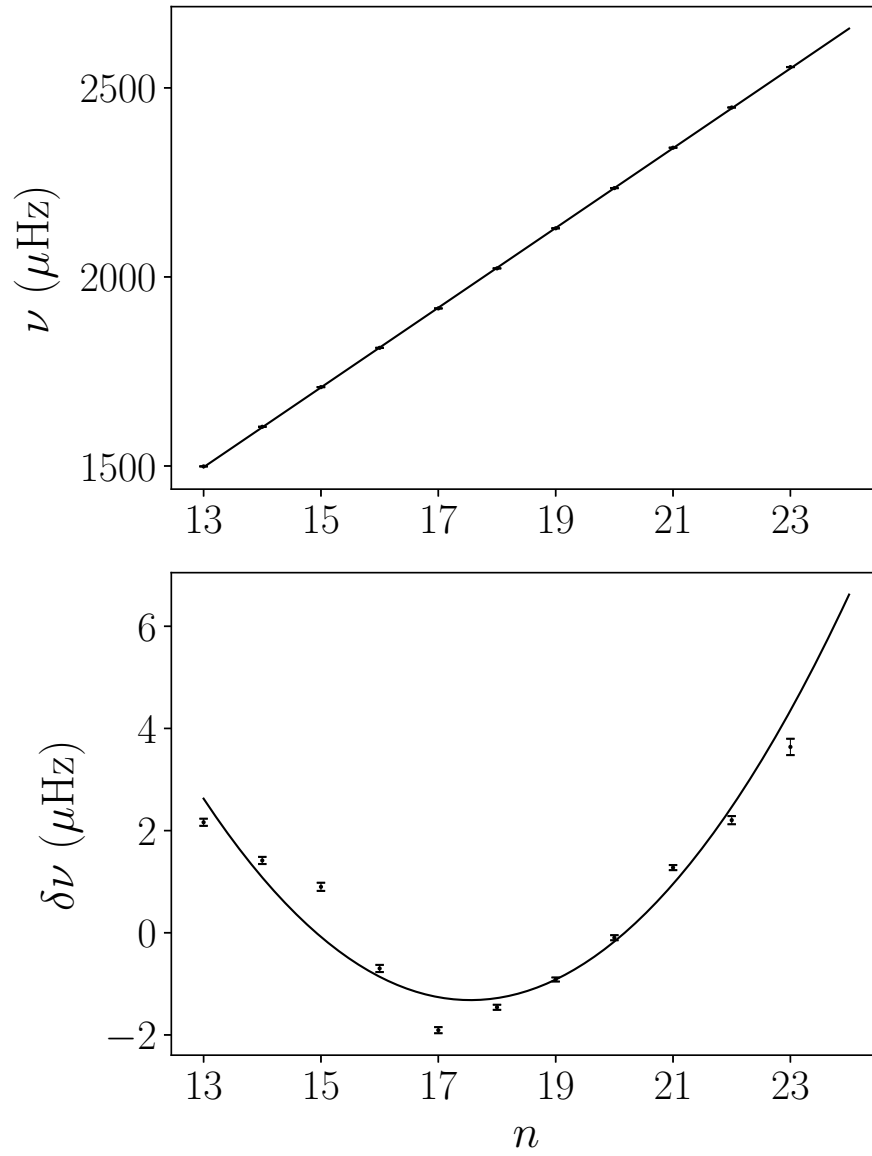


Figure 3.3: Visualisation of the orthonormalisation process and fitting procedure for the smooth component of the oscillation spectrum. *Top*: reference radial frequencies as a function of the modes radial order. The solid line represents the first order adjustment. *Bottom*: residuals of the first order adjustment of radial modes as a function of the radial order. The solid line represents the second order basis element.

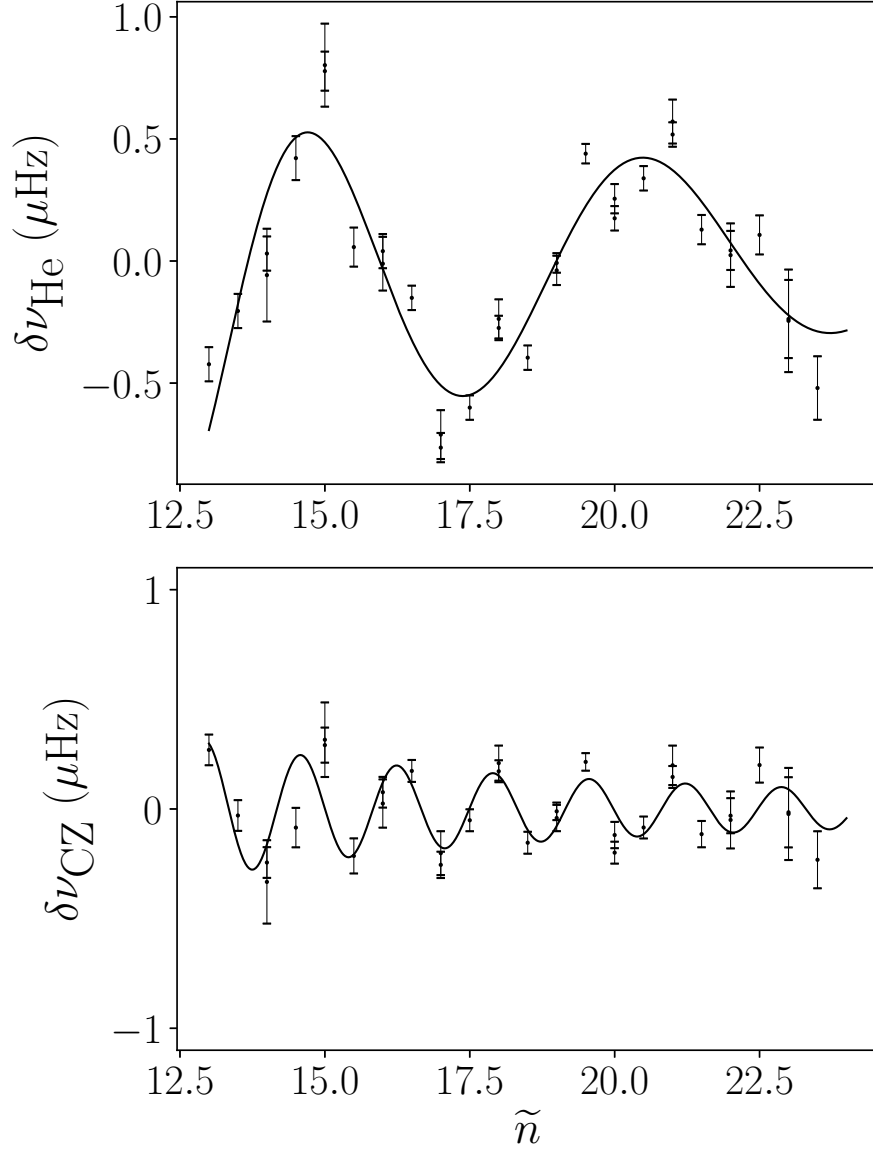


Figure 3.4: Visualisation of the orthonormalisation process and fitting procedure for the glitch component of the oscillation spectrum. *Top*: residuals of the smooth component adjustment of all the modes as a function of $\tilde{n} = n + l/2$. The solid line represents the helium glitch basis element. *Bottom*: residuals of the smooth and helium glitch components adjustment of all the modes as a function of \tilde{n} . The solid line represents the convection zone glitch basis element.

3.2.3 Seismic indicators

In the present section, we define seismic indicators of the WhoSGIAd method relevant to the stellar structure which will be used as constraints to stellar models.

Stellar models

To study the probing potential of the seismic indicators that we define in the present section, we built a series of models with the CLES stellar evolution code (Scuflaire et al. 2008b) and computed the frequencies associated with each model using the LOSC oscillation code (Liège Oscillation code Scuflaire et al. 2008a). We used the 16 Cygni A frequencies measured by Davies et al. (2015) as a reference to keep consistent basis elements throughout the grid of models. This ensures that our results are comparable. The reference stellar parameters are given in Table 3.1. The choices of physical reference tables are detailed in (Farnir et al. 2019, Sect. 3.1).

The large separation

One crucial step of the method is the Gram-Schmidt orthonormalisation. To construct the basis, we proceed in a carefully chosen order to easily define seismic indicators. First, we orthonormalise basis elements of the smooth component for each spherical degree with increasing polynomial degrees. Thus, the first element considered is the constant contribution for the radial modes ($l = 0, k = 0$). Next comes the first order polynomial for radial modes ($l = 0, k = 1$), and so on. This is especially interesting as, to first order, frequencies may be approximated by the asymptotic formulation (Eq. (3.13)) which is a linear function of the radial order and its slope is $\Delta\nu$, the asymptotic large separation (see the top panel of Fig. 3.3 for a representation). Therefore, for each spherical degree, the projection of the frequencies over the two first basis elements ($k = 0, 1$) provides us with a linear adjustment of the frequencies and an estimator of the large separation. For a given spherical degree l and limiting the development to the first order ($k = 1$), Eq. (3.4) combined with Eq. (3.7) yields

$$\begin{aligned}\nu_{\text{fit}, k \leq 1} &= \sum_{k=0}^1 a_{l,k} \sum_{k_0}^k R_{l,k_0,k}^{-1} n^{k_0} \\ &= a_{l,0} R_{l,0,0}^{-1} + a_{l,1} \left(R_{l,0,1}^{-1} + R_{l,1,1}^{-1} n \right),\end{aligned}\quad (3.23)$$

where the spherical degree, l , is explicitly written in order to ease the understanding.

We easily identify the slope in n and we define the estimator of the large separation for each individual spherical degree,

$$\Delta_l = a_{l,1} R_{l,1,1}^{-1}. \quad (3.24)$$

It may also be expressed more explicitly as a function of frequencies and radial orders as follows; Given the vector of frequencies associated with the spherical degree l , $\boldsymbol{\nu}_l$, and the vector of corresponding radial orders, \boldsymbol{n}_l , we may write:

$$\Delta_l = \frac{\langle \boldsymbol{\nu}_l | \boldsymbol{n}_l \rangle / \|\mathbf{1}\|^2 - \overline{\boldsymbol{n}_l} \overline{\boldsymbol{\nu}_l}}{\|\boldsymbol{n}_l\|^2 / \|\mathbf{1}\|^2 - \overline{\boldsymbol{n}_l}^2}, \quad (3.25)$$

Table 3.1: Reference stellar parameters.

Parameter	Value
X_0	0.734
Y_0	0.25
Z_0	0.016
$(Z/X)_0$	0.022
α_{MLT}	1.82
α_{ov}	0
α_{un}	0

where the $\bar{\cdot}$ symbol represents the weighted mean of a given quantity and is defined as

$$\bar{\nu}_l = \frac{\langle \nu_l | \mathbf{1} \rangle}{\|\mathbf{1}\|^2} = \frac{\sum_{i=1}^N \nu_{l,n_i} / \sigma_i^2}{\sum_{i=1}^N 1 / \sigma_i^2}. \quad (3.26)$$

Eq. (3.25) is equivalent to its standard definition obtained through a linear regression (see e.g. [Reese et al. \(2012\)](#)). We provide additional mathematical developments to retrieve this form in App. 3.A.

We may also define the mean large separation over all spherical degrees corresponding to the weighted mean value, $\bar{\Delta}_l$, of the individual large separations for each spherical degree. We get

$$\Delta = \bar{\Delta}_l = \frac{\sum_l \Delta_l / \sigma^2(\Delta_l)}{\sum_l 1 / \sigma^2(\Delta_l)}, \quad (3.27)$$

with $\sigma(\Delta_l) = R_{l,1,1}^{-1}$ the uncertainty on the large separation of degree l . This is an indicator of the mean stellar density ([Ulrich 1986](#)) and it is mostly sensitive to the mass and age of the star. Therefore, on the main sequence, at a given mass, composition, and set of input physics, it is an indicator of stellar evolution. Indeed, its value decreases along the stellar evolution. This is also true on the subgiant phase and for most of the red giant phase (see for example [Christensen-Dalsgaard 1988](#); [Mosser et al. 2011](#)).

Normalised small separations

Common and useful seismic indicators are the small separations of modes, which isolate the contribution of the second term in Eq. (3.21). They are usually defined by comparison of higher-degree modes with radial modes as, for example,

$$d_{01} = (\nu_{n,1} - 2\nu_{n,0} + \nu_{n+1,1}) / 2, \quad (3.28)$$

$$d_{02} = \nu_{n,0} - \nu_{n-1,2}. \quad (3.29)$$

However, these are sensitive to the surface effects, mostly caused by the non-adiabaticity in the outermost layers of the star, which we poorly understand. For this reason, [Roxburgh & Vorontsov \(2003\)](#) proposed to define frequency ratios which they empirically demonstrated to be almost independent of these outermost layers

$$r_{01}(n) = \frac{d_{01}}{\Delta_{r,1}(n)}, \quad (3.30)$$

$$r_{02}(n) = \frac{d_{02}}{\Delta_{r,1}(n)}, \quad (3.31)$$

with $\Delta_{r,l}(n) = \nu_{n,l} - \nu_{n-1,l}$ the local large separation associated with the degree l . Taking inspiration in their definition, we define our estimator of the small separation ratio between the spherical degrees 0 and l as

$$\hat{r}_{0l} = \frac{\bar{\nu}_0 - \bar{\nu}_l}{\Delta_0} + \bar{n}_l - \bar{n}_0 + \frac{l}{2}. \quad (3.32)$$

By definition, these quantities are dimensionless.

We show in Fig. 3.5 the evolution of the small separation ratios for degrees 1 (top), 2 (middle) and 3 (bottom) with Δ_0 over a grid of models extending from the zero-age main sequence (ZAMS) to the terminal-age main sequence (TAMS). As Δ_0 decreases with the evolution on the main sequence, the evolution goes from right to left. The models span masses from $0.9 M_\odot$ to $1.3 M_\odot$ with a step of $0.1 M_\odot$. Except for the coloured tracks, all the models have the reference values for the stellar parameters presented in Table 3.1. The sequence for $1.06 M_\odot$, close to the expected mass for 16 Cyg A ([Ramírez et al. 2011](#); [White et al. 2013](#)), is shown as a thick line. We show variations of this track with different colours; in blue for $Y_0 = 0.27$ and with the reference value for $(Z/X)_0$, orange for $\alpha_{\text{MLT}} = 1.5$, and pink for $(Z/X)_0 = 0.018$ and the reference Y_0 value. We also display the measured value of the separation ratios for 16 Cyg A as blue markers. In addition, we show the value corrected for the surface effects following [Kjeldsen et al. \(2008\)](#) and using the fitted coefficients from [Sonoï et al. \(2015\)](#), in red.

We first observe in this figure that the small separation ratios are indeed almost independent of the surface effects, with \hat{r}_{02} being the most impacted. We observe that \hat{r}_{02} (middle panel) monotonously

decreases with evolution, similarly to Δ_0 , making it an excellent indicator of the central conditions and stellar evolution. We note the same trend as the so-called ‘seismic HR diagram’ defined by [Christensen-Dalsgaard \(1988\)](#) who showed that placing an observed star in such a diagram allows us to constrain its mass and age. We also observe on the top panel that, while the evolution of \hat{r}_{01} is not monotonous, it follows a different trend than \hat{r}_{02} . This indicator therefore bears information that are not redundant with \hat{r}_{02} . Conversely, \hat{r}_{03} follows the same trend as \hat{r}_{02} and therefore does not bring any new piece of information.

We observe in the middle and bottom panels of Fig. 3.5 that the inclusion of a reduced mixing length parameter ($\delta\alpha_{\text{MLT}} = 0.3$), at fixed stellar parameters, is similar to an increase in the stellar mass (of about $\delta M \sim 0.05 M_{\odot}$), as the orange track illustrates. Similarly, increasing the initial helium content ($\delta Y_0 = 0.02$), showed by the blue line, also impacts the seismic indicator similarly to an increase in the stellar mass (of about $\delta M \sim 0.04 M_{\odot}$). We also note that the slope of the \hat{r}_{02} - Δ_0 track is slightly modified, reducing the rate of decrease in \hat{r}_{02} with evolution. Finally, increasing the metal content ($\delta(Z/X)_0 \simeq 0.04$), in pink, again produces similar results to an increase in the stellar mass ($\delta M \sim 0.02 M_{\odot}$) with a reduction of the slope in \hat{r}_{02} as for the case with increased helium content. All these observations are in perfect agreement with the results of [Mazumdar \(2005\)](#).

We represent in Fig. 3.6 the evolution of the small separation ratios as defined in [Roxburgh & Vorontsov \(2003\)](#) (Eq. (3.30)) evaluated at $n = 21$ with Δ_0 . The trends presented in Fig. 3.5 and 3.6 are comparable; with our representation displaying a smoother evolution. Furthermore, because we define the small separation ratios as an average over the complete set of radial orders while [Roxburgh & Vorontsov \(2003\)](#) use a local definition, we should obtain reduced uncertainties compared to them. It is indeed what we observe from the red marker in Fig. 3.6, with $\sigma(r_{0l}) \sim 3\sigma(\hat{r}_{0l})$.

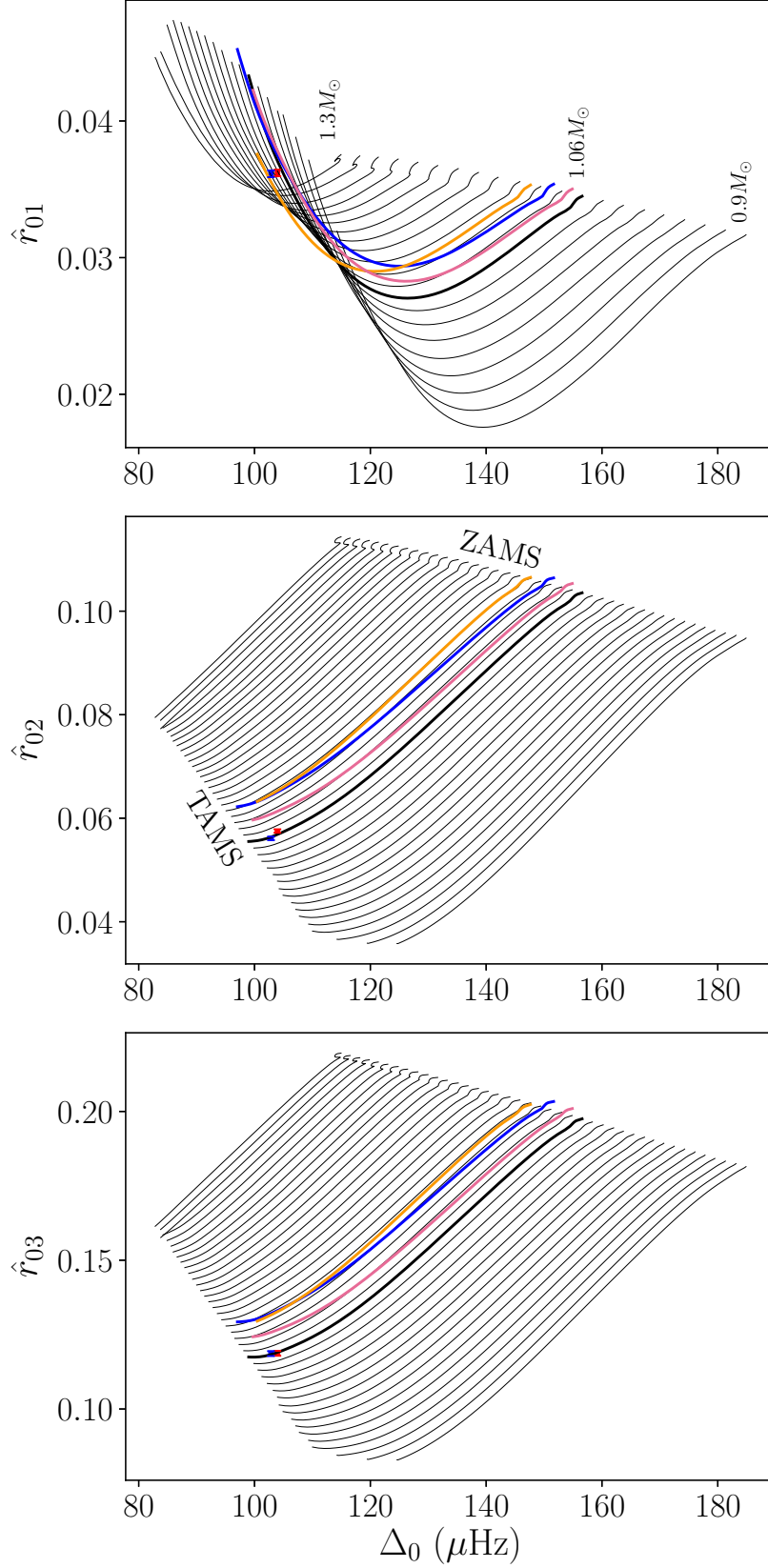


Figure 3.5: Evolution of the small separation ratios defined in Eq. (3.32) over a grid of models with $X_0 = 0.734$, $Y_0 = 0.25$, $Z_0 = 0.016$, and $\alpha_{\text{MLT}} = 1.82$. The models span masses in the range $[0.9 M_\odot, 1.3 M_\odot]$ ($0.01 M_\odot$ step). The thick line corresponds to the $1.06 M_\odot$ track, the blue line to $Y_0 = 0.27$ at reference $(Z/X)_0$ ratio, the orange one to $\alpha_{\text{MLT}} = 1.5$, and the pink one to $(Z/X)_0 = 0.018$ at reference Y_0 value.

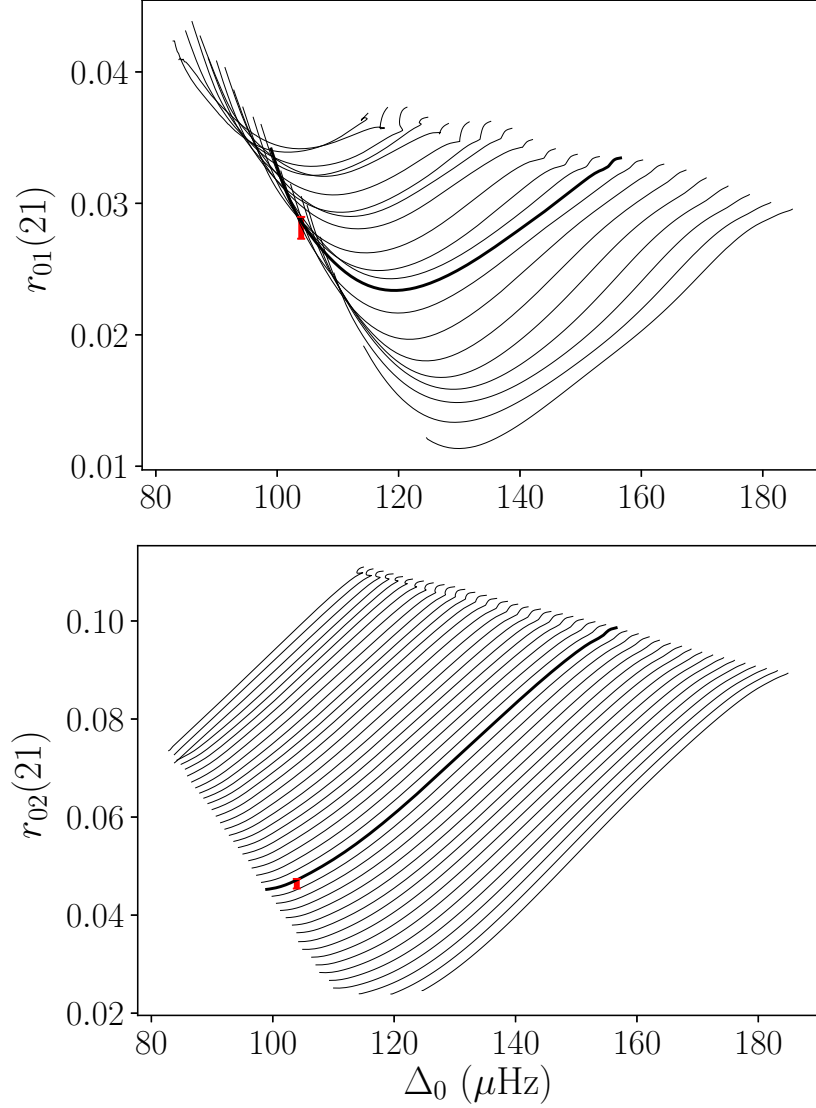


Figure 3.6: Evolution of the small separation ratios as defined in Eq. (3.30) (Roxburgh & Vorontsov 2003) over the same grid as in Fig. 3.5.

Large separation differences

These are the differences between the large separations of individual spherical degrees 0 and l normalised to the large separation of radial modes,

$$\Delta_{0l} = \frac{\Delta_l}{\Delta_0} - 1. \quad (3.33)$$

Δ_{01} corresponds to the slope of the local small separation ratio between orders 0 and 1 as a function of n . Indeed, by defining a local version of Eq. (3.32),

$$\hat{r}_{0,l}(n) \simeq \frac{\nu_{n,0} - \nu_{n,l}}{\Delta_0}, \quad (3.34)$$

we easily obtain this slope, with an opposite sign compared to Eq. (3.33). Combined with our indicator \hat{r}_{01} , which provides an estimate of the mean $r_{01}(n)$ value, we obtain information relative to the amount of core overshooting. We present in Fig. 3.7 a \hat{r}_{01} - Δ_{01} diagram for $1.2 M_{\odot}$ tracks with different overshooting parameter values in the range $[0.005, 0.300]$. This figure was also presented in Farnir et al. (2019), Fig. 3. Indeed, the evolutionary tracks occupy different regions according to the amount of overshooting included in the model. This coincides with observations from Deheuvels et al. (2016) who noted that

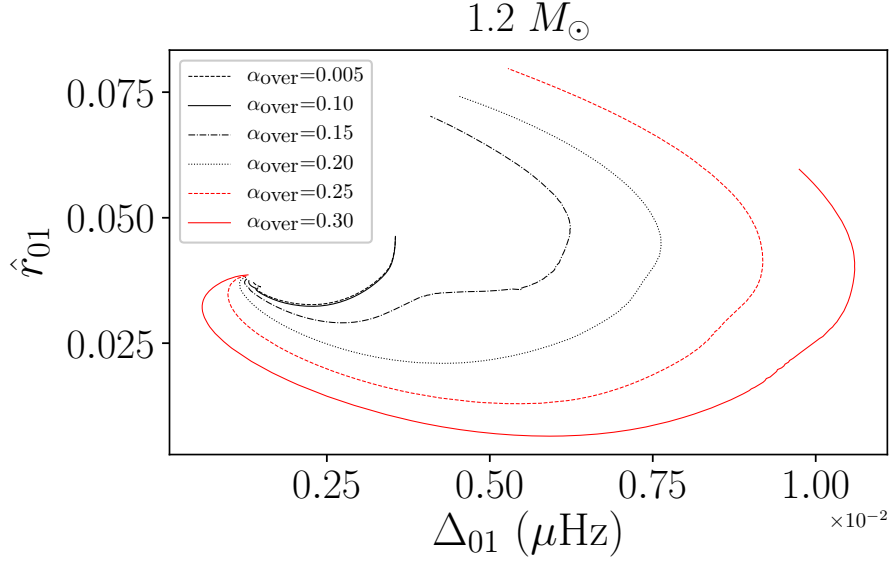


Figure 3.7: \hat{r}_{01} - Δ_{01} diagram for several main sequence $1.2 M_{\odot}$ tracks with different overshooting parameter values as in [Farnir et al. \(2019\)](#), Fig. 3.

the simultaneous use of the mean value, denoted a_0 , and slope, a_1 , of the small separation ratio between degrees 0 and 1 allows us to constrain central overshooting. We further illustrate this potential in Figs. 3.9 and 3.10. These represent the \hat{r}_{01} and Δ_{01} values for a set of models adjusting the Δ value of KIC7510397 and KIC7206837, respectively. The different colours correspond to different values of the overshooting parameter (0.00, 0.10, 0.15, 0.20, 0.25, and 0.30) and individual models to different masses in the range $[1.10 M_{\odot}, 1.50 M_{\odot}]$ with a step of $0.02 M_{\odot}$. The masses increase from the top to the bottom of both figures. We also represent the observed \hat{r}_{01} and Δ_{01} values by the errorbars. We observe that placing a star in such a diagram constrains both its mass and overshooting parameter. For KIC7510397 we expect a low overshooting parameter value, close to zero, while we expect a value of about 0.15 in the case of KIC7206837. The advantage of our method is that these indicators are automatically included and are as little correlated as possible to the other ones. This is important when using several indicators alongside one another to retrieve the most robust inferences possible.

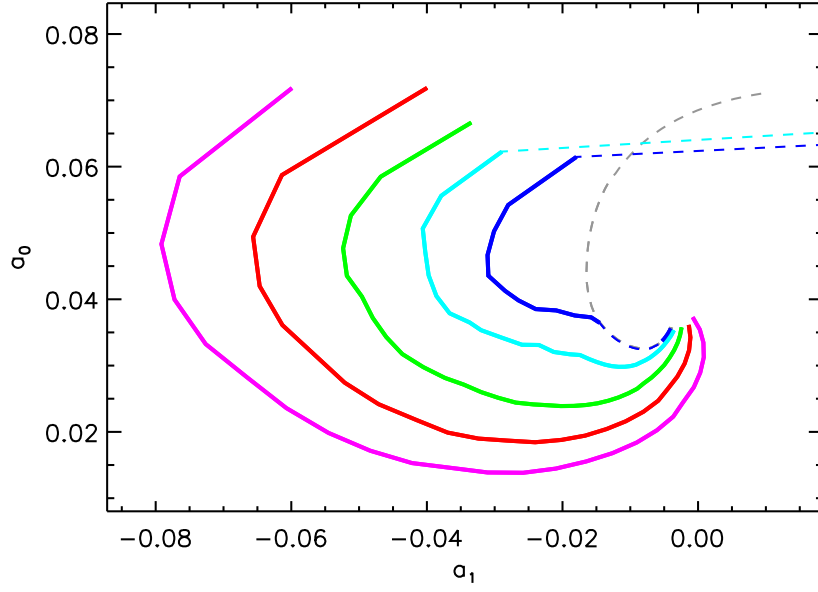


Figure 3.8: Fig. 3 of [Deheuvels et al. \(2016\)](#). a_0 represents the mean value of the small separation ratio between degrees 0 and 1 and a_1 is the slope in n of this ratio. The different colours correspond to different overshooting parameter values $\alpha_{\text{ov}} = 0$ (grey), $\alpha_{\text{ov}} = 0.1$ (blue), $\alpha_{\text{ov}} = 0.15$ (cyan), $\alpha_{\text{ov}} = 0.2$ (green), $\alpha_{\text{ov}} = 0.25$ (red), and $\alpha_{\text{ov}} = 0.3$ (pink).

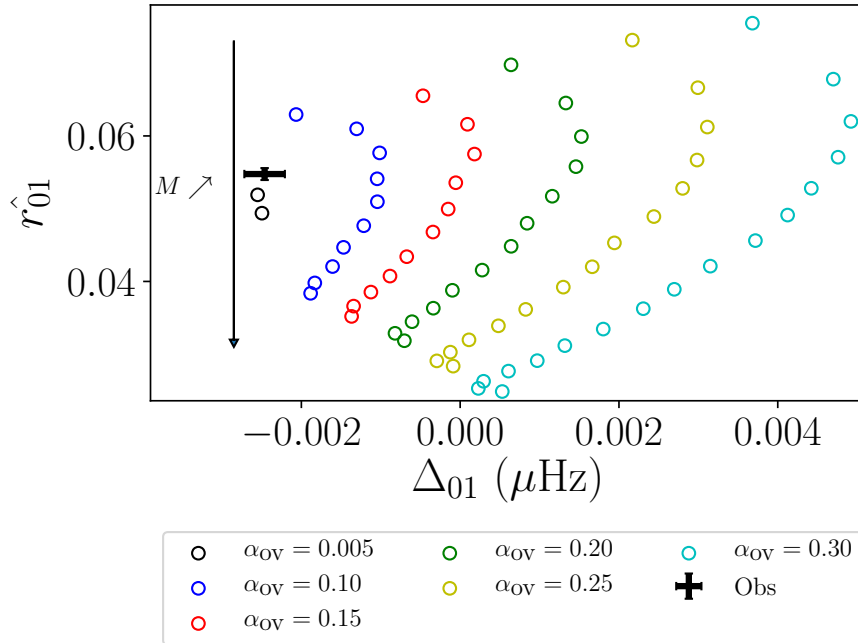


Figure 3.9: \hat{r}_{01} - Δ_{01} diagram for models adjusting the large separation, Δ , of KIC7510397 for several masses and overshooting parameter values, represented by the colours. The masses range from $1.10 M_{\odot}$ (top) to $1.50 M_{\odot}$ (bottom) with a step of $0.02 M_{\odot}$. The observed values are represented by the errorbars.

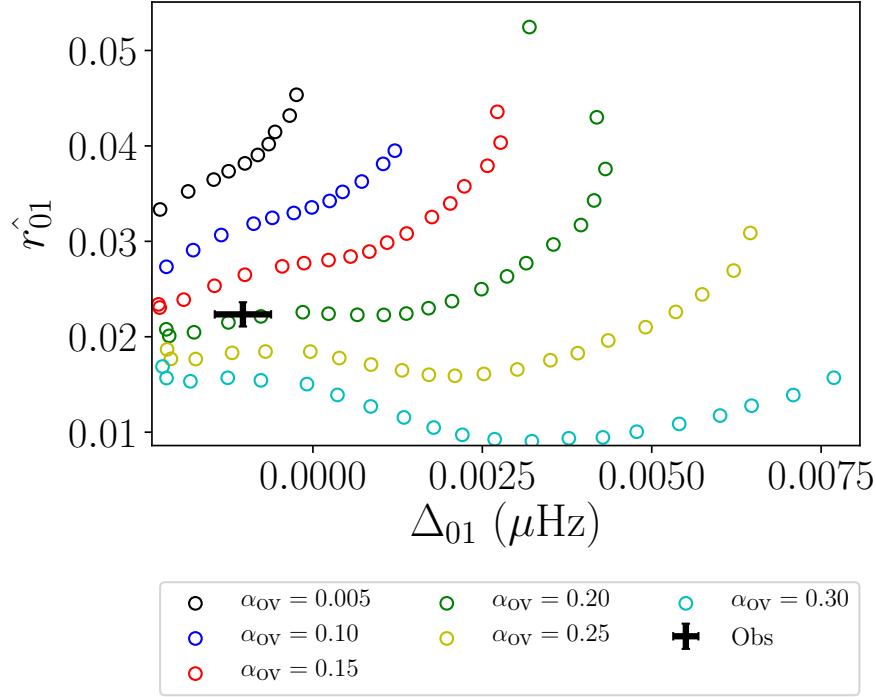


Figure 3.10: \hat{r}_{01} - Δ_{01} diagram for models adjusting the large separation, Δ , of KIC7206837 for several masses and overshooting parameter values, represented by the colours. The masses range from $1.10 M_{\odot}$ (top) to $1.50 M_{\odot}$ (bottom) with a step of $0.02 M_{\odot}$. The observed values are represented by the errorbars.

$\hat{\epsilon}$ indicator

We may provide an estimator, $\hat{\epsilon}$, of the constant term, ϵ , in the asymptotic formulation (Eq. (3.13)). This term is mostly affected by the surface effects, as we showed in [Farnir et al. \(2019\)](#). To define its estimator, we define a vector subspace in which frequencies are described as

$$\nu(n, l) = \left(n + \frac{l}{2} + \epsilon\right) \hat{\Delta} = \left(n + \frac{l}{2}\right) \hat{\Delta} + K, \quad (3.35)$$

where $\hat{\Delta}$ and K are free parameters, and project the observed frequencies over this subspace. We then identify the coefficients to retrieve an expression for $\hat{\epsilon}$,

$$\hat{\epsilon} = \frac{\overline{\nu}}{\hat{\Delta}} - \overline{n}. \quad (3.36)$$

We note that $\hat{\Delta}$ has a different expression from our indicator Δ as a result of the slightly different basis. Its exact expression is not relevant to the current discussion.

We represent in Fig. 3.11, the evolution of the $\hat{\epsilon}$ indicator over the same grid of models as in Fig. 3.5. The observed value is shown in red, the corrected value for the surface effects following [Kjeldsen et al. \(2008\)](#) with the fitted coefficients of [Sonoi et al. \(2015\)](#) is shown in blue, and the one corrected as in [Sonoi et al. \(2015\)](#) is shown in green. We observe that the tracks are nearly degenerated for most of the stellar evolution on the main sequence. This makes this indicator difficult to exploit in order to constrain the stellar structure. Furthermore, we observe that its value is greatly impacted by the surface effects, as the coloured markers demonstrate. We therefore expect that measuring its value could help to provide information on the outermost layers of the star. Nevertheless, we were not able to efficiently exploit this indicator to constrain stellar models.

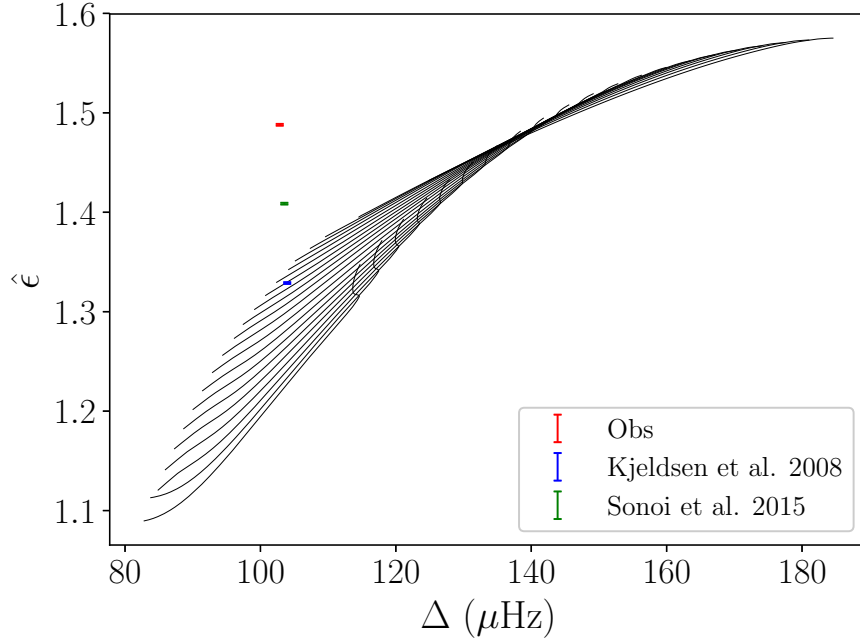


Figure 3.11: Evolution of $\hat{\epsilon}$ with Δ over the same grid of models as in Fig. 3.5. The observed value is shown in red, the one corrected for the surface effects as in Kjeldsen et al. (2008) with the fitted coefficients of Sonoai et al. (2015) is displayed in blue, and the one corrected as in Sonoai et al. (2015) is shown in green. This corresponds to Fig. 4 of Farnir et al. (2019).

Glitch amplitude

The last indicators we defined are the glitches amplitudes. Taking advantage of the orthonormalisation and the scalar product, it corresponds to the norm of the glitch term,

$$A_{\bullet} = \|\delta_{\bullet}\|, \quad (3.37)$$

with δ_{\bullet} being the considered glitch term (either helium or convection zone) symbolised by the \bullet index.

Because of this definition and of the orthonormalisation, the uncertainty on this indicator is always of unity and the contribution of the glitches is completely decorrelated of the smooth component of the spectrum. Furthermore, the helium glitch and convection zone glitch are independent of one another.

For the helium glitch, the amplitude is a proxy of the surface helium abundance but it also strongly depends on the metals mass fraction and the total mass (Farnir et al. (2019)). Figure 3.12 represents the evolution of the helium glitch amplitude with the surface helium abundance at fixed large separation, that of 16 Cyg A, and fixed metallicity. We consider different masses ($1 M_{\odot}$, $1.025 M_{\odot}$, and $1.052 M_{\odot}$) and also assess the impact of the surface effects (Kjeldsen et al. 2008 with the coefficients from Sonoai et al. 2015). We observe that, on each track, the helium glitch amplitude is directly correlated to the surface helium content. This is a direct consequence of the evolution of the shape of the Γ_1 index with the helium abundance (see Fig. 3.2). The greater the helium abundance, the more pronounced the Γ_1 depletion and the greater the helium glitch amplitude. We also observe by comparing the individual tracks that, the greater the mass, the greater the helium glitch amplitude. We note that, at fixed helium glitch amplitude, an increase in the mass of about $0.025 M_{\odot}$ requires a decrease in the surface helium abundance of about 0.01. The helium glitch amplitude is therefore degenerate with the mass. This is more easily interpreted with $\ln T - \ln P$ diagrams, in which the curves of different models are parallel in the second ionisation zone of helium. Only the height of these curves varies, the higher the curve, the shallower the Γ_1 dip and the lower the helium glitch amplitude. In such a diagram, the most massive models lie the lowest. Finally, the green track illustrates the impact of the surface effects on the helium glitch amplitude. We note that it has a negligible impact, compared to the uncertainty on the amplitude, as represented by the black symbol.

The helium glitch amplitude also exhibits an anti-correlation with the metals content. This is represented in Fig. 3.13 showing the evolution of the helium glitch amplitude at fixed $Y_0 = 0.24$ and Δ

values for different masses. The black curve corresponds to $1 M_{\odot}$, the blue to $1.025 M_{\odot}$, and the red to $1.052 M_{\odot}$. This means that a measurement of the helium glitch amplitude alone is not sufficient to constrain the surface helium content. This agrees with the findings of [Basu et al. \(2004\)](#). Nevertheless, the smooth component indicators may help to further constrain the chemical composition, namely \hat{r}_{01} , and thus to lift this degeneracy. To better understand the origin of this degeneracy, we built a toy model of the first adiabatic index (see Sect. 3.4). This allows us to isolate the impact of the helium and metals abundances from that of stellar evolution on the shape of the Γ_1 index. We find that an increased helium abundance leads to a more pronounced Γ_1 depletion in the helium second-ionisation zone. The same goes for a decreased metals abundance. We represent in Fig. 3.14 this toy model for different abundances. We show, as a black curve, the reference model. The red curves correspond to models with modified compositions and the blue ones to models for which the composition was modified without impacting the temperature and density profiles. The top panel corresponds to modifications in the helium content while the bottom panel corresponds to variations in the metals abundance. We observe, in the top panel, that the effect of the helium abundance on the Γ_1 profile is mainly due to the change in abundance rather than the modification of the stratification, as the blue and red curves are close to one another. Conversely, the impact of the metals abundance on Γ_1 is the result of the different T and ρ profiles after evolution. Indeed, we observe that the isolated effect of the modification of the composition is not significant, while the models with modified T and ρ profiles are significantly impacted.

We now turn our attention to the convection zone glitch amplitude, which is a proxy of the sharpness of the temperature gradient transition at the base of the convection zone. This is illustrated in Fig. 3.15 which represents the evolution of A_{CZ} with the amount of undershooting below the base of the convection zone. Including undershooting moves the base of the convection zone inwards. The nature of the undershooting, with the temperature gradient ∇ either being fixed at the adiabatic one ∇_{ad} or at the radiative one ∇_{rad} in the undershooting region, determines the nature of the discontinuity, as illustrated in Fig. 3.16. If we were to include radiative undershooting, only the derivative of the temperature stratification would be discontinuous and no glitch would arise. Conversely, with adiabatic undershooting, there is a discontinuity in the gradient and a glitch is created. As both Figs. 3.15 and 3.16 show, increasing the amount of undershoot increases the size of the jump in ∇ and thus leads to a greater glitch amplitude.

One advantage of our definition of the glitch amplitude (Eq. (3.37)) is that the associated uncertainty is always equal to unity. The strength of the glitch signal is always to be compared with 1. However, when comparing our results with other works, this may seem counter-intuitive. Indeed, an increase in the observed uncertainties leads to a reduced glitch amplitude, instead of increased uncertainties on that quantity. Therefore, to ease the comparison, we propose an alternate definition

$$A'_{\bullet} = \frac{A_{\bullet}}{\sqrt{\sum_{i=1}^N 1/\sigma_i^2}}. \quad (3.38)$$

This new definition has the units of frequencies. Moreover, it is invariant under a multiplication of the σ_i by a given factor. Finally, the uncertainty on the parameter is now given by

$$\sigma(A'_{\bullet}) = \frac{1}{\sqrt{\sum_{i=1}^N 1/\sigma_i^2}}, \quad (3.39)$$

which is proportional to the uncertainties on the frequencies. In the case of 16 Cygni A and B, switching from the first definition (Eq. 3.12) to the second (Eq. 3.38) corresponds to a multiplication by 0.15 of both the glitch amplitude and its uncertainty. We give both values in Table 3.2.

Table 3.2: Glitches amplitudes for 16 Cyg A and B uncorrected frequencies.

	A_{He}	A'_{He}	A_{CZ}	A'_{CZ}
16 Cyg A	29.59 ± 1	$4.44 \pm 0.15 \mu\text{Hz}$	1.84 ± 1	$0.28 \pm 0.15 \mu\text{Hz}$
16 Cyg B	33.42 ± 1	$5.01 \pm 0.15 \mu\text{Hz}$	1.58 ± 1	$0.24 \pm 0.15 \mu\text{Hz}$

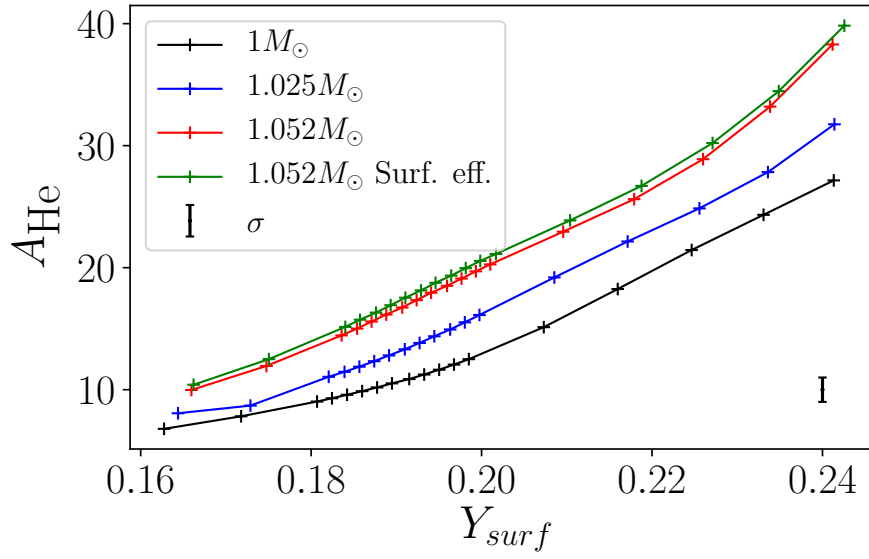


Figure 3.12: Helium glitch amplitude evolution with the surface helium abundance at fixed $(Z/X)_0 = 0.022$ value. We consider different masses, shown in different colours $1M_{\odot}$ (black), $1.025 M_{\odot}$ (blue), and $1.052 M_{\odot}$ (red). The green track corresponds to models corrected for the surface effects as in [Kjeldsen et al. \(2008\)](#) with the coefficients from [Sonoai et al. \(2015\)](#) for $1.052 M_{\odot}$. The black symbol corresponds to the uncertainty σ on the amplitude.

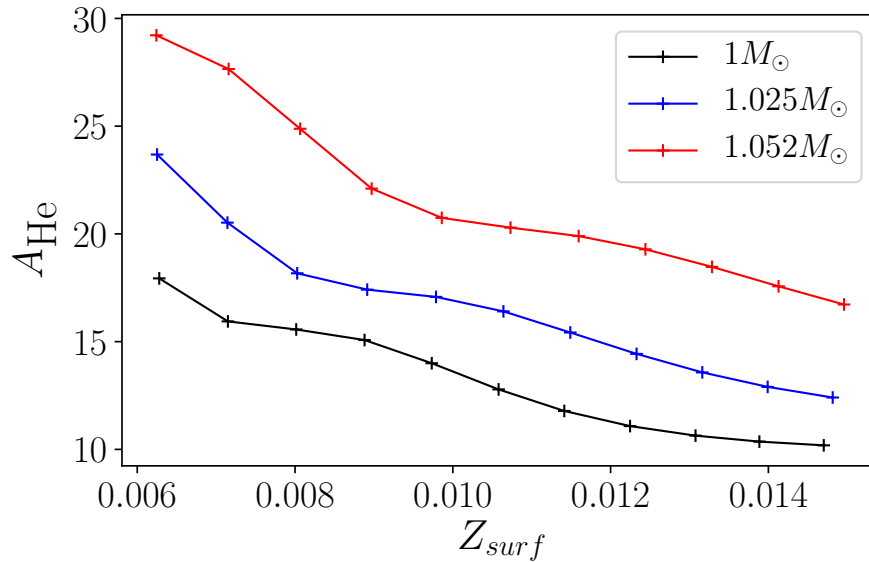


Figure 3.13: Helium glitch amplitude evolution with the surface metals abundance at fixed $Y_0 = 0.24$ value. We consider different masses, shown in different colours $1 M_{\odot}$ (black), $1.025 M_{\odot}$ (blue), and $1.052 M_{\odot}$ (red).

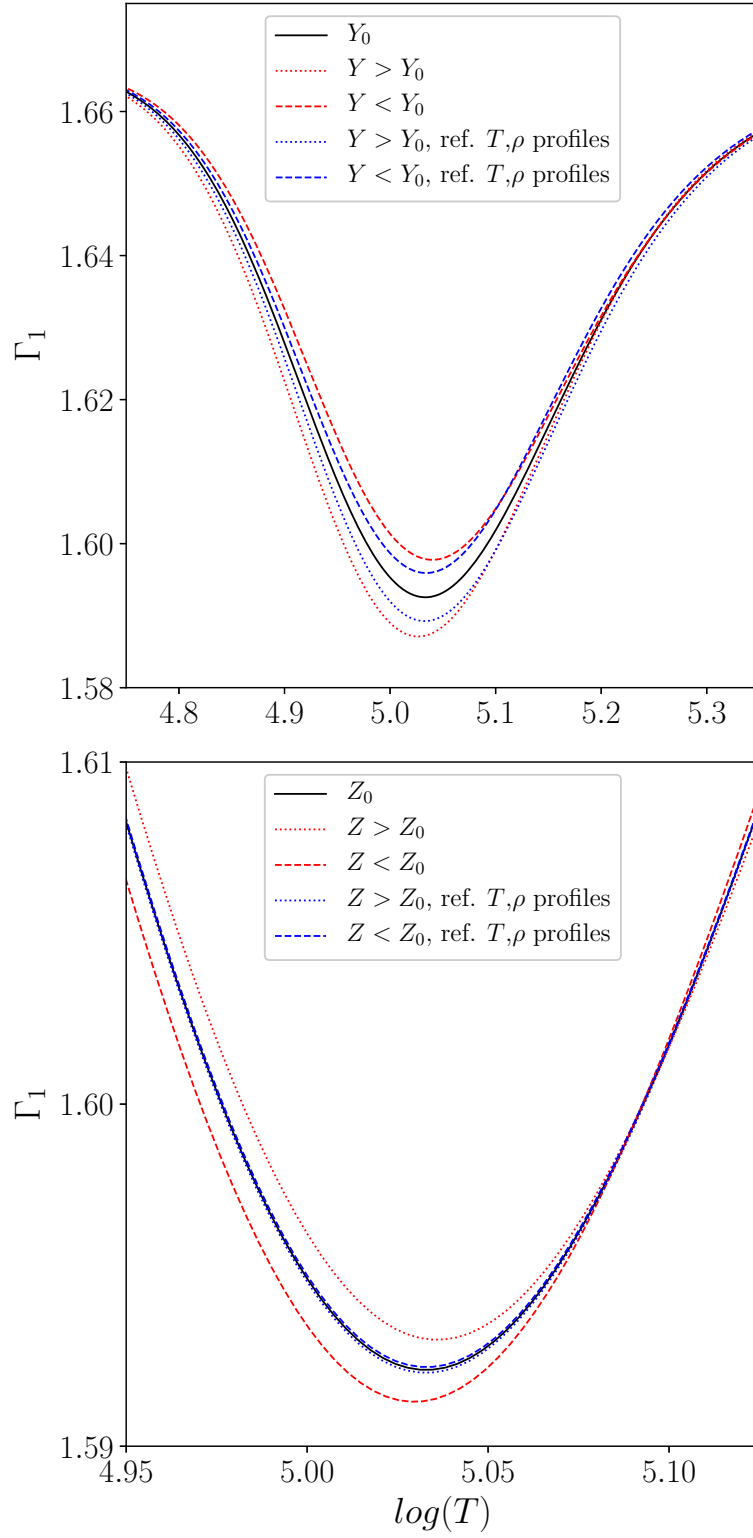


Figure 3.14: Γ_1 toy model in the helium second-ionisation zone. The reference model is shown in black, models with modified compositions but fixed ρ and T profiles are in blue and models with modified compositions and profiles are in red. The top panel shows the evolution with Y . Dotted lines have an increased abundance compared to the reference while dashed lines have a decreased abundance. The bottom panel shows the evolution with the metals abundance. The line styles have the same meaning.

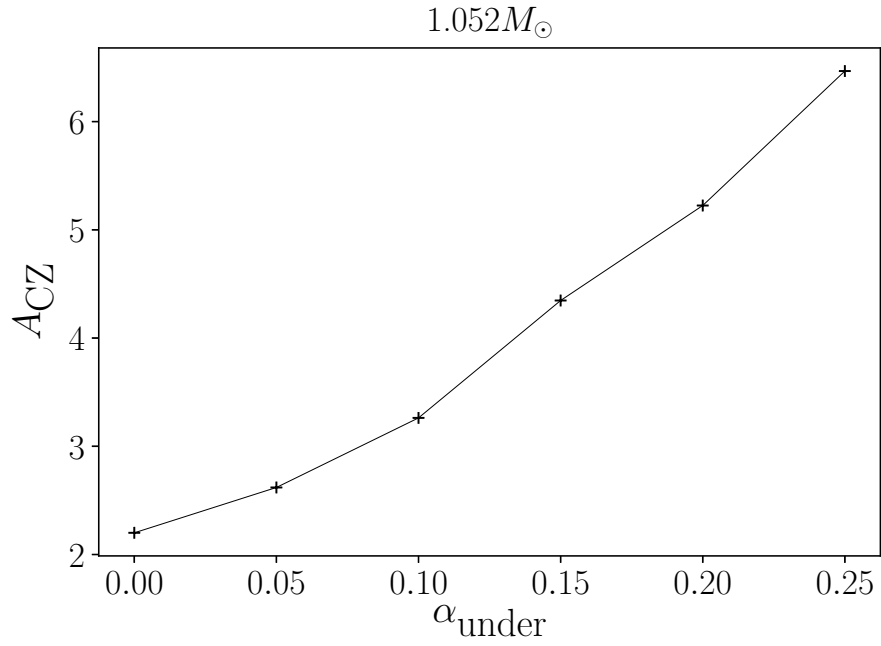


Figure 3.15: Evolution of the convection zone glitch amplitude with the amount of undershooting below the base of the convection zone.

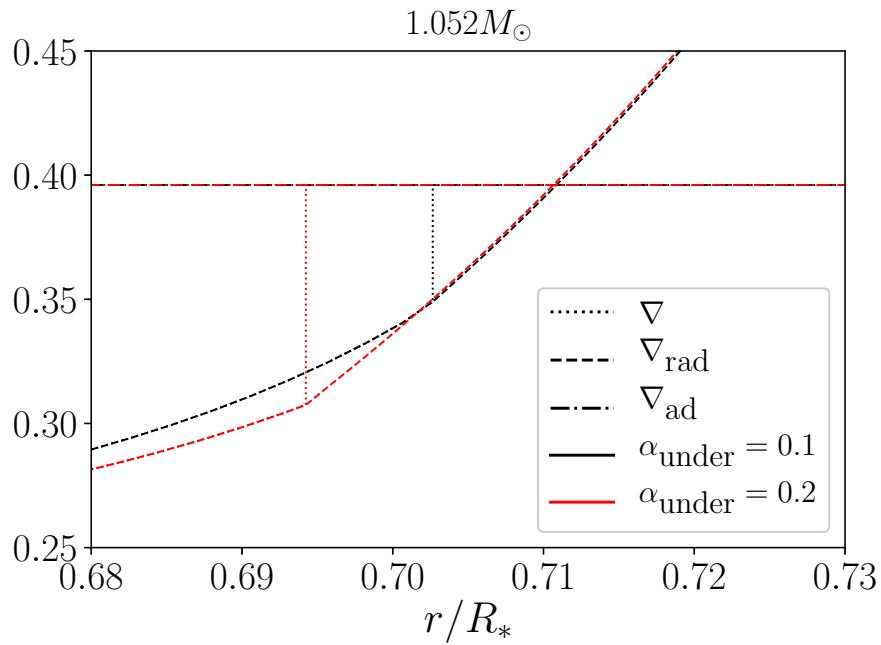


Figure 3.16: Temperature gradients around the base of the convection zone. The real gradient is represented by the dotted lines, the radiative gradient by the dashed lines, and the adiabatic one by the dot-dashed lines. The three gradients are displayed for a value of $\alpha_{\text{un}} = 0.1$ in black and for $\alpha_{\text{un}} = 0.2$ in red.

3.3 Advantages and limitations

The great advantage of the WhoSGIAd method is that the formulation used is linear. Therefore, the construction of the basis, adjustment of frequencies, and retrieval of the seismic indicators relies only on linear algebra. The fitting coefficients and associated seismic indicators are simply defined as linear combinations of the observed frequencies. This makes the method extremely fast and efficient. Furthermore, because of the orthonormalisation, we ensure that the fitting coefficients are fully independent, therefore uncorrelated. As a consequence, the definition of seismic indicators as presented in Sect. 3.2.3 allows them to be as little correlated as possible and makes them relevant and robust constraints of the stellar structure. This already makes the technique an efficient means to automatically study the stellar structure of stellar models (Farnir et al. 2019). We further illustrate that the method efficiently adjusts a reference oscillation spectrum and retrieves the signature of the acoustic glitches in Fig. 3.17. We represent the observed 16CygA frequencies (Davies et al. 2015) (errorbars), the fitted helium glitch alone (dashed line), and the fitted contribution of both the helium and convection zone glitches (continuous line). We observe that the fitted curve tightly agrees with the observed data, which shows that our method yields robust results. We also observe that the contribution of the convection zone glitch is tiny in comparison to that of the helium glitch and that it does not significantly improve the agreement with the observed data. This results from the small amplitude of this glitch (see Table 3.2).

However, the analysis of observed data is a little more tedious. Indeed, from Eq. (3.17), we immediately note the dependency of the basis functions on T_{He} and T_{CZ} . These parameters are kept at fixed values to maintain the linearity of the method. It is therefore crucial to properly estimate their values. This was done by a preliminary modelling of the observed data. Because of the orthonormalisation, the indicators relative to the smooth part of the oscillation spectrum are completely independent of the glitch part. Therefore, they may be used as constraints in the search of a first stellar model, representative of most of the stellar structure features. These are the Δ , \hat{r}_{01} , and \hat{r}_{02} indicators previously defined. The acoustic depth of both glitches may be retrieved in the optimal model by a simple integration (Eq. (2.112)). Nevertheless, because of the modelling involved, this is a lengthy process. In addition, the acoustic depth estimation is model dependent. Consequently, this has to be improved for the automated treatment of observed data. We developed an improved technique to estimate the acoustic depth of the helium glitch with a master student, Angelo Valentino. This is presented in Sect. 3.5. Beside the need for estimates of the acoustic glitches depths, we demonstrated that this procedure remains very efficient and provides excellent results, putting stellar models to the test (Farnir et al. 2019, 2020a).

Another limitation of the method again concerns the glitches signatures. We observed that the helium glitch amplitude is only a valid proxy of the surface helium abundance for stellar models with masses $\lesssim 1.25 M_{\odot}$ (Farnir et al. 2019). This is illustrated in Fig. 3.18. We observe that, for the $1.3 M_{\odot}$ model, the helium glitch amplitude does not monotonously increase with the surface helium abundance. We attributed this effect to the microscopic diffusion in these models. The size of the surface convection zone becomes so thin that the gravitational settling, which is more efficient close to the surface, is efficient enough to significantly decrease the surface helium abundance. The same goes for the surface metallicity. As a consequence, we observe a large increase in the helium glitch amplitude ($A_{\text{He}} \sim 96$). Indeed, A_{He} is both correlated with Y_{surf} and anti-correlated with Z_{surf} .

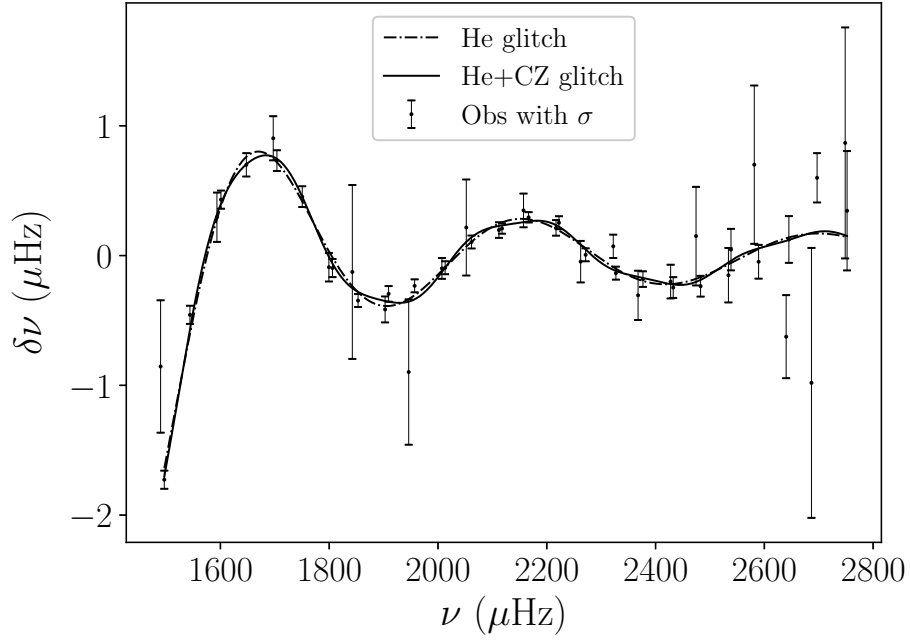


Figure 3.17: Fitted glitches signatures to the 16CygA frequencies measured by [Davies et al. \(2015\)](#). The observed data is represented by the errobars, the fitted helium glitch by a dashed line and the contribution of both the helium, and convection zone glitch by a continuous line.

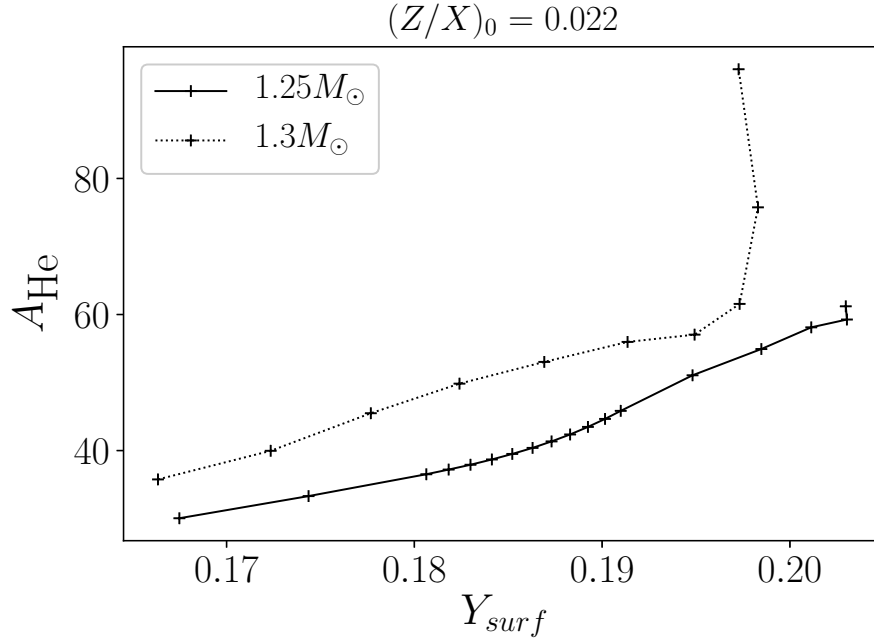


Figure 3.18: Evolution of the helium glitch amplitude with the surface helium abundance in the limit case ($1.25 M_{\odot}$ and $1.3 M_{\odot}$).

3.4 Toy model of the first adiabatic index

In Farnir et al. (2019), we provided a toy model for the first adiabatic index, Γ_1 , in order to study the impact of the stellar mass and composition on its local shape, in the helium second-ionisation zone. In the present section, we further explicit the mathematical developments leading to its final expression.

For that purpose, we consider a perfect gas composed of three different species: the hydrogen, X , the helium, Y , and the metals Z . In the helium second-ionisation zone, we consider the hydrogen atoms to be fully ionised, the helium to be partially ionised, and the metals to be neutral. From Fig. 14.1 from Kippenhahn et al. (2012) (which we included as Fig. 3.19) representing individual ionisation states of a hydrogen-helium mixture representative of the Sun, we see that this is a sound hypothesis. Because of individual ionisation energies (H ionisation, first and second helium ionisations), the individual ionisation states are almost completely distinct of one another (i.e. first ionisation of He starts when almost all the H atoms are completely ionised and second He ionisation happens once the first ionisation has been completed). In addition, when the second helium ionisation starts to play a role, the hydrogen is already fully ionised. Because of neutrality of the gas, we have that the number of negative particles must equal that of positive ones,

$$e = H + He^+ + 2He^{++}, \quad (3.40)$$

where e is the number of electrons, H that of ionised hydrogen, He^+ that of partially ionised helium, and He^{++} that of fully ionised helium. We thus have the total number of particles,

$$n = 2H + 2He^+ + 3He^{++} + Z. \quad (3.41)$$

Expressing the mass fraction of each element as a function of its number density, we obtain

$$H = \rho \frac{X}{m_u}, \quad (3.42)$$

$$He \equiv He^+ + He^{++} = \rho \frac{Y}{4m_u}, \quad (3.43)$$

$$Z = \frac{\rho}{m_u} \sum_i \frac{Z_i}{A_i} \equiv \frac{\rho}{m_u} \frac{\bar{Z}}{\bar{A}}, \quad (3.44)$$

where m_u is the atomic mass unit, Z_i and A_i are the mass fraction and number of individual elements, respectively.

Defining, $x_{He} = \frac{He^{++}}{He^+ + He^{++}}$ the fraction of fully ionised helium atoms and using Eq. (3.43) we write

$$He^+ = (1 - x_{He}) \rho \frac{Y}{4m_u}, \quad (3.45)$$

$$He^{++} = x_{He} \rho \frac{Y}{4m_u}. \quad (3.46)$$

The fraction of fully ionised helium atoms over the number of atoms partially ionised is determined by Saha's equation

$$\mathcal{F} \equiv \frac{He^{++}e}{He^+} = \frac{g}{h^3} (2\pi m_e k_B T)^{3/2} e^{-\frac{\xi}{k_B T}}, \quad (3.47)$$

where g is the statistical weight of the fully ionised state, h is Planck's constant, m_e the electronic mass, and ξ the energy difference between the two states.

Considering small perturbations in the pressure, we may relate partial derivatives of the pressure with the adiabatic indexes introduced by Chandrasekhar

$$\begin{aligned} P_\rho &= \left. \frac{\partial \ln P}{\partial \rho} \right|_T \\ &= \Gamma_1 - (\Gamma_3 - 1)^2 \frac{c_v \rho T}{P}, \end{aligned} \quad (3.48)$$

$$\begin{aligned} P_T &= \left. \frac{\partial \ln P}{\partial T} \right|_\rho \\ &= (\Gamma_3 - 1)^2 \frac{c_v \rho T}{P}, \end{aligned} \quad (3.49)$$

with $c_v = \left. \frac{\partial S}{\partial T} \right|_\rho$ the isochoric heat capacity and

$$\Gamma_1 = \left. \frac{\partial \ln P}{\partial \ln \rho} \right|_s, \quad (3.50)$$

$$\Gamma_3 - 1 = \left. \frac{\partial \ln T}{\partial \rho} \right|_s, \quad (3.51)$$

the first and third adiabatic indexes.

In the case of a monoatomic perfect gas, we have $c_v = \frac{3}{2} \frac{P}{\rho T}$ and we obtain the expression for the first adiabatic index

$$\Gamma_1 = P_\rho + \frac{2}{3} P_T^2. \quad (3.52)$$

Furthermore, we have the law of perfect gases

$$P = \frac{\rho k_B T}{\mu m_u} = n k_B T, \quad (3.53)$$

with μ the mean molecular weight, n the number of particles, and k_B Boltzmann's constant. As a consequence, we obtain from Eqs. (3.48) and (3.49),

$$P_\rho = \left. \frac{\partial \ln n}{\partial \ln \rho} \right|_T \equiv n_\rho, \quad (3.54)$$

$$P_T = 1 + \left. \frac{\partial \ln n}{\partial \ln T} \right|_\rho \equiv 1 + n_T. \quad (3.55)$$

Therefore, we need to find expressions for n_ρ and n_T to represent Γ_1 .

Perturbing Eq. (3.41) and combining it with Eqs. (3.42) and (3.43) yields

$$dn = 2 \frac{X}{m_u} d\rho + \frac{3}{4} \frac{Y}{m_u} d\rho - dHe^+ + dZ. \quad (3.56)$$

Similarly, from the neutrality (Eq. (3.40)), we also obtain

$$de = \frac{X}{m_u} d\rho + \frac{Y}{2m_u} d\rho - dHe^+. \quad (3.57)$$

We need an expression for the variation in the number of partially ionised helium atoms, dHe^+ . It may be retrieved from the derivative of Saha's equation (Eq. (3.47))

$$\frac{d\mathcal{F}}{\mathcal{F}} = \frac{de}{e} + \frac{dHe^{++}}{He^{++}} - \frac{dHe^+}{He^+}. \quad (3.58)$$

Identifying the individual terms leads to

$$dHe^+ = \left\{ \left[X + \frac{Y}{2} + \frac{em_u}{x_{He}\rho} \right] \frac{d\rho}{m_u} - e \frac{d\mathcal{F}}{\mathcal{F}} \right\} N, \quad (3.59)$$

with N defined as

$$N = \left(1 + \frac{e}{x_{He} (1 - x_{He}) \frac{Y\rho}{4m_u}} \right). \quad (3.60)$$

We then obtain, after a few manipulations of N , the expression

$$dn = \left\{ (2 - N)X + [2 + x_{He}] - (x_{He} + 1)N \right\} \frac{Y}{4} + \frac{\overline{Z}}{A} \left\{ \frac{d\rho}{m_u} + eN \frac{d\mathcal{F}}{\mathcal{F}} \right\}. \quad (3.61)$$

We now have all the necessary ingredients to n_ρ and n_T ,

$$n_\rho = \left\{ (2 - N)X + [2 + x_{He}] - (x_{He} + 1)N \right\} \frac{Y}{4} + \frac{\overline{Z}}{A} \left\{ \frac{\rho}{nm_u} \right\}, \quad (3.62)$$

$$n_T = eN \frac{d\mathcal{F}/\mathcal{F}}{nd \ln T} = \left(\frac{3}{2} + \frac{\xi}{k_B T} \right) \frac{eN}{n}. \quad (3.63)$$

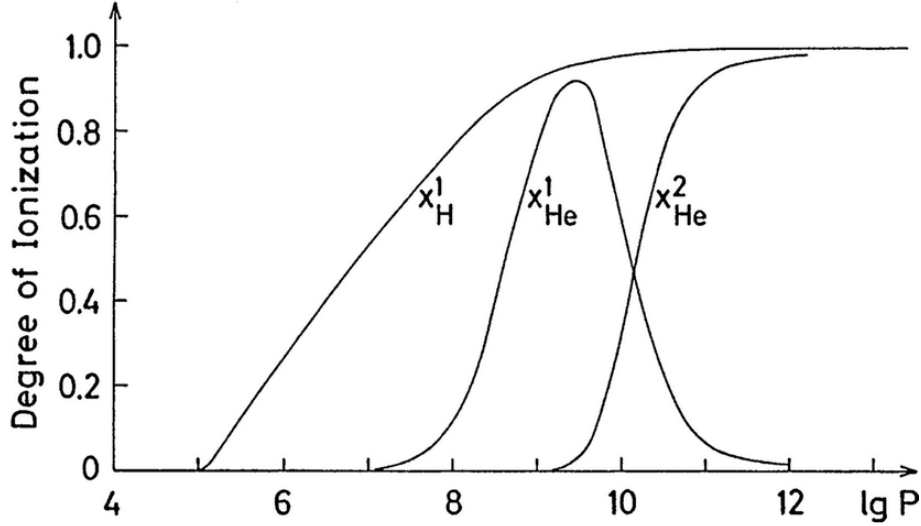


Figure 3.19: Evolution of the degrees of ionisation x of hydrogen and helium as a function of the pressure in a solar model presented in (Kippenhahn et al. 2012, Fig. 14.1). x ranges between zero, for a neutral species, and unity, for a fully ionised species.

These quantities may be inserted in Eq. (3.52) to obtain our toy model for Γ_1 .

Finally, we must account for the impact of the ionisation on the isochoric specific heat, as some of the energy from the heating of the gas will be converted into gas ionisation instead of increasing the temperature. The internal energy per unit volume is the following

$$u = \frac{3}{2} \frac{P}{\rho} + (x_{\text{He}} - 1) \xi \frac{Y}{4m_u}, \quad (3.64)$$

where the second term accounts for the energy of the ionised particles. The specific heat then comes naturally as the partial derivative of the energy with respect to the temperature, for a fixed volume

$$c_v = \left. \frac{du}{dT} \right|_V = \frac{3}{2} \frac{k_B P_T}{\mu m_u} + \frac{Y \xi}{4m_u} \frac{dx_{\text{He}}}{dT}. \quad (3.65)$$

From the expressions of the number of particles (Eq. (3.41)) and the law of perfect gases (Eq. (3.53)), we may identify μ

$$\mu = \left[2X + (2 + x_{\text{He}}) \frac{Y}{4} + \frac{\bar{Z}}{A} \right]^{-1}. \quad (3.66)$$

Finally, from Eq. (3.58), we get

$$\frac{dx_{\text{He}}}{dT} = \frac{(1 - x_{\text{He}}) \left(\frac{3}{2} + \frac{\xi}{k_B T} \right) \frac{m_u \mathcal{F}}{\rho T}}{X + \frac{Y}{2} \left(\frac{1}{2} + x_{\text{He}} \right) + \frac{m_u}{\rho} \mathcal{F}}, \quad (3.67)$$

and the final expression for Γ_1 yields

$$\Gamma_1 = n_\rho + 4(1 + n_T) \frac{1}{6 + \frac{Y \xi}{(1 + n_T) k_B} \left[2X + (2 + x_{\text{He}}) \frac{Y}{4} + \frac{\bar{Z}}{A} \right] \frac{dx_{\text{He}}}{dT}}. \quad (3.68)$$

3.5 Providing an estimate for the acoustic depth of the helium glitch

3.5.1 Motivation

One criticism that may be made about the WhoSGlAd technique is its need for an estimate of the acoustic depth of both glitches (τ_{He} and τ_{CZ}). Indeed, we chose to use a fixed value of these acoustic depth (or rather their dimensionless counterpart: $T = \tau \Delta$) in order to avoid introducing unnecessary correlations

between the parameters of the fit by carrying out a minimisation over the acoustic depths and to have a linear relation between the frequencies and the parameters. Therefore, it is essential to provide a proper estimate. In the case of theoretical data, this does not represent a limitation as it may be computed directly from the model. Equation (2.112) providing the acoustic depth of the helium glitch can be generalised to any glitch

$$\tau_{\bullet} = \int_{r_{\bullet}}^R \frac{dr}{c(r)}, \quad (3.69)$$

with r_{\bullet} the position of the stellar feature creating the glitch. In the case of the helium glitch, it was shown that this is the maximum between the two minima of the Γ_1 function (e.g. [Broomhall et al. 2014](#)).

However, in the case of observed data, estimating the acoustic depth of a glitch, which determines the period of the oscillation in the frequencies, proves to be more difficult. We initially proceeded as follows:

1. Retrieve several seismic indicators associated with the smooth part of the observed data and representative of the stellar structure (i.e. Δ , \hat{r}_{01} , and \hat{r}_{02});
2. Find a model adjusting these indicators. Its stellar structure is thus close to the one of the target;
3. Measure τ on this model, via Eq. (3.69).

As the above procedure illustrates, this is a lengthy and model dependent procedure. Nonetheless, we showed that this estimation yields excellent results and allows us to carry out precise seismic measurements ([Farnir et al. 2019, 2020a,b](#)). Indeed, a small excursion from the optimal value (around 10% in relative variation) was shown to have a negligible impact on the measured glitch amplitude. However, it came as a necessity to estimate the acoustic depth in a model independent and faster way to, for example, allow for the automated adjustment of large amounts of data, as the PLATO mission ([Rauer et al. 2014](#)) will produce.

As a consequence, I proposed as part of a master thesis project, to find an automated way to estimate the acoustic depth of the helium glitch. As we noted that the convection zone glitch is of negligible amplitude, we did not interest ourselves in it. This was the work of Angelo Valentino. The idea was to relate $T_{\text{He}} = \tau_{\text{He}}\Delta$ with seismic indicators associated with the smooth part of the spectrum: Δ_0 and \hat{r}_{02} . It was demonstrated that a seismic HR diagram built using Δ_0 and \hat{r}_{02} (or indicators that bear similar information) is relevant to the study of the stellar evolution ([Christensen-Dalsgaard 1988](#); [Farnir et al. 2019](#)). Furthermore, the second helium ionisation, regardless of the pressure conditions, happens around a fixed temperature of about $10^5 K$. We can thus expect that it would be mostly determined by the gross stellar properties. Finally, [Mazumdar \(2005\)](#) showed that τ - Δ_0 diagrams, τ being the acoustic depth of either the helium or convection zone glitch, could be built as a replacement for the seismic diagrams ([Christensen-Dalsgaard 1988](#)). He also showed that his diagrams can help in constraining stellar models, as the tracks in these diagrams are distinct in regard to the expected precision on both parameters. It is also worth noting that models with masses between $0.8 M_{\odot}$ and $1.1 M_{\odot}$ evolve monotonously and almost linearly in these diagrams. Consequently, relating the evolution T_{He} with that of Δ_0 and \hat{r}_{02} seems to be a reasonable choice.

3.5.2 Results

Over a grid of main-sequence stellar models, we showed that we may, at first order, assume that the dimensionless acoustic depth follows a linear relation in both Δ and \hat{r}_{02} ,

$$T_{\text{He}} \simeq a\Delta_0 + b\hat{r}_{02} + c, \quad (3.70)$$

with a , b , and c being 3 parameters to be adjusted. This is what is represented in Fig. 3.20. The value of T_{He} , represented by the colour gradient, is depicted along our grid of models computed with CLES ([Scuflaire et al. 2008a](#)) with an initial composition of $X_0 = 0.75$ and $Z_0 = 0.012$ and using the same set of input physics as in ([Farnir et al. 2019, Sect. 3.1](#)). The grid spans masses between $0.80 M_{\odot}$ and $1.15 M_{\odot}$ with a step of $0.05 M_{\odot}$. We did not expand beyond $1.15 M_{\odot}$ as the subsistence of a convective core in heavier stars leads to non-linearities.

We indeed observe in Fig. 3.20 that T_{He} monotonously increases with both Δ_0 and \hat{r}_{02} . We therefore adjusted the linear relation given by Eq. (3.70) to this grid and retrieved the coefficients:

$$a \simeq 8.1 \cdot 10^{-5}, \quad b \simeq -2.5 \cdot 10^{-1}, \quad c \simeq 7.9 \cdot 10^{-2}. \quad (3.71)$$

We note the value resulting from our relation (Eq. (3.70)) and the fitted coefficients (Eq. (3.71)), $T_{\text{He,fit}}$, the value obtained from models, $T_{\text{He,mod}}$, and define their relative difference as

$$\delta T_{\text{He}} = \frac{T_{\text{He,fit}} - T_{\text{He,mod}}}{T_{\text{He,mod}}}. \quad (3.72)$$

To show the agreement between our relation and the model value, we represent in Fig. 3.21 this relative difference, depicted by the colour gradient, on the same grid of models as in Fig. 3.20. We observe that in the worst case, the relative difference is of about $\sim 1.5\%$. Which remains small in comparison with the 10% excursion we demonstrated to have a negligible impact on the glitch amplitude (Farnir et al. 2019). Indeed, in that case the difference in helium glitch amplitude, normalised to its uncertainty is of $\sim 5\%$, which is not significant. We also observe that the relative difference does not vary monotonously, displaying a distinct minimum for each track. While the agreement between fitted and model values is already sufficient, this indicates that a second order relation could further improve this agreement.

We also tested the impact of the chemical composition on the quality of the inferred value. We compared the results yielded by our reference composition to the integrated values from grids with a different composition, $X_0 = 0.725$ and $Z_0 = 0.014$. The maximum relative variation in acoustic depth is of $\sim 3\%$ and the helium amplitude is unaffected (the change is on the order of 0.01σ). This is shown in Fig. 3.22. Therefore, we are confident that this relation may be used with observed data. This is the natural next step.

We applied the relation to 16 Cygni A data and computed a dimensionless acoustic depth of $6.5 \cdot 10^{-2}$. This is 30% lower than the value obtained via a modelling of the smooth component ($9.1 \cdot 10^{-2}$). However, the impact on the measured helium glitch amplitude remains small in comparison with the uncertainties on this indicator: 29.1 with the relation and 29.6 via modelling (i.e. 0.5σ change). Therefore, this modified value of the glitch amplitude should not significantly impact the modelling of the star. In addition, we may carry out a minimisation of the WhoSGLAd cost function (Eq. (3.12)), therefore reducing at most the difference between reference and fitted frequencies, with the acoustic depth as the only free parameter to further improve the results. This is done via a Brent minimisation procedure (Brent 1973, see also Sect. 3.C). The optimal value retrieved is situated within 1% of the one obtained via a partial modelling of the star. This further demonstrates the validity of the presented technique to provide an estimate of T_{He} . Consequently, this enables us to efficiently measure the glitch signature in main sequence solar-like stars without the need for a preliminary modelling of the observed target.

While the proposed estimation of T_{He} proves to be efficient, we must proceed with care. Indeed, we restricted ourselves to main-sequence models with radiative cores, in order to avoid non-linear behaviours. Therefore, additional test will be necessary to assess the reliability of the estimated values in models with convective cores, in which Δ and \hat{r}_{02} are not monotonous and T_{He} may vary non-linearly. Considering a higher order expression, as Figs. 3.21 and 3.22 would suggest, may be necessary. These concerns will be addressed in future works.

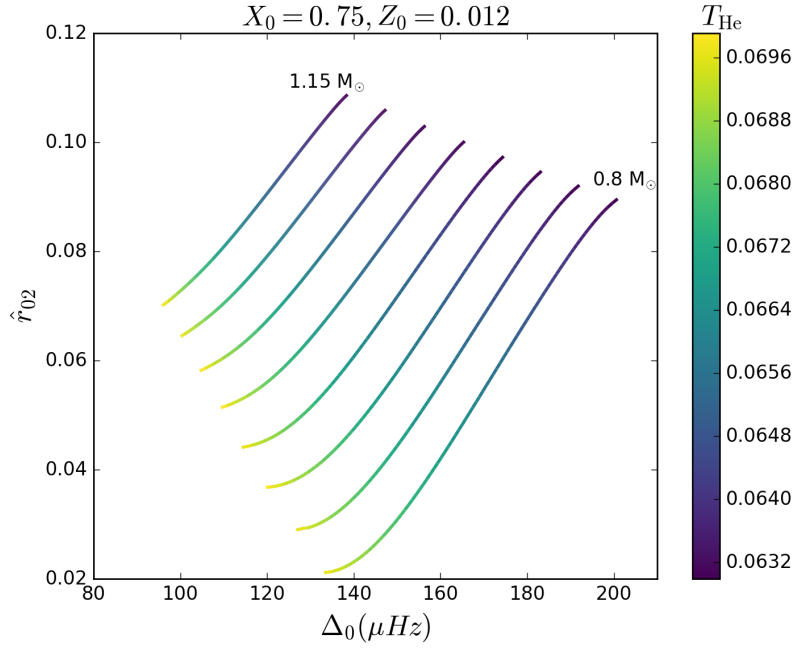


Figure 3.20: Evolution of the acoustic depth of the helium glitch for a grid of models with masses in $[0.80M_\odot, 1.15M_\odot]$ ($0.05M_\odot$ step) for the initial composition $X_0 = 0.75$ and $Z_0 = 0.012$.

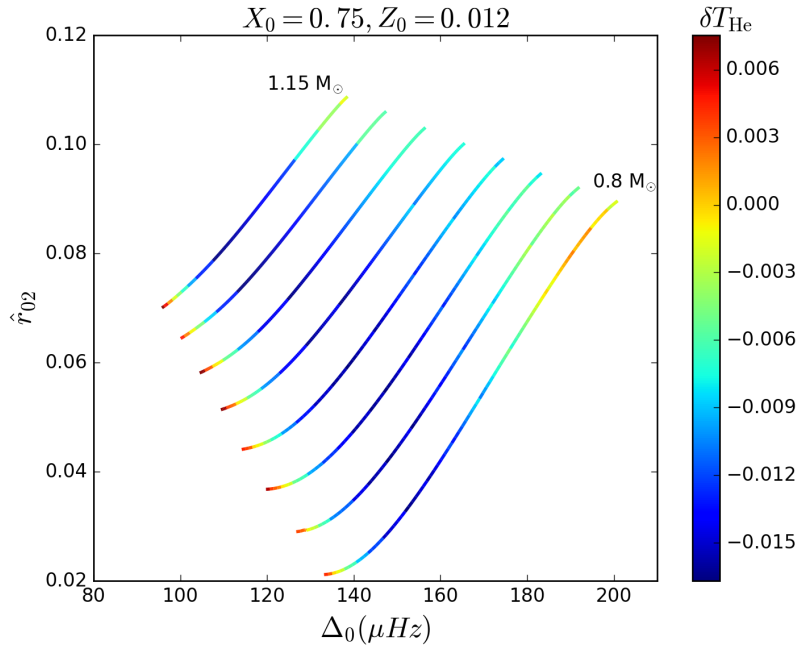


Figure 3.21: Relative difference between the fitted and model acoustic depth of the helium glitch for a grid of models with masses in $[0.80M_\odot, 1.15M_\odot]$ ($0.05M_\odot$ step) for the initial composition $X_0 = 0.75$ and $Z_0 = 0.012$.

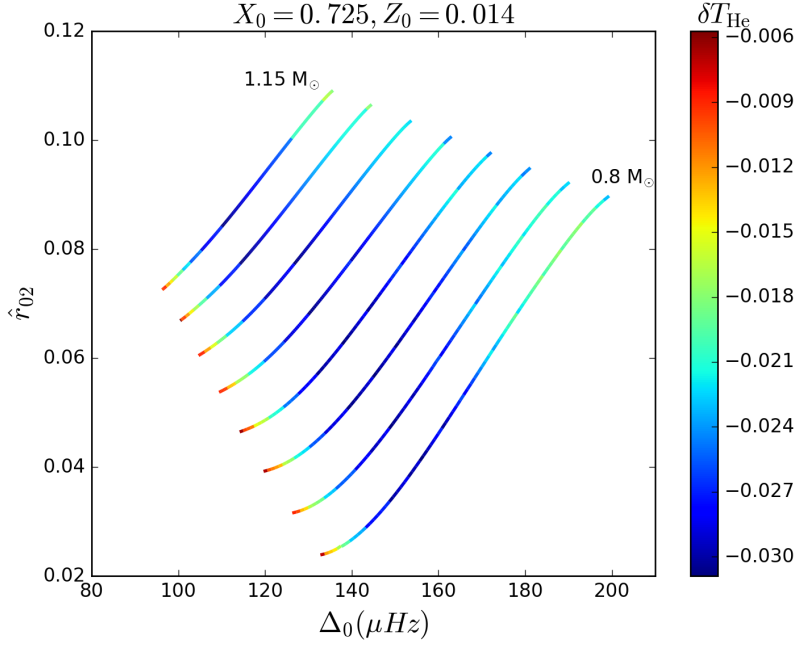


Figure 3.22: Relative difference between the fitted and model acoustic depth of the helium glitch for a grid of models with masses in $[0.80M_\odot, 1.15M_\odot]$ ($0.05M_\odot$ step) for the initial composition $X_0 = 0.725$ and $Z_0 = 0.014$.

3.6 Conclusion

Thanks to the Gram-Schmidt orthonormalisation process, we have defined a method that efficiently adjusts the complete oscillation spectrum of main-sequence low-mass stars. A consequence of the orthonormalisation is that the fitted coefficients are completely independent of one another. These coefficients are in turn used to build seismic indicators relevant of the stellar structure and with reduced correlations. For example, the helium and convection zone glitches amplitudes are completely independent of one another but also of the smooth component. We also showed that the helium amplitude allows us to precisely constrain the helium surface mass fraction but that this indicator is correlated with the metals surface mass fraction and the stellar mass as well. Nevertheless, using the helium amplitude in combination with the other indicators we defined, it is possible to unambiguously constrain the stellar age, mass, radius, composition (including the helium abundance), and central overshooting (for stars with a convective core).

We noted two main limitations to our technique. First, for stars with masses exceeding $\sim 1.25 M_\odot$, the microscopic diffusion may become so efficient that there is not a monotonous relation between the helium glitch amplitude and the helium surface abundance any more, disrupting our ability to constrain Y_{surf} . The second limitation comes from the acoustic depths of the glitches. These were fixed in order to maintain a linear formulation for the glitches. This allowed us, through the orthonormalisation, to ensure that the fitted parameters were indeed completely independent of each other. It was therefore necessary to estimate these acoustic depths. For model data, this does not constitute a problem as we have access to the stellar structure and it can be easily retrieved. Conversely, the case of stellar observations is more complex and requires a partial modelling of the stellar structure, accounting for the smooth component indicators.

To circumvent this problem, we used a linear relation between the dimensionless acoustic depth of the helium glitch (T_{He}), Δ , and \hat{r}_{02} . This proved efficient and cancelled the necessity to carry out partial modelling to retrieve this quantity. Indeed, it allows us to estimate this quantity using only observable seismic indicators, independent of the glitch contribution. This therefore opens the possibility to automatically measure the helium glitch signature in a large sample of stars. While we observed that the composition does not have a significant impact, the use of our formulation on 16 Cyg A data lead to a 30% excursion from the model value. This however did not

affect significantly the measured glitch amplitude (0.5σ change) but demonstrates the necessity to use this relation with care. Furthermore, minimising the difference between the WhoSGLAd fitted frequencies and the reference ones allows us to retrieve the model value of T_{He} . While this estimation requires further testing, it proves to be a significant asset to our technique.

Appendices

3.A Large frequency separation in common notations

In the present section, we relate the expression of the large frequency separation at a given spherical degree l (Eq. (3.24)) to its expression in notations more commonly used (Eq. (3.25)). To do so, from the matrix expression of the Gram-Schmidt process (Eq. (3.4)) and the formal one (Eqs. (3.2) and (3.3)), we may identify the transformation matrix elements,

$$R_{l,0,0}^{-1} = \frac{1}{\|\mathbf{1}\|}, \quad (3.73)$$

$$\mathbf{q}_{l,1} = R_{l,0,1}^{-1} \mathbf{1} + R_{l,1,1}^{-1} \mathbf{n}_l \quad (3.74)$$

$$= \frac{\mathbf{n}_l - \langle \mathbf{n}_l | \mathbf{q}_{l,0} \rangle \mathbf{q}_{l,0}}{\|\mathbf{n}_l - \langle \mathbf{n}_l | \mathbf{q}_{l,0} \rangle \mathbf{q}_{l,0}\|} \quad (3.75)$$

$$= \frac{\mathbf{n}_l - \langle \mathbf{n}_l | \mathbf{1} \rangle \mathbf{1} \left(R_{l,0,0}^{-1} \right)^2}{\left\| \mathbf{n}_l - \langle \mathbf{n}_l | \mathbf{1} \rangle \mathbf{1} \left(R_{l,0,0}^{-1} \right)^2 \right\|}. \quad (3.76)$$

Thus,

$$\left(R_{l,1,1}^{-1} \right)^2 = \frac{1}{\|\mathbf{n}_l\|^2 - \langle \mathbf{n}_l | \mathbf{1} \rangle^2 \left(R_{l,0,0}^{-1} \right)^2} \quad (3.77)$$

$$= \frac{1}{\|\mathbf{n}_l\|^2 - \bar{n}_l^2 \|\mathbf{1}\|^2}, \quad (3.78)$$

$$R_{l,0,1}^{-1} = -\langle \mathbf{n}_l | \mathbf{1} \rangle \left(R_{l,0,0}^{-1} \right)^2 R_{l,1,1}^{-1}. \quad (3.79)$$

Finally, we may expand Eq. (3.24) and introduce Eqs. (3.74), (3.78) and (3.79) to obtain

$$\Delta_l = a_{l,1} R_{l,1,1}^{-1} \quad (3.80)$$

$$= \langle \mathbf{n}_l | \mathbf{q}_{l,1} \rangle R_{l,1,1}^{-1} \quad (3.81)$$

$$= \left[\langle \nu_l | \mathbf{1} \rangle R_{l,0,1}^{-1} + \langle \nu_l | \mathbf{n}_l \rangle R_{l,1,1}^{-1} \right] R_{l,1,1}^{-1} \quad (3.82)$$

$$= \frac{\langle \nu_l | \mathbf{n}_l \rangle / \|\mathbf{1}\|^2 - \bar{n}_l \bar{\nu}_l}{\|\mathbf{n}_l\|^2 / \|\mathbf{1}\|^2 - \bar{n}_l^2}, \quad (3.83)$$

which matches expression (3.25).

3.B The case of correlated frequencies

During a PLATO Hands On Workshop session, O. Benomar showed that individual frequencies may be correlated to one another, as a result of the prior necessary to the identification of the modes. This was illustrated in the specific case of the 16 Cyg B star, one of our benchmark stars. He showed that radial and quadrupolar modes exhibit a significant correlation. These correlations may amount to up to 20% of diagonal terms in the covariance matrix. Consequently, once such data has been published, it will be necessary to account for these correlations in order to draw proper statistical inferences. Indeed, the WhoSGLAd method aims at reducing at most correlations between the adjusted parameters. However, this

is carried under the hypothesis that individual frequencies are independent of each other. This assumption is crucial to demonstrate that the fitted coefficients are uncorrelated (see Eq.(3.11)). However, as O. Benomar demonstrated, it collapses. It would be very useful to have a method that takes these frequency correlations into account and still provides independent fitted parameters to be used as seismic indicators. As we show now, WhoSGlAd can be easily adapted to reach this goal.

When correlations are present between individual modes, the method has to be adapted to make use of the full correlation matrix instead of the diagonal elements only, which correspond to individual modes uncertainties. This problematic has not yet been tackled. To do so, one has to adapt the definition of the scalar product (Eq. (3.5)) by introducing the correlation matrix \mathbb{C} such that individual elements are:

$$\mathbb{C}_{ij} = \sigma_{ij}^2, \quad (3.84)$$

with σ_{ij}^2 the correlation between individual frequencies labelled i and j . σ_{ii}^2 is therefore the variance associated with the i^{th} frequency.

The scalar product (Eq. (3.5)) between two vector quantities, \mathbf{x} and \mathbf{y} , then takes the form

$$\langle \mathbf{x} | \mathbf{y} \rangle = \mathbf{x}^T \mathbb{C}^{-1} \mathbf{y} = \sum_{i,j} x_i (\mathbb{C}^{-1})_{ij} y_j, \quad (3.85)$$

where the T superscript represents the matrix transpose operation and \mathbb{C}^{-1} is the inverse of the covariance matrix. The construction of the orthonormal basis elements, \mathbf{q}_k , via the Gram-Schmidt orthonormalisation follows from this definition. The transformation matrix is slightly modified to account for individual correlations through the new scalar product definition.

With this scalar product, we may show that the fitted parameters remain uncorrelated. First, the fitting coefficients are expressed as

$$a_k = \langle \nu_{\text{obs}} | \mathbf{q}_k \rangle = \sum_{i=1}^N (\mathbb{C}^{-1})_{ij} \nu_{\text{obs},i} q_{k,j}. \quad (3.86)$$

Second, the covariance between a_k and a_l becomes

$$\text{cov}(a_k, a_l) = \sum_{ij} (\mathbb{C}^{-1})_{ij} q_{k,i} q_{l,j} = \delta_{kl}, \quad (3.87)$$

because of orthonormality of the \mathbf{q}_k basis vectors. We have proven the independence of the fitted coefficients, which is an essential ingredient to produce the least correlated possible seismic indicators.

Finally, to account for the correlations while assessing the quality of the adjustment, Eq. (3.12) becomes:

$$\begin{aligned} \chi^2 &= \|\nu_{\text{obs}} - \nu_{\text{fit}}\|^2 = (\nu_{\text{obs}} - \nu_{\text{fit}})^T \mathbb{C}^{-1} (\nu_{\text{obs}} - \nu_{\text{fit}}) \\ &= \sum_{i,j} (\nu_{\text{obs}} - \nu_{\text{fit}})_i (\mathbb{C}^{-1})_{ij} (\nu_{\text{obs}} - \nu_{\text{fit}})_j. \end{aligned} \quad (3.88)$$

Naturally, in the case of uncorrelated frequencies, the correlation matrix becomes

$$\mathbb{C}_{ij} = \delta_{ij} \sigma_{ij}^2, \quad (3.89)$$

and Eqs. (3.85) and (3.88) reduce to their usual forms.

3.C Brent minimisation

To optimise over the T_{He} value estimated in Sect. 3.5, we make use of the one-dimensional Brent minimum search (Brent 1973). This method assumes the function to be well-behaved and to take a parabolic form in the vicinity of the minimum. It thus performs a three-points parabolic interpolation to estimate this minimum. If we write the function, f and the three points x_1 , x_2 , and x_3 (in increasing order), the estimated position of the minimum, x , is

$$x = x_2 - \frac{1}{2} \frac{(x_2 - x_1)^2 |f(x_2) - f(x_3)| - (x_2 - x_3)^2 |f(x_2) - f(x_1)|}{(x_2 - x_1) |f(x_2) - f(x_3)| - (x_2 - x_3) |f(x_2) - f(x_1)|}. \quad (3.90)$$

At each step of Brent’s minimisation technique, the algorithm evaluates the function at 6 points: x_{\min} and x_{\max} , two user supplied values bracketing the minimum, x the current minimum, x_2 the current second lowest value, $x_{2,\text{prev}}$ the previous value of x_2 , and x_{last} the last function evaluation. If $f(x_{\text{last}}) \leq f(x)$, the values are replaced accordingly. The method converges when the size of individual steps becomes comparable to the root of the machine’s precision (see [Press et al. 1992](#), Eq. 10.1.2 for a justification).

In practice, because Eq. (3.90) is not guaranteed to succeed, Brent’s method will alternate between parabolic steps and golden section minimum search steps. This is the equivalent of the bisection root search for minima and with asymmetric (based on the golden ratio, hence the name) intervals sizes. The transition to the golden section step happens either when the new estimate falls out of bounds ($x_{\text{new}} \notin [x_{\min}, x_{\max}]$) or when the step is too large (typically $\delta_{\text{curr}} \geq 0.5\delta_{\text{prev}}$, with δ the step size).

Because the method is very simple, it converges extremely fast and fits well within the WhoSGlAd implementation. This allows for the fast, reliable, and automated estimation of T_{He} necessary to the glitch amplitude measurement in observations.

Comprehensive stellar seismic analysis

New method exploiting the glitches information in solar-like pulsators

M. Farnir¹, M.-A. Dupret¹, S. J. A. J. Salmon¹, A. Noels¹, and G. Buldgen²

¹ Institut d'Astrophysique et Géophysique de l'Université de Liège, Allée du 6 août 17, 4000 Liège, Belgium
e-mail: martin.farnir@uliege.be

² School of Physics and Astronomy, University of Birmingham, Edgbaston, Birmingham B15 2TT, UK

Received 8 August 2018 / Accepted 10 December 2018

ABSTRACT

Aims. We develop a method that provides a comprehensive analysis of the oscillation spectra of solar-like pulsators. We define new seismic indicators that should be as uncorrelated and as precise as possible and should hold detailed information about stellar interiors. This is essential to improve the quality of the results obtained from asteroseismology as it will provide better stellar models which in turn can be used to refine inferences made in exoplanetology and galactic archaeology.

Methods. The presented method – WhoSGLAd – relies on Gram-Schmidt's orthogonalisation process. A Euclidean vector sub-space of functions is defined and the oscillation frequencies are projected over an orthonormal basis in a specific order. This allowed us to obtain independent coefficients that we combined to define independent seismic indicators.

Results. The developed method has been shown to be stable and to converge efficiently for solar-like pulsators. Thus, detailed and precise inferences can be obtained on the mass, the age, the chemical composition and the undershooting in the interior of the studied stars. However, attention has to be paid when studying the helium glitch as there seems to be a degeneracy between the influence of the helium abundance and that of the heavy elements on the glitch amplitude. As an example, we analyse the 16CygA (HD 186408) oscillation spectrum to provide an illustration of the capabilities of the method.

Key words. asteroseismology – stars: oscillations – stars: solar-type – stars: abundances – methods: numerical

1. Introduction

Since the launch of CoRoT (Baglin et al. 2009) and *Kepler* (Borucki et al. 2010) missions, the scientific community has access to a tremendous amount of asteroseismic data of unprecedented quality. Such data are essential to better constrain stellar structure and evolution and, in turn, improve the characterisation of exoplanets and stellar populations. However, it is essential to develop techniques that are able to retrieve stellar parameters as accurately as possible in order to benefit from the quality of the data. A very complex problem in determining stellar parameters is the model dependency of the results. The results are intrinsically dependent on the input physics such as the equation of state as well as the opacity tables used. It therefore becomes of prime importance to develop techniques that are able to test the influence of the input physics on stellar parameters or even techniques that provide results as model independent as possible.

With such precision in the data, and the precision of the future missions TESS (Ricker et al. 2014) and PLATO (Rauer et al. 2014), studying the signature of acoustic glitches becomes a natural step towards better models. This idea was originally proposed by Vorontsov (1988) and Gough (1990). They both highlighted the effect of a sharp feature in the stellar structure on the frequencies, either directly or on the second differences. Such considerations have already been the subject of several studies. As an example of the several techniques used, Mazumdar et al. (2014) illustrate four techniques either using the second frequency differences or striving to isolate the glitch oscillation directly from the frequencies. Also, most

of the current methods focus on the localisation of the helium second ionisation zone or the base of the envelope convection zone (e.g. Monteiro et al. 2000). This is a crucial first step on the way to a better understanding of stellar physics. Indeed, a characterisation of the convective envelope extension allows to get constraints on convection itself as well as on overshooting (both its efficiency and nature). Therefore, the glitch provides the necessary observational data needed to refine current convection theories. Also, the study of the helium glitch should provide information on the helium surface content in low-mass stars. This is essential as, in such stars, it cannot be derived from spectroscopic data. Therefore, a methodology taking advantage of most of the oscillation spectrum aspects is required.

Finally, it is sometimes the case that studies use correlated constraints or discard pieces of information in their studies. For example, in method *C* from Verma et al. (2014), the information that is not contained in the glitch (the smooth component) is not used directly as the glitch information is isolated to draw inferences. Therefore, the usual indicators (e.g. large separation, small separation ratios, ...) are computed separately from the glitch and no method is proposed to determine properly the correlation between those indicators and that of the glitch.

For those reasons, we propose a method: Whole Spectrum and Glitches Adjustment (WhoSGLAd) that takes as much of the available spectral information as possible into account. This method defines new seismic indicators in such a way that they are as independent as possible and significant from a statistical

point of view. To do so, it relies on linear algebra via Gram-Schmidt's algorithm.

The present paper is organised as follows. We first present the method in a very general and mathematical way in Sect. 2. Then Sect. 3 defines the seismic indicators and their diagnosis power will be used to study solar-like pulsators. In the following section, we demonstrate its ability to extract and analyse the glitches signal. We also show its limitations. We present a first application to the case of 16 Cygni A (HD 186408) in Sect. 5. Let us insist on the fact that we do not present here a thorough study of 16 Cygni A but we rather show an example of the ability of the method to provide constraints on stellar structure. We conclude the paper by discussing the results and detailing future perspectives.

2. Method

In the present section, we describe the method we developed. It aims at using as much as possible of the information available in the oscillation spectrum of a star. Therefore, both the oscillatory and smooth part of the spectrum are simultaneously analysed in a single adjustment. This avoids multiple usage of the same information to draw different inferences. The very strength of the proposed method is that the different parameters obtained will be independent of each other, meaning that their covariance matrix will be the identity matrix. This will allow to build indicators which also are independent of each other and draw statistically relevant inferences. The independence of the parameters will be ensured by using Gram-Schmidt's (Gram 1883; Schmidt 1907) algorithm. Then, the defined seismic indicators will be used as constraints to provide improved models in the framework of forward seismic modelling (see for example Miglio & Montalbán 2005 for one of the first use of Levenberg-Marquardt's algorithm to adjust a model to seismic and non-seismic observables). Finally, such models may be used as initial guesses for inverse seismic modelling. (see Roxburgh & Vorontsov (2002a,b) for the application of the inversion technique on an artificial target, which shows the feasibility of such techniques, and Buldgen et al. (2016a,b) for examples of inversions in the case of 16 Cygni A.)

2.1. Mathematical description

Non-radial pulsation frequencies can be mathematically defined by three integer numbers; the radial order n , the spherical degree l , and the azimuthal order m (in this paper, we do not consider the seismic probing of rotation and consider only $m = 0$). The method we developed – WhoSGIAd – is based on linear algebra in a Euclidean space. The vector space we consider is the set of N observed oscillation frequencies ν_i . The standard deviation for each frequency is written σ_i . Given two frequency vectors \mathbf{x} and \mathbf{y} we define their scalar product as

$$\langle \mathbf{x} | \mathbf{y} \rangle = \sum_{i=1}^N \frac{x_i y_i}{\sigma_i^2}. \quad (1)$$

Often in asteroseismology, it is useful to compare two sets of frequencies (e.g. theoretical and observed frequencies) using a merit function defined as

$$\chi^2 = \sum_{i=1}^N \frac{(\nu_{\text{obs},i} - \nu_{\text{th},i})^2}{\sigma_i^2}, \quad (2)$$

with ν_{th} and ν_{obs} , the theoretical and observed¹ frequencies. Taking advantage of the scalar product defined above and the associated norm, this simply becomes

$$\chi^2 = \|\nu_{\text{obs}} - \nu_{\text{th}}\|^2. \quad (3)$$

In the presence of a glitch, Houdek & Gough (2007) showed that the oscillatory component in frequencies due to the glitch can be isolated from the rest of the spectrum, called the smooth component. Thus, to represent observed frequencies, we define a vector sub-space that is typically a polynomial space – the smooth component – associated with an oscillating component – the glitch –. The analytical formulation of those two components will be given in the following sections. This is very similar to what has been done by Verma et al. (2014).

The method consists in the projection of the observed and theoretical frequencies over the vector sub-space. Then, we define seismic indicators from the projections. Their definitions are given in Sect. 3. To do so, it is useful to define an orthonormal basis over the vector sub-space. This is done via Gram-Schmidt's orthogonalisation process associated with the definition of the scalar product (1). For more information about this process as well as its equivalent form as a QR decomposition, the interested reader may read Appendix D.

If we write j and j_0 the indices associated with the basis elements, \mathbf{p}_j the former basis elements, \mathbf{q}_{j_0} the orthonormal basis elements, and R_{j,j_0}^{-1} the transformation matrix, we have:

$$\mathbf{q}_{j_0}(n, l) = \sum_{j \leq j_0} R_{j,j_0}^{-1} \mathbf{p}_j(n, l), \quad (4)$$

where the dependence in n and l translates that the basis elements are evaluated at each observed value of the radial order n and the spherical degree l .

It is essential that the projections be done in a specific order to obtain the lowest possible value of the merit function. This will be the subject of the following subsection. Finally, we write $a_j = \langle \nu | \mathbf{q}_j \rangle$ the projections of the frequencies over the basis elements. The fitted frequencies are then given by

$$\nu_f(n, l) = \sum_j a_j \mathbf{q}_j(n, l). \quad (5)$$

Let us add that, thanks to the orthonormalisation, the standard deviations of the coefficients a_j are $\sigma(a_j) = 1$ and they are independent (their covariance matrix is the identity).

2.2. Smooth component

Now that the mathematical context is given, we may detail the vector sub-space we selected to fit the smooth component of the frequency spectrum. As the set of observed radial orders and σ_i are usually different for each spherical degree and the smooth component depends on l , the smooth component basis elements depend on l . For each value of l , the frequencies will be projected over the different powers considered. We also point out that, for each spherical degree, the method requires at least the same number of frequencies as of powers considered in the formulation. The polynomials are then of the general form:

$$p_{lk}(n, l') = \delta_{ll'} p_k(n), \quad (6)$$

¹ We denote with the subscript *obs* both the observed frequencies and the frequencies derived from a reference model – which constitutes an artificial target – and we denote by the subscript *th* the frequencies that we adjust to those observations.

where $\delta_{ll'}$ is the *Kronecker* delta which compares two spherical degrees l and l' , $p_k(n)$ is a polynomial in the radial order n and k represents its ordering. We note that the previously defined j is now separated into two indices, the spherical degree l and the ordered power k . For a better understanding, the spherical degree and ordering will be explicitly written for the smooth component transformation matrix as R_{l,k,k_0}^{-1} . And the orthonormal basis elements are

$$q_{lk}(n, l') = \delta_{ll'} q_{lk}(n), \quad (7)$$

which yield:

$$a_{lk} = \langle \mathbf{v} | \mathbf{q}_{lk} \rangle = \sum_n \frac{v(n, l) q_{lk}(n, l)}{\sigma^2(n, l)}, \quad (8)$$

where thanks to the introduction of $\delta_{ll'}$ in Eqs. (6) and (7), the sum over l' collapses over one fixed degree l . For the smooth component, we treat separately each spherical degree, the parameters associated to a given degree only depend on the frequencies of this degree.

According to the asymptotic theory of non-radial oscillations (Gough 1986), we have the following formulation of the expected frequencies as a function of n and l :

$$v(n, l) \simeq \left(n + \frac{l}{2} + \epsilon \right) \Delta, \quad (9)$$

where $\Delta = \left(2 \int_0^{R_*} \frac{dr}{c(r)} \right)^{-1}$ is the asymptotic large frequency separation, $c(r)$ is the adiabatic sound speed, and R_* is the radius at the photosphere of the star.

It follows that the first two polynomials in n (taken from the right hand side of Eq. (6)) used to depict the spectrum smooth component will be:

$$p_0(n) = 1, \quad (10)$$

$$p_1(n) = n. \quad (11)$$

Then, to provide the best fit to the observed frequencies, we methodically tested several combinations of powers to find the set giving the best agreement with the observations – the observations actually referring to theoretical models taken as observed stars in a set of calibrations –, hence the lowest χ^2 value. We get:

$$p_2(n) = n^2. \quad (12)$$

At this point, it is of prime importance to note that the construction of the basis via Gram-Schmidt's process will have to be done following the ordering of the degrees because it will allow us to associate the seismic indicators to the projection of the frequencies on the successive basis elements. For example, the projection of the frequencies on the 0 order polynomial corresponds to a fit to a constant value. This estimates the mean frequency value. Moreover, we did not include other degrees as the fit of the smooth component was already very good². Also, adding higher order polynomials to the smooth component might account for some of the glitch oscillating features. It is essential to avoid such a behaviour as the definitions of the seismic indicators, and the inferences we draw from them, will be impacted.

Furthermore, we could also include a regularisation parameter λ (as in Verma et al. 2014, method C) in order to prevent those behaviours. This requires a new definition of the vector

² Appendix E shows that adding new elements to the set of basis functions is indeed not relevant.

sub-spaces. The vectors are now of dimension $2N$. The first N components are defined as before while the components from $N + 1$ to $2N$ are 0 for both the frequencies and the glitch polynomial, and the second derivative of the polynomial for the smooth part. The vectors are now:

$$\begin{aligned} \mathbf{v} &\rightarrow \mathbf{v}' = (v_{i,i \leq N}, 0_{N < i \leq 2N}) \\ \text{smooth} &\rightarrow \mathbf{q}'_j = \left(\mathbf{q}_j, \frac{\partial^2 \mathbf{q}_j}{\partial n^2} \right) \\ \text{glitch} &\rightarrow \mathbf{q}'_j = (\mathbf{q}_j, \mathbf{0}). \end{aligned} \quad (13)$$

Then, we have to define the scalar product of \mathbf{x} and \mathbf{y} as

$$\langle \mathbf{x} | \mathbf{y} \rangle = \sum_{i=1}^N \frac{x_i y_i}{\sigma_i^2} + \lambda^2 \sum_{i=N+1}^{2N} x_i y_i. \quad (14)$$

Therefore, using the definition (3) with the new scalar product gives another value of the merit function. The inclusion of the regularisation parameter allows to minimise the oscillation of the smooth component as the minimisation of the merit function will lead to a minimisation of the second derivatives of the smooth component. Let us note that, for the regularisation constant to have an influence on the results, it must at least be of the order of the inverse of the frequencies standard deviation. However, we performed some tests with and without regularisation terms and it appears that the method is very stable without it. Moreover, we observed in many cases that the results were degraded when including it (see also Appendix A for an illustrative example). Therefore, it is not necessary to include these regularisation terms to properly extract the glitch in our method. As a consequence, the results presented in this paper do not include such terms. The fact that we use fewer fitting parameters than in (Verma et al. 2014; they consider polynomials up to the fourth degree whereas we only reach the second) might explain that the regularisation constant is not necessary in our case. In addition, we note that using $\lambda = 0$ leads to the classical χ^2 fitting.

Finally, as we have three polynomials for each value of l , we built, for the smooth component, a vector sub-space of dimension $3 \times l$ which equals 12 if we have four values for l (e.g. 0, 1, 2, 3). As hinted earlier, more than three observed frequencies of each degree are necessary to apply the developed method.

2.3. Glitch

The formulations used by Verma et al. (2014) and Houdek & Gough (2007) allow us to fit properly the helium and convection zone glitches but they are highly non linear with respect to the free parameters. Below is the expression from Verma et al. (2014), which we adapted:

$$\begin{aligned} \delta v_{g, \text{Verma}} &= \mathcal{A}_{\text{He}} v e^{-c_2 v^2} \sin(4\pi \tau_{\text{He}} v + \phi_{\text{He}}) \\ &\quad + \frac{\mathcal{A}_{\text{CZ}}}{v^2} \sin(4\pi \tau_{\text{CZ}} v + \phi_{\text{CZ}}), \end{aligned} \quad (15)$$

where the first term takes the helium glitch into account and the second, the convection zone glitch. The quantities τ_{He} , ϕ_{He} , and \mathcal{A}_{He} represent respectively the acoustic depth of the second ionisation zone of helium, the phase of the helium glitch, and its amplitude. The same goes for the quantities τ_{CZ} , ϕ_{CZ} , and \mathcal{A}_{CZ} in the case of the base of the envelope convective zone. Finally, c_2 is the rate of decrease in amplitude of the helium glitch with the squared frequency.

Moreover, Eq. (15) is implicit since the frequency appears on the right-hand side. To adjust at best the frequencies, it is therefore necessary to use non-linear least square fitting algorithms (e.g. Levenberg-Marquardt's method, genetic algorithms, ...) which can be unstable and are very sensitive to the initial guesses on the optimal parameters.

For this reason, we decided to adopt the following *linearised* functions, expressed as a function of $\tilde{n} = (n + \frac{l}{2})$ for the helium glitch:

$$p_{\text{HeCk}}(\tilde{n}) = \cos(4\pi T_{\text{He}}\tilde{n})\tilde{n}^{-k}, \quad (16)$$

$$p_{\text{HeSk}}(\tilde{n}) = \sin(4\pi T_{\text{He}}\tilde{n})\tilde{n}^{-k}, \quad (17)$$

with $k = (4, 5)$; and, for the convection zone glitch:

$$p_{\text{CC}}(\tilde{n}) = \cos(4\pi T_{\text{CZ}}\tilde{n})\tilde{n}^{-2}, \quad (18)$$

$$p_{\text{CS}}(\tilde{n}) = \sin(4\pi T_{\text{CZ}}\tilde{n})\tilde{n}^{-2}. \quad (19)$$

To obtain the above expressions we replaced the value of the frequency ν by its first order approximation from the asymptotic formulation (9): $\tilde{n}\Delta$. We also defined $T_{\text{He}} = \tau_{\text{He}}\Delta$ and $T_{\text{CZ}} = \tau_{\text{CZ}}\Delta$.

Moreover, we approximated the exponential decrease in frequency by the combination of two polynomials in $\tilde{n}\Delta$. The degrees -4 and -5 have been chosen to reproduce at best the decrease of the glitch amplitude towards high frequencies (which was described using a gaussian by Houdek & Gough 2007). To do so, we compared the polynomial formulation with the exponential one (Eq. (15)). Let us add that we adjusted the helium glitch using several sets of degrees and the method proved to be very stable and the results remained good. Both the fitted coefficients and defined indicators values were quasi unaffected by the choice of degrees. The glitch then writes

$$\delta\nu_{\text{He}}(\tilde{n}) = \sum_{k=5}^4 [c_{\text{He},k}p_{\text{HeCk}}(\tilde{n}) + s_{\text{He},k}p_{\text{HeSk}}(\tilde{n})], \quad (20)$$

$$\delta\nu_{\text{CZ}}(\tilde{n}) = [c_{\text{CZ}}p_{\text{CC}}(\tilde{n}) + s_{\text{CZ}}p_{\text{CS}}(\tilde{n})]. \quad (21)$$

Furthermore, such a formulation allows us to move on with Gram-Schmidt's process and generate orthonormal vectors to append the smooth component basis. As the glitch is generated in the superficial layers, it should not depend on l . Therefore, we defined the coefficients c and s to be independent of l . By doing so, the vector sub-space associated with the glitch is only of dimension 6 and this sub-space is used to complete the orthonormal basis over which frequencies are projected. We are thus able to write the glitch contribution to the frequencies as

$$\delta\nu_g(\tilde{n}) = \sum_{k=5}^4 [C_{\text{He},k}q_{\text{HeCk}}(\tilde{n}, T_{\text{He}}) + S_{\text{He},k}q_{\text{HeSk}}(\tilde{n}, T_{\text{He}})] + C_{\text{CZ}}q_{\text{CC}}(\tilde{n}, T_{\text{CZ}}) + S_{\text{CZ}}q_{\text{CS}}(\tilde{n}, T_{\text{CZ}}). \quad (22)$$

At this point, one should be aware to the fact that the basis functions depend on the acoustic depths of the second ionisation zone of helium and the base of the envelope convective zone, respectively – through T_{He} and T_{CZ} –. We observe that the functions depend non-linearly on the values of T_{He} and T_{CZ} . To preserve the linearity of the method, it is necessary to provide values for τ_{He} and τ_{CZ} and leave them unchanged to generate the basis and project the observed frequencies over it. In the case of a theoretical model, this estimation is done using the definition of the acoustic depth, that is:

$$\tau_{\text{He/CZ}} = \int_{R_*}^{r_{\text{He/CZ}}} \frac{dr}{c(r)}, \quad (23)$$

where R_* is the radius at the photosphere, $r_{\text{He/CZ}}$ represents the radius of the helium second ionisation zone or of the base of the envelope convection zone (in practice we take the corresponding local maximum between the two local minima of Γ_1 due to the partial ionisation of He and H for r_{He} and the last point below the surface for which $\nabla < \nabla_{\text{rad}}$ for r_{CZ}).

For observed data, we first generate the optimal model that does not take the glitches into account. We then fit this model for the glitches and retrieve the model values of the acoustic depths as estimators of the optimal values. Therefore, we do not provide any new means to estimate the involved acoustic depths.

Eventually, we may optimise over the values of τ_{He} and τ_{CZ} to get the best results. This is done through the use of Brent (1973)'s minimisation algorithm. However, it makes the problem non linear again. Furthermore, the optimised estimations of τ_{He} and τ_{CZ} always remain very close to the theoretical value and do not decrease significantly the χ^2 value. Also, we observed that by using an initial value of τ_{He} different from that at the Γ_1 maximum (e.g. at the minimum of the helium second ionisation zone) and adjusting it, we found back the value at the maximum. Moreover, we tried to find the value of Y_f giving the best agreement with the helium amplitude (defined in Sect. 3.3.1) observed in the case of 16 Cyg A at fixed values of τ_{He} corresponding either to the second local minimum or the local maximum of the Γ_1 profile. We noted that the difference between both values of Y_f is smaller than the standard deviation. In addition, freeing τ_{He} does not impact the surface helium abundance retrieved in a significant way. This stems from the fact that the acoustic depth value changes at most of 10% and has little influence on the measured helium glitch amplitude. Therefore, the influence on the calculated Y_f is negligible as well. Thus we finally decided to give up that last non-linear minimisation for theoretical models.

By keeping a fully linear implementation of the spectrum fitting we guarantee the stability of the algorithm, the independence³ of the parameters obtained via the projection on the orthonormal basis as well as small computation times. This is essential for it has to be included into a non-linear routine that searches for a stellar model accounting at best for the seismic and non-seismic observables.

3. Seismic indicators

The main advantage of the developed method is that it provides – via Gram-Schmidt's process – fitted coefficients which are independent of each other. It therefore allows us to derive seismic indicators as uncorrelated as possible. We will define the ones that we explored in the current section. To characterise those indicators, we computed their evolution along the grid of models presented in the next subsection and using the set of modes observed for 16 Cyg A.

3.1. Models

The grid of models we used was computed using CLES (Scuflaire et al. 2008a) combined with LOSC (Scuflaire et al. 2008b) stellar evolution and oscillation codes. The models used the FreeEOS software (Cassisi et al. 2003) to generate the equation of state table, the reaction rates prescribed by Adelberger et al. (2011), the metal mixture of AGSS09 (Asplund et al. 2009), and the OPAL opacity table (Iglesias & Rogers 1996)

³ Provided that the measurements of the frequencies are independent, which is not always the case.

combined with that of [Ferguson et al. \(2005\)](#) at low temperatures. Moreover, the mixing inside convective regions was computed according to the mixing length theory ([Cox & Giuli 1968](#)) and using the value $\alpha_{\text{MLT}} = l/H_p = 1.82$ (where l is the mixing length and H_p the pressure scale height) that we obtained via a solar calibration. Microscopic diffusion was taken into account in the computation by using [Thoul et al. \(1994\)](#)'s routine. For each model, the temperature at the photosphere and the conditions above the photosphere are determined by using an Eddington $T(\tau)$ relationship. The models have masses ranging from $0.90 M_\odot$ to $1.30 M_\odot$ by steps of $0.01 M_\odot$ and are in the main sequence phase. Moreover, each model has an initial composition of $Y_0 = 0.25$ and $Z_0 = 0.016$ to remain close to the solar case. Finally, unless specified otherwise, the observed frequencies have been corrected for the surface effects using [Kjeldsen et al. \(2008\)](#)'s prescription of which the coefficients a and b have been calibrated by [Sonoi et al. \(2015\)](#).

3.2. Smooth component indicators

3.2.1. Large separation

A commonly used indicator is the large separation which holds a local (i.e. based on the individual frequencies) and an asymptotic definition. To construct an estimator of the large separation, we will take inspiration in the asymptotic definition. In the asymptotic regime ($n \gg l$), Eq. (9) is satisfied. We notice that, in this formulation, Δ represents the slope in n of the straight line fitting at best the frequencies. Moreover, to fit the spectrum smooth component, we project the frequencies over the basis in a specific order given by the sequence of degrees (0, 1, 2). This means that keeping only the expression of order 0 will give an adjustment of the frequencies by a constant term, thus estimating the mean value. Furthermore, if we now keep the expression of first order, we adjust the frequencies to a straight line of which the slope, if we rely on Eq. (9), is Δ . This is the most common way to define the mean large separation in seismic analyses. However, we must note that we have different basis vectors depending on the spherical degree considered. This means that, for each value of l , we will have a different regression to a straight line, therefore a different estimate of the large separation Δ_l . Using expressions (4), (5), (7), and (8), we isolate this slope to write:

$$\Delta_l = a_{l,1} R_{l,1,1}^{-1}. \quad (24)$$

We may finally average these indicators over l to estimate at best the large separation. Knowing that the standard deviation of $a_{l,1}$ is 1, $(R_{l,1,1}^{-1})^2$ is the variance of Δ_l . The weighted mean of the large separations thus yields

$$\Delta = \frac{\sum_l a_{l,1} / R_{l,1,1}^{-1}}{\sum_l 1 / (R_{l,1,1}^{-1})^2}. \quad (25)$$

Finally, we expect from [Ulrich \(1986\)](#) that Δ should be an estimator of the mean stellar density.

3.2.2. Normalised small separation

Two commonly used indicators are the small separations $d_{01}(n)$ and $d_{02}(n)$ of which the definitions are:

$$d_{01}(n) = (\nu(n-1, 1) - 2\nu(n, 0) + \nu(n, 1)) / 2, \quad (26)$$

$$d_{02}(n) = (\nu(n, 0) - \nu(n-1, 2)). \quad (27)$$

They allow a measurement of the spacing between the observations and the asymptotic relation (9). However, they happen to be sensitive to the surface effects. Therefore, [Roxburgh & Vorontsov \(2003\)](#) suggested to divide these expressions by the large separation in order to minimise such effects. Indeed, they showed that those ratios are almost independent of the structure of the outer layers of the star.

We thus introduce estimators of these ratios. Such ratios represent the spacing between ridges of spherical degrees 0 and 1 for Eq. (26) and degrees 0 and 2 for Eq. (27) in the échelle diagram ([Grec et al. 1983](#)). In a more general way, we approximate the mean difference between the ridges of spherical degrees 0 and l by comparing the mean values of the frequencies for those degrees. That is $(\bar{\nu}_0 - \bar{\nu}_l) / \Delta_0$. Assuming expression (9) to be exact, this difference is $\bar{n}_0 + \epsilon_0 - (\bar{n}_l + \epsilon_l + l/2)$. Then, we added $-\bar{n}_0 + \bar{n}_l + l/2$ to the expression to make its value come close to $\epsilon_0 - \epsilon_l$. We then obtained the following expression:

$$\hat{r}_{0l} = \frac{\bar{\nu}_0 - \bar{\nu}_l}{\Delta_0} + \bar{n}_l - \bar{n}_0 + \frac{l}{2}, \quad (28)$$

where $\bar{\nu}_l$ and \bar{n}_l are respectively the weighted mean values of $\nu(n, l)$ and of n for the spherical degree l in accordance with the definition of the scalar product. In addition, the mean value $\bar{\nu}_l$ equals $a_{l,0} R_{l,0,0}^{-1}$ as it is the fitting of the frequencies of degree l to a constant value. Finally, we stress that the above expression is slightly different from Eqs. (26) and (27) as they represent the local spacing between ridges in the échelle diagram and Eq. (28) corresponds to the mean spacing. Figure 1 shows the evolution of those indicators along the grid presented in Sect. 3.1⁴ for the set of modes observed in 16 Cygni A. The x-axis is the large separation of spherical degree 0 as we defined above and the y-axis is the considered indicator. We also display the observed values for 16 Cygni A (HD 186408) using the frequencies determined by [Davies et al. \(2015\)](#). In blue is the observed value and, in red, the value corrected for the surface effects according to [Kjeldsen et al. \(2008\)](#)'s prescription. We note that these indicators are almost insensitive to surface effects excepted for the case of \hat{r}_{02} , which value is changed by about 1σ . We only show the standard deviation for the estimators of the small separation as the one for the large separation is too small to be visible on the plot. Indeed, we computed a standard deviation for Δ_0 of $\sigma(\Delta_0) = 5 \times 10^{-3} \mu\text{Hz}$.

To provide a comparison, we computed the evolution of the ‘‘usual’’ indicators along the same tracks as in Fig. 1 and display it in Fig. B.1. We observe that the new indicators exhibit the same behaviour as the usual ones and provide smaller standard deviations, therefore, tighter constraints.

We note on Fig. 1 that \hat{r}_{02} is a very good indicator of the core conditions and should hold information about the evolutionary stage on the main sequence as its evolution is almost monotonic. It is therefore very similar to the small separation that has been shown to carry information on the evolution ([Christensen-Dalsgaard 1988](#)) as it is sensitive to the sound speed gradient which in turn is sensitive to the chemical composition changes. On the other hand, \hat{r}_{01} is not a good indicator of the evolution but carries additional information. For example, [de Meulenaer et al. \(2010\)](#) showed that, for stars with masses and metallicities close to that of α Centauri A (HD 128620), it should provide an upper limit on the amount of convective-core overshooting. We also draw attention to the fact that \hat{r}_{01} shows a turn off for evolved stars. This means that we have to be cautious when fitting models to the observations as, for specific sets of input physics, there

⁴ However, in the case of the indicator \hat{r}_{01} we used a $0.02 M_\odot$ step for a better visibility.

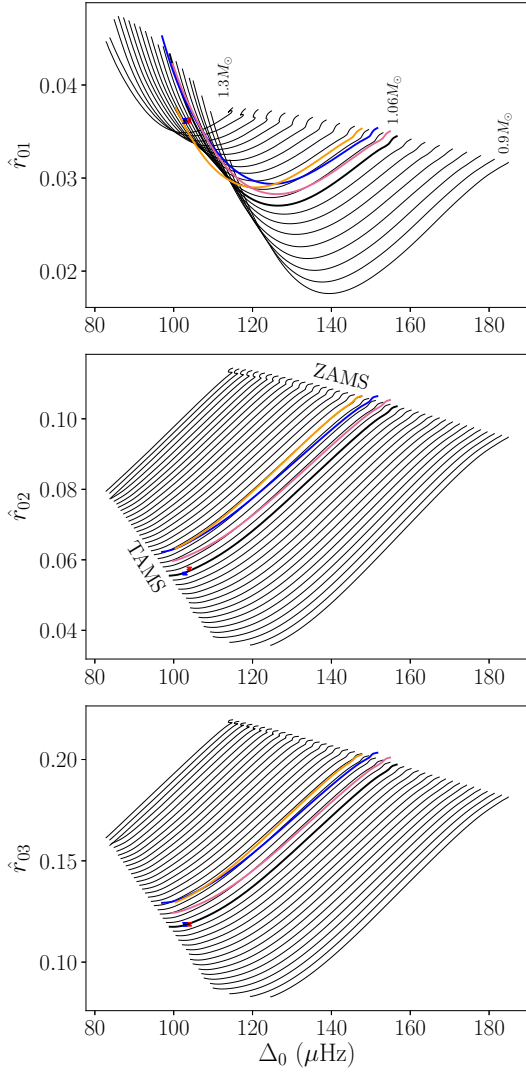


Fig. 1. Seismic HR diagram defined with the new indicators \hat{r}_{0l} and computed along the grid presented in Sect. 3.1. The masses increase from right to left. The blue marker shows the observed value for 16 Cyg A while the red one shows the value corrected for the surface effects following Kjeldsen et al. (2008)’s prescription. The thick line represents the track for $1.06 M_{\odot}$. The blue line has been computed for $Y_0 = 0.27$, the orange one for $\alpha_{\text{MLT}} = 1.5$, and the pink one for $(Z/X)_0 = 0.018$. All the coloured lines have been computed for $1.06 M_{\odot}$.

exists inaccessible regions. This should allow to constrain the input physics.

Finally, \hat{r}_{03} does not provide new information. In addition, we may observe from the comparison between the observations and the theoretical tracks that the expected masses retrieved from the different indicators are in agreement. Indeed, from \hat{r}_{01} , we should expect masses between $1.06 M_{\odot}$ and $1.11 M_{\odot}$. Then, from \hat{r}_{02} , the expected values are in between $1.06 M_{\odot}$ and $1.07 M_{\odot}$. Again, \hat{r}_{03} does not add some information as the values range from $1.05 M_{\odot}$ to $1.06 M_{\odot}$. As a consequence, we would expect the mass of 16 Cygni A to be around $1.06 M_{\odot}$. This value has been highlighted on the figure by using a thick line. However, we must observe that this does not provide a precise estimate of 16 Cyg A mass as we only tested a specific chemical composition – $Y_0 = 0.25$, $Z_0 = 0.016$ – as well as given choice

of $\alpha_{\text{MLT}} = 1.82$. A proper adjustment is needed to draw conclusions. Those values are only given to illustrate the compatibility between the different indicators. We also show the influence of the composition and α_{MLT} on the coloured tracks. The blue line is for a higher initial helium abundance. Then, the orange line depicts the influence of a lower value of α_{MLT} . Finally, the pink line shows how a higher metallicity modifies the results. We observe in all cases that the inferred mass should be lower.

3.2.3. Δ_{0l} indicators

As it has been shown in several studies, the combination of the small separation ratios r_{01} and r_{10} first introduced by Roxburgh & Vorontsov (2003) into r_{010} allows to provide inferences about the stellar central mixed region extension (Popielski & Dziembowski 2005; Deheuvels et al. 2010; Silva Aguirre et al. 2011). Indeed, the mean value and slope of this indicator occupy very specific regions in the parameter space according to the extent of the central mixed region. This should therefore provide constraint on the amount of overshooting necessary to reproduce observations. As an example, an extensive study of several *Kepler* targets has been realised by Deheuvels et al. (2016) who have been able to provide constraints on the overshooting parameter α_{ov} for eight of those targets. In the framework of this paper, the indicator \hat{r}_{01} represents an estimator of the mean value of r_{010} . We may therefore build an indicator for its slope as follows:

$$\Delta_{0l} = \frac{\Delta_l}{\Delta_0} - 1, \quad (29)$$

with Δ_l the large separation for modes of spherical degree l defined by Eq. (24). It is straightforward to show that, in the asymptotic regime, Δ_{01} indeed represents the slope of the frequency ratio r_{01} .

As for the small separation indicators, we computed the evolution of such indicators along the grid of models presented in Sect. 3.1 to demonstrate their regularity and validity. This is shown in Fig. 2. We also display the observed value for the case of 16 Cygni A. This value is corrected for the surface effect using Kjeldsen et al. (2008)’s prescription. As in Fig. 1, the error on Δ_0 is too small to be visible. Moreover, we show the influence of a change in the composition and of α_{MLT} with the coloured tracks. The colours are the same as in Fig. 1.

Again, it is possible to get an estimate of the mass value for the given composition and physics. From Δ_{01} , we expect masses ranging from $1.06 M_{\odot}$ to $1.07 M_{\odot}$. Then, from Δ_{02} , we expect that they lie between $1.05 M_{\odot}$ and $1.07 M_{\odot}$. Finally, from Δ_{03} , the mass should be between $1.00 M_{\odot}$ and $1.05 M_{\odot}$. This time, we observe a slight incompatibility between the first two indicators and the last one. Let us add that we highlighted the value of $1.06 M_{\odot}$ as in Fig. 1. Moreover, we note that, as opposed to the small separation ratio indicators, the relative behaviours of the coloured tracks are different for the three indicators. This could allow to discriminate various choices in the physics of the models considered as they represent different values of α_{MLT} , Y_0 , and Z/X_0 and also to solve the slight mass discrepancy observed.

Finally, as detailed above, the simultaneous use of both \hat{r}_{01} and Δ_{01} allows to provide estimations of the extent of stellar mixed cores. To illustrate this, we plotted main sequence evolutionary tracks for a $1.2 M_{\odot}$, $Y_0 = 0.25$ and $X_0 = 0.734$ with several overshooting parameter values ranging from 0.005 to

0.3. The overshooting parameter gives the extent of the mixed core above the Schwarzschild limit through $d = \alpha_{\text{ov}} \min(H_p, h)$ where H_p is the pressure scale height and h the thickness of the convection zone. This is shown in Fig. 3. The ZAMS is at the converging point of the tracks and the TAMS is at their end. We observe that the various tracks occupy very specific regions in the $(\Delta_{01}, \hat{r}_{01})$ diagram. Moreover, we note the striking resemblance of Fig. 3 and Fig. 3 of Deheuvels et al. (2016). This should allow us to constrain the amount of overshooting. However, Deheuvels et al. (2016) noted that for this diagnostic tool to be efficient, the mean large separation of the target should not exceed $\sim 110 \mu\text{Hz}$ and mixed modes should not be present in the oscillation spectrum.

3.2.4. $\hat{\epsilon}$

To provide an estimate of ϵ , we define the following vector sub-space, where frequencies are described as

$$v(n, l) = \left(n + \frac{l}{2} + \epsilon \right) \hat{\Delta} = \left(n + \frac{l}{2} \right) \hat{\Delta} + K, \quad (30)$$

where $\hat{\Delta}$ and K are free parameters.

Then, we define an orthonormal basis over this sub-space: \tilde{q}_0 and \tilde{q}_1 . Finally, by projection of the frequencies over this basis and identification of the several coefficients with the asymptotic formulation, we can retrieve an expression for $\hat{\epsilon}$, the estimator of ϵ . We note that this projection also provides an expression to estimate the large separation that is different from Eq. (25).

Figure 4 shows the evolution of the indicator $\hat{\epsilon}$ along the grid presented in Sect. 3.1 but with a step of $0.02 M_\odot$. We may observe that this indicator is almost insensitive to the mass for the early stages of the main sequence. The influence of the mass only becomes visible when the stars become older. Moreover, the red marker in Fig. 4 shows the observed value for 16 Cygni A. We note a disagreement between theoretical and observed data. This disagreement can however be tackled by correcting the observed frequencies for the surface effects. This is what the blue and green markers represent. For the blue one, we have computed a correction to the surface effects following Kjeldsen et al. (2008)'s prescription. Then, for the green one, we have computed the correction prescribed by Sonoi et al. (2015). Therefore, it seems reasonable that the indicator we defined could be of some use to constrain the surface effects. It could provide a complementary method to that of Roxburgh (2016). Indeed the method presented uses differences between observed and model ϵ values – under the hypothesis that both the model and observed star have the same inner structure – to isolate only the surface contribution to the measured frequencies. This allows to account for surface effects without the need of empirical corrections. On the other hand, the present indicator should allow to discriminate several surface effects corrections without the need of any physical assumption.

3.3. Glitch indicators

3.3.1. Helium amplitude

With the aim of retrieving the photospheric helium abundance, we built an indicator of the helium glitch amplitude. Verma et al. (2014) obtain their indicator via an integration of the glitch amplitude over the spectrum. We prefer taking advantage of the

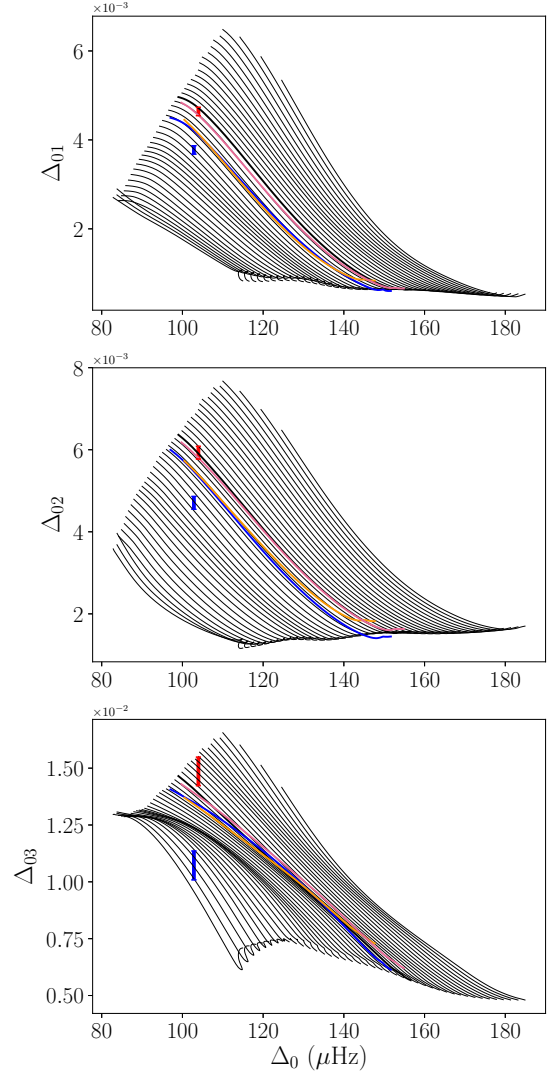


Fig. 2. Seismic HR diagram defined with the new indicators Δ_{0l} and computed along the grid presented in Sect. 3.1. The masses increase from right to left. The red marker shows the observed value corrected for the surface effects following Kjeldsen et al. (2008)'s prescription. The thick line represents the track for $1.06 M_\odot$. The blue line has been computed for $Y_0 = 0.27$, the orange one for $\alpha_{\text{MLT}} = 1.5$, and the pink one for $(Z/X)_0 = 0.018$. All the coloured lines have been computed for $1.06 M_\odot$.

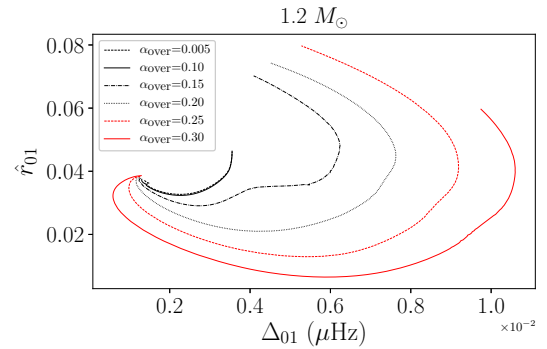


Fig. 3. MS evolutionary tracks in the $(\Delta_{01}, \hat{r}_{01})$ plane for models of $1.2 M_\odot$ with $Y_0 = 0.25$ and $X_0 = 0.734$ for several values of the overshooting parameter α_{ov} shown in the legend.

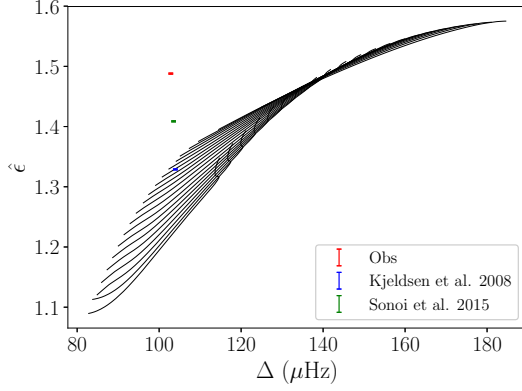


Fig. 4. Evolution of $\hat{\epsilon}$ along the grid presented in Sect. 3.1. The masses increase from top to bottom. The step is here of $0.02 M_{\odot}$. The red, green, and blue markers respectively represent the observation for 16 Cygni A, the observation for 16 Cygni A corrected for the surface effects using Kjeldsen et al. (2008)’s prescription and the one corrected using Sonoii et al. (2015)’s prescription.

scalar product and define the indicator as the norm of the helium glitch component, thus generating the following expression:

$$A_{\text{He}} = \sqrt{C_{\text{He},5}^2 + S_{\text{He},5}^2 + C_{\text{He},4}^2 + S_{\text{He},4}^2} \quad (31)$$

Thanks to the orthonormalisation, it is independent of the other indicators and its standard deviation equals 1. We calculated the evolution of this indicator with respect to the surface helium mass fraction Y_f and the surface mass fraction of metals Z_f . This is shown in Figs. 5 and 6. Figure 5 has been computed for stars with a fixed $(Z/X)_0$ ratio of 0.022 for several surface helium mass fractions, displayed on the abscissa, and for the three values of the mass shown in the legend. To have a reference, we imposed the models to have a fixed value of the large separation – the one observed for 16 Cyg A. In a similar way, Fig. 6 has been computed for a fixed value of $Y_0 = 0.24$ and for several masses shown in the legend. The helium glitch amplitude has then been computed for the values of Z_f displayed on the abscissa. We insist on the fact that these tracks do not represent the evolution of the helium amplitude with the surface composition along the evolution of a given model. Instead, each point corresponds to a given stellar model that fits the observed 16 Cygni A large separation for a given surface composition. This means that those models were not selected from the grid presented in Sect. 3.1.

We observe in Fig. 5 an increasing trend in the helium glitch amplitude with the helium mass fraction as well as with the mass. This has to be expected as a larger quantity of helium inside the star would lead to a more important depression of the first adiabatic index Γ_1 at the second ionisation zone of helium, and, therefore, a glitch of greater amplitude. Moreover, we also show the influence of the surface effects by computing the amplitude evolution for a $1.052 M_{\odot}$ star for which the surface effects have been taken into account via Kjeldsen et al. (2008)’s prescription (dot-dashed line). It is apparent that they have little influence on the amplitude as the values remain in the 1σ error bars of the uncorrected models. This was expected as the glitch is of greater amplitude in the low frequencies regime while the surface effects corrections are greater in the high frequencies regime.

Furthermore, as shown in Fig. 6, the glitch amplitude and the metallicity are anti-correlated. This corroborates Basu et al.

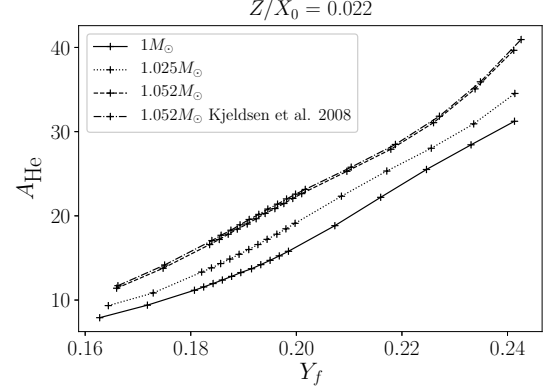


Fig. 5. Evolution of the helium glitch amplitude A_{He} with the surface helium abundance Y_f . Each track corresponds to a given mass, written in the legend. The dot-dashed line represents the amplitude for a $1.052 M_{\odot}$ model of which the frequencies have been corrected for surface effects as in Kjeldsen et al. (2008). Every model has an initial heavy elements abundance of $(Z/X)_0 = 0.022$. Each point has been computed with the same large separation to remain at the same evolutionary stage.

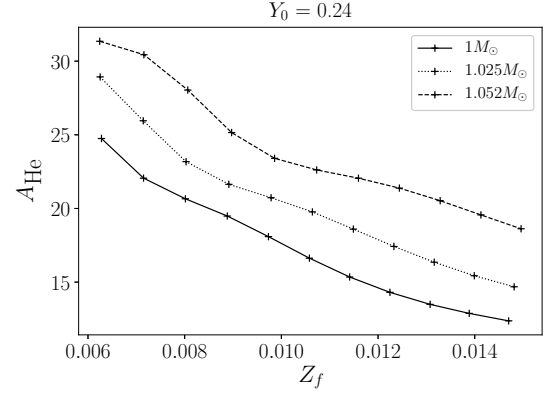


Fig. 6. Evolution of the helium glitch amplitude A_{He} with the surface heavy elements abundance Z_f . Each track corresponds to a given mass labeled in the legend.

(2004)’s observations. Therefore, we are facing a degeneracy and the glitch amplitude alone will not be sufficient to estimate properly the surface helium mass fraction. Thus, the smooth component indicators defined above will be of great help. This clearly shows that the $A_{\text{He}}-Y_f$ relation is model dependent which should never be forgotten.

Figure 7 illustrates this degeneracy. It represents the profile of Γ_1 as a function of the reduced radius in the superficial layers of stars of a fixed large separation but with several chemical compositions. We immediately notice that both an increase of the surface helium abundance and a decrease of the surface heavy elements abundance lead to a minimum that increases in magnitude. Therefore, the helium glitch amplitude becomes greater as well. We provide an interpretation of this phenomenon in Sect. 4.2.

3.3.2. Convection zone amplitude

The definition of the envelope convective zone glitch amplitude we provide is very similar to that of the helium glitch and is the following:

$$A_{\text{CZ}} = \sqrt{C_{\text{CZ}}^2 + S_{\text{CZ}}^2} \quad (32)$$

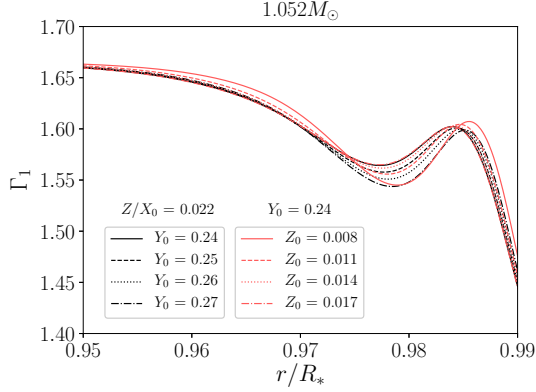


Fig. 7. Evolution of Γ_1 as a function of the reduced radius in the superficial layers of stars of fixed large separation. Every star has a mass of $1.052 M_\odot$. Two families of curves are displayed. The black ones have a fixed value of the ratio between the initial hydrogen and heavy elements abundances of $(Z/X)_0 = 0.022$ and variable initial helium abundance. The red ones have a fixed initial helium abundance of $Y_0 = 0.24$ and a variable initial heavy elements abundance. The different values are displayed on the figure.

We expect this indicator to be a proxy of the sharpness of the transition between the envelope convective zone and the radiative zone. Again, thanks to the orthonormalisation, it is independent of the other indicators and its standard deviation is equal to 1. We present in Fig. 8 its evolution with the importance of the undershooting, characterised by the coefficient α_{under} . This coefficient determines the size d of the undershooting region at the bottom of the convective envelope. This size is given by $d = \alpha_{\text{under}} \min(H_p, h)$ where H_p is the pressure scale height and h the thickness of the convection zone. In the undershoot region, the temperature gradient is set to the adiabatic one and the mixing is assumed to be instantaneous.

We expect an increase of A_{CZ} with α_{under} as the introduction of undershooting in a stellar model will create a discontinuity of the temperature gradient. The temperature gradient jump increases with the value of α_{under} . Thus, the glitch amplitude increases as well. This is what we show in Fig. 8 where the computed models have a mass of $1.052 M_\odot$, an initial hydrogen mass fraction of $X_0 = 0.744$, and an initial metal mass fraction of $Z_0 = 0.016$. As for the case of the helium amplitude evolution, we kept a fixed large separation – which is that of 16 Cyg A – for each model. Moreover, we noted that each computed model was at the same evolutionary stage (constant central hydrogen mass fraction). Therefore, the observed effect is not evolutionary but rather the effect of the temperature gradient discontinuity as expected. Finally, we may add that, when setting the temperature gradient to the radiative one in the undershoot region, we do not observe any significant trend in the amplitude with α_{under} . We may thus conclude that we observe the effect of the temperature gradient and not of the chemical composition.

4. Method characterisation

4.1. Capabilities

For the observed data, we have chosen the frequencies computed by Davies et al. (2015) for the component A of the binary system 16 Cygni (HD 186408). We come back to the particular case of 16 Cyg A in Sect. 5. Figure 9 shows the difference

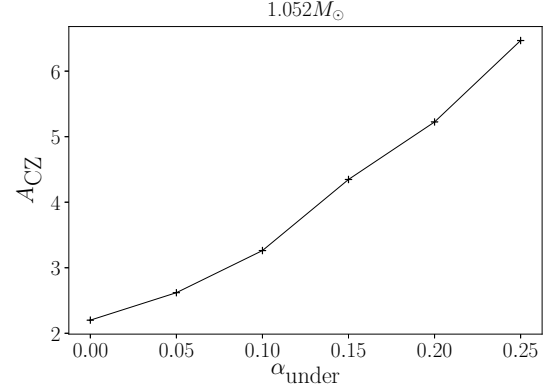


Fig. 8. Evolution of the convection zone glitch amplitude A_{CZ} with α_{under} for a star of mass $1.052 M_\odot$, $X_0 = 0.744$, $Z_0 = 0.016$ and at a constant value of the large separation.

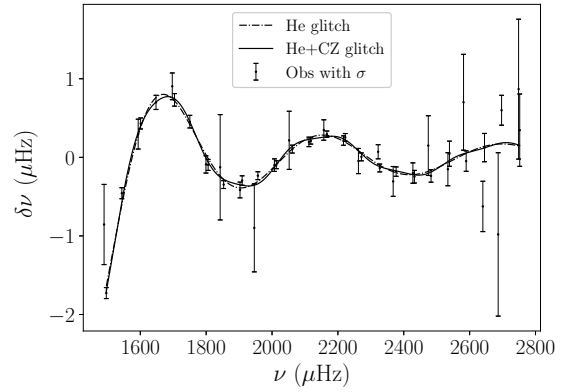


Fig. 9. Fitted glitch to 16CygA (HD 186408) data (Davies et al. 2015). Only the $l = 0$ fitted curves are displayed.

between the observed frequencies and the smooth component of the fitted frequencies, the fitted helium glitch alone and the fitted helium and convection zone glitches. Only the $l = 0$ fitted curves are displayed. We observe that the fit is good and that the helium glitch has been properly isolated. However, the convection zone glitch is of very low amplitude, compared to the helium glitch, and has a negligible contribution. This is visible in the negligible improvement of the χ^2 value from the results without including the convective zone glitch (about 10% variation). These results are similar to those of Verma et al. (2014).

4.2. Limitations

The presented method has been developed for the study of solar-like pulsators and to provide a comprehensive analysis of their oscillation spectra. However, it is not yet adapted to study evolved stars which exhibit mixed modes.

In addition, from masses around $1.25 M_\odot$ and above as well as for the highest values of the helium abundances considered (from $Y_f \sim 0.195$ and above), the evolution of the helium glitch amplitude with the surface helium mass fraction is less monotonic and inferences become unreliable. Figure 10 shows this limitation. Indeed, for $1.25 M_\odot$ we observe a very sharp increase of the helium amplitude as we defined in Sect. 3.3.1 for a quasi constant surface helium mass fraction. This corresponds to a

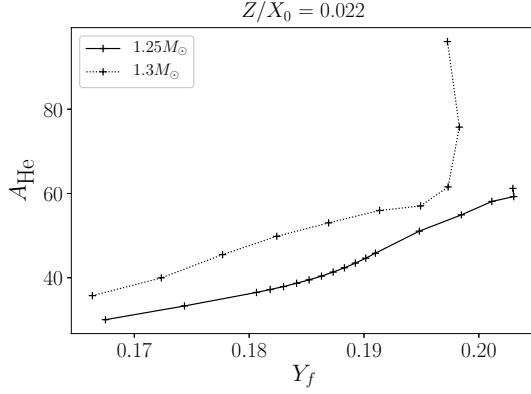


Fig. 10. Evolution of the helium glitch amplitude A_{He} with the surface helium abundance Y_f for high masses.

decrease of the surface Z/X ratio which is shown in Sect. 3.3.1 to lead to a higher amplitude.

Also, we observe for $1.3 M_{\odot}$ that the last point ($Y_f \sim 0.197$ and $A_{\text{He}} \sim 96$) moves backwards. This is due to microscopic diffusion. We observe that the size of the convective envelope decreases with the initial helium abundance. This leads to a more efficient gravitational settling as the diffusion velocities are greater close to the surface. Therefore, the surface abundance becomes smaller than for the previous point that had a lower initial helium abundance. We observe the same decrease in the surface metallicity which explains the increase of the amplitude even though the surface helium mass fraction remained constant.

We also noted in Sect. 3.3.1 that the surface abundance of metals has a relevant influence on the helium glitch amplitude and separating its contribution from that of the helium is not an easy task. To investigate such a behaviour, we developed a toy model for the first adiabatic index Γ_1 which is thought to be the main contributor to the helium glitch amplitude (Gough 1990; Houdek & Gough 2007). In this model, we trace back the influence of the helium and metals abundances on the dip of Γ_1 in the helium second ionisation zone. More information about the construction of this model is given in Appendix C. Using it, we were able to test the influence of the chemical composition decoupled from its evolutionary effect on the temperature and density profiles. To do so, we artificially modified the chemical composition profile of a reference model (black curve in Fig. 11), without changing its temperature and density profiles, to match the surface abundance, in either metals or helium, of a second reference model. This way, we were able to isolate the contribution of the chemical composition alone. Figure 11 shows the comparison between the helium second ionisation zone toy models with modified chemical composition profiles only (blue curves) and toy models with the same composition but for which its effect on temperature and density have been taken into account (red curves). We observe in the top panel that the effect of the helium abundance dominates over the effect of temperature. In the bottom panel, we observe that the metal abundance alone does not modify by a significant amount the dip in the helium second ionisation zone. However, when taking its influence on the temperature and density profiles into account, the effect becomes significant. This allows to better understand the degeneracy in composition on the helium amplitude. One effect, that of the helium abundance is direct on the shape of the Γ_1 profile in the helium second ionisation zone while the second, that of the metal abundances, is indirect as it influences the

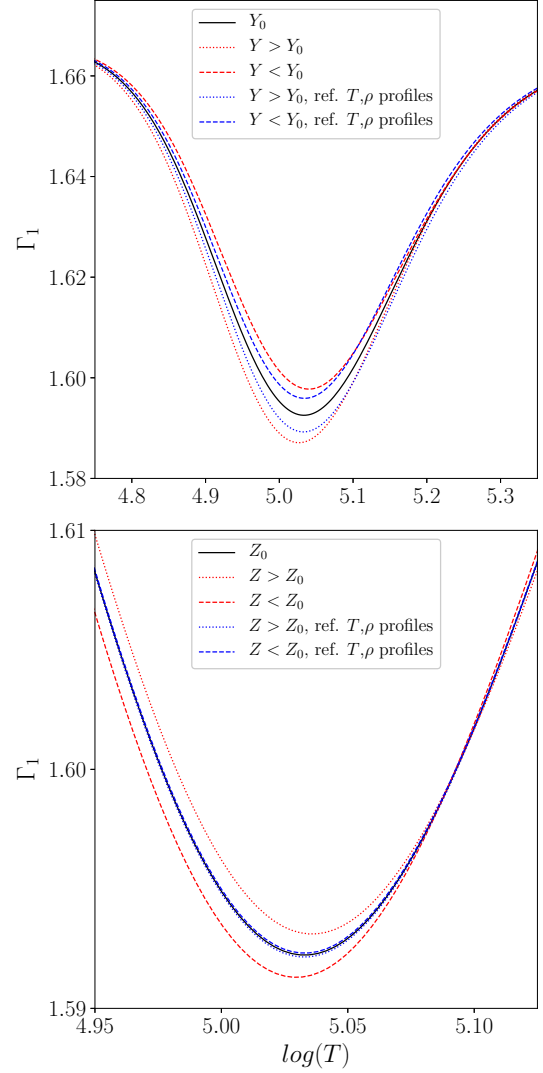


Fig. 11. Comparison with a reference model (black curve) of the toy model Γ_1 profiles in cases for which the temperature and density profiles have been decoupled from the composition profiles (blue curves) and coupled cases (red curves). The dashed lines have a common decreased abundance of the considered element and the dotted lines have an increased abundance. *Top panel:* effect of the helium abundance; *bottom panel:* effect of the metals abundance.

temperature and density profiles which in turn modify the Γ_1 profile.

Finally, we observe that, in a $\ln P - \ln T$ diagram, the curves for the different models in the temperature region of the Γ_1 dip are parallel to each other but at various height. A higher $\ln P - \ln T$ curve corresponds to a shallower Γ_1 dip. We also observe this behaviour with a fixed composition and a variable mass. Higher masses models have lower curves and deeper depressions in Γ_1 . Therefore, the toy model allows to understand the influence of the mass on the helium glitch amplitude as well.

5. Illustration with 16 Cygni A (HD 186408) observations

16 Cyg A (HD 186408) is one of the brightest stars in the *Kepler* field of view. It belongs to a binary system of solar analogs, both exhibiting solar-like pulsations. The quality and length of the

Table 1. Observed seismic indicators.

Indicator	Value		σ
	Kjeldsen	Sonoi	
$\Delta(\mu\text{Hz})$	104.088	103.611	0.005
A_{He}	30.4	30.1	1.0
A_{CZ}	2.2	1.5	1.0
$\bar{\epsilon}$	1.3288	1.4086	0.0009
\hat{r}_{01}	0.0362	0.0362	0.0002
\hat{r}_{02}	0.0575	0.0561	0.0003
\hat{r}_{03}	0.1187	0.1184	0.0008
Δ_{01}	4.6×10^{-3}	3.8×10^{-3}	0.1×10^{-3}
Δ_{02}	5.9×10^{-3}	4.8×10^{-3}	0.1×10^{-3}
Δ_{03}	14.9×10^{-3}	10.6×10^{-3}	0.6×10^{-3}

Table 2. Adjusted stellar parameters.

Quantity	Value		σ
	Kjeldsen	Sonoi	
	n^0, n, n^2	n^{-1}	
$M(M_{\odot})$	1.06	1.06	0.02
$R(R_{\odot})$	1.218	1.219	0.001
age (Gyr)	6.8	6.9	0.1
X_0	0.684	0.697	0.010
$(Z/X)_0$	0.035	0.031	0.002
Y_f	0.242	0.232	0.028
[Fe/H]	0.188	0.131	0.03

collected time series make it the ideal subject to test the method. It should be noted that we do not provide a detailed study of 16 Cygni A. Indeed, we only present here the capability of the method to provide structural constraints. A detailed study will be the object of a future paper.

5.1. Methodology

To obtain constraints on 16 Cyg A, we compute the value of the seismic indicators using the frequencies determined by Davies et al. (2015). We have corrected the surface effects for the observed frequencies by using the power law prescribed by Kjeldsen et al. (2008) and the a and b coefficients fitted by Sonoi et al. (2015) as a function of T_{eff} and g . The authors have done this coefficient adjustment by comparing the adiabatic frequencies of patched models based on 3D simulations and that of unpatched standard 1D models. We then fit the observed values of Δ , \hat{r}_{01} , \hat{r}_{02} , and A_{He} with the age, mass, initial mass fraction of hydrogen, and the initial heavy elements over hydrogen abundance ratio as free parameters. To do so, we select an initial guess value of X_0 and derive the best fit values of Δ , \hat{r}_{01} , and \hat{r}_{02} . This results in a set of values for the mass, the age, and $(Z/X)_0$. Then, the adjustment is done by applying the secant method to find the value of X_0 in best agreement with the target A_{He} . At each step of the secant algorithm – at each value of X_0 –, Levenberg-Marquardt’s algorithm (L-M) computes the optimal set of stellar parameters giving the best fit of Δ , \hat{r}_{01} , and \hat{r}_{02} . Finally, when we have a good estimate for A_{He} , we use L-M’s algorithm one last time to derive the complete set of values for the mass, the age, X_0 , and $(Z/X)_0$ fitting the observed parameters. We used the secant method in order to diminish the computational time needed to converge towards the solution.

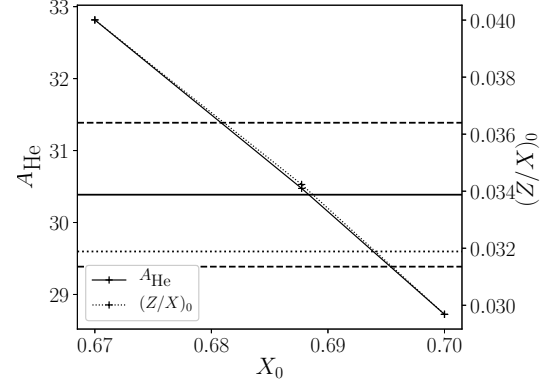


Fig. 12. Helium amplitude (solid line) and $(Z/X)_0$ ratio (dotted line) versus the initial hydrogen abundance. The horizontal solid line represents the target value for the amplitude – corrected for the surface effects following Kjeldsen et al. (2008) – while the dashed lines represent the 1σ interval. The horizontal dotted line is the value of the amplitude without surface effects correction.

5.2. Results

The values of the relevant seismic indicators as well as the associated standard deviations computed from the observed frequencies are given in Table 1. The column labeled Kjeldsen refers to the observed indicators corrected for the surface effects using Sonoi et al. (2015)’s coefficient fitted to Kjeldsen et al. (2008)’s prescription as explained in Sect. 3.1. The Sonoi column corresponds to the correction of surface effects using a Lorentzian profile as in Sonoi et al. (2015). We also derived the seismic indicators while adding smooth basis elements with n^{-1} . As the frequencies are projected in a specific order to build the seismic indicators, only the glitches amplitudes are affected and we have: $A_{\text{He}} = 27.6$ and $A_{\text{CZ}} = 3.3$. Using the methodology described above, we managed to derive the stellar parameters given in Table 2 for the different sets of observed seismic indicators. We note that changing the treatment of surface effects or adding the n^{-1} basis elements have an impact on the fitted parameters comparable to that of the frequencies uncertainties. Thus, we will only discuss here the parameters adjusted to the data corrected for the surface effects using Kjeldsen et al. (2008)’s prescription and without adding n^{-1} basis elements. The parameters we derived do not constitute a detailed characterisation of the target 16 Cyg A. Rather, they illustrate the ability of the method to provide constraints on a solar analog. Indeed, only one single set of input physics was tested. Therefore, the standard deviations tend to be underestimated as they are the ones intrinsic to the method. The abundances used for the computations were the solar ones determined by Asplund et al. (2009). Let us add that we obtain a surface helium abundance of $Y_f = 0.242 \pm 0.028$ which lies in the interval obtained by Verma et al. (2014), $Y_{f,V} \in [0.231, 0.251]$. This is comforting us in the idea that the developed method is efficient in isolating the glitches and drawing inferences from their signatures. In Fig. 12, we show the evolution of the helium glitch amplitude resulting from the three parameters adjustment of Δ , \hat{r}_{01} , and \hat{r}_{02} as a function of X_0 . We also show the evolution of the value of $(Z/X)_0$. The very linear trend justifies that we used the secant method to provide successive estimates of A_{He} in order to lessen the computational charge. In addition, we illustrate both the observed value for A_{He} and the corrected value under Kjeldsen et al. (2008)’s prescription. We note that the corrected value is of about 0.79σ lower than the uncorrected one. Using Sonoi et al. (2015)’s prescription only leads to a 0.55σ

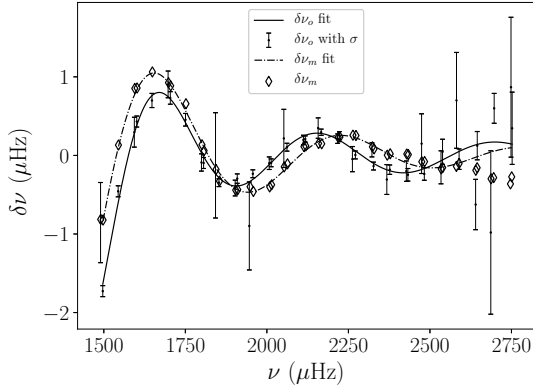


Fig. 13. Comparison between the observed helium glitch $\delta\nu_o$ (solid line) and the one resulting from the best fit model $\delta\nu_m$ (dot-dashed line), for $l = 0$. We also display the observed glitch as a function of the frequencies (errorbars) as well as the best model glitch associated with the theoretical frequencies (diamond).

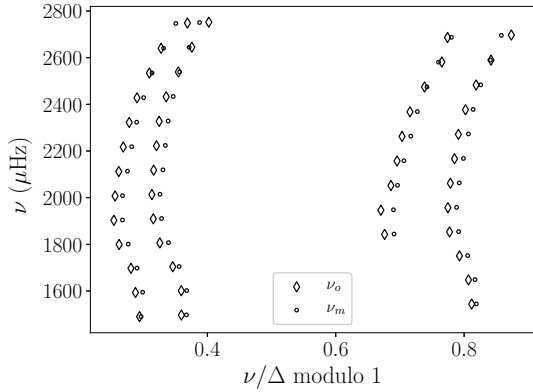


Fig. 14. Comparison between the observed frequencies (diamonds) and the best model frequencies (circles) in an échelle diagram.

variation of the measured amplitude. This demonstrates that the surface effects have a small influence on the amplitude we derive using the method. Also, we retrieved a value of 970.97 s for τ_{He} and 3042.32 s for τ_{CZ} . As they were fixed to model values and, as a consequence, were neither parameters nor constraints of the adjustment, we do not provide uncertainties. However, we may compare their values to the ones adjusted by Verma et al. (2014). They obtained $\tau_{\text{He}} \in [868, 944]$ s and $\tau_{\text{CZ}} \in [2992, 3234]$ s. We observe that τ_{CZ} lies in the interval calculated by Verma et al. (2014) while the value of τ_{He} is slightly above the upper limit. However, as we show in Sect. 2.3 this does not impact the inferences drawn from the helium glitch amplitude in a significant way. To illustrate this statement, we freed the value of τ_{He} (but not that of τ_{CZ} as the convection zone glitch is of negligible amplitude compared to that of the helium glitch). The relative change between the optimised τ_{He} and its estimator is of only 6%. Moreover, the observed value of the helium glitch amplitude remains unchanged compared to its standard deviation (we observe a change of 0.06σ). As expected, the best fit Y_f also remains untouched. At this point, one should be reminded that we focus on the glitch amplitude to draw our inferences. And, as we showed in Sect. 2.3, the exact location of the glitch does not have a significant impact on its amplitude as well as on the derived surface helium abundance. Finally, Fig. 13 shows the fit-

ted helium glitches⁵ for the observed data and the 4 parameters best fit model. It is visible that the observed and fitted glitches are close in amplitude and period. This demonstrates the ability of the method to both isolate the glitch and the related parameters and to provide a model reproducing at best those parameters. We also show in Fig. 14 the comparison in an échelle diagram of the observed frequencies and those of the best fit model. We observe in this last figure that the smooth component of the spectrum (not visible in the previous figure) is properly adjusted. Thus, by fitting the set of indicators Δ_0 , \hat{r}_{01} , \hat{r}_{02} , and A_{He} we obtain a good representation of the observed frequencies. We also show in Appendix F the adjustment to frequencies corrected for surface effects using a Lorentzian profile as in Sonoi et al. (2015). We observe in Fig. F.1 that the agreement between the model and observed glitches is better than in Fig. 13. However, we also note in the corresponding échelle diagram (Fig. F.2) that there is an offset between observed and model ridges. This corresponds to different values of $\hat{\epsilon}$. Figure 4 also illustrates this behaviour as it is clearly visible that only Kjeldsen et al. (2008)’s prescription allow to reproduce the observed value for $\hat{\epsilon}$.

6. Discussion and conclusions

6.1. Principle

In the present paper, we provide a new method that uses as much of the available seismic information as possible. Indeed, we take advantage of the information contained in both the glitches and the smooth component (usually discarded in glitches analyses but then used separately for forward seismic modelling, see Verma et al. 2014 for example) of the spectrum to define indicators that are as independent as possible of each other. To do so, we take advantage of Gram-Schmidt’s algorithm to create an orthonormal basis over which we project the frequencies. The obtained coefficients are therefore independent of each other and consist in a linear combination of the frequencies. Thus, using the appropriate combination of those allows us to define uncorrelated indicators. Such indicators are constructed in order to reproduce the behaviour of “usual” indicators such as the large frequency separation. Up to this day and to our knowledge, no method, has been proposed to provide proper correlations between the smooth and glitch indicators as they are built separately. Therefore, our method provides the asteroseismologists with new diagnosis means.

6.2. Advantages

As the method only relies on linear algebra, it is very stable and the computation times are negligible – of the order of a fraction of a second –. Thus, it could easily be implemented in stellar model fitting algorithms, which are non-linear, without impacting the total computational time. This can be done with any algorithm as the method only focuses on the definition of new seismic indicators and does not rely on the physics of the model itself. Let us add that the defined indicators should be used in combination with non-seismic constraints through a single merit function while searching for a stellar model in order to obtain proper covariances between the inferred quantities – which is not often the case in seismic analyses. The illustration for 16 Cyg A

⁵ We do not display the envelope convective zone glitch as its amplitude is negligible compared to that of the helium glitch, as mentioned in Sect. 4.

truly demonstrates the possibility to use the new indicators to provide further constraints on stellar structure in the framework of forward seismic modelling.

In addition, the usual indicators often hold a local definition and may use correlated information while the new ones are built in a way that the information used is averaged over the whole frequency range and that it is not redundant (each observed frequency is used only once for each indicator). This results in smaller standard deviations and smoother behaviours. Appendix B shows the evolution of the classical indicators $r_{01}(n)$ and $r_{02}(n)$ as defined by [Roxburgh & Vorontsov \(2003\)](#). We indeed observe that the new definitions of the indicators give smaller error bars while preserving the expected trends, providing tighter constraints. Finally, the method has the advantage that it can be implemented even in cases where some modes are missing. It is not the case of the “usual” methods as they need successive modes to define some of their indicators. For example, the classical local definitions of the large separation and second differences require at least two consecutive frequencies. Therefore, whenever some modes are missing, pieces of information might be discarded.

6.3. Information carried by the indicators

We have defined indicators that provide estimates for the classical indicators that are the large separation, Δ and Δ_l , and the small separation ratios, \hat{r}_{0l} . As expected, Δ provides an estimation of the stellar mean density ([Ulrich 1986](#)). Also, we defined the indicators Δ_{0l} which combine the large separations associated with the spherical degrees 0 and l which are known to give an estimate of the resonant cavity of the l degree modes ([Monteiro 2002](#)). Those indicators provide an estimator of the slope of r_{010} which, combined with \hat{r}_{01} can be used to constrain the overshooting parameter as shown in Fig. 3.

Moreover, we observe in Fig. 1 that the indicator \hat{r}_{02} , defined to estimate the small separation ratio between the spherical degrees 0 and 2, is a proper indicator of the evolution of the star, as expected from [Christensen-Dalsgaard \(1988\)](#). Also, we observe that the indicator \hat{r}_{01} presents a degeneracy, as a turn-off occurs in the Δ_0 – \hat{r}_{01} plane, and there is an inaccessible region. This is a very interesting observation as it should provide tight constraints on the stellar structure. Indeed, we show that a change in composition or in the value of α_{MLT} allows to modify that region. It will therefore be necessary to use such parameters to reproduce observed values.

Furthermore, Fig. 4 shows that we might get constraints on the surface effects from the indicator $\hat{\epsilon}$ we defined. It should allow to discriminate from several empirical formulations meant to account for the surface effects. We have tested both formulations from [Kjeldsen et al. \(2008\)](#) and [Sono et al. \(2015\)](#) as an illustration of the diagnosis power of the indicator $\hat{\epsilon}$. However, we are aware of the existence of the formulation from [Ball & Gizon \(2014\)](#) and it should also be inspected in further studies. Besides, we showed that the helium amplitude indicator is almost unaffected by the surface effects as it has to be expected (see for example Fig. 12). Indeed, empirical surface effects corrections are important for the high frequencies compared to ν_{max} while the glitch is of great amplitude only for the low frequencies. Also, the helium glitch amplitude should allow to draw inferences on the surface helium abundance as shown by Fig. 5. However, attention has to be paid as it is also anti-correlated with the metallicity (see Fig. 6). We have demonstrated via a toy model for the first adiabatic index that both effects on the amplitude stem from the position of the adiabat which in turn

determines the amplitude of the second local Γ_1 minimum due to helium partial ionisation.

In addition, we observe that the convective zone glitch amplitude has a significantly lower amplitude than that of the helium glitch and is correlated with the amount of undershooting at the base of the envelope convection zone (in agreement with [Verma et al. 2014](#)).

Finally, let us add that it is possible to define other indicators than those presented in this paper. This should therefore be carefully studied to take advantage of as much of the available information as possible.

6.4. Limitations

However, we show that the method is only fit to draw inferences about solar-like stars, that is low-mass stars on the main-sequence. Indeed, Fig. 10 illustrates that from masses around $1.3 M_{\odot}$ and above, diffusion plays an important role and the relation between helium surface abundance and the helium glitch amplitude is not monotonic anymore. Therefore, the method will have to be adapted for massive and evolved stars.

Moreover, one could argue that using model values as estimators of the acoustic depths of the glitches is a major drawback of the method. However, the proposed method does not focus on those quantities. Rather, we focus on the information that the amplitude of the glitch (not the period of the signal) carries. This means that we only need proper, but not exact, estimators for the acoustic depths in order to draw inferences. Indeed, we showed in Sect. 2.3, in the case of the helium glitch, that a small excursion from the estimated value (either by manually setting another value, that of the second minimum in the first adiabatic index for the helium glitch, or by optimising over its value) does not lead to a significant change in the measured amplitude. Therefore, the inferences drawn remained unchanged. However, one could still regard this as a flaw of the method as we do not provide a new way of retrieving the acoustic depths of glitches. This could be explored in future studies by, for example, finding the global optimum for the acoustic depths of the glitches and then using the measured value as a constraint for the best fit model. Nevertheless, this would make the calculations more time consuming and annihilate the benefit of the orthonormalisation that is the independence of the fitted parameters.

Also, the indicators should be used to complement non-seismic data as we have shown that, for example, there exists a degeneracy between the helium glitch amplitude, the helium surface abundance and the metallicity⁶ (see Figs. 5 and 6). Therefore, the helium amplitude alone is not sufficient and additional information are needed to lift such a degeneracy – these information may be contained in other indicators (seismic and non-seismic).

6.5. Future perspective

The next step will be the detailed study with the new method of several stars from the *Kepler* legacy sample ([Lund et al. 2017](#)). This sample consists of 66 main sequence stars for which at least one year of continuous observations has been made. Having such long time series provides the necessary precision to study glitches. Let us add that this future study is intended to be independent of what has been done in [Verma et al. \(2017\)](#).

⁶ Which we have shown in Sect. 4.2 to be an indirect effect as it is due to the influence on density and temperature profiles for the metallicity.

Also, another important step will be the improvement of the method by enabling the study of glitches present in red subgiants spectra. The peculiarity of such pulsators is that they exhibit mixed modes. This will consist in a new challenge as their analytical formulation is not a simple task. However, this is a necessary step to improve our knowledge of the evolution of a star such as the Sun. Moreover, this will allow a better description of such stars and will provide a deeper understanding of their properties via, for example, the characterisation of the mixing processes.

Acknowledgements. The authors would like to thank the referee for their very constructive remarks that improved the paper in a significant way. M.F. is supported by the FRIA (Fond pour la Recherche en Industrie et Agriculture) – FNRS PhD grant. S.J.A.J.S. is funded by ARC grant for Concerted Research Actions, financed by the Wallonia-Brussels Federation. GB acknowledges support from the ERC Consolidator Grant funding scheme (project ASTEROCHRONOMETRY, G.A. no. 772293).

References

- Adelberger, E. G., García, A., Robertson, R. G. H., et al. 2011, *Rev. Mod. Phys.*, **83**, 195
- Asplund, M., Grevesse, N., Sauval, A. J., & Scott, P. 2009, *ARA&A*, **47**, 481
- Baglin, A., Auvergne, M., Barge, P., et al. 2009, in *Transiting Planets*, eds. F. Pont, D. Sasselov, & M. J. Holman, *IAU Symp.*, **253**, 71
- Ball, W. H., & Gizon, L. 2014, *A&A*, **568**, A123
- Basu, S., Mazumdar, A., Antia, H. M., & Demarque, P. 2004, *MNRAS*, **350**, 277
- Bedding, T. R., Mosser, B., Huber, D., et al. 2011, *Nature*, **471**, 608
- Böhm-Vitense, E. 1958, *ZAp*, **46**, 108
- Borucki, W. J., Koch, D., Basri, G., et al. 2010, in *American Astronomical Society Meeting Abstracts*, BAAS, **42**, 215
- Brent, R. P. 1973, *Algorithms for Minimization without Derivatives* (Englewood Cliffs, NJ: Prentice-Hall)
- Buldgen, G., Reese, D. R., & Dupret, M. A. 2016a, *A&A*, **585**, A109
- Buldgen, G., Salmon, S. J. A. J., Reese, D. R., & Dupret, M. A. 2016b, *A&A*, **596**, A73
- Cassisi, S., Salaris, M., & Irwin, A. W. 2003, *ApJ*, **588**, 862
- Christensen-Dalsgaard, J. 1988, in *Advances in Helio- and Asteroseismology*, eds. J. Christensen-Dalsgaard, & S. Frandsen, *IAU Symp.*, **123**, 295
- Cox, J. P., & Giuli, R. T. 1968, *Principles of Stellar Structure* (New York: Gordon and Breach)
- Davies, G. R., Chaplin, W. J., Farr, W. M., et al. 2015, *MNRAS*, **446**, 2959
- Deheuvels, S., Michel, E., Goupil, M. J., et al. 2010, *A&A*, **514**, A31
- Deheuvels, S., Brandão, I., Silva Aguirre, V., et al. 2016, *A&A*, **589**, A93
- de Meulenaer, P., Carrier, F., Miglio, A., et al. 2010, *A&A*, **523**, A54
- Ferguson, J. W., Alexander, D. R., Allard, F., et al. 2005, *ApJ*, **623**, 585
- Gough, D. O. 1986, *Highlights Astron.*, **7**, 283
- Gough, D. O. 1990, in *Progress of Seismology of the Sun and Stars*, eds. Y. Osaki, & H. Shibahashi (Berlin: Springer Verlag), *Lect. Notes Phys.*, **367**, 283
- Gram, J. P. 1883, *J. Reine Angew. Math.*, **94**, 41
- Grec, G., Fossat, E., & Pomerantz, M. A. 1983, *Sol. Phys.*, **82**, 55
- Houdek, G., & Gough, D. O. 2007, *MNRAS*, **375**, 861
- Iglesias, C. A., & Rogers, F. J. 1996, *ApJ*, **464**, 943
- Kjeldsen, H., Bedding, T. R., & Christensen-Dalsgaard, J. 2008, *ApJ*, **683**, L175
- Lund, M. N., Silva Aguirre, V., Davies, G. R., et al. 2017, *ApJ*, **835**, 172
- Manchon, L., Belkacem, K., Samadi, R., et al. 2018, *A&A*, **620**, A107
- Mazumdar, A., Monteiro, M. J. P. F. G., Ballot, J., et al. 2014, *ApJ*, **782**, 18
- Miglio, A., & Montalbán, J. 2005, *A&A*, **441**, 615
- Monteiro, M. J. P. F. G. 2002, in *Observed HR Diagrams and Stellar Evolution*, eds. T. Lejeune, & J. Fernandes, *ASP Conf. Ser.*, **274**, 77
- Monteiro, M. J. P. F. G., Christensen-Dalsgaard, J., & Thompson, M. J. 2000, *MNRAS*, **316**, 165
- Popielski, B. L., & Dziembowski, W. A. 2005, *Acta Astron.*, **55**, 177
- Ramírez, I., Meléndez, J., & Asplund, M. 2009, *A&A*, **508**, L17
- Rauer, H., Catala, C., Aerts, C., et al. 2014, *Exp. Astron.*, **38**, 249
- Ricker, G. R., Winn, J. N., Vanderspek, R., et al. 2014, in *Space Telescopes and Instrumentation 2014: Optical, Infrared, and Millimeter Wave*, Proc. SPIE, **9143**, 914320
- Roxburgh, I. W. 2016, *A&A*, **585**, A63
- Roxburgh, I. W., & Vorontsov, S. V. 2002a, in *Stellar Structure and Habitable Planet Finding*, eds. B. Battrick, F. Favata, I. W. Roxburgh, & D. Galadi, *ESA Spec. Pub.*, **485**, 337
- Roxburgh, I. W., & Vorontsov, S. V. 2002b, in *Stellar Structure and Habitable Planet Finding*, eds. B. Battrick, F. Favata, I. W. Roxburgh, & D. Galadi, *ESA Spec. Pub.*, **485**, 341
- Roxburgh, I. W., & Vorontsov, S. V. 2003, *A&A*, **411**, 215
- Saha, M. N. D. 1920, *Lond. Edinb. Phil. Mag. J. Sci.*, **40**, 472
- Schmidt, E. 1907, *Math. Ann.*, **63**, 433
- Scuflaire, R., Théado, S., Montalbán, J., et al. 2008a, *Ap&SS*, **316**, 83
- Scuflaire, R., Montalbán, J., Théado, S., et al. 2008b, *Ap&SS*, **316**, 149
- Silva Aguirre, V., Ballot, J., Serenelli, A. M., & Weiss, A. 2011, *A&A*, **529**, A63
- Sonoi, T., Samadi, R., Belkacem, K., et al. 2015, *A&A*, **583**, A112
- Thoul, A. A., Bahcall, J. N., & Loeb, A. 1994, *ApJ*, **421**, 828
- Ulrich, R. K. 1986, *ApJ*, **306**, L37
- Verma, K., Faria, J. P., Antia, H. M., et al. 2014, *ApJ*, **790**, 138
- Verma, K., Raodeo, K., Antia, H. M., et al. 2017, *ApJ*, **837**, 47
- Vorontsov, S. V. 1988, in *Advances in Helio- and Asteroseismology*, eds. J. Christensen-Dalsgaard, & S. Frandsen, *IAU Symp.*, **123**, 151

Appendix A: Effect of the regularisation constant

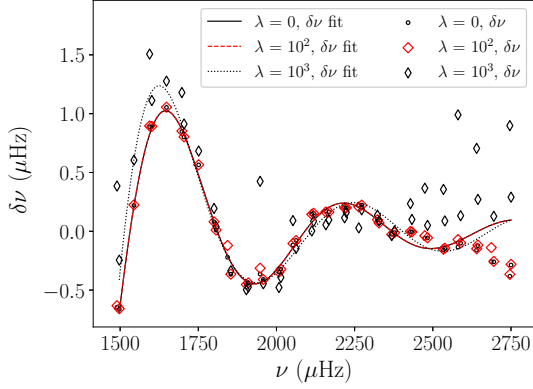


Fig. A.1. Comparison between the glitch adjustment for several values of the regularisation constant λ for 16 Cyg A best model determined in Sect. 5.2. The values are given in the legend. The lines correspond to the fitted glitch and the markers to the observed glitch. Only the fitted curves for $l = 0$ are displayed.

Figure A.1 shows the influence of the regularisation constant λ on the quality of the fitted glitch. We fitted the glitch of the best model obtained in Sect. 5.2 using the values of λ shown in the legend. We observe that, when using a value of 10^2 which is already significant as discussed in Sect. 2.2, the fit (red dashed curve) remains close to the one obtained without including regularisation terms (solid black curve). There is only a slightly higher dispersion in the model frequencies subtracted from the smooth part of the spectrum. To show the degradation caused by a regularisation constant that dominates the adjustment, we used $\lambda = 10^3$. We observe both a discrepancy between results without and with (dotted black curve) regularisation terms and a higher dispersion. This translates in a higher value of the merit function (from $\chi^2 \sim 1$ without regularisation to $\chi^2 \sim 500$ with $\lambda = 10^3$).

Appendix B: Comparison with usual indicators

We present in Fig. B.1 the evolution of the “usual” indicators $r_{01}(n)$ and $r_{02}(n)$ (Roxburgh & Vorontsov 2003) used in asteroseismology in order to compare them with the new indicators. They are evaluated at the value of $n = 21$ which corresponds to the measured value of n_{\max} for 16 Cyg A (n_{\max} being the value of n at $l = 0$ of closest frequency to the ν_{\max} value). First let us draw the attention to the fact that the usual indicators hold a local value, as Eqs. (26) and (27) show, while the new indicators are averaged over the complete set of available modes. It results from this averaging a lower standard deviation. Then, we notice that the behaviour of both the usual indicators and the new ones follow similar trends. This means that the definition is consistent with what has been done up to now and that it should hold the same information. Therefore, it should be able to provide similar diagnostics, but with higher precisions.

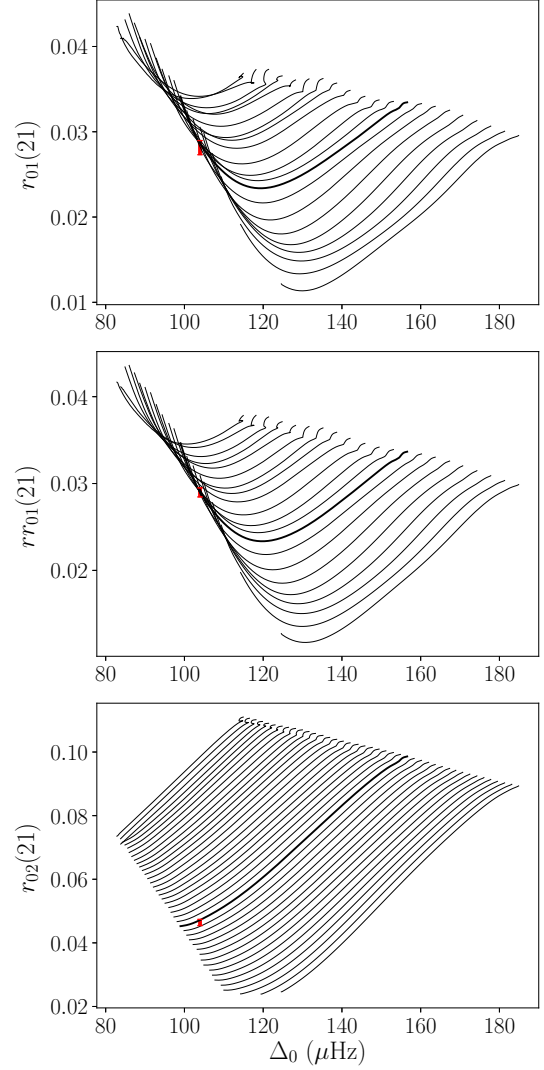


Fig. B.1. Evolution of the normalised small separation as defined by Roxburgh & Vorontsov (2003) and evaluated at $n = 21$ along the grid presented in Sect. 3.1. The red marker shows the observed value corrected for the surface effects following Kjeldsen et al. (2008)’s prescription. The thick line represents the track for $1.06 M_{\odot}$. *Top panel:* three points normalised small separation between spherical degrees 0 and 1; *middle panel:* five points normalised small separation between spherical degrees 0 and 1; *bottom panel:* normalised small separation between spherical degrees 0 and 2.

Appendix C: Γ_1 toy model

To build a toy model for Γ_1 that replicates at best its behaviour in the helium second ionisation zone we use the following hypotheses:

- In the helium second ionisation zone, hydrogen is fully ionised;
- Metals are in their atomic form;

- We consider a perfect gas.

We then define:

- The once ionised helium number of particles per unit volume He^+ and twice ionised helium number of particles per unit volume He^{++} such that:

$$\text{He}^+ + \text{He}^{++} = \frac{Y\rho}{4m_u}, \quad (\text{C.1})$$

where m_u is the atomic mass unit;

- The helium ionisation fraction:

$$x_{\text{He}} = \frac{\text{He}^{++}}{\text{He}^+ + \text{He}^{++}}, \quad (\text{C.2})$$

which equals 0 if the helium is ionised only once and 1 if it is fully ionised;

- The number of electrons per unit volume:

$$e = \left(X + (1 + x_{\text{He}}) \frac{Y}{4} \right) \frac{\rho}{m_u}; \quad (\text{C.3})$$

- The total number of particles:

$$n = \left(2X + (2 + x_{\text{He}}) \frac{Y}{4} + \sum_i \frac{Z_i}{A_i} \right) \frac{\rho}{m_u}, \quad (\text{C.4})$$

where Z_i is the mass fraction of the metal labeled i and A_i its mass number.

Using Saha's equation (Saha 1920):

$$S a = \frac{\text{He}^{++} e}{\text{He}^+} = \frac{g}{h^3} (2\pi m_e k_B T)^{\frac{3}{2}} e^{-\frac{\chi}{k_B T}}, \quad (\text{C.5})$$

where g is the statistical weight of helium at its fundamental state, h is Planck's constant, k_B is Boltzmann's constant, m_e the electron mass, and χ the helium second ionisation energy, we may obtain a second order equation for x_{He} :

$$\frac{Y\rho}{4m_u} x_{\text{He}}^2 + \left[\left(X + \frac{Y}{4} \right) \frac{\rho}{m_u} + S a \right] x_{\text{He}} - S a = 0, \quad (\text{C.6})$$

which we solve to obtain the evolution of x_{He} with temperature and density. We may also derive this expression with respect to temperature at constant density. This yields

$$\left. \frac{\partial x_{\text{He}}}{\partial T} \right|_{\rho} = \frac{(1 - x_{\text{He}}) \left(\frac{3}{2} + \frac{\chi}{k_B T} \right) \frac{m_u S a}{\rho T}}{X + \left(\frac{1}{2} + x_{\text{He}} \right) \frac{Y}{4} + \frac{m_u}{\rho} S a}. \quad (\text{C.7})$$

Then we have the following expressions:

$$P_T = \left. \frac{\partial \ln P}{\partial \ln T} \right|_s = 1 + \frac{eD}{n} \left(\frac{3}{2} + \frac{\chi}{k_B T} \right), \quad (\text{C.8})$$

$$P_{\rho} = \left. \frac{\partial \ln P}{\partial \ln \rho} \right|_s = \left[(2 - D)X + (2 + x_{\text{He}} - (1 + x_{\text{He}})D) \frac{Y}{4} + \sum_i \frac{Z_i}{A_i} \right] \frac{\rho}{m_u n}, \quad (\text{C.9})$$

$$c_v = \frac{3}{2} \frac{k_B P_T}{\mu m_u} + \frac{Y\chi}{4m_u} \left. \frac{\partial x_{\text{He}}}{\partial T} \right|_{\rho}, \quad (\text{C.10})$$

where μ is the mean molecular weight and

$$D = \left(\frac{e}{x_{\text{He}}(1 - x_{\text{He}})} \frac{4m_u}{Y\rho} + 1 \right)^{-1}. \quad (\text{C.11})$$

Finally, we may insert their values in the relation linking Γ_1 , P_T , P_{ρ} , and c_v :

$$\Gamma_1 = P_{\rho} + P_T^2 \frac{P}{c_v \rho T}. \quad (\text{C.12})$$

Appendix D: Gram-Schmidt's process and QR decomposition

As a reminder, Gram-Schmidt's algorithm consists in the construction of orthonormal basis elements from a set of non-orthonormal basis elements. Let us consider the element of index $j_0 : \mathbf{p}_{j_0}$. Let us also assume that we have already built the set of orthonormal basis functions up to index $j_0 - 1$, that is the set $(\mathbf{q}_1, \dots, \mathbf{q}_{j_0-1})$. To build element \mathbf{q}_{j_0} , we first subtract to \mathbf{p}_{j_0} its projection over the successive previous basis elements. We thus have

$$\mathbf{u}_{j_0} = \mathbf{p}_{j_0} - \sum_{j=1}^{j_0-1} \langle \mathbf{p}_{j_0} | \mathbf{q}_j \rangle \mathbf{q}_j, \quad (\text{D.1})$$

where \mathbf{u}_{j_0} is the basis element orthogonal to the set $(\mathbf{q}_1, \dots, \mathbf{q}_{j_0-1})$. Finally, it is normalised to obtain

$$\mathbf{q}_{j_0} = \frac{\mathbf{u}_{j_0}}{\|\mathbf{u}_{j_0}\|}. \quad (\text{D.2})$$

It is also possible to express this process as a QR decomposition. To do so we call \mathcal{P}_l the matrix of initial polynomials and \mathcal{Q}_l the matrix of orthonormal polynomials for a given spherical degree:

$$\mathcal{P}_l = \begin{pmatrix} p_0(n_{\min}) & \cdots & p_2(n_{\min}) \\ \vdots & & \vdots \\ p_0(n_{\max}) & \cdots & p_2(n_{\max}) \end{pmatrix} = (\mathbf{p}_0 \cdots \mathbf{p}_2)_l, \quad (\text{D.3})$$

$$\mathcal{Q}_l = \begin{pmatrix} q_0(n_{\min}) & \cdots & q_2(n_{\min}) \\ \vdots & & \vdots \\ q_0(n_{\max}) & \cdots & q_2(n_{\max}) \end{pmatrix} = (\mathbf{q}_0 \cdots \mathbf{q}_2)_l, \quad (\text{D.4})$$

where n_{\min} is the lowest observed radial order and n_{\max} the highest one for the spherical degree considered.

We may then express Gram-Schmidt's procedure in a matrix form as a QR decomposition as follows:

$$\mathcal{Q}_l = \mathcal{P}_l R_l^{-1}, \quad (\text{D.5})$$

where, using our definition of the scalar product

$$R_l = \begin{pmatrix} \langle \mathbf{q}_0 | \mathbf{p}_0 \rangle_l & \cdots & \langle \mathbf{q}_0 | \mathbf{p}_2 \rangle_l \\ & \ddots & \vdots \\ 0 & & \langle \mathbf{q}_2 | \mathbf{p}_2 \rangle_l \end{pmatrix}, \quad (\text{D.6})$$

is an upper triangular matrix.

We may now generalise by considering several spherical degrees. For the smooth part, the matrices become block matrices which are the combination of the matrices for the several spherical degrees considered. This block disposition illustrates the fact that we have different basis functions for the different spherical degrees – this is not the case for the glitch part –. This is represented by a *Kronecker* delta in Eq. (6). In these matrices, each row corresponds to a given mode and each column corresponds to a given element of the basis. Finally, we append the glitch part to those block matrices. They take the following form (we remind that the independent variable for the glitch basis is $\tilde{n} = n + l/2$):

$$\mathbb{P} = \left(\begin{array}{ccc|ccc} \mathcal{P}_0 & & 0 & \mathbf{p}_{\text{He},C,5}(n) & \cdots & \mathbf{p}_{C,S}(n) \\ & \ddots & & \vdots & & \vdots \\ 0 & & \mathcal{P}_3 & \mathbf{p}_{\text{He},C,5}(n+3/2) & \cdots & \mathbf{p}_{C,S}(n+3/2) \end{array} \right), \quad (\text{D.7})$$

$$\mathbf{Q} = \left(\begin{array}{cc|cc} \mathbf{Q}_0 & 0 & \mathbf{q}_{\text{He},C,5}(n,l) & \cdots & \mathbf{q}_{C,S}(n,l) \\ & \ddots & \vdots & & \vdots \\ 0 & \mathbf{Q}_3 & \mathbf{q}_{\text{He},C,5}(n,l) & \cdots & \mathbf{q}_{C,S}(n,l) \end{array} \right), \quad (\text{D.8})$$

And the \mathbf{R} matrix becomes

$$\mathbf{R} = \left(\begin{array}{cc|ccc} R_0 & 0 & \langle \mathbf{q}_k | \mathbf{p}_{\text{He},C,5} \rangle_{l=0} & \cdots & \langle \mathbf{q}_k | \mathbf{p}_{C,S} \rangle_{l=0} \\ & \ddots & \vdots & & \vdots \\ 0 & R_3 & \langle \mathbf{q}_k | \mathbf{p}_{\text{He},C,5} \rangle_{l=3} & \cdots & \langle \mathbf{q}_k | \mathbf{p}_{C,S} \rangle_{l=3} \\ & 0 & \langle \mathbf{q}_{\text{He},C,5} | \mathbf{p}_{\text{He},C,5} \rangle & \cdots & \langle \mathbf{q}_{\text{He},C,5} | \mathbf{p}_{C,S} \rangle \\ & & & \ddots & \vdots \\ & & 0 & & \langle \mathbf{q}_{C,S} | \mathbf{p}_{C,S} \rangle \end{array} \right), \quad (\text{D.9})$$

where $\langle \mathbf{q}_k | \mathbf{p}_g \rangle_{l=0}$ is a column vector of which the rows are the successive scalar products of the basis elements with the glitch function – denoted with the g index – such that $\langle \mathbf{q}_k | \mathbf{p}_g \rangle_{l=0} = (\langle \mathbf{q}_0 | \mathbf{p}_g \rangle_{l=0} \cdots \langle \mathbf{q}_2 | \mathbf{p}_g \rangle_{l=0})^T$. We may again write the QR decomposition as

$$\mathbf{Q} = \mathbf{P}\mathbf{R}^{-1}. \quad (\text{D.10})$$

Appendix E: A numerical example

We generated a set of frequencies for spherical degrees from 0 to 2 (listed in Table E.1) and applied our method. We show in Figs. E.1 and E.2 the successive adjustments of the basis functions. This shows the validity of using the set of functions described in Sect. 2 and allows oneself to compare their results with ours. As a reminder, we project the frequencies over the basis in the specific order explained in Sect. 2. Therefore, taken in the correct order, these plots provide intermediary results for the glitch adjustment. We also show in Table E.2 the values of the fitted coefficients. In this example, we also fitted n^{-1} polynomials – inspired by the second order form of the asymptotic expansion – to show that it is not necessary, nor relevant, to add supplementary basis elements to our method. Indeed, the fitted coefficient values become comparable to the standard deviation that is equal to 1, through the orthonormalisation. Such values and plots were obtained as follows:

1. Considering the set of standard deviations from Table E.1, we use Gram-Schmidt procedure (Eq. (4)) associated with the definition of the scalar product (Eq. (1)) to produce the ordered orthonormal basis functions for each value of the spherical degree l . Thus, we successively project the former basis elements $p_j(n, l)$ (i.e. the ordered set of polynomials n^0, n^1, n^2 and the glitch functions for each spherical degree) on the already defined orthonormal basis elements $q_{j_0}(n, l)$. Then, we normalise those projections. This provides us with the orthonormal basis elements $q_{j_0}(n, l)$, as well as the transformation matrix R_{j,j_0}^{-1} .
2. For the smooth part and one spherical degree at a time, the frequencies from Table E.1 are projected on the orthonor-

Table E.1. Example set of frequencies.

l	n	$\nu(\mu\text{Hz})$	$\sigma(\mu\text{Hz})$
0	13	1498.89	0.07
0	14	1603.60	0.07
0	15	1708.55	0.08
0	16	1812.40	0.07
0	17	1916.65	0.06
0	18	2022.56	0.05
0	19	2128.56	0.04
0	20	2234.84	0.05
0	21	2341.67	0.05
0	22	2448.06	0.08
0	23	2554.95	0.16
1	13	1546.42	0.07
1	14	1651.36	0.09
1	15	1755.56	0.08
1	16	1860.40	0.05
1	17	1965.44	0.05
1	18	2071.47	0.05
1	19	2178.50	0.04
1	20	2284.98	0.05
1	21	2391.77	0.06
1	22	2499.11	0.08
1	23	2606.15	0.13
2	13	1596.42	0.19
2	14	1701.68	0.17
2	15	1805.69	0.11
2	16	1910.30	0.10
2	17	2016.47	0.08
2	18	2122.70	0.06
2	19	2229.41	0.06
2	20	2336.56	0.09
2	21	2443.24	0.13
2	22	2550.54	0.21

Table E.2. Fitted parameters to the frequencies of Table E.1.

	$l = 0$	$l = 1$	$l = 2$
a_{l0}	112948.0	117296.1	72112.2
a_{l1}	14952.0	14674.1	6882.0
a_{l2}	74.0	79.4	35.4
a_{l-1}	-3.5	9.0	6.3
A_{He}		27.5	
A_{CZ}		9.4	

mal basis elements following the proper order to produce the fitted frequencies, $\nu_f(n, l)$, according to Eq. (5) where the fitted coefficients are given by Eq. (8). Then, for the glitch part, the frequencies are projected simultaneously for every spherical degree on the glitch basis elements following the same procedure. This is due to the fact that the glitch coefficients should not depend on l . This produces the coefficients from Table E.2.

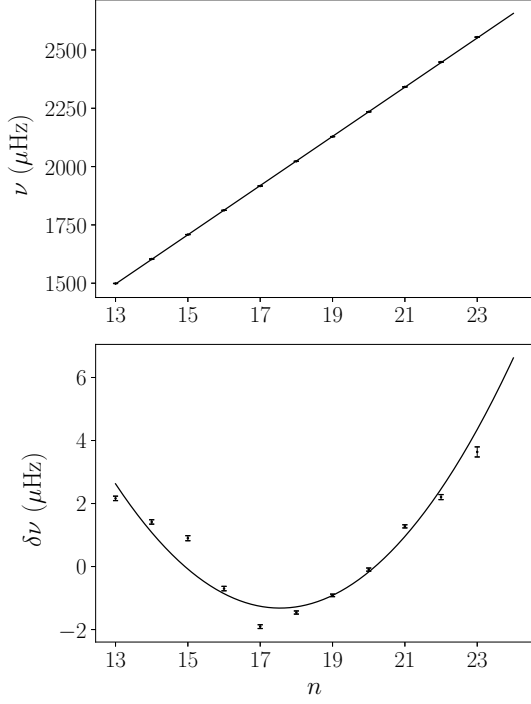


Fig. E.1. Comparison between the successive adjustments and the observed radial modes frequencies listed in Table E.1. *Upper panel:* observed frequencies compared to the first order adjustment; *lower panel:* residual of the first order adjustment compared to the second order fit to those residuals.

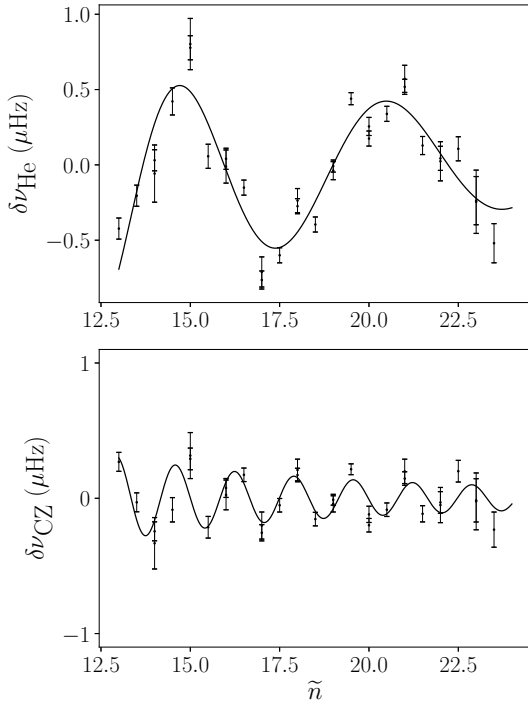


Fig. E.2. Separated glitches adjustments to the frequencies in Table E.1 of both glitches shown for the spherical degree $l = 0$. *Upper panel:* helium glitch; *lower panel:* convection zone glitch.

Appendix F: Supplementary adjustments

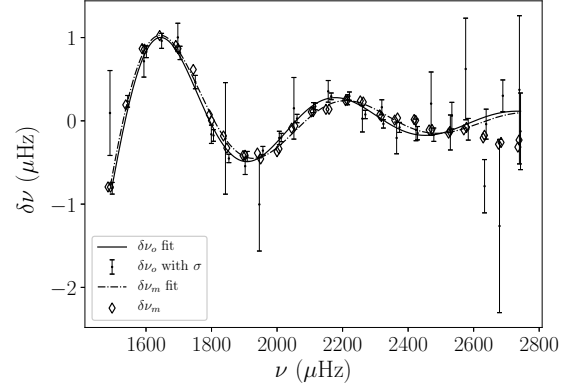


Fig. F.1. Comparison between the observed helium glitch $\delta\nu_o$ (solid line) and the one resulting from the best fit model $\delta\nu_m$ (dot-dashed line) for $l = 0$. We also display the observed glitch as a function of the frequencies (errorbars) as well as the best model glitch associated with the theoretical frequencies (diamond). The observed frequencies have been corrected for surface effects using Sonoi et al. (2015)'s prescription.

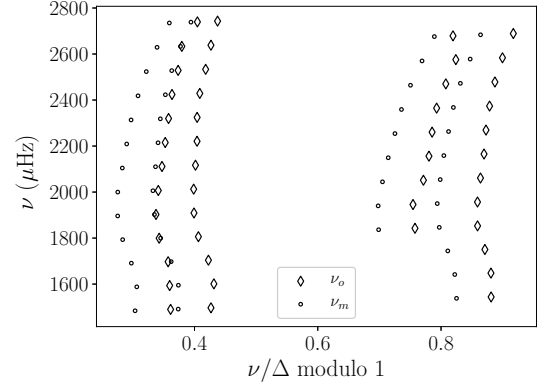


Fig. F.2. Comparison between the observed frequencies (diamonds) and the best model frequencies (circles) in an échelle diagram. The observed frequencies have been corrected for surface effects using Sonoi et al. (2015)'s prescription.

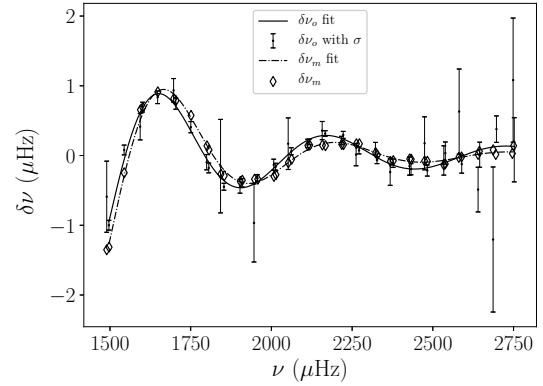


Fig. F.3. Comparison between the observed helium glitch $\delta\nu_o$ (solid line) and the one resulting from the best fit model $\delta\nu_m$ (dot-dashed line) for $l = 0$. We also display the observed glitch as a function of the frequencies (errorbars) as well as the best model glitch associated with the theoretical frequencies (diamond). We include polynomials in n^{-1} to the basis functions.

We show in the present section the best fit model frequencies adjusted to the observed 16 Cygni A frequencies for several cases. First we show the adjustment to the frequencies corrected for surface effects using a Lorentzian profile as in [Sonoï et al. \(2015\)](#). Figure [F.1](#) shows that both glitches are in good agreement. However, the frequencies are systematically shifted, as Fig. [F.2](#) illustrates, as a consequence of the difference between the observed and theoretical $\hat{\epsilon}$ values. Figure [4](#) illustrates such a discrepancy. This shows that, even though [Sonoï et al. \(2015\)](#) showed that for high frequency regimes [Kjeldsen et al. \(2008\)](#)'s prescription is not able to reproduce frequency differences between patched and unpatched model, it is

the only tested empirical correction that allowed us to reproduce the observed value for $\hat{\epsilon}$. In a further study, it would be appropriate to try out a scaled formulation of [Ball & Gizon \(2014\)](#)'s correction such as presented in [Manchon et al. \(2018\)](#).

We also provide in Fig. [F.3](#) the best fit model including terms in n^{-1} in the basis functions for the smooth part of the spectrum. By eye, the glitch adjustment seems better than in Fig. [13](#). However, as shown in Table [E.2](#), the improvement is not significant as the fitted parameters values are comparable to their standard deviation. Moreover, Table [2](#) demonstrates that the effect of including such terms in the adjustment is comparable to a variation of 1σ in the frequencies.

CHAPTER 4

Application of the WhoSGIAd method

In the present chapter we provide several applications of the WhoSGIAd method to observed targets. We take advantage of the seismic indicators defined in the method to provide robust constraints on the stellar structure (see Sect. 3.2.3). The first part of this chapter focuses on the detailed adjustment of the 16 Cygni system, using a Levenberg-Marquardt minimisation algorithm. This has been presented in our second paper (Farnir et al. 2020b, see also Sect. 4.A) while the second part provides a more superficial adjustment of the Kepler LEGACY sample (Lund et al. 2017) using the grid-based model search algorithm, AIMS (Asteroseismic Inference on a Massive Scale, Rendle et al. 2019). This was the topic of a presentation at the *Stars and their variability observed from the sky* conference in Vienna (Farnir et al. 2020b, see also Sect. 4.B).

4.1 Minimisation schemes

Before diving into specific applications of the WhoSGIAd technique, we recall several aspects of the forward stellar modelling. In all cases, the goal is to find a model, namely the associated set of K stellar parameters a_k , with $k = 1 \dots K$, that allows us to reproduce at best a set of N observed constraints $C_{i,\text{obs}}$, with $i = 1 \dots N$. To assess the quality of the model, it is customary to define a cost function,

$$\chi^2(\mathbf{a}) = \sum_{i=1}^N \frac{(C_{i,\text{obs}} - C_{i,\text{mod}}(\mathbf{a}))^2}{\sigma_i^2}. \quad (4.1)$$

We use here a compact vectorial representation set of the K stellar parameters, \mathbf{a} . The ‘mod’ and ‘obs’ subscripts respectively correspond to model and observed quantities and the σ are the associated uncertainties. We note that the $C_{i,\text{mod}}$ quantities are complex (non-analytical) functions of the stellar parameters.

The objective of any minimisation scheme will then be to reduce at most the value of the cost function, which measures the squared distance between modelled and observed constraints. In the course of this thesis, we considered two minimisation schemes: the Levenberg-Marquardt, which was applied to the thorough characterisation of the 16 Cygni system, and the Markov-Chain Monte-Carlo technique (henceforth MCMC), via the AIMS algorithm (Rendle et al. 2019), to model the Kepler LEGACY sample.

4.1.1 Levenberg-Marquardt minimisation algorithm

We now present the mathematical grounds behind the Levenberg-Marquardt technique (Marquardt 1963). Our use of this technique to obtain accurate stellar models is not the first reported in the literature. For example, Miglio & Montalbán (2005) present one of the first applications of this technique to the stellar modelling, in the case of the α Centauri system. To find the best fit models of the 16 Cygni system, we used the min-cles minimisation algorithm, which we updated during this PhD to meet our needs. The current developments follow that of Press et al. (1992).

Finding the minimum of the χ^2 function, as a function of the stellar parameters, amounts to finding the set of parameters that cancels the gradient of this function, $\nabla\chi^2 = 0$. Assuming the current parameters estimate, \mathbf{a}_{curr} , is close to the parameters corresponding to the minimum, \mathbf{a}_{min} , we approximate the cost-function by a quadratic form,

$$\chi^2(\mathbf{a}) \sim \gamma - \mathbf{d} \cdot \mathbf{a} + \frac{1}{2} \mathbf{a} \cdot \mathbf{D} \cdot \mathbf{a}, \quad (4.2)$$

with a constant γ , a K -vector, \mathbf{d} , and a $K \times K$ -matrix \mathbf{D} .

If the current estimate is close enough to the minimum, we may use the second order Taylor expansion to find the minimum, remembering that $\nabla\chi^2(\mathbf{a}_{\min}) = 0$,

$$\mathbf{a}_{\min} = \mathbf{a}_{\text{curr}} - \mathbf{D}^{-1} \cdot \nabla\chi^2(\mathbf{a}_{\text{curr}}). \quad (4.3)$$

\mathbf{D} here represents the second derivatives, the so-called Hessian matrix. When the second order approximation is not good enough, the only possibility is to follow the gradient in the direction of steepest descent,

$$\mathbf{a}_{\text{next}} = \mathbf{a}_{\text{curr}} - J\nabla\chi^2(\mathbf{a}_{\text{curr}}), \quad (4.4)$$

with J , some constant.

Writing

$$\beta_k \equiv -\frac{1}{2} \frac{\partial\chi^2}{\partial a_k}, \quad (4.5)$$

$$\alpha_{kl} \equiv \frac{1}{2} \frac{\partial^2\chi^2}{\partial a_k \partial a_l}, \quad (4.6)$$

$$\delta a_l \equiv a_{l,\text{next}} - a_{l,\text{curr}}, \quad (4.7)$$

with $\delta\mathbf{a}$ the vector of small increments, δa_l , in stellar parameters, it is possible to rewrite Eq. (4.3) in the linear form,

$$\sum_{l=1}^K \alpha_{kl} \delta a_l = \beta_k. \quad (4.8)$$

This is a linear system of equations of which the set of δa_l are the unknowns.

And the steepest descent formula (Eq. (4.4)) becomes

$$\delta a_l = J\beta_l. \quad (4.9)$$

Because second-order derivatives may have a destabilising effect, when the model badly fits or is contaminated by outliers, a more stable definition of the α matrix is used, considering only first-order derivatives

$$\alpha_{kl} \equiv \sum_{i=1}^N \frac{1}{\sigma_i^2} \left[\frac{\partial C_{i,\text{mod}}}{\partial a_k} \frac{\partial C_{i,\text{mod}}}{\partial a_l} \right]. \quad (4.10)$$

Modifying the form of α will not prevent us from finding the proper minimum as the condition for the minimum is $\beta = \mathbf{0}$. Only the route towards this minimum will be affected.

The constant J in Eq. (4.9) has to be carefully chosen. From its definition (Eq. (4.5)), β_l has the units of the inverse of a_l (the cost-function is dimensionless) while δa_l naturally has the dimensions of a_l . To preserve the units, the constant J must have the units of a_l^2 . Hopefully, α_{ll} is of the units $1/a_l^2$. As a consequence, we may set the scale of the J constant using diagonal elements of the α matrix,

$$\delta_l = \frac{1}{\lambda\alpha_{ll}}\beta_l, \quad (4.11)$$

with λ a dimensionless scaling parameter that allows us to reduce the step size, if necessary, and prevents to move too far from the current estimation.

This estimation of J is the first difference of the Levenberg-Marquardt method compared to the steepest descent. The second difference comes from the redefinition of the α matrix by combination of Eqs. (4.8) and (4.11)

$$\alpha'_{ll} = (1 + \lambda)\alpha_{ll}, \quad (4.12)$$

$$\alpha'_{lkl} = \alpha_{kl} \quad k \neq l. \quad (4.13)$$

$$(4.14)$$

We then obtain

$$\sum_{l=1}^K \alpha'_{kl} \delta a_l = \beta_k, \quad (4.15)$$

which is hybrid between Eqs. (4.8) and (4.11). For large λ values, the α' matrix is dominated by its diagonal elements and Eq. (4.15) is equivalent to Eq. (4.11). Conversely, for values of λ approaching zero, $\alpha' \simeq \alpha$ and we go back to Eq. (4.8).

All the strength of the Levenberg-Marquardt method will be in the control of the size of the λ parameter to alternate between the two cases and converge to a solution. We then proceed as follows. At the initial guess of the parameters, we estimate the cost function $\chi(\mathbf{a})^2$. From a small value of the scaling parameter, we solve Eq. (4.15) for $\delta\mathbf{a}$ and compute the cost function at this point $\chi(\mathbf{a} + \delta\mathbf{a})^2$. According to the new χ^2 value, we either increase the λ factor, when the trial has failed (i.e. the estimate strayed further from the minimum), or decrease the λ factor, when the trial has succeeded. The previous steps are repeated until a condition for convergence (or non-convergence) has been met.

Finally, at the minimum, one may estimate the uncertainties on the individual parameters of the fit by setting $\lambda = 0$. The covariance matrix is then

$$\mathbf{C} \equiv \boldsymbol{\alpha}^{-1}, \quad (4.16)$$

of which the diagonal elements correspond to the standard deviations on individual parameters,

$$\sigma(a_k) = \sqrt{(\boldsymbol{\alpha}^{-1})_{kk}}. \quad (4.17)$$

Here $\boldsymbol{\alpha}^{-1}$ means the inverse of the matrix $\boldsymbol{\alpha}$ and $(\boldsymbol{\alpha}^{-1})_{kl}$ is the element kl of that matrix.

Naturally, this method has its limitations. First of all, this is a local minimum search algorithm, as Eq. (4.4) clearly illustrates. The ability of the technique to reach a solution, and the number of required iterations, directly depend on the quality of the initial estimate of the optimal parameters. It therefore requires a good knowledge of the function we are trying to optimise. Hopefully, in stellar modelling problems, it is often the case that we can provide educated guesses about the solution.

Another drawback of the method comes from the derivatives computation. For stellar models, the $C_{\text{mod},i}$ functions, necessary to compute the cost-function, and their derivatives (see Eqs. (4.1), (4.5), and (4.10)) do not have an analytical form. It is therefore not possible to obtain a formal representation of these derivatives either. Instead, we estimate them by finite (forward) difference

$$\frac{\partial C_{\text{mod},i}(a_k)}{\partial a_k} \simeq \frac{C_{\text{mod},i}(a_k + h) - C_{\text{mod},i}(a_k)}{h}, \quad (4.18)$$

where h is the derivation step, small enough for the derivative to be accurate but not too small to avoid numerical noise to dominate. Iott et al. (1985) argue that the finite difference formulation (Eq. (4.18)) suffers from two different sources of error: the truncation error, resulting from the truncation of the Taylor series expansion of the perturbed function, and the condition error, representing the difference between the numerical evaluation of a function and its exact value. The truncation error is proportional, at leading orders, to the second derivative of the function while the condition error is estimated to be inversely proportional to the finite difference step size. The total error is then the sum of both contributions, truncation and condition. Finding the optimal step size then amounts to minimising this total error.

Two main consequences arise from this estimate of the derivative. First, inaccuracies may arise in the derivatives estimation. This means that the parameters uncertainties, Eq. (4.17), are affected as well. Therefore, a better computation of the uncertainties is in order, such as Monte-Carlo sampling. We did not implement such improvement for the time being. However, this will be carried out in future works.

Second, for each derivative in Eq. (4.18), two stellar models are required. Hopefully, one of these is readily available, as it serves to evaluate the quality of the estimate at the current position. Nevertheless, this means that one additional model is necessary per derivative, associated with a free parameter. Therefore, per iteration of the Levenberg-Marquardt algorithm, and for K free parameters, $K + 1$ stellar models are necessary. This can become rather time consuming as the number of free parameters rises.

4.1.2 Visualisation of the stellar modelling procedure

We provide in Fig. 4.1 a schematic representation of the stellar modelling procedure involving the WhoSGLAd indicators. Independently of the technique used, observed and modelled seismic indicators will be compared at each iterative step. This illustration clearly shows the necessity for the WhoSGLAd method to be as fast and reliable as possible, to ensure the fast determination of optimal stellar parameters with great confidence.

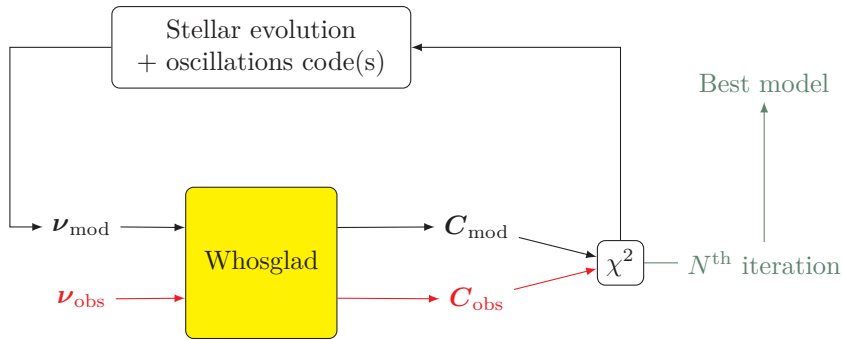


Figure 4.1: Schematic modelling procedure.

4.2 Application to the 16 Cygni system

In the current section, we summarise the results obtained in [Farnir et al. \(2020a\)](#) concerning the extensive characterisation of the 16Cyg system with the WhoSGlAd method.

4.2.1 Interest of the system

The 16 Cygni system is a binary system composed of two solar analogues. Because they have been observed continuously for 928 days with the *Kepler* satellite ([Borucki et al. 2010](#)), the seismic data available for these stars is part of the best currently available. Aside seismic data, precise spectroscopic and photometric data have also been gathered for both stars. As a consequence, this system was already subject to several studies providing accurate stellar parameters determinations, either by spectroscopic, photometric or seismic means (see Table 4.1 for a summary of some of the past determinations). Nevertheless, the system displays several unexpected features which are to be accounted for and remain, to this day, open questions. We do not pretend answering such questions but rather add up the amount of information that might help in constraining them.

Several studies noted that the A component of the system is significantly metal-rich than the B one (e.g. [Maia et al. 2019](#); [Morel et al. 2021](#)). One feature that stands out is the apparent difference in surface Lithium abundances. Although the two stars have similar masses and are expected to have a common origin, thus a common composition, 16CygB has been observed to be around four times more Li depleted than 16CygA ([Friel et al. 1993](#); [King et al. 1997](#)). As hypothesised by [Deal et al. \(2015\)](#), this could result from the presence of a jovian companion to the B component ([Cochran et al. 1997](#)). If 16CygB would have accreted a fraction of the Earth’s mass from its companion, it could have lead to fingering convection, which would have precipitated the lithium where it can be burned by nuclear reactions. The consequence is a reduced Li abundance while preserving the metals abundance. This is a clear example where regular standard models become insufficient and additional physical processes (in that case thermohaline, or fingering, convection) must be invoked to explain the complexity of the data at hand. This agrees with the computations from [Maia et al. \(2019\)](#). Placing the system in a broader context leads to different conclusions. Indeed, when comparing it to other analogues, [Carlos et al. \(2016\)](#) observed that 16CygB follows the age - lithium abundance trend, while 16CygA is significantly over-abundant. This suggests that 16CygA is the anomalous component of the system, which would require additional processes to explain such a difference.

Furthermore, the highly precise data gathered for the system allows for the reliable detection of acoustic glitches signatures in their oscillation spectra ([Verma et al. 2014, 2017](#); [Farnir et al. 2019, 2020a,b](#)) as well as to carry detailed seismic inversions ([Buldgen et al. 2016a,b](#)). This represents another excellent opportunity to highlight caveats in current stellar models and inch towards plausible solutions. We presented in [Farnir et al. \(2020a\)](#) a thorough study of the system considering both stars as separate components or as a whole (assuming common formation scenario, i.e. identical compositions and ages). We exploited the helium glitch signatures in both stars and tested a large sample of choices of physical ingredients in order to highlight the necessary improvements that would have to be included in stellar models to improve the agreement with the data. This paper is part of a series that approaches the problematic with different point of views. The first makes use of WhoSGlAd in a forward seismic modelling scheme. The second will go one step further by inverting structural profiles over the stellar interior ([Buldgen et al. 2021, in prep.](#)). The last one will study the impact of angular momentum and planetary

Table 4.1: Summary of literature properties of the 16 Cygni system.

	16CygA	16CygB	Ref.
$T_{\text{eff}}(K)$	5839 ± 42	5809 ± 39	a
$\log g$	4.33 ± 0.07	4.34 ± 0.07	b
$[\text{Fe}/\text{H}]$	0.096 ± 0.026	0.052 ± 0.021	b
$L (L_{\odot})$	1.56 ± 0.05	1.27 ± 0.04	c
$M (M_{\odot})$	1.07 ± 0.05	1.05 ± 0.04	a
	1.05 ± 0.02	1.00 ± 0.01	d
	0.98 ± 0.02	0.945 ± 0.015	e
	1.11 ± 0.02	1.07 ± 0.02	c
$R (R_{\odot})$	1.10 ± 0.01	1.06 ± 0.01	f
	1.10 ± 0.02	1.00 ± 0.03	g
	1.218 ± 0.012	1.098 ± 0.010	a
	1.195 ± 0.005	1.09 ± 0.01	e
	1.243 ± 0.008	1.127 ± 0.007	c
	1.24 ± 0.01	1.13 ± 0.01	f
	1.237 ± 0.010	1.102 ± 0.015	g
	$7.15^{+0.04}_{-1.03}$	$7.26^{+0.69}_{-0.33}$	d
Age (Gyr)	7.2 ± 0.2	7.2 ± 0.2	e
	6.4 ± 0.4	6.4 ± 0.4	f
	6.7 ± 0.3	6.9 ± 0.3	g
	$[0.670, 0.681]$	$[0.671, 0.685]$	e'
X_0	0.726 ± 0.010	0.727 ± 0.010	c'
	0.716	0.176	f'
	$[0.30, 0.31]$	$[0.30, 0.31]$	e
	0.25 ± 0.01	0.25 ± 0.01	c
Z_0	0.26	0.26	f
	$[0.0194, 0.0199]$	$[0.0151, 0.0186]$	e
	0.024 ± 0.002	0.023 ± 0.002	c
	0.024	0.024	f
Y_{surf}	0.2226	0.2265	f
	$[0.23, 0.25]$	$[0.218, 0.260]$	h
Z_{surf}	0.0221	0.0223	f

References. a: White et al. (2013), b: Ramírez et al. (2009), c: Metcalfe et al. (2012), d: Ramírez et al. (2011), e: Buldgen et al. (2016a), f: Deal et al. (2015), g: Verma et al. (2017), h: Verma et al. (2014), The ' symbol signifies that values are propagated from values in the corresponding reference.

formation on the evolution of the system.

4.2.2 Philosophy of the study

The study presented in Farnir et al. (2020a) aims at providing a thorough adjustment of the 16Cyg system while testing the impact of several hypotheses on the retrieved optimal models. We tested several choices of constraints, either only seismic or in combination with non-seismic data, a wide variety of variations in the input physics (solar mixture reference, opacity, equation of state, mixing length parameter, hypothesis on chemical diffusion, extension of convective layers, atmospheric temperature profile, and surface effects), and the hypothesis of a common origin for both stars (identical age and/or initial composition).

The modelling of the system was carried in several steps. First, both stars were considered to be independent of one another. Therefore, it was not required of the stars to have any stellar parameters in common. Second, we tested the hypothesis of a common origin requiring a common age and/or common composition. Both steps were also divided into two sub-steps: We started by considering only seismic constraints, which were Δ , \hat{r}_{01} , \hat{r}_{02} , and A_{He} (presented in Sect. 3.2.3), and used the four following free parameters, the mass, the age, X_0 , and $(Z/X)_0$. The values of the seismic constraints are gathered in Table. 4.2. We then included non-seismic constraints to assess their impact on the optimal models. We

Table 4.2: Observed seismic indicators, as in [Farnir et al. \(2020a\)](#). These are computed with the set of frequencies given in [Davies et al. \(2015\)](#) and corrected for the surface effects following [Sonoi et al. \(2015\)](#). The standard deviations result from the propagation of the uncertainties on the observed frequencies.

Indicator	16CygA	16CygB
$\Delta(\mu\text{Hz})$	104.024 ± 0.005	117.911 ± 0.004
A_{He}	30 ± 1	36 ± 1
\hat{r}_{01}	$(3.62 \pm 0.02) \cdot 10^{-2}$	$(2.52 \pm 0.02) \cdot 10^{-2}$
\hat{r}_{02}	$(5.75 \pm 0.03) \cdot 10^{-2}$	$(5.53 \pm 0.03) \cdot 10^{-2}$

therefore introduced additional free parameters, either the mixing-length parameter or the turbulent diffusion coefficient.

From a reference model (of which the physical components are given in Table 4.3), we changed one ingredient at a time. The variations in the input physics were the following:

- The GN93 solar-reference mixture ([Grevesse & Noels 1993](#)), in light blue in the figures;
- The opacities from the opacity project ([Badnell et al. 2005](#)), denoted OP in light brown, the Los Alamos opacities ([Colgan et al. 2016](#)), written OPLIB, in beige;
- The CEFF equation of state ([Christensen-Dalsgaard & Daeppen 1992](#)), in dark brown, and the revised OPAL equation of state ([Rogers & Nayfonov 2002](#)), written OPAL05, in grey;
- A different choice of mixing length coefficient ($\alpha_{\text{MLT}} = 1.7$), in yellow;
- The non-inclusion of microscopic diffusion, in light pink;
- The inclusion of turbulent mixing of chemical elements following the relation for the turbulent mixing coefficient, $DDT = D_{\text{turb}} \left(\frac{\rho}{\rho_0} \right)^n + D_{\text{ct}}$ (in cm^2s^{-1}), where ρ is the density, ρ_0 the density at the bottom of the convective envelope, and D_{turb} , n , and D_{ct} are fixed at 7500, -3 , and 0 respectively ([Proffitt & Michaud 1991](#)), shown in purple;
- The inclusion of overshooting extending outside convective regions over a distance $d = \alpha_{\text{ov}} \min(H_p, h)$, where α_{ov} is the overshooting parameter, H_p the local pressure scale height, and h the thickness of the convective region. The temperature gradient in the overshooting region is set to the radiative one and the mixing is instantaneous. We either include overshooting above the convective core, denoted α_{ov} and shown in red, or below the convective envelope, written α_{un} in khaki and referred to as ‘undershoot’. Both values are set to 0.1;
- The effect of a different choice of temperature profile above the stellar photosphere, in orange. We use the model temperature profile of the quiet sun by [Vernazza et al. \(1981\)](#) for which an analytical formulation may be found in [Paxton et al. \(2013\)](#);
- The impact of the surface effects, by computing a model fitting seismic indicators defined with stellar frequencies which are not corrected for surface effects, in dark green.

4.2.3 Results considering the stars as separate

For each star, seen as independent of its twin, we computed 15 individual models. These are presented in Figs. 4.2 and 4.3 that place these models in a mass - age diagram (top panel), HR diagram (middle panel), where we display the observed effective temperature and luminosity (from the interferometric radius and effective temperature measured by [White et al. 2013](#), and the Stefan-Boltzmann relation, Eq. (2.41)) as a black box, and in a initial hydrogen - metals diagram (bottom panel). These are also gathered in a diagram representing the surface metallicity and helium abundance in Figs. 4.4 and 4.5. The observed metallicity ([Ramírez et al. 2009](#)) and computed Y_s range ([Verma et al. 2014](#)) are again shown as a black box.

It clearly stands out that seismic constraints alone are not sufficient. Indeed, we observe that most models do not fall within the observed ranges of the non-seismic data. While non-seismic constraints were not yet part of the adjustment, we observed that only models with a modified diffusion efficiency were able to reproduce both the position in the HR diagram and the observed metallicity. In the case of 16CygA,

Table 4.3: Set of reference physical ingredients.

Ingredient	Choice	Additional information
Evolution code	Scuflaire et al. (2008a)	CLES
Oscillation code	Scuflaire et al. (2008b)	LOSC
Solar mixture	Asplund et al. (2009)	AGSS09
Equation of state	Cassisi et al. (2003)	FreeEOS
Opacity	Iglesias & Rogers (1996)	OPAL
	Ferguson et al. (2005)	at low T
Nuclear reaction rates	Adelberger et al. (2011)	NACRE
Mixing length parameter	$\alpha_{\text{MLT}} = 1.82$	Cox & Giuli (1968)
Microscopic diffusion	Thoul et al. (1994)	
Turbulent diffusion	none	
Overshooting	none	
Undershooting	none	
Atmosphere	Eddington	
Surface effects correction	Sonoi et al. (2015)	

it was the model including turbulent diffusion, and therefore partially compensating the microscopic diffusion of chemical elements, while using a different opacity table (OPLIB) that performed the best. For 16CygB, completely turning down microscopic diffusion allowed us to obtain the agreement with both seismic and non-seismic data.

On a side note, looking closely at the models with and without microscopic diffusion, we observe that these are systematically heavier, by about $0.05 M_{\odot}$, than those including diffusion. As a consequence, the surface helium content is reduced by about 0.02. This actually coincides with the impact of the mass on the helium amplitude we noted in Sect. 3.2.3. From Fig. 3.12, we may estimate that, when increasing the stellar mass by $0.025 M_{\odot}$, the surface helium abundance should decrease by about 0.01 to preserve a fixed glitch amplitude.

The impact of non-seismic data

We then tried to adjust the non-seismic constraints, which are the spectroscopic metallicity (Ramírez et al. 2009) and effective temperature (White et al. 2013). We first tested the impact of the mixing-length coefficient and turbulent mixing coefficient on the retrieved T_{eff} and $[\text{Fe}/\text{H}]$. We did so by computing models at fixed values of these coefficients with only seismic constraints. We observed that both parameters have a significant impact. Nonetheless, while the inclusion of turbulent mixing clearly improved the agreement, we noted that it saturated early (well below the values considered in this study), making it useless as a free parameter. As we also observed that increasing the mixing-length parameter value clearly allows us to approach the observed effective temperature, we computed models using it as a free parameter while setting the effective temperature as a constraint. This was done by either including turbulent mixing, with a fixed value of $D_{\text{turb}} = 7500 \text{ cm}^2\text{s}^{-1}$, or not (as turbulent diffusion improves both the modelled effective temperature and metallicity). In both cases, the effective temperature was properly accounted for. Nevertheless, neither of them performed better than the model with turbulent diffusion and the OPLIB opacity table for 16CygA and the model without microscopic diffusion for 16CygB.

We further noted that the adjusted values of α_{MLT} significantly varied from one star to the other, $\alpha_{\text{MLT},B} - \alpha_{\text{MLT},A} = 0.1$. However, from the works of Magic et al. (2015, Fig. 2), we expect both values to be similar, as the stars have similar effective temperatures and surface gravities. In addition, when compared to the solar case, with a calibrated mixing-length parameter of $\alpha_{\text{MLT}} = 1.82$ and a lower effective temperature and surface gravity, we expect their value to slightly decrease. Finally, at a fixed $\log g$ value, such a difference in the mixing-length parameter corresponds in Fig. 2 of Magic et al. (2015) to a difference in effective temperature around 500 – 1000 K, which is obviously not compatible with observations.

Another consequence of the inclusion of the non-seismic constraints was the increased difficulty to find a satisfactory model. This directly stems from the large differences in relative uncertainties ($\sigma(C)/C$) of these constraints compared to the seismic ones. Indeed, the relative uncertainty on the spectroscopic metallicity is on the order of 25%, which is extremely large compared to the $5 \times 10^{-3}\%$ for the large separation. Of course, through the course of this thesis we developed a few means to

improve the convergence of the Levenberg-Marquardt algorithm. For example, an efficient ‘recipe’ consists in a preliminary minimisation with relative uncertainties of every constraint boosted up to a common level, ensuring that none of them dominates over the others, preventing a proper convergence. Once an acceptable minimum has been reached, we may carry one last minimisation step with the proper uncertainties to retrieve the correct Hessian matrix and correlations. Nevertheless, in the present case, this was not sufficient to reach an acceptable solution in most cases. This explains why we adjusted these non-seismic constraints for a specific set of input physics only instead of all the presented choices. Furthermore, the large uncertainties on individual constraints favoured large uncertainties on the fitted stellar parameters. Nonetheless, we already discussed the limited confidence that can be attributed to the confidence intervals computed with the Levenberg-Marquardt algorithm. A more robust way to estimate such interval is the one we presented in this paper, by testing several physical hypotheses and measuring the scatter of the stellar parameters. Finally, the extremely small uncertainties on the large separation, resulting from the averaging and propagation of individual frequencies uncertainties, may be considered unrealistic. A more physically meaningful estimate of this uncertainty comes from a measurement of the impact of the surface effects on the large separation value. The relative uncertainty now becomes approximately 1.1%, which is much larger but remains significantly smaller than for the metallicity. The above considerations therefore remain valid.

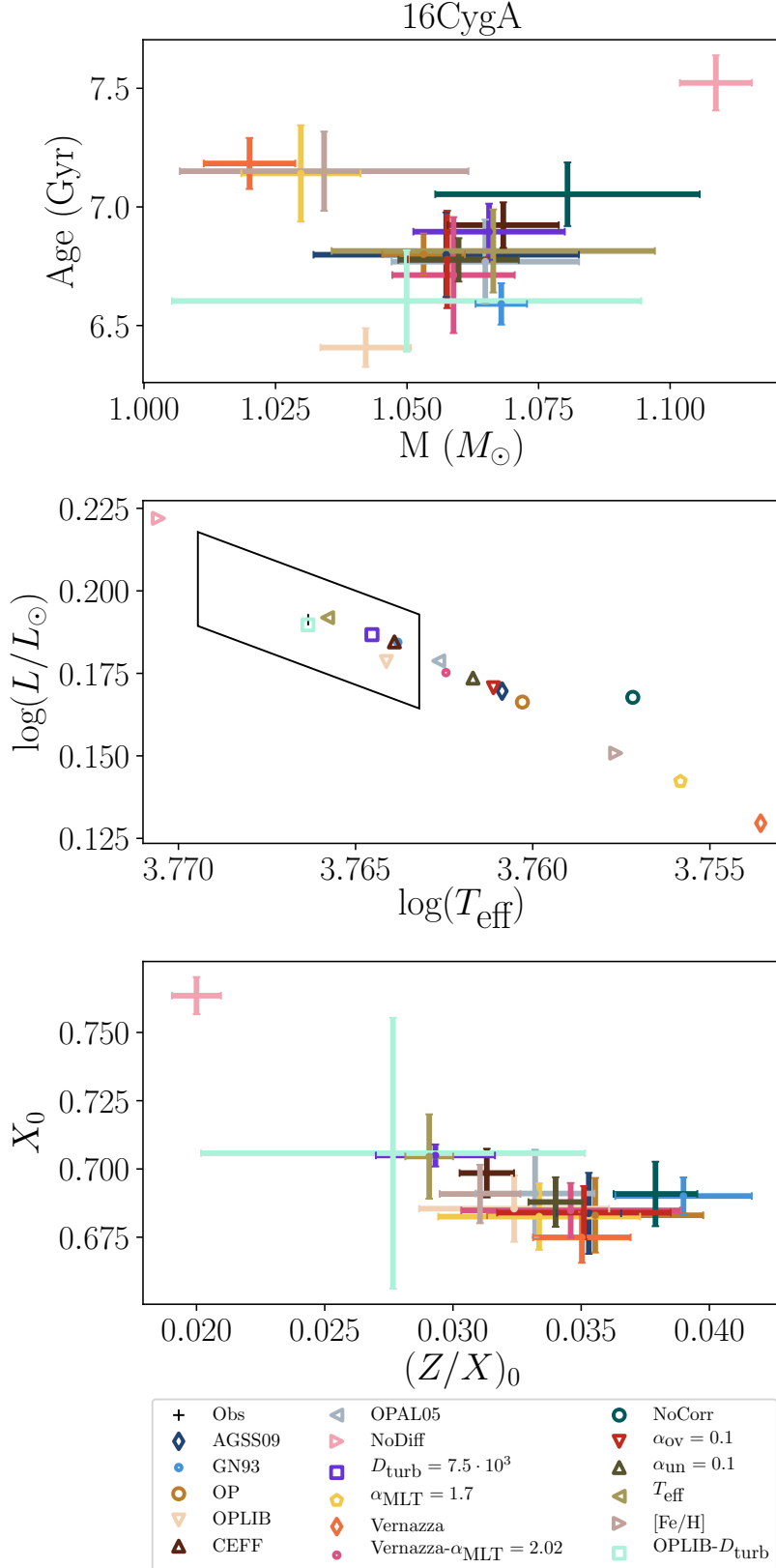


Figure 4.2: Summary of the adjusted stellar models for 16CygA, considering it as an isolated star. *top panel:* Mass - age diagram. *middle panel:* Hertzsprung-Russell diagram. The black cross represents the observed value and the black box the uncertainties (White et al. 2013, see also Table 4.1). *bottom panel:* Initial hydrogen - metals abundances diagram. The legend gives the colour code used. Error bars represent the error propagation through the Levenberg-Marquardt method (Eq. (4.17)).

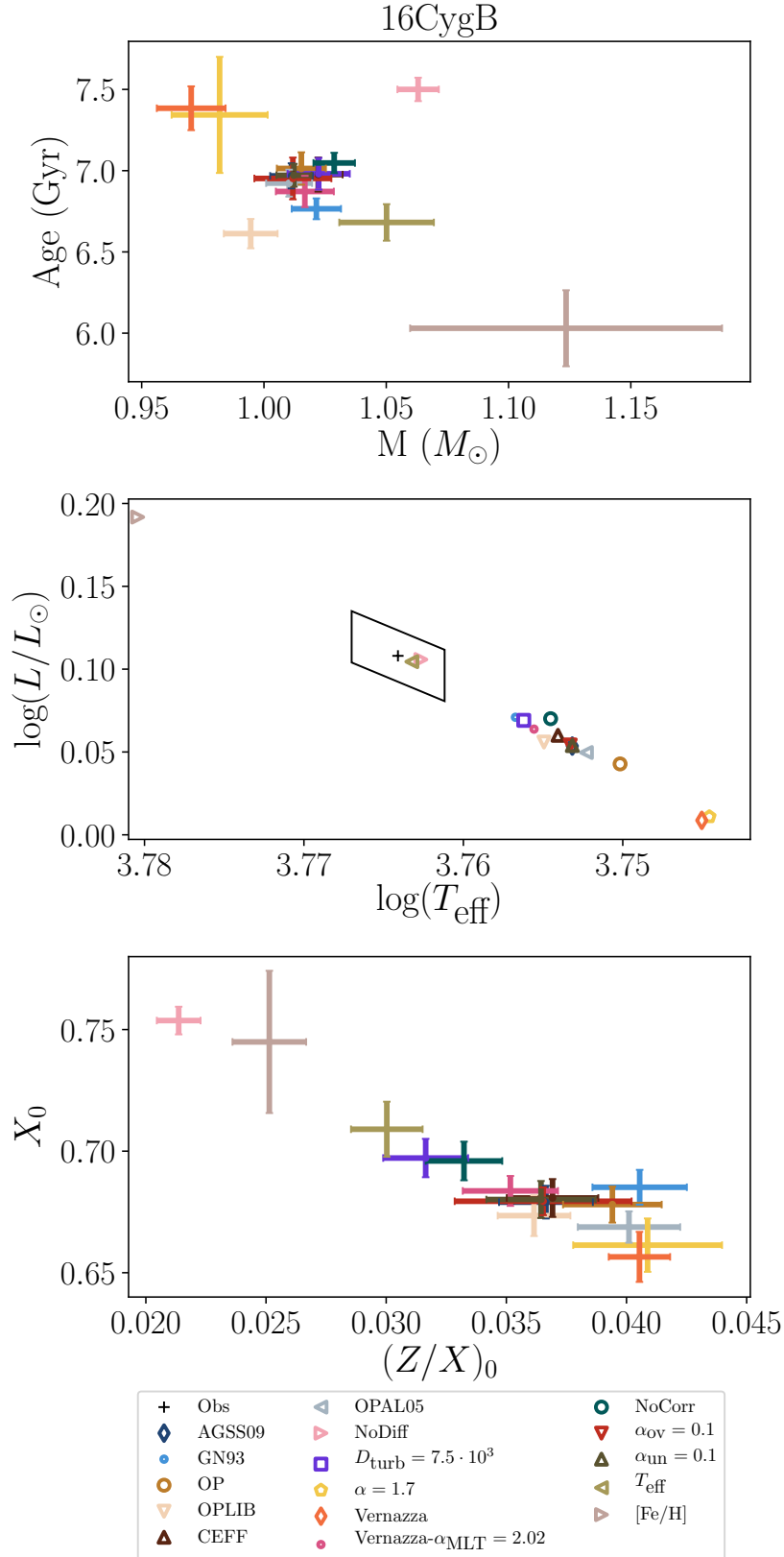


Figure 4.3: Summary of the adjusted stellar models for 16CygB, considering it as an isolated star. *top panel:* Mass - age diagram. *middle panel:* Hertzsprung-Russell diagram. The black cross represents the observed value and the black box the uncertainties (White et al. 2013, see also Table 4.1). *bottom panel:* Initial hydrogen - metals abundances diagram. The legend gives the colour code used. Error bars represent the error propagation through the Levenberg-Marquardt method (Eq. (4.17)).

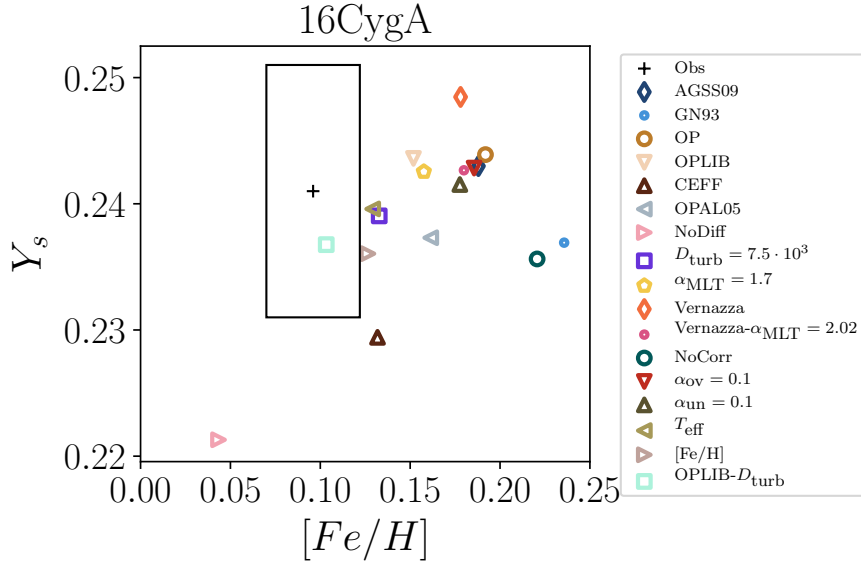


Figure 4.4: Surface metallicity and helium abundance of the set of models presented in Fig. 4.2 compared to the reference values of [Ramírez et al. \(2009\)](#) (metallicity) and [Verma et al. \(2014\)](#).

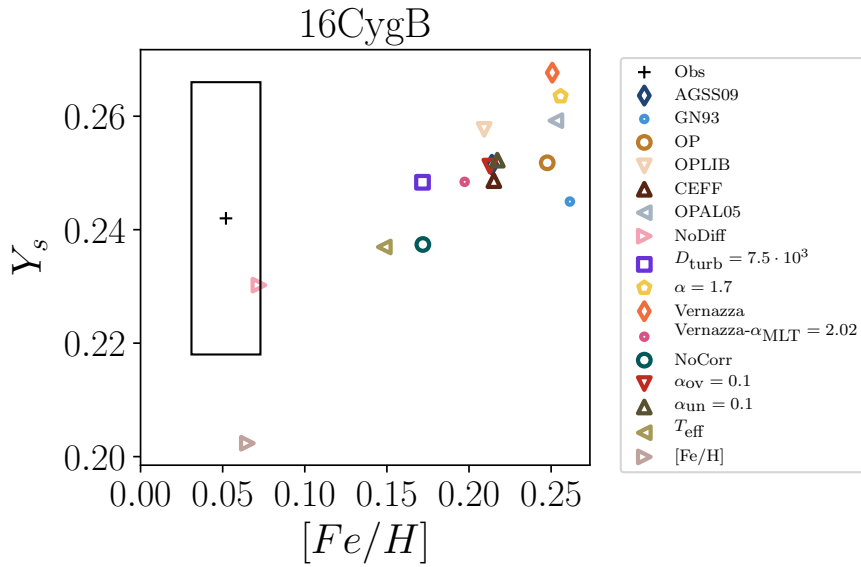


Figure 4.5: Surface metallicity and helium abundance of the set of models presented in Fig. 4.3 compared to the reference values of [Ramírez et al. \(2009\)](#) (metallicity) and [Verma et al. \(2014\)](#).

4.2.4 Results of the joint analysis

As the next step of our modelling procedure assumed both stars to have a common origin, hence a common age and initial composition, we selected a subset of models that had compatible ages and initial compositions. By compatible, we mean that the 1σ range around each value overlap. These models are referred to as ‘accepted’ models and correspond to:

- The reference models;
- The ones including turbulent mixing;
- Those with overshooting ($\alpha_{\text{ov}} = 0.1$);
- Those without diffusion;
- Those with an atmosphere as in [Vernazza et al. \(1981\)](#) and a specifically calibrated $\alpha_{\text{MLT}} = 2.02$ value.

The accepted range of stellar parameters, defined by the centroid of all values and the necessary variations to reach the extrema is given in Table 4.4. The accepted models served as the basis for the joint analysis of both stars. We already note that, obviously, while individual ages and initial compositions ranges overlap one another, central values are not identical. Iterating over these values was therefore necessary.

By imposing a common age and composition, the set of free parameters was reduced by three while maintaining the same amount of constraints, namely Δ , \hat{r}_{01} , \hat{r}_{02} , and A_{He} for each star. The system to solve becomes overdetermined, with five free parameters and eight constraints. This greatly increases the difficulty to find a suitable solution, for which the reduced $\chi^2_{\text{red}} = \chi^2/(N - M) < 1$, with $N - M = 3$ being the number of degrees of freedom, N the number of constraints and M the number of free parameters. As a consequence, such a solution was never found when common compositions and ages were required. However, two choices of input physics clearly outperformed the others, the one with the temperature profile prescribed by [Vernazza et al. \(1981\)](#) with the calibrated mixing-length parameter and the one without diffusion, with $\chi^2_{\text{red}} = 2.9$ and 3.4 , respectively. While these did not reach the limit of acceptability, we can still observe that the large separation is the most difficult to reproduce, as a consequence of its extremely stringent uncertainty. Often, because of the common properties of the stars, the algorithm favoured one component over the other, allowing for all its indicators to be properly reproduced compromising the agreement with the constraints of the second component.

Adding degrees of freedom

We observed that the reduced number of parameters might explain this inadequacy. Thus, a first attempt to introduce new degrees of freedom to the system was carried by freeing the mixing-length parameter of each star. Nonetheless, this parameter did not vary significantly and remained close to the solar value. This has to be expected from the works of [Magic et al. \(2015\)](#). We also noted that there were sometimes large reduced difference between initial metallicities of both components (in the accepted set of models). Therefore, we relaxed the common composition hypothesis. In most cases, this largely improved the results while only introducing small compositions differences (at most 0.008 dex^1 in X_0 and 0.002 dex in $(Z/X)_0$, for the model with turbulent diffusion). More specifically, for models without diffusion, the χ^2_{red} value reached below 1 and the model could be accepted. This was the only one. We recall that, while this model does not include microscopic diffusion, this does certainly not mean that it should never be included in the modelling of the system. This simply demonstrates the complexity of the modelling procedure and the necessity to include processes that act against microscopic diffusion.

Finally, we observed that most models did not account for the non-seismic data. This was not a surprise as the reference models did not account for them either. Furthermore, the inclusion of these constraints would have only rendered the task of finding a suitable model (according to our criterion $\chi^2_{\text{red}} < 1$) even more difficult. The only model that almost reproduced observed data was the one without diffusion. This had to be expected as the separate model for 16Cyg B reproduced all the constraints (seismic and non-seismic) while the one for the A star was close to the observed non-seismic ranges. We obtained $\delta T_{\text{eff}}/\sigma(T_{\text{eff}}) = 1.3$ and $\delta [\text{Fe}/\text{H}]/\sigma([\text{Fe}/\text{H}]) = 1.4$.

¹There was a mistake in the paper, an order of magnitude was left out.

Table 4.4: Accepted stellar range defined as the centroid of the extremum values for each parameter of the set of accepted models.

Quantity	16CygA	16CygB
$M (M_{\odot})$	1.08 ± 0.04	1.03 ± 0.03
X_0	0.72 ± 0.05	0.72 ± 0.04
$(Z/X)_0$	0.028 ± 0.009	0.03 ± 0.01
Y_0	0.26 ± 0.05	0.26 ± 0.05
t (Gyr)	7.1 ± 0.5	7.2 ± 0.4

4.2.5 Conclusions of the study

In this study, we demonstrated the necessity of high-precision probing techniques, such as WhoSGLAd, to thoroughly constrain the stellar structure. Such techniques provide means to establish realistic stellar parameters ranges, accounting for various physical hypotheses, and allow us to point to missing non-standard physical processes. Two illustrations were the necessity to reduce the efficiency of microscopic diffusion (even shutting it down for 16Cyg B) to account simultaneously for seismic and non-seismic data and the difficulty to provide models of the system requiring identical ages and initial compositions. We showed that small differences in initial composition (at most of 0.008 dex in X_0 and 0.002 dex in $(Z/X)_0$, for a common age) allowed us to greatly improve the agreement with the seismic data. This highlights the plausible necessity to separate the contribution of metals (often gathered in stellar models) in sub-species. [Maia et al. \(2019\)](#) and [Morel et al. \(2021\)](#) demonstrated that there exist small differences in individual species between the two stars. Both studies demonstrated that 16Cyg A is overabundant in metals compared to its sister. From the former study, it even stands out that there is a correlation between the element overabundance and its condensation temperature, which is compatible with planet engulfment by the A component. They also note that the planet engulfment hypothesis is consistent with the overabundance in Li et Be observed in 16Cyg A. This also agrees with the studies of [Montalbán & Rebolo \(2002\)](#) and [Carlos et al. \(2016\)](#). The opposite scenario, where it would be 16Cyg B that accreted planetary matter, triggering thermohaline convection and destructing Li et Be, has also been put forward by [Deal et al. \(2015\)](#). This represents an excellent opportunity to ally asteroseismology and exoplanetology to study and model the traces of such processes in order to further constrain our knowledge of stellar and planetary formation, evolution, and interaction. A collaboration would therefore benefit both fields.

Another clue that non-standard physical processes might be necessary to the proper depiction of the system comes from the fact that the models that performed the best at accounting for seismic and non-seismic data required to reduce the efficiency of microscopic diffusion and a different opacity table for 16Cyg A. This shows that additional mixing is necessary to counteract microscopic diffusion. This additional mixing could originate from the stellar rotation, which is not included in the CLES evolution but of which the effect can be mimicked by turbulent mixing (see for example [Rosu et al. 2020](#), who showed that the inclusion of turbulent mixing can produce similar results on the evolution of a massive star as the inclusion of rotation). Indeed, both [Davies et al. \(2015\)](#) and [Bazot et al. \(2019\)](#) demonstrated that both stars exhibit non-negligible rotation rates.

Finally, an important conclusion of the study is the importance of using all the available data at hand, with the emphasis on non-seismic data. Effectively, we determined that, while seismic models produced excellent results, most of them failed to reproduce the non-seismic data. Even worse, accounting for such data proved to be a difficult task for many of the considered variations in the input physics. This illustrates the necessity to include such constraints in the modelling procedure, in order to generate the most accurate models possible. Nevertheless, we were not able to account for these constraints while requiring a common origin for both stars.

4.2.6 Extensions of the study and future prospects

This study is the first of a three papers series and opens the way to multiple synergies between astrophysical fields. The second paper, [Buldgen et al. \(2021, in prep.\)](#), builds upon the extensive set of models computed in the first paper and carries out seismic inversions with in mind the goal to refine the results and pinpoint

stellar models shortcomings. The most striking conclusion of their paper is the dependency of the inversion results on the preliminary forward modelling step. They clearly demonstrate that, while a slight mass and radius discrepancy stands out of the inversion of their central conditions indicator (Buldgen et al. 2015, 2018), the necessity for a correction and therefore the inclusion of non-standard processes is not as clear as in their other study (Buldgen et al. 2016a), slightly above the 1σ significance level. For 16Cyg B, the models provided by the forward modelling in the first paper of the series are already in excellent agreement with inversions, requiring no further improvement. This is a clear demonstration that the WhoSGLAd indicators provide first-rate constraints relevant to the stellar structure. This also hints towards the possible necessity of non-linear seismic inversions to further probe the stellar structure.

Finally, the third paper of the series will be devoted to the study of the relation between the planetary companion and the host star, planetary formation scenarios, and the macroscopic transport of elements and angular momentum. These results will be put in the light of the differential Li and Be abundances in both stars as well as the inverted rotation profile retrieved by Bazot et al. (2019).

4.3 Application to the Kepler LEGACY sample

The second application of the WhoSGLAd method concerns the Kepler LEGACY sample (Lund et al. 2017). Part of these results were presented at the *Stars and their variability observed from the sky* conference in Vienna (Farnir et al. 2020b, and Sect. 4.B). We present here those results in more details and further discuss them.

4.3.1 The Kepler LEGACY sample

This sample consists of 66 main-sequence solar-like pulsators that have been observed continuously by the *Kepler* spacecraft during at least 1 year. This therefore constitutes the best seismic data at hand for solar-like pulsators. It also constitutes a valid sample to carry meaningful statistical studies of main-sequence stellar populations. As a consequence, several authors carried out characterisations of this ensemble of stars (e.g. Verma et al. 2017, 2019; Silva Aguirre et al. 2017). Such a large sample can, for example, test galactic enrichment relations (e.g. Verma et al. 2019; Nsamba et al. 2021) or put forward a possible correlation between the amount of central overshooting and the stellar mass (as was observed by Claret & Torres 2017, 2018, for intermediate mass eclipsing binaries). As a matter of fact, the question of overshooting in Kepler targets was already addressed by Deheuvels et al. (2016). Using the mean value and slope as a function of the radial order of the small separation between radial and dipolar modes, they demonstrated the possibility to constrain central overshooting. However, they restricted themselves to eight stars. Our goal was then to extend their work and to try to put forward the possible relations between overshooting and mass as well as between initial helium and metals abundances.

4.3.2 Fitting procedure

To model the Kepler LEGACY stars, we used the AIMS minimisation tool (Rendle et al. 2019) which consists in a grid-based approach relying on the MCMC sampling technique and in which we implemented the WhoSGLAd method. These results were then refined via the same Levenberg-Marquardt approach as for the case of 16 Cygni (Sect. 4.1.1). The preliminary minimisation with AIMS is essential to provide reliable stellar parameters guesses for the Levenberg-Marquardt step. However, as the quality of the adjustment is directly conditioned by the grid of models used, the Levenberg-Marquardt step also plays an important role and allows us to precisely navigate outside of the fixed grid elements. The set of seismic constraints used in this study were very similar to those used to characterise the 16Cyg system: that is to say Δ , \hat{r}_{01} , \hat{r}_{02} , and A_{He} . However, we also included the Δ_{01} constraint as we have shown that, in combination with \hat{r}_{01} , it may probe the amount of central overshooting (Farnir et al. 2019, and Sect. 3.2.3), one of the objectives of this study. Overall, three sets of models were computed:

- Purely seismic models, adjusting only the 5 seismic indicators: Δ , \hat{r}_{01} , \hat{r}_{02} , Δ_{01} , and A_{He} (seismic only);
- Models for which the helium glitch amplitude constraint was replaced by the surface metallicity measured by spectroscopy (metal);
- Models including both the helium glitch amplitude and metallicity (both).

A summary of reference effective temperatures and metallicities for each star is given in Table 4.5. We do not include T_{eff} as a constraint as we observed in our study of the 16Cyg that its inclusion tended to impair the convergence of our technique. Nevertheless, they remain essential data for the validation of our models. We also gather in Table 4.6 the measured values for the seismic indicators used in the adjustment for each individual star of the sample. When possible, we provide the amplitude and acoustic depth of the helium glitch. Indeed, the measurement of those quantities relies on a partial seismic modelling (excluding the glitch signature as described in Sect. 3.5.1). However, we were not able in all cases to carry this partial seismic modelling. Therefore, in these difficult cases, we measured the helium glitch amplitude using the dimensionless helium acoustic depth estimation defined in Sect. 3.5. These models are marked with an asterisk *.

Table 4.5: Observed effective temperature and surface metallicity of the Kepler LEGACY stars. Some of the other identifiers are gathered.

KIC ID	Other IDs	T_{eff} (K)	$[Fe/H]$	Refs
KIC1435467		6265 ± 60	-0.01 ± 0.06	Bruntt et al. (2012)
KIC2837475	HD179260	6700 ± 60	-0.02 ± 0.06	Bruntt et al. (2012)
KIC3427720		6040 ± 60	-0.03 ± 0.06	Bruntt et al. (2012)
KIC3456181		6270 ± 60	-0.19 ± 0.06	Bruntt et al. (2012)
KIC3632418	HIP94112, HD179070	6190 ± 60	-0.16 ± 0.06	Bruntt et al. (2012)
KIC3656476		6710 ± 60	0.34 ± 0.06	Bruntt et al. (2012)
KIC3735871		6080 ± 25	0.04 ± 0.01	Brewer et al. (2016)
KIC4914923	HIP94734	5905 ± 60	0.17 ± 0.06	Bruntt et al. (2012)
KIC5184732	/	5840 ± 60	0.38 ± 0.06	Bruntt et al. (2012)
KIC5773345		6130 ± 60	0.21 ± 0.06	Bruntt et al. (2012)
KIC5950854		5853 ± 77	-0.23 ± 0.10	Buchhave & Latham (2015)
KIC6106415	HIP93427, HD177153	5990 ± 60	-0.09 ± 0.06	Bruntt et al. (2012)
KIC6116048		5935 ± 60	-0.24 ± 0.06	Bruntt et al. (2012)
KIC6225718	HIP97527, HD187637	6230 ± 60	-0.17 ± 0.06	Bruntt et al. (2012)
KIC6508366		6354 ± 60	-0.08 ± 0.06	Bruntt et al. (2012)
KIC6603624		5625 ± 60	0.28 ± 0.06	Bruntt et al. (2012)
KIC6679371		6260 ± 60	-0.13 ± 0.06	Bruntt et al. (2012)
KIC6933899		5860 ± 60	0.02 ± 0.06	Bruntt et al. (2012)
KIC7103006		6394 ± 60	0.05 ± 0.06	Bruntt et al. (2012)
KIC7106245		6068 ± 102	-0.12 ± 0.01	Brewer et al. (2016)
KIC7206837	/	6304 ± 60	0.14 ± 0.06	Bruntt et al. (2012)
KIC7296438		5775 ± 77	0.19 ± 0.10	Brewer et al. (2016)
KIC7510397	Krazy, HIP93511, HD177412	6110 ± 60	-0.23 ± 0.06	Bruntt et al. (2012)
KIC7680114		5855 ± 60	0.11 ± 0.06	Bruntt et al. (2012)
KIC7771282		6248 ± 77	-0.02 ± 0.10	Brewer et al. (2016)
KIC7871531		5400 ± 60	-0.24 ± 0.06	Bruntt et al. (2012)
KIC7940546	HIP92615, HD175226	6264 ± 60	-0.19 ± 0.06	Bruntt et al. (2012)
KIC7970740	HD186306	5290 ± 60	-0.49 ± 0.06	Bruntt et al. (2012)
KIC8006161	Doris, HIP91949	5390 ± 60	0.34 ± 0.06	Bruntt et al. (2012)
KIC8150065		6173 ± 101	-0.13 ± 0.15	Huber et al. (2013)
KIC8179536		6344 ± 60	0.01 ± 0.06	Bruntt et al. (2012)
KIC8228742	HIP95098	6042 ± 60	-0.14 ± 0.06	Bruntt et al. (2012)
KIC8379927		6067 ± 120	-0.10 ± 0.15	Ramírez et al. (2009)
KIC8394589		6114 ± 60	-0.36 ± 0.06	Bruntt et al. (2012)
KIC8424992		5719 ± 77	-0.12 ± 0.10	Buchhave & Latham (2015)
KIC8694723		6120 ± 60	-0.59 ± 0.06	Bruntt et al. (2012)
KIC8760414		5727 ± 60	-1.14 ± 0.06	Bruntt et al. (2012)
KIC8938364		5630 ± 60	-0.20 ± 0.06	Bruntt et al. (2012)
KIC9025370		5270 ± 180	-0.12 ± 0.18	Pinsonneault et al. (2012)
KIC9098294		5840 ± 60	-0.13 ± 0.06	Bruntt et al. (2012)
KIC9139151	HIP92961	6125 ± 60	0.11 ± 0.06	Bruntt et al. (2012)
KIC9139163	HIP92962, HD176071	6400 ± 60	0.15 ± 0.06	Bruntt et al. (2012)
KIC9206432		6608 ± 60	0.23 ± 0.06	Bruntt et al. (2012)
KIC9353712		6278 ± 77	-0.05 ± 0.10	Buchhave & Latham (2015)
KIC9410862		6047 ± 77	-0.31 ± 0.10	Buchhave & Latham (2015)
KIC9414417		6253 ± 75	-0.13 ± 0.10	Chaplin et al. (2014)
KIC9812850		6325 ± 60	-0.16 ± 0.06	Bruntt et al. (2012)
KIC9955598		5410 ± 60	0.11 ± 0.06	Bruntt et al. (2012)

4. Application of the WhoSGIAd method

KIC ID	Other IDs	T_{eff} (K)	$[Fe/H]$	Refs
KIC9965715		5860 ± 180	-0.20 ± 0.01	Brewer et al. (2016)
KIC10068307	HIP94675, HD180867	6114 ± 60	-0.22 ± 0.06	Bruntt et al. (2012)
KIC10079226		5949 ± 77	0.11 ± 0.10	Buchhave & Latham (2015)
KIC10162436	HIP97992	6200 ± 60	-0.08 ± 0.06	Bruntt et al. (2012)
KIC10454113	HIP92983	6120 ± 60	-0.06 ± 0.06	Bruntt et al. (2012)
KIC10516096		5940 ± 60	-0.06 ± 0.06	Bruntt et al. (2012)
KIC10644253		6230 ± 60	0.12 ± 0.06	Bruntt et al. (2012)
KIC10730618		6150 ± 180	0.04 ± 0.01	Brewer et al. (2016)
KIC10963065		6060 ± 60	-0.20 ± 0.06	Bruntt et al. (2012)
KIC11081729		6630 ± 60	-0.12 ± 0.06	Bruntt et al. (2012)
KIC11253226	HIP97071, HD186700	6605 ± 60	-0.08 ± 0.06	Bruntt et al. (2012)
KIC11772920		5180 ± 180	-0.09 ± 0.18	Pinsonneault et al. (2012)
KIC12009504		6065 ± 60	-0.09 ± 0.06	Bruntt et al. (2012)
KIC12069127		6276 ± 77	0.08 ± 0.10	Buchhave & Latham (2015)
KIC12069424	16CygA	5839 ± 42^a	0.096 ± 0.026^b	^a White et al. (2013) ^b Ramírez et al. (2009)
KIC12069449	16CygB	5809 ± 39^a	0.051 ± 0.021^b	^a White et al. (2013) ^b Ramírez et al. (2009)
KIC12258514		5990 ± 60	0.04 ± 0.06	Bruntt et al. (2012)
KIC12317678		6580 ± 77	-0.28 ± 0.10	Buchhave & Latham (2015)

Table 4.6: Values of the seismic indicators measured with WhoSGIAd for the complete LEGACY sample. When possible, we provide the value of the acoustic depth of the helium glitch.

Star	Δ (μHz)	\hat{r}_{01} ($\times 10^{-2}$)	\hat{r}_{02} ($\times 10^{-2}$)	Δ_{01} ($\times 10^{-3}$)	A_{He}	τ_{He} (s)
KIC1435467	70.50 ± 0.02	3.9 ± 0.2	8.2 ± 0.3	2.3 ± 0.5	15.0 ± 1.0	1224.89
KIC2837475	75.68 ± 0.02	3.1 ± 0.2	8.3 ± 0.4	1.4 ± 0.6	16.3 ± 1.0	1048.91
KIC3427720	119.63 ± 0.01	3.03 ± 0.05	8.67 ± 0.07	2.60 ± 0.02	14.3 ± 1.0	775.10
KIC3456181	52.29 ± 0.02	7.6 ± 0.3	9.0 ± 0.4	2.2 ± 0.8	12.1 ± 1.0	1856.10
KIC3632418	60.488 ± 0.008	6.44 ± 0.09	7.28 ± 0.15	5.6 ± 0.3	22.2 ± 1.0	1636.07
KIC3656476	93.144 ± 0.009	5.11 ± 0.04	5.16 ± 0.04	2.3 ± 0.2	16.9 ± 1	1108.15
KIC3735871	122.71 ± 0.02	2.95 ± 0.08	8.95 ± 0.15	-1.4 ± 0.4	8.5 ± 1.0	733.30
KIC4914923	88.364 ± 0.009	5.20 ± 0.04	6.05 ± 0.07	3.2 ± 0.2	18.6 ± 1.0	1124.33
KIC5184732	95.393 ± 0.008	3.04 ± 0.04	6.41 ± 0.05	3.5 ± 0.2	18.5 ± 1.0	1001.23
KIC5773345	57.00 ± 0.01	1.8 ± 0.2	7.8 ± 0.4	-4.4 ± 0.4	13.3 ± 1.0	1421.21
KIC5950854	96.87 ± 0.03	5.25 ± 0.09	5.29 ± 0.16	5.8 ± 0.7	4.6 ± 1.0	1095.36
KIC6106415	103.945 ± 0.008	3.35 ± 0.04	7.01 ± 0.06	3.8 ± 0.2	18.9 ± 1.0	934.16
KIC6116048	100.653 ± 0.008	3.74 ± 0.04	6.32 ± 0.06	2.8 ± 0.2	19.3 ± 1.0	1007.70
KIC6225718	105.111 ± 0.007	3.06 ± 0.04	8.28 ± 0.06	2.1 ± 0.1	28.0 ± 1.0	843.08
KIC6508366	51.59 ± 0.02	7.1 ± 0.3	6.3 ± 0.4	2.7 ± 0.7	11.2 ± 1.0	1954.58
KIC6603624	110.046 ± 0.005	2.72 ± 0.02	4.86 ± 0.2	2.4 ± 0.1	25.3 ± 1.0	918.68
KIC6679371	50.68 ± 0.01	5.7 ± 0.2	6.2 ± 0.4	0.1 ± 0.6	14.9 ± 1.0	1829.04
KIC6933899	71.797 ± 0.007	7.16 ± 0.05	7.02 ± 0.07	-0.9 ± 0.2	$23.4 \pm 1.0^*$	
KIC7103006	59.72 ± 0.02	4.8 ± 0.2	7.3 ± 0.5	3.1 ± 0.6	11.2 ± 1.0	1510.33
KIC7106245	111.23 ± 0.02	3.20 ± 0.08	5.9 ± 0.1	2.4 ± 0.5	5.4 ± 1.0	898.48
KIC7206837	78.80 ± 0.01	2.4 ± 0.1	6.3 ± 0.2	-0.07 ± 0.42	10.9 ± 1.0	1124.43
KIC7296438	88.51 ± 0.02	5.07 ± 0.07	5.98 ± 0.09	1.6 ± 0.4	11.1 ± 1.0	1149.45
KIC7510397	61.747 ± 0.007	5.80 ± 0.08	7.7 ± 0.1	-1.7 ± 0.3	21.6 ± 1.0	1528.36
KIC7680114	85.02 ± 0.01	6.00 ± 0.05	6.10 ± 0.07	0.7 ± 0.3	13.1 ± 1.0	1227.89
KIC7771282	72.39 ± 0.04	4.7 ± 0.3	6.5 ± 0.5	7.1 ± 1.2	6.2 ± 1.0	1304.71
KIC7871531	151.25 ± 0.01	1.62 ± 0.03	5.08 ± 0.09	3.1 ± 0.2	9.0 ± 1.0	685.37
KIC7940546	58.784 ± 0.009	6.5 ± 0.1	7.8 ± 0.2	0.7 ± 0.3	18.9 ± 1.0	1532.56
KIC7970740	173.137 ± 0.009	1.53 ± 0.02	5.16 ± 0.05	1.8 ± 0.1	$9.8 \pm 1.0^*$	
KIC8006161	149.214 ± 0.006	2.19 ± 0.02	6.83 ± 0.03	1.04 ± 0.09	14.6 ± 1.0	645.81
KIC8150065	88.83 ± 0.041	2.8 ± 0.2	7.2 ± 0.3	-4.5 ± 1.2	4.9 ± 1.0	1027.41
KIC8179536	94.93 ± 0.03	3.3 ± 0.1	8.7 ± 0.3	2.9 ± 0.6	9.2 ± 1.0	865.63
KIC8228742	61.697 ± 0.009	6.52 ± 0.08	7.3 ± 0.1	3.6 ± 0.3	$19.4 \pm 1.0^*$	
KIC8379927	120.058 ± 0.009	3.15 ± 0.04	9.37 ± 0.06	1.8 ± 0.1	23.8 ± 1.0	744.10
KIC8394589	109.15 ± 0.02	3.23 ± 0.06	7.5 ± 0.1	3.9 ± 0.3	14.2 ± 1.0	867.63
KIC8424992	120.81 ± 0.02	2.53 ± 0.08	4.34 ± 0.10	2.8 ± 0.5	4.8 ± 1.0	869.78

Star	Δ (μHz)	\hat{r}_{01} ($\text{in } 10^{-2}$)	\hat{r}_{02} ($\text{in } 10^{-2}$)	Δ_{01} ($\text{in } 10^{-3}$)	A_{He}	τ_{He} (s)
KIC8694723	74.727 \pm 0.008	6.78 \pm 0.07	8.05 \pm 0.13	-0.4 \pm 0.2	18.8 \pm 1.0	1323.06
KIC8760414	117.227 \pm 0.009	4.25 \pm 0.03	5.05 \pm 0.04	5.0 \pm 0.2	9.8 \pm 1.0*	
KIC8938364	85.402 \pm 0.008	7.70 \pm 0.04	6.38 \pm 0.05	1.3 \pm 0.2	18.1 \pm 1.0	1354.64
KIC9025370	132.60 \pm 0.02	2.34 \pm 0.04	6.89 \pm 0.08	1.1 \pm 0.2	7.5 \pm 1.0	735.69
KIC9098294	108.83 \pm 0.01	3.20 \pm 0.04	5.05 \pm 0.07	3.6 \pm 0.2	12.1 \pm 1.0	956.42
KIC9139151	116.98 \pm 0.01	2.94 \pm 0.06	8.52 \pm 0.12	2.5 \pm 0.3	13.1 \pm 1.0	764.86
KIC9139163	80.96 \pm 0.01	2.6 \pm 0.1	7.6 \pm 0.2	2.5 \pm 0.3	21.7 \pm 1.0	1034.51
KIC9206432	84.86 \pm 0.02	3.8 \pm 0.2	8.2 \pm 0.4	0.2 \pm 0.6	14.2 \pm 1.0	999.68
KIC9353712	51.32 \pm 0.02	6.4 \pm 0.3	7.2 \pm 0.5	-3.7 \pm 1.0	8.3 \pm 1.0	1886.80
KIC9410862	107.32 \pm 0.02	3.80 \pm 0.08	5.83 \pm 0.17	3.2 \pm 0.5	7.7 \pm 1.0	944.33
KIC9414417	59.93 \pm 0.01	6.7 \pm 0.1	8.1 \pm 0.3	4.0 \pm 0.4	14.2 \pm 1.0	1528.81
KIC9812850	64.85 \pm 0.02	3.9 \pm 0.2	7.3 \pm 0.5	5.9 \pm 0.7	12.2 \pm 1.0	1425.83
KIC9955598	153.07 \pm 0.01	1.95 \pm 0.03	6.09 \pm 0.06	2.5 \pm 0.2	6.6 \pm 1.0	651.93
KIC9965715	96.95 \pm 0.02	4.0 \pm 0.1	8.3 \pm 0.2	2.1 \pm 0.5	11.3 \pm 1.0	889.00
KIC10068307	53.572 \pm 0.007	7.37 \pm 0.09	7.48 \pm 0.013	0.8 \pm 0.3	22.4 \pm 1.0	1876.55
KIC10079226	116.15 \pm 0.04	3.0 \pm 0.1	8.3 \pm 0.3	-2.1 \pm 0.6	5.7 \pm 1.0	789.35
KIC10162436	55.475 \pm 0.008	6.0 \pm 0.1	7.3 \pm 0.2	-3.0 \pm 0.3	19.8 \pm 1.0	1643.92
KIC10454113	104.333 \pm 0.008	1.71 \pm 0.09	9.3 \pm 0.1	-2.6 \pm 0.2	17.8 \pm 1.0	824.98
KIC10516096	84.17 \pm 0.01	5.95 \pm 0.05	4.30 \pm 0.69	2.6 \pm 0.2	16.3 \pm 1.0	1258.08
KIC10644253	122.62 \pm 0.02	3.08 \pm 0.8	9.58 \pm 0.11	-1.5 \pm 0.4	11.9 \pm 1.0	715.18
KIC10730618	65.90 \pm 0.02	2.1 \pm 0.3	6.7 \pm 0.6	-7.7 \pm 0.9	9.7 \pm 1.0	1200.54
KIC10963065	102.82 \pm 0.01	3.61 \pm 0.05	7.11 \pm 0.08	3.0 \pm 0.2	17.4 \pm 1.0	938.27
KIC11081729	89.95 \pm 0.02	4.2 \pm 0.2	8.2 \pm .5	2.3 \pm 0.6	7.0 \pm 1.0	1015.86
KIC11253226	76.98 \pm 0.02	2.6 \pm 0.2	8.3 \pm 0.5	3.8 \pm 0.4	14.9 \pm 1.0	1231.96
KIC11772920	157.61 \pm 0.02	1.55 \pm 0.03	5.24 \pm 0.09	1.5 \pm 0.2	5.4 \pm 1.0	665.31
KIC12009504	87.75 \pm 0.01	4.07 \pm 0.07	7.1 \pm 0.1	2.4 \pm 0.3	18.1 \pm 1.0	1092.63
KIC12069127	48.16 \pm 0.02	6.7 \pm 0.3	7.9 \pm 0.5	-0.2 \pm 0.9	9.9 \pm 1.0	1862.68
KIC12069424	103.070 \pm 0.005	3.61 \pm 0.02	5.61 \pm 0.03	3.77 \pm 0.10	29.6 \pm 1.0	973.14
KIC12069449	116.761 \pm 0.005	2.49 \pm 0.02	5.31 \pm 0.03	2.75 \pm 0.09	28.9 \pm 1.0	858.47
KIC12258514	74.442 \pm 0.005	5.49 \pm 0.04	6.49 \pm 0.05	1.0 \pm 0.1	31.6 \pm 1.0	133.83
KIC12317678	63.35 \pm 0.01	-2.1 \pm 0.2	3.4 \pm 0.7	2.0 \pm 0.4	19.8 \pm 1.0	1352.45

Note. * A_{He} obtained with T_{He} estimated as in Sect. 3.5.

Stellar grid

The grid of models we used with AIMS was computed with the CLES stellar evolution code (Scuflaire et al. 2008b), with the same set of input physics as for the 16Cyg case (see Farnir et al. 2020a, and Table 4.3). For each model, adiabatic oscillation frequencies were computed with the LOSC oscillation code (Scuflaire et al. 2008a) (we computed frequencies in a broad range to encompass observed frequency ranges). We computed stellar evolution models along the main sequence phase only for masses in the range $M \in [0.90 M_{\odot}, 1.40 M_{\odot}]$ ($0.02 M_{\odot}$ step), initial hydrogen abundances in the range $X_0 \in [0.68, 0.74]$ (0.02 step), initial metals content in $Z_0 \in [0.008, 0.024]$ (0.004 step) and overshooting parameter in $\alpha_{\text{ov}} \in [0.0, 0.4]$ (0.1 step). This represents 1200 evolutionary tracks and over 450000 individual models.

4.3.3 Results of the adjustment

We present here the results of each type of adjustment. From our experience with the case of 16Cyg A, we now know that the inclusion of overshooting in stars close to the limit at which convective cores start to subsist ($M \gtrsim 1.1 M_{\odot}$) can lead to unexpected and complex behaviours. Therefore, for models for which we expected a mass $\lesssim 1.1 M_{\odot}$ (from preliminary modelling or literature values) and the absence of a convective core, the overshooting parameter becomes irrelevant. For such stars, we computed models without overshooting and excluding the Δ_{01} constraint. Our results are therefore separated into two categories with respect to the inclusion of overshooting. These considerations put aside, the grid we used might be too coarse. The overshooting parameter step size may be too large to properly interpolate between grid points. Furthermore, we know from our past experience that the metallicity constraint (non-seismic data in a broader sense) is often difficult to reconcile with seismic data. As a consequence, the results presented here must be regarded with caution as it will be necessary to further improve them.

Our results are presented in Figs. 4.6 to 4.10. We selected the 14 best purely seismic models including overshooting (i.e. with Δ , \hat{r}_{01} , \hat{r}_{02} , Δ_{01} , and A_{He} as constraints) and the associated metallicity models ($[\text{Fe}/\text{H}]$ replacing A_{He}) and the nine best models without overshooting. Models with overshooting are represented by filled symbols while the empty symbols correspond to models without overshooting. Within those models we distinguish

seismic models, represented by diamonds, from the metallicity models, represented by triangles. Individual stars are associated with different colors and linked by a straight line. The associated stellar parameters are gathered in Tables 4.7 and 4.8 where we separated the models with and without overshooting with the horizontal line.

In the selected sample of models, only five seismic models (two with overshooting and three without) and eight metallicity models (two with overshooting and six without) have a $\chi^2 \leq 1$. This illustrates the difficulty to retrieve acceptable models. A less conservative criterion can be to require the χ^2 value to never exceed N , the number of constraints. This is a sensible criterion as each constraint is authorised to contribute to, at most, one to the total cost function and is therefore within 1σ of its target value. The number of acceptable models increases to 16 and 13 for seismic and metallic models, respectively.

Figure 4.6 represents the selected sample of models in a HR diagram. Except for a few cases, the difference between seismic and metallic models is not large. However, this observation allows us to conclude that models including both the metallicity and helium glitch amplitude are uninformative. Indeed, whenever one of the two constraints dominates, the algorithm will settle for a model adjusting that constraint. This is what we actually observed when trying to compute such models. As a consequence, we do not present these results. We also represent the observed effective temperature and their associated uncertainties for each star, using the same color coding. We note that about half of the models agree with the observed effective temperature.

In Fig. 4.7 we represent the age of individual stars as a function of their mass. We note a clear anti-correlation between those two quantities. As these stars are expected to be main-sequence stars, we may expect this relation to result from the typical hydrogen nuclear burning time scale (Eq. (2.28)). We also observe that, in most cases, using the metallicity constraint over the helium glitch amplitude has a little impact. This is to be expected as both constraints mostly impact the chemical composition (which can still impact stellar age and mass but with a reduced magnitude in comparison with the Δ constraint, for example).

We also represent the amount of overshooting included in optimal models as a function of their mass in Fig. 4.8. While we cannot assert a definitive trend. The amount of overshooting indeed seems to increase with stellar mass. To demonstrate it, we carried a linear fit of the amount of overshooting as a function of the mass. This is represented by the straight line in Fig. 4.8. However, the scatter around the slight trend is rather large. This is in agreement with the observations of (Claret & Torres 2017, 2018) in eclipsing binaries. The range of masses included in our study is much narrower than theirs, because solar-like stars correspond to low-mass stars. We further note that using either the metallicity constraint or the helium glitch amplitude constraint has, in most cases, little impact on the solution retrieved. However, we note for some stars that the use of the helium glitch amplitude produces models with a significantly reduced amount of overshooting. Nevertheless, the mass of such models is almost unaffected, their ages and positions in the HR diagram as well. Amongst the stars presenting such a difference, two striking examples stand out: KIC10162436 (filled blue symbols) and KIC11081729 (filled peach symbols). The former actually corresponds to a star that produced a satisfying seismic model but that did not reach a proper solution including the metallicity constraint. The latter is more interesting as both solutions are excellent. This shows that the selection of constraints, while having little impact on regular non-seismic data, can play an essential role in determining the optimal set of parameters. Another interesting example is that of KIC10454113 (filled light-brown symbols). While preserving similar amounts of overshooting, the optimal mass is smaller by about $0.1 M_{\odot}$ when using A_{He} instead of the metallicity.

Finally, the composition of the best models is depicted in Figs. 4.9 and 4.10. They represent the initial helium mass fraction as a function of the initial metals abundance and the surface helium abundance as a function of the surface metallicity, respectively. It is again difficult to affirm that a clear trend stands out. However, via a linear adjustment of our data (represented by a straight line), we obtain in Fig. 4.9 $\Delta Y/\Delta Z = 1.92 \pm 0.79$ and $Y_p = 0.26 \pm 0.01$. This is in relative agreement with the determination of Verma et al. (2019). While our values are lower than theirs, they are comprised within their uncertainties. Our values are also compatible with the numerous past determinations (e.g. Ribas et al. 2000; Lebreton et al. 2001; Peimbert et al. 2002; Balser 2006; Casagrande et al. 2007; Nsamba et al. 2021) that span a broad range of values: $\Delta Y/\Delta Z \in [1.4, 3.5]$ and $Y_p \in [0.18, 0.24]$. This is to be expected as the chemical evolution of our galaxy is far from being homogeneous (Vincenzo et al. 2019). Furthermore, the chosen solar-reference mixture must have an impact and on the inferred $\Delta Y/\Delta Z$ and Y_p . We note that, contrary to these studies, we have used the AGSS09 solar mixture (Asplund et al. 2009), which is the less metallic of the commonly used references. When modelling the 16Cyg system, we observed that the use of GN93 (Grevesse & Noels 1993) over AGSS09 lead to more metallic models but also initially less abundant in helium. Altogether, this could result in an increased $\Delta Y/\Delta Z$ and a reduced Y_p . When looking at Fig. 4.10, a positive correlation between the surface helium abundance and surface metallicity seems to exist. We observed the same correlation between our models of the 16Cyg system (Figs. 4.4 and 4.5). However, the interpretation must be different as we do not adjust the same glitch signature, which is both correlated to the helium surface content and anti-correlated to the metallicity.

4.3. Application to the Kepler LEGACY sample

Table 4.7: Stellar parameters obtained by adjusting Δ , \hat{r}_{01} , \hat{r}_{02} , Δ_{01} , and A_{He} . The results are ordered in increasing χ^2 values. Only the 14 best models with overshooting and the nine best without are displayed.

Star	$M (M_{\odot})$	$R (R_{\odot})$	$t (Gyrs)$	α_{ov}	$L (L_{\odot})$	T_{eff}	Y_s	$(Z/X)_s$	$[Fe/H]$	M_{mix}/M	χ^2
KIC10454113	1.171 ± 0.187	1.231 ± 0.065	1.615 ± 1.119	0.134 ± 0.059	2.28	6396.38	0.24	0.02	-0.03	0.06	0.44E+00
KIC6225718	1.143 ± 0.041	1.219 ± 0.015	2.395 ± 0.121	0.128 ± 0.003	2.16	6341.96	0.22	0.01	-0.15	0.03	0.91E+00
KIC7296438	1.121 ± 0.048	1.378 ± 0.020	6.447 ± 0.339	0.008 ± 0.362	1.97	5824.47	0.23	0.03	0.18	0.00	0.15E+01
KIC11081729	1.223 ± 0.572	1.389 ± 0.217	3.052 ± 1.483	0.033 ± 1.498	2.63	6238.95	0.21	0.02	0.02	0.03	0.26E+01
KIC8150065	1.135 ± 0.058	1.365 ± 0.023	2.745 ± 0.267	0.087 ± 0.049	2.63	6289.23	0.26	0.02	0.07	0.08	0.28E+01
KIC5184732	1.142 ± 0.055	1.313 ± 0.021	4.211 ± 0.119	0.125 ± 0.135	2.06	6036.05	0.24	0.02	0.13	0.06	0.39E+01
KIC7510397	1.340 ± 0.035	1.828 ± 0.016	2.977 ± 0.257	0.067 ± 0.031	4.75	6302.77	0.16	0.01	-0.22	0.07	0.39E+01
KIC10068307	1.298 ± 0.009	1.997 ± 0.005	3.357 ± 0.123	0.178 ± 0.013	5.23	6175.06	0.20	0.01	-0.17	0.09	0.40E+01
KIC6508366	1.323 ± 0.069	2.071 ± 0.036	3.391 ± 0.328	0.243 ± 0.054	5.24	6066.32	0.24	0.02	0.03	0.12	0.87E+01
KIC7206837	1.234 ± 0.264	1.514 ± 0.108	2.553 ± 0.627	0.156 ± 0.121	3.36	6350.65	0.21	0.02	0.01	0.12	0.89E+01
KIC8179536	1.281 ± 0.174	1.351 ± 0.061	1.419 ± 0.281	0.101 ± 0.032	2.86	6459.50	0.22	0.02	0.03	0.06	0.96E+01
KIC10162436	1.385 ± 0.529	1.984 ± 0.253	2.440 ± 8.265	0.040 ± 1.314	5.57	6295.68	0.19	0.02	-0.05	0.06	0.10E+02
KIC5773345	1.573 ± 0.152	2.014 ± 0.065	1.764 ± 0.275	0.211 ± 0.068	6.26	6434.16	0.12	0.02	0.06	0.00	0.11E+02
KIC7771282	1.321 ± 0.117	1.646 ± 0.049	2.974 ± 0.589	0.092 ± 0.104	3.75	6260.70	0.19	0.02	-0.00	0.09	0.11E+02
KIC9353712	1.397 ± 0.013	2.111 ± 0.006	2.917 ± 0.134	0.117 ± 0.034	5.60	6109.50	0.23	0.02	0.09	0.07	0.12E+02
KIC8006161	0.989 ± 0.038	0.932 ± 0.012	5.609 ± 0.158	0.000 ± 0.000	0.56	5168.07	0.24	0.04	0.34	0.00	0.67E+00
KIC8394589	1.085 ± 0.028	1.177 ± 0.010	3.532 ± 0.156	0.000 ± 0.000	1.82	6177.52	0.23	0.01	-0.10	0.00	0.81E+00
KIC9955598	0.901 ± 0.081	0.888 ± 0.027	7.122 ± 0.902	0.000 ± 0.000	0.56	5309.23	0.24	0.02	0.11	0.00	0.87E+00
KIC7871531	0.840 ± 0.068	0.875 ± 0.024	9.431 ± 1.934	0.000 ± 0.000	0.53	5261.47	0.27	0.03	0.19	0.00	0.14E+01
KIC7106245	0.972 ± 0.031	1.124 ± 0.012	5.750 ± 0.328	0.000 ± 0.000	1.51	6035.34	0.24	0.01	-0.12	0.00	0.18E+01
KIC7680114	1.098 ± 0.015	1.405 ± 0.007	6.797 ± 0.284	0.000 ± 0.000	2.18	5913.33	0.21	0.02	0.02	0.00	0.24E+01
KIC9098294	1.006 ± 0.016	1.156 ± 0.109	7.704 ± 0.208	0.000 ± 0.000	1.42	5865.45	0.20	0.01	-0.11	0.00	0.37E+01
KIC8424992	0.927 ± 0.070	1.052 ± 0.026	9.851 ± 0.375	0.000 ± 0.000	1.01	5635.74	0.22	0.02	-0.02	0.00	0.40E+01
KIC6603624	1.023 ± 0.023	1.155 ± 0.009	8.351 ± 0.123	0.000 ± 0.000	1.16	5568.94	0.25	0.03	0.28	0.00	0.62E+01

Note. Models with overshooting are presented above the horizontal separation. Models without overshooting are situated below.

Table 4.8: Stellar parameters obtained by adjusting Δ , \hat{r}_{01} , \hat{r}_{02} , Δ_{01} , and $[Fe/H]$. The results are ordered in increasing χ^2 values. Only the 14 best models with overshooting and the nine best without are displayed.

Star	$M (M_{\odot})$	$R (R_{\odot})$	$t (Gyrs)$	α_{ov}	$L (L_{\odot})$	T_{eff}	Y_s	$(Z/X)_s$	$[Fe/H]$	M_{mix}/M	χ^2
KIC6225718	1.141 ± 0.105	1.217 ± 0.037	2.377 ± 0.149	0.126 ± 0.016	2.18	6355.31	0.21	0.01	-0.17	0.03	0.44E+00
KIC10454113	1.267 ± 0.430	1.267 ± 0.143	1.665 ± 0.272	0.143 ± 0.037	2.31	6323.26	0.20	0.02	-0.06	0.06	0.57E+00
KIC7296438	1.121 ± 0.092	1.378 ± 0.038	6.447 ± 0.761	0.008 ± 0.513	1.97	5824.47	0.23	0.03	0.18	0.00	0.13E+01
KIC11081729	1.241 ± 0.460	1.395 ± 0.172	3.232 ± 1.109	0.100 ± 0.339	2.73	6283.37	0.18	0.01	-0.12	0.02	0.28E+01
KIC6508366	1.336 ± 0.122	2.071 ± 0.063	3.115 ± 1.064	0.231 ± 0.068	5.59	6167.57	0.22	0.02	-0.05	0.12	0.31E+01
KIC8150065	1.129 ± 0.149	1.362 ± 0.060	2.893 ± 0.384	0.117 ± 0.040	2.67	6319.22	0.24	0.02	-0.03	0.08	0.49E+01
KIC7771282	1.331 ± 0.147	1.651 ± 0.061	3.128 ± 1.489	0.094 ± 0.085	3.73	6244.28	0.18	0.02	-0.02	0.08	0.69E+01
KIC10068307	1.286 ± 0.007	1.990 ± 0.003	3.206 ± 0.090	0.167 ± 0.015	5.24	6191.34	0.21	0.01	-0.15	0.09	0.81E+01
KIC7510397	1.340 ± 0.098	1.828 ± 0.045	2.977 ± 0.618	0.069 ± 0.028	4.75	6303.13	0.16	0.01	-0.22	0.07	0.84E+01
KIC8179536	1.281 ± 0.339	1.351 ± 0.119	1.417 ± 0.239	0.099 ± 0.091	2.86	6459.93	0.22	0.02	0.03	0.06	0.97E+01
KIC9353712	1.397 ± 12.186	2.115 ± 6.147	2.926 ± 299.365	0.131 ± 27.973	5.54	6088.69	0.24	0.02	0.09	0.08	0.13E+02
KIC5773345	1.573 ± 0.220	2.015 ± 0.094	1.767 ± 0.537	0.194 ± 0.066	6.23	6423.29	0.13	0.02	0.08	0.00	0.16E+02
KIC5184732	1.137 ± 0.017	1.311 ± 0.007	4.104 ± 0.184	0.120 ± 0.027	2.07	6044.76	0.25	0.02	0.14	0.06	0.19E+02
KIC7206837	1.228 ± 0.199	1.523 ± 0.082	3.600 ± 0.531	0.146 ± 0.012	2.93	6118.45	0.24	0.02	0.14	0.10	0.23E+02
KIC10162436	1.388 ± 0.140	1.984 ± 0.067	2.464 ± 0.178	0.124 ± 0.039	5.61	6304.88	0.19	0.02	-0.05	0.10	0.47E+02
KIC8394589	1.107 ± 0.037	1.181 ± 0.013	3.896 ± 0.167	0.000 ± 0.000	1.91	6243.17	0.17	0.01	-0.36	0.00	0.37E+02
KIC6603624	1.020 ± 0.306	1.155 ± 0.115	8.263 ± 3.198	0.000 ± 0.000	1.16	5568.94	0.25	0.03	0.28	0.00	0.18E+00
KIC7106245	0.971 ± 0.034	1.123 ± 0.013	5.723 ± 0.394	0.000 ± 0.000	1.51	6039.24	0.24	0.01	-0.12	0.00	0.23E+00
KIC8006161	0.956 ± 0.010	0.921 ± 0.003	5.365 ± 0.803	0.000 ± 0.000	0.59	5268.17	0.27	0.04	0.34	0.00	0.92E+00
KIC7871531	0.909 ± 0.043	0.898 ± 0.014	9.987 ± 0.804	0.000 ± 0.000	0.61	5377.51	0.17	0.01	-0.23	0.00	0.98E+00
KIC9955598	0.901 ± 0.128	0.888 ± 0.042	7.056 ± 1.459	0.000 ± 0.000	0.57	5314.82	0.24	0.02	0.11	0.00	0.15E+01
KIC7680114	1.099 ± 0.025	1.405 ± 0.011	6.773 ± 0.766	0.000 ± 0.000	2.18	5916.19	0.21	0.02	0.01	0.00	0.18E+01
KIC9098294	1.006 ± 0.019	1.156 ± 0.007	7.706 ± 0.249	0.000 ± 0.000	1.42	5864.84	0.20	0.01	-0.11	0.00	0.38E+01
KIC8424992	0.910 ± 0.065	1.045 ± 0.025	9.831 ± 1.792	0.000 ± 0.000	1.03	5685.50	0.23	0.02	-0.07	0.00	0.58E+01

Note. Models with overshooting are presented above the horizontal separation. Models without overshooting are situated below.

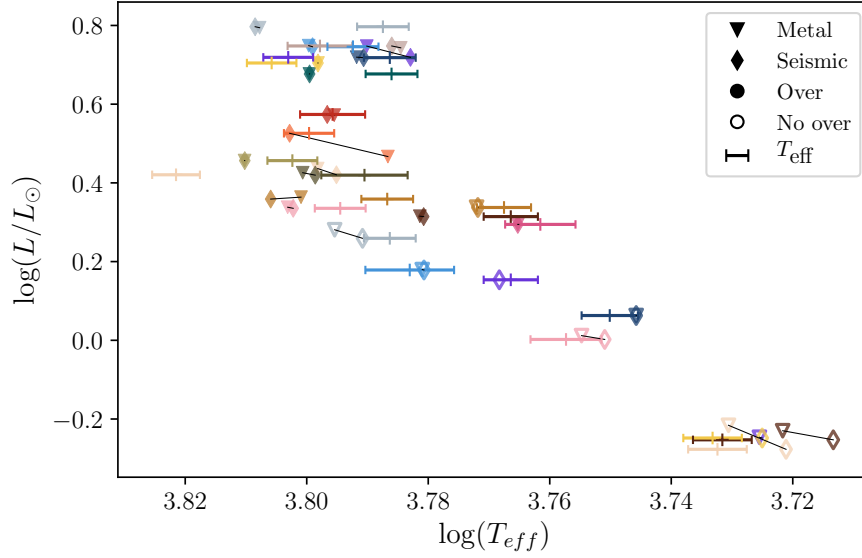


Figure 4.6: HR diagram representing the best fit models considering either only seismic constraints (diamonds) or the metallicity constraint instead of A_{He} (triangles). Models with overshooting are shown as filled symbols while models without are represented by empty symbols. Individual stars are associated with a single colour and are linked with a straight line. For each star and in the corresponding colour, we represent the observed effective temperature and its uncertainties as the errorbars.

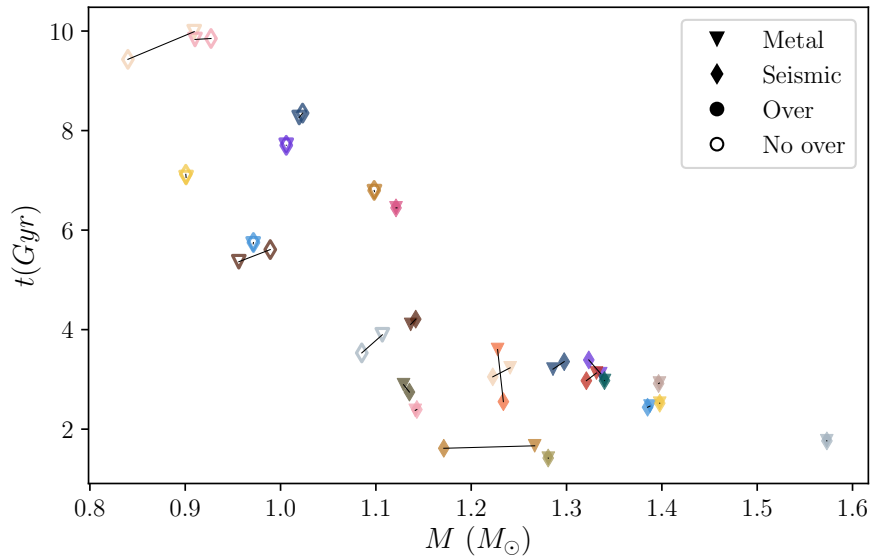


Figure 4.7: Age (in Gyrs) as a function of the mass for the best fit models considering either only seismic constraints (diamonds) or the metallicity constraint instead of A_{He} (triangles). Models with overshooting are shown as filled symbols while models without are represented by empty symbols. Individual stars are associated with a single colour and are linked with a straight line.

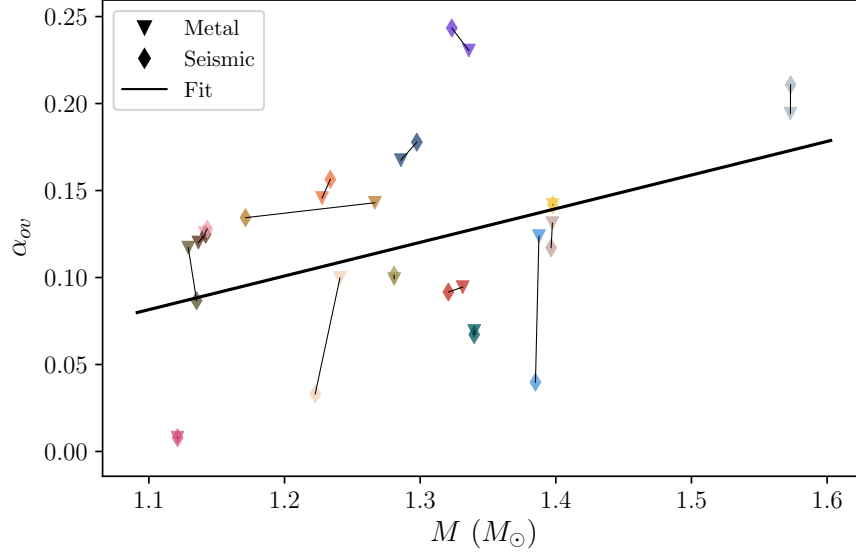


Figure 4.8: Overshooting parameter as a function of the mass for the best fit models considering either only seismic constraints (diamonds) or the metallicity constraint instead of A_{He} (triangles). Models with overshooting are shown as filled symbols while models without are represented by empty symbols. Individual stars are associated with a single colour and are linked with a straight line. A linear fit to the data is also represented by the black line.

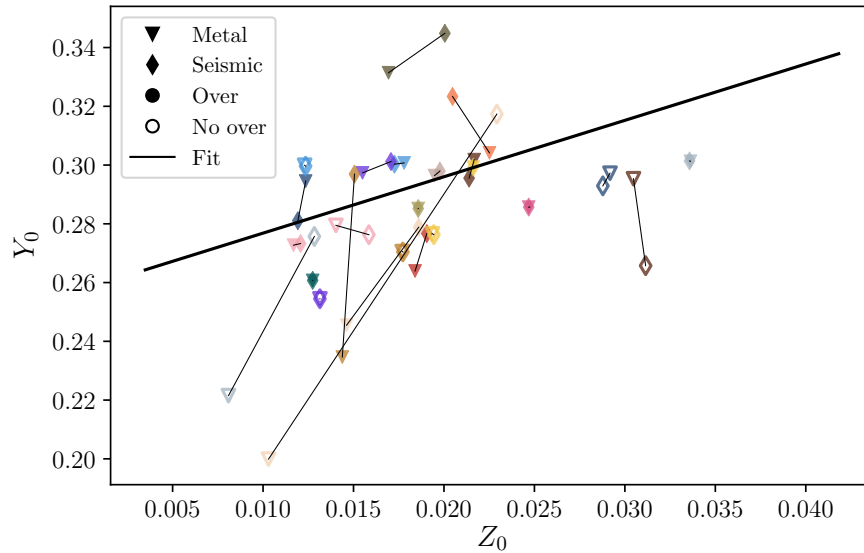


Figure 4.9: Initial helium abundance as a function of $(Z/X)_0$ for the best fit models considering either only seismic constraints (diamonds) or the metallicity constraint instead of A_{He} (triangles). Models with overshooting are shown as filled symbols while models without are represented by empty symbols. Individual stars are associated with a single colour and are linked with a straight line. A linear fit to the data is also represented by the black line.

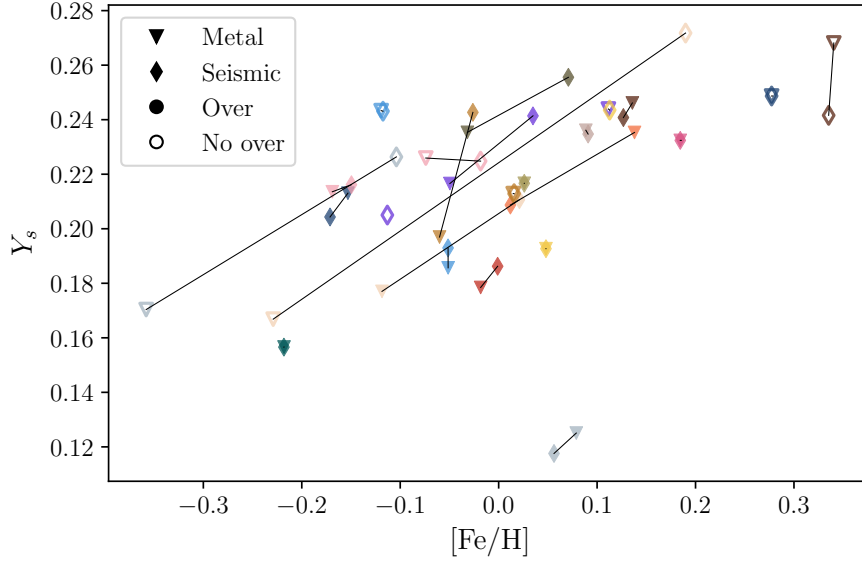


Figure 4.10: Surface helium abundance as a function of the surface (Z/X) ratio for the best fit models considering either only seismic constraints (diamonds) or the metallicity constraint instead of A_{He} (triangles). Models with overshooting are shown as filled symbols while models without are represented by empty symbols. Individual stars are associated with a single colour and are linked with a straight line.

4.3.4 Conclusions of the analysis

While the grid we used to model the Kepler LEGACY sample might be too coarse to properly infer central overshooting in most of the stars, we managed to retrieve satisfying results for about 20 stars out of the 66 that constitute the sample. This allowed us to show that for stars with masses $\gtrsim 1.1 M_{\odot}$, there might exist a correlation between the amount overshooting and the stellar mass (as shown in [Claret & Torres 2017, 2018](#)). For masses below this threshold, there is no convective core and the overshooting parameter is irrelevant. We also inferred the primordial helium abundance and enrichment ratio of $Y_p = 0.26 \pm 0.01$ and $\Delta Y/\Delta Z = 1.92 \pm 0.79$, respectively. The primordial abundance is larger than most literature values (e.g. [Ribas et al. 2000](#); [Lebreton et al. 2001](#); [Peimbert et al. 2002](#); [Balser 2006](#); [Casagrande et al. 2007](#); [Verma et al. 2019](#)). This could in fact result from our choice of the AGSS09 solar mixture which tend to produce less metallic and more helium abundant models than the reference mixtures used in other studies.

Overall, it would be interesting to extend the present study by improving our grid, in order to obtain acceptable models for a greater number of stars. We could also compute sets of models without overshooting for stars with masses $\gtrsim 1.1 M_{\odot}$ to observe its effect on the final stellar parameters over the complete sample. Finally, selecting a few targets to carry an in-depth characterisation, as we did for the 16Cyg system, will be particularly interesting, to further test the limitations of our technique as well as of the stellar models. This would represent the opportunity to fully exploit the $\Delta_{01}-\hat{r}_{01}$ combination of seismic indicators and to study the impact of the set of input physics on the inferred properties of convective cores.

Thorough characterisation of the 16 Cygni system

I. Forward seismic modelling with WhoSGLAd

M. Farnir¹, M.-A. Dupret¹, G. Buldgen², S. J. A. J. Salmon¹, A. Noels¹, C. Pinçon^{1,3},
C. Pezzotti², and P. Eggenberger²

¹ Institut d'Astrophysique et Géophysique de l'Université de Liège, Allée du 6 août 17, 4000 Liège, Belgium
e-mail: martin.farnir@uliege.be

² Observatoire de Genève, Université de Genève, 51 Ch. Des Maillettes, 1290 Sauverny, Switzerland

³ LESIA, Observatoire de Paris, PSL Research University, CNRS, Université Pierre et Marie Curie, Université Paris Diderot, 92195 Meudon, France

Received 28 May 2020 / Accepted 7 October 2020

ABSTRACT

Context. Being part of the brightest solar-like stars, and close solar analogues, the 16 Cygni system is of great interest to the scientific community and may provide insight into the past and future evolution of our Sun. It has been observed thoroughly by the *Kepler* satellite, which provided us with data of an unprecedented quality.

Aims. This paper is the first of a series aiming to extensively characterise the system. We test several choices of micro- and macro-physics to highlight their effects on optimal stellar parameters and provide realistic stellar parameter ranges.

Methods. We used a recently developed method, WhoSGLAd, that takes the utmost advantage of the whole oscillation spectrum of solar-like stars by simultaneously adjusting the acoustic glitches and the smoothly varying trend. For each choice of input physics, we computed models which account, at best, for a set of seismic indicators that are representative of the stellar structure and are as uncorrelated as possible. The search for optimal models was carried out through a Levenberg-Marquardt minimisation. First, we found individual optimal models for both stars. We then selected the best candidates to fit both stars while imposing a common age and composition.

Results. We computed realistic ranges of stellar parameters for individual stars. We also provide two models of the system regarded as a whole. We were not able to build binary models with the whole set of choices of input physics considered for individual stars as our constraints seem too stringent. We may need to include additional parameters to the optimal model search or invoke non-standard physical processes.

Key words. asteroseismology – stars: oscillations – stars: solar-type – stars: abundances

1. Introduction

In the past decade, the CoRoT (Baglin et al. 2009) and *Kepler* (Borucki et al. 2010) space missions have provided the stellar physics community with a wealth of data of unprecedented quality for solar-like stars. Such data allow stellar scientists, through the use of asteroseismology, to put their models to the test and to provide stringent constraints on the physical processes at hand, therefore highlighting the current shortcomings in the modelling (e.g. mixing processes, angular momentum transport, star-planet interaction). In addition, studying solar-like stars enables us to gather invaluable insight into the past and future of our Sun.

The 16 Cygni system is of great interest as it consists of binary solar twins which have been observed continuously for 928 days. Both stars are therefore among the solar-like pulsators with the best data available for seismic studies. Moreover, a great amount of information has yet to be accounted for. For example, differences in superficial lithium abundances remain unexplained (Friel et al. 1993 and King et al. 1997) observed that the B component is at least four times more Li depleted than its twin). The presence of a jovian companion to 16 Cygni B (Cochran et al. 1997) has been argued by Deal et al. (2015) to be the possible cause. This specific example illustrates that the system is an ideal test-bench to constrain stellar models as well as

to test non-standard physical processes while taking advantage of asteroseismic techniques.

Solar-like oscillations, as both stars display, are stochastically excited by the outer convective layer. Such oscillation spectra may present the following two main features: a regular pattern, referred to as the smooth part of the spectrum, and an oscillating pattern of low amplitude, the glitch. An acoustic glitch is the oscillating signal observed in frequencies, which is caused by a sharp variation – compared to the wavelength of the oscillating mode – variation in the stellar structure. The first mention of the possible use of such signatures was by Vorontsov (1988) and Gough (1990) who theoretically demonstrated the effect of a sharp feature in the stellar structure on oscillation frequencies, either directly or in the second frequency differences. For example, in solar-like stars, we have the helium glitch, caused by a depression in the first adiabatic index¹ in the second helium ionisation zone, and the convection zone glitch, due to the variation of the temperature gradient at the base of the convective envelope zone. They may constrain the surface helium content, inaccessible by other means for solar-like stars, (e.g. Basu et al. 2004; Verma et al. 2014) and the total extent of the envelope convective

¹ We recall the definition of the first adiabatic index: $\Gamma_1 = \frac{d \ln P}{d \ln \rho} \Big|_S$, where ρ is the density, P is the pressure, and S is the entropy.

zone, as well as the mixing processes at hand that might explain such an extent (e.g. Monteiro et al. 2000).

In a previous paper, Farnir et al. (2019) described a new method to provide a robust analysis of the solar-like oscillation frequencies simultaneously accounting for the smooth and glitch parts, the WhoSGIAd (Whole Spectrum and Glitches Adjustment) method. This method relies on the *Gram-Schmidt* orthonormalisation process to define seismic indicators as uncorrelated as possible. It shows a great potential to provide precise, accurate and statistically relevant constraints on stellar physics. Compared to other seismic methods accounting for the glitches signature, the WhoSGIAd method has the advantage of decorrelating the information contained in both components of the oscillation spectrum (smooth and glitch parts) while accounting for them simultaneously. This leads to constraints which are, in turn, the least correlated possible and more stringent. Moreover, the measured frequencies are not fitted individually as it introduces large correlations. Rather, we use seismic indicators defined to be representative of the stellar structure and as little correlated as possible. This enables us to compute optimal models as accurate as possible.

This paper is part of a series of publications dedicated at providing the most accurate and complete picture of the 16Cyg binary system. In this first study, our goal is to establish a large sample of reliable structural models analysing the degeneracies stemming from variations in the micro- and macro-physical prescriptions using our new consistent seismic modelling technique, WhoSGIAd. We model the system using asteroseismic, spectroscopic and interferometric constraints considering both 16CygA (KIC12069424) and 16CygB (KIC12069449) independently and as a joint system. We provide a suitable set of models for structural inversions to be studied in a second paper. Our thorough analysis also paves the way for an in-depth description of potential traces of non-standard processes acting (or having acted) during the history of the system. These include the effects of angular momentum transport processes (Eggenberger et al. 2010, 2019) as well as the effects of planetary formation and accretion on the lithium abundances of both stars (Deal et al. 2015; Thévenin et al. 2017).

The paper is structured as follows. First, we present in Sect. 2 the general methodology and recall the basics of the WhoSGIAd method. We then model the system. This is done in two steps. To take advantage of the great precision of the data for each star, we first provide, in Sect. 3, separate adjustments while testing different choices of micro- and macro-physics. This allows to provide robust stellar parameter ranges accounting for the modelling uncertainties as well as to show discrepancies in the modelling for some cases. We select in Sect. 4 the models having consistent ages and initial compositions as initial guesses to compute models imposing a common age and initial composition, as those stars should have formed from a single molecular cloud. Even though no specific interaction between both stars is taken into account during their evolution, we refer to those models as binary models. We discuss the results in Sect. 5. Finally, we conclude our paper in Sect. 6.

2. Methodology

In the current section, we describe the optimisation scheme and the seismic and non-seismic constraints used. We then present the basic principle of the WhoSGIAd method. Finally, we describe the physics included in the models as well as the considered variations.

Table 1. Set of non-seismic data used throughout this paper.

Quantity	16CygA	16CygB	Refs.
$R(R_\odot)$	1.22 ± 0.02	1.12 ± 0.02	a
$T_{\text{eff}}(\text{K})$	5839 ± 42	5809 ± 39	a
$L(L_\odot)$	1.56 ± 0.05	1.27 ± 0.04	b
[Fe/H] (dex)	0.096 ± 0.026	0.052 ± 0.021	c
Y_f	[0.23, 0.25]	[0.218, 0.260]	d

References. a: White et al. (2013), b: Metcalfe et al. (2012), c: Ramírez et al. (2009), d: Verma et al. (2014).

2.1. Best-fit model search

The search for best-fit models is undertaken by a *Levenberg-Marquardt* (L-M) algorithm. In doing so, we compare observed values of a set of constraints with model values, computed on the fly, through a χ^2 function, to be minimised, defined as:

$$\chi^2 = \sum_{i=1}^N \frac{(C_{\text{obs},i} - C_{\text{mod},i})^2}{\sigma_i^2}, \quad (1)$$

where C represents the N constraints, the obs (resp. mod) subscript the observed (resp. model) values and σ their associated standard deviations.

Except when mentioned otherwise, the set of constraints consists of the Δ , \hat{r}_{01} , \hat{r}_{02} , and A_{He} seismic indicators (Farnir et al. 2019) presented in Sect. 2.2 and the free parameters adopted in the modelling procedure are the mass (M), age (t), initial hydrogen abundance (X_0) and, metallicity (Z/X_0) of the considered star. Other non-seismic data, such as the effective temperature (T_{eff}), interferometric radius (R), or the metallicity ([Fe/H]), are used to discriminate between the several choices of input physics. In some cases, and when so stated, non-seismic data may be used as constraints to the model search while relaxing the mixing length parameter or including turbulent diffusive mixing with a free coefficient (see Sect. 2.3 for a description of the physics included in the models). Those data are gathered in Table 1. Finally, we do not use as a constraint the luminosity (L) from Metcalfe et al. (2012) as it results from asteroseismic modelling and would not be independent of our study. Instead, we compute it from the observed interferometric radius (White et al. 2013) and the definition of the effective temperature: $sT_{\text{eff}}^4 = \frac{L}{4\pi R^2}$, where s is the Stefan-Boltzmann constant.

2.2. WhoSGIAd principle and seismic indicators

We recall here the set of WhoSGIAd seismic indicators used in the fitting procedure as well as the basics of the method. For a more detailed description, see Farnir et al. (2019).

Principle. The WhoSGIAd method relies on *Gram-Schmidt's* orthogonalisation. To represent the observed frequencies, we define a Euclidean vector space of functions of the spherical degree, l , and radial order, n (only $m = 0$ modes are considered). The N observed frequencies at a given value of l are regarded as unknown vector functions of n and l which we write $\mathbf{v}_l = (v_{l,n_1}, \dots, v_{l,n_N})$. Two notable functions are the identity, $\mathbf{1}$, and linear function of the radial order, $\mathbf{n}_l = (n_{l,1}, \dots, n_{l,N})$.

Given two vector quantities, say the observed and theoretical vectors of frequencies, \mathbf{v}_{obs} and \mathbf{v}_l , we may define their scalar product as:

$$\langle \mathbf{v}_{\text{obs}} | \mathbf{v}_l \rangle = \sum_{i=1}^N \frac{v_{\text{obs},n_i} v_{l,n_i}}{\sigma_i^2}, \quad (2)$$

with σ_i the uncertainties associated with each component. From this scalar product is defined the norm of a vector \mathbf{v}_{obs} :

$$\|\mathbf{v}_{\text{obs}}\| = \sqrt{\langle \mathbf{v}_{\text{obs}} | \mathbf{v}_{\text{obs}} \rangle}. \quad (3)$$

We may also define the weighted mean of a quantity, according to our scalar product and normalisation, as:

$$\overline{\mathbf{v}_{\text{obs}}} = \frac{\langle \mathbf{v}_{\text{obs}} | \mathbf{1} \rangle}{\|\mathbf{1}\|^2} = \frac{\sum_{i=1}^N \mathbf{v}_{\text{obs},i} / \sigma_i^2}{\sum_{i=1}^N 1 / \sigma_i^2}. \quad (4)$$

The functions used to describe the frequencies are separated into two contributions: a smooth part, represented by second-order polynomials of n , and a glitch part, represented by oscillating functions of the frequency. The form of those functions is given in Appendix A. Using *Gram-Schmidt's* orthogonalisation process, we build a basis of functions over that vector space. To provide an adjustment of the observed frequencies, those are projected over the basis elements. This provides completely independent coefficients which are combined into seismic indicators as little correlated as possible. One of the main advantages of this approach is that the glitch part of the adjustment is completely independent of the smooth part, even though both adjustments are carried out simultaneously. We define the seismic indicators as follows:

The large separation for modes of degree l . Corresponds to the value of the slope of the frequencies decorrelated from the contribution of the acoustic glitches and expressed as a linear function of the radial order n for each spherical degree l :

$$\Delta_l = \frac{\langle \mathbf{v}_l | \mathbf{n}_l \rangle / \|\mathbf{1}\|^2 - \overline{\mathbf{n}_l} \overline{\mathbf{v}_l}}{\|\mathbf{n}_l\|^2 / \|\mathbf{1}\|^2 - \overline{\mathbf{n}_l}^2}. \quad (5)$$

This is equivalent to its standard definition obtained through a linear regression (see e.g. Reese et al. 2012).

The large separation. Corresponds to the weighted mean value, $\overline{\Delta_l}$, of the individual large separations for each spherical degree l

$$\Delta = \overline{\Delta_l} = \frac{\sum_l \Delta_l / \sigma^2(\Delta_l)}{\sum_l 1 / \sigma^2(\Delta_l)}, \quad (6)$$

with $\sigma(\Delta_l)$ the uncertainty on the large separation of degree l .

The normalised small separations between degrees 0 and l .

$$\hat{r}_{0l} = \frac{\overline{\mathbf{v}_0} - \overline{\mathbf{v}_l}}{\Delta_0} + \overline{\mathbf{n}_l} - \overline{\mathbf{n}_0} + \frac{l}{2}. \quad (7)$$

Those indicators are analogous to the mean value of the local small separation ratios defined by Roxburgh & Vorontsov (2003) but are again completely independent from the contribution of acoustic glitches.

The helium glitch amplitude.

$$A_{\text{He}} = \|\delta \mathbf{v}_{\text{He}}\|, \quad (8)$$

where $\delta \mathbf{v}_{\text{He}}$ is the helium glitch component.

Beside those indicators, we may define complementary seismic indicators which are presented in Appendix B. Those were not part of the constraints.

Table 2. Observed seismic indicators.

Indicator	16CygA	16CygB
$\Delta(\mu\text{Hz})$	104.024 ± 0.005	117.911 ± 0.004
A_{He}	30 ± 1	36 ± 1
\hat{r}_{01}	$(3.62 \pm 0.02) \cdot 10^{-2}$	$(2.52 \pm 0.02) \cdot 10^{-2}$
\hat{r}_{02}	$(5.75 \pm 0.03) \cdot 10^{-2}$	$(5.53 \pm 0.03) \cdot 10^{-2}$

Notes. The standard deviations result from the propagation of the uncertainties on the observed frequencies.

Table 2 gathers the values of the considered seismic indicators computed using the modes defined over the full length of the *Kepler* mission determined by Davies et al. (2015). We take out from those modes the ones with uncertainties above $1.5 \mu\text{Hz}$. This mostly corresponds to high frequency modes. A brief discussion of this choice is given in Appendix C. We have corrected the frequencies for the surface effects by using the power law prescribed by Kjeldsen et al. (2008) and the a and b coefficients fitted by Sonoi et al. (2015) as a function of T_{eff} and g . The authors have undertaken this coefficient adjustment by comparing the adiabatic frequencies of patched models based on 3D simulations and that of unpatched standard 1D models.

2.3. Models

Unless specified otherwise all the models are computed using the CLES stellar evolution code (Scuflaire et al. 2008b) with the AGSS09 solar chemical mixture (Asplund et al. 2009), the OPAL opacity table (Iglesias & Rogers 1996) combined with that of Ferguson et al. (2005) at low temperatures, the FreeEOS software to generate the equation of state table (Cassisi et al. 2003), and the nuclear reactions rates prescribed by Adelberger et al. (2011). We also use the mixing length theory (Cox & Giuli 1968), with the solar calibrated value of $\alpha_{\text{MLT}} = l/H_p = 1.82$ (where l is the mixing length and H_p the pressure scale height), to parametrise the mixing inside convective regions. This value is the result of a solar calibration that we carried out using the same set of input physics as described in the present section. The microscopic diffusion of elements is included and treated as in Thoul et al. (1994). The models do not include rotation and, therefore, rotation-induced mixing. Unless specified otherwise, models do not include overshooting at the boundary of convective layers. The temperature conditions above the photosphere are determined using an Eddington $T(\tau)$ relation, τ being the optical depth. We choose such a relation to remain consistent with Sonoi et al. (2015) whose fitted coefficients are used to correct surface effects on the observed frequencies. From now on, to distinguish from the several physical variations, we refer to the models with this specific set of input physics as the reference models. Finally, we compute theoretical adiabatic oscillation frequencies for each model via the LOSC oscillation code (Scuflaire et al. 2008a).

2.4. Variations in the input physics

As mentioned earlier, to provide the most reliable set of stellar parameter ranges while accounting for the choice of micro- and macro-physics, we test choices by changing one ingredient at the time from the reference models. Those variations are:

- The GN93 solar reference mixture (Grevesse & Noels 1993), in light blue in the figures (see Sect. 3.1.2);

- The opacities from the opacity project (Badnell et al. 2005), denoted OP in light brown, the Los Alamos opacities (Colgan et al. 2016), written OPLIB in beige (see Sect. 3.1.2);
- The CEFF equation of state (Christensen-Dalsgaard & Daeppen 1992), in dark brown, and the revised OPAL equation of state (Rogers & Nayfonov 2002), written OPAL05 in grey (see Sect. 3.1.2);
- A different choice of mixing length coefficient ($\alpha_{\text{MLT}} = 1.7$), in yellow (see Sects. 3.1.2 and 3.2);
- The inclusion (or not) of microscopic diffusion, in light pink (see Sect. 3.1.3);
- The inclusion of turbulent mixing of chemical elements following the relation for the turbulent mixing coefficient $\text{DDT} = D_{\text{turb}} \left(\frac{\rho}{\rho_0} \right)^n + D_{\text{ct}}$ (in $\text{cm}^2 \text{s}^{-1}$), where ρ is the density, ρ_0 the density at the bottom of the convective envelope and D_{turb} , n and D_{ct} are fixed at 7500, -3 and 0 respectively (Proffitt & Michaud 1991), shown in purple (see Sects. 3.1.3 and 3.2);
- The inclusion of overshooting extending outside convective regions over a distance $d = \alpha_{\text{ov}} \min(H_p, h)$ where α_{ov} is the overshooting parameter, H_p the local pressure scale height and h the thickness of the convective region. The temperature gradient in the overshooting region is set to the radiative one and the mixing is instantaneous. We either include overshooting above the convective core, denoted α_{ov} and shown in red, or below the convective envelope, written α_{un} in khaki and referred to as “undershoot”. Both values are set to 0.1 (see Sect. 3.1.4);
- The effect of a different choice of temperature profile above the stellar photosphere, in orange. We use the model temperature profile of the quiet sun by Vernazza et al. (1981) for which an analytical formulation may be found in Paxton et al. (2013) (see Sect. 3.1.5);
- The impact of the surface effects, computing a model fitting seismic indicators defined with stellar frequencies which are not corrected for surface effects in dark green. Their values are shown in Table D.1. See also Sect. 5.2 and Appendix D.

3. 16 Cygni A and B seen as separate stars

In the present section, we look for individual models of each star representative of the observed data and accounting at best for the modelling uncertainties. The stellar parameters for every best model estimates are displayed in Appendix E. To find individual models, we test several choices of input physics without any specific hypothesis about the binarity of the stars. This allows to take advantage of the unprecedented quality of the data. The first part of this study is subdivided in two steps. We start by only considering seismic constraints. Then, we add non-seismic constraints, in Sect. 3.2, to further improve the models. The advantage of first computing individual models for each star is that it allows to have the same amount of constraints as free parameters and to obtain an exact solution, from a statistical point of view, to the minimisation process.

3.1. Fitting seismic constraints only

In the present section, we present the results of the modelling considering only seismic indicators. This allows to show the impact of the seismic indicators alone on optimal results as well as the possible limitations of such an exclusive approach. Furthermore, we test several choices of micro- and macro-physics.

This enables us to highlight their influence on the set of optimal parameters we retrieve. The models are computed as described in Sect. 2.3 while changing only one physical ingredient at a time.

The individual models for both components are shown in Figs. 1 and 2 (see Table E.3 for individual parameter values.) We show, in the upper panel of the figures the age versus the mass of the optimal model for each variation in the input physics along with the associated uncertainties. The middle panel displays the position of those models in a Hertzsprung-Russell (HR) diagram. We also represent, as a black box, the observed effective temperature and luminosity computed from the interferometric radius (White et al. 2013). Finally, the lower panels represent the initial hydrogen versus initial metallicity and their uncertainties for each model.

In both figures, the reference model is represented in dark blue and denoted AGSS09. For 16 Cyg A, it actually corresponds to the model presented in Sect. 5 of Farnir et al. (2019). Their Fig. 14 illustrates that the use of the WhoSGLAd seismic indicators as constraints allows to provide a proper agreement between observed and model frequencies.

3.1.1. Influence of seismic constraints on stellar parameters

Farnir et al. (2019) showed that the WhoSGLAd helium glitch amplitude is a good proxy of the surface helium abundance. This means that, when requiring our models to reproduce the observed helium glitch amplitude, we require a specific helium abundance. To illustrate this statement, we plot in Figs. 3 and 4 the surface helium content as a function of the surface metallicity of each model. We also represent, as a black box, the spectroscopic metallicity from Ramírez et al. (2009) and the asteroseismic Y_s range computed by Verma et al. (2014), taking advantage of the information contained in the helium glitch, along with their associated uncertainties. We indeed observe that the surface helium abundance is well constrained and, in most cases, in agreement with the study of Verma et al. (2014). They computed ranges of $[0.231, 0.251]$ and $[0.218, 0.266]$ for the A and B components respectively, which encapsulate most of our values. However, we also note a small scatter in the values. Again, Farnir et al. (2019) showed that the helium glitch amplitude is both correlated to the surface helium and metal abundances, with the helium abundance being the dominant factor. They indeed observe that, at constant surface helium abundance, a lower surface metal abundance or, at constant surface metal abundance, a higher surface helium abundance may both lead to a greater glitch amplitude. This is in fact due to a shift in the position of the adiabat in the second helium ionisation zone, where the first adiabatic index, $\Gamma_1 = \frac{d \ln P}{d \ln \rho}|_s$, presents a large depression. This allows us to account for the small scatter observed. A direct consequence of the helium glitch amplitude constraint is the anti-correlation between the initial metallicity and helium abundance that we observe in the lower panels of Figs. 1 and 2.

Moreover, we point out that most models do not account for the spectroscopic metallicity constraint. This is clearly visible in Figs. 3 and 4. This does not come as a surprise as the presented models do not yet include the metallicity constraint in the fitting procedure. This also shows that the information contained in the helium glitch amplitude and the surface metallicity are complementary and it comes as a necessity to take advantage of both to provide the most accurate model possible.

Now looking at the middle panels of Figs. 1 and 2, the first striking feature is the fact that most models lie on a straight line. Such line corresponds to the locus of models of constant radius.

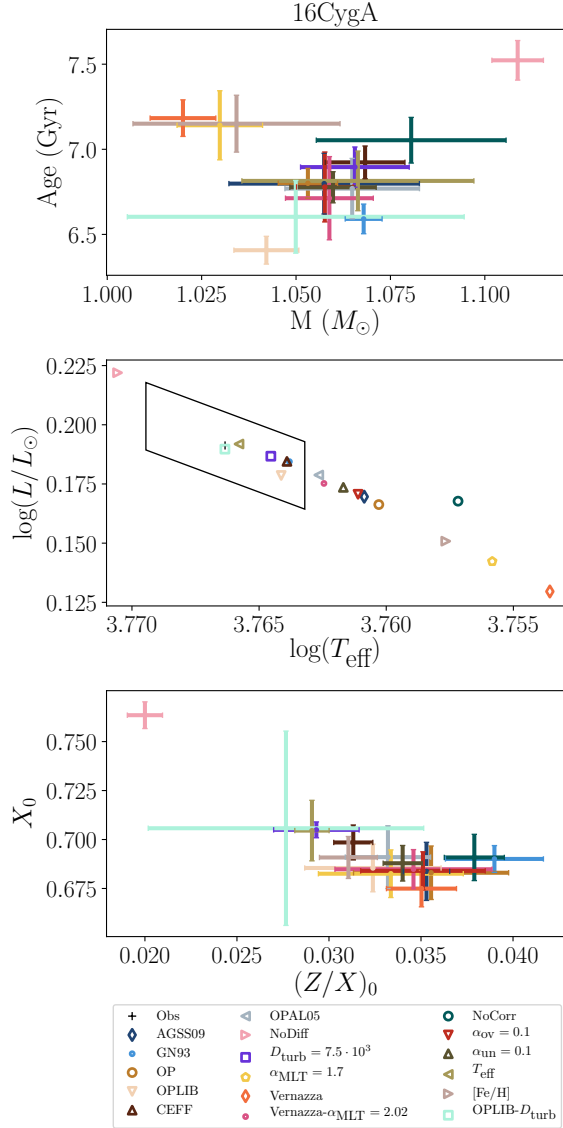


Fig. 1. Summary of 16 Cyg A best-fit models represented in a Mass – Age diagram (*top panel*), HR diagram (*middle panel*) and initial hydrogen abundance versus metal composition diagram (*bottom panel*). The luminosity and effective temperature constraints from White et al. (2013) are represented in the HR diagram as a black box.

This almost constance of the radii stems from the Δ indicator which provides a constraint on the mean stellar density (Farnir et al. 2019; Ulrich 1986). Thus, the models of constant mean density have almost constant stellar radii, as long as the mass remains close to constant. Actually, this is what we observe as the mean radius values of our models are $1.22 R_{\odot}$ and $1.11 R_{\odot}$ for 16CygA and B respectively (Typical uncertainties are of $0.02 R_{\odot}$ and $0.01 R_{\odot}$ respectively. Individual values are shown in Table E.3). This is in good agreement with the values in Table 1. We note that some models do not lie on the straight line with the other models. Such models are those with masses values that differ significantly from the mean value of other models. Finally, we observe that many models do not fall in the effective

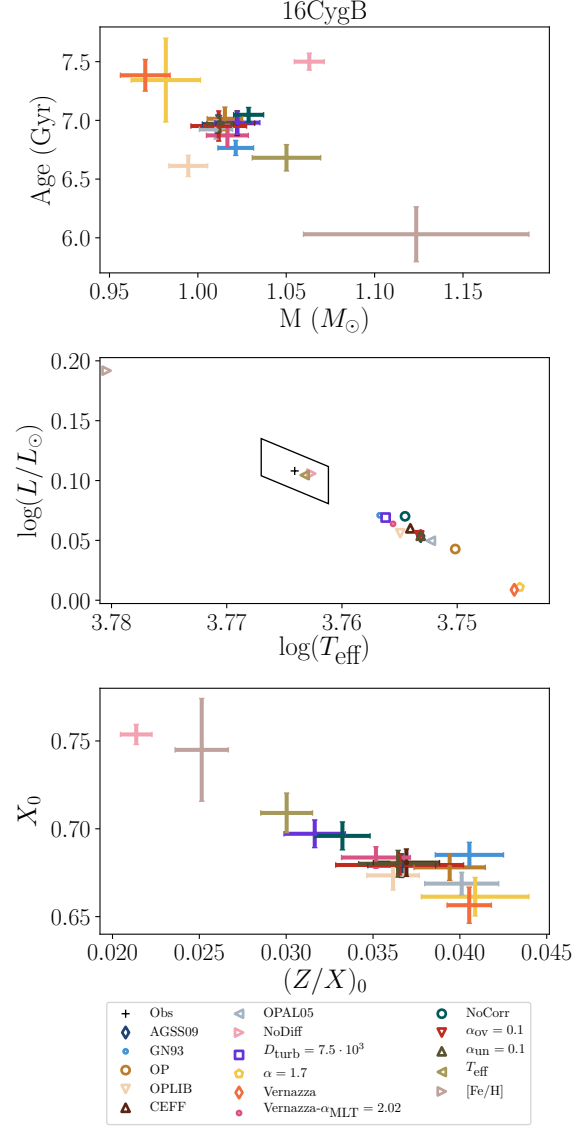


Fig. 2. Summary of 16 Cyg B best-fit models. The colours are the same as in Fig. 1.

temperature and luminosity observational boxes. This comes from the fact that those constraints are not yet part of the modelling procedure and shows that their inclusion is necessary to provide the most accurate picture of the system.

3.1.2. Effect of the metallicity reference, opacity table, and equation of state

As is clearly visible in Figs. 1 and 2 using either the GN93 solar reference mixture or a greater value of the mixing length parameter produces models for both stellar components which are more luminous and have a greater effective temperature than the reference models. Furthermore, looking at Figs. 3 and 4, we observe that the GN93 solar reference tends to produce more metallic models, directly stemming from the fact that this solar reference is indeed more metallic than the AGSS09 one. However, in terms

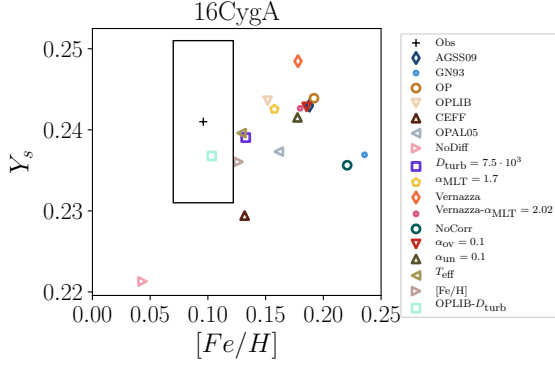


Fig. 3. Surface helium abundance versus metallicity for 16 Cygni A. The black box represents the spectroscopic metallicity value computed by Ramírez et al. (2009) and the surface helium value from Verma et al. (2014) along with the corresponding uncertainties.

of metallicity, the mixing length parameter has opposite impacts on the two stellar components. A decrease of its value leads, in the case of 16 Cyg A, to models which become less metallic, while it produces more metallic models for 16 Cyg B.

Now looking at the influence of the opacity tables, we note that the OPLIB table leads to a model for 16 Cyg A which has a greater effective temperature while the effect is barely visible for 16 Cyg B. Conversely, the OP opacity table leads to models which are cooler for both stars but the effect is not as pronounced. The effect of the opacity tables is not clear on the surface composition as both models react in different ways.

Finally, the use of a different equation of state table also produces differential effects on both stars. On the first hand, in the case of 16 Cygni A, using either the CEFF or OPAL05 tables lead to hotter, more luminous stars and with decreased surface helium and metal abundances. On the other hand, for 16 Cygni B, both tables have very little influence on the position of the star in the HR diagram (see Fig. 2). However, the use of the OPAL05 table leads to a model of the B component which is both richer in helium and metals at its surface. The impact of the CEFF equation of state is barely visible.

3.1.3. Impact of diffusion

We note that the models we compute without diffusion of chemical elements are both older, heavier and richer in hydrogen than the reference, as represented in light pink in Figs. 1 and 2. As showed by Farnir et al. (2019), at a specific composition, more massive models present a stronger helium glitch signature. Therefore, to reproduce the observed signature of both stars, the models need to be poorer in helium as more massive models are favoured. This is even reinforced by the fact that no diffusion is included and the initial helium abundance has to match that of the surface. Moreover, the difference in surface helium abundance between models with and without diffusion is systematically of about 0.02 as was noted by Verma et al. (2019). This confirms their observation of the importance of diffusion in low mass stars of solar metallicity.

We observe that non-seismic data, that will be considered in Sect. 3.2, are not accounted for in most cases. We note that one way to account for them is to reduce the impact of microscopic diffusion, either partially for 16 Cygni A – by involving additional mixing processes as turbulent mixing – or completely for 16 Cygni B. This contradicts the conclusions of Buldgen et al.

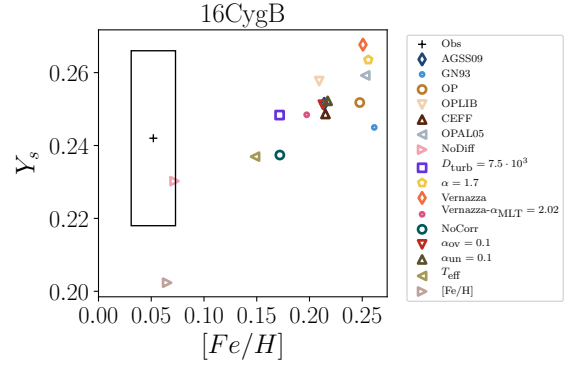


Fig. 4. Surface helium abundance versus metallicity for 16 Cygni B. The black box represents the spectroscopic metallicity value computed by Ramírez et al. (2009) and the surface helium value from Verma et al. (2014) along with the corresponding uncertainties.

(2016a) who determined that models with increased diffusion efficiency (with diffusion velocities higher of about 10%) could help reproduce inversion results for the A star. However, this agrees with their second study (Buldgen et al. 2016b) where they noted that reducing the efficiency of diffusion allowed the computation of models consistent with the inversion results. This, however, lead their study to inconsistencies in surface composition between the two stars.

We also show the impact of the inclusion of turbulent mixing on the modelling by computing models with a turbulent mixing coefficient fixed at a value of $D_{\text{turb}} = 7500 \text{ cm}^2 \text{ s}^{-1}$. We note that those models tend, for both stars, to be more luminous, hotter and less metallic. The overall agreement with non-seismic data is thus improved. We show in Sect. 3.2.1 the influence of the value of the turbulent mixing coefficient on the optimal results.

3.1.4. Extension of convective layers

To analyse the effect of the extension of the convective core – during pre-main sequence – on the stellar evolution, we include instantaneous overshooting in some of our models. Those are displayed in red in the figures. We note that the effect on the optimal models is not obvious. Indeed, such models are almost indistinguishable from the reference ones and lie within one another uncertainties. The same goes for the surface compositions retrieved. Including a greater value of the overshooting parameter ($\alpha_{\text{ov}} = 0.2$ instead of 0.1) leads to great differences in the behaviours of both stars. Indeed, while the model for 16 Cyg B remains rather similar to that with a lower value of overshooting, thus similar to the one without overshooting, the model for the A component becomes significantly less massive, older, metal poor and with a smaller radius (see Table E.3). The reason for such a difference is that only the A component, because of its slightly greater mass and smaller metallicity, is able to maintain a convective core during the main sequence with such an overshooting parameter value. Therefore, its structure becomes significantly different from that of a model without overshooting which has a radiative core during the main sequence. However, this model maintaining a convective core on the main sequence seems to be a curiosity of the minimisation method. The retro-action of the presence of the convective core ultimately leads to a significant decrease of the optimal mass as well as the metallicity, becoming significantly sub-solar

($[\text{Fe}/\text{H}] = -0.39 \pm 0.01$). This further indicates the necessity to use non-seismic constraints to obtain proper models. We can therefore safely discard this model. Additionally, we may note that the significantly lower mass of the A model leads to a significantly smaller radius because of the Δ constraint, which again contradicts observations. Moreover, this pair of model has now a less massive A component than the B. Although, by a simple argument of scaling relations, we obtain a hint that the A component should be heavier than the B. Indeed, from [Kjeldsen & Bedding \(1995\)](#) we have that $\frac{M_A}{M_B} \simeq \left(\frac{\nu_{\text{max},A}}{\nu_{\text{max},B}}\right)^3 \left(\frac{\Delta\nu_A}{\Delta\nu_B}\right)^{-4} \left(\frac{T_{\text{eff},A}}{T_{\text{eff},B}}\right)^{3/2}$. With $\nu_{\text{max},A} = 2188 \mu\text{Hz}$, $\nu_{\text{max},B} = 2561 \mu\text{Hz}$ taken from [Lund et al. \(2017\)](#), and the values of the effective temperatures and large separations presented earlier, we expect the mass of the A component to be larger than the other ($M_A \simeq 1.04 M_B$). This is what we observe for most of our models.

The inclusion of undershooting below the base of the convective zone has no significant impact on the optimal stellar parameters beside a reduction of the individual uncertainties. Initial compositions and ages for both stars now fall out of each others uncertainties and the models are dismissed as valid candidates to compute binary models in Sect. 4. This statement is clearly illustrated in Fig. 7 where the initial hydrogen, metal abundances and ages of both stars are plotted against one another. The straight line displays the locus of identical parameters for both stars. In the upper panel, the khaki cross, representing the model with undershooting, does not meet the line any more.

3.1.5. Effects of the atmosphere and mixing length coefficient

We show the influence of the atmosphere on the optimal stellar parameters by using a temperature profile above the photosphere as in [Vernazza et al. \(1981\)](#) with a specifically calibrated value of $\alpha_{\text{MLT}} = 2.02$ (dark pink small circle in the figures). We observe that the optimal model is very similar to the reference model. Indeed, both pairs of models lie within the uncertainties of one another. The optimal parameters are given in Table E.4. However, the models become hotter and more luminous. They are thus closer to the observed luminosities and effective temperatures. This indicates that it allows to provide better models in terms of spectroscopic constraints while preserving rather similar stellar parameters compared to the case using the Eddington relation. We must also point out that the use of a different temperature profile leads to significant changes from the reference models but the calibration of the mixing length parameter compensates for it. To illustrate this, we compute models with the temperature profile of [Vernazza et al. \(1981\)](#) while using the reference value of $\alpha_{\text{MLT}} = 1.82$ calibrated for an Eddington $T - \tau$ relation. We observe that our models, shown in orange in the figures, are very similar to models using a lower value of the mixing length parameter, displayed in yellow. This is especially true for 16 Cygni B for which both models lie within respective uncertainties. For both stars, the computed models are older and lighter.

3.2. Fitting non-seismic constraints

To further improve individual models for each star, we may include non-seismic constraints into the minimisation process. We indeed note that, in most cases, they are not accounted for. Therefore, we use those constraints and include additional free parameters to add degrees of freedom. The considered constraints are the effective temperature ([White et al. 2013](#)) and the spectroscopic metallicity ([Ramírez et al. 2009](#)). The additional

free parameters are the mixing length parameter α_{MLT} and the turbulent mixing coefficient D_{turb} . In what follows, we specify in every case which of those constraints and free parameters are used.

3.2.1. Accounting for the effective temperature

From Figs. 1 and 2, we expect that it is possible to improve the agreement with the observed effective temperature by increasing the value of α_{MLT} . As a consequence of the Δ constraint, which we showed in Sect. 3.1.1 to be a proper constraint on the radius, we also expect to produce better model luminosities.

To demonstrate that a variation in the mixing length parameter is indeed responsible for the improvement of the model effective temperature, we compute several models with different mixing length parameters. We only include seismic constraints in the fitting procedure to show the influence of α_{MLT} alone on optimal parameters. This is shown in Figs. 5 and 6 for 16 Cyg A and B respectively and the stellar parameters are given in Table E.5. The values considered are 1.7 [light blue], the solar value of 1.82 [dark blue], and 2.0 [brown]. Those models are connected with a blue line to improve visibility. We also display models with several choices for the turbulent mixing coefficient: $D_{\text{turb}} = 2000 \text{ cm}^2 \text{ s}^{-1}$ [light pink], $5000 \text{ cm}^2 \text{ s}^{-1}$ [brown], $7500 \text{ cm}^2 \text{ s}^{-1}$ [grey], $10000 \text{ cm}^2 \text{ s}^{-1}$ [dark pink], and no turbulent mixing [dark blue]. These are connected in red and stellar parameters are gathered in Table E.6. We observe that an increase of α_{MLT} leads to a better agreement with the observed effective temperature for both stars. Moreover, we note that the inclusion of turbulent mixing improves the agreement in effective temperature and metallicity for both stars. Even so, both stars exhibit too large values of the metallicity compared to the observed ones. We also note that, for 16 Cyg B, turbulent mixing alone is not sufficient for the observed and model T_{eff} to match. In addition, we observe a clear effect of saturation of the turbulent mixing coefficient, which occurs above a threshold value that is already exceeded by the considered values. The results are almost indistinguishable no matter which value is chosen. Therefore, the turbulent mixing and mixing length coefficient both have a impact on the model effective temperature (and thus luminosity) but using the turbulent mixing coefficient as a free parameter would be meaningless. Furthermore, we also display in both figures models which did not include microscopic diffusion of the chemical elements. We observe that those two models differ greatly from the models including turbulent diffusion, both being highly hotter and less metallic. The model for 16 Cygni B even properly reproduces the observed metallicity and effective temperature, although they are not yet part of the constraints.

Finally, we compute two models for each star with a free mixing length coefficient and including T_{eff} as a constraint, with and without turbulent mixing ($D_{\text{turb}} = 7500 \text{ cm}^2 \text{ s}^{-1}$). The set of input physics is that of the reference model. Both are displayed in Figs. 5 and 6 as orange diamonds labelled “ $T_{\text{eff}} - D_{\text{turb}}$ ” and as yellow pentagons labelled “ T_{eff} ”. For the A component, we see that including turbulent mixing improves the results. However the agreement with the non-seismic constraints is not improved compared to the model including only turbulent mixing and the opacity table OPLIB with only seismic constraints, that already accounted for the effective temperature, as displayed on Fig. 1. Conversely, for the B component, the improvement is significant and the effective temperature is now well adjusted. Nevertheless, the inclusion of turbulent mixing does not have a significant impact on the resulting agreement with the non-seismic data. Furthermore, in both cases, the metallicity is still

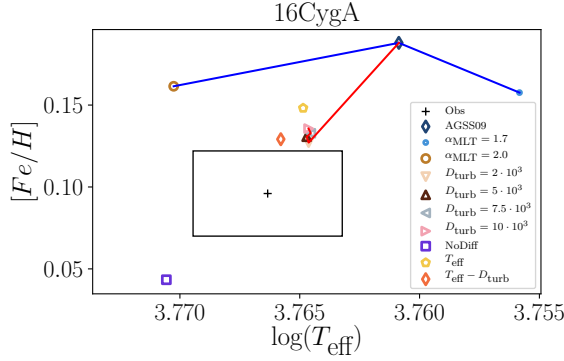


Fig. 5. Variation of the optimal metallicity and effective temperature for 16 Cyg A with the mixing length parameter and turbulent mixing. Models of different α_{MLT} values are connected in blue while models with various turbulent mixing are connected by a red line.

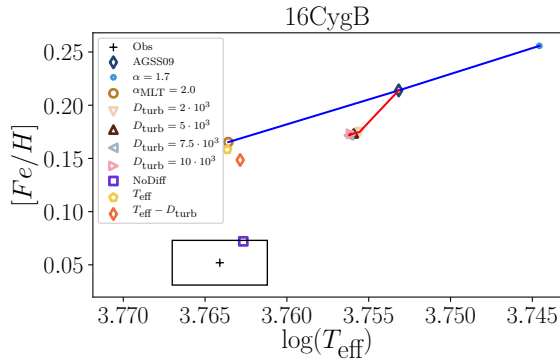


Fig. 6. Variation of the optimal metallicity and effective temperature for 16 Cyg B with the mixing length parameter and turbulent mixing. Models of different α_{MLT} values are connected in blue while models with various turbulent mixing are connected by a red line.

Table 3. Adjusted stellar parameters including the T_{eff} with the reference set of input physics.

Quantity	16CygA	16CygB
$M(M_{\odot})$	1.1 ± 0.1	1.05 ± 0.02
X_0	0.69 ± 0.04	0.70 ± 0.01
$(Z/X)_0$	0.032 ± 0.002	0.032 ± 0.002
Y_0	0.28 ± 0.04	0.027 ± 0.01
$[\text{Fe}/\text{H}]$	0.15 ± 0.05	0.16 ± 0.03
Y_s	0.23 ± 0.02	0.233 ± 0.007
$t(\text{Gyr})$	6.7 ± 0.4	6.6 ± 0.1
$R(R_{\odot})$	1.2 ± 0.1	1.12 ± 0.02
α_{MLT}	1.9 ± 0.2	1.99 ± 0.06
χ^2	1.1	0.2

not properly accounted for. The corresponding set of stellar parameters is presented in Tables 3 and 4.

Analysing our results, we first notice from Table 3 that the calibrated mixing length parameters are very different. Indeed, looking at Fig. 2 from Magic et al. (2015), who used the same solar reference mixture as we do, we would expect that both adjusted values would remain rather close to the solar calibrated value (1.82 in our case) while being smaller as both stars have

Table 4. Adjusted stellar parameters including the T_{eff} constraint and turbulent mixing with a coefficient of $D_{\text{turb}} = 7500 \text{ cm}^2 \text{ s}^{-1}$.

Quantity	16CygA	16CygB
$M(M_{\odot})$	1.07 ± 0.03	1.05 ± 0.02
X_0	0.70 ± 0.01	0.71 ± 0.01
$(Z/X)_0$	0.0291 ± 0.0009	0.0298 ± 0.0008
Y_0	0.27 ± 0.02	0.027 ± 0.01
$[\text{Fe}/\text{H}]$	0.13 ± 0.02	0.15 ± 0.01
Y_s	0.24 ± 0.01	0.238 ± 0.009
$t(\text{Gyr})$	6.8 ± 0.2	6.7 ± 0.1
$R(R_{\odot})$	1.22 ± 0.03	1.12 ± 0.03
α_{MLT}	1.84 ± 0.08	1.94 ± 0.07
χ^2	0.6	0.7

higher effective temperatures and smaller surface gravities than the Sun. Thus, both differences should translate into a lower mixing length parameter. However, we observe that for 16 Cygni A, and within the error bars, α_{MLT} remains solar while the calibrated value for 16 Cygni B is significantly higher than the solar value. We may need to invoke a special physical process acting on any of the components while being inefficient for the second to produce such a differential effect. Some of the possible scenarios are discussed in Sect. 5.3.

We note that slightly more massive and less metallic models than previously are favoured. Such an effect stems from the fact that more massive models are hotter and thus in better agreement with the observed effective temperature, while keeping the same density, because of the Δ constraint.

Another way to better reproduce the observed position in the HR diagram is to include extra mixing counteracting the diffusion of chemical elements. Indeed, for 16 Cyg B, the model computed without diffusion already accounts for these constraints. Which is striking as those were not yet constraints of the fit. What is more striking is that it also reproduces the spectroscopic metallicity. This strongly suggests that additional mixing processes may be necessary to properly and accurately model this star. For its twin, we note that the inclusion of turbulent mixing, a different opacity table, the Los Alamos one, or the use of a different equation of state, either CEFF or OPAL05, could help us account for the observed luminosity and effective temperature. Therefore, we perform another fit using the OPLIB opacity table, including turbulent mixing with a coefficient of $D_{\text{turb}} = 2000 \text{ cm}^2 \text{ s}^{-1}$, and adding the effective temperature to the set of constraints. We do not include the turbulent mixing coefficient into the free parameters as Figs. 5 and 6 clearly demonstrate that it saturates. The set of constraints is now composed of our seismic indicators and the effective temperature and the free parameters are the age, mass, and initial composition. We are now able to get a suitable model which, again, accounts for the position in the HR diagram but also for the spectroscopic metallicity, which was not required. This is illustrated as a cyan square in the figures, with the label “OPLIB – D_{turb} ”. This shows that modified opacities could help model the 16 Cyg A star as accurately as possible and also reinforces the argument that additional mixing processes might be necessary to model both stars. The values of the several stellar parameters are gathered in Table E.7.

3.2.2. Accounting for the metallicity

Up to now, the only two models accounting for the spectroscopic metallicity constraint from Ramírez et al. (2009) are

Table 5. Adjusted stellar parameters including the metallicity constraint.

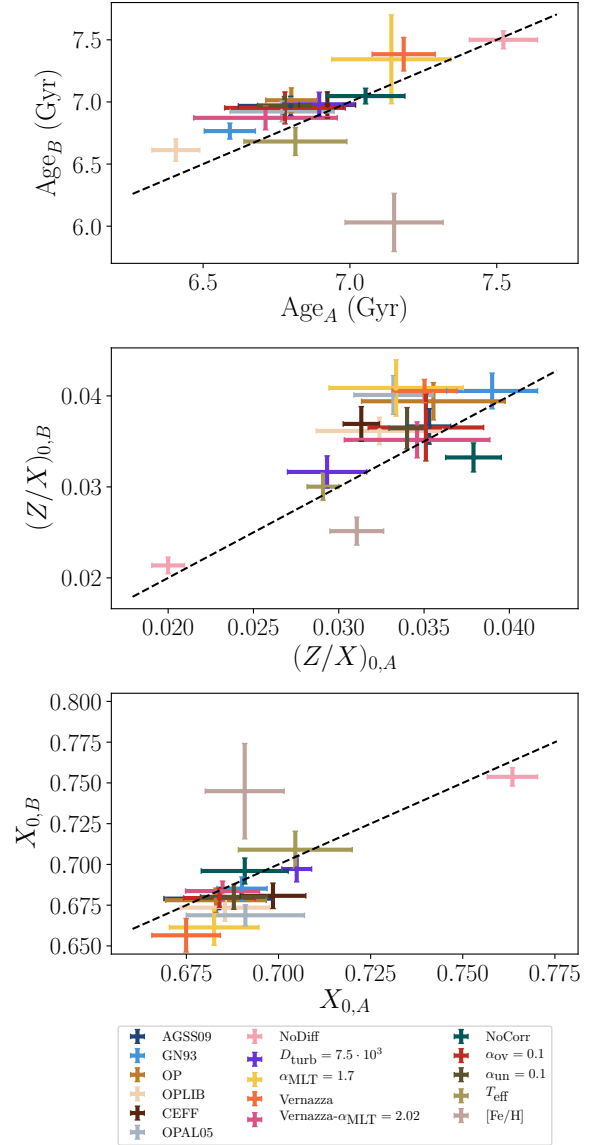
Quantity	16CygA	16CygB
$M(M_{\odot})$	1.03 ± 0.03	1.12 ± 0.06
X_0	0.69 ± 0.01	0.74 ± 0.03
$(Z/X)_0$	0.031 ± 0.003	0.025 ± 0.001
Y_0	0.29 ± 0.01	0.24 ± 0.03
$[\text{Fe}/\text{H}]$	0.12 ± 0.04	0.06 ± 0.04
Y_s	0.236 ± 0.006	0.20 ± 0.02
$t(\text{Gyr})$	7.1 ± 0.2	6.0 ± 0.2
$R(R_{\odot})$	1.21 ± 0.03	1.14 ± 0.06
α_{MLT}	1.71 ± 0.04	2.3 ± 0.2
χ^2	3.2	1.2

models with a reduced impact of diffusion. Those correspond to the one with the OPLIB opacity table and including turbulent mixing with a fixed coefficient of $D_{\text{turb}} = 2000 \text{ cm}^2 \text{ s}^{-1}$, labelled “OPLIB – D_{turb} ” in the figures, for 16 Cyg A and the one without diffusion for 16 Cyg B. Both models reproduce the complete set of seismic and non-seismic constraints (that is Δ , \hat{r}_{01} , \hat{r}_{02} , A_{He} , T_{eff} , L , and $[\text{Fe}/\text{H}]$). However, the spectroscopic metallicity was not yet part of the fitting constraints. Moreover, as Figs. 3 and 4 clearly illustrate, most of the computed models do not agree with the spectroscopic metallicities.

As Figs. 5 and 6 clearly show, the turbulent mixing coefficient saturates and freeing its value cannot enable us to produce models that reproduce the metallicity. We also note that the impact of the mixing length parameter is mostly focused on the effective temperature. As a consequence, we expect a large variation of this parameter will be necessary to reproduce the metallicity. In order to verify this hypothesis, we compute models with a free mixing length parameter and the metallicity as a constraint. The set of free parameters is made of the age, mass, composition and, mixing length of the star and the constraints are the set of seismic constraints and the metallicity. The results are given in Table 5 and shown in grey brown with the label $[\text{Fe}/\text{H}]$ in Figs. 1 through 4. We indeed observe that the necessary variations in α_{MLT} are incompatible with those to reproduce T_{eff} . Indeed, now that the model and observed metallicities agree, the effective temperature values do not. Trying to include both non-seismic constraints, using the mixing length parameter as a free coefficient and either including turbulent mixing or not did not lead to a satisfactory adjustment (i.e. with a reduced χ^2 value inferior to 1). This clearly shows that we are not able, with the current set of parameters, to reproduce the complete set of seismic and non-seismic constraints without invoking special physical processes. We also note that the model for 16 Cyg B is both too massive and young compared to other studies (e.g. Buldgen et al. 2016b; Verma et al. 2017). This illustrates that one has to proceed with caution when modelling data as it is possible to provide a model which is representative of these data while having no physical meaning.

3.3. Individual best models

In the present section, we summarise and further analyse the two best models we obtain while regarding both stars as separate, that is to say without imposing a common initial composition and age. Those are the only models which simultaneously account for seismic and non seismic constraints and are the ones denoted “OPLIB – D_{turb} ” for 16 Cyg A and “NoDiff” for 16 Cyg

**Fig. 7.** Comparison of adjusted stellar parameters for both stars at a given physics. The straight line shows the locus of identical stellar parameters for both stars.

B. Table 6 shows the choice of input physics as well as the set of optimal parameters of those models. As both models do not have the same set of input physics, they may not be regarded as valid candidates to study the system as a whole as is done in Sect. 4. We indeed expect from binary stars with close stellar parameters that their internal physics should overall be identical. The goal of the present section is only to analyse in more depth models which fitted the complete set of considered constraints and to investigate whether those models still may be further improved.

We display the échelle diagrams of each star in Figs. 8 and 9. We observe that the frequency trend for both stars is well accounted for. However, we note a drift at high frequencies. We expect this effect to mainly result from the surface effects. To illustrate this claim, we display the échelle diagram of optimal

Table 6. Best individual models for each star, accounting for both seismic and non-seismic constraints.

Quantity	16CygA	16CygB
Solar Ref.	AGSS09	AGSS09
Opacity	OPLIB	OP
Eq. state	Free	Free
Atmos	Eddington	Eddington
Diffusion	Yes	No
Turb. mix.	Yes	No
α_{MLT}	1.82	1.82
$M(M_{\odot})$	1.07 ± 0.03	1.063 ± 0.008
X_0	0.70 ± 0.03	0.754 ± 0.006
$(Z/X)_0$	0.029 ± 0.004	0.0214 ± 0.009
Y_0	0.27 ± 0.03	0.230 ± 0.009
$t(\text{Gyr})$	6.8 ± 0.2	7.50 ± 0.07
D_{turb}	$0.2 \cdot 10^4$	/
χ^2	0.9	0.6

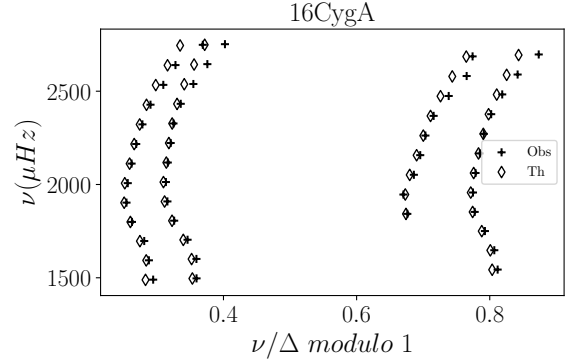
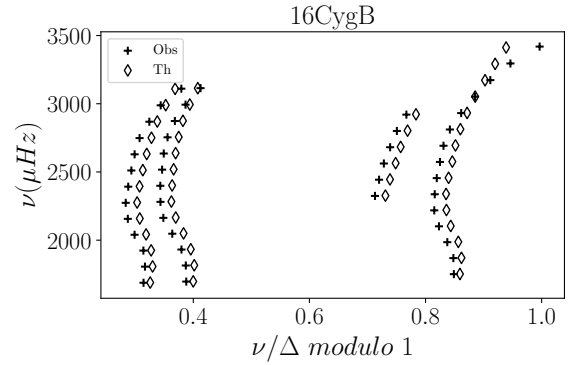
models for both stars computed with seismic indicators which are not corrected for surface effects in Figs. D.1 and D.2. We indeed observe that the high frequency drift is reinforced.

We also note that, in the case of 16 Cygni B, the theoretical ridges are shifted with respect to the observed ones. This effect should mainly be due to the $\hat{\epsilon}$ seismic indicator defined in Farnir et al. (2019). It corresponds to an estimator of the constant term in n in the asymptotic expression of frequencies as in Gough (1986) and has been shown to be sensitive to the surface effects. Its value along with several other WhoSGLAd indicators for every computed model are displayed in Figs. 10 and 11 (their definitions and observed values are given in Appendix B). We observe that the $\hat{\epsilon}$ is not properly accounted for. However, it is worse in the case of 16 Cyg B, which explains why this effect is much more visible.

In Appendix B, we define other seismic indicators that were not part of the constraints. Now looking at those indicators displayed in Figs. 10 and 11, we see that, in most cases, none of them are properly accounted for. In the lower panels, we display the values of the base of the convection zone glitch amplitude and note that only a few models are within the one σ uncertainty region. However, one should not be alarmed by this observation as its value is hardly significant in the case of the 16 Cygni system ($A_{\text{CZ}} = 2 \pm 1$ for both stars) and, therefore, bears little information.

We also represent the values for both Δ_{01} and Δ_{02} which represent the slopes of the individual frequency ratios r_{01} and r_{02} expressed as a function of the radial order. Again, every model presents a value which is significantly different from the observed ones. Nonetheless, accounting for such data is a complex task and we note that, in the present situation, only the modification of diffusion seems to provide an improvement for both stars.

We do not include the $\hat{\epsilon}$ indicator in the modelling procedure as it has been shown by Farnir et al. (2019, Fig. 4) to be sensitive mostly to the surface effects and highly degenerate in the stellar mass. Moreover, it is tightly correlated to the large separation (see Eq. (B.2) and the asymptotic formulation of the frequencies in Gough 1986). The Δ_{0l} indicators are not used as they mostly carry information about central overshooting (Farnir et al. 2019, Fig. 3) which we presumed would not happen as both stars are below the approximative limit of $\sim 1.1 M_{\odot}$ and are expected to have a radiative core.

**Fig. 8.** Échelle diagram of 16 Cygni A best-fit model. The crosses are the observed frequencies and the diamonds the theoretical ones.**Fig. 9.** Échelle diagram of 16 Cygni B best-fit model. The crosses are the observed frequencies and the diamonds the theoretical ones.

Finally, we plot in Figs. 12 and 13 the observed individual frequency ratios defined in Roxburgh & Vorontsov (2003), which we recall are not used as constraints in our fits, as a function of frequency against the best model ones. We observe that, although the overall agreement is good, the oscillation which is present in the observed ratios is not properly accounted for in the model frequencies. This clearly indicates that some information remains to be exploited to model the system as comprehensively as we can and inversion techniques may be of great help in doing so. However, with the use of only our indicators, instead of individual ratios, the overall trend seems to be well respected in both cases.

4. The system as a whole

In this section, we select the set of individual models which respect the binarity constraint and try to provide models while imposing a common age and initial composition.

4.1. Accepted models

The models satisfying the binarity constraint are those that have, within one another uncertainties, identical ages and initial composition. Figure 7 provides a clear illustration. Only models represented by a cross that meets the line, corresponding to identical stellar parameters in the three panels, are kept. Those models are referred to as the accepted models and are: the reference models (AGSS09, dark blue), those with turbulent mixing

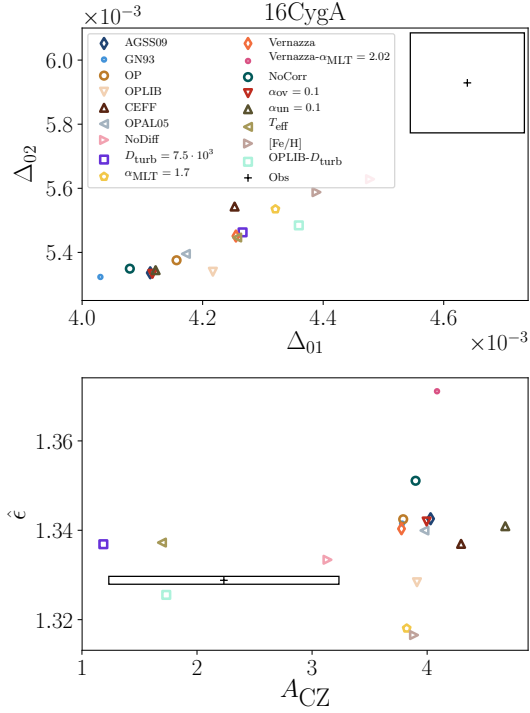


Fig. 10. Values of complementary seismic indicators for 16 Cyg A. Observed values along with their uncertainties are shown as a black box.

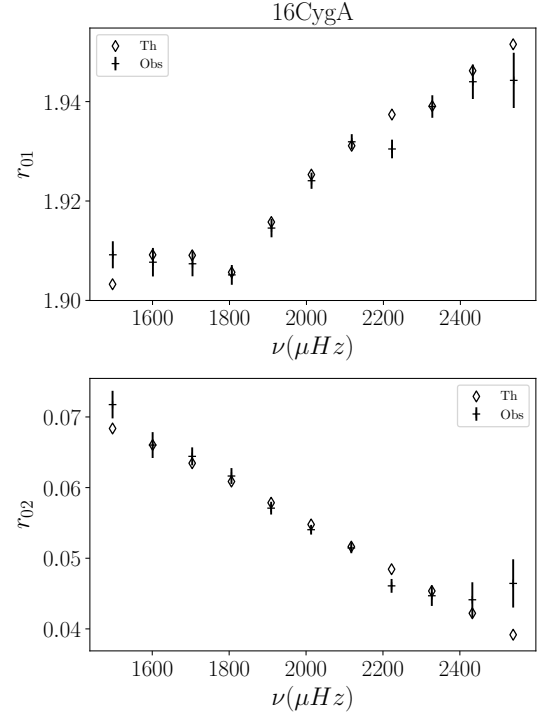


Fig. 12. Individual ratios for 16 Cygni A. Observed values along with their uncertainties are shown as crosses, best model values are represented by diamonds.

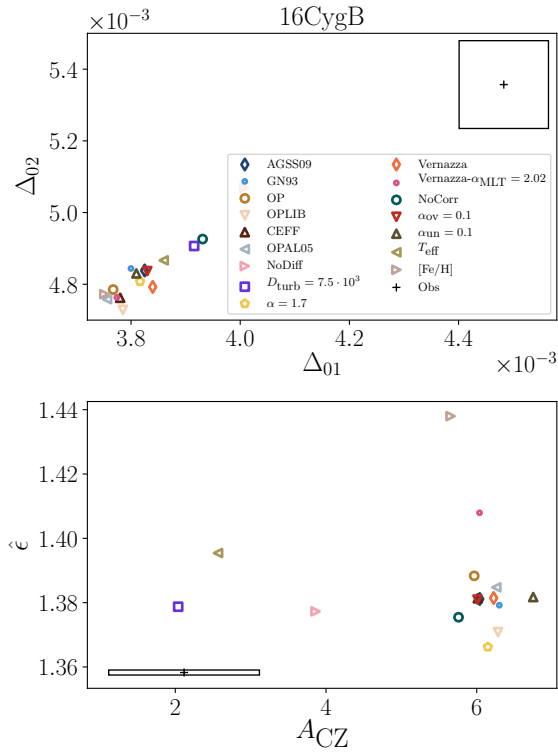


Fig. 11. Values of complementary seismic indicators for 16 Cyg B. Observed values along with their uncertainties are shown as a black box.

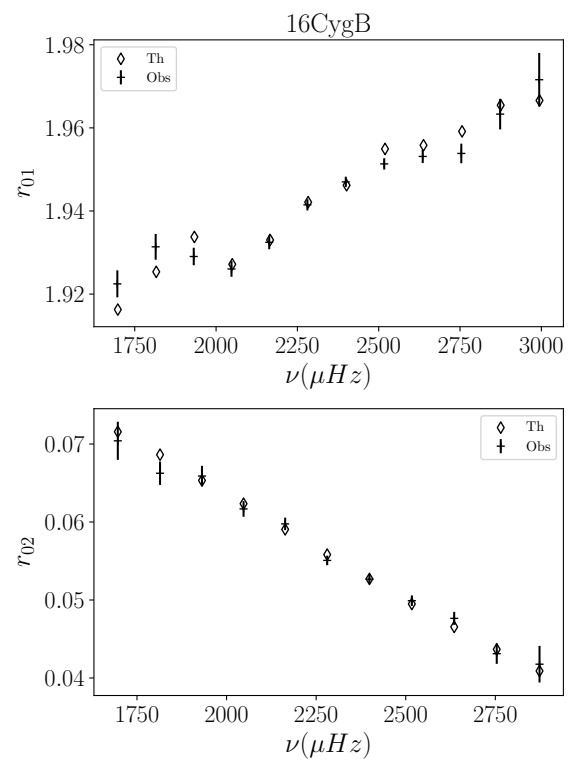


Fig. 13. Individual ratios for 16 Cygni B. Observed values along with their uncertainties are shown as crosses, best model values are represented by diamonds.

(D_{turb} , purple), without diffusion (NoDiff, light pink), with over-shooting (α_{ov} , red), the models with the mixing length coefficient adjusted for the effective temperature (T_{eff} , light green), and with a temperature profile above the photosphere as in Vernazza et al. (1981) with a calibrated α_{MLT} of 2.02 (Vernazza α_{MLT} dark pink). From those models, we define the range of accepted stellar parameters given in Table 7.

Even though models without diffusion are included in the set of accepted models, we emphasise that it does not mean that microscopic diffusion should not be included when modelling the system but that other mixing processes might occur to counteract it. Moreover, those models largely shift the accepted parameter ranges to heavier, older and hydrogen rich – thus metal and helium poor – models. This significant difference in composition is a clear illustration of the degeneracy between helium and metal abundances in the helium glitch amplitude.

We previously noted that the only models accounting simultaneously for the complete set of seismic and non-seismic constraints were the model with the OPLIB opacity table and turbulent mixing, for 16 Cygni A, and the one without diffusion for 16 Cygni B. This again hints at the necessity to include non-standard physical processes. However, we must point out that they are incompatible for a joint analysis, as is carried out in the present section, as their ages and compositions are significantly different. Moreover, as we use different opacity tables for both stars, they may not be used simultaneously to analyse the system as a whole.

4.2. Binary models

We now use the individual accepted models to compute models imposing a common age and composition. The adjustment is carried out as in the previous section (that is, with the same set of free parameters and constraints as in Sect. 3) only ages and initial compositions are required to be identical, reducing the set of free parameters by three. We use the average values of the initial composition and ages as initial guesses. The set of free parameters is composed of: one value of the age, initial hydrogen and metal fraction for both stars, and a different value of the mass for each star. The set of constraints corresponds to the individual values of the 4 seismic constraints considered in this paper (Δ , \hat{r}_{01} , \hat{r}_{02} , and A_{He}).

We are not able to provide an exact adjustment of both stars simultaneously (“exact” meaning that the reduced χ^2 value should not exceed a value of 1). This may result from the fact that the size of the parameters space is reduced by three. Effectively, even though the accepted ages and initial compositions agree within their uncertainties (see Table 7), they are not identical and our seismic constraints may be too stringent to allow for an exact simultaneous fit while imposing identical ages and compositions. To illustrate this statement, we have plotted the optimal ages and initial composition of one stellar component against the other for each choice of input physics in Fig. 7. We observe in this figure that the three common free parameters almost never simultaneously agree for a given choice of input physics. As further illustration, we may compute the relative difference in the initial metallicity between both stars normalised by the quadratic sum of their uncertainties

$(|(Z/X)_{0,A} - (Z/X)_{0,B}| / \sqrt{\sigma^2(Z/X)_{0,A} + \sigma^2(Z/X)_{0,B}})$. In the most favourable case, we obtain 0.2, while we get 2.7 in the least favourable one. This shows that the difference in initial composition for individual models is sometimes significant and may impair the convergence of the Levenberg-Marquardt procedure.

Table 7. Accepted stellar range defined as the centroid of the extremum values for each parameter.

Quantity	16CygA	16CygB
$M(M_{\odot})$	1.08 ± 0.04	1.03 ± 0.03
X_0	0.72 ± 0.05	0.72 ± 0.04
$(Z/X)_0$	0.028 ± 0.009	0.03 ± 0.01
Y_0	0.26 ± 0.05	0.26 ± 0.05
$t(\text{Gyr})$	7.1 ± 0.5	7.2 ± 0.4

Notes. The uncertainties are the necessary variations to reach those extrema. The accepted models used to define this range are: the reference models, the ones including turbulent mixing, those with over-shooting, those without diffusion and those with a temperature profile above the photosphere as in Vernazza et al. (1981) and with a calibrated α_{MLT} value.

One could argue that our inability to provide an exact adjustment for both stars comes from the reduced number of free parameters. Therefore, we try to include the mixing length parameter into the fitting parameters, allowing it to vary freely and independently for each star. However, this does not improve the results. As a matter of fact, the mixing length parameter value does not significantly vary. We retrieve optimal values of $\alpha_{\text{MLT},A} = 1.8 \pm 0.2$ and $\alpha_{\text{MLT},B} = 1.8 \pm 0.1$ respectively, compared to the fixed solar value of $\alpha_{\text{MLT}} = 1.82$. From Magic et al. (2015) and the solar-twin character of both stars (see also the discussion in Sect. 3.2.1) one might expect that the mixing length parameter value should remain close to solar.

Although we do not obtain models that exactly reproduce the seismic constraints, in some cases, we may find a reasonable agreement with most of them (but not all, therefore having a reduced χ^2 value greater than 1). We obtain two sets of convincing results: one for models without diffusion, the other for models with a temperature profile above the photosphere as in Vernazza et al. (1981) and a corresponding solar calibrated $\alpha_{\text{MLT}} = 2.02$ value. The optimal model stellar parameters are gathered in Tables 8 and 9, respectively, and Tables 10 and 11 show the differences between the observed and model seismic indicators normalised to the observed uncertainties. We also show the complete set of “optimal” model parameters, for each choice of input physics, as well as their relative agreement with the seismic constraints in Tables E.8 and E.9. We observe for the models without diffusion in Table 10 that, out of the 8 seismic constraints, only the large separation of 16 Cygni A was not properly accounted for. All the other indicators are within the 1σ uncertainty. For the models with a temperature profile above the photosphere as in Vernazza et al. (1981), both the large separation and small frequency ratio between radial and dipolar modes are poorly reproduced.

For the other models, presented in Tables E.8 and E.9, we note that it is always the large separation of the A star which is poorly fitted. The other indicators are rather well adjusted but the small separation ratios often fall out, while remaining close, of the 1σ uncertainty box. This difference in fitting between the several indicators mainly stems from the difference in their relative uncertainties. Indeed, the helium glitch amplitudes have relative uncertainties of about 3% and, by far, are the least stringent constraints. Then come the ratios with relative uncertainties around 0.8%. Finally, the Δ constraint relative uncertainties are of approximately 0.004%. Moreover, it was shown by Farnir et al. (2019) that the \hat{r}_{01} ratio is mostly sensitive to the evolutionary state of the star, therefore at a given composition and mass,

Table 8. Best set of adjusted stellar parameters, models without diffusion, imposing a common age and initial composition for both stars.

Quantity	16CygA	16CygB
$M(M_{\odot})$	1.10 ± 0.01	1.068 ± 0.004
$[\text{Fe}/\text{H}]$	0.058 ± 0.009	0.058 ± 0.009
Y_s	0.225 ± 0.004	0.225 ± 0.004
$R(R_{\odot})$	1.24 ± 0.01	1.114 ± 0.004
X_0	0.759 ± 0.004	
$(Z/X)_0$	0.0207 ± 0.0004	
Y_0	0.225 ± 0.004	
$t(\text{Gyr})$	7.50 ± 0.05	

to the stellar age. Then, the large separation is a proxy of the mean stellar density and decreases along the main sequence. As both stars are required to have identical ages and compositions, and with such stringent constraints, we may understand that only one large separation may be fitted at a time and that all the other constraints, from the clear imbalance in the relative uncertainties will adjust to it. To find a simultaneous agreement for those models that did not reach satisfactory convergence, we either need to relax this assumption, allowing for example different values for the initial composition, or to relax the seismic constraints.

We also display in Fig. 14 the agreement of the models with the non-seismic data for each of the considered variations in input physics, represented by the different symbols. The observed values along with their uncertainties are shown as boxes. We display the results for 16 Cyg A in blue and for 16 Cyg B in red. We note, as in the previous section, that the models for each star are almost constant in radius. We also note that very few models account for the position of the stars in the HR diagram. Actually, those are the models which, individually accounted for these data. It does not come as a surprise as the minimisation aims at finding a compromise between all the seismic constraints for both stars. Then, looking at the lower panel, we note that no model for 16 Cyg A is representative of the surface composition. For 16 Cyg B, only the model without diffusion agrees with these data – again with no surprise as the individual model already agreed – Let us add that, as the models without diffusion for both stars must have the same initial composition, their surface compositions are identical and both markers are indistinguishable in the lower panel of the figure.

In a nutshell, we are able to produce two pairs of binary models that are in reasonable agreement with our seismic constraints. However, no model accounts simultaneously for the seismic and non-seismic data of both stars. This may result from a differential effect between both stellar components which could, for example, create differences in compositions as has been discussed by [Maia et al. \(2019\)](#). This would require the inclusion of non-standard physical processes in the modelling.

4.3. Relaxing the common composition hypothesis

We noted in the previous section that simultaneously providing models of both stars while imposing them to have identical initial compositions as well as ages is a difficult task. In most cases, this resulted in our inability to build such models. Therefore, we try to model the system requiring only an identical age for both stars. The set of free parameters is thus made of the age, the individual initial hydrogen, and metal abundances and the individual masses. This adds up to 7 free parameters. The constraints are the

Table 9. Best set of adjusted stellar parameters, models with a temperature profile above the photosphere as in [Vernazza et al. \(1981\)](#) and with $\alpha_{\text{MLT}} = 2.02$, imposing a common age and initial composition for both stars.

Quantity	16CygA	16CygB
$M(M_{\odot})$	1.054 ± 0.006	1.016 ± 0.006
$[\text{Fe}/\text{H}]$	0.18 ± 0.01	0.19 ± 0.01
Y_s	0.244 ± 0.003	0.249 ± 0.003
$R(R_{\odot})$	1.216 ± 0.007	1.105 ± 0.006
α_{MLT}	2.02	
X_0	0.682 ± 0.005	
$(Z/X)_0$	0.0352 ± 0.0007	
Y_0	0.293 ± 0.005	
$t(\text{Gyr})$	6.82 ± 0.05	

Table 10. Differences between theoretical, model without diffusion, and observed values for the seismic constraints defined as $\delta = |I_{\text{obs}} - I_{\text{th}}|$, in the units of the constraint.

Quantity	16CygA		16CygB	
	δ	δ/σ	δ	δ/σ
$\Delta (\mu\text{Hz})$	0.01	3.0	$3 \cdot 10^{-5}$	0.007
A_{He}	0.7	0.7	0.3	0.3
\hat{r}_{01}	10^{-4}	0.4	10^{-4}	0.7
\hat{r}_{02}	10^{-4}	0.4	10^{-4}	0.4
χ^2_{red}	3.4			

Notes. $\chi^2_{\text{red}} = \chi^2/(N - k)$ is the reduced χ^2 value where N is the number of constraints to the fit and k the number of free parameters.

Table 11. Same as in Table 10, but for models model with a temperature profile above the photosphere as in [Vernazza et al. \(1981\)](#) and $\alpha_{\text{MLT}} = 2.02$.

Quantity	16CygA		16CygB	
	δ	δ/σ	δ	δ/σ
$\Delta (\mu\text{Hz})$	$6 \cdot 10^{-3}$	1.3	$7 \cdot 10^{-4}$	0.1
A_{He}	0.5	0.5	0.6	0.6
\hat{r}_{01}	$6 \cdot 10^{-4}$	1.9	$4 \cdot 10^{-4}$	1.1
\hat{r}_{02}	$3 \cdot 10^{-4}$	1.1	$2 \cdot 10^{-4}$	0.8
χ^2_{red}	2.9			

seismic indicators used throughout this paper which represent 8 constraints.

We compute models for the several sets of input physics considered in the previous section. The individual stellar parameters of those models are given in Table E.10. To quantify whether the improvement of the results is significant given the increased number of parameters, we introduce the Bayesian Information Criterion (BIC; [Schwarz 1978](#)). It allows to compare models of different dimensionalities and provides a criterion for making a selection. It has the advantage over the simple χ^2 value to penalise over the number of fitting parameters and may pinpoint overfitting models. Under the assumption that model errors are independent and normally distributed, it takes the form:

$$\text{BIC} = \chi^2 + k \ln(N), \quad (9)$$

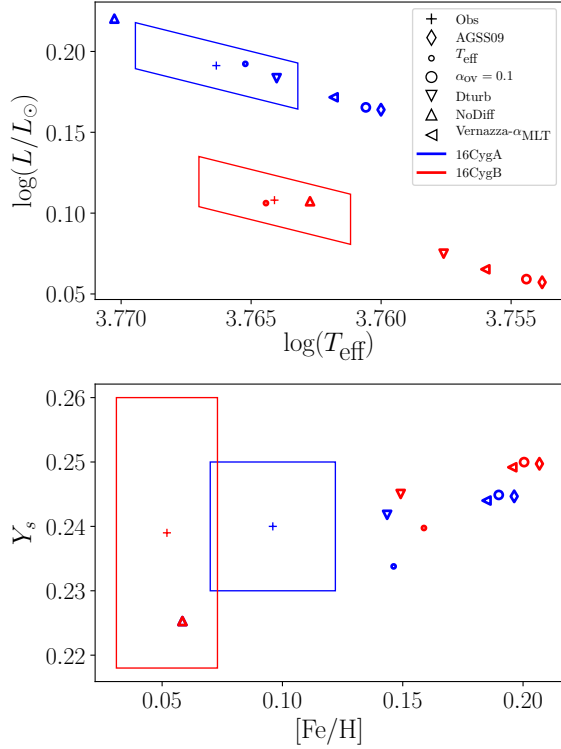


Fig. 14. Computed values of non-seismic constraints against the observed ones, symbolised by a box, for the system seen as a whole (i.e. with common ages and initial compositions). Each variation in input physics is represented by a different symbol. The colour represents the star, blue for 16 Cyg A and red for 16 Cyg B. The *upper panel* is a HR diagram. The *lower panel* shows the surface helium abundance versus the metallicity.

with the χ^2 value as defined previously, k the number of free parameters and N the number of constraints. When comparing different models, the key ingredient is not the BIC value itself but rather the difference between values – one must however keep in mind that the lower the value, the better – For the BIC difference to be significant, it has to exceed 2. BIC differences from 6 and above will be regarded as strongly significant (Kass & Raftery 1995). In this specific case, we compare models from the previous section that had 5 free parameters and 8 constraints, the added term to the χ^2 value thus equals 10.4. In the current section, it is equal to 14.6. The difference is 4.2 which the χ^2 improvement has to exceed so that the model may be regarded as improved.

Looking at the models in Table E.10, we observe that the relative difference in compositions between the two stars is very small (the maximum difference reaches up to 0.07 dex in X_0 and 0.002 dex in $(Z/X)_0$). However, that variation alone is able to greatly improve the BIC values, as the comparison of Tables E.9 and E.11 shows. Only two models were not significantly improved. The model considering the mixing length parameters calibrated over the effective temperature of the stars could not be improved. Also, the one using the temperature profile of Vernazza et al. (1981) above the photosphere and a calibrated value of α_{MLT} is not improved, BIC-wise (the raw χ^2 value did decrease of about 1.7). The BIC variation is of about 2 which makes this difference barely relevant. Therefore, in most cases,

it is relevant to allow the composition to slightly vary between the two stars. This again points toward the necessity to include non-standard physical processes. We also note that it is often the case that the uncertainties on the individual stellar parameters are degraded. Finally, we note that, in most cases, 16 Cyg B is initially richer in metals and poorer in hydrogen than its twin. This validates the trend we observe in the middle and lower panels of Fig. 7. Therefore, we observe that, seismically speaking, the B component of the system is more metallic than the A, which is in opposition with the spectroscopic observations (see Table 1).

5. Discussion

5.1. General considerations about the approach

Compared to other asteroseismic approaches aiming at the modelling of solar-like pulsators, the greatest difference of our approach is that we do not use directly the complete set of individual frequencies or of individual frequency ratios as constraints. Instead, we build seismic indicators, via the WhoSGLAd method, which are as little correlated as possible and relevant to the stellar structure. Moreover, the search for optimal models is carried out by minimising a single cost function comparing simultaneously theoretical seismic and non-seismic constraints to observed data. This has the advantage of avoiding unnecessary correlations.

Furthermore, the direct use of the helium glitch amplitude in our modelling also makes up the peculiarity of our approach. Indeed, in several other studies, it is not used directly as a constraint to the modelling. For example, Verma et al. (2014, 2019) calibrate the model helium glitch amplitude with respect to the surface helium abundance in a set of optimal models representative of other constraints (namely individual frequencies, ratios, effective temperature and metallicity) to provide an estimate. In the present case, including the helium glitch amplitude as a constraint to the fit acts as a constraint on the model helium abundance, with some correlation with the metal content as showed in Sect. 3.1.1. This means that we do not assume a specific relation between the two quantities and the resulting helium abundance stems from the best model search only.

We noted that providing models of both stars while requiring a common age and composition proves to be an arduous task. For most choices of micro- and macro-physics, we are not able to produce satisfactory models. However, when completely inhibiting the microscopic diffusion of chemical elements or imposing a temperature relation above the photosphere following the prescription of Vernazza et al. (1981) while using a specifically calibrated value of the mixing length parameter, we obtained a reasonable agreement, but did not go below the value of 1 for the reduced χ^2 . On the first hand, the fact that including extra mixing produces better results illustrates the need to include non-standard physical processes to properly model such complex data. On the other hand, the improvement of the results while using another temperature profile above the photosphere demonstrates the impact of the surface effects on the seismic indicators. Even though those indicators were defined in such a way to lessen this effect at most. We must also add that non-seismic constraints are not simultaneously accounted for in both stars (see Fig. 14). This clearly illustrates the need to include such constraints in the fitting procedure as well as additional physical processes. Some of the possible non-standard physical processes that could be included in the modelling are discussed in Sect. 5.3. Another way to improve models of the system as a whole is to relax the hypothesis of a common composition.

This leads to small differences in composition between both stars (never exceeding 0.07 dex in X_0 and 0.002 dex in $(Z/X)_0$). This is however sufficient in many cases to improve the results significantly as the BIC values testify.

5.2. Impact of the surface effects

The impact of the surface effects correction of the frequencies on the optimal model is not clear. We computed models that adjusted seismic indicators built over the uncorrected frequencies. Those are displayed in dark green in the figures throughout the paper. Although it is barely significant we note that those models are heavier and older than models with corrected frequencies.

Furthermore, we noted in Sect. 4.2 that the large separation we compute is the most stringent of our indicators with a relative uncertainty of approximately 0.004%. However, this specific value of the uncertainty, resulting from the error propagation of the individual frequencies, is unrealistic. To provide a more robust estimate, we can quantify the contribution of the surface effects by computing the difference between corrected and uncorrected values. We obtain $\sigma(\Delta_A) = 0.9 \mu\text{Hz}$ and $\sigma(\Delta_B) = 1.0 \mu\text{Hz}$, for 16 Cyg A and B respectively, which amounts to 1.1% relative uncertainty. This shows that, even though we build seismic indicators in such way that makes them the less dependent on the surface effects as possible, they are still impacted by the surface conditions.

The impact of the surface effects correction is further illustrated in Appendix D where we give the values of the seismic indicators for uncorrected frequencies and display the best-fit models échelle diagrams of both stars. We also compute models with frequencies corrected according to the prescription of Ball & Gizon (2014). The optimal parameters are given in Table D.2. We observe, compared to the reference models, that both stars become older and hydrogen rich. We also note that, while the A component becomes more metallic, the B one is then less metallic. 16 Cygni B also becomes heavier while it is not the case for its twin. Nonetheless, the differences are such that we could include those models in the set of accepted ones.

5.3. Non-standard physical processes and modelling improvements

As was shown by Verma et al. (2019) and as we illustrate in Sect. 3.1.3, diffusion is very important in the modelling of solar-like stars. However, the models computed with CLES currently consider only three chemical species, the hydrogen, the helium and the metals. A significant improvement would stem from the consideration of several sub-species in the metals. For example, we may retrieve invaluable information by following the lithium evolution with the star. Indeed, the discussion regarding the effects of potential non-standard processes is tightly linked to the lithium abundance in both stars and its connection with the formation and orbital evolution of planetary systems. Deal et al. (2015) have proposed that, since the B component was orbited by a Jovian planet (Cochran et al. 1997), accretion of matter from the planetary disc in the envelope of 16CygB would have triggered fingering convection and thus led to a strong decrease in the lithium abundance. They determined that the accretion of $0.66 M_\oplus$ would be enough to reproduce the lithium abundance of 16CygB that is 4 times lower than that of 16CygA (Friel et al. 1993; King et al. 1997), despite both stars having very similar rotational and structural properties. It is also interesting to note that, in the broader context of the Li abundance of solar-twins,

16CygA seems to be more Li-rich than similar solar-twins, while 16CygB seems to follow the trend observed with age for these stars (Carlos et al. 2016). This could suggest a reverse scenario that should explain the high lithium abundance of 16CygA and in particular the possibility of an increase in lithium abundance related to planet engulfment (e.g. Montalbán & Rebolo 2002; Carlos et al. 2016). In this context, analysing both scenarios in light of potential traces of such events in seismic indicators may lead to new synergies between asteroseismology and exoplanetology, namely in the analysis of planetary formation and material accretion onto the surface of planet-host stars.

Furthermore, our models do not include rotation, nor rotation-induced mixing. As a matter of fact, Davies et al. (2015) and Bazot et al. (2019) showed that rotation indeed occurs in both stars taking advantage of the rotational splitting present in stellar oscillation spectra of rotating stars. Bazot et al. (2019) even showed that differential rotation occurs in both stars, in a similar way to our Sun. Such a process could significantly affect the diffusion of chemical elements. This could be argued to be a flaw in our models. However, the additional mixing induced may be approximated by the turbulent mixing of elements as was performed for several models in this study. This prescription consists of an approximation and the models may still be improved. Therefore, we may, in the future, use improved models which account for the rotation. This will be discussed in further papers of the series.

Finally, we noted that choosing a different opacity profile, that of the Los Alamos project, while including turbulent mixing of elements, which counteracts diffusion, allowed to reproduce both seismic and non seismic constraints for 16 Cygni A. This provides clues that we may need to modify the opacity profile of the star to properly account for all the observed constraints. Therefore, inversion techniques could help us to further improve our models. However, the OPLIB opacity table has two different effects on the stellar structure. On the one hand, it modifies slightly the size of the convective envelope. On the other hand, it changes the temperature gradient in the central regions. According to which effects dominates this could be the illustration of the need of non-standard mixing processes as well.

6. Conclusion

With the aim of characterising the 16 Cygni system as thoroughly as possible, we took advantage of the seismic indicators defined via the WhoSGLAd method to provide stringent constraints on the stellar structure and test several choices of micro- and macro-physics. We built those indicators using the frequencies computed over the full length of the *Kepler* data by Davies et al. (2015) and corrected for the surface effects according to Kjeldsen et al. (2008)'s power law adjusted by Sonoi et al. (2015). The several choices of micro- and macro-physics used in stellar models we tested are: the solar reference mixture, opacity and equation of state tables as well as the inclusion of turbulent mixing or of diffusion of chemical elements, a different choice for the mixing length parameter, the inclusion of overshooting outside of convective regions, a different choice of temperature profile above the photosphere or the effect of the correction of the frequencies for the surface effects.

Overall, our results agree with previous studies with slight differences according to the choice of physics included in the models. We showed that the use of the WhoSGLAd indicators allows to discriminate between several of those choices. However, we also note that those indicators alone do not suffice to provide a complete adjustment of the stars as, in most cases,

the non-seismic constraints (i.e. luminosity, effective temperature, and metallicity) are not satisfied. Therefore, they need to be included in the fitting process to provide the most representative model. We show in Sect. 3.2.1 that the mixing length parameter has a clear effect on the modelled effective temperature of the star. Indeed, a value greater than the solar one allows to greatly improve the agreement with the observed value in the case of 16 Cyg B. Moreover, we also study the impact of the inclusion of turbulent mixing and show that it leads to a better fit of the effective temperature and metallicity. However, we observe that the turbulent mixing coefficient saturates and using it as a free parameter of the modelling procedure would be meaningless. Therefore, using a free α_{MLT} and T_{eff} as a constraint, we are able to produce models in agreement with this constraint. However, the observed metallicities are not reproduced by those models. We also demonstrate in Sect. 3.2.2 that varying the mixing length parameter while using the metallicity constraint allows to better reproduce its value for both stars but at the cost of the agreement with the observed effective temperatures. This illustrates the necessity to build more complex models in order to reproduce both seismic and non-seismic constraints.

Indeed, we show that, to reproduce the non-seismic constraints, we have to select only specific choices of input physics or even include non-standard physical processes. Indeed, for 16 Cygni A, only a model with a modified opacity profile, from the Los Alamos Opacity Project, and including turbulent mixing of the chemical elements reproduced all constraints. For 16 Cygni B, it was a model that did not include diffusion that was able to account for these constraints. This illustrates in both cases that non-standard physical processes may be necessary to inhibit diffusion and to properly model those stars. Such processes could be the accretion of planetary matter or rotation-induced mixing.

Adjusting both stars simultaneously while imposing a common age and composition proved to be a difficult task. In most cases, with models that were consistent within mutual uncertainties for both stars as initial guesses, we could not obtain a satisfactory adjustment. The large separation of 16 Cyg B, because of the high precision of the Δ constrain defined in our study, was dominant and the free parameters adapted at best to provide a compromise for the other constraints. This resulted in models that did not exactly fit the large separation of 16 Cygni A while reasonably fitting other constraints (only a few σ difference from the required value). Nonetheless, for models without diffusion or with a different temperature profile above the photosphere (that of Vernazza et al. 1981) and a calibrated value of α_{MLT} , we were able to account for the seismic constraints of both stars with a reduced χ^2 of 3.4 and 2.9 respectively. The difficulty to provide satisfactory models of both stars with other choices of input physics indicates that it can be necessary to either relax the common initial composition assumption, the seismic constraints or to invoke special physical processes. For example, we showed in Sect. 4.2 that the differences in the initial metallicity between both stellar components of optimal individual models may sometimes be significant. Therefore, we computed models relaxing the common composition hypothesis in Sect. 4.3 and were able to significantly improve the results. We observe that a small difference between the initial compositions of both stars is sufficient.

With the aim of providing a broad sample of reliable models of the system, the extensive analysis of the degeneracies carried out by combining seismic and non-seismic constraints is of prime importance to fully grasp the uncertainties of inverse analysis but also to the extent in which we can constrain physical processes not implemented in standard stellar models linked for

example to the effects of accretion of planetary matter, angular momentum transport and their link to both seismic indices and the lithium and beryllium abundances of both stars.

We showed that, even for our models that reproduced both seismic and non-seismic constraints, information remain to be analysed as we observe that other indicators defined in Farnir et al. (2019) are not properly represented (i.e. $\hat{\epsilon}$, Δ_{01} , Δ_{02} , and A_{CZ}). Further studies could focus on those other constraints. Finally, as the WhoSGIAd method also proves to provide very stringent seismic constraints, we will, in future studies, undertake the adjustment of the *Kepler* LEGACY sample (Lund et al. 2017) to try and retrieve global trends in solar-like oscillators. This data set contains the best set of solar-like oscillation spectra available to the community to this day as it is composed of 66 solar-like stars which have been continuously observed from space for at least one year. Therefore, we would be able to realise an ensemble study of stellar parameters. For example, we could study the evolution of the amount of central overshooting with the stellar mass.

Acknowledgements. The authors would like to thank the referee for their careful reading of the paper as well as for their very constructive remarks. M. F. is supported by the FRiA (Fond pour la Recherche en Industrie et Agriculture) – FNRS PhD Grant. G. B. acknowledges fundings from the SNF AMBIZIONE Grant No. 185805 (Seismic inversions and modelling of transport processes in stars). C. Pinçon is supported by the F. R. S – FNRS as a Chargé de Recherche. P. E. and S. J. A. J. S. have received funding from the European Research Council (ERC) under the European Union’s Horizon 2020 research and innovation programme (Grant agreement No. 833925, project STAREX). C. Pezzotti is sponsored by the Swiss National Science Foundation (project number 200020 – 172505).

References

- Adelberger, E. G., García, A., Robertson, R. G. H., et al. 2011, *Rev. Mod. Phys.*, **83**, 195
- Asplund, M., Grevesse, N., Sauval, A. J., & Scott, P. 2009, *ARA&A*, **47**, 481
- Badnell, N. R., Bautista, M. A., Butler, K., et al. 2005, *MNRAS*, **360**, 458
- Baglin, A., Auvergne, M., Barge, P., et al. 2009, in *Transiting Planets*, eds. F. Pont, D. Sasselov, M. J. Holman, et al., *IAU Symp.*, **253**, 71
- Ball, W. H., & Gizon, L. 2014, *A&A*, **568**, A123
- Basu, S., Mazumdar, A., Antia, H. M., & Demarque, P. 2004, *MNRAS*, **350**, 277
- Bazot, M., Benomar, O., Christensen-Dalsgaard, J., et al. 2019, *A&A*, **623**, A125
- Borucki, W. J., Koch, D., Basri, G., et al. 2010, in *American Astronomical Society Meeting Abstracts #215*, *Bull. Am. Astron. Soc.*, **42**, 215
- Buldgen, G., Salmon, S. J. A. J., Reese, D. R., & Dupret, M. A. 2016a, *A&A*, **596**, A73
- Buldgen, G., Reese, D. R., & Dupret, M. A. 2016b, *A&A*, **585**, A109
- Carlos, M., Nissen, P. E., & Meléndez, J. 2016, *A&A*, **587**, A100
- Cassisi, S., Salaris, M., & Irwin, A. W. 2003, *ApJ*, **588**, 862
- Christensen-Dalsgaard, J., & Däppen, W. 1992, *A&A Rev.*, **4**, 267
- Cochran, W. D., Hatzes, A. P., Butler, R. P., & Marcy, G. W. 1997, *ApJ*, **483**, 457
- Colgan, J., Kilcrease, D. P., Magee, N. H., et al. 2016, *ApJ*, **817**, 116
- Cox, J. P., & Giuli, R. T. 1968, *Principles of Stellar Structure* (New York: Gordon and Breach)
- Davies, G. R., Chaplin, W. J., Farr, W. M., et al. 2015, *MNRAS*, **446**, 2959
- Deal, M., Richard, O., & Vauclair, S. 2015, *A&A*, **584**, A105
- Eggenberger, P., Miglio, A., Montalbán, J., et al. 2010, *A&A*, **509**, A72
- Eggenberger, P., Buldgen, G., & Salmon, S. J. A. J. 2019, *A&A*, **626**, L1
- Farnir, M., Dupret, M. A., Salmon, S. J. A. J., Noels, A., & Buldgen, G. 2019, *A&A*, **622**, A98
- Ferguson, J. W., Alexander, D. R., Allard, F., et al. 2005, *ApJ*, **623**, 585
- Friel, E., Cayrel de Strobel, G., Chmielewski, Y., et al. 1993, *A&A*, **274**, 825
- Gough, D. O. 1986, *Highlights Astron.*, **7**, 283
- Gough, D. O. 1990, in *Progress of Seismology of the Sun and Stars*, eds. Y. Osaki, & H. Shibahashi (Berlin Springer Verlag), *Lect. Notes Phys.*, **367**, 283
- Grevesse, N., & Noels, A. 1993, in *Origin and Evolution of the Elements*, eds. N. Prantzos, E. Vangioni-Flam, & M. Casse, **15**
- Iglesias, C. A., & Rogers, F. J. 1996, *ApJ*, **464**, 943
- Kass, R. E., & Raftery, A. E. 1995, *J. Am. Stat. Assoc.*, **90**, 773
- King, J. R., Deliyannis, C. P., Hiltgen, D. D., et al. 1997, *AJ*, **113**, 1871
- Kjeldsen, H., & Bedding, T. R. 1995, *A&A*, **293**, 87

- Kjeldsen, H., Bedding, T. R., & Christensen-Dalsgaard, J. 2008, *ApJ*, **683**, L175
- Lund, M. N., Silva Aguirre, V., Davies, G. R., et al. 2017, *ApJ*, **835**, 172
- Magic, Z., Weiss, A., & Asplund, M. 2015, *A&A*, **573**, A89
- Maia, M. T., Meléndez, J., Lorenzo-Oliveira, D., Spina, L., & Jofré, P. 2019, *A&A*, **628**, A126
- Manchon, L., Belkacem, K., Samadi, R., et al. 2018, *A&A*, **620**, A107
- Metcalfe, T. S., Chaplin, W. J., Appourchaux, T., et al. 2012, *ApJ*, **748**, L10
- Montalbán, J., & Rebolo, R. 2002, *A&A*, **386**, 1039
- Monteiro, M. J. P. F. G., Christensen-Dalsgaard, J., & Thompson, M. J. 2000, *MNRAS*, **316**, 165
- Paxton, B., Cantiello, M., Arras, P., et al. 2013, *ApJS*, **208**, 4
- Proffitt, C. R., & Michaud, G. 1991, *ApJ*, **380**, 238
- Ramírez, I., Meléndez, J., & Asplund, M. 2009, *A&A*, **508**, L17
- Reese, D. R., Marques, J. P., Goupil, M. J., Thompson, M. J., & Deheuvels, S. 2012, *A&A*, **539**, A63
- Rogers, F. J., & Nayfonov, A. 2002, *ApJ*, **576**, 1064
- Roxburgh, I. W., & Vorontsov, S. V. 2003, *A&A*, **411**, 215
- Schwarz, G. 1978, *Ann. Stat.*, **6**, 461
- Scuflaire, R., Théado, S., Montalbán, J., et al. 2008a, *Ap&SS*, **316**, 83
- Scuflaire, R., Montalbán, J., Théado, S., et al. 2008b, *Ap&SS*, **316**, 149
- Sonoi, T., Samadi, R., Belkacem, K., et al. 2015, *A&A*, **583**, A112
- Tassoul, M. 1980, *ApJS*, **43**, 469
- Thévenin, F., Oreshina, A. V., Baturin, V. A., et al. 2017, *A&A*, **598**, A64
- Thoul, A. A., Bahcall, J. N., & Loeb, A. 1994, *ApJ*, **421**, 828
- Ulrich, R. K. 1986, *ApJ*, **306**, L37
- Verma, K., Faria, J. P., Antia, H. M., et al. 2014, *ApJ*, **790**, 138
- Verma, K., Raodeo, K., Antia, H. M., et al. 2017, *ApJ*, **837**, 47
- Verma, K., Raodeo, K., Basu, S., et al. 2019, *MNRAS*, **483**, 4678
- Vernazza, J. E., Avrett, E. H., & Loeser, R. 1981, *ApJS*, **45**, 635
- Vorontsov, S. V. 1988, in *Advances in Helio- and Asteroseismology*, eds. J. Christensen-Dalsgaard, & S. Frandsen, *IAU Symp.*, **123**, 151
- White, T. R., Huber, D., Maestro, V., et al. 2013, *MNRAS*, **433**, 1262

Appendix A: WhoSGIAd decomposition

We describe here the basis of functions which are used to represent the oscillation spectrum of a solar-like pulsator. First, the smooth part of the spectrum is represented by a second-order polynomial of n , the radial order. We thus have the following succession of polynomials:

$$p_{lk}(n, l') = \delta_{ll'} p_k(n), \quad (\text{A.1})$$

with $p_k(n) = n^k$, $k = 0, 1, 2$ and $\delta_{ll'}$ the Kronecker delta comparing two values of the spherical degree l and l' .

Then, the helium glitch is described by the following oscillating functions:

$$\delta\nu_{\text{He}} = \sum_{k=-4}^{-5} [\cos(4\pi\tau\Delta\nu\tilde{n}) + \sin(4\pi\tau\Delta\nu\tilde{n})] \tilde{n}^k, \quad (\text{A.2})$$

where τ is the acoustic depth of the glitch, $\Delta\nu$ the asymptotic large frequency separation and $\tilde{n} = n + l/2$. $\tilde{n}\Delta\nu$ is actually the first order approximation of $\nu_{l,n}$. The asymptotic large frequency separation is defined as $\Delta\nu = \left(2 \int_0^{R_*} \frac{dr}{c(r)}\right)^{-1}$ (Tassoul 1980), with the local radius r , the local sound speed $c(r)$ and R_* the radius of the star at the photosphere.

We must add that the values of τ and $\Delta\nu$ are estimated via a model that is representative of the seismic indicators of the smooth part, namely Δ , \hat{r}_{01} and \hat{r}_{02} . Farnir et al. (2019) showed that the exact value of $\tau\Delta\nu$ has a negligible impact on the amplitude of the glitch. A 10% percent excursion from the optimal value is of negligible impact.

Finally, orthonormalisation of the basis function is carried out via *Gram-Schmidt*'s process. This produces the orthonormal elements over which we may project the frequencies to represent them. We thus retrieve completely independent coefficients.

Appendix B: Additional seismic indicators

In the present section, we describe supplementary seismic indicators defined in the WhoSGIAd method but that are not used directly in our optimisation for a model representative of the 16 Cygni system. The values of those indicators are given in Table B.1.

$\hat{\epsilon}$: In taking inspiration in the asymptotic formulation of the frequencies (Gough 1986)

$$\nu(n, l) \simeq \left(n + \frac{l}{2} + \epsilon\right) \Delta, \quad (\text{B.1})$$

we may construct a vector subspace over which frequencies are represented by the function:

$$\nu(n, l) = \left(n + \frac{l}{2} + \epsilon\right) \hat{\Delta} = \left(n + \frac{l}{2}\right) \hat{\Delta} + K, \quad (\text{B.2})$$

where $\hat{\Delta}$ and K are free parameters. By defining an orthonormal basis over this subspace, projecting the frequencies and identifying the several coefficients with the asymptotic expression we may get an expression for $\hat{\epsilon}$.

A_{CZ} .

$$A_{\text{CZ}} = \|\delta\nu_{\text{CZ}}\|, \quad (\text{B.3})$$

where $\delta\nu_{\text{CZ}}$ is the base of the convection zone glitch component.

A37, page 18 of 24

Table B.1. Additional observed seismic indicators.

Indicator	16CygA	16CygB
$\hat{\epsilon}$	1.3288 ± 0.0009	1.3583 ± 0.0008
A_{CZ}	2 ± 1	2 ± 1
Δ_{01}	$(4.64 \pm 0.09) \cdot 10^{-3}$	$(4.48 \pm 0.08) \cdot 10^{-3}$
Δ_{02}	$(5.9 \pm 0.2) \cdot 10^{-3}$	$(5.4 \pm 0.1) \cdot 10^{-3}$

Notes. The standard deviations result from the propagation of the uncertainties on the observed frequencies.

Δ_{0l} . Corresponds to the slope of the individual frequency ratios r_{0l} as a function of the radial order n and is defined as:

$$\Delta_{0l} = \frac{\Delta_l}{\Delta_0} - 1. \quad (\text{B.4})$$

Appendix C: Impact of high uncertainties modes

Table C.1. Stellar parameters retrieved with the reference set of input physics and the complete set of frequencies.

Quantity	16CygA	16CygB
$M(M_\odot)$	1.06 ± 0.01	1.011 ± 0.006
X_0	0.684 ± 0.009	0.679 ± 0.006
$(Z/X)_0$	0.035 ± 0.004	0.037 ± 0.002
Y_0	0.292 ± 0.009	0.296 ± 0.006
$[\text{Fe}/\text{H}]$	0.19 ± 0.05	0.21 ± 0.03
Y_s	0.243 ± 0.005	0.251 ± 0.003
$R(R_\odot)$	1.22 ± 0.01	1.104 ± 0.006
$t(\text{Gyr})$	6.8 ± 0.1	6.97 ± 0.07
χ^2	1.0	0.7

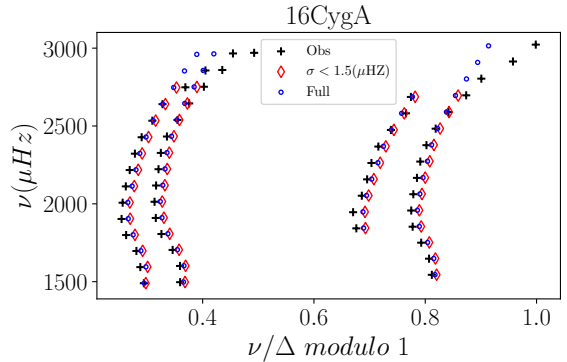


Fig. C.1. Échelle diagram of 16 Cygni A comparing optimal reference model with full set of frequencies (blue circles) from Davies et al. (2015; black crosses) with the optimal model with a set restricted to frequencies with uncertainties lower than $1.5 \mu\text{Hz}$ (red diamonds).

From the modes computed by Davies et al. (2015) we select those with uncertainties below $1.5 \mu\text{Hz}$. Those high uncertainty modes have a limited and negligible impact on the results as our indicators are averaged over the whole spectrum. Furthermore, as the high frequency modes are the ones which are the most affected by the surface effects this may render our results more

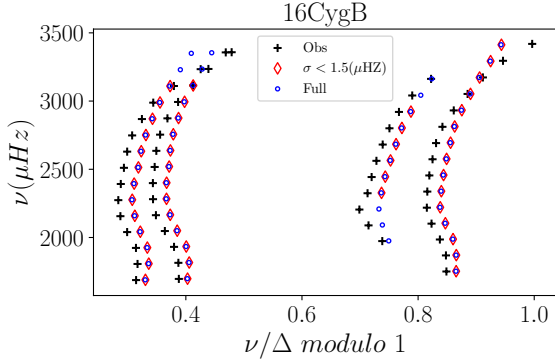


Fig. C.2. Échelle diagram of 16 Cygni B comparing optimal reference model with full set of frequencies (blue circles) from (Davies et al. 2015; black crosses) with the optimal model with a set restricted to frequencies with uncertainties lower than $1.5 \mu\text{Hz}$ (red diamonds).

robust. In Table C.1 we show the optimal set of stellar parameters retrieved when using the full set of frequencies. We observe that the results do not vary significantly from the case considering modes with uncertainties below the $1.5 \mu\text{Hz}$ threshold, presented in Table E.3 under the label AGSS09. Only the uncertainties on the individual parameters are affected which should not be of any concern as the dominant factor remains the choice of input physics. As further validation of this choice, we display in Figs. C.1 and C.2 a comparison of the échelle diagram of optimal models of both stars using the complete set of frequencies (blue circle) with the ones with the reduced set (red diamond) and the observations (black crosses). We observe that the results do not significantly differ, only that the high frequency drift is more visible as more frequencies are displayed.

Appendix D: Influence of the surface effects

Table D.1. Observed seismic indicators with frequencies uncorrected for surface effects.

Indicator	16CygA	16CygB
$\Delta(\mu\text{Hz})$	103.070 ± 0.005	116.706 ± 0.004
A_{He}	30 ± 1	33 ± 1
\hat{r}_{01}	$(3.61 \pm 0.02) \cdot 10^{-2}$	$(2.55 \pm 0.02) \cdot 10^{-2}$
\hat{r}_{02}	$(5.61 \pm 0.03) \cdot 10^{-2}$	$(5.41 \pm 0.03) \cdot 10^{-2}$

Notes. The standard deviations result from the propagation of the uncertainties on the observed frequencies.

We computed both models for frequencies which were not corrected for the surface effects or with theoretical frequencies corrected as in Ball & Gizon (2014) with the adjusted relation in large separation, effective temperature, surface gravity and opacity of Manchon et al. (2018). Table D.1 displays seismic indicators computed with frequencies which are not corrected for the surface effects. The échelle diagram for the models computed with these set of indicators are displayed in Figs. D.1 and D.2. The most striking feature is the large shift between theoretical and observed ridges in both figures which shows that the ϵ indicator is not well accounted for as Figs. 10 and 11 show. Moreover, the overall shape of the individual ridges is well represented by the theoretical frequencies. Table D.2 displays the set

Table D.2. Adjusted stellar parameters with theoretical frequencies corrected as in Ball & Gizon (2014) with the adjusted relation in Manchon et al. (2018).

Quantity	16CygA	16CygB
$M(M_{\odot})$	1.07 ± 0.04	1.027 ± 0.008
X_0	0.687 ± 0.007	0.692 ± 0.006
$(Z/X)_0$	0.039 ± 0.006	0.034 ± 0.002
Y_0	0.285 ± 0.009	0.292 ± 0.006
$[\text{Fe}/\text{H}]$	0.23 ± 0.07	0.19 ± 0.03
Y_s	0.238 ± 0.005	0.240 ± 0.04
$R(R_{\odot})$	1.23 ± 0.04	1.118 ± 0.008
$t(\text{Gyr})$	7.1 ± 0.2	7.04 ± 0.08
χ^2	0.8	0.4

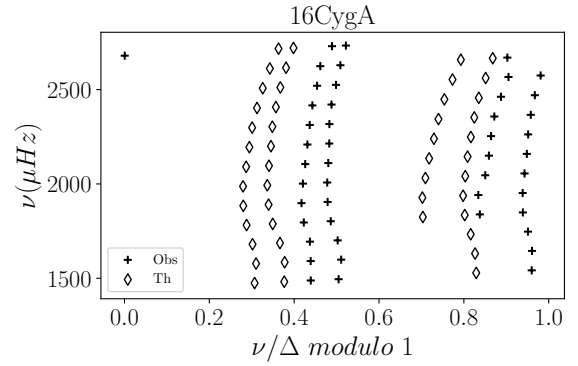


Fig. D.1. Échelle diagram of 16 Cygni A optimal model calculated with seismic indicators defined over frequencies which are not corrected for the surface effects. The crosses are the observed frequencies and the diamonds the theoretical ones.

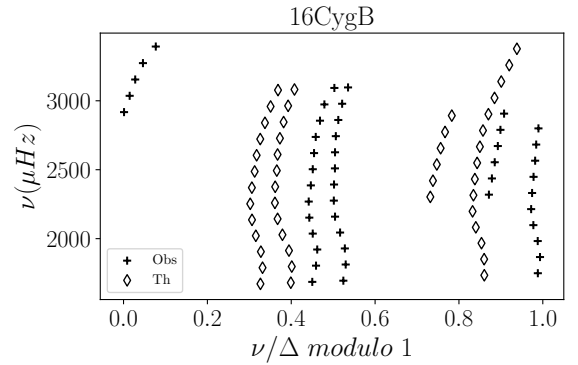


Fig. D.2. Échelle diagram of 16 Cygni B optimal model calculated with seismic indicators defined over frequencies which are not corrected for the surface effects. The crosses are the observed frequencies and the diamonds the theoretical ones.

of optimal parameters for models using frequencies corrected as in Ball & Gizon (2014).

Appendix E: Individual models

In this section, we summarise the set of input physics used in the reference models and gather the individual stellar parameters as well as the uncertainties propagated during the

Table E.1. Summary of the physical ingredients included in the reference models, denoted AGSS09.

Inp. Phys.	Value	Refs.
Solar mixture	AGSS09	Asplund et al. (2009)
Eq. of state	Free EOS	Cassisi et al. (2003)
Opacity	OPAL	Iglesias & Rogers (1996)
α_{MLT}	1.82	Solar calibration
Overshoot	None	/
Diffusion	Yes	Thoul et al. (1994)
Turbulent mix.	None	/
Atmosphere	Eddington $T - \tau$ relation	/
Surf. eff. corr.	Yes	Kjeldsen et al. (2008)

Table E.2. Variations in the input physics, corresponding name and reduced χ^2 values.

Name	Inp. Phys.	Value	χ^2_{A}	χ^2_{B}
AGSS09	Sol. mix.	AGSS09	1.0	0.8
GN93	Sol. mix.	GN93	1.0	1.0
OP	Opac.	OP	0.6	0.6
OPLIB	Opac.	OPLIB	1.2	1.0
CEFF	Eq. of state	CEFF	1.0	0.9
OPAL05	Eq. of state	OPAL05	0.2	1.1
No diff.	Diff.	No	0.9	0.6
D_{turb}	Turb. mix.	$D_{\text{turb}} = 7500$	0.5	0.9
$\alpha_{\text{MLT}} = 1.7$	α_{MLT}	1.7	1.3	0.3
Vernazza	Atmos.	Vernazza et al. (1981)	0.3	0.8
No surf. corr.	Surf. eff. corr.	No	0.1	0.0
$\alpha_{\text{ov}} = 0.1$	Overshoot	0.1	0.8	0.3
$\alpha_{\text{ov}} = 0.2$	Overshoot	0.2	0.4	0.2
$\alpha_{\text{un}} = 0.1$	Undershoot	0.1	0.9	0.7

Levenberg-Marquardt adjustment for each model presented in this paper. Table E.1 presents the set of input physics used in the reference model while Table E.2 summarises the several variations of input physics considered throughout the paper. In the latter, the first column gives the label given to the models considering that specific choice of input physics, the second column is the physical ingredient which is varied upon, the third column is the corresponding value and columns 4 and 5 display the χ^2 values obtained for the optimal models of both stars in each case. Finally, Tables E.3 through E.11 give the complete set of stellar parameters obtained for every case considered in the present paper.

Table E.3. Summary of the fitted models with only the seismic constraints.

Model	Quantity	16CygA	16CygB
AGSS09	$M(M_{\odot})$	1.06 ± 0.02	1.011 ± 0.009
	X_0	0.68 ± 0.01	0.679 ± 0.007
	$(Z/X)_0$	0.035 ± 0.001	0.037 ± 0.002
	Y_0	0.30 ± 0.01	0.296 ± 0.007
	[Fe/H]	0.19 ± 0.01	0.22 ± 0.03
	Y_s	0.243 ± 0.009	0.251 ± 0.004
	$R(R_{\odot})$	1.22 ± 0.03	1.104 ± 0.009
	$t(\text{Gyr})$	6.8 ± 0.2	6.97 ± 0.08
Dark blue GN93	$M(M_{\odot})$	1.068 ± 0.005	1.02 ± 0.01
	X_0	0.690 ± 0.007	0.685 ± 0.007
	$(Z/X)_0$	0.039 ± 0.003	0.040 ± 0.002
	Y_0	0.283 ± 0.008	0.288 ± 0.007
	[Fe/H]	0.23 ± 0.03	0.26 ± 0.03
	Y_s	0.237 ± 0.004	0.245 ± 0.005
	$R(R_{\odot})$	1.222 ± 0.006	1.11 ± 0.01
	$t(\text{Gyr})$	6.59 ± 0.09	6.76 ± 0.06
Light blue OP	$M(M_{\odot})$	1.053 ± 0.008	1.01 ± 0.01
	X_0	0.68 ± 0.01	0.678 ± 0.007
	$(Z/X)_0$	0.035 ± 0.004	0.039 ± 0.002
	Y_0	0.30 ± 0.01	0.296 ± 0.007
	[Fe/H]	0.19 ± 0.06	0.25 ± 0.03
	Y_s	0.244 ± 0.008	0.252 ± 0.005
	$R(R_{\odot})$	1.217 ± 0.009	1.11 ± 0.01
	$t(\text{Gyr})$	6.80 ± 0.09	7.0 ± 0.1
Light brown OPLIB	$M(M_{\odot})$	1.042 ± 0.009	0.99 ± 0.01
	X_0	0.68 ± 0.01	0.673 ± 0.008
	$(Z/X)_0$	0.032 ± 0.004	0.036 ± 0.001
	Y_0	0.30 ± 0.01	0.303 ± 0.008
	[Fe/H]	0.16 ± 0.05	0.20 ± 0.01
	Y_s	0.244 ± 0.007	0.258 ± 0.005
	$R(R_{\odot})$	1.21 ± 0.01	1.10 ± 0.01
	$t(\text{Gyr})$	6.41 ± 0.08	6.61 ± 0.09
Beige CEFF	$M(M_{\odot})$	1.07 ± 0.01	1.02 ± 0.01
	X_0	0.698 ± 0.009	0.681 ± 0.008
	$(Z/X)_0$	0.031 ± 0.001	0.037 ± 0.002
	Y_0	0.280 ± 0.009	0.294 ± 0.008
	[Fe/H]	0.12 ± 0.02	0.22 ± 0.03
	Y_s	0.229 ± 0.005	0.249 ± 0.005
	$R(R_{\odot})$	1.22 ± 0.01	1.11 ± 0.01
	$t(\text{Gyr})$	6.9 ± 0.1	7.0 ± 0.1
Dark brown OPAL05	$M(M_{\odot})$	1.06 ± 0.02	1.010 ± 0.009
	X_0	0.69 ± 0.02	0.669 ± 0.006
	$(Z/X)_0$	0.033 ± 0.002	0.040 ± 0.002
	Y_0	0.29 ± 0.02	0.304 ± 0.004
	[Fe/H]	0.16 ± 0.03	0.25 ± 0.03
	Y_s	0.237 ± 0.009	0.259 ± 0.004
	$R(R_{\odot})$	1.22 ± 0.02	1.10 ± 0.01
	$t(\text{Gyr})$	6.8 ± 0.2	6.92 ± 0.08
Grey No diff.	$M(M_{\odot})$	1.109 ± 0.007	1.063 ± 0.008
	X_0	0.763 ± 0.007	0.754 ± 0.006
	$(Z/X)_0$	0.020 ± 0.001	0.0214 ± 0.0009
	Y_0	0.22 ± 0.01	0.230 ± 0.009
	[Fe/H]	0.04 ± 0.02	0.07 ± 0.02
	Y_s	0.221 ± 0.007	0.230 ± 0.006
	$R(R_{\odot})$	1.237 ± 0.008	1.123 ± 0.009
	$t(\text{Gyr})$	7.5 ± 0.1	7.50 ± 0.07
Light pink	$M(M_{\odot})$	1.109 ± 0.007	1.063 ± 0.008
	X_0	0.763 ± 0.007	0.754 ± 0.006
	$(Z/X)_0$	0.020 ± 0.001	0.0214 ± 0.0009
	Y_0	0.22 ± 0.01	0.230 ± 0.009
	[Fe/H]	0.04 ± 0.02	0.07 ± 0.02
	Y_s	0.221 ± 0.007	0.230 ± 0.006
	$R(R_{\odot})$	1.237 ± 0.008	1.123 ± 0.009
	$t(\text{Gyr})$	7.5 ± 0.1	7.50 ± 0.07

Notes. The reference model, labelled AGSS09, corresponds to the choice of physics described in Sects. 2.3 and E.1. The individual uncertainties result from the error propagation during the Levenberg-Marquardt adjustment.

Table E.3. continued.

Model	Quantity	16CygA	16CygB
D_{turb}	$M(M_{\odot})$	1.07 ± 0.01	1.02 ± 0.01
	X_0	0.705 ± 0.004	0.697 ± 0.008
	$(Z/X)_0$	0.029 ± 0.002	0.032 ± 0.002
	Y_0	0.274 ± 0.004	0.281 ± 0.008
	$[\text{Fe}/\text{H}]$	0.14 ± 0.03	0.17 ± 0.03
	Y_s	0.239 ± 0.003	0.248 ± 0.006
	$R(R_{\odot})$	1.22 ± 0.02	1.11 ± 0.01
Purple	$t(\text{Gyr})$	6.9 ± 0.1	7.0 ± 0.1
$\alpha_{\text{MLT}} = 1.7$	$M(M_{\odot})$	1.03 ± 0.01	0.98 ± 0.02
	X_0	0.68 ± 0.01	0.66 ± 0.01
	$(Z/X)_0$	0.033 ± 0.004	0.041 ± 0.003
	Y_0	0.30 ± 0.01	0.31 ± 0.01
	$[\text{Fe}/\text{H}]$	0.16 ± 0.07	0.26 ± 0.04
	Y_s	0.242 ± 0.007	0.263 ± 0.006
	$R(R_{\odot})$	1.21 ± 0.01	1.09 ± 0.02
Yellow	$t(\text{Gyr})$	7.1 ± 0.2	7.3 ± 0.4
Vernazza	$M(M_{\odot})$	1.020 ± 0.009	0.97 ± 0.01
	X_0	0.675 ± 0.009	0.66 ± 0.01
	$(Z/X)_0$	0.035 ± 0.002	0.040 ± 0.001
	Y_0	0.30 ± 0.01	0.32 ± 0.01
	$[\text{Fe}/\text{H}]$	0.17 ± 0.03	0.25 ± 0.01
	Y_s	0.248 ± 0.005	0.268 ± 0.006
	$R(R_{\odot})$	1.20 ± 0.01	1.09 ± 0.02
No surf. corr.	$t(\text{Gyr})$	7.2 ± 0.1	7.4 ± 0.1
	$M(M_{\odot})$	1.08 ± 0.02	1.028 ± 0.009
	X_0	0.69 ± 0.01	0.696 ± 0.008
	$(Z/X)_0$	0.038 ± 0.002	0.033 ± 0.002
	Y_0	0.28 ± 0.01	0.281 ± 0.008
	$[\text{Fe}/\text{H}]$	0.22 ± 0.03	0.17 ± 0.03
	Y_s	0.236 ± 0.007	0.237 ± 0.005
Dark green	$R(R_{\odot})$	1.24 ± 0.03	1.12 ± 0.01
	$t(\text{Gyr})$	7.0 ± 0.1	7.05 ± 0.06
$\alpha_{\text{ov}} = 0.1$	$M(M_{\odot})$	1.058 ± 0.007	1.01 ± 0.02
	X_0	0.68 ± 0.01	0.679 ± 0.006
	$(Z/X)_0$	0.035 ± 0.003	0.036 ± 0.004
	Y_0	0.30 ± 0.01	0.297 ± 0.007
	$[\text{Fe}/\text{H}]$	0.19 ± 0.05	0.20 ± 0.04
	Y_s	0.243 ± 0.006	0.251 ± 0.004
	$R(R_{\odot})$	1.218 ± 0.09	1.10 ± 0.02
Red	$t(\text{Gyr})$	6.8 ± 0.2	6.9 ± 0.1
$\alpha_{\text{ov}} = 0.2$	$M(M_{\odot})$	0.920 ± 0.009	1.016 ± 0.009
	X_0	0.700 ± 0.006	0.682 ± 0.007
	$(Z/X)_0$	0.0106 ± 0.0002	0.036 ± 0.002
	Y_0	0.293 ± 0.006	0.293 ± 0.007
	$[\text{Fe}/\text{H}]$	-0.39 ± 0.01	0.21 ± 0.02
	Y_s	0.217 ± 0.002	0.249 ± 0.004
	$R(R_{\odot})$	1.16 ± 0.01	1.11 ± 0.01
$\alpha_{\text{un}} = 0.1$	$t(\text{Gyr})$	7.16 ± 0.06	6.97 ± 0.09
	$M(M_{\odot})$	1.06 ± 0.01	1.012 ± 0.007
	X_0	0.688 ± 0.009	0.680 ± 0.008
	$(Z/X)_0$	0.034 ± 0.001	0.036 ± 0.002
	Y_0	0.289 ± 0.009	0.295 ± 0.008
	$[\text{Fe}/\text{H}]$	0.17 ± 0.02	0.22 ± 0.03
	Y_s	0.241 ± 0.005	0.252 ± 0.005
Khaki	$R(R_{\odot})$	1.22 ± 0.01	1.105 ± 0.008
	$t(\text{Gyr})$	6.78 ± 0.09	6.97 ± 0.07

Table E.4. Adjusted stellar parameters using the temperature profile from Vernazza et al. (1981) with a solar calibrated value of $\alpha_{\text{MLT}} = 2.02$.

Quantity	16CygA	16CygB
$M(M_{\odot})$	1.06 ± 0.01	1.02 ± 0.01
X_0	0.68 ± 0.01	0.684 ± 0.006
$(Z/X)_0$	0.035 ± 0.004	0.035 ± 0.002
Y_0	0.29 ± 0.01	0.292 ± 0.006
$[\text{Fe}/\text{H}]$	0.20 ± 0.03	0.18 ± 0.06
Y_s	0.243 ± 0.006	0.248 ± 0.04
$R(R_{\odot})$	1.22 ± 0.01	1.10 ± 0.01
$t(\text{Gyr})$	6.7 ± 0.2	6.9 ± 0.1
α_{MLT}	2.02	

Table E.5. Results of the modelling considering only seismic constraints with different values of the mixing length coefficient.

α_{MLT}	Quantity	16CygA	16CygB
1.7	$M(M_{\odot})$	1.03 ± 0.01	0.98 ± 0.02
	X_0	0.68 ± 0.01	0.66 ± 0.01
	$(Z/X)_0$	0.033 ± 0.004	0.041 ± 0.003
	Y_0	0.30 ± 0.01	0.31 ± 0.01
	$[\text{Fe}/\text{H}]$	0.16 ± 0.07	0.26 ± 0.04
	Y_s	0.242 ± 0.007	0.263 ± 0.006
	$R(R_{\odot})$	1.21 ± 0.01	1.09 ± 0.02
1.82	$t(\text{Gyr})$	7.1 ± 0.2	7.3 ± 0.4
	$M(M_{\odot})$	1.06 ± 0.02	1.011 ± 0.009
	X_0	0.68 ± 0.01	0.679 ± 0.007
	$(Z/X)_0$	0.035 ± 0.001	0.037 ± 0.002
	Y_0	0.30 ± 0.01	0.296 ± 0.007
	$[\text{Fe}/\text{H}]$	0.19 ± 0.01	0.22 ± 0.03
	Y_s	0.243 ± 0.009	0.251 ± 0.004
2.0	$R(R_{\odot})$	1.22 ± 0.03	1.104 ± 0.009
	$t(\text{Gyr})$	6.8 ± 0.2	6.97 ± 0.08
	$M(M_{\odot})$	1.108 ± 0.009	1.058 ± 0.009
	X_0	0.705 ± 0.007	0.705 ± 0.06
	$(Z/X)_0$	0.033 ± 0.002	0.032 ± 0.002
	Y_0	0.272 ± 0.007	0.272 ± 0.06
	$[\text{Fe}/\text{H}]$	0.16 ± 0.03	0.16 ± 0.04
	Y_s	0.227 ± 0.004	0.232 ± 0.004
	$R(R_{\odot})$	1.23 ± 0.01	1.12 ± 0.01
	$t(\text{Gyr})$	6.4 ± 0.1	6.6 ± 0.1

Table E.6. Results of the modelling considering only seismic constraints and including turbulent mixing with different values of the turbulent mixing coefficient.

D_{turb} ($\text{cm}^2 \text{s}^{-1}$)	Quantity	16CygA	16CygB
2000	$M(M_{\odot})$	1.07 ± 0.01	1.024 ± 0.008
	X_0	0.70 ± 0.01	0.697 ± 0.007
	$(Z/X)_0$	0.029 ± 0.001	0.032 ± 0.002
	Y_0	0.27 ± 0.01	0.281 ± 0.007
	$[\text{Fe}/\text{H}]$	0.12 ± 0.02	0.17 ± 0.02
	Y_s	0.236 ± 0.007	0.246 ± 0.005
	$R(R_{\odot})$	1.22 ± 0.01	1.109 ± 0.009
	$t(\text{Gyr})$	6.9 ± 0.1	6.99 ± 0.07
5000	$M(M_{\odot})$	1.1 ± 0.1	1.023 ± 0.007
	X_0	0.7 ± 0.1	0.697 ± 0.006
	$(Z/X)_0$	0.03 ± 0.01	0.032 ± 0.001
	Y_0	0.3 ± 0.1	0.280 ± 0.006
	$[\text{Fe}/\text{H}]$	0.1 ± 0.2	0.17 ± 0.02
	Y_s	0.24 ± 0.07	0.247 ± 0.004
	$R(R_{\odot})$	1.2 ± 0.1	1.109 ± 0.007
	$t(\text{Gyr})$	6.8 ± 0.8	6.99 ± 0.06
7500	$M(M_{\odot})$	1.07 ± 0.01	1.02 ± 0.01
	X_0	0.705 ± 0.004	0.697 ± 0.008
	$(Z/X)_0$	0.029 ± 0.002	0.032 ± 0.002
	Y_0	0.274 ± 0.004	0.281 ± 0.008
	$[\text{Fe}/\text{H}]$	0.14 ± 0.03	0.17 ± 0.03
	Y_s	0.239 ± 0.003	0.248 ± 0.006
	$R(R_{\odot})$	1.22 ± 0.02	1.11 ± 0.01
	$t(\text{Gyr})$	6.9 ± 0.1	7.0 ± 0.1
10 000	$M(M_{\odot})$	1.03 ± 0.01	0.98 ± 0.02
	X_0	0.70 ± 0.01	0.66 ± 0.01
	$(Z/X)_0$	0.029 ± 0.001	0.032 ± 0.001
	Y_0	0.27 ± 0.01	0.280 ± 0.006
	$[\text{Fe}/\text{H}]$	0.14 ± 0.02	0.17 ± 0.02
	Y_s	0.240 ± 0.007	0.248 ± 0.004
	$R(R_{\odot})$	1.22 ± 0.01	1.109 ± 0.007
	$t(\text{Gyr})$	6.9 ± 0.1	6.99 ± 0.06

Table E.7. Adjusted stellar parameters including the effective temperature constraint with the OPLIB opacity table and with a fixed turbulent mixing coefficient.

Quantity	16CygA
$M(M_{\odot})$	1.05 ± 0.07
X_0	0.70 ± 0.08
$(Z/X)_0$	0.028 ± 0.001
Y_0	0.27 ± 0.08
$[\text{Fe}/\text{H}]$	0.1 ± 0.1
Y_s	0.24 ± 0.03
$R(R_{\odot})$	1.21 ± 0.05
$t(\text{Gyr})$	6.6 ± 0.4
D_{turb}	$0.2 \cdot 10^4$

Table E.8. Adjusted stellar parameters imposing a common age and initial composition for both stars for the different variations in physics.

Model	Quantity	16CygA	16CygB
AGSS09	$M(M_{\odot})$	1.05 ± 0.01	1.015 ± 0.006
	$[\text{Fe}/\text{H}]$	0.20 ± 0.01	0.21 ± 0.01
	Y_s	0.245 ± 0.003	0.250 ± 0.003
	$R(R_{\odot})$	1.21 ± 0.01	1.106 ± 0.007
	X_0	0.681 ± 0.006	
	$(Z/X)_0$	0.0360 ± 0.0009	
	Y_0	0.294 ± 0.006	
	$t(\text{Gyr})$	6.87 ± 0.04	
D_{turb}	$M(M_{\odot})$	1.063 ± 0.006	1.024 ± 0.005
	$[\text{Fe}/\text{H}]$	0.144 ± 0.009	0.15 ± 0.01
	Y_s	0.242 ± 0.003	0.245 ± 0.004
	$R(R_{\odot})$	1.220 ± 0.007	1.109 ± 0.006
	X_0	0.702 ± 0.005	
	$(Z/X)_0$	0.0300 ± 0.0006	
	Y_0	0.277 ± 0.005	
	$t(\text{Gyr})$	0.692 ± 0.006	
No Diff.	$M(M_{\odot})$	1.10 ± 0.01	1.068 ± 0.004
	$[\text{Fe}/\text{H}]$	0.058 ± 0.009	0.058 ± 0.009
	Y_s	0.225 ± 0.004	0.225 ± 0.004
	$R(R_{\odot})$	1.24 ± 0.01	1.114 ± 0.004
	X_0	0.759 ± 0.004	
	$(Z/X)_0$	0.0207 ± 0.0004	
	Y_0	0.225 ± 0.004	
	$t(\text{Gyr})$	7.50 ± 0.05	
$\alpha_{\text{ov}} = 0.1$	$M(M_{\odot})$	1.052 ± 0.007	1.013 ± 0.006
	$[\text{Fe}/\text{H}]$	0.19 ± 0.01	0.20 ± 0.01
	Y_s	0.245 ± 0.003	0.250 ± 0.003
	$R(R_{\odot})$	1.214 ± 0.008	1.105 ± 0.006
	X_0	0.681 ± 0.005	
	$(Z/X)_0$	0.0355 ± 0.0007	
	Y_0	0.294 ± 0.005	
	$t(\text{Gyr})$	6.85 ± 0.04	
α_{MLT} from T_{eff} fit	$M(M_{\odot})$	1.072 ± 0.004	1.039 ± 0.003
	$[\text{Fe}/\text{H}]$	0.145 ± 0.007	0.159 ± 0.007
	Y_s	0.234 ± 0.002	0.240 ± 0.002
	$R(R_{\odot})$	1.226 ± 0.006	1.114 ± 0.004
	α_{MLT}	1.85	1.99
	X_0	0.696 ± 0.003	
	$(Z/X)_0$	0.0320 ± 0.0004	
	Y_0	0.282 ± 0.003	
	$t(\text{Gyr})$	6.63 ± 0.05	
Vernazza calibrated α_{MLT}	$M(M_{\odot})$	1.054 ± 0.006	1.016 ± 0.006
	$[\text{Fe}/\text{H}]$	0.18 ± 0.01	0.19 ± 0.01
	Y_s	0.244 ± 0.003	0.249 ± 0.003
	$R(R_{\odot})$	1.216 ± 0.007	1.105 ± 0.006
	α_{MLT}	2.02	
	X_0	0.682 ± 0.005	
	$(Z/X)_0$	0.0352 ± 0.0007	
	Y_0	0.293 ± 0.005	
	$t(\text{Gyr})$	6.82 ± 0.05	

Table E.9. Differences between theoretical and observed values for the seismic constraints, for the several variations in physics, defined as $\delta = |I_{\text{obs}} - I_{\text{th}}|$, in the units of the constraint.

Model	Quantity	16CygA		16CygB	
		δ	δ/σ	δ	δ/σ
AGSS09	Δ (μHz)	0.2	47.4	10^{-3}	0.2
	A_{He}	0.7	0.7	0.7	0.7
	$\hat{\nu}_{01}$	$5 \cdot 10^{-5}$	0.2	10^{-4}	0.8
	$\hat{\nu}_{02}$	$6 \cdot 10^{-4}$	2.0	$4 \cdot 10^{-4}$	1.4
	χ^2_{red}	751.9			
	BIC	2266.2			
D_{turb}	Δ (μHz)	0.06	13.6	$7 \cdot 10^{-3}$	1.6
	A_{He}	0.4	0.4	0.2	0.2
	$\hat{\nu}_{01}$	$2 \cdot 10^{-5}$	0.1	$3 \cdot 10^{-4}$	1.3
	$\hat{\nu}_{02}$	$4 \cdot 10^{-4}$	1.2	$3 \cdot 10^{-4}$	1.1
	χ^2_{red}	63.3			
	BIC	200.4			
No Diff.	Δ (μHz)	0.01	3.0	$3 \cdot 10^{-5}$	0.007
	A_{He}	0.7	0.7	0.3	0.3
	$\hat{\nu}_{01}$	10^{-4}	0.4	10^{-4}	0.7
	$\hat{\nu}_{02}$	10^{-4}	0.4	10^{-4}	0.4
	χ^2_{red}	3.4			
	BIC	20.7			
$\alpha_{\text{ov}} = 0.1$	Δ (μHz)	0.3	59.7	$1 \cdot 10^{-4}$	0.03
	A_{He}	0.8	0.8	0.6	0.6
	$\hat{\nu}_{01}$	$3 \cdot 10^{-5}$	0.1	$2 \cdot 10^{-4}$	0.9
	$\hat{\nu}_{02}$	$5 \cdot 10^{-4}$	1.6	$4 \cdot 10^{-4}$	1.6
	χ^2_{red}	1188.8			
	BIC	3576.7			
α_{MLT} from T_{eff} fit	Δ (μHz)	0.2	52.8	10^{-3}	0.2
	A_{He}	0.2	0.2	0.5	0.5
	$\hat{\nu}_{01}$	$2 \cdot 10^{-4}$	1.0	$4 \cdot 10^{-4}$	2.0
	$\hat{\nu}_{02}$	$4 \cdot 10^{-4}$	1.3	$6 \cdot 10^{-4}$	2.2
	χ^2_{red}	928.4			
	BIC	2795.6			
Vernazza calibrated α_{MLT}	Δ (μHz)	0.01	3.0	$7 \cdot 10^{-4}$	0.1
	A_{He}	0.7	0.7	0.3	0.3
	$\hat{\nu}_{01}$	10^{-4}	0.4	10^{-4}	0.7
	$\hat{\nu}_{02}$	10^{-4}	0.4	10^{-4}	0.4
	χ^2_{red}	2.9			
	BIC	19.2			

Notes. $\chi^2_{\text{red}} = \chi^2/(N - k)$ is the reduced χ^2 value where N is the number of constraints to the fit and k the number of free parameters. The BIC value is defined in Sect. 4.3.

Table E.10. Same as Table E.8, but without imposing a common composition for the two stars.

Model	Quantity	16CygA	16CygB
AGSS09	$M(M_{\odot})$	1.05 ± 0.04	1.017 ± 0.007
	[Fe/H]	0.20 ± 0.05	0.23 ± 0.02
	Y_s	0.25 ± 0.01	0.251 ± 0.004
	$R(R_{\odot})$	1.21 ± 0.04	1.106 ± 0.008
	X_0	0.68 ± 0.02	0.679 ± 0.006
	$(Z/X)_0$	0.037 ± 0.003	0.038 ± 0.002
	Y_0	0.29 ± 0.02	0.295 ± 0.006
	$t(\text{Gyr})$	6.86 ± 0.06	
	D_{turb}	1.1 ± 0.1	1.02 ± 0.05
	[Fe/H]	0.1 ± 0.1	0.2 ± 0.1
D_{turb}	Y_s	0.24 ± 0.04	0.25 ± 0.03
	$R(R_{\odot})$	1.2 ± 0.1	1.11 ± 0.05
	X_0	0.70 ± 0.06	0.70 ± 0.05
	$(Z/X)_0$	0.029 ± 0.007	0.031 ± 0.009
	Y_0	0.27 ± 0.06	0.28 ± 0.04
	$t(\text{Gyr})$	6.9 ± 0.1	
	No Diff.	1.11 ± 0.02	1.064 ± 0.006
	[Fe/H]	0.04 ± 0.02	0.06 ± 0.02
	Y_s	0.221 ± 0.008	0.228 ± 0.005
	$R(R_{\odot})$	1.23 ± 0.02	1.123 ± 0.007
$\alpha_{\text{ov}} = 0.1$	X_0	0.763 ± 0.008	0.756 ± 0.005
	$(Z/X)_0$	0.0200 ± 0.0008	0.021 ± 0.001
	Y_0	0.221 ± 0.008	0.228 ± 0.005
	$t(\text{Gyr})$	7.51 ± 0.07	
	$M(M_{\odot})$	1.05 ± 0.02	1.010 ± 0.009
	[Fe/H]	0.19 ± 0.03	0.19 ± 0.02
	Y_s	0.245 ± 0.007	0.250 ± 0.003
	$R(R_{\odot})$	1.21 ± 0.02	1.10 ± 0.01
	X_0	0.68 ± 0.01	0.681 ± 0.006
	$(Z/X)_0$	0.035 ± 0.002	0.035 ± 0.002
α_{MLT} from T_{eff} fit	Y_0	0.29 ± 0.01	0.295 ± 0.006
	$t(\text{Gyr})$	6.86 ± 0.05	
	$M(M_{\odot})$	1.072 ± 0.004	1.039 ± 0.003
	[Fe/H]	0.145 ± 0.007	0.159 ± 0.007
	Y_s	0.234 ± 0.002	0.240 ± 0.002
	$R(R_{\odot})$	1.226 ± 0.006	1.114 ± 0.004
	α_{MLT}	1.85	1.99
	X_0	0.696 ± 0.003	0.696 ± 0.003
	$(Z/X)_0$	0.0320 ± 0.0004	0.0320 ± 0.0004
	Y_0	0.282 ± 0.003	0.282 ± 0.003
Vernazza calibrated α_{MLT}	$t(\text{Gyr})$	6.63 ± 0.05	
	$M(M_{\odot})$	1.05 ± 0.02	1.017 ± 0.008
	[Fe/H]	0.18 ± 0.02	0.20 ± 0.02
	Y_s	0.244 ± 0.007	0.249 ± 0.004
	$R(R_{\odot})$	1.21 ± 0.02	1.105 ± 0.009
	α_{MLT}	2.02	
	X_0	0.68 ± 0.01	0.683 ± 0.007
	$(Z/X)_0$	0.035 ± 0.002	0.035 ± 0.001
	Y_0	0.29 ± 0.01	0.293 ± 0.007
	$t(\text{Gyr})$	6.82 ± 0.06	

Table E.11. Same as Table E.9, but without imposing a common composition for the two stars.

Model	Quantity	16CygA		16CygB	
		δ	δ/σ	δ	δ/σ
AGSS09	Δ (μHz)	0.1	31.7	$6 \cdot 10^{-3}$	1.3
	A_{He}	0.9	0.9	1.5	1.5
	\hat{r}_{01}	$4 \cdot 10^{-5}$	0.1	$5 \cdot 10^{-4}$	0.2
	\hat{r}_{02}	$6 \cdot 10^{-4}$	1.9	$4 \cdot 5 \cdot 10^{-4}$	1.7
	χ^2_{red}			1020.9	
	BIC			1035.5	
D_{turb}	Δ (μHz)	$3 \cdot 10^{-3}$	0.2	$2 \cdot 10^{-5}$	0.05
	A_{He}	0.3	0.3	0.6	0.6
	\hat{r}_{01}	$3 \cdot 10^{-5}$	0.1	$3 \cdot 10^{-4}$	1.4
	\hat{r}_{02}	$2 \cdot 10^{-4}$	0.6	$3 \cdot 10^{-4}$	1.2
	χ^2_{red}			4.4	
	BIC			19.0	
No Diff.	Δ (μHz)	$3 \cdot 10^{-3}$	0.6	$0.2 \cdot 10^{-3}$	0.05
	A_{He}	0.002	0.002	0.02	0.02
	\hat{r}_{01}	10^{-4}	0.5	$0.4 \cdot 10^{-4}$	0.2
	\hat{r}_{02}	$0.2 \cdot 10^{-4}$	0.07	$0.5 \cdot 10^{-4}$	0.2
	χ^2_{red}			0.8	
	BIC			15.3	
$\alpha_{\text{ov}} = 0.1$	Δ (μHz)	0.2	49.1	$3 \cdot 10^{-4}$	0.007
	A_{He}	0.7	0.7	0.2	0.2
	\hat{r}_{01}	$3 \cdot 6 \cdot 10^{-5}$	0.2	$2 \cdot 10^{-4}$	0.9
	\hat{r}_{02}	$6 \cdot 10^{-4}$	1.7	$3 \cdot 10^{-4}$	1.2
	χ^2_{red}			2426.7	
	BIC			2441.3	
α_{MLT} from T_{eff} fit	Δ (μHz)	0.2	52.8	10^{-3}	0.2
	A_{He}	0.2	0.2	0.5	0.5
	\hat{r}_{01}	$2 \cdot 10^{-4}$	1.0	$4 \cdot 10^{-4}$	2.0
	\hat{r}_{02}	$4 \cdot 10^{-4}$	1.3	$6 \cdot 10^{-4}$	2.2
	χ^2_{red}			928.4	
	BIC			2795.6	
Vernazza calibrated α_{MLT}	Δ (μHz)	$2 \cdot 10^{-4}$	0.05	$5 \cdot 10^{-6}$	0.001
	A_{He}	0.5	0.5	0.7	0.7
	\hat{r}_{01}	$6 \cdot 10^{-4}$	1.9	10^{-4}	0.9
	\hat{r}_{02}	$3 \cdot 10^{-4}$	1.1	$2 \cdot 10^{-4}$	0.8
	χ^2_{red}			7.1	
	BIC			21.7	

DETERMINATION OF PRECISE STELLAR PARAMETERS OF KEPLER LEGACY TARGETS USING THE WHOSGLAD METHOD

M. Farnir¹, M.-A. Dupret¹, S.J.A.J. Salmon¹, A. Noels¹ and G. Buldgen²

Abstract. We developed a method, WhoSGLAd, that provides a comprehensive adjustment of solar like oscillations spectra. It allows for tighter constraints (up to four times smaller standard deviations than that of analogous ones). We take advantage of this new method and of the quality of the *Kepler* LEGACY data to highlight trends in the stellar parameters as well as the limitations of the current generation of stellar models.

Keywords: asteroseismology, stars: oscillations, stars: solar-type, stars: abundances, methods: numerical

1 Introduction

In the recent years, space missions such as *Kepler* (Borucki et al. 2010), CoRoT (Baglin et al. 2009) and BRITE (Weiss et al. 2014) provided a wealth of data of unprecedented quality. This has allowed asteroseismology to become a very efficient tool to constrain the stellar structure. Moreover, owing to the high quality of the data, it becomes possible to study acoustic glitches. Those are oscillating signatures in frequency spectra that are caused by a sharp variation* in the stellar structure. Therefore, they provide very localised and invaluable information. For example, several studies have taken advantage of the glitches to infer the surface helium content in solar-like pulsators, which cannot be measured by any other technique. The idea to use such glitches to constraint the stellar structure was first formulated by Gough (1990) and Vorontsov (1988). Since then, several studies including acoustic glitches have been carried out, among which we may cite Basu et al. (2004) and Verma et al. (2014). In a previous paper (Farnir et al. 2019), we have presented a new method, WhoSGLAd, to adjust simultaneously the signature of such glitches and the smoothly varying component of the oscillation spectrum. This method has the advantage of providing constraints correlated as little as possible thanks to the use of Gram-Schmidt's orthogonalisation process. Moreover, the standard deviation of the defined seismic indicators are up to four times smaller than the usual ones. In these proceedings, we shortly recall the principle of the WhoSGLAd method and present its application to the study of the *Kepler* LEGACY sample (Lund et al. 2017) as well to the in depth study of 16 Cygni A.

2 Principle

2.1 Mathematical description

This section consists of a very brief description of the WhoSGLAd method's principle. More information may be found in Farnir et al. (2019). To describe a set of observed frequencies, ν_{obs}^\dagger , we built a euclidean vector space of functions. The following scalar product is defined:

$$\langle \mathbf{x} | \mathbf{y} \rangle = \sum_{i=1}^N \frac{x_i y_i}{\sigma_i^2}, \quad (2.1)$$

¹ Institut d'Astrophysique et Géophysique de l'Université de Liège, Allée du 6 août 17, 4000 Liège, Belgium

² Observatoire de Genève, Université de Genève, 51 Ch. Des Maillettes, 1290 Sauverny, Switzerland

*compared to the wavelength of the incoming wave

[†]We here denote by the *obs* subscript, frequencies to be adjusted, be them observed or model frequencies.

where \mathbf{x} and \mathbf{y} are two sets of N frequencies and σ_i are the individual standard deviations. In this vector space we represent the smooth part of the oscillation spectrum as polynomials in the radial order n and the glitch part as oscillating functions linearised for the fitted coefficients. Then, using the Gram-Schmidt's orthogonalisation process, we build an orthonormal basis over this vector space. If we write $p_j(n, l)$ the former basis elements, $q_{j_0}(n, l)$ the orthonormal basis elements and R_{j,j_0}^{-1} the transformation matrix, we have:

$$q_{j_0}(n, l) = \sum_{j \leq j_0} R_{j,j_0}^{-1} p_j(n, l). \quad (2.2)$$

Finally, using the scalar product 2.1, we project the frequencies over the successive basis elements. The fitted frequencies are thus:

$$\nu_f(n, l) = \sum_j a_j q_j(n, l), \quad (2.3)$$

where a_j are the fitted coefficients and $q_j(n, l)$ the orthonormal basis elements. It is essential to note that, owing to the orthonormalisation, all the coefficients a_j are completely independent of each other. Therefore, while the glitch and smooth components are treated simultaneously they are fully uncorrelated.

2.2 Useful seismic indicators

Combining in a clever way the adjusted coefficients, we may construct seismic indicators as uncorrelated as possible for the stellar structure that are proxies of the 'usual' ones.

Large separation: At first order, the smooth part of the spectrum is approximated by a straight line. For a given spherical degree, the slope of this line is the large separation for this degree. In our formulation, we obtain[‡]

$$\Delta_l = a_{l,1} R_{l,1,1}^{-1} \quad (2.4)$$

Averaging this quantity over the range of observed spherical degrees, we get:

$$\Delta = \frac{\sum_l a_{l,1} / R_{l,1,1}^{-1}}{\sum_l 1 / \left(R_{l,1,1}^{-1}\right)^2} \quad (2.5)$$

Small separation ratios: Analogous to Roxburgh & Vorontsov (2003), we may define averaged small separation ratios as:

$$\hat{r}_{0,l} = \frac{\bar{\nu}_0 - \bar{\nu}_l}{\Delta_0} + \bar{n}_l - \bar{n}_0 + \frac{l}{2}, \quad (2.6)$$

where the overlined symbols represent the mean value of those quantities calculated using our scalar product. We show in Farnir et al. (2019) that these ratios are almost independent of the surface effects, as expected from Roxburgh & Vorontsov (2003).

Large separation ratios: We define:

$$\Delta_{0l} = \frac{\Delta_l}{\Delta_0} - 1 \quad (2.7)$$

It is straightforward to show that it represents the mean slope of r_{010} , which is the combination of the small separation ratios r_{01} and r_{10} (Roxburgh & Vorontsov 2003).

Helium glitch amplitude: We define the amplitude of the helium glitch, $\delta\nu_{\text{He}}$, as the norm of the helium glitch term, i.e.:

$$A_{\text{He}} = \|\delta\nu_{\text{He}}\| = \sqrt{\sum_j a_{j,\text{He}}^2}. \quad (2.8)$$

[‡]Note that, for the smooth part, the j index has been separated into the spherical degree l and the polynomial degree k , as we have different polynomials for each spherical degree.

3 Applications

3.1 Models

Unless specified otherwise, every model was constructed using the CLES stellar evolution code (Scuflaire et al. 2008b) with the AGSS09 solar chemical mixture (Asplund et al. 2009), the OPAL opacity table (Iglesias & Rogers 1996) combined with that of Ferguson et al. (2005) at low temperatures, the FreeEOS software to generate the equation of state table (Cassisi et al. 2003) and the reactions rates prescribed by Adelberger et al. (2011). We also used the mixing length theory (Cox & Giuli 1968), with the solar calibrated value of $\alpha_{\text{MLT}} = l/H_p = 1.82$ (where l is the mixing length and H_p the pressure scale height), to parametrise the mixing inside convective regions. The microscopic diffusion of elements was included and treated as in Thoul et al. (1994). Moreover, the temperature conditions above the photosphere were determined using an Eddington $T(\tau)$ relationship, τ being the optical depth. Finally, the model frequencies were calculated using the LOSC oscillation code (Scuflaire et al. 2008a) which were corrected for the surface effects according to Kjeldsen et al. (2008)'s prescription using the a and b coefficients fitted by Sonoi et al. (2015).

3.2 The *Kepler* LEGACY sample

The *Kepler* LEGACY sample consists of 66 main sequence solar-like stars which have been observed by the *Kepler* telescope for at least one continuous year (Lund et al. 2017). This is therefore the best data available to the asteroseismology of main sequence solar-like pulsators.

For each star in the sample, we tried to provide a fitted model to the observed seismic indicators defined in the previous section and built over the frequencies from Lund et al. (2017). To do so, we first used the AIMS algorithm (Rendle et al. 2019) to provide initial guesses that were then used as starting points by a Levenberg-Marquardt algorithm.

The constraints used are the following seismic indicators: Δ , \hat{r}_{01} , \hat{r}_{02} , Δ_{01} and A_{He} and the metallicity. The free parameters are: the mass, age, initial hydrogen and metal abundances and the overshooting parameter.

From the whole sample, only 18 stars were properly fitted, with a $\chi^2 = \sum_i \left(\frac{y_{\text{th},i} - y_{\text{obs},i}}{\sigma_{\text{obs},i}} \right)^2 \leq 40$. The results are shown in Figs. 1 and 2. Figure 1 shows the initial helium content as a function of the initial metallicity. We observe a correlation which could be a clue of a galactic enrichment. In Fig.2 we show the adjusted overshooting parameter versus the stellar mass. We do not observe a correlation between those two quantities as expected from Claret & Torres (2019). However, the range of masses depicted in their Fig. 10 is much broader than ours and the apparent absence of correlation could result from our restricted mass range. Therefore, to validate both observations, it will be necessary to provide a proper adjustment for as many stars from the sample as possible.

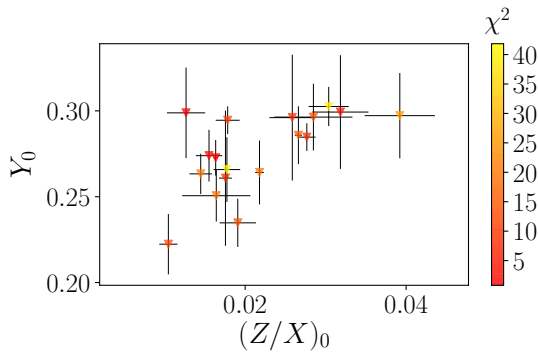


Fig. 1: Best fit values for the initial helium abundance as a function of the initial metallicity. The color code represents the χ^2 value for each model.

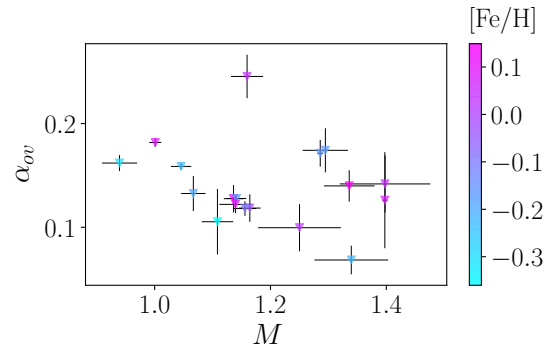


Fig. 2: Best fit values for the step overshooting parameter as a function of the mass. The color code represents the metallicity of the models.

3.3 Application to 16 Cygni A

In the previous subsection, we showed adjustments that were done by considering only one set of physical ingredients. To properly understand the dependency of the stellar parameters on the physics as well as to provide proper standard deviations for these parameters, one has to test different physical ingredients. This is what we did for the specific case of 16 Cyg A. We show in Fig. 3 the results for the different choices of microphysics we considered. The frequencies from which we built our seismic indicators were those determined by Davies et al. (2015). We calculated the models shown in the figure by changing one microphysical ingredient from the reference described in Sec. 3.1 at a time. The reference is shown in black. The considered variations were: the GN93 solar reference (Grevesse & Noels 1993) (in red), the opacity table from the opacity project OP (Badnell et al. 2005) (in green), the LANL/OPLIB opacity table (Colgan et al. 2016) (in blue), the CEFF equation of state (Christensen-Dalsgaard & Daeppen 1992) (in yellow), the OPAL05 equation of state (Rogers & Nayfonov 2002) (in magenta), the inclusion of turbulent mixing (in cyan) following the relation $DDT = D_{\text{turb}} \left(\frac{\rho}{\rho_0} \right)^n + D_{\text{ct}}$, where ρ is the density, ρ_0 the surface density and D_{turb} , n and D_{ct} were fixed at -7500 , -3 and 0 respectively (Proffitt & Michaud 1991). A reduced value of 1.7 for the mixing length parameter (in light green) was also considered. We used Δ , \hat{r}_{01} , \hat{r}_{02} and A_{He} as constraints and the mass, age, initial helium abundance and metallicity as free parameters.

We observe that, given the current precision of both the data and the method, it becomes possible to discriminate between different choices of input physics. We also show with a grey box the luminosity (deduced from the interferometric radius) and effective temperature (White et al. 2013). These constraints were not included during the fit, we merely show the discrepancy of the results with those. Only a few models lie in the box, one of them relying on non classical physics (the cyan model includes turbulent mixing). This clearly illustrates the limitations of the forward approach for the stellar modelling as well as that of our knowledge about the stellar structure. To further improve our results and highlight the necessary improvements to the stellar models, one should consider making use of inverse techniques as in Buldgen et al. (2016).

4 Conclusions

The WhoSGLAd method allows us to provide a comprehensive adjustment of solar-like pulsators oscillations spectra as a whole (glitch and smooth parts) and to put tighter seismic constraints (up to four time smaller than ‘classical’ ones) on the stellar structure. Combined with the precision of the *Kepler* LEGACY data, it becomes possible to observe trends over the whole sample (we note a correlation between the initial helium content and the initial metallicity) as well as the limitations of the current stellar models. It therefore becomes necessary to refine those by, for example, improving the treatment of convection or including non-standard physics (e.g. turbulent mixing, revised abundances and opacities). Moreover, to go even further in the modelling, combining the promising WhoSGLAd method with inverse techniques may be of great help. Finally, the adaptation of the method to the more complex case of subgiants exhibiting mixed modes will be a natural step as those present the regularities of p and g modes, which are well suited for such an approach.

M.F. is supported by the FRIA (Fond pour la Recherche en Industrie et Agriculture) - FNRS PhD grant. S.J.A.J.S. is funded by ARC grant for Concerted Research Actions, financed by the Wallonia-Brussels Federation. G. Buldgen is supported by the Swiss National Science Foundation (project number 200020_172505)

References

- Adelberger, E. G., García, A., Robertson, R. G. H., et al. 2011, *Reviews of Modern Physics*, 83, 195
- Asplund, M., Grevesse, N., Sauval, A. J., & Scott, P. 2009, *ARA&A*, 47, 481
- Badnell, N. R., Bautista, M. A., Butler, K., et al. 2005, *MNRAS*, 360, 458
- Baglin, A., Auvergne, M., Barge, P., et al. 2009, in *IAU Symposium*, Vol. 253, *Transiting Planets*, ed. F. Pont, D. Sasselov, & M. J. Holman, 71–81
- Basu, S., Mazumdar, A., Antia, H. M., & Demarque, P. 2004, *MNRAS*, 350, 277
- Borucki, W. J., Koch, D., Basri, G., et al. 2010, in *Bulletin of the American Astronomical Society*, Vol. 42, *American Astronomical Society Meeting Abstracts #215*, 215
- Buldgen, G., Reese, D. R., & Dupret, M. A. 2016, *A&A*, 585, A109
- Cassisi, S., Salaris, M., & Irwin, A. W. 2003, *ApJ*, 588, 862

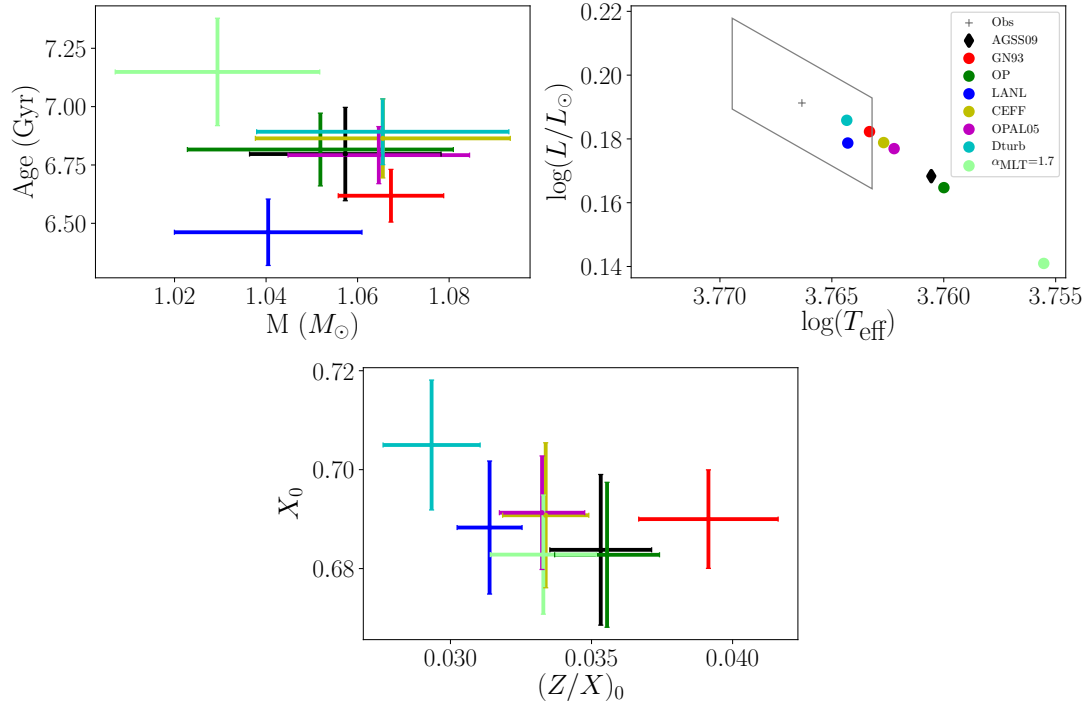


Fig. 3: Ensemble of 16Cyg A best fit models represented in an age - mass diagram (upper left panel), HR diagram (upper right panel) and inial hydrogen - metallicity diagram (lower panel). The different choices of microphysics are represented by the colors. The luminosity (deduced from the interferometric radius) and effective temperature (White et al. 2013) observed values and standard deviations are represented by the grey box in the upper right panel.

- Christensen-Dalsgaard, J. & Daeppen, W. 1992, *A&A Rev.*, 4, 267
- Claret, A. & Torres, G. 2019, *ApJ*, 876, 134
- Colgan, J., Kilcrease, D. P., Magee, N. H., et al. 2016, *ApJ*, 817, 116
- Cox, J. P. & Giuli, R. T. 1968, *Principles of stellar structure*
- Davies, G. R., Chaplin, W. J., Farr, W. M., et al. 2015, *MNRAS*, 446, 2959
- Farnir, M., Dupret, M. A., Salmon, S. J. A. J., Noels, A., & Buldgen, G. 2019, *A&A*, 622, A98
- Ferguson, J. W., Alexander, D. R., Allard, F., et al. 2005, *ApJ*, 623, 585
- Gough, D. O. 1990, in *Lecture Notes in Physics*, Berlin Springer Verlag, Vol. 367, *Progress of Seismology of the Sun and Stars*, ed. Y. Osaki & H. Shibahashi, 283
- Grevesse, N. & Noels, A. 1993, in *Origin and Evolution of the Elements*, ed. N. Prantzos, E. Vangioni-Flam, & M. Casse, 15–25
- Iglesias, C. A. & Rogers, F. J. 1996, *ApJ*, 464, 943
- Kjeldsen, H., Bedding, T. R., & Christensen-Dalsgaard, J. 2008, *ApJ*, 683, L175
- Lund, M. N., Silva Aguirre, V., Davies, G. R., et al. 2017, *ApJ*, 835, 172
- Proffitt, C. R. & Michaud, G. 1991, *ApJ*, 380, 238
- Rendle, B. M., Buldgen, G., Miglio, A., et al. 2019, *MNRAS*, 484, 771
- Rogers, F. J. & Nayfonov, A. 2002, *ApJ*, 576, 1064
- Roxburgh, I. W. & Vorontsov, S. V. 2003, *A&A*, 411, 215
- Scuflaire, R., Montalbán, J., Théado, S., et al. 2008a, *Ap&SS*, 316, 149
- Scuflaire, R., Théado, S., Montalbán, J., et al. 2008b, *Ap&SS*, 316, 83
- Sonoi, T., Samadi, R., Belkacem, K., et al. 2015, *A&A*, 583, A112
- Thoul, A. A., Bahcall, J. N., & Loeb, A. 1994, *ApJ*, 421, 828

- Verma, K., Faria, J. P., Antia, H. M., et al. 2014, *ApJ*, 790, 138
- Vorontsov, S. V. 1988, in *IAU Symposium*, Vol. 123, *Advances in Helio- and Asteroseismology*, ed. J. Christensen-Dalsgaard & S. Frandsen, 151
- Weiss, W. W., Rucinski, S. M., Moffat, A. F. J., et al. 2014, *PASP*, 126, 573
- White, T. R., Huber, D., Maestro, V., et al. 2013, *MNRAS*, 433, 1262

PART II

The subgiants and red-giants

CHAPTER 5

The EGGMiMoSA method



Figure 5.1: The EGGMiMoSA logo.

As we have seen, as a consequence of the contraction of their core and expansion of their envelope, red-giant and subgiant stars display mixed-mode oscillation spectra (Sects. 2.1.4 and 2.2.4). These modes represent a unique opportunity to probe the entire stellar structure of evolved solar-like stars, unveiling the future of our Sun. A method accounting for such information was therefore necessary, this is why EGGMiMoSA (**E**xtracting **G**uesses about **G**iants via **M**ixed-**M**odes **S**pectrum **A**djustment) was developed. This has been presented in an article (Farnir et al. 2021, accepted for publication in A&A, see also Sect. 5.A). In the present chapter, we present notable results of the technique.

5.1 Introduction

Owing to their large luminosities, red-giant stars can be observed at large distances. Furthermore, such stars cover a wide range of stellar masses and compositions. Combined with precise positions and velocities, obtained for example with the GAIA mission (Perryman et al. 2001), they constitute key elements to the characterisation and understanding of our host galaxy, the Milky-Way. This is the topic of galactic archaeology, which aims at studying the Milky-Way’s dynamical and chemical evolution (e.g. Miglio et al. 2013; Noels et al. 2016). However, galactic archaeology strongly relies on precise ages and composition measurements. This was enabled by the detection of non-radial oscillation modes (De Ridder et al. 2009). Among these were also detected modes of mixed pressure and gravity characters (Bedding et al. 2010). This is an important breakthrough for asteroseismology, allowing us to retrieve such precise ages and compositions, but also to probe the structure of these stars from their surfaces to their cores.

5.1.1 Anatomy of a mixed-mode

Oscillation modes either behave as pressure modes, with the pressure gradient acting as the restoring force of the oscillation, or as a gravity mode, with the buoyancy being the restoring force (see Sect. 2.2.4). In low-mass main-sequence stars, the g-modes propagate in the innermost regions, the g-cavity, and have little amplitude at the surface, as they are damped in the radiative region. Therefore, they have not been detected yet. Conversely, the p-modes propagate in the outermost regions of the star, the p-cavity, and are ‘easily’ detected. As a consequence, only information about these shallow regions can be retrieved and their deepest regions cannot be probed via asteroseismology. However, in condensed stars, such as subgiants and red giants, these modes can couple to create modes of mixed p- and g- natures, behaving as g-modes in the central regions and as p-modes in the envelope. These are the so-called mixed-modes and constitute a unique opportunity to probe most of the interior of low-mass stars (see Sect. 2.2.4).

The existence of modes of mixed character, was theoretically discussed early on by Dziembowski (1971) in a Cepheid model and by Scuflaire (1974) in polytropic models. Such modes exist because of the large density contrast appearing in subgiant and red-giant stars. Indeed, as the star evolves after the main sequence, its core contracts and its envelope expands significantly. The frequencies of g-modes increase and those of p-modes decrease. Hence, around the frequency of maximum power, ν_{\max} , non-radial modes behave like gravity modes in the core and like pressure modes in the envelope. These are the so-called **mixed-modes**, which propagate over most of the stellar interior. The two propagation cavities of these mixed modes are coupled through the thin evanescent zone between them. The first consequence of this coupling is the **avoided crossing** (Osaki 1971; Aizenman et al. 1977). Instead of crossing, the two modes exchange nature and avoid each other.

In addition, as evolution proceeds from the subgiant phase to the red-giant phase, the number of modes with a dominant gravity character per modes of dominant pressure character increases. This is represented by the g-dominated modes density around ν_{\max} defined by Mosser et al. (2015),

$$\mathcal{N}(\nu_{\max}) = \frac{\Delta\nu}{\Delta\pi_1\nu_{\max}^2}, \quad (5.1)$$

with $\Delta\nu$ the large frequency separation between two consecutive p-dominated modes and $\Delta\pi_1$ the period spacing between two consecutive g-dominated modes. Spectra with $\mathcal{N} \ll 1$ are dominated by the presence of the p-dominated modes. We expect most of the behaviour of the spectrum to follow that of pure pressure mode spectra with an almost constant frequency separation $\Delta\nu$, such as in main-sequence solar-like stars. Conversely, spectra with $\mathcal{N} \gg 1$ show a dominant g-character and are expected to present a regular spacing between individual modes periods, $\Delta\pi_1$, such as white dwarfs and γ -Dor stars exhibit. However, the coupling between the two cavities introduces complex behaviours and disrupts these regularities. Plotting the frequency separation as a function of the period ($\mathcal{N} \ll 1$, p-dominated spectra) or the period spacing as a function of the frequency ($\mathcal{N} \gg 1$, g-dominated spectra) displays a characteristic shape with periodic local decreases in these quantities, called ‘dips’. This is referred to as **modes bumping** and corresponds to the signature of the presence of modes of g-dominated nature ($\mathcal{N} \ll 1$, p-dominated spectra) or p-dominated nature ($\mathcal{N} \gg 1$, g-dominated spectra). We represent this phenomenon of modes bumping for theoretical frequencies obtained via LOSC (Scuflaire et al. 2008a) for a typical subgiant model and a typical red-giant model computed with CLES (Scuflaire et al. 2008b) in Figs. 5.2 and 5.3, respectively. The periodic excursions from the constant $\Delta\nu$ and $\Delta\pi_1$, shown in green, are clearly visible. We also observe that the presence of periodic dips provides an information about $\Delta\pi_1$ or $\Delta\nu$, as displayed by the double-sided black arrows.

5.1.2 Describing the mixed-modes pattern

Despite the apparent complexity exhibited by the mixed-mode oscillation spectra, several approaches have been developed to analyse them. One of them, developed by Deheuvels & Michel (2011) for subgiant stars, models the mixed-mode spectrum as a series of coupled harmonic oscillators. This approach was also adopted by Benomar et al. (2012) who were able to show the correlation between the coupling strength, between the p- and g-cavities, and the stellar mass in the subgiant phase. However, the connection between this approach and the stellar structure is not straightforward.

Another widely used approach, exploiting physical knowledge about the stellar structure, relies on the asymptotic description of mixed modes (Shibahashi 1979; Tassoul 1980). The most commonly used formulation is the one presented in (Shibahashi 1979),

$$\tan \theta_p = q \tan \theta_g, \quad (5.2)$$

where θ_p represents the phase contribution of the pressure cavity, θ_g that of the gravity cavity, and q the coupling strength between these cavities through the evanescent region. Solving Eq. (5.2) provides the asymptotic frequencies. Originally, Shibahashi (1979) assumed a thick evanescent region, corresponding to a weak coupling between the two oscillating cavities, never allowing q to exceed a value of 0.25. This is valid for most of the red-giant phase evolution. Nevertheless, on the subgiant phase, it may be necessary to allow for greater values of the coupling factor. Takata (2016a) treated the case of a strong coupling where the evanescent zone is thin and demonstrated that Eq. (5.2) remains valid in this case, with greater values of the coupling factor, with a maximum of 1. This is

referred to as the strong coupling. He also properly accounted for the perturbation of the gravitational potential, often neglected under Cowling's approximation (Cowling 1941, see also Sect. 2.2.3), on the adiabatic equations of oscillations. He also showed that the large density contrast between the core and the envelope impacts the positions of the turning points, affecting the definition of the resonant cavities. This lead to the definition of modified Lamb and Brunt-Väisälä frequencies

$$\hat{L}_l \equiv L_l J \quad (5.3)$$

and

$$\hat{N} \equiv \frac{N}{J}, \quad (5.4)$$

such that we find the usual conditions for the propagation of modes. A mode is propagative in a region where its frequency σ is such that $\sigma^2 < \hat{L}_l^2, \hat{N}^2$ or $\sigma^2 > \hat{L}_l^2, \hat{N}^2$ and it is evanescent otherwise. The local density contrast between the local density, ρ , and the mean density of the encapsulated sphere, $\bar{\rho} = \frac{m(r)}{4/3\pi r^3}$,

$$J(r) \equiv 1 - \rho(r)/\bar{\rho}(r), \quad (5.5)$$

has been introduced.

5.1.3 Measuring the asymptotic parameters

Since the prediction of the existence and detectability of mixed-modes (Scuflaire 1974; Dupret et al. 2009), a lot of effort for their observations has been made. Thanks to the high quality data collected by spacecrafts such as CoRoT (Baglin et al. 2009) and *Kepler* (Borucki et al. 2010), these were detected by Bedding et al. (2010). The observations and characterisations of these modes then multiplied. With a parametric revision of the asymptotic formulation, Mosser et al. (2012c) were able to measure the period spacing, $\Delta\pi_1$, in a large sample of red-giant stars and demonstrated that it is possible to clearly identify mixed-modes. This formulation was later revised and the pressure and gravity phases took the empirical form (Mosser et al. 2015),

$$\theta_p = \pi \left[\frac{\nu}{\Delta\nu} - \frac{1}{2} - \epsilon_p \right] \quad (5.6)$$

and

$$\theta_g = \pi \left[\frac{1}{\nu\Delta\pi_1} - \epsilon_g \right], \quad (5.7)$$

with ϵ_p and ϵ_g the pressure and gravity offsets, respectively. Introducing an appropriate variable change, allowing the regularity of the spectrum to be restored, Vrad et al. (2016) and Mosser et al. (2017, 2018) again extended the number of measured $\Delta\pi_1$, as well as q , to several thousands of red giants. As the asymptotic formulation has been shown to be valid for subgiant stars, Eq. (5.2) was applied to about 40 of these stars to retrieve a measurement of $\Delta\pi_1$ (Appourchaux 2020).

The measurement of the period spacing is of great interest. Indeed, it was shown that measuring both $\Delta\pi_1$ and $\Delta\nu$ is sufficient to recognise H-shell burning from core-He burning stars, otherwise indistinguishable (Bedding et al. 2011; Mosser et al. 2014). This is illustrated in Fig. 5.4, taken from Mosser et al. (2014, Fig. 3). The distinction between subgiants (upper right), H-shell burning giants (bottom left) and core-He burning giants is very clear. This results from the large difference in the density contrast between these phases, which has been shown to impact the value of $\Delta\pi_1$ (Montalbán et al. 2010). In addition, by measuring the mass of the core in core-He burning stars, Montalbán et al. (2013) demonstrated that it is possible to obtain a diagnosis for the amount of overshooting in intermediate-mass stars. The amount and nature of the overshooting have an important impact on the central composition and the duration of the main sequence, which in turn impacts our inference of stellar ages.

In addition, the other asymptotic parameters are important to a proper characterisation of the mixed-mode oscillation spectra. For example, (Buysschaert et al. 2016) measured $\Delta\pi_1$, ϵ_g , and q in three red giants and concluded that using ϵ_g as a free parameter, when adjusting mixed-mode spectra, is necessary to retrieve reliable confidence intervals on the measurement of $\Delta\pi_1$. Nevertheless, there currently does not exist studies that are able to retrieve reliable values for the ϵ_g parameter. Relying on analytical models of the stellar structure, Pinçon et al. (2019) later demonstrated that the gravity offset is sensitive to the core-envelope density contrast in red giants and that it should hold information about the localisation of the base of the convective zone. The efforts to robustly measure this quantity, must endure.

Finally, the coupling factor was measured in a large number of stars (Mosser et al. 2012c; Vrad et al. 2016; Mosser et al. 2017), demonstrating the important change in its value throughout stellar evolution. On the subgiant phase, the coupling factor starts with a low value of about 0.1. Then, by the end of the subgiant phase, it sharply increases to approximately 0.6. This largely exceeds the limits of 1/4 foreseen by the weak coupling of Shibahashi (1979) and corroborates the necessity of Takata (2016b)'s work. At the beginning of the red-giant phase, the coupling factor decreases around 0.25 and steadily decreases during this phase, until reaching a final drop by the very end of the phase. This is illustrated in Fig. 5.5, which is presented in Mosser et al. (2017, Fig. 6). By means of stellar models Jiang & Christensen-Dalsgaard (2014), Hekker et al. (2018), and Jiang et al. (2020) also observed the decrease in the coupling factor on the red-giant phase which they showed to be correlated with the increase in the width of the evanescent region. Using analytical models, Pinçon et al. (2020) further demonstrated that the thickening of the evanescent region is a result of its migration towards the base of the convective region, where the Brunt-Väisälä frequency drops to zero.

Rotation

Thanks to rotational splittings, it was possible to measure the core rotation rate of a large sample of giant stars. First, [Beck et al. \(2012\)](#) measured the core-rotation rate of three red giants then [Mosser et al. \(2012b\)](#) and [Gehan et al. \(2018\)](#) extended this measurement to several hundreds of stars. They noted that, despite its contraction, the core spins down as the star evolves on the red-giant branch, hence contradicting simple assumptions about angular momentum conservation and requiring a spin-up of the core. Indeed, the core-rotation rates predicted by stellar models exhibit too large values (e.g. [Marques et al. 2013](#); [Cantiello et al. 2014](#)). This demonstrated the necessity to account for a process that efficiently transports angular momentum but that is not efficient enough to impose a rigid rotation of the complete star. Several authors provided candidates to explain this transport of angular momentum such as the redistribution by mixed-modes ([Belkacem et al. 2015a,b](#)), the diffusion of angular momentum ([Spada et al. 2016](#)), and its transport by internal gravity waves ([Pinçon et al. 2017](#)).

[Deheuvels et al. \(2014\)](#) also noted that the core of subgiants first spins up before reaching the red-giant branch. They also estimated that the redistribution of angular momentum from the core to the envelope, deemed necessary to account for the low core-rotation rates (e.g. [Eggenberger et al. 2012](#)), is still not sufficient. This nevertheless constitutes a constraint on such transport processes. In addition, [Pinçon et al. \(2017\)](#) showed that the combination of the core contraction (expected on the subgiant phase) and the angular momentum transport by internal gravity waves leads to a stabilisation of the rotation profile and strikingly agrees with the observations of [Deheuvels et al. \(2014\)](#). [Deheuvels et al. \(2020\)](#) later demonstrated that two early subgiants exhibit near solid-body rotation, hinting at the possibility that the efficiency of angular momentum transport decreases with the stellar evolution. Based on red-giant models, [Goupil et al. \(2013\)](#) demonstrated that the rotational splittings are mostly impacted by the central regions and they provided a parametric expression relating these splittings to the ratio between core and envelope rotation rates.

5.1.4 Extensions of the asymptotic theory

Finally, the asymptotic expansion can be extended. We have seen in Sect. 2.2.5 that sharp features in the stellar structure can cause oscillating features in the oscillation spectrum, the glitches. Beside the helium glitch, which has already been addressed in the case of red giants by several authors (e.g. [Miglio et al. 2010](#); [Broomhall et al. 2014](#); [Vrard et al. 2015](#); [Dréau et al. 2020](#)) and which the WhoSGLAd method has been developed for main-sequence stars, there exist buoyancy glitches. These buoyancy glitches, as their name would suggest, are sharp features in the buoyancy frequency, remnants, for example, of the first dredge up. These have been extensively studied by [Cunha et al. \(2015\)](#) who provided an analytical expression for these glitches and demonstrated that we should expect to observe them at the luminosity bump and at the early phases of core-He burning, providing tight evolutionary constraints.

5.1.5 Our work

We note from all the previous studies that they suffer from one main flaw. Up to this day, there exists no unified approach, relying on the asymptotic expression and tackling the problem of both subgiant and red-giant stars, often because of underlying simplifying assumptions. Furthermore, many of them require heavy and non-local minimisation techniques, that can be costly both in time and computing resources. Consequently, we constructed a method, EGGMiMoSA, of which the aim is to adjust the asymptotic expression to both subgiant and red-giant oscillation spectra ([Farnir et al. 2021, accepted for publication in A&A](#)). We neglect the effect of rotation as low-mass subgiant and red-giant stars are slow rotators (e.g. [Gehan et al. 2018](#)), so that the $m = 0$ modes, which we consider here, are not perturbed at first order. The strength of this method relies on educated guesses for the asymptotic parameters (i.e. $\Delta\nu$, $\Delta\pi_1$, ϵ_p , ϵ_g , and q) and on a local minimisation scheme, the Levenberg-Marquardt technique. Nevertheless, this method does not pretend to replace identification methods such as the one proposed by [Mosser et al. \(2015\)](#). Rather, after a proper detection of mixed-modes has been carried out, our method comes into play to define robust seismic indicators, bearers of relevant structural information, and to adjust stellar models to these indicators.

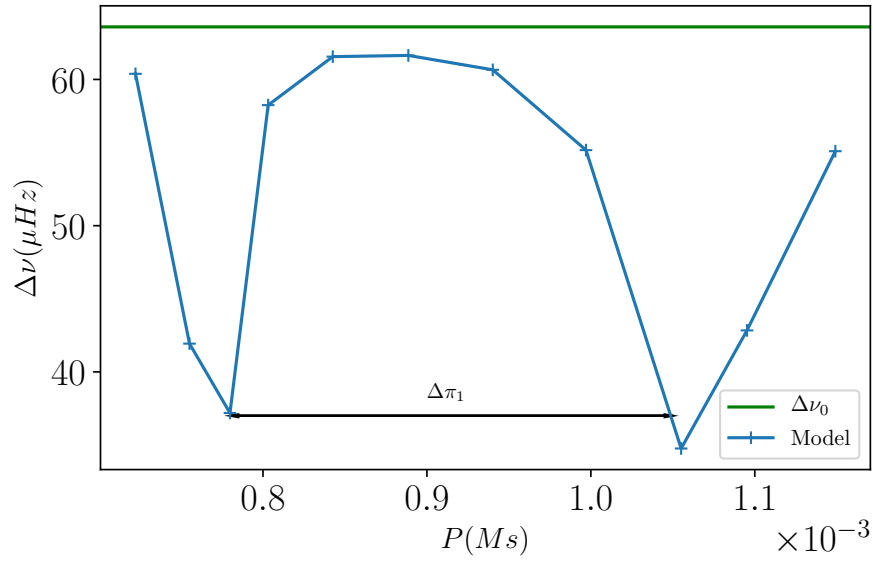


Figure 5.2: Large frequency separation as a function of the period for a $1 M_{\odot}$, $X_0 = 0.72$, $Z_0 = 0.015$ subgiant model. The asymptotic frequency separation is represented by the green horizontal line and the asymptotic period spacing by the black double-headed arrow.

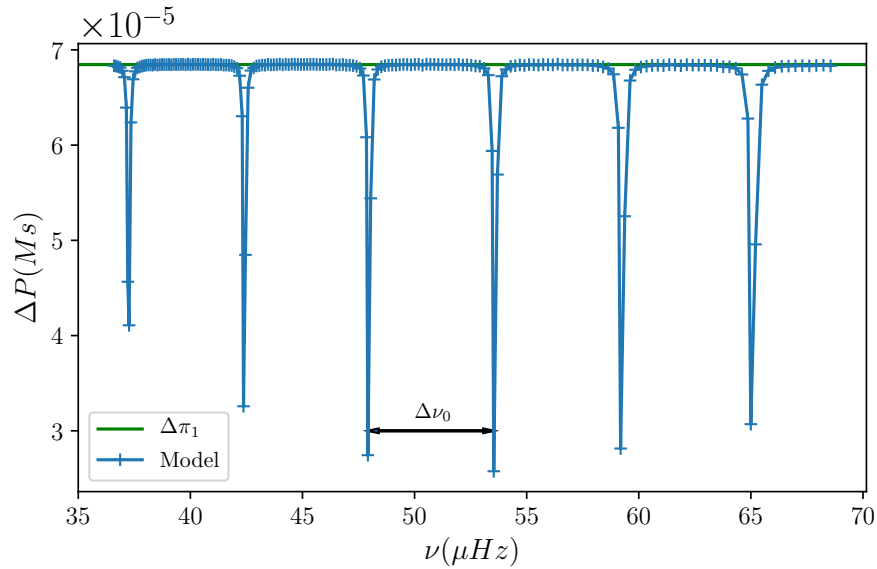


Figure 5.3: Period spacing as a function of the frequency for a $1 M_{\odot}$, $X_0 = 0.72$, $Z_0 = 0.015$ red-giant model. The asymptotic period spacing is represented by the green horizontal line and the asymptotic frequency separation by the black double-headed arrow.

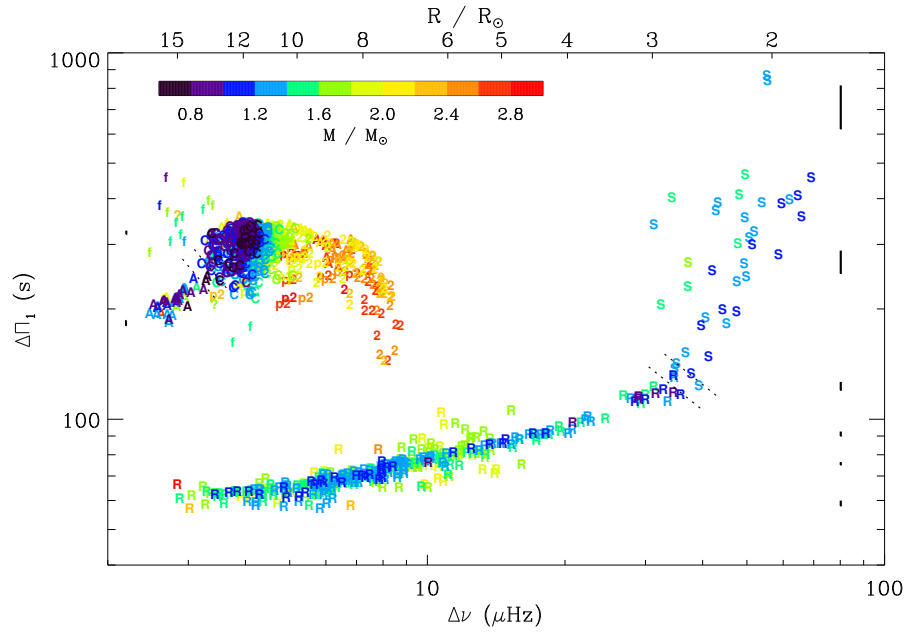


Figure 5.4: Measured values of $\Delta\nu$ and $\Delta\Pi_1$ for almost 1200 evolved *Kepler* stars taken from Mosser et al. (2014, Fig. 3).

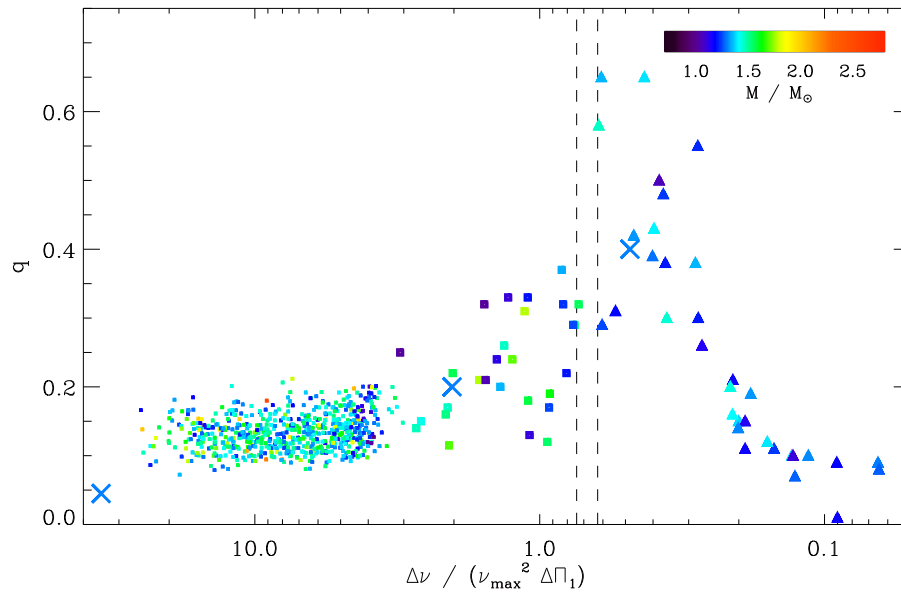


Figure 5.5: Evolution of the coupling factor as a function of the g-dominated modes density, taken from Mosser et al. (2017, Fig. 6).

5.2 The method

In the current section, we recall the different steps of the EGGMiMoSA method (All the technical details of the approach are given in [Farnir et al. 2021, accepted for publication in A&A](#)). The goal is to find the set of frequencies, ν_{fit} , that are the closest possible to reference frequencies, ν_{ref} . As is often the case in minimisation problems, we want to retrieve the set of parameters: $\Delta\nu$, $\Delta\pi_1$, ϵ_p , ϵ_g , and q that minimise the cost function,

$$\chi^2 = \sum_{i=1}^N \frac{[\nu_{\text{ref},i} - \nu_{\text{fit},i}(\Delta\nu, \Delta\pi_1, \epsilon_p, \epsilon_g, q)]^2}{\sigma_i^2}, \quad (5.8)$$

where the σ_i are the uncertainties on individual reference frequencies.

As our goal is to find a fast and robust technique to provide the five optimal parameters we avoid global minimisation techniques. We rather use a Levenberg-Marquardt technique and rely on appropriate parameters initial guesses in order to ensure the convergence. However, as illustrated by Eq. (5.2), the problem is non-linear and there exist several correlations between individual parameters (see Eqs. (5.6) and (5.7)). To cope with the most problematic correlations we use frequency or period differences as an intermediate step.

The five steps of the procedure are the following:

1. Estimate $\Delta\nu$ and ϵ_p on radial modes using WhoSGIAd. This corresponds to a linear fit of the frequencies;
2. Estimate the g-dominated modes density, \mathcal{N} . This is done via the second frequency difference $\delta\nu_{2,i} = \frac{\nu_{i+1} - \nu_{i-1}}{\Delta\nu}$;
3. According to the \mathcal{N} value, estimate $\Delta\pi_1$, ϵ_g , and q ;
4. Adjust individual frequency ($\mathcal{N} < 1$) or period ($\mathcal{N} > 1$) differences. In doing so, we avoid the $\Delta\nu$ - ϵ_p or $\Delta\pi_1$ - ϵ_g correlations, respectively;
5. Adjust individual frequencies, to retrieve robust parameters as well as uncertainties.

5.3 Notable results

Thanks to the appropriate estimation of the five mixed-mode parameters, their adjustment is carried out in a fast, robust and automated way. This allows us to follow their evolution along several evolutionary tracks, from the subgiant phase to the red-giant phase, for different masses and compositions. We now detail several notable results we obtained with the EGGMiMoSA method.

5.3.1 The models

For masses in the range $[0.9, 2.1]$, adopting a step of 0.1, we computed evolutionary tracks of models from the subgiant phase to the RGB luminosity bump with the CLES ([Scuflaire et al. 2008b](#)) evolution code. All the models have an initial composition of $X_0 = 0.72$ and $Z_0 = 0.015$. Frequencies are obtained using the LOSC ([Scuflaire et al. 2008a](#)) adiabatic oscillation code. We selected the frequency range following [Mosser et al. \(2012a\)](#). They estimated that the extent around ν_{max} of the modes that are efficiently excited, therefore observable, in red-giant stars follow the simple relation $0.66 \nu_{\text{max}}^{0.88}$. Typical observations from [Appourchaux et al. \(2012\)](#) for a subgiant star with $\nu_{\text{max}} \sim 1000 \mu\text{Hz}$ show that a little more than 10 radial modes may be clearly identified. Therefore, to match such observed ranges and ensure computing a sufficient amount of modes, we choose a slightly broader range of about $\nu_{\text{max}} \pm 0.4 \nu_{\text{max}}^{0.88}$. This corresponds, for red giants (resp. subgiants), to approximately three (resp. five) p-dominated modes on both sides of ν_{max} , as expected from observations.

5.3.2 General results

For each of the fitted mixed-mode parameters ($\Delta\pi_1$, ϵ_p , ϵ_g , and q), we observed a clear distinction between the subgiant and red-giant phases. The subgiant models present different evolutions according to the stellar mass. Evolutionary tracks then converge to a common evolution on the red-giant branch. This is a result of the important density contrast between the core and the envelope on the red-giant phase.

5.3.3 Evolution of the period spacing

By studying the evolution of the period spacing with stellar evolution, we obtained very interesting results. We represent in Fig. 5.6 the evolution of the fitted $\Delta\pi_1$ as a function of the large frequency separation of radial modes,

which is a good proxy for the evolution during these phases (Mosser et al. 2011), for all the tracks in our grid of models. As the period spacing decreases with evolution on the subgiant and red-giant phases, the evolution proceeds from right to left. We also represent the asymptotic value of the period spacing $\Delta\pi_{1,\text{as}}$ (Eq. (2.85)) as dashed lines. We mark the transition between the subgiant and red-giant phases as vertical coloured dotted lines.

The first striking feature is the clear difference between the subgiant phase, on the right of the dotted lines, and the red-giant phase, on the left. Indeed, the period spacing strongly decreases with evolution on the subgiant phase while the rate of decrease is significantly reduced on the red-giant phase. By comparing Figs. 5.4 and 5.6, we note that our computations qualitatively agree with the observations of Mosser et al. (2014). We confirm that the subgiant and red-giant stars occupy different regions in a $\Delta\nu$ - $\Delta\pi_1$ diagram. We also observe that the fitted $\Delta\pi_1$ values agree with the asymptotic ones. This remains true during the subgiant phase (see also Lagarde et al. 2016), where we do not expect the asymptotic formulation to hold for g-dominated modes, as the g-radial order is low ($n_g \sim 3$). We note that the relative difference between the fitted and asymptotic period spacing, $\delta\Delta\pi_1 = \frac{|\Delta\pi_{1,\text{as}} - \Delta\pi_{1,\text{fit}}|}{\Delta\pi_{1,\text{as}}}$, starts with a large value of about 10 – 15% then quickly decreases to around 5 – 10%. Once on the red-giant phase, it never exceeds 0.2%. This shows that the fitted period spacing is a potent proxy of the asymptotic one. Finally, using Eq. (2.85) we may roughly estimate $\Delta\pi_1$ to be inversely proportional to the maximum of the Brunt-Väisälä frequency in the radiative region, which has been demonstrated by Pinçon et al. (2020) to be approximately proportional to the square root of the helium core’s density. We represent this helium core’s density as a function of the helium core’s mass in Fig. 5.7. The abscissa has been flipped to match the direction of the evolution (right to left) presented in the other figures. We indeed observe the expected trend: The helium core’s density increases with evolution, leading to the observed decrease in $\Delta\pi_1$.

Furthermore, on the subgiant phase, all the tracks are well separated while, on the red-giant phase, only tracks with masses above $M \gtrsim 1.8 M_\odot$ are distinct. Tracks with lower masses are degenerate on the red-giant phase. This suggests that measuring both $\Delta\nu_0$ and $\Delta\pi_1$ of subgiants should allow us to infer their masses, radii, and ages. To further illustrate this, we plot the evolution of the asymptotic period spacing (to smooth out the small oscillations) as a function of $\Delta\nu_0$ in Fig. 5.8. We represent the age of the models as a colour gradient, and models with the same radius as black symbols (a diamond corresponds to $2 R_\odot$, a pentagram to $3 R_\odot$, and a star to $4 R_\odot$). We observe that individual tracks are significantly separated, compared to typical observed relative uncertainties of 1% on $\Delta\pi_1$ retrieved by Appourchaux (2020). Therefore, a measure of $\Delta\nu_0$ and $\Delta\pi_1$ allows us to infer the stellar mass with a greater precision than $0.1 M_\odot$. Because the age on the subgiant phase is dominated by the duration of the main sequence, which is mostly determined by the stellar mass (Eq. (2.28)), we may in turn infer the stellar age. This is again visible through the different colours of individual tracks. Finally, the black symbols, representing iso-radius curves, illustrate the possibility to also constrain the radius of the star by placing it in such a diagram.

We note a degeneracy of the tracks for red giants with masses $\lesssim 1.8 M_\odot$. This can be explained as a result of the electron degeneracy in the core. Indeed, because of the large core-envelope density contrast, we demonstrated in Sect. 2.1.4 that the properties of the H-shell are dependent on the helium core’s mass and radius only. Furthermore, the electron degeneracy leads to a relation between the mass and radius of the core. The evolution of the helium core’s density is therefore independent of the total stellar mass. This is what we observe in Fig. 5.7 representing the core’s density as a function of its mass. Because of the relation between the core’s mass and radius, the properties of the shell thus only depend on the core’s mass. In addition, because the luminosity is constant above the shell, the total luminosity only depends on the core’s mass. Then, as the effective temperature is almost constant on the red-giant branch (the stars rises almost vertically in the HR diagram, cf. Sect. 2.1.4) and because of Stefan-Boltzmann’s law (Eq. (2.41)), the stellar radius is also only a function of the core’s mass. The mean density, which is predominantly a function of the stellar radius, is therefore mostly determined by the core’s mass. Consequently, the same goes for $\Delta\nu$ which is a proxy of the mean density (Ulrich 1986; Farnir et al. 2019). The density contrast defined as $\rho_c/\bar{\rho}$, with ρ_c the central density, is also degenerate in mass for stars with an electron-degenerate core. This is represented in Fig. 5.9, where we indeed observe this degeneracy. This results in the degeneracy in the $\Delta\pi_1$ indicator as a function of $\Delta\nu$. Finally, the separation of the tracks for masses $\gtrsim 1.8 M_\odot$ opens the possibility to constrain the stellar mass, radius, and age, similarly to the subgiant phase.

We also studied the impact of the chemical composition on the evolution of $\Delta\pi_1$. To do so, we build a set of $1 M_\odot$ models varying either X_0 or Z_0 from the reference values ($X_0 = 0.72$ and $Z_0 = 0.015$). The variations in composition considered are $X_0 = 0.68$, $Z_0 = 0.011$, and $Z_0 = 0.019$. This is represented in Fig. 5.10. While we observe that the impact of the composition seems restricted, it has a comparable impact on $\Delta\pi_1$ during the subgiant phase as in the case of the \hat{r}_{01} and \hat{r}_{02} WhoSGIAd indicators. To highlight the effect of composition during the subgiant phase, we magnify this phase in Fig. 5.11. We indeed observe that, at fixed $\Delta\nu_0$ and $\Delta\pi_1$ values, a variation of 0.008 in Z_0 would modify the inferred mass by about $0.1 M_\odot$. This is very similar to what we observe in Fig. 3.5. Therefore, for a proper determination of the mass, radius and, age of a subgiant, it will be necessary to precisely measure the chemical composition. Conversely, the red-giant tracks are again degenerate.

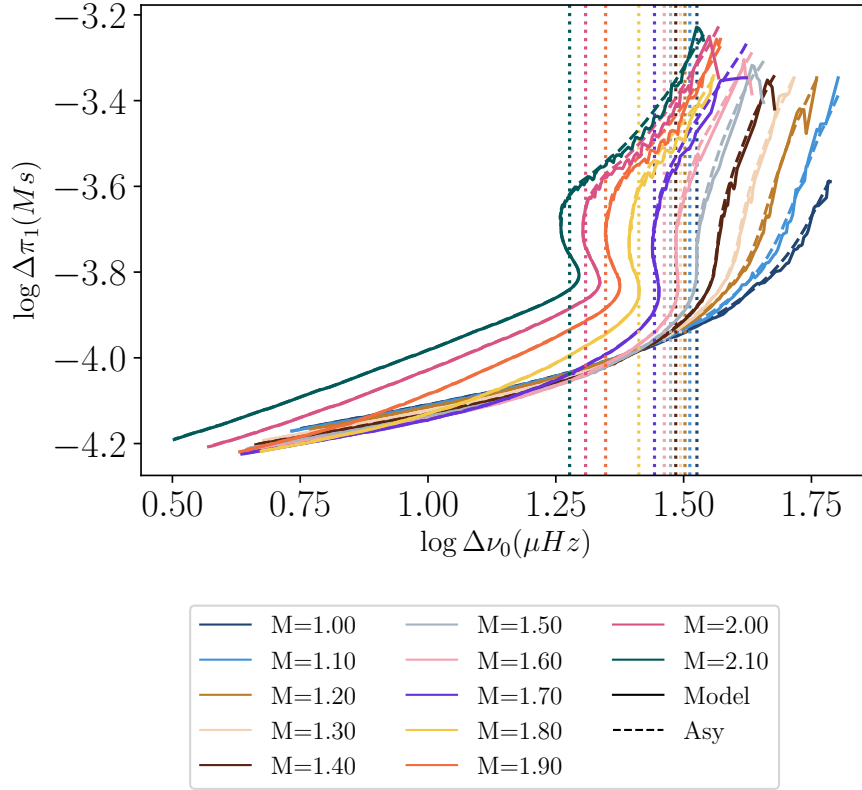


Figure 5.6: Evolution of $\Delta\pi_1$ as a function of $\Delta\nu_0$ for different masses, represented by the different colours. The dashed lines represent the asymptotic period spacing, $\Delta\pi_{1,as}$, and the vertical dotted lines the transition between subgiant and red-giant phases.

With a determination of the chemical composition, we noted the possibility to precisely constrain the stellar mass, radius, and age of subgiant stars. In addition, we demonstrated that the presence of central electron degeneracy combined with the large core-envelope density contrast in red-giant stars with masses $\lesssim 1.8 M_\odot$ leads to a degeneracy in the evolution of $\Delta\pi_1$ with $\Delta\nu_0$ for these stars. For heavier red-giant stars, the degeneracy is lifted and it should be possible to constrain their masses, radii, and ages, as in the subgiant case.

5.3.4 Evolution of the gravity offset

To our knowledge, we presented for the first time the evolution of the gravity offset over a complete grid of models, including both subgiant and red-giant models. This is represented in Fig. 5.12 for masses of $1 M_\odot$, $1.2 M_\odot$, $1.5 M_\odot$, and $1.8 M_\odot$ as a function of ν_{\max} which decreases with the evolution. We chose ν_{\max} to ease the comparison with the work of Pinçon et al. (2019, Fig. 4), given in Fig. 5.13. They compare the values observed by Mosser et al. (2018) with their analytical determinations, represented by the different lines. We first observe the clear difference in behaviour between the subgiant and red-giant phases, which we expect to stem from the qualitative differences in core-envelope density contrast between these stages.

While our computations extend to slightly greater values of ν_{\max} than the work of Pinçon et al. (2019), we observe the same trends. We first note that there is a systematic shift of 0.5 in our values compared to theirs. This results from the inclusion of a $1/2$ factor in the θ_g phase in our study while they omitted this term. During the red-giant phase, the ϵ_g value is almost constant at a value of approximately 0.75 which then drops for ν_{\max} between ~ 60 to ~ 40 (μHz) to approximately zero. This agrees with their computations, predicting a plateau at 0.25 and a sudden drop to about -0.2 in the range $\nu_{\max} \in [50 \mu\text{Hz}, 110 \mu\text{Hz}]$.

Pinçon et al. (2019) predicted that we should measure a constant gravity offset for most of the red-giant phase (represented by the grey rectangle) because the Brunt-Väisälä and Lamb frequencies are almost parallel and can be approximated by a power-law in the evanescent zone. This is what we illustrate in Fig. 5.14 where we represent the propagation diagram between the center and a reduced radius of $0.3 r/R$ of a $1 M_\odot$ young red giant.

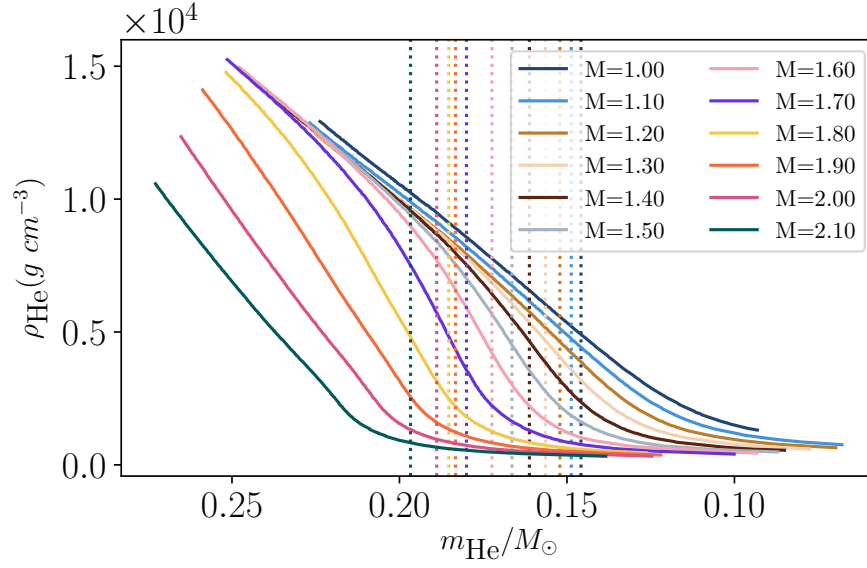


Figure 5.7: Density of the helium core as a function of its mass (in solar units) for every track presented in Fig. 5.6. The colours and vertical dotted lines have the same meaning.

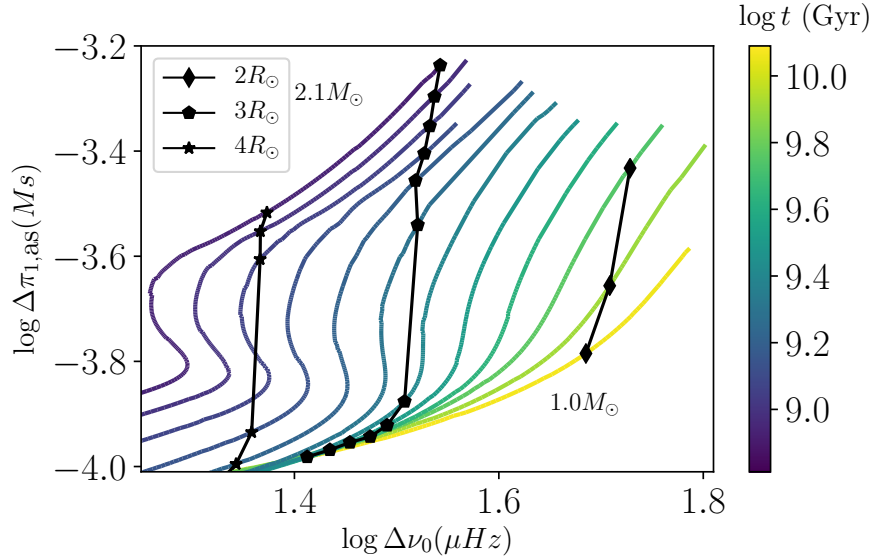


Figure 5.8: Evolution of $\Delta\pi_{1,\text{as}}$ as a function of $\Delta\nu_0$ on the subgiant phase for the different masses considered in Fig. 5.6. The colour gradient corresponds to the age. We show models with a radius of $2 R_{\odot}$ as black diamonds, those with $3 R_{\odot}$ as black pentagons, and those with $4 R_{\odot}$ as black stars.

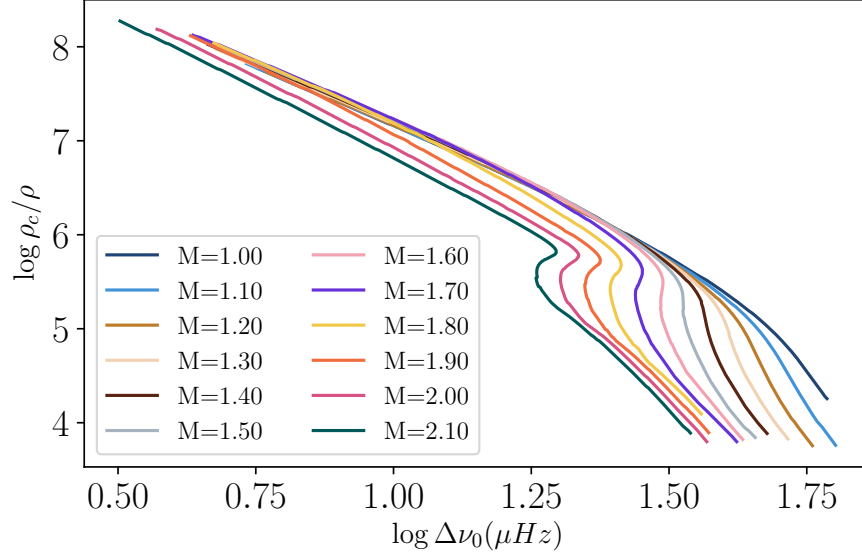


Figure 5.9: Evolution of the ratio of the central density over the mean stellar density with the evolution, represented by $\Delta\nu_0$. The colours are the same as in Fig. 5.6.

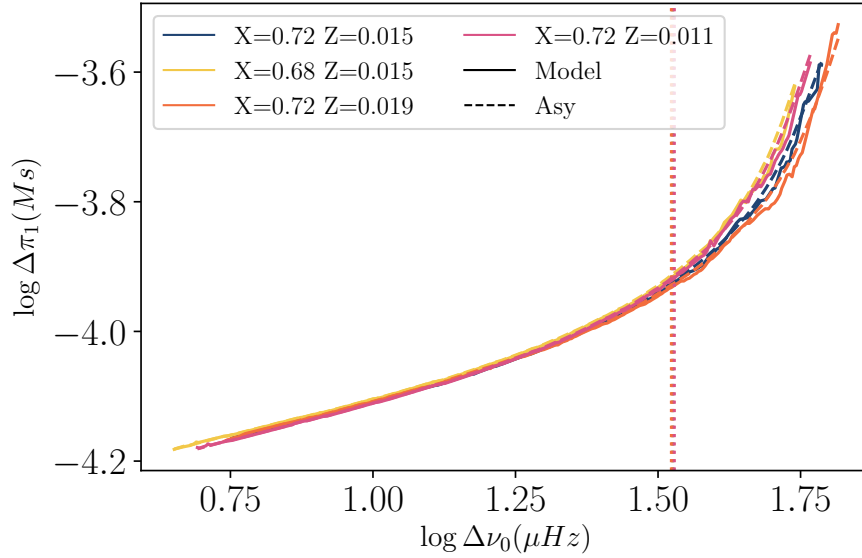


Figure 5.10: Evolution of $\Delta\pi_1$ as a function of $\Delta\nu_0$ for a $1 M_\odot$ track and different initial compositions represented by the colours. The dashed lines represent the asymptotic period spacing, $\Delta\pi_{1,\text{as}}$, and the vertical dotted lines the transition between subgiant and red-giant phases.

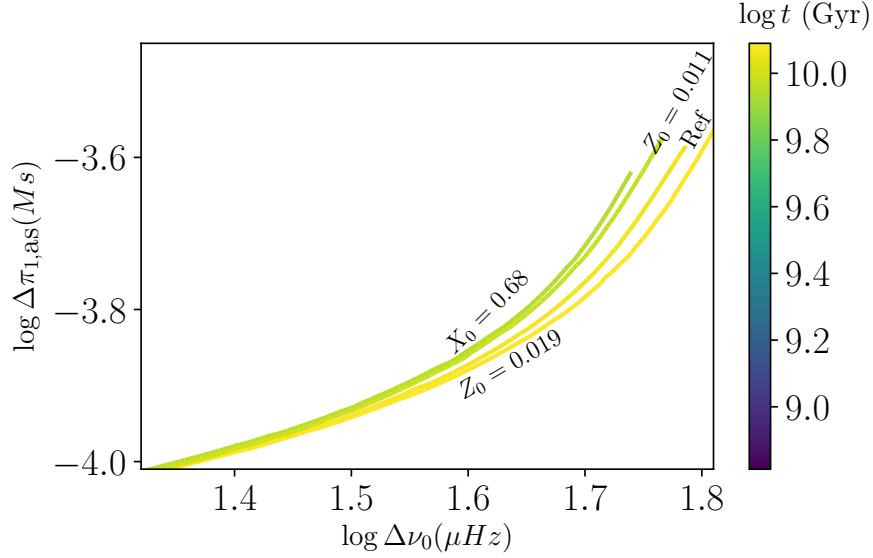


Figure 5.11: Evolution of $\Delta\pi_{1,as}$ as a function of $\Delta\nu_0$ on the subgiant phase for different compositions considered in Fig. 5.10. The colour gradient corresponds to the age.

The squared modified Brunt-Väisälä frequency (Eq. (5.4)) is shown in orange and the squared modified Lamb frequency (Eq. (5.3)) in blue. The squared computed frequency range is represented by the dashed green lines while the squared frequency at maximum power is represented by the continuous green line. The two characteristic frequencies are indeed, in very good approximation, parallel to one another in the radiative core. The Brunt-Väisälä frequency then drops in the convective envelope. Nonetheless, the two frequencies are parallel to each other in most of the considered frequency range. It does not remain valid as evolution proceeds. The frequency range decreases in frequency along with ν_{\max} and the evanescent region moves outwards. Both frequencies cannot be assumed parallel any more. This is represented in Fig. 5.15.

For subgiant stars, we noted a dependency of ϵ_g on the stellar mass, which we expect to result from the moderate and mass-dependent core-envelope density in the evanescent region. This density contrast is represented as a function of \mathcal{N} in Fig. 5.16 for each of the tracks presented in Fig. 5.6. We also note that ϵ_g is less regular in the subgiant phase than in the red-giant phase. However, individual spectra are well adjusted (see Farnir et al. 2021, accepted for publication in A&A, Figs. 6 to 8) and we expect this to be a result of structural features.

Concerning the chemical composition, we note that the composition only has a notable impact on the ϵ_g drop close to the luminosity bump. Its position in ν_{\max} shifts to lower values for a decrease in either X_0 or Z_0 . The evolution during earlier phases is fairly unaffected by the changes in composition considered in the present study.

Our results qualitatively agree with the observations of Mosser et al. (2018) and the asymptotic predictions of Pinçon et al. (2019). We also extend the range of measured gravity offsets and propose for the first time a determination of its values for both subgiant and red-giant models with a unique method. The composition is shown to only affect the position of the drop with ν_{\max} .

5.3.5 Evolution of the coupling factor

We represent in Fig. 5.17 the evolution of the coupling factor with the g-dominated modes density. We chose \mathcal{N} as a proxy of evolution to ease the comparison with the observations of Mosser et al. (2017, Fig. 6). We provide this figure in Fig. 5.5. In agreement with Benomar et al. (2012), we observed that the coupling factor strongly increases during the subgiant phase and then abruptly drops right before the start of the red-giant branch. The value of q then settles and slowly decreases from around 0.25 to approximately 0.1. In some cases, we also observe a last drop of its value before the luminosity bump. This agrees with the observations of Mosser et al. (2017).

Assuming the Brunt-Väisälä and Lamb frequencies to be parallel in the radiative region, Pinçon et al. (2020) demonstrated that the coupling factor should be correlated with the width of the evanescent region. An increase in the width of the evanescent region would lead to a decrease in the coupling factor, and conversely, a decrease in the width of the evanescent region would lead to a stronger coupling. Defining this width at ν_{\max} as

$$\delta_{\text{ev}} = \frac{r_2 - r_1}{(r_2 + r_1)/2}, \quad (5.9)$$

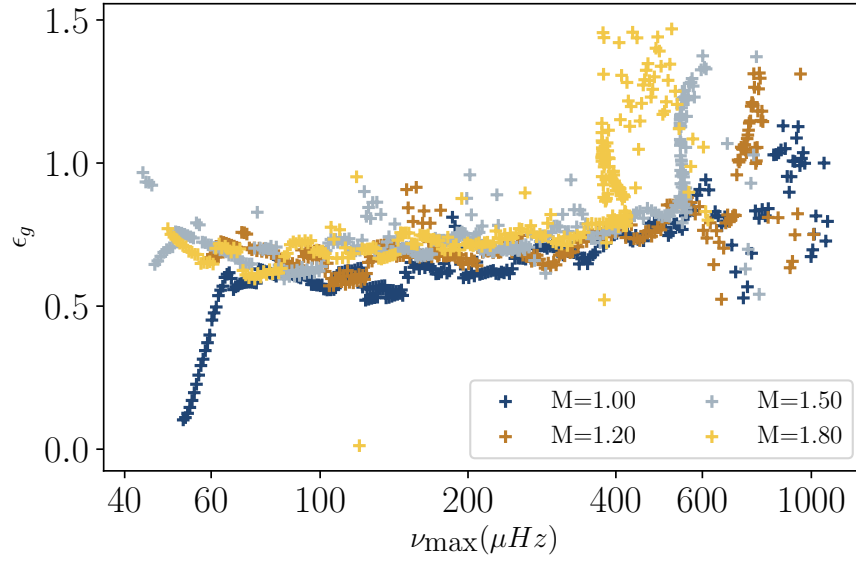


Figure 5.12: Evolution of the gravity offset as a function of ν_{\max} for different masses represented by the colours.

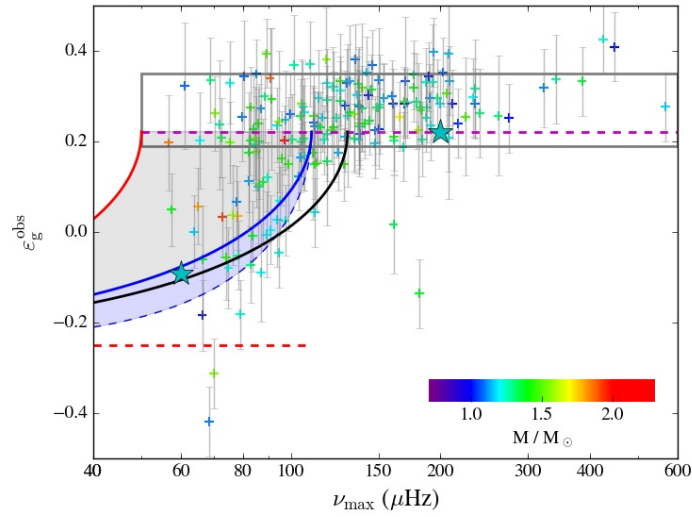


Figure 5.13: Evolution of the gravity offset with ν_{\max} on the red-giant phase taken from [Pinçon et al. \(2019, Fig. 4\)](#). The errorbars represent measured values from [Mosser et al. \(2018\)](#) while the different lines represent analytical determinations of ϵ_g for different hypotheses.

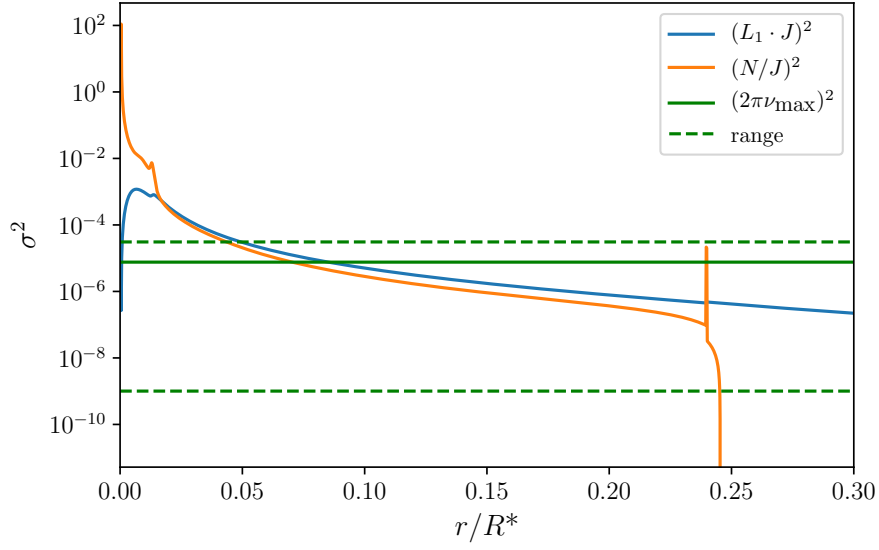


Figure 5.14: Propagation diagram for a $1 M_{\odot}$ young red giant between the center and a reduced radius of $r/R = 0.3$. We represent the squared modified Brunt-Väisälä frequency $(N/J)^2$ in orange and the squared modified Lamb frequency $(L_1 \cdot J)^2$ in blue. We also represent the squared frequency of maximum power as a continuous green line and the computed squared frequency range as dashed green lines.

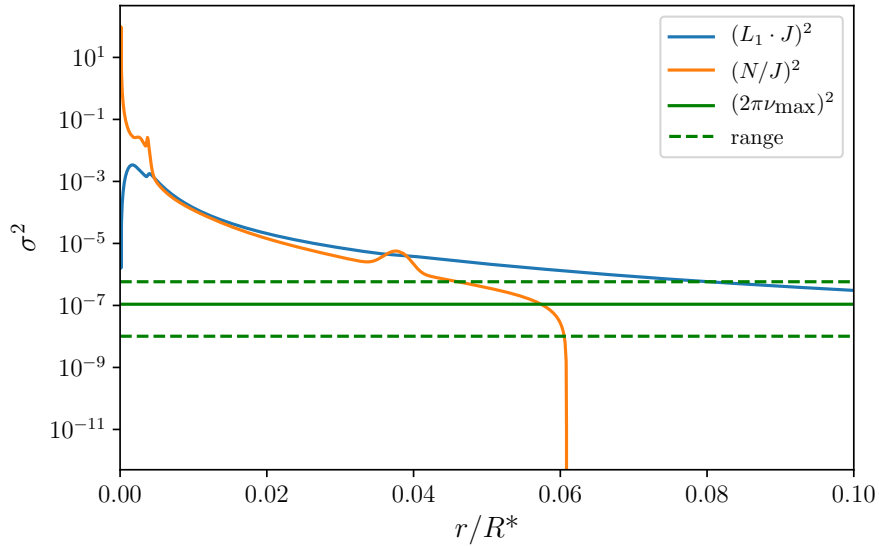


Figure 5.15: Propagation diagram for a $1 M_{\odot}$ red giant, right before the luminosity bump, between the center and a reduced radius of $r/R = 0.1$. We represent the squared modified Brunt-Väisälä frequency $(N/J)^2$ in orange and the squared modified Lamb frequency $(L_1 \cdot J)^2$ in blue. We also represent the squared frequency of maximum power as a continuous green line and the computed squared frequency range as dashed green lines.

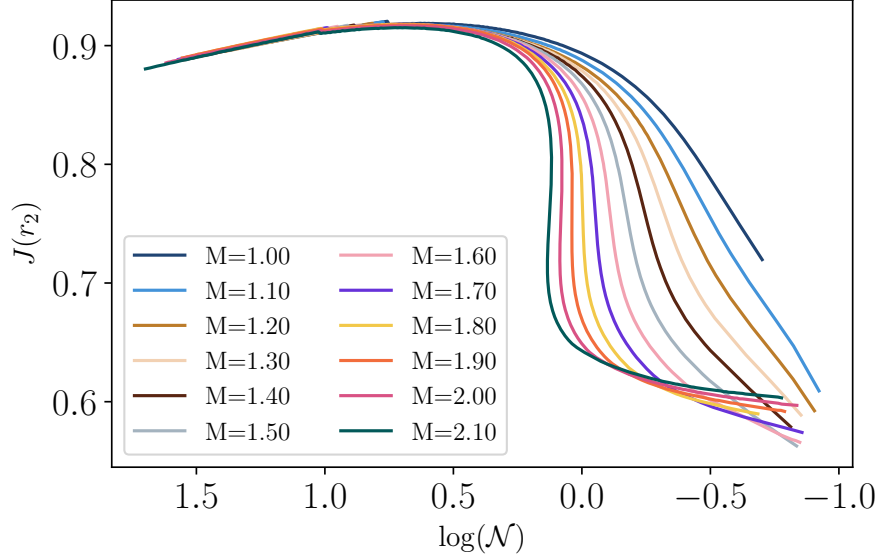


Figure 5.16: Evolution of the density contrast in the evanescent region as a function of \mathcal{N} for all the tracks of Fig. 5.6, with the corresponding colour code.

with r_1 and r_2 the positions of the inner and outer edges of the evanescent region (respectively), we plotted its variation along stellar evolution for different masses (Fig. 5.18). We indeed observe a sharp decrease in its value on the subgiant phase. The consequence is an important increase in the coupling factor, exceeding the $1/4$ limit imposed by Shibahashi (1979) therefore showing the necessity of the strong coupling formalism introduced by Takata (2016a). The width of the evanescent region then steadily increases, while the coupling factor decreases. On the red-giant branch, we also observe discontinuities in the width of the evanescent zone which we attribute to discontinuities in the composition at the base of the convective envelope. The composition discontinuities create peaks in the Brunt-Väisälä frequency and, consequently, in δ_{ev} . We observe such a peak in Fig. 5.14, although, because of the relatively large value of ν_{max} , it does not impact our determination of the width of the evanescent region (see also for example Cunha et al. 2015).

Similarly to the other indicators, we observe that q depends strongly on the stellar mass for subgiant models while its evolution is almost independent of the mass on the red-giant branch. This is again expected to result from the differences in the density contrast in the evanescent region (see Fig. 5.16). During the subgiant phase, the density contrast is moderate and strongly depends on the stellar mass. Therefore, the width of the evanescent region is also strongly impacted by the stellar mass. This is reinforced by the fact that, for a moderate density contrast, we may not assume the Lamb and Brunt-Väisälä frequencies to be log-parallel. For the $1.8 M_{\odot}$ track, this even leads to an oscillation in the width of the evanescent region. This stems from the fact that, as the star evolves, ν_{max} decreases. Furthermore, as the Brunt-Väisälä and Lamb frequencies are not parallel, they may cross. This crossing of the frequencies may also change with time. This results in ν_{max} meeting the crossing of both frequencies at several occasions, creating very thin evanescent regions. This is a phenomenon which will be investigated in future papers (Pinçon et al. 2021, in prep.).

While we noted the evolution of q on the RGB to be little affected by the stellar mass, it still has a visible impact. First, we observe on the red-giant branch that the greater the mass, the lower the coupling factor. This is again correlated with the evolution of the width of the evanescent region, which we observe to be slightly impacted by the stellar mass (compare Figs. 5.17 and 5.18). The other visible influence of the mass on q during the red-giant phase happens by the end of the sequence. Indeed, the position in ν_{max} of the last drop in the coupling factor depends on the mass.

The impact of the composition on the coupling factor is negligible. Only its drop before the luminosity bump is affected. This could be the result of a slight modification of the position of the convective zone as demonstrated by Pinçon et al. (2020). Our results do not agree with the work of Jiang et al. (2020) who noted a difference in the rate of decrease in q for different masses during the red-giant phase. This difference is more pronounced for the youngest red giants, which seem to finally settle to a common rate of decrease. Furthermore, they considered the coupling factor to be a function of the radial order and followed its evolution at fixed radial orders. This could explain the discrepancies we observe as we consider a constant value of q over the complete spectrum and, contrary to them, we do not fix the radial orders along the evolution in our fits. While following a constant radial order is questionable, as the set of observable modes strongly changes with evolution (e.g. Mosser et al. 2012a), it remains necessary to account for the variation of q with the frequency (Cunha et al. 2019), as the width of the evanescent region may not be constant with frequency. This will be discussed in Sect. 5.4.3.

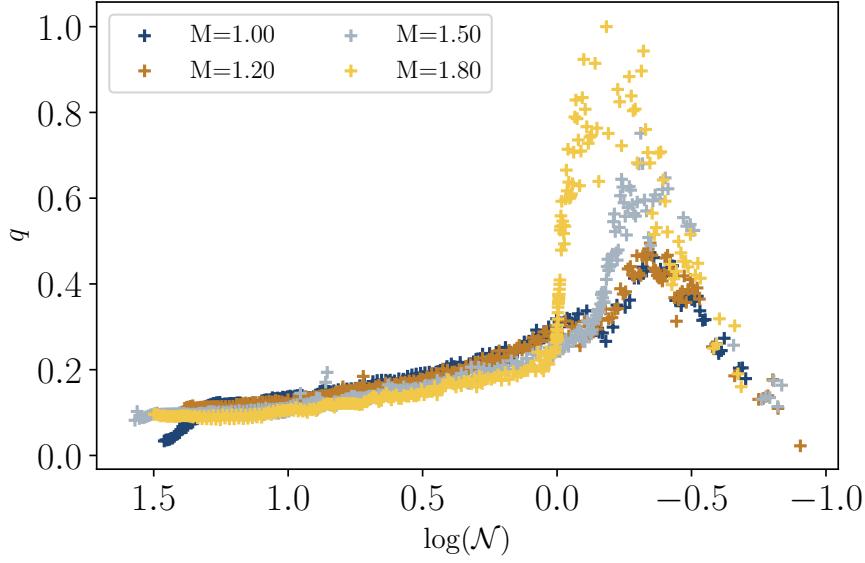


Figure 5.17: Evolution of the coupling factor with \mathcal{N} for different masses represented by the colours.

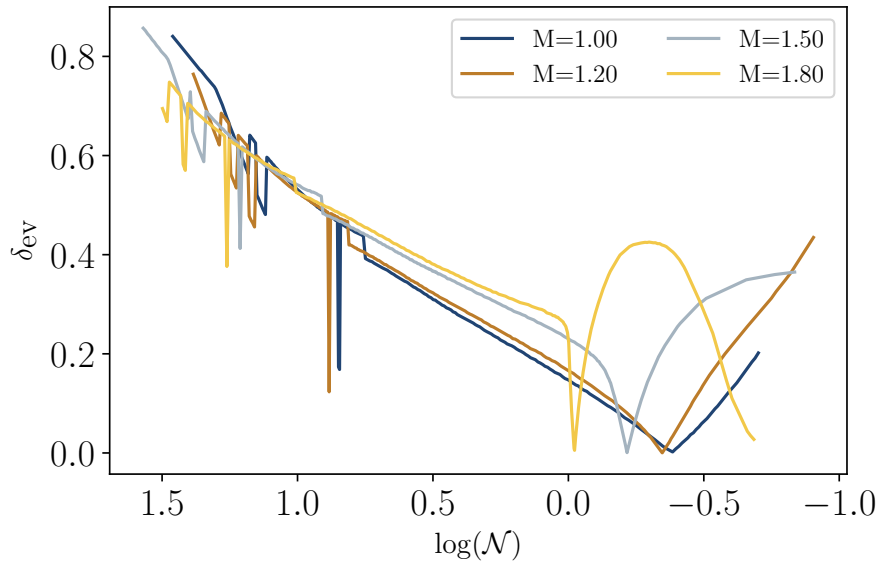


Figure 5.18: Evolution of the width of the evanescent region (Eq. (5.9)) for different masses represented by the colours.

We demonstrated that the coupling factor strongly depends on the width of the evanescent region, calculated at ν_{\max} . We noted a strong influence of the mass during the subgiant phase, where the density contrast is moderate and the Brunt-Väisälä and Lamb frequencies may not be assumed log-parallel. On the red-giant phase, only a small anti-correlation of the mass with the coupling factor is noted. Overall, the coupling factor strongly increases then sharply decreases on the subgiant phase. This is followed by a steady decrease during the red-giant phase. We did not note a significant impact of the composition beside a change in the position of the drop before the luminosity bump.

5.4 Improvements of the method

We consider in the present section several refinements that we plan on including in the EGGMiMoSA method.

5.4.1 Spectra with holes

A limitation of the proposed technique is that it has been developed assuming all the successive modes to be observed. This is a very reasonable assumption in the case of model data, for which we can compute the frequency of every excited mode. This therefore enabled us to follow the evolution of the mixed-mode parameters along a grid of models. However, this hypothesis collapses with observed data. Indeed, some of the modes might not be observed. For example, [Grosjean et al. \(2014\)](#) predict that for a $1.5 M_{\odot}$ star with $\Delta\nu \lesssim 4.6 \mu\text{Hz}$ star, quadrupole mixed-modes should not be detected after 360 days of the *Kepler* spacecraft observation. This agrees with the works of [Mosser et al. \(2018\)](#) who found a limit of $\Delta\nu \lesssim 6 \mu\text{Hz}$ for the detection of g-dominated mixed-modes.

Two main consequences arise from the lack of detection of several modes. The first one is that we have to account for the radial order difference between individual modes, which we assumed to be successive. However, starting from a reliable modes identification (such as presented in [Mosser et al. 2015](#); [Gehan et al. 2018](#); [Appourchaux 2020](#)), this problem is easily solved. Indeed, our method uses a parameter to describe this radial order difference ([Farnir et al. 2021, accepted for publication in A&A](#), Eqs. (13) and (16)).

The second complication, which is more complex to tackle, comes from the parameters estimation. For example, [Mosser et al. \(2018\)](#) expect that g-dominated modes should not be detected for stars with $\Delta\nu \lesssim 6 \mu\text{Hz}$ and only p-dominated modes would be detected. However, the g-dominated modes are crucial to both the estimation of $\Delta\pi_1$, through the maximum of the period differences curve, and of q , through the ratio of the maximum and minimum of the ΔP curve. Missing g-dominated modes, which are expected to lie close to the maximum of the ΔP curve, can therefore severely impair the estimation of both indicators. Special care will need to be undertaken in their estimation for observed stars. This will be investigated in future studies. In addition, the number of observed g-dominated modes should increase as we go down the red-giant branch. Younger stars should thus consist in less of a problem.

5.4.2 Higher-order contributions

In the present work, we used a linear expression for the pressure phase, θ_p , to represent the pressure contribution to the mixed-modes. However, in the case of evolved red-giant stars, the pressure radial order is low, on the order of $n_p \sim 5$. The asymptotic expression is therefore not applicable as is, as the condition requiring large radial order modes (therefore small wavelengths) is not verified. It may be necessary to include higher-order contributions to the pressure phase. This is indeed what many authors consider (see for example [Mosser et al. 2013](#); [Vrard et al. 2016](#); [Cunha et al. 2019](#)). As a matter of fact, we observed for an evolved red giant ([Farnir et al. 2021, accepted for publication in A&A](#), Fig. 8) that there is a slight shift in the position of the fitted ΔP dips relative to the reference ones, as well as differences in their magnitudes at high frequencies, where the second order contribution is expected to be the most important. This illustrates the need to include higher-order contributions to the pressure phase of evolved red giants.

During the subgiant phase, we noted that the width of the considered set of modes is so large (about $10 \Delta\nu$ wide) that the large separation cannot be considered constant over the considered set of modes, as we assume by setting it to its radial value (with WhoSGIAd). Indeed, we observed that the relative difference between the constant large separation and the actual value as a function of frequency over the set of radial modes is of about $\frac{\delta\Delta\nu}{\Delta\nu_0} \sim 5\%$ ([Farnir et al. 2021, accepted for publication in A&A](#), Fig. 6). In addition, a typical value for the pressure radial order in these stars is of $n_p \sim 20$. The consequence is that their product $\frac{\delta\Delta\nu}{\Delta\nu_0} n_p$, representing the error made by considering a constant large separation, is of the order of unity. This means that it is comparable to the uncertainties on the pressure offset. This again shows the necessity to include higher-order contributions to the pressure phase as, otherwise, it could lead to a misidentification of the modes. In the worst cases, overlooking the second-order contributions could lead to the addition or removal of a p-dominated mode in the considered set.

Finally, as the g-dominated modes span a wide range of radial orders in the red-giant stars, we would expect the second-order contribution to the gravity phase to be significant as well. Nevertheless, [Pinçon et al. \(2019\)](#) showed analytically that this contribution should be small compared to the uncertainties on the gravity offset for stars observed before the luminosity bump.

5.4.3 Variation of q with frequency

For evolved red giants, [Cunha et al. \(2019\)](#) demonstrated the necessity to include a dependency of q on the frequency. Indeed, as the Brunt-Väisälä and the Lamb frequencies cannot be considered parallel in the evanescent region, because it has penetrated the convective region and the Brunt-Väisälä frequency dropped to zero, the width of the evanescent region varies in the frequency range considered. Figure 5.15 provides a good illustration of this phenomenon. As the width of the evanescent region depends on frequency, so does the coupling factor ([Pinçon et al. 2019](#)). To mimic the dependency of the coupling factor on frequency, we selected an evolved giant and binned the reference spectrum into symmetrical sub-spectra around each dip of the period spacing. This is presented in Fig. 23 of [Farnir et al. \(2021, accepted for publication in A&A\)](#). We allowed the coupling factor to vary from one sub-spectrum to the other (freezing the other parameters). In doing so, we observed that the coupling factor varies almost linearly with the frequency corresponding to the central frequency of each bin (see [Farnir et al. 2021, accepted for publication in A&A](#), Fig. 24). In addition, allowing q to vary with frequency improved the

agreement between the reference and the adjusted spectra. Furthermore, we observed that the variation of q over the spectrum is significant, from about 0.11 to 0.22. This is important in comparison with the constant value of 0.12 (consistent with the observations of Mosser et al. 2017) adjusted over the complete spectrum. We therefore expect that, for evolved giants, it will be necessary to account for the linear dependency of q on the frequency to improve the robustness of our technique.

5.4.4 Glitches

Interesting phenomena providing valuable insight into the stellar structure are the glitches. Because of sharp features in the stellar structure (sharp in comparison to the wavelength of the mode), an oscillating signal with frequency appears in the measured frequencies (see Sect. 2.2.5). In evolved stars, as modes are of mixed nature, both types of modes may present such glitches. Sharp variations in the Brunt-Väisälä frequency, impacting the gravity contribution to the spectrum, cause the buoyancy glitches. Conversely, variations in the sound speed create the acoustic glitches, already studied in the case of solar-like stars in the present study (Chaps. 3 and 4).

The acoustic glitch caused by the helium second-ionisation zone has already been studied on numerous occasions in red-giant stars. Miglio et al. (2010) demonstrated the existence of such a signal in the frequency spectrum of the red giant HR7349 using the large frequency separation. Using a set of stellar models, the work of Broomhall et al. (2014) showed that this signature can be efficiently recovered for red giants with $\nu_{\max} > 40 \mu\text{Hz}$ and that the localisation of the second-ionisation zone could be formally retrieved. However, this signature could hardly be used to measure the helium abundances in these stars. With a sample of more than 500 red-giants, Vrad et al. (2015) confirmed that the current uncertainties on the helium glitch amplitude are too large to precisely infer the helium abundance. Finally, Dréau et al. (2020) demonstrated that including the dipolar p-dominated modes in the glitch fitting procedure slightly improves the robustness of this procedure. Consequently, a precise adjustment of the helium glitch using both radial and dipolar modes is in order to precisely retrieve the glitch signature. Using the WhoSGLAd method could constitute a significant asset and provide reliable inferences on the helium surface abundance of subgiant and red-giant stars. We will investigate this possibility in future works.

The second type of glitches encountered in red-giant stars corresponds to buoyancy glitches. These are the signatures left by a sharp variation in the Brunt-Väisälä frequency. Cunha et al. (2015) demonstrated the necessity to account for the signature of such glitches in determining the asymptotic parameters (such as the period spacing) and provided a formulation describing the combined impact of a buoyancy glitch and of modes coupling. They also demonstrated that the signature of buoyancy glitches should be present for stars at the luminosity bump and for early stages of helium burning. These signatures therefore constitute a proxy of the evolutionary stage of the evolved red giants. As we limited our study to stars before the luminosity bump, we should not expect to detect such glitches and neglecting them is not a crude approximation. Nonetheless, to extend our method to later evolutionary stages, accounting for buoyancy glitches will be necessary. Indeed, they provide necessary insight into red giant's cores, for example bearing the trace of the retreating convective core. This will be considered in future studies.

5.5 Conclusion

We developed a fast and efficient technique to adjust the complex pattern of mixed-mode oscillation spectra displayed by low-mass subgiant and red-giant stars. Relying on the asymptotic description of mixed-modes (Shibahashi 1979; Takata 2016b) and educated mixed-mode parameters guesses, the technique can be consistently and robustly applied to subgiant and red-giant spectra. Our results qualitatively agree with both observational and theoretical studies (e.g. Mosser et al. 2017, 2018; Pinçon et al. 2019, 2020). We then proceeded to demonstrate on a grid of stellar models the probing potential as seismic indicators held by the mixed-mode parameters. These allow us, for example, to precisely measure the mass, radius, and age of subgiant stars. This should also be possible for red giants with a mass $M \gtrsim 1.8 M_{\odot}$. This is not possible for less massive red giants as a result of the central electron degeneracy and the large core-envelope density contrast, leading to a degeneracy in the evolution of $\Delta\pi_1$ as a function of $\Delta\nu_0$.

There remains a need to assess the ability to adjust the mixed-mode spectrum of observed stars as several complications may arise (e.g. missing modes, glitches) and there also is a need to include further refinements of the asymptotic formulation used (e.g. higher-order contribution to the pressure phase, dependency of q on the frequency). Nonetheless, after modes identification, the EGGMiMoSA method will constitute an excellent tool to the automated study of large samples of evolved solar-like stars, as the PLATO mission (Rauer et al. 2014) is expected to observe. Combined with modelling tools such as AIMS (Rendle et al. 2019), this will provide us with the means to automatically compute stellar models representative of the observed mixed-mode parameters.

Asteroseismology of evolved stars with EGGMiMoSA

I. Theoretical mixed-mode patterns from the subgiant to the RGB phase

M. Farnir, C. Pinçon, M-A. Dupret, A. Noels, and R. Scuflaire

Institut d'Astrophysique et Géophysique de l'Université de Liège, Allée du 6 août 17, 4000 Liège, Belgium
e-mail: martin.farnir@uliege.be

Received 17/05/2021 / Accepted 30/06/2021

ABSTRACT

Context. In the context of an ever increasing amount of highly precise data, thanks to the numerous space-borne missions, came a revolution in stellar physics. This data allowed asteroseismology to thrive and improve our general knowledge of stars. Important results were obtained about giant stars owing to the presence of ‘mixed modes’ in their oscillation spectra. These modes carry information about the whole stellar interior, enabling the comprehensive characterisation of their structure.

Aims. The current study is part of a series of papers that provide a technique to coherently and robustly analyse the mixed-modes frequency spectra and characterise the stellar structure of stars on both the subgiant branch and red-giant branch (RGB). In this paper we aim at defining seismic indicators, relevant of the stellar structure, as well as studying their evolution along a grid of models.

Methods. The proposed method, EGGMiMoSA, relies on the asymptotic description of mixed modes. It defines appropriate initial guesses for the parameters of the asymptotic formulation and uses a Levenberg-Marquardt minimisation scheme in order to adjust the complex mixed-modes pattern in a fast and robust way.

Results. We are able to follow the evolution of the mixed-modes parameters along a grid of models from the subgiant phase to the RGB bump, therefore extending previous works. We show the impact of the stellar mass and composition on the evolution of these parameters. We observe that the evolution of the period spacing $\Delta\pi_1$, pressure offset ϵ_p , gravity offset ϵ_g , and coupling factor q as a function of the large frequency separation $\Delta\nu$ is little affected by the chemical composition and that it follows two different regimes depending on the evolutionary stage. On the subgiant branch, the stellar models display a moderate core-envelope density contrast. Therefore, the evolution of $\Delta\pi_1$, ϵ_p , ϵ_g , and q significantly changes with the stellar mass. Furthermore, we demonstrate that, for a given metallicity and with proper measurements of the period spacing $\Delta\pi_1$ and large frequency separation $\Delta\nu$, we may unambiguously constrain the stellar mass, radius and age of a subgiant star. Conversely, as the star reaches the red-giant branch, the core-envelope density contrast becomes very large. Consequently, the evolution of ϵ_p , ϵ_g and q as a function of $\Delta\nu$ becomes independent of the stellar mass. This is also true for $\Delta\pi_1$ in stars with masses $\lesssim 1.8M_\odot$ because of core electron degeneracy. This degeneracy in $\Delta\pi_1$ is lifted for higher masses, again allowing for a precise measurement of the stellar age. Overall, our computations qualitatively agree with previous observed and theoretical studies.

Conclusions. The method provides automated measurements of the adjusted parameters along a grid of models and opens the way to the precise seismic characterisation of both subgiants and red giants. In the following papers of the series, we will explore further refinements to the technique as well as its application to observed stars.

Key words. asteroseismology – stars:oscillations – methods:numerical – stars:low mass

1. Introduction

Red giant and subgiant stars constitute essential ingredients to our understanding of the Universe. Indeed, such stars are very bright and may therefore be observed at large distances and in great numbers. Firstly, the determination of their properties is crucial to galactic archaeology, which is aimed at tracing the structural and dynamical evolution of the Milky Way (e.g. Miglio et al. 2017). Secondly, these stars are key targets with regard to the precise characterisation of stellar structure and evolution. In the recent decades, the data of unprecedented quality collected by the CoRoT (Baglin et al. 2009) and Kepler (Borucki et al. 2010) spacecrafts have enabled us to make a sizeable leap towards the characterisation of red giants and subgiants, thanks to the detection of mixed modes (Bedding et al.

2011). Even though their detection is recent, their theoretical existence and detectability was predicted early on (Scuflaire 1974; Dupret et al. 2009). These modes exhibit a twofold nature: they behave as pressure modes in the outermost regions of the star, with the pressure gradient as the restoring force, and as gravity modes in the innermost regions, with the buoyancy being the restoring force. Both cavities are coupled through an evanescent region, the properties of which determine the coupling strength (e.g. Hekker & Christensen-Dalsgaard 2017). These modes constitute a unique opportunity to probe the entire stellar structure as they propagate from the surface to the core. It is not the case in solar-type stars that exhibit pure pressure modes, that propagate in an outer pressure cavity. Consequently, it is only information about the outermost layers of these stars that may be retrieved.

The coupling between gravity modes (g-modes) and pressure modes (p-modes) leads to complex behaviours, that evolve in tandem with the star. On the main sequence, a solar-like oscillator presents a p-modes spectrum that displays significant regularity in frequency. At first order, oscillation modes of a given spherical degree l are separated by a constant quantity, the large separation $\Delta\nu$ (Tassoul 1980; Gough 1986). The observed frequency range is almost constant and lies around the frequency of maximum power, ν_{\max} . As the star evolves along the subgiant branch, ν_{\max} decreases. At some point, the observed frequencies of the p-modes become so small that they can couple with the g-modes and create so-called mixed modes. This leads to the phenomenon called avoided crossings (Osaki 1971; Aizenman et al. 1977). This creates a bumping of the frequency spacing of the modes, perturbing the apparent regularity of the spectrum. Later on, during the red giant phase, as ν_{\max} continues to decrease the frequency pattern is composed of a large number of modes that behave, at leading order, as gravity modes with a constant separation between successive mode periods, the period spacing $\Delta\pi_1$ (Tassoul 1980). Again, because of the coupling between p and g-modes, this regularity is disturbed and mode bumping appears, the local period spacing between consecutive modes decreases when encountering p-modes. Despite the apparent complexity exhibited by mixed modes, several studies have demonstrated that their frequency pattern can be described via a limited number of parameters.

On the one hand, Deheuvels & Michel (2011) described avoided crossings via a series of coupled harmonic oscillators, mimicking the coupling between p- and g-modes. This approach was later used by Benomar et al. (2012) who demonstrated on a grid of subgiants that the coupling strength was predominantly function of the mass. Furthermore, they noted that it should increase right before the transition to the red giant phase. However, linking this approach to the stellar structure is not straightforward.

On the other hand, to exploit the physical knowledge we have about the stellar structure, many authors rely on the asymptotic description of mixed modes (Shibahashi 1979; Takata 2016), which assumes that the oscillating modes are of a short wavelength compared to the variations in the stellar structure (i.e., the modes radial order is large). In this formalism, the resonance condition takes the following form

$$\tan \theta_p = q \tan \theta_g, \quad (1)$$

where θ_p and θ_g are phase terms describing the propagation of the modes in the pressure and gravity cavities, respectively, and q is the coupling factor describing the level of interaction between both cavities. In this general form, the analytical expressions of these parameters directly depend on the stellar structure properties and the frequency. Based on observations, Mosser et al. (2012b, 2015) proposed explicit formulations for both phases of dipolar modes, which are the most observed:

$$\theta_p = \pi \left(\frac{\nu}{\Delta\nu} - \epsilon_p \right), \quad (2)$$

$$\theta_g = \pi \left(\frac{1}{\nu\Delta\pi_1} - \epsilon_g + \frac{1}{2} \right). \quad (3)$$

We present here the gravity phase with an opposite sign for the $1/2$ term. Assuming in addition that q is independent

of the frequency, the asymptotic expression is then a function of 5 frequency-independent parameters (henceforth referred to as the ‘mixed-modes parameters’): the large separation $\Delta\nu$, the period spacing $\Delta\pi_1$, the pressure offset ϵ_p , the gravity offset ϵ_g , and the coupling factor q . Solving Eq. (1) for ν provides the theoretical asymptotic frequencies of the dipolar modes. Under the form given by Eqs. (1)–(3), the asymptotic formulation has already been shown to be a very powerful tool that allowed us to interpret both observed and model data as functions of the stellar structure.

Indeed, the asymptotic formulation has successfully been applied to adjust observed data in several studies. For example, Mosser et al. (2015) use the asymptotic formulation along with a carefully defined variable such that it restores the regularity in the oscillation spectrum and eases its adjustment, the so-called period stretching. This technique was then used by Vrad et al. (2016) and Mosser et al. (2017, 2018) to generate an automated adjustment of a large sample of giant stars. These studies provided an accurate measurement of $\Delta\pi_1$ and q in more than 5000 stars. They were also able to measure ϵ_g in several hundreds of red giant stars. In addition, the asymptotic formalism was shown to be valid on the subgiant branch. For example, Eqs. (1)–(3) were also fitted for about 40 stars observed by *Kepler* for which we could measure the mixed-mode parameters (Mosser et al. 2014; Appourchaux 2020).

In order to interpret the observed variations in these parameters, numerous authors took interest in the mixed-modes oscillation spectra from a theoretical point of view, most of them using a grid-based approach. These studies provide invaluable insight on the evolution of the mixed-modes parameters with the stellar parameters. Namely, Jiang & Christensen-Dalsgaard (2014), Hekker et al. (2018), and Jiang et al. (2020) provided adjustments for q on theoretical frequency spectra computed from red giant stellar models. These studies showed that the decrease observed in the value of q during the evolution along the red giant branch is correlated with the increase in the size of the evanescent region. Pinçon et al. (2020) demonstrated by means of analytical models that the thickening of this region on the red giant branch actually results from its migration to the radiative core towards the base of the convective envelope. This fact also explains the variations observed in the measurement of the gravity offset (Pinçon et al. 2019). Other studies demonstrated the interest of the period spacing and large frequency separation as constraints to the stellar structure. Indeed, measuring both $\Delta\pi_1$ and $\Delta\nu$ allows us to distinguish between core helium burning and hydrogen shell burning stages, which are otherwise indistinguishable (Bedding et al. 2011; Mosser et al. 2014). This is due to the fact that the core density greatly differs in these stages, therefore impacting the value of $\Delta\pi_1$ (Montalbán et al. 2010). Also, by measuring the mass of the core in core helium burning stars models, Montalbán et al. (2013) demonstrated the possibility to constrain the convective overshooting in intermediate mass stars, the amount and nature of which greatly impacts the central stellar composition as well as the duration of the main sequence, directly influencing the inferred stellar age.

All the aforementioned works have demonstrated the high potential of mixed modes to probe and characterise the properties of evolved stars. However, all the information carried by seismic data still remains to be exploited

in full. In particular, previous theoretical works mainly focused on the red giant branch and on only one parameter at a time. It is thus necessary to extend these works to the subgiant branch and to account for all the mixed-mode parameters together in a robust and convenient way. Consequently, the present paper is part of a series aiming at providing a method to precisely adjust the mixed-modes pattern of evolved solar-like stars, either extracted from observed seismic data or predicted by a pulsation code, and to tightly constrain the stellar structure. We present in this paper the seismic method we developed, namely: **Extracting Guesses about Giants via Mixed-Modes Spectrum Adjustment** (EGGMiMoSA), which relies on the asymptotic formulation (Eq. Eq. (1)). In this method, the adjustment is performed thanks to the use of appropriate initial estimations of the five parameters of the asymptotic formulation and a Levenberg-Marquardt minimisation scheme. In the current paper, the aim is to depict the evolution of the five mixed-mode parameters across a grid of models of different masses and chemical compositions, extending from the subgiant phase to the red-giant phase. We insist that our goal is not to provide a detection and identification of mixed modes but rather to assess the relevance of the five mixed-modes parameters as probes of the stellar structure. Therefore, we do not pretend to replace identification methods of the likes of Mosser et al. (2015), as our method should come as a secondary step to such techniques in order to put constraints on stellar models.

This paper is structured as follows. We first present the method and its fitting procedure in Sect. 2. In Sect. 3, we demonstrate the ability of the technique to properly account for mixed-mode spectra and display the evolution of the adjusted parameters with stellar evolution, mass, and composition. This is followed by a discussion in Sect. 4 and we present out the conclusions in Sect. 5.

2. Method

In its current version, the EGGMiMoSA method relies on the adapted asymptotic description of the mixed-modes pattern given by Eqs. Eq. (1)-Eq. (3). The core element of the method is the computation of educated initial guesses of the five mixed-mode parameters, enabling a fast adjustment of a reference spectrum via a Levenberg-Marquardt minimisation algorithm. Before describing the parameter estimation and the fitting procedure, we first recall a few aspects relevant to the subgiant and red-giant spectra. The generation of the models used for illustration is detailed in Sect. 3.

2.1. Typical oscillation spectra

As a star evolves along the subgiant branch and then rises on the red giant branch, the properties of its spectrum evolve as well. As an illustration, we display the theoretical frequency and period differences between consecutive modes for two typical $1M_{\odot}$ solar subgiant and red giant stars in Figs. 1 and 2, respectively. Their parameters are summarised in Table 1. The models and their theoretical frequencies were computed with the CLES evolution code and the LOSC pulsation code (Scuflaire et al. 2008b,a). First, on the subgiant branch, the oscillation spectrum in Fig. 1 departs from a pure pressure behaviour, such as solar-like stars display on the main sequence. Nonetheless,

Table 1. Parameters of the $1M_{\odot}$ models used to compute the frequencies presented in Figs. 1 and 2.

	Subgiant	Red giant
\mathcal{N}	0.16	29.85
$\log L/L_{\odot}$	0.35	1.39
$\log T_{\text{eff}}$	3.74	3.65

the spectrum still shows a majority of pressure-dominated (p-dominated) modes and very few gravity-dominated (g-dominated) modes. As a consequence, successive frequencies are almost evenly spaced. However, the presence of g-dominated modes locally decreases the frequency difference. This results in mode bumping. Conversely, the oscillation spectrum for the red giant star in Fig. 2 displays a greater number of g-dominated modes per p-dominated modes. The modes periods (instead of frequencies) are now predominantly evenly separated. Again, the presence of p-dominated modes locally reduces the period difference, which also corresponds to mode bumping.

To make the distinction between pressure and gravity dominated spectra the g-dominated modes density has been conveniently defined in Mosser et al. (2015) as

$$\mathcal{N}(\nu_{\text{max}}) = \frac{\Delta\nu}{\Delta\pi_1\nu_{\text{max}}^2}, \quad (4)$$

with ν_{max} the frequency of maximum power in the power spectrum. This number represents the ratio of g-dominated modes per p-dominated modes. A g-dominated spectrum will display an \mathcal{N} value greater than unity, while a p-dominated spectrum will have a value lower than unity. For instance, the models plotted in Figs. 1 and 2 have $\mathcal{N}(\nu_{\text{max}}) \approx 0.16$ and 30, respectively.

Moreover, in Fig. 1, we see that the maximum value of the frequency difference in p-dominated spectra is close to the large separation of radial modes, $\Delta\nu_0$ (green horizontal line). We also see that successive bumps are separated by approximately one asymptotic period spacing (black arrow). We recall that the asymptotic period spacing, $\Delta\pi_{1,\text{as}}$, is related to the integration of the Brunt-Väisälä frequency, N , from the center to the base of the convection zone, r_{BCZ} , by the expression

$$\Delta\pi_{1,\text{as}} = 2\pi^2 \left(\int_0^{r_{\text{BCZ}}} \frac{N}{r} dr \right)^{-1}, \quad (5)$$

with r the distance from the center of the star. Conversely, in Fig. 2, we see that the maximum value of the period difference in g-dominated spectra is very close to the asymptotic period spacing (green horizontal line), while the bumps are separated by about the large frequency separation of the radial modes (black arrow). Through an inspection of both figures, we therefore note that we may retrieve estimations for both the large separation and the period spacing directly from such plots.

2.2. Fitting the spectrum

In the present section, we describe the fitting procedure. In its present version, the goal of the EGGMiMoSA method is

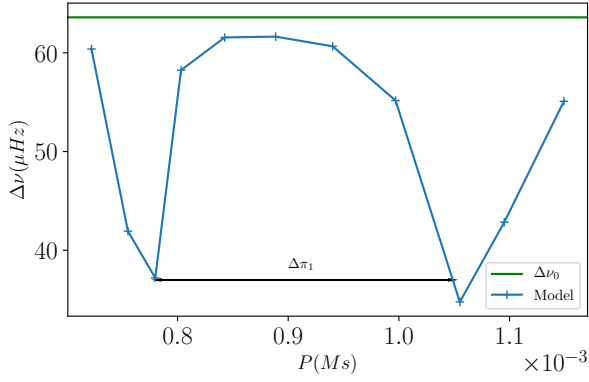


Fig. 1. Oscillation frequency differences between consecutive modes as a function of the period in the $1M_{\odot}$ subgiant model presented in Table 1. The green horizontal line represents the large separation value calculated for radial modes. The double-sided arrow shows the approximate asymptotic period spacing.

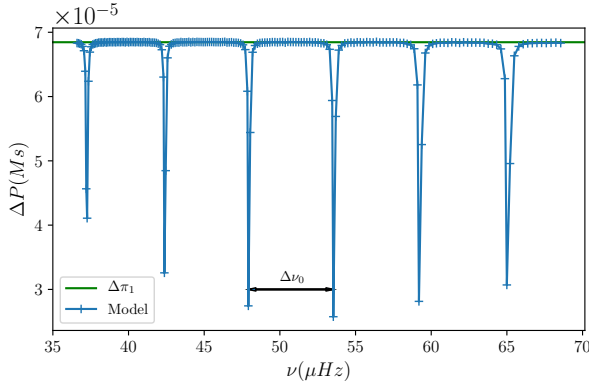


Fig. 2. Oscillation period differences between consecutive modes as a function of the frequency in the $1M_{\odot}$ red giant model presented in Table 1. The green horizontal line represents the asymptotic period spacing. The double-sided arrow shows the large separation value calculated for radial modes.

to find the values of the five frequency independent mixed-modes parameters ($\Delta\nu$, $\Delta\pi_1$, ϵ_p , ϵ_g , and q) in Eqs. Eq. (1)-Eq. (3) that provide the best agreement between the reference and theoretical asymptotic frequencies. Subgiant and red giant stars are known to be slow rotators (e.g. [Deheuvels et al. 2014](#); [Gehan et al. 2018](#)), so that rotation perturbs at first-order only the frequencies of the prograde and retrograde modes. We focus on the $m=0$ modes in the present paper and thus do not include the contributions of rotation. The adjustment is carried in the following steps: **1.** We estimate $\Delta\nu$ and ϵ_p with WhoSGIAd. **2.** We estimate the g -dominated mode density. **3.** We provide the initial estimates for $\Delta\pi_1$, ϵ_g , and q . **4.** We adjust frequency (p-dominated spectrum) or period (g-dominated) differences. **5.** We adjust individual frequencies.

As the spectrum adjustment is to be carried via a Levenberg-Marquardt algorithm, which is local, it is crucial to provide proper initial estimates of the parameters. This is even more important as strong correlations exist between the individual parameters of the fit. Indeed, from

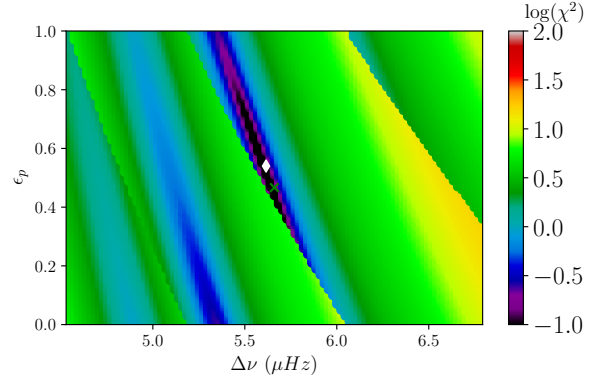


Fig. 3. Cost function landscape in the neighbourhood of the known solution as a function of the parameters $\Delta\nu$ and ϵ_p . The minimum of the χ^2 landscape is represented by the white diamond and the fitted value by the green cross.

Eqs. Eq. (2) and Eq. (3), we observe tight correlations between $\Delta\nu$ and ϵ_p and between $\Delta\pi_1$ and ϵ_g . This is also illustrated in Figs. 3 and 4. Both figures show the evolution of the χ^2 cost function (measuring the squared difference between the reference and asymptotic frequencies) as a function of two of the five fitted parameters (the three remaining parameters are frozen at their final fitted values). We observe in Fig. 3 (respectively Fig. 4) that $\Delta\nu$ and ϵ_p (resp. $\Delta\pi_1$ and ϵ_g) show an important correlation. In the most extreme case, because of the large value of the pressure (resp. gravity) radial order, a small deviation in the value of $\Delta\nu$ (resp. $\Delta\pi_1$) leads to large differences in ϵ_p (resp. ϵ_g). Furthermore, we observe steep χ^2 discontinuities. These are the consequence of an improper mode identification caused by the incorrect $\Delta\nu$ and ϵ_p values. Because of these important correlations, which may impair the convergence of the method, we took special care in devising the initial parameters estimation. In order to provide a first glimpse of the efficiency of the developed method, we represent in these figures the values of the parameters fitted with EGGMiMoSA as green crosses and the minima of the χ^2 in the 2D landscape as white diamonds. We see that they greatly match in both cases. We note nevertheless that there is a slight difference, especially in Fig. 3, because both figures constitute a restricted picture of the five-parameter space and the minimum in this restricted space does not necessarily constitute the global five-parameter minimum.

2.2.1. Estimating $\Delta\nu$ and ϵ_p with WhoSGIAd

Since the first detections of solar-like oscillations in red giants (e.g. [Frandsen et al. 2002](#)), it has been known that their spectra always display several radial modes. These may be used in order to estimate a priori the value of the mixed-modes large separation, $\Delta\nu$, and pressure offset, ϵ_p . To do so, we rely on the estimate computed with the WhoSGIAd method ([Farnir et al. 2019](#)) applied to radial modes. This ensures a robust, precise, and fast estimation. This estimation corresponds to a least-squares linear fit of the radial frequencies. We have already highlighted the fact that in order to improve the stability of the method, we maintain the value of $\Delta\nu$ fixed at the first guess.

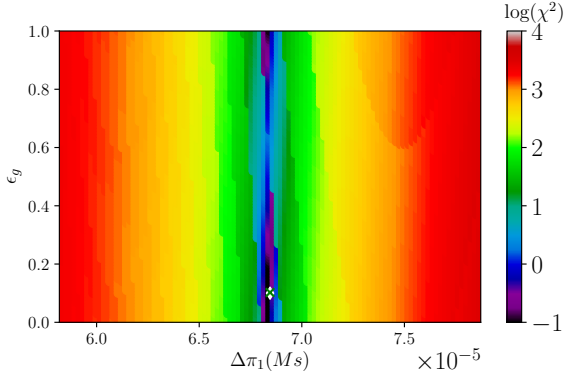


Fig. 4. Cost function landscape in the neighbourhood of the known solution as a function of the parameters $\Delta\pi_1$ and ϵ_g . The minimum of the χ^2 landscape is represented by the white diamond and the fitted value by the green cross.

2.2.2. Estimating the g-dominated modes density

As the parameter estimation and subsequent steps depend on the g-dominated mode density (Eq. Eq. (4)), we first need to provide an estimate of this quantity. Nonetheless, as we aim at applying the technique to observed spectra, we cannot assume that we will have access to a measure of $\Delta\pi_1$. We thus provide in this section a technique to recognise g-dominated spectra, p-dominated spectra and intermediate cases. To do so, we take advantage of the following second difference in frequencies:

$$\delta\nu_{2,i} = \frac{\nu_{i+1} - \nu_{i-1}}{\Delta\nu}, \quad (6)$$

where the i index is an integer ordering the frequencies in ascending values, and thus the periods in decreasing values. We recall that the $\Delta\nu$ value was previously retrieved via the WhoSGLad method on radial modes.

In the case of a mixed-mode oscillation spectrum, the second difference is expected to take values between 0 and 2. In a pressure-dominated spectrum, as the number of p-dominated modes exceeds that of g-dominated modes, individual modes are almost evenly spaced in frequency of one large separation. As a consequence, the second difference takes a value between 1 and 2. Conversely, in a gravity dominated spectrum, the modes are now almost evenly spaced in period of one period spacing. To make the link with the second frequency difference, we can write using $\nu_i = 1/P_i$ such that

$$\delta\nu_{2,i} = \frac{\Delta\pi_1 \nu_{i+1} \nu_{i-1}}{\Delta\nu} \delta P_{2,i}, \quad (7)$$

where $\delta P_{2,i} = (P_{i-1} - P_{i+1})/\Delta\pi_1$ is defined as the second period difference. In Eq. Eq. (7), the first factor is smaller than $\mathcal{N}(\nu_j)^{-1}$, which is much smaller than unity in g-dominated spectra, and $\delta P_{2,i} = (P_{i-1} - P_{i+1})/\Delta\pi_1 \lesssim 2$. Consequently, the second frequency difference now ranges between 0 and 1. Finally, if the g-dominated modes density was exactly equal to 1, this would mean that the spectrum would alternate between p-dominated and g-dominated modes and the second difference would be exactly equal to 1 as well. Therefore, using the second difference, we may

easily distinguish the different types of spectra. We will consider a spectrum with $\delta\nu_{2,i} > 1$ everywhere as completely p-dominated; a spectrum with $\delta\nu_{2,i} < 1$ everywhere as completely g-dominated; and a spectrum for which the second difference crosses the value of 1 as an intermediate case. We provide in Appendix A a visual and mathematical justification of the validity of these previous heuristic arguments.

2.2.3. $\Delta\pi_1$, ϵ_g and q initial estimation

We now present the estimation of the remaining three parameters. They are estimated according to the nature of the spectrum, that is: completely g-dominated, completely p-dominated or intermediate.

g-dominated estimation ($\mathcal{N} \gg 1$, $\delta\nu_2 < 1$): In the g-dominated case, the spectrum presents a majority of gravity dominated modes. Also, the gravity dominated modes closest to pure g-modes are located midway between two dips of the period difference curve. As illustrated in Fig. 2, the maximum of the local period spacing between consecutive modes, denoted ΔP_{\max} , provides a first proper estimate for $\Delta\pi_1$.

Next, we use the ζ function defined by Mosser et al. (2015) to provide an initial value for the coupling factor q . This function is defined as

$$\zeta = \left\{ 1 + \frac{q}{\mathcal{N}} \frac{1}{q^2 \cos^2 \theta_p + \sin^2 \theta_p} \right\}^{-1}, \quad (8)$$

such that $\frac{dP}{dn} = \zeta \Delta\pi_1$, with $n = n_p - n_g$ the mixed-mode radial order. In the case of g-dominated spectra, $\mathcal{N} \gg 1$, the θ_p phase is almost constant between successive modes. Assuming in addition that the $\mathcal{N}(\nu)$ function provided in Eq. Eq. (4) does not vary between successive modes, ζ is thus almost constant, and we may integrate the expression for two successive radial orders so that we obtain $\Delta P_i \simeq \zeta(\nu_i) \Delta\pi_1$. We then use this relation to estimate q . First, we define the ratio $Z = \zeta_{\min}/\zeta_{\max}$ with ζ_{\min} and ζ_{\max} corresponding, respectively, to the minimum (i.e., close to a pure p-mode with $\theta_p = k\pi, k \in \mathbb{N}$) and maximum (i.e., close to a pure g-mode with $\theta_p = \pi/2 + k\pi, k \in \mathbb{N}$) values of the ζ function. From the analytical expressions of ζ_{\min} and ζ_{\max} , we can thus get an expression of the coupling factor as a function of \mathcal{N} and Z :

$$q = \left[(Z - 1) \mathcal{N} + \sqrt{(1 - Z)^2 \mathcal{N}^2 + 4Z} \right] / 2. \quad (9)$$

Second, as $\Delta P_i \simeq \zeta(\nu_i) \Delta\pi_1$, we can estimate Z from the ratio of the minimum and maximum values of the individual observed period spacings. Note that, as we have a first estimate for $\Delta\pi_1$, we also have an estimate of \mathcal{N} . Therefore, according to Eq. Eq. (9), we can obtain an estimate for the coupling factor.

In addition, having an estimate of \mathcal{N} and q , we can now compute the ζ function for any frequency. This allows us in a final step to correct by iteration the first estimated $\Delta\pi_1$ value using the relation $\Delta\pi_1 \simeq \Delta P_{\max}/\zeta(\nu_{\max})$, where ν_{\max} is the frequency at the maximum value of the individual period spacings.

Finally, we note that, for g-dominated spectra, the gravity offset will not be adjusted in the subsequent step as period differences will be adjusted (Sect. 2.2.4). Therefore,

we do not need to provide an estimate for its value in the present step.

p-dominated estimation ($\mathcal{N} \ll 1$, $\delta\nu_2 > 1$): For pressure-dominated spectra, the gravity-dominated modes correspond to the dips in the frequency difference curve. In that case, both $\Delta\pi_1$ and ϵ_g are estimated through a linear fit of the identified gravity-dominated modes. The slope of the fit corresponds to $\Delta\pi_1$ and the intercept to ϵ_g .

As the approximation $\Delta P_i \simeq \zeta(\nu_i)\Delta\pi_1$ is only valid for g-dominated spectra where $\mathcal{N} \gg 1$, we need an alternative to estimate the coupling factor in p-dominated spectra. For a p-dominated spectrum, $\mathcal{N} \ll 1$, we define the ζ' function (see App. B) to express the variation of frequency with the mixed-mode radial order, n :

$$\zeta' = \left\{ 1 + \frac{q\mathcal{N}}{\cos^2 \theta_g + q^2 \sin^2 \theta_g} \right\}^{-1}, \quad (10)$$

such that $\frac{d\nu}{dn} = \zeta'\Delta\nu$. Because the θ_g function is almost constant between two dips in p-dominated spectra where $\mathcal{N} \ll 1$, ζ' is almost constant as well within the assumption that \mathcal{N} is quasi constant. We may thus integrate over n the previous expression between two successive modes. This yields $\Delta\nu_i \simeq \zeta'(\nu_i)\Delta\nu$, where the dependency on individual frequencies is shown explicitly. Using Eq. (1), we can easily show that $\zeta' = 1 - \zeta$.

Similarly to the g-dominated case, we define $Z' = \zeta'_{\max}/\zeta'_{\min}$ where ζ'_{\max} is the maximum value of ζ' obtained for $\theta_g = k\pi$, $k \in \mathbb{N}$ (i.e., close to a pure p-mode) and ζ'_{\min} is the minimum value for $\theta_g = \pi/2 + k\pi$, $k \in \mathbb{N}$ (i.e., close to a pure g-mode). We thus can get an analytical expression of q based on this ratio, that is,

$$q = \left[(1 - Z') + \sqrt{(Z' - 1)^2 + 4Z'\mathcal{N}^2} \right] / (2\mathcal{N}Z'). \quad (11)$$

Using the fact that $\Delta\nu_i \simeq \zeta'(\nu_i)\Delta\nu$, the maximum and minimum values of the ζ' function can then be estimated with the maximum and minimum values of the individual frequency differences. This provides an estimate of Z' that, combined with the estimate of \mathcal{N} from the estimate of $\Delta\pi_1$, provides an estimate of q according to Eq. (11).

Intermediate case ($\mathcal{N} \sim 1$, $\delta\nu_2 \sim 1$): When we have comparable p-dominated and g-dominated modes densities, that is, $\mathcal{N} \sim 1$, we cannot rely on the characteristic shape of the frequency or period differences to estimate individual parameters. Nevertheless, we may use the transition in the spectrum where $\delta\nu_2 \simeq 1$ to carry this estimation. From Sect. 2.2.2, we know that $\delta\nu_{2,i} \simeq 1$ and $\delta P_{2,i} \simeq 1$ at the transition, where we have the same amount of p-dominated and g-dominated modes. As a consequence, the first factor in the right-hand side of Eq. (6) is close to unity and we may retrieve an estimate for $\Delta\pi_1$:

$$\Delta\pi_1 \simeq \frac{\Delta\nu}{\nu_{t+1}\nu_{t-1}}. \quad (12)$$

with t being the mode index closest to the transition, that is, where $\delta\nu_{2,t}$ is the closest to unity.

The coupling factor, q , is then estimated on the part of the spectrum being the most dominated by one character. If we note ν_{\inf} and ν_{\sup} the lower and upper bounds of

the considered frequency range, this corresponds to the p-dominated part around ν_{\sup} if $1/\mathcal{N}(\nu_{\sup}) > \mathcal{N}(\nu_{\inf})$ or the g-dominated part around ν_{\inf} if $1/\mathcal{N}(\nu_{\sup}) < \mathcal{N}(\nu_{\inf})$. We then follow the usual previous procedure associated with the dominant character to estimate q .

2.2.4. Fitting differences

After providing proper estimates for the mixed-modes parameters, we adjust the values of these parameters that allow us to reproduce individual period spacings or frequency differences between consecutive modes (according to the nature of the spectrum). By doing so, we cancel out the correlation with ϵ_g (resp. ϵ_p), which remains fixed and will be adjusted in subsequent steps. This differs from most techniques present in the literature as they directly adjust the individual frequencies (e.g. Mosser et al. 2012b; Hekker et al. 2018). Techniques that adjust period differences also exist (Cunha et al. 2015, 2019), similarly to what we propose, however, those are only valid for red giants, which have a g-dominated spectrum ($\mathcal{N} \gg 1$). The present study therefore represents an extension of such works.

g-dominated spectrum: When the spectrum is dominated by the contribution of g-dominated modes, we fit individual period spacings. From Eq. (1), it is possible to find an expression for individual period spacings:

$$\Delta P_i = P_i - P_{i+1} = (\Delta n_g + \Delta\psi_i/\pi)\Delta\pi_1, \quad (13)$$

with Δn_g , the difference of gravity radial order between two successive modes, $\Delta\psi_i = \psi_i - \psi_{i+1}$ and $\psi_i = \arctan(\tan\theta_{p,i}/q)$. The i index in the $\theta_{p,i}$ term represents the value of θ_p evaluated at the period of index i . The difference Δn_g takes either a value of 1 when two successive modes are g-dominated or 0 when encountering a p-dominated mode, resulting in a change of the pressure radial order. In practice, we keep $\Delta n_g = 1$ to compute the theoretical period difference ΔP_i in a first step and then subtract $\Delta\pi_1$ to ΔP_i where its estimate is greater than unity, which is not permitted. A further justification of the value of Δn_g is given in Appendix C. The three remaining parameters ($\Delta\pi_1$, ϵ_p and q) may be adjusted to reproduce the reference individual period spacings.

Second, having adjusted individual period spacings, we may find a value of ϵ_g such that we minimise the difference between reference and fitted periods expressed with the following function:

$$\chi^2 = \sum_{i=1}^N \frac{(P_{i,\text{ref}} - P_{i,\text{fit}})^2}{\sigma_i^2}, \quad (14)$$

with N the number of modes to be adjusted and σ_i the uncertainties on the period of each mode.

As there only remains one free parameter to be fitted, ϵ_g , minimising the distance between reference and theoretical periods amounts to compute $\frac{\partial\chi^2}{\partial\epsilon_g} = 0$. This yields an analytical expression for ϵ_g :

$$\epsilon_g = \left[\sum_{i=1}^N \frac{P_{i,\text{ref}}}{\sigma_i^2} + \sum_{i=1}^N \sum_{j=1}^{i-1} \frac{\Delta P_{j,\text{fit}}}{\sigma_i^2} \right] \frac{1}{\Delta\pi_1 \sum_{i=1}^N 1/\sigma_i^2} - (n_{g,1} - 1/2 + \psi_1/\pi), \quad (15)$$

where $\Delta P_{j,\text{fit}}$ represent individual period spacings from the previous step and $n_{g,1}$ is the gravity radial order of the first mode in the observed set. Because ϵ_g is defined modulo 1 and $n_{g,1}$ is an integer, its actual value does not impact ϵ_g .

p-dominated spectrum: In the case of a pressure dominated spectrum, we proceed in a very similar fashion. First, to avoid the correlation between $\Delta\nu$ and ϵ_p , the individual frequency spacings are adjusted. Their expressed as follows:

$$\Delta\nu_i = \nu_{i+1} - \nu_i = (\Delta n_p + \Delta\phi_i/\pi) \Delta\nu, \quad (16)$$

where Δn_p is the difference of pressure radial order between two successive modes and $\phi_i = \arctan(q \tan \theta_{g,i})$. Similarly to the g-dominated case, Δn_p takes either a value of 1, for two successive p-dominated mixed-modes, or 0 when alternating between p-dominated and g-dominated character.

Finally we get the following expression for ϵ_p , minimising the difference between reference and asymptotic frequencies:

$$\epsilon_p = \left[\sum_{i=1}^N \frac{\nu_{i,\text{ref}}}{\sigma_i^2} - \sum_{i=1}^N \sum_{j=1}^{i-1} \frac{\Delta\nu_{j,\text{fit}}}{\sigma_i^2} \right] \frac{1}{\Delta\nu \sum_{i=1}^N 1/\sigma_i^2} - (n_{p,1} + \phi_1/\pi), \quad (17)$$

with $n_{p,1}$ the radial order of the first mode in the set. As ϵ_p is defined modulo 1 and $n_{p,1}$ is an integer, its actual value is not important. We note that, in this context, the σ_i now represent uncertainties on the frequencies of each mode.

2.2.5. Fitting frequencies

Independently of the nature of the spectrum, a last Levenberg-Marquardt minimisation step is carried to simultaneously adjust the four parameters $\Delta\pi_1$, ϵ_p , ϵ_g , and q in such a way that the individual theoretical frequencies, that are solutions of Eq. (1), reproduce at best the reference frequencies. This last complete adjustment further improves the agreement with the data and also ensures the reduction the uncertainties on the parameters of the adjustment. Before assessing the probing potential of the individual parameters of the adjustment, we tested the ability of the EGGMiMoSA method to retrieve parameters from frequencies that were generated with the asymptotic formulation and known parameters. The results were excellent and did not introduce unwanted biases.

3. Seismic indicators

In this section we apply the above-described method to several sequences of giant models and display the evolution of the individual parameters to assess their probing potential as relevant proxies of the stellar structure and evolution. The models were computed with the CLES evolution code (Scuflaire et al. 2008b) as described in Farnir et al. (2019). The reference model has a mass of $1M_\odot$, with an initial hydrogen abundance of $X_0 = 0.72$ and metal abundance of $Z_0 = 0.015$. Oscillation modes are computed using the LOSC oscillation code (Scuflaire et al. 2008a). Therefore, the reference modes are not the solution of the asymptotic formulation. Regarding the frequency range considered for

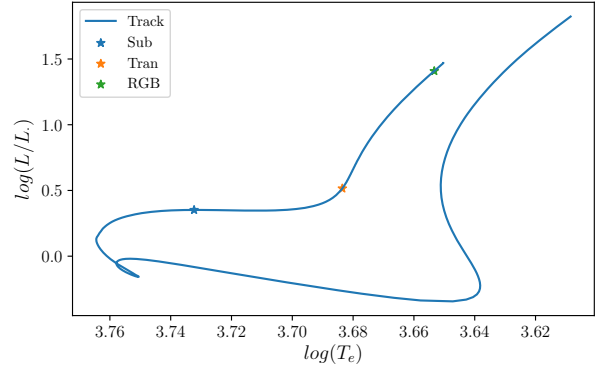


Fig. 5. Position of the models presented in Figs. 6 to 8

each model, Mosser et al. (2012a) estimated that the extent around ν_{max} of the modes that are efficiently excited, therefore observable, in red giant stars follow the simple relation $0.66\nu_{\text{max}}^{0.88}$. Typical observations from Appourchaux et al. (2012) for a subgiant star with $\nu_{\text{max}} \sim 1000\mu\text{Hz}$ show that a little more than ten radial modes may be clearly identified. Therefore, to match such observed ranges and ensure computing a sufficient amount of modes, we chose a slightly broader range of about $\nu_{\text{max}} \pm 0.4\nu_{\text{max}}^{0.88}$. This corresponds, for red giants (resp. subgiants) to approximately three (resp. 5) p-dominated modes on both sides of ν_{max} , as expected from the observations.

3.1. Individual spectra

In the present section we display adjusted oscillation spectra of models typical of the Sun ($1M_\odot$, $X_0 = 0.72$ and $Z_0 = 0.015$) at different stages of evolution: at the beginning of the subgiant phase (subsequently referred to as 'Sub'), at the transition between subgiant and red giant phases ('Tran') and at the tip of the red giant branch, before the luminosity bump ('RGB'). These spectra are represented as frequency or period differences (resp. for pressure or gravity dominated spectra) as a function of the frequency. Those stages are represented in a HR diagram in Fig. 5 and correspond to \mathcal{N} values of respectively 0.16, 0.98, and 29.85. Figures 6 to 8 compare the reference spectra obtained with LOSC (in blue) with the fitted spectra (in orange). To produce these results, the adjustment was undertaken in an automated fashion following the methodology described in Sect. 2.

Early subgiant: Figure 6 corresponds to an early subgiant model (marked 'Sub' in Fig. 5), the first one on the sequence displaying two local minima in the individual period spacing, corresponding to mixed modes. This is the much lower threshold of applicability with regard to the EGGMiMoSA technique. Nonetheless, we observe that it is very efficient at providing a qualitative adjustment of the data. Both the shape and position of individual bumps are properly accounted for. However, we note a slight offset in the bump height around a frequency of $1000\mu\text{Hz}$. This offset is similar in amplitude to the error made by assuming the large separation of radial modes to be constant even

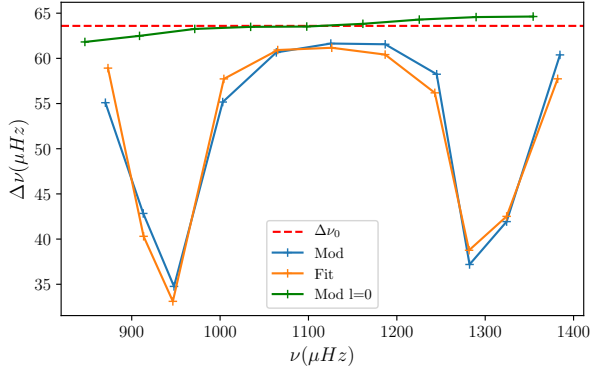


Fig. 6. Fitted frequency differences as a function of frequency for an early $1M_{\odot}$ subgiant model, denoted ‘Sub’ in Fig. 5.

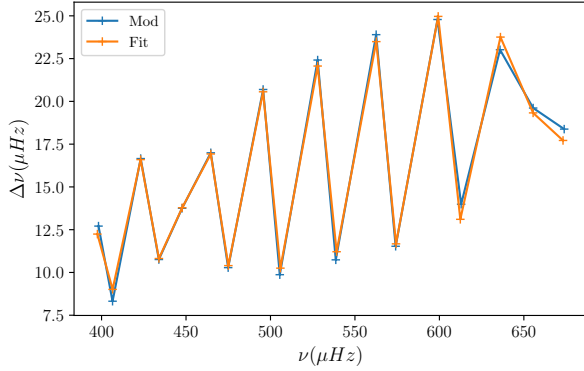


Fig. 7. Fitted frequency differences as a function of frequency for a $1M_{\odot}$ model with similar numbers of p-dominated and g-dominated modes. It is denoted ‘Tran’ in Fig. 5.

though it presents a slight dependency with the frequency. This is illustrated by the dashed red line, corresponding to the constant estimate of the large separation of radial modes obtained with WhoSGLAd (Farnir et al. 2019), compared to the local value in green. We observe that the offset between the green and red curves is similar to that between the blue and orange ones.

Late subgiant: We represent a model presenting a comparable amount of pressure dominated modes and gravity dominated ones in Fig. 7 (marked ‘Tran’ in Fig. 5). It corresponds to $\mathcal{N} \simeq 1$. Although the shape of the spectrum is complex, we find a proper fit to the data. This is possible thanks to the proper estimation of the parameters beforehand.

Evolved red giant: For the more evolved star displayed in Fig. 8, we again observe a very good agreement with the data. However, we note a slight shift in the position of dips towards low frequencies. Furthermore, we also observe that the adjusted dips tend to be shallower than the data suggests. Possible reasons for such discrepancies will be discussed in Sects. 4.3 and 4.4.

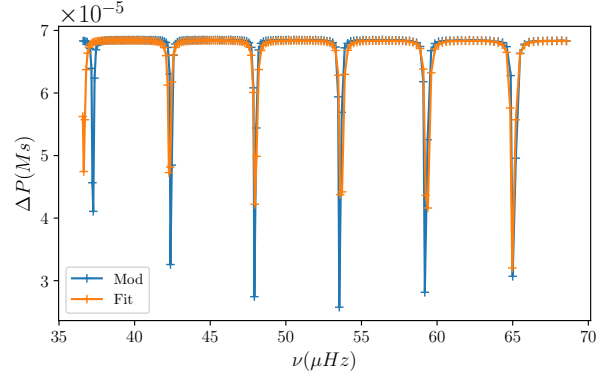


Fig. 8. Fitted individual period spacings as a function of frequency for a late $1M_{\odot}$ red giant model. It is denoted ‘RGB’ in Fig. 5.

3.2. Variation with mass along the evolution

We present in the current section the variation of the parameters of the adjustment with stellar evolution and mass. The models were computed from the beginning of the subgiant phase up to the RGB-bump. The results are displayed in Figs. 9 through 17. To ease the comparison with other works, stellar evolution goes from right to left.

3.2.1. Period spacing, $\Delta\pi_1$

Figure 9 represents the evolution of the period spacing as a function of the large separation of radial modes which decreases with evolution. The large separation is indeed a proxy of the mean density (Ulrich 1986; Farnir et al. 2019) which decreases with evolution during the subgiant and red giant phases. We represent tracks for stellar masses in the range $[1.0M_{\odot}, 2.1M_{\odot}]$ ($0.1M_{\odot}$ step) in different colours. We represent the transition between subgiant and red giant phases (at $\mathcal{N} = 1$) by dotted lines. We thus observe that the period spacing decreases with the evolution, at different rates according to the evolutionary phase, the decrease on the subgiant phase being the steepest.

We first note that our computations in Fig. 9 qualitatively agree with the observations of Mosser et al. (2014, see Fig. 1). This confirms that subgiant and red-giant stars occupy distinct regions in a seismic HR diagram. We also note an excellent agreement between the fitted period spacing and its asymptotic value, $\Delta\pi_{1,as}$, represented by dashed lines (see also Lagarde et al. 2016). Assessing the normalised difference between the fitted and asymptotic values of the large separation, given by $\delta\Delta\pi_1 = \frac{|\Delta\pi_{1,fit} - \Delta\pi_{1,as}|}{\Delta\pi_{1,as}}$, we observe that it never exceeds 0.2% on the red-giant phase. On the subgiant phase, this difference is greater and decreases as the star evolves. It is below 10 – 15% at the beginning of the subgiant phase and quickly drops below 5 – 10%. This demonstrates that as n_g increases, the validity of the asymptotic analysis improves. Finally, only a few models exceed the 15% disagreement and they correspond to models with only two g-dominated modes, which stands as the very limit of applicability of our technique. This suggests that the adjusted value is a valid proxy of the asymptotic one. This agreement demonstrates that, al-

though the asymptotic approximation is questionable for g-dominated modes in the subgiant phase (the number of nodes of the g-dominated mode eigenfunction in the buoyancy cavity is $n_g \sim 3$ in an early subgiant, and its wavelength is thus large), it globally yields valid results. Using the asymptotic expression in Eq. (5), we can crudely estimate that $\Delta\pi_1$ is about inversely proportional to the maximum of the Brunt-Väisälä frequency in the radiative region, which was shown by Pinçon et al. (2020) to be approximately proportional to the square root of the helium core density. The evolution of the helium core density as a function of its mass is plotted in Fig. 10 for different stellar masses. During these stages, the helium core mass increases as $\Delta\nu$ decreases. We can thus see that the helium core density progressively increases during evolution, leading to the global decrease in the period spacing, as expected.

We further note that the subgiant tracks in Fig. 9, corresponding to different masses, are separated to a significant extent. This trend with the stellar mass can again be explained by the dependence of the helium core density on the stellar mass during the subgiant branch as illustrated in Fig. 10. We see in Fig. 9 that the $\Delta\pi_1$ separation between successive tracks is much larger than the typical observed relative uncertainties from Appourchaux (2020), which are smaller than 1% in most cases. This demonstrates that the measure of both $\Delta\nu_0$ and $\Delta\pi_1$ should allow us to infer the mass of an observed star with a precision much better than $0.1M_\odot$. Consequently, because the age of a subgiant star is dominated by the duration of the main sequence phase, which is a function of the mass, we may in turn constrain the stellar age. This holds great promises for the accurate characterisation of stellar populations. To further demonstrate that the age of a subgiant may indeed be constrained by the measure of $\Delta\nu_0$ and $\Delta\pi_1$, we display in Fig. 11, the evolution of the asymptotic period spacing, $\Delta\pi_{as}$, with $\Delta\nu_0$ along the subgiant phase. The colour gradient corresponds to the stellar age. We observe that individual tracks indeed represent distinct ages. We also show iso-radius values with the black symbols. Models with $2R_\odot$ are symbolised by a diamond, models with $3R_\odot$ by a pentagon and those with $4R_\odot$ by a star. We observe that measuring both $\Delta\pi_1$ and $\Delta\nu_0$ allows us to position a star on this diagram and to constrain its mass, radius and age at a given metallicity. Nevertheless, assuming the duration of the main sequence to be mainly a function of the stellar mass only holds when there is no overshooting during this phase, as is the case for solar-like stars. However, stars with a mass greater than $\sim 1.2M_\odot$ have a convective core, and the overshooting may therefore impact the inferred age. For example, Noll et al. (2021) demonstrated in the specific case of the KIC10273246 subgiant that models with a finite amount of overshooting are in better agreement with observed data than models without overshooting. Including the effect of overshooting will thus be mandatory in more quantitative studies that will follow the preliminary exploratory work presented here.

In red giants with masses $\lesssim 1.8M_\odot$, we see in Fig. 9 that the evolution of $\Delta\pi_1$ as a function of $\Delta\nu$ converges to a degenerate track. This degeneracy is actually the result of the electron degeneracy in the helium core at these low masses. In these evolved stars, the density contrast between the core and the envelope is such that the mass of the envelope is negligible compared to that of the core. Therefore, we may show by homology that the properties of the shell are determined by the mass and radius of the helium core

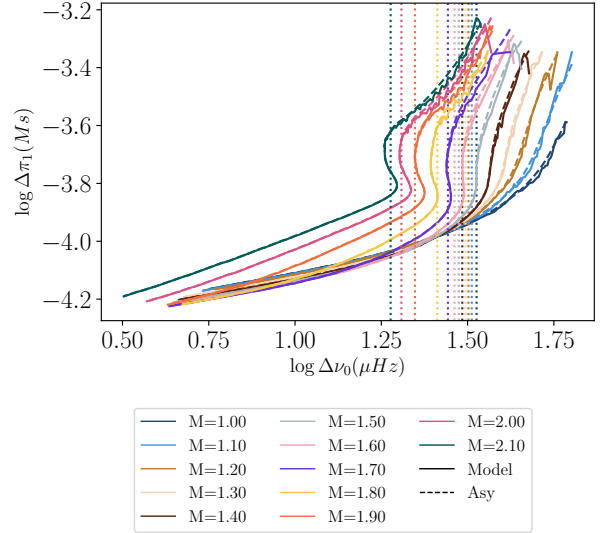


Fig. 9. Variation of $\Delta\pi_1$ with $\Delta\nu_0$ for different masses, depicted by the colours. The dashed lines correspond to the asymptotic value. The dotted vertical lines correspond to the transition between subgiant and red-giant phases.

(Refsdal & Weigert 1970; Kippenhahn et al. 2012). Furthermore, because of the central electron degeneracy, the mass and radius of the core are related and the density of the core is a function of the core mass only. As a consequence, the evolution of the helium core density, in these stars with a degenerate core, should be independent of the total stellar mass and vary only with the mass of the helium core. In particular, this is what we observe in Fig. 10. The low-mass tracks indeed converge to an identical evolution once the transition to the red-giant phase, represented by the dotted vertical lines, has been crossed. The consequence of this relation between the core mass and radius is that the properties of the shell are solely determined by the mass of the helium core. The temperature and luminosity of the shell, which, in turn determine the total luminosity, are then only a function of the mass of the core. As the effective temperature is almost constant on the red-giant branch, the stellar radius thus also predominantly depends on the mass of the core. This is also true for the mean density, $\bar{\rho}$, as it is predominantly a function of the stellar radius. Consequently, the same goes for the large frequency separation $\Delta\nu$ that is a proxy of the mean density. This results in a helium core density and a density contrast $\rho_c/\bar{\rho}$, with ρ_c the central density, which only depend on the mass of the helium core. These quantities are therefore degenerate as well as a function of the stellar mass for low mass stars with a degenerate core. This is indeed what we observe in Figs. 10 and 12. The consequence of this degeneracy in the core helium density as a function of $\Delta\nu$ is the degeneracy in period spacing observed in Fig. 9. Finally, as the degeneracy is lifted in red-giant stars with masses $\gtrsim 1.8M_\odot$, it is theoretically possible to constrain the mass, radius and age of these stars by measuring $\Delta\nu_0$ and $\Delta\pi_1$, similarly to the case of the subgiants. However, in practice, it might not be possible to observe such stars as they evolve fast.

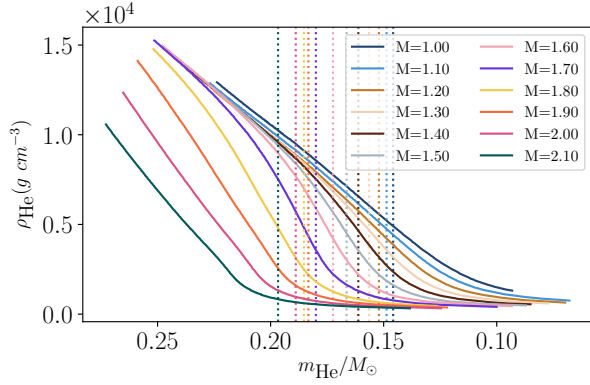


Fig. 10. Evolution of the helium core density as a function of its mass. The colours and different line styles have the same indications as in Fig. 9.

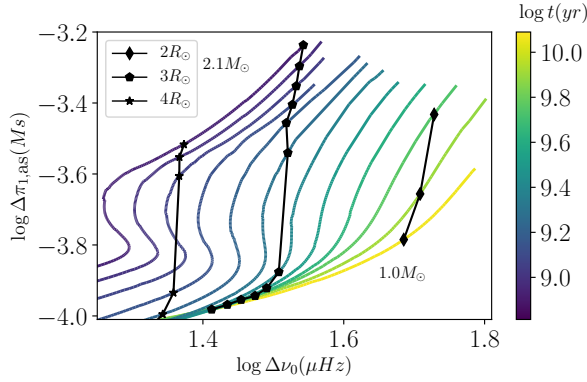


Fig. 11. Variation of $\Delta\pi_{1,as}$ with $\Delta\nu_0$ on the subgiant phase for different masses. The colour gradient represents the age. The black symbols correspond the models at fixed radius. The diamonds correspond to models of $2R_\odot$, pentagons to $3R_\odot$, and stars to $4R_\odot$.

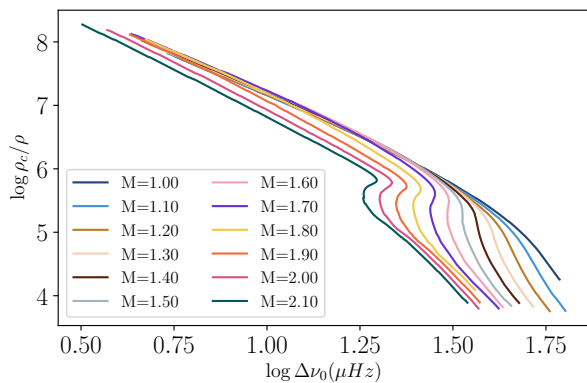


Fig. 12. Evolution of the ratio of the central density to the mean stellar density as a function of the large separation of radial modes. The colours represent different total stellar masses, as in Fig. 9.

3.2.2. Pressure offset, ϵ_p

Figure 13 shows the evolution of the pressure offset as a function of \mathcal{N} , which increases with evolution. From now on, we restrict the sample of masses to a sub-sample ($1.0, 1.2, 1.5$ and $1.8M_\odot$) for better clarity. The same trend is followed by models with masses above $1.8M_\odot$. The first striking feature is that there exist two regimes, depending on the evolution stage. During the subgiant phase, we observe that ϵ_p mostly displays an increasing trend, of which the slope as a function of \mathcal{N} increases with mass. This increase is followed by a steady decrease along the red giant phase with a slope that is independent of the mass. This is in qualitative agreement with the measured evolution from (Mosser et al. 2013, Fig.7). We note that their measurements are shifted up by 0.5. This is to be expected as they consider radial modes while we consider $l = 1$ dipolar modes, which introduces a shift of $l/2$.

We further investigate the two apparent regimes in the evolution of the pressure offset. As it represents the phase lag induced at the boundaries of the pressure cavities, we expect its behaviour to be influenced by their properties. As a consequence, we display in Fig. 14 the density contrast compared to the inner sphere at the lower boundary of the pressure cavity, corresponding to the outer edge of the evanescent region. The local density contrast is defined in (Takata 2016) by:

$$J(r) = 1 - \rho(r) / \bar{\rho}(r), \quad (18)$$

which compares the local density ρ and local mean density $\bar{\rho}(r) = \frac{m(r)}{4/3\pi r^3}$, with $m(r)$ the mass encapsulated by the sphere of radius r . As an example, a value of $J = 0.7$ means the inner sphere is on average three times denser than the local layer whereas a value of $J = 0.9$ means the inner sphere is, on average, ten times denser. As the density contrast compared to the inner sphere tends to zero, J tends towards unity. We observe that the density contrast at the outer edge of the evanescent region, r_2 , is moderate and strongly varies with the mass in the subgiant phase. Then, all the tracks converge towards a similar and high density contrast during the red giant phase (i.e., $J \sim 0.9$). This matches the observations for the pressure offset, indicating that the pressure offset holds an information about the density contrast and the structure in the evanescent region. Indeed, Pinçon et al. (2020) showed that the structure of the intermediate evanescent region behaves as power laws of the radius when the density contrast between the core and the evanescent region is large, independently of the stellar mass. This also goes for the Brunt-Väisälä and Lamb frequencies. In contrast, the structure deviates from such a configuration for lower core-envelope density contrast as observed in subgiant stars (see also discussion in Sect. 3.2.4). This suggests that the evolution of the core-envelope density contrast between the subgiant and the red giant branches is the main responsible for the different regimes observed in the pressure offset.

In Fig. 13, during the red giant phase, we observe discontinuities, that result in a seesaw behaviour. This is a direct consequence of the set of modes considered and does not question the quality of the adjustment. Indeed, for such an extended evolution, we may not consider a fixed set of modes, that is, of fixed radial orders. As a consequence, the set shifts towards lower pressure modes orders and disconti-

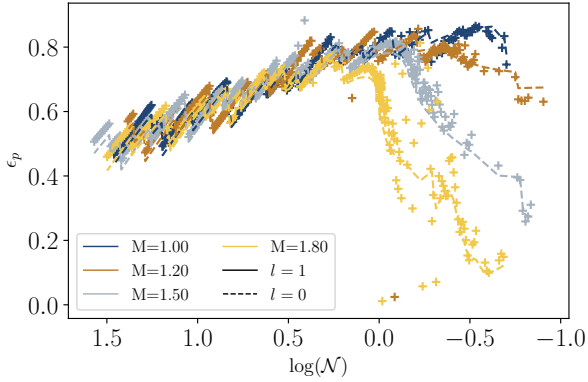


Fig. 13. Variation of ϵ_p as a function of \mathcal{N} . The dashed line correspond to the value estimated with WhoSGLAd on the radial modes.

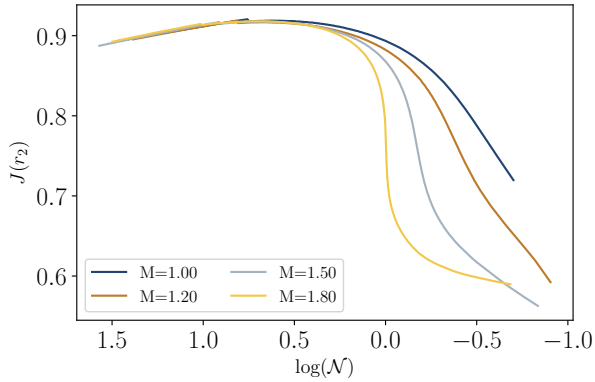


Fig. 14. Variation of the density contrast compared to the inner encapsulated sphere at the outer edge of the evanescent region, r_2 , as in Fig. 9.

nities in the evolution are representative of this shift. Such an effect is discussed in more details in Sect. 4.1.

In this figure, we also represent (as dashed lines) the $\epsilon_{p,0}$ value retrieved for the radial modes via WhoSGLAd. The displayed values account for the $l/2$ shift in value compared with dipolar modes. We observe that the trends of radial and dipolar modes are in excellent agreement, with a slight offset for the most evolved stars. This illustrates that it is a proper estimate for the pressure offset of the dipolar mixed modes. The seesawing of the radial value of ϵ_p further demonstrates that this is not caused by any improper convergence of the technique.

In addition, we note that the behaviour is rather erratic during the subgiant phase. This may be a direct consequence of the need to include higher order contributions to the pressure phase, θ_p , because of the extended set of modes. This aspect is further discussed in Sect. 4.4.

3.2.3. Gravity offset, ϵ_g

Figure 15 represents the evolution of ϵ_g with ν_{\max} (to ease the comparison with Pinçon et al. 2019, Fig. 4). This is, to our knowledge, the first representation of the gravity

offset on a grid of models from the subgiant phase to the red giant phase. As for the case of the pressure offset, we observe two regimes, each depending on the evolutionary phase. We expect that this also stems from the qualitative difference in the evolution of the density contrast in the evanescent region.

On the red giant branch, when comparing our results with Fig. 4 of Pinçon et al. (2019) (which confronts their asymptotic computations with observations from Mosser et al. 2018) the agreement is convincing. We must bear in mind that we include an additional $1/2$ term in the θ_g phase compared to their study. As a consequence, the values of ϵ_g we measure will be shifted up of that same factor compared to theirs. Indeed, in the red giant phase, we observe a plateau at a value of approximately 0.75 of the gravity offset. Accounting for the shift in values of 0.5, this is in excellent agreement with their observation of a plateau at an approximate value of 0.25. This plateau is then followed by a sudden drop of the gravity offset happening in the range of $\nu_{\max} \in [50\mu\text{Hz}, 110\mu\text{Hz}]$.

The constant value of the gravity offset during the first part of the red giant branch comes from the fact that, as mentioned earlier, the profiles of the Brunt-Väisälä and Lamb frequencies may be assumed to be parallel and represented by a power-law of radius in the evanescent region because of the high density contrast between the core and the surface. The slope of the Brunt-Väisälä frequency is then constant and determines the gravity offset value. As the star evolves, ν_{\max} decreases along with the set of excited modes. Therefore, the evanescent region moves outwards, up to the point where it penetrates the convective zone. The Brunt-Väisälä frequency then suddenly drops. Both frequencies can no longer be considered parallel to one another. The gravity offset then drops, as observed in Fig. 15 and predicted by Pinçon et al. (2019).

In the subgiant phase, we first note that the evolution of ϵ_g depends on the stellar mass. Similarly to the pressure offset, we expect this dependence to stem from the low and mass-dependent density contrasts displayed by these stars in the evanescent region (see Fig. 14), in opposition to the high and almost mass-independent density contrasts in red giant stars. We also note that the behaviour is less regular than in the red giant phase. However, individual spectra are properly adjusted, as illustrated in Fig. 6 for the most extreme case. We thus expect this effect to either results from structural features or the necessity to extend the asymptotic formulation to higher orders. Another feature in the subgiant phase is the apparent oscillation for low-mass stars, which should be caused by variations in the evanescent region.

Finally, similarly to the case of the pressure offset, we note a seesaw behaviour. This is again a consequence of the varying set of modes. This will be addressed in the discussion (Sect. 4.1).

3.2.4. Coupling factor, q

The evolution of the coupling factor is displayed in Fig. 16. We see that the value of q first increases to a high value in the subgiant phase. This corresponds to the case of a strong coupling (Takata 2016). To be complete, we also note that, for the lowest masses ($1.0M_\odot$ and $1.2M_\odot$), there is a local minimum of the coupling factor before the sharp increase at the end of the subgiant phase. Then it suddenly drops

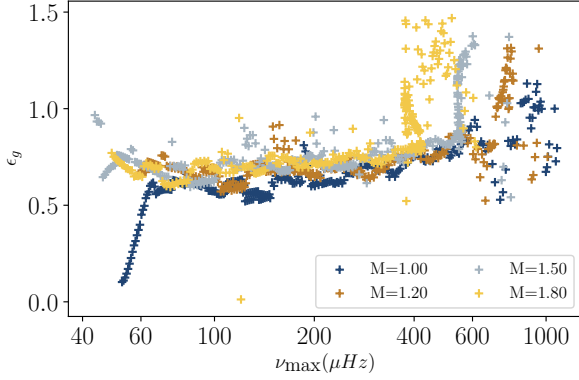


Fig. 15. Variation of ϵ_g as a function of ν_{\max} for different masses.

before the red giant phase. Finally, during the red giant phase, the coupling factor steadily decreases from a value of about 0.25 to approximately 0.10, corresponding this time to a weak coupling. Eventually, the value of q further drops by the end of the RGB phase. As our sequences stop at the RGB bump, this drop is not visible for all of them.

This predicted evolution of the coupling factor is very similar to observations made by Mosser et al. (2017, namely Fig. 6). As demonstrated by Pinçon et al. (2020) under the assumption that the Brunt-Väisälä frequency and the Lamb frequency are log-parallel, the coupling strength should be a proxy of the width of the evanescent zone; thus the larger the evanescent zone, the lower the coupling. To check whether the width of the evanescent region is correlated with the coupling factor, we display in Fig. 17 the evolution of this relative width at ν_{\max} , denoted δ_{ev} , as a function of the g-dominated modes density. It is defined as:

$$\delta_{\text{ev}} = \frac{r_2 - r_1}{(r_1 + r_2)/2}, \quad (19)$$

with r_1 and r_2 the positions of the inner and outer edges of the evanescent region (respectively). For all masses, we indeed observe a global rapid decrease in the size of the evanescent zone during the subgiant phase (with $\mathcal{N} < 1$) followed by a steady increase of this size during the red giant phase (with $\mathcal{N} > 1$). This coincides with the evolution of the coupling factor. We note that the discontinuities in the evolution on the red giant branch come from the discontinuity in composition at the base of the convective envelope, which, in turn, creates a peak of the Brunt-Väisälä frequency (see for example Cunha et al. 2015).

Regarding the dependence of q with the stellar mass, the two regimes are again observed, as expected from the behaviour of the density contrast in the evanescent region. During the subgiant phase, the coupling factor strongly depends on the mass while, on the red giant branch, the coupling factor is much less sensitive to the stellar mass. In both cases, the same global trend is nevertheless observed: the higher the mass, the lower the q value. Firstly, on the red giant branch, the density contrast in the evanescent region compared to the inner sphere is large enough for the profiles of the Brunt-Väisälä and Lamb frequencies to be assumed to be parallel and the structure of the evanescent region is quite comparable for all the masses at a given

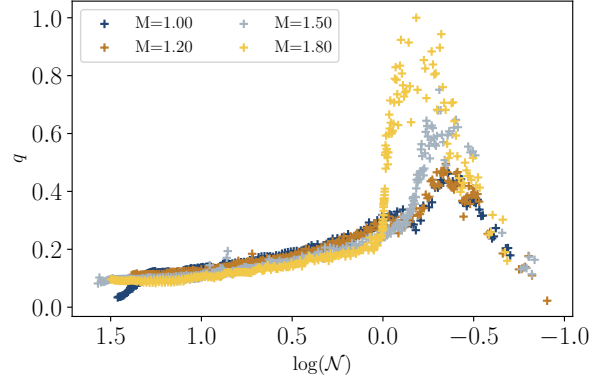


Fig. 16. Variation of q as a function of \mathcal{N} for different masses.

value of \mathcal{N} . The width of the evanescent region nevertheless depends slightly on the stellar mass, as seen in Fig. 17, explaining the slight dependence on q observed in Fig. 16 on the red giant branch. Only the position of the ultimate drop of the coupling factor by the end of the sequences appears to be significantly affected by the stellar mass. However, as we restricted ourselves to models before the luminosity bump, this drop is not visible for every track. Secondly, on the subgiant branch, the density contrast is moderate and depends on the stellar mass (see Fig. 14). Because of this lower density contrast than on the red giant branch, the Brunt-Väisälä profile does not follow a simple power-law relation with the radius and may not be assumed to be parallel to the profile of the Lamb frequency. This impacts the evolution of the width of the evanescent region for the different masses, as shown in Fig. 17, and thus explains the significant mass dependence of the coupling factor on the subgiant branch. We even note that the $1.8M_{\odot}$ model exhibits an oscillation with regard to the size of its evanescent region. Indeed, both critical frequencies may cross in this model. As the star evolves, ν_{\max} decreases. It therefore reaches this crossing of the frequencies, corresponding to a very narrow evanescent region. Then, as the star continues to evolve, the evanescent region increases in size again. Furthermore, as the frequency profiles also evolve with time (mainly due to the evolution of the density contrast), the point at which they cross may evolve as well and other minima of the width of the evanescent zone may occur, as we observe in Fig. 17. This phenomenon will be further discussed in Pinçon et al. (2021, in prep.).

3.3. Variation with chemical composition along the evolution

To study the impact of the chemical composition on the fitted parameters, we computed several tracks for a $1M_{\odot}$ star with different initial hydrogen and metals abundances. We consider pairs of initial hydrogen and metal abundances in $X_0 \in [0.68, 0.72]$ and $Z_0 \in [0.011, 0.019]$. The results are shown in Figs. 18 to 21 for $\Delta\pi_1$, ϵ_p , ϵ_g and q , respectively. In Fig. 18, we observe that the several tracks for $\Delta\pi_1$ are almost indistinguishable from one another during the red giant phase. Only a small difference is visible on the subgiant phase. Nevertheless, thanks to a close inspection of our Fig. 18, alongside Fig. 1 of Farnir et al. (2019), we expect that an improper determination of the metallicity will

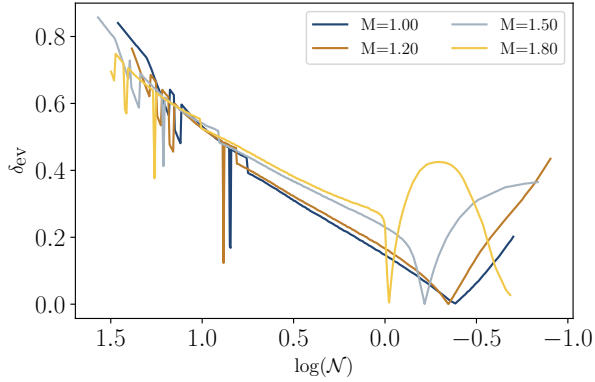


Fig. 17. Variation of width of the evanescent zone as a function of \mathcal{N} for different masses.

impact the inferred mass in a similar way as it does in the main sequence case. Indeed, at fixed $\Delta\pi_1$ and $\Delta\nu_0$ values, a variation of 0.008 in Z_0 could change the estimated mass of about $0.1M_\odot$. This suggests that, in addition to the measurements of $\Delta\nu$ and $\Delta\pi_1$, a spectroscopic measurement of the composition will be necessary to a good determination of the mass, radius and age of subgiant stars. Indeed, the initial composition may impact the inferred stellar mass, thus the inferred age. Regarding ϵ_p , we do not note any significant impact of the chemical composition on the evolution of this indicator, as illustrated in Fig. 19. Finally, concerning q and ϵ_g , we note in Figs. 20 and 21 that only the position (in either ν_{\max} or $\log\mathcal{N}$) of the drop in the values of ϵ_g and q just before the luminosity bump is significantly affected by the composition. As shown by Pinçon (2020), this likely results from a modification of the position of the base of the convective envelope.

The impact of the metallicity on the measured value of the period spacing and coupling factor has already been studied by Jiang et al. (2020). In this work, they looked at the evolution of these indicators on a grid of red-giant models, but their fits were made around a fixed value of the pressure radial order n_p only. While they also observe that there is no significant impact of the metallicity on the evolution of $\Delta\pi_1$, they note a slight impact of the metallicity on the rate of decrease of q . A close look at their Fig. 9 also seems to indicate that this dependency with metallicity mostly appears for the youngest stars. The individual trends seem to settle to a common one as the stellar evolution goes on during the red giant branch. Nevertheless, we do not observe such distinction with the composition. A possible reason for this difference might stem from the fact that they consider the coupling factor to depend on the radial order, n_p , and represent its evolution following specific modes; whereas we consider the coupling factor to be constant over the spectrum with a typical set of frequencies representative of the observations all along the subgiant and red giant branches. This is further discussed in Sect. 4.4.

Finally, what is striking in Figs. 18 to 21 is that some subtle features are present for every composition considered. For example, looking at the evolution of the gravity offset in Fig. 20, it stands out that the oscillation present on the subgiant phase is present for all the compositions.

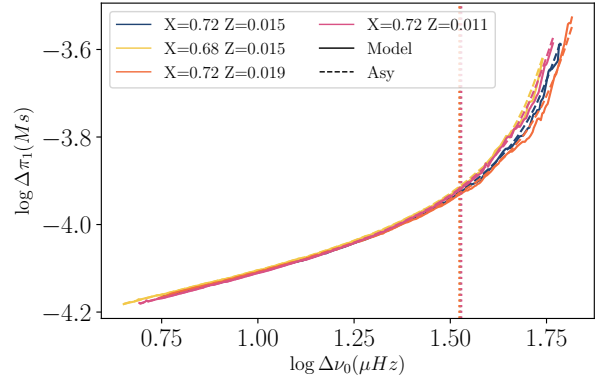


Fig. 18. Variation of $\Delta\pi_1$ as a function of $\Delta\nu_0$ for $1M_\odot$ models with several compositions, represented by the colours. The dashed lines correspond to the asymptotic values and the vertical dotted lines to the transition at $\mathcal{N} = 1$.

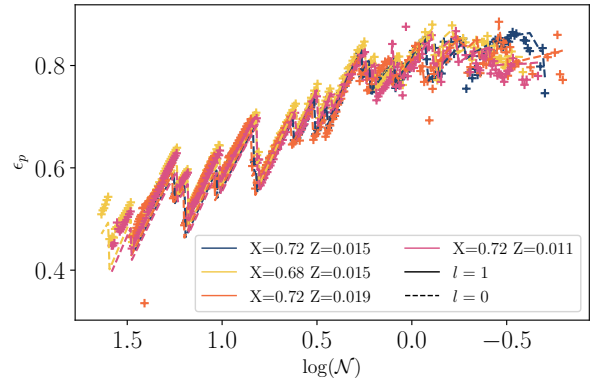


Fig. 19. Variation of ϵ_p as a function of \mathcal{N} for $1M_\odot$ models with several compositions, represented by the colours. The dashed lines correspond to the values computed with WhoSGLAd on the radial modes.

Furthermore, in Fig. 21, we also observe that the local minimum in the coupling factor, right before the transition at $\mathcal{N} = 1$, is present for every track. This might result from the fact that the changes in composition considered might not significantly affect the evolution on the subgiant phase and, therefore, the evolution of the indicators during this phase. Another striking feature is the homology between the track with $X_0 = 0.68$ and $Z_0 = 0.015$ and the one with $X_0 = 0.72$ and $Z_0 = 0.011$. The tracks are almost identical.

Overall, we may assert that the indicators are degenerate with the chemical composition on the red giant phase, except for the latest stages of evolution: for instance the drops in ϵ_g and q before the luminosity bump.

4. Discussion

In the present section, we further discuss the results presented in Sect. 3 as well as possible improvements of the EGGMiMoSA method.

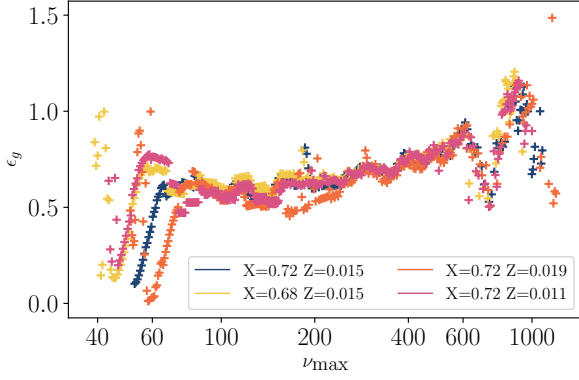


Fig. 20. Variation of ϵ_g as a function of ν_{\max} for $1M_{\odot}$ models with several compositions, represented by the colours.

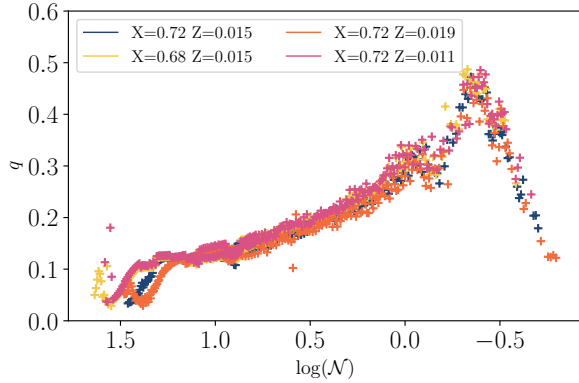


Fig. 21. Variation of q as a function of \mathcal{N} for $1M_{\odot}$ models with several compositions, represented by the colours.

4.1. Impact of the considered set of modes

In the present paper, we considered modes in the range of the width $0.8\nu_{\max}^{0.88}$ around ν_{\max} , determined to include at least ten radial modes for the youngest subgiant models (Mosser et al. 2012b; Appourchaux 2020). We immediately see that this range evolves with ν_{\max} , both in terms of its central frequency ν_{\max} and in the number of modes. As the number of modes is discrete its evolution experiences discontinuities. This creates the saw-like pattern we observe in the pressure and gravity offsets (Figs. 13, 15, 19 and 20). To illustrate this effect, we plot in Fig. 22 the evolution of ϵ_p for the $1M_{\odot}$ track as well as the mean radial order of pressure modes, \bar{n}_p . This value is divided by 15, an arbitrary value, such that ϵ_p and \bar{n}_p have comparable values. We observe that both behave as a seesaw and that the discontinuities in the values are synchronous along evolution. In the case of the observations, the set of modes also changes with evolution, which should also create the discontinuities we observe theoretically. Nevertheless, when attempting to carry stellar modelling of a given star considering ϵ_p as a constraint, this will not constitute a problem as the set of modes will be fixed by the observations.

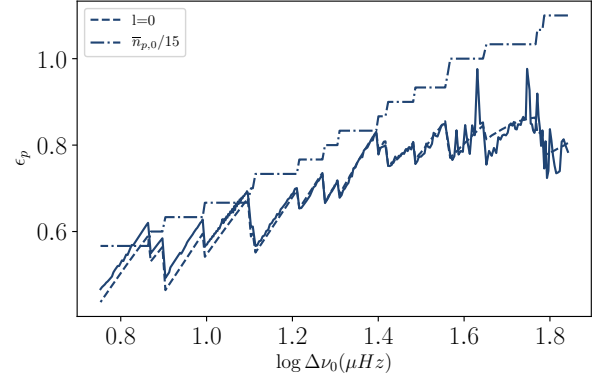


Fig. 22. Variation of ϵ_p with evolution for the $1M_{\odot}$ track. The dashed line represents the variation of the estimation with WhoSGLAd on radial modes and the dot-dashed line the mean pressure radial order of modes considered divided by 15.

4.2. Generalisation to spectra with holes

When adjusting the spectrum, we assume in this paper that the modes that are adjusted are successive, that is, the difference in radial order between the considered modes, Δn_g and Δn_p , are equal to either 0 or 1. However, when applying the method on observational spectra, it may be the case that some modes are not detected. Consequently, the period and frequency difference formulations in Eqs. Eq. (13) and Eq. (16) will have to be adapted considering proper values for the Δn_g and Δn_p parameters in these equations. This will thus require that a proper identification of the modes has been carried out.

Moreover, regarding the initial estimation of the parameters to be adjusted, the position and number of holes might be problematic in some specific cases. For example, as we estimated $\Delta\pi_1$ via the maximum of the local period differences in g-dominated spectra, missing several modes in the central region between dips would lead to an underestimation of its value. In addition, the coupling factor is estimated from the ratio between the maximum and minimum of the local difference in period (for g-dominated spectra) or in frequency (p-dominated). Therefore, missing modes close to these minima or maxima might severely impact the initial estimate of q . However, Mosser et al. (2018) have showed that, with *Kepler* data, g-dominated mixed modes should be below the limit of observability only for evolved giant stars with $\Delta\nu \leq 6\mu\text{Hz}$, for which only p-dominated mixed modes would be detected. This actually corresponds to the most evolved stars, which are close to the luminosity bump, considered in this study. The number of observed g-dominated modes should increase as we go down the red giant branch, meaning that younger stars should constitute less of a problem. Therefore, it will be necessary in future studies to test the ability of the method to provide correct results in such evolved cases.

4.3. Higher order contributions to the asymptotic formulation

In the present paper, we considered the pressure phase, θ_p , to depend linearly on the frequency. However, because the set of modes is broad in the case of subgiant stars (about $10\Delta\nu$ wide), the large separation may not be considered to

be constant over this interval. As an illustration, its relative variation in the subgiant star considered in Fig. 6 is of about $\frac{\delta\Delta\nu}{\Delta\nu} \sim 5\%$. Furthermore, the mean value of the pressure radial order is of $n_p \sim 20$ in such stars. As a consequence, the product of both quantities, corresponding to the error made by considering only a linear pressure phase, is on the order of unity. It is therefore not negligible compared to typical observed uncertainties on ϵ_p . In such a case, the assumed formulation for the pressure phase may not be valid any more. Therefore, it may be necessary to include second-order contributions to this phase. This effect may be so important that it may result in the addition or removal of a p-dominated mode to the set of considered frequencies. Following this discussion, the case of the gravity phase of evolved red-giants naturally comes to mind, as such stars span a large range of gravity radial orders. However, Pinçon et al. (2019) analytically showed that the second order contribution to the gravity phase remains small compared to the current observed uncertainties on the gravity offset for stars typically observed before the luminosity bump.

For the evolved red giant stars, it may again be necessary to include higher order contributions to the pressure phase (Mosser et al. 2013). Indeed, we noted in Fig. 8 that there is a slight shift in the position of the ΔP dips as well as small differences in their exact magnitude. This can now be caused by the fact that the hypothesis that the number of nodes in the pressure cavity is large and thus that the local wavelength is small is not verified for the pressure dominated modes. Indeed, the radial order of p-dominated modes is very low, namely, $n_p \sim 5$.

The inclusion of such higher order contributions to the pressure phase might be necessary to improve the robustness of the method and of the measured seismic indicators. As a consequence, it will be implemented and tested in subsequent papers of this series.

4.4. Frequency dependence of the coupling factor in evolved red giants

Cunha et al. (2019) showed that, for evolved models, the coupling factor may depend on the frequency. This is due to the fact that the evanescent zone has penetrated into the convective zone. As a consequence, the Brunt-Väisälä frequency drops to zero and is no longer log-parallel to the Lamb frequency. The relative width of the evanescent region defined in Eq. (19) may not be considered constant with respect to the frequency any longer. Therefore, the coupling factor may in turn depend on the frequency (Pinçon et al. 2020). To mimic this effect, we binned the oscillation spectrum of the evolved giant presented in Fig. 8 into sub-spectra containing only one dip each. The binned spectrum is shown in Fig. 23. We then fitted individual q values in each sub-spectra. The evolution of the coupling factor as a function of the central frequency of each bin is displayed in Fig. 24. We indeed observe that it may vary with the frequency in an almost linear fashion. Only the coupling factor in the lowest frequency bin strays far from the linear trend. This may result from the asymmetric number of modes around the dip. Finally, we note that the variation of the coupling factor on the spectrum is significant when compared to the constant fitted value. Indeed, while the fitted value is of about 0.12 (comparable to values in the literature, see Mosser et al. 2017), it changes from ~ 0.11 to ~ 0.22 along the spectrum. This illustrates the necessity

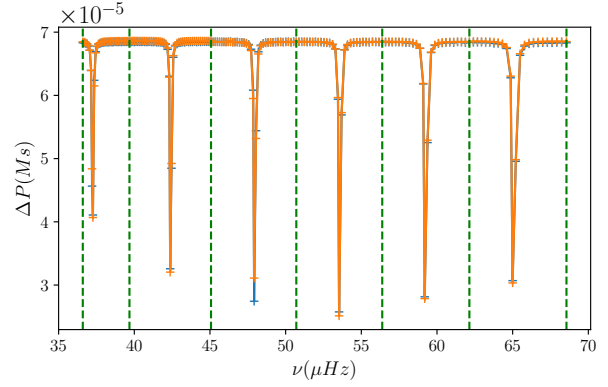


Fig. 23. Fitted individual period spacings as a function of frequency for the same red-giant model as in Fig. 8, but the spectrum has been binned for each individual bump. The green vertical dashed lines delimit each bin.

to account for its dependency with the frequency in order to properly interpret its value.

4.5. Glitches

A further refinement of the technique would be the inclusion of glitches in the formulation used. These glitches are the result of a sharp variation (compared to the wavelength of the incoming mode) in the stellar structure. Their signature is an oscillating feature in the oscillation spectrum. Cunha et al. (2015) showed that buoyancy glitches, caused by a sharp variation in the Brunt-Väisälä frequency, are mainly found for red giant stars at the luminosity bump, at the early phases of helium core burning and at the beginning of helium shell burning. In this paper, we only consider models before the luminosity bump. Therefore, we should not expect the detection of such glitches in these models. Nonetheless, their inclusion will be a necessary step to the application of the EGGMiMoSA method to more evolved stellar models and data. Furthermore, such glitches carry essential information for constraining the stellar cores of giants as well as the transport processes of chemical elements.

Aside from buoyancy glitches, there are the acoustic glitches, found in the pressure part of the spectrum. In the case of red giants, we may observe the signature of the helium glitch, created by the second ionisation zone of helium. Therefore, it holds information about the surface helium content, providing additional constraints to stellar models. The study of such glitches in giant stars has been carried in the past (e.g. Miglio et al. 2010; Dréau et al. 2020). Combining the present method with WhoSGLAd (Farnir et al. 2019) we will be able to retrieve this signature in the p-dominated modes in a robust way. The inclusion of both the buoyancy and acoustic glitches in the dipolar modes will be discussed in subsequent papers of this series.

5. Conclusion

With the aim of defining relevant seismic indicators and relying on a prior modes extraction (e.g. Mosser et al. 2015; Gehan et al. 2018; Appourchaux 2020), we present a method of automated, consistent, robust, and fast adjust-

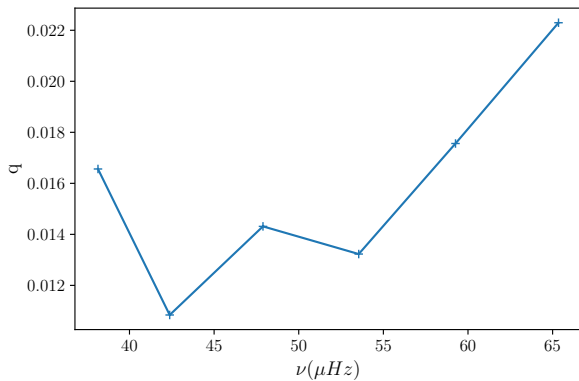


Fig. 24. Evolution of q throughout the binned spectrum presented in Fig. 23

ment of observed and theoretical mixed-mode oscillation spectra. Theoretical oscillations spectra of low-mass subgiant and red-giant stars are well adjusted, as illustrated in Figs. 6 - 8.

We explored the probing potential of the mixed-mode parameters ($\Delta\nu$, $\Delta\pi_1$, ϵ_p , ϵ_g , and q) as indicators of the stellar structure of subgiant and red giant stars, along a grid of models for masses between $1.0M_\odot$ and $1.8M_\odot$ (extended to $2.1M_\odot$ in the case of $\Delta\pi_1$) and initial chemical compositions in $X_0 \in [0.68, 0.72]$ and $Z_0 \in [0.011, 0.019]$. Overall, the evolution of the indicators displays clear trends and the chemical composition has only a slight impact. In contrast, we note that the evolution of the parameters with the mass follows two regimes, depending on the evolutionary stage of the star.

During the subgiant phase, because of a moderate core-envelope density contrast, the mixed-mode parameters evolve differently with $\Delta\nu$ according to the stellar mass. Notably, the evolution of $\Delta\pi_1$ in subgiants is such that it may be used, combined with $\Delta\nu$ and a proper measurement of the metallicity, to infer the stellar mass, radius and age (Fig. 11). We also demonstrate that the asymptotic period spacing tightly agrees with the fitted one. This came as a surprise as the contribution of the gravity modes departs from the asymptotic regime for these stars.

As the stars evolve to the red giant phase, the core-envelope density contrast becomes large. As a consequence, the structure of the evanescent region is almost independent of the stellar mass and the evolutions of the pressure offset, gravity offset, and coupling factor as a function of $\Delta\nu$ are not really affected by the stellar mass in this phase. We showed that this is also true for $\Delta\pi_1$ in stars with masses $\lesssim 1.8M_\odot$ because of the core electron degeneracy, which makes the helium core density quasi independent of the stellar mass at a given value of $\Delta\nu$. Above this threshold, the electron degeneracy is lifted and the evolution of $\Delta\pi_1$ again depends on the mass. Observing stars in that region would therefore allow us to constraint their masses, radii, and ages, similarly to the case of subgiants. However, such stars evolve swiftly and might not be observed.

Here, we provide the first depiction, to our knowledge, of the gravity offset evolution along a grid of models during both the subgiant and red giant phases. The evolution during the red-giant phase agrees with the observations of

Mosser et al. (2018) and the asymptotic computations from Pinçon et al. (2019). As the gravity offset corresponds to the phase lag of the g-dominated modes induced at the inner edge of the evanescent region, we expect it should hold information about this region. However, some issues remain to be tackled as the behaviour of this indicator remains erratic in the subgiant phase.

The evolution of the coupling factor along our grid of models also qualitatively agrees with the observations of Mosser et al. (2017). We also show, based on the study of Pinçon et al. (2020), that its evolution is concordant with that of the width of the evanescent region (see Fig. 17).

Owing to the use of the asymptotic formulation and appropriate estimation of the mixed-mode parameters, the EGGMiMoSA technique offers a robust and fast¹ adjustment of the mixed-mode spectra displayed by subgiant and red giant stars. Furthermore, we also plan on extending the method to include refinements of the asymptotic formulation such as higher order contributions and glitches. Finally, we expect that the technique would represent a great asset to the automated treatment of large samples of data as will be generated by spacecrafts such as PLATO (Rauer et al. 2014), which will observe a great number of subgiant stars (core program) and red-giant stars (secondary science program). Indeed, after a proper modes extraction, the measured seismic indicators can be used as constraints on stellar models to automatically compute stellar parameters with model search algorithms such as AIMS (Rendle et al. 2019).

6. Acknowledgments

M.F. is supported by the FRIA (Fond pour la Recherche en Industrie et Agriculture) - FNRS PhD grant. C.P. is supported by the F.R.S - FNRS as a Chargé de Recherche.

References

- Aizenman, M., Smeyers, P., & Weigert, A. 1977, A&A, 58, 41
- Appourchaux, T. 2020, A&A, 642, A226
- Appourchaux, T., Chaplin, W. J., García, R. A., et al. 2012, A&A, 543, A54
- Baglin, A., Auvergne, M., Barge, P., et al. 2009, in IAU Symposium, Vol. 253, Transiting Planets, ed. F. Pont, D. Sasselov, & M. J. Holman, 71–81
- Bedding, T. R., Mosser, B., Huber, D., et al. 2011, Nature, 471, 608
- Benomar, O., Bedding, T. R., Stello, D., et al. 2012, ApJ, 745, L33
- Borucki, W. J., Koch, D., Basri, G., et al. 2010, in Bulletin of the American Astronomical Society, Vol. 42, American Astronomical Society Meeting Abstracts #215, 215
- Cunha, M. S., Avelino, P. P., Christensen-Dalsgaard, J., et al. 2019, MNRAS, 490, 909
- Cunha, M. S., Stello, D., Avelino, P. P., Christensen-Dalsgaard, J., & Townsend, R. H. D. 2015, ApJ, 805, 127
- Deheuvels, S., Doğan, G., Goupil, M. J., et al. 2014, A&A, 564, A27
- Deheuvels, S. & Michel, E. 2011, A&A, 535, A91
- Dréau, G., Cunha, M. S., Vrad, M., & Avelino, P. P. 2020, MNRAS, 497, 1008
- Dupret, M. A., Belkacem, K., Samadi, R., et al. 2009, A&A, 506, 57
- Farnir, M., Dupret, M. A., Salmon, S. J. A. J., Noels, A., & Buldgen, G. 2019, Astronomy and Astrophysics, 622, A98
- Frandsen, S., Carrier, F., Aerts, C., et al. 2002, A&A, 394, L5
- Gehan, C., Mosser, B., Michel, E., Samadi, R., & Kallinger, T. 2018, A&A, 616, A24
- Gough, D. O. 1986, Highlights of Astronomy, 7, 283
- Hekker, S. & Christensen-Dalsgaard, J. 2017, A&A Rev., 25, 1

¹ Computation times are much smaller than those necessary to compute theoretical adiabatic frequencies.

- Hekker, S., Elsworth, Y., & Angelou, G. C. 2018, *A&A*, 610, A80
- Jiang, C. & Christensen-Dalsgaard, J. 2014, *MNRAS*, 444, 3622
- Jiang, C., Cunha, M., Christensen-Dalsgaard, J., & Zhang, Q. 2020, *MNRAS*, 495, 621
- Kippenhahn, R., Weigert, A., & Weiss, A. 2012, *Stellar Structure and Evolution*
- Lagarde, N., Bossini, D., Miglio, A., Vrad, M., & Mosser, B. 2016, *MNRAS*, 457, L59
- Miglio, A., Chiappini, C., Mosser, B., et al. 2017, *Astronomische Nachrichten*, 338, 644
- Miglio, A., Montalbán, J., Carrier, F., et al. 2010, *A&A*, 520, L6
- Montalbán, J., Miglio, A., Noels, A., et al. 2013, *ApJ*, 766, 118
- Montalbán, J., Miglio, A., Noels, A., Scuflaire, R., & Ventura, P. 2010, *ApJ*, 721, L182
- Mosser, B., Benomar, O., Belkacem, K., et al. 2014, *A&A*, 572, L5
- Mosser, B., Elsworth, Y., Hekker, S., et al. 2012a, *A&A*, 537, A30
- Mosser, B., Gehan, C., Belkacem, K., et al. 2018, *A&A*, 618, A109
- Mosser, B., Goupil, M. J., Belkacem, K., et al. 2012b, *A&A*, 540, A143
- Mosser, B., Michel, E., Belkacem, K., et al. 2013, *A&A*, 550, A126
- Mosser, B., Pinçon, C., Belkacem, K., Takata, M., & Vrad, M. 2017, *A&A*, 600, A1
- Mosser, B., Vrad, M., Belkacem, K., Deheuvels, S., & Goupil, M. J. 2015, *A&A*, 584, A50
- Noll, A., Deheuvels, S., & Ballot, J. 2021, *A&A*, 647, A187
- Osaki, Y. 1971, *PASJ*, 23, 485
- Pinçon, C. 2020, in *Stars and their Variability Observed from Space*, ed. C. Neiner, W. W. Weiss, D. Baade, R. E. Griffin, C. C. Lovekin, & A. F. J. Moffat, 313–315
- Pinçon, C., Goupil, M. J., & Belkacem, K. 2020, *A&A*, 634, A68
- Pinçon, C., Takata, M., & Mosser, B. 2019, *A&A*, 626, A125
- Rauer, H., Catala, C., Aerts, C., et al. 2014, *Experimental Astronomy*, 38, 249
- Refsdal, S. & Weigert, A. 1970, *A&A*, 6, 426
- Rendle, B. M., Buldgen, G., Miglio, A., et al. 2019, *MNRAS*, 484, 771
- Scuflaire, R. 1974, *A&A*, 36, 107
- Scuflaire, R., Montalbán, J., Théado, S., et al. 2008a, *Ap&SS*, 316, 149
- Scuflaire, R., Théado, S., Montalbán, J., et al. 2008b, *Ap&SS*, 316, 83
- Shibahashi, H. 1979, *PASJ*, 31, 87
- Takata, M. 2016, *PASJ*, 68, 91
- Tassoul, M. 1980, *ApJS*, 43, 469
- Ulrich, R. K. 1986, *ApJ*, 306, L37
- Vrad, M., Mosser, B., & Samadi, R. 2016, *A&A*, 588, A87

Appendix A: Bounds of the asymptotic frequency differences

The method presented in Sect. 2 takes advantage of the theoretical bounds of the first and second frequency differences of the asymptotic frequency pattern. On the one hand, the first frequency (resp. period) difference between two consecutive modes normalised by $\Delta\nu$ (resp. $\Delta\pi_1$) is always smaller than unity. On the other hand, the second frequency difference in (Eq. Eq. (6)) displays values greater than 1 in a p-dominated spectrum while it presents values lower than 1 in g-dominated spectra. In the current section, we mathematically demonstrate these statements.

Appendix A.1: Case $\mathcal{N} < 1$ over the spectrum

In a first step, we study the properties of the asymptotic frequency pattern focusing on the case where the local g-dominated mode density $\mathcal{N}(\nu) < 1$. Using the expression of the pressure phase (Eq. Eq. (2)), we may first rewrite the asymptotic resonance condition (Eq. Eq. (1)) as a function of the independent variable $x = \nu/\Delta\nu$. In this form, the asymptotic frequency pattern is obtained by solving the implicit relation

$$x = \mathcal{F}(n_p, x) = n_p + \epsilon_p + \frac{1}{\pi} \arctan[q \tan(\theta_g(x))] , \quad (\text{A.1})$$

where n_p is the pressure radial order and the gravity phase θ_g (Eq. Eq. (3)) is also expressed as a function of the variable x , that is,

$$\theta_g(x) = \pi [x\mathcal{N}(x) - \epsilon_g + 1/2] , \quad (\text{A.2})$$

with $\mathcal{N}(x) = (x^2 \Delta\nu \Delta\pi)^{-1}$ the local g-dominated modes density defined in Eq. Eq. (4) but rewritten in terms of the x variable.

As an illustration, the \mathcal{F} function in the case $\mathcal{N}(x) < 1$ is plotted as a function of x in Fig. A.1 for different values of n_p . To plot this figure, we choose $\Delta\pi_1 \Delta\nu \approx 200$, which is a typical value for an observed subgiant star. The solutions of the implicit equation in Eq. Eq. (A.1) are provided by the intersection between the \mathcal{F} function and the identity function $f(x) = x$ represented by the solid black line. These solutions are shown as red filled circles. In this figure, a given value of n_p is associated with a horizontal strip located in the range $[n_p + \epsilon_p - 1/2, n_p + \epsilon_p + 1/2[$ in the vertical axis. In such a horizontal strip, we see that the \mathcal{F} function exhibits discontinuities as a function of x . These discontinuities occur at values, x_{n_g} , which correspond to the frequencies of pure g-modes verifying the condition $\theta_g = (n_g + 1/2)\pi$ with $n_g \in \mathbb{N}$ the gravity radial order. The values of x_{n_g} are thus provided by

$$x_{n_g} = \frac{1}{\Delta\pi_1 \Delta\nu} (n_g + \epsilon_g)^{-1} . \quad (\text{A.3})$$

The positions, x_{n_g} , for different values of n_g are represented by vertical dashed lines in Fig. A.1. As the gravity phase θ_g has a local period in x of $\mathcal{N}(x) < 1$, it is obvious that two consecutive pure gravity modes are such that: $x_{n_g} - x_{n_g+1} > 1$, as confirmed in Fig. A.1. Over a range $I_{n_g} =]x_{n_g+1}, x_{n_g}]$ (referred to as ‘g-subset’) and for a given value of n_p , we also note that $\mathcal{F}(n_p, x)$ is continuous and monotonically decreasing as a function of x , which can be easily checked by deriving this function with respect to x .

With framework set out thus far, it is now possible to study the bounds of the first and second differences of the solution pattern in a simple way. For the sake of convenience, we start the investigation with the first difference. Firstly, we focussed on a g-subset I_{n_g} . Over such an interval, we distinguished three cases:

1. On each subset $I_{n_p} = [n_p + \epsilon_p - 1/2, n_p + \epsilon_p + 1/2[$ (referred to as ‘p-subset’) such that $I_{n_p} \subset I_{n_g}$, the f function monotonically and continuously increases from $n_p + \epsilon_p - 1/2$ to $n_p + \epsilon_p + 1/2$. In contrast, the $\mathcal{F}(n_p, x)$ function monotonically and continuously decreases and is such that: $n_p + \epsilon_p - 1/2 < \mathcal{F}(n_p, x) < n_p + \epsilon_p + 1/2$. Therefore, both functions intersect only once and there is only one solution in the p-subset I_{n_p} .
2. Over the subset $I_{n_p} =]x_{n_g+1}, n_p + \epsilon_p + 1/2]$, where n_p^- is the lowest integer such as $x_{n_g+1} \leq n_p^- + \epsilon_p + 1/2$, according to the continuity and the monotonic behaviour of the \mathcal{F} and f functions, we still have only one solution since $\mathcal{F}(n_p^-, x_{n_g+1}) = n_p^- + \epsilon_p + 1/2 \geq x_{n_g+1}$ and $\mathcal{F}(n_p^-, n_p^- + \epsilon_p + 1/2) \leq n_p^- + \epsilon_p + 1/2$.
3. Over the subset $I_{n_p}^+ = [n_p^+ + \epsilon_p - 1/2, x_{n_g}]$ where n_p^+ is the largest integer such as $x_{n_g} \geq n_p^+ + \epsilon_p - 1/2$, according to the continuity and the monotonic behaviour of the \mathcal{F} and f functions, we again have only one solution since $\mathcal{F}(n_p^+, x_{n_g}) = n_p^+ + \epsilon_p - 1/2 \leq x_{n_g}$ and $\mathcal{F}(n_p^+, n_p^+ + \epsilon_p - 1/2) \geq n_p^+ + \epsilon_p - 1/2$.

As a result, over a g-subset I_{n_g} , each solution is associated with a unique value of n_p . Now, because $n_p^+ - n_p^- \geq 1$ since $x_{n_g} - x_{n_g+1} > 1$ when $\mathcal{N} < 1$, there are at least two solutions over I_{n_g} , and we call x_k the solution associated with the pressure radial order $n_{p,k} = n_p^- + k$ with $0 \leq k \leq n_p^+ - n_p^-$. We thus have for each successive solutions

$$\begin{aligned} x_{k+1} - x_k &= \mathcal{F}(n_{p,k+1}, x_{k+1}) - \mathcal{F}(n_{p,k}, x_k) \\ &= 1 + \mathcal{F}(n_{p,k}, x_{k+1}) - \mathcal{F}(n_{p,k}, x_k), \end{aligned} \quad (\text{A.4})$$

where the last equality comes from the definition of the phase function (Eq. Eq. (A.1)) and the fact that the difference of pressure radial order between two successive solutions is $\Delta n_p = n_{p,k+1} - n_{p,k} = 1$. Because $\theta_g(x)$ monotonically decreases over I_{n_g} , the \mathcal{F} function continuously decreases as well and we have:

$$\theta_g(x_k) > \theta_g(x_{k+1}) \Rightarrow \mathcal{F}(n_{p,k}, x_{k+1}) - \mathcal{F}(n_{p,k}, x_k) < 1 , \quad (\text{A.5})$$

such that $x_{k+1} - x_k < 1$. Finally, the last case to tackle is when two successive solutions belong to two successive distinct g-subsets I_{n_g} and I_{n_g-1} . We have just shown that these two solutions belong to the same p-subset I_{n_p} such as $x_{n_g} \in I_{n_p}$. The difference of pressure radial order between these two successive solutions is thus $\Delta n_p = 0$ and it is trivial to conclude that the difference between the two solutions remains lower than unity. All these findings are well illustrated in the square grey domains in Fig. A.1, which represent the ‘p-domain’ $I_{n_p} \times I_{n_p}$ that contains the solutions of the implicit relation. To summarize this first part, we have thus shown that the difference between two successive solutions of the implicit equation is smaller than unity. Converting this result as a function of the frequency

ν_j (listed in ascending order with respect to the subscript j), we therefore obtain in pressure-dominated spectra such as $\mathcal{N}(\nu) < 1$, such that

$$\frac{\nu_{j+1} - \nu_j}{\Delta\nu} < 1, \quad (\text{A.6})$$

which in terms of period $P_j = 1/\nu_j$ is equivalent to

$$\begin{aligned} \frac{P_j - P_{j+1}}{\Delta\pi_1} &= \frac{\nu_{j+1} - \nu_j}{\Delta\nu} \frac{\Delta\nu}{\Delta\pi_1 \nu_{j+1} \nu_j} \\ &< \frac{\nu_{j+1} - \nu_j}{\Delta\nu} \mathcal{N}(\nu_j) < 1, \end{aligned} \quad (\text{A.7})$$

because $\mathcal{N}(x) < 1$ in the present case. Moreover, we have shown that the difference of pressure radial orders between two successive modes is either equal to unity when the modes belong to the same g-subset associated with a unique gravity radial order n_g (i.e., $\Delta n_p = 1$ and $\Delta n_g = 0$), or equal to zero when the modes belong to two successive distinct g-subsets associated with successive gravity radial orders n_g and $n_g - 1$, respectively (i.e., $\Delta n_p = 0$ and $\Delta n_g = -1$).

Secondly, we now search the bounds of the second difference between two solutions x_{j+1} and x_{j-1} . According to the previous paragraph, we always have $x_{j+1} - x_j < 1$ when $\mathcal{N} < 1$, so that the upper bound of the second difference is directly $x_{j+1} - x_{j-1} < 2$. Regarding the lower bound, we first note that when the three considered solutions, x_{j-1} , x_j , and x_{j+1} , are part of the same g-subset I_{n_g} , they are associated with successive values of the pressure radial order; thus, it is obvious that $1 < x_{j+1} - x_{j-1}$ since $\Delta n_p = n_{p,j+1} - n_{p,j-1} = 2$. When the three solutions are spread over two g-subsets, such that $x_j \in I_{n_g}$ and $x_{j+1} \in I_{n_g-1}$, we cannot directly draw a conclusion. To demonstrate that the result also holds in that case, we define the functions around the pure g-mode x_{n_g} :

$$\begin{aligned} \tilde{\mathcal{F}}(n_p, x; x_{n_g}) &= n_p + \epsilon_p \\ &+ \frac{1}{\pi} \arctan \left[q \tan \left\{ \tilde{\theta}_g(x; x_{n_g}) \right\} \right], \end{aligned} \quad (\text{A.8})$$

and

$$\tilde{\theta}_g(x; x_{n_g}) = \pi(x_{n_g} - x) + \theta_g(x_{n_g}), \quad (\text{A.9})$$

where we recall that $\theta_g(x_{n_g}) = \pi(1/2 + n_g)$. In an analogous way to the previous steps, we define the three consecutive solutions \tilde{x}_{j-1} , \tilde{x}_j , and \tilde{x}_{j+1} around x_{n_g} of the new implicit equation:

$$\tilde{x} = \tilde{\mathcal{F}}(n_p, \tilde{x}; x_{n_g}). \quad (\text{A.10})$$

As shown previously, the solutions \tilde{x}_{j+1} and \tilde{x}_{j-1} around x_{n_g} are respectively associated with the radial orders $n_{p,j+1}$ and $n_{p,j-1} = n_{p,j+1} - 1$, as consecutive solutions on both sides of x_{n_g} verify $\Delta n_p = 0$. In this case, the $\tilde{\mathcal{F}}$ function has a period of 1 and it is obvious that $\tilde{x}_{j+1} - \tilde{x}_{j-1} = \Delta n_p = 1$. To go further, we then express the θ_g phase in Eq. Eq. (A.2) as

$$\begin{aligned} \frac{\theta_g(x)}{\pi} &= x\mathcal{N}(x) - \epsilon_g + 1/2 \\ &= x\mathcal{N}(x) - x_{n_g}\mathcal{N}(x_{n_g}) + n_g + 1/2 \\ &= \frac{x_{n_g}}{x} \mathcal{N}(x_{n_g}) (x_{n_g} - x) + n_g + 1/2, \end{aligned} \quad (\text{A.11})$$

where the second equality comes from Eq. Eq. (A.3). By comparing Eq. Eq. (A.11) with the definition of $\tilde{\theta}_g$ in Eq. Eq. (A.10), we can determine that:

$$\tilde{\theta}_g(\tilde{x}_{j+1}; x_{n_g}) < \theta_g(\tilde{x}_{j+1}), \quad (\text{A.12})$$

since $\tilde{x}_{j+1} > x_{n_g}$ and $\mathcal{N}(x_{n_g}) < 1$, which implies that

$$\tilde{x}_{j+1} = \tilde{\mathcal{F}}(n_{p,j+1}, \tilde{x}_{j+1}; x_{n_g}) < \mathcal{F}(n_{p,j+1}, \tilde{x}_{j+1}). \quad (\text{A.13})$$

In other words, this means that the identity function and the \mathcal{F} function do not intercept for $x < \tilde{x}_{j+1}$ inside the considered interval $I_{n_{p,j+1}} \cap I_{n_g-1}$, so that they will necessarily intercept at a higher value (since we have shown before that there is a unique solution in such an interval), that is,

$$x_{j+1} > \tilde{x}_{j+1}. \quad (\text{A.14})$$

Similarly, for $\tilde{x}_{j-1} < x_{n_g}$, we have:

$$\tilde{\theta}_g(\tilde{x}_{j-1}; x_{n_g}) > \theta_g(\tilde{x}_{j-1}), \quad (\text{A.15})$$

implying

$$\tilde{x}_{j-1} = \tilde{\mathcal{F}}(n_{p,j-1}, \tilde{x}_{j-1}; x_{n_g}) > \mathcal{F}(n_{p,j-1}, \tilde{x}_{j-1}). \quad (\text{A.16})$$

This means that the identity function and the \mathcal{F} function do not intercept for $x > \tilde{x}_{j+1}$ inside the considered interval $I_{n_{p,j-1}} \cap I_{n_g}$, so that they will necessarily intercept at a lower value, that is,

$$x_{j-1} < \tilde{x}_{j-1}. \quad (\text{A.17})$$

As a result, we find that:

$$x_{j+1} - x_{j-1} > \tilde{x}_{j+1} - \tilde{x}_{j-1} = 1. \quad (\text{A.18})$$

In summary, we thus conclude that for $\mathcal{N} < 1$, the second frequency difference is bounded, such that:

$$1 < \delta\nu_{2,j} = \frac{\nu_{j+1} - \nu_{j-1}}{\Delta\nu} < 2. \quad (\text{A.19})$$

Appendix A.2: Case $\mathcal{N} > 1$ over the spectrum

In a g-dominated spectrum, the analysis can be put in a similar form to the case treated in App. A.1 if we apply the following substitutions

$$\begin{aligned} \nu &\leftarrow P, & \Delta\pi_1 &\leftarrow \Delta\nu, & \Delta\nu &\leftarrow \Delta\pi_1, \\ \epsilon_g - 1/2 &\leftarrow \epsilon_p, & \epsilon_p &\leftarrow \epsilon_g - 1/2, & \mathcal{N} &\leftarrow \mathcal{N}'' \equiv \frac{1}{\mathcal{N}}, \\ q &\leftarrow \frac{1}{q}, & n_p &\leftarrow n_g, & n_g &\leftarrow n_p, \\ \theta_g &\leftarrow \theta_p. \end{aligned} \quad (\text{A.20})$$

Indeed, in the case $\mathcal{N} > 1$, we have $\mathcal{N}'' < 1$, and it is possible to follow the same reasoning as in the previous section.

On the one hand, for the first difference, when $\mathcal{N} > 1$ over the considered spectrum, we obtain:

$$\frac{P_j - P_{j+1}}{\Delta\pi_1} < 1 \quad (\text{A.21})$$

$$\begin{aligned} \frac{\nu_{j+1} - \nu_j}{\Delta\nu} &= \frac{P_j - P_{j+1}}{\Delta\pi_1} \frac{\Delta\pi_1 \nu_j \nu_{j+1}}{\Delta\nu} \\ &< \frac{P_j - P_{j+1}}{\Delta\pi_1} \mathcal{N}(\nu_{j+1})^{-1} < 1. \end{aligned} \quad (\text{A.22})$$

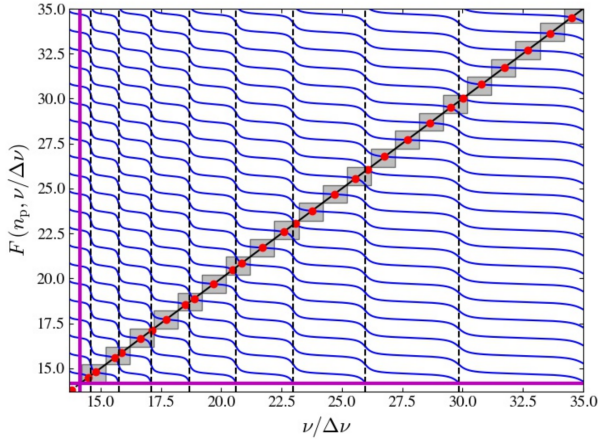


Fig. A.1. Evolution of the phase function with the frequency over the large operation. The phase function for different pressure radial orders is represented in blue. The straight line represents the identity function $f(x) = x$. Its intersections with the phase function are the solutions, in red. The grey square domains represent regions of constant n_p values. The vertical dashed lines are the positions of pure g-modes. The mixed-mode parameters used are $q = 0.2$ and $\Delta\nu\Delta\pi_1 = 200$

Moreover, the difference of gravity radial orders between two successive modes (i.e., still listed in ascending order with frequency) is either equal to -1 when the modes belong to the same p-subset associated with a unique pressure radial order n_p (i.e., $\Delta n_g = -1$ and $\Delta n_p = 0$), or equal to zero when the modes belong to two successive distinct p-subsets associated with successive pressure radial orders n_p and $n_p + 1$, respectively (i.e., $\Delta n_g = 0$ and $\Delta n_p = 1$).

On the other hand, for the second period difference, we obtain when $\mathcal{N} > 1$ over the considered spectrum

$$1 < \frac{P_{j-1} - P_{j+1}}{\Delta\pi_1} < 2. \quad (\text{A.23})$$

For the second frequency difference, when $\mathcal{N} > 1$, we can solely determine:

$$\delta\nu_{2,j} = \frac{\nu_{j+1} - \nu_{j-1}}{\Delta\nu} = \frac{P_{j-1} - P_{j+1}}{\Delta\pi_1} \mathcal{N}'_{j-1}, \quad (\text{A.24})$$

where an alternative definition for the g-dominated mode density naturally appears, namely,

$$\mathcal{N}'_j = \frac{\Delta\nu}{\Delta\pi_1 \nu_{j+1} \nu_{j-1}}. \quad (\text{A.25})$$

Since $\mathcal{N}(\nu_{j+1}) < \mathcal{N}'_j$, we have $\mathcal{N}'_j > 1$ over the considered spectrum. As soon as $\mathcal{N}' > 2$, Eq. Eq. (A.24) shows us that $\delta\nu_{2,j} < 1$. In the case $1 < \mathcal{N}' < 2$, we can adapt the reasoning made in App. A.1. Indeed, either the solutions x_{j-1} and x_{j+1} are associated with the same pressure radial order (i.e., $\Delta n_p = 0$ and $\Delta n_g = -2$) and $x_{j+1} - x_{j-1} < 1$, or the difference in n_p is equal to unity (i.e., with $\Delta n_g = -1$)². In the second case, this means that the solutions x_{j-1} and x_{j+1} are located on both sides of a pure g-mode x_{n_g} . Applying the reasoning as in App. A.1 to determine the bounds of

² We recall that $\Delta n_p < 2$ between x_{j+1} and x_{j-1} when $\mathcal{N} > 1$, in a similar way that $\Delta n_g > -2$ when $\mathcal{N} < 1$.

the second frequency difference, we obtain $x_{j+1} - x_{j-1} < 1$ as $\mathcal{N} > 1$ in the present case. We therefore conclude that over a spectrum such as $\mathcal{N} > 1$, we have

$$\delta\nu_{2,j} = \frac{\nu_{j+1} - \nu_{j-1}}{\Delta\nu} < 1. \quad (\text{A.26})$$

Appendix A.3: Case $\mathcal{N} = 1$ somewhere in the spectrum

The last case to tackle is when the two solutions that are compared are located from each side of the transition point x^* where $\mathcal{N}(x^*) = 1$.

For the first difference, the demonstration is simple. We denote x_q (resp. x_{q+1}) as the largest (the smallest) solution lower (resp. greater) than x^* . If we note n_g^* as the lowest gravity radial order such a $x_{n_g^*} \leq x^*$, we have $x^* - x_{n_g^*} < 1$ since otherwise n_g^* would not be the highest lowest gravity radial order such that $x_{n_g^*} \leq x^*$ as $x_{n_g^*} - x_{n_g^*+1} < 1$ when $\mathcal{N} > 1$. Therefore, we have two cases. If $x_q < x_{n_g^*}$, x_{q+1} is then necessarily comprised in the same p-subset as x_q . If $x_q > x_{n_g^*}$, either $x_{q+1} > x_{n_g^*+1}$ and x_{q+1} is then again necessarily comprised in the same p-subset as x_q ; or $x_{q+1} < x_{n_g^*+1}$ and x_{q+1} then belongs to an adjacent p-subset to that of x_q . In all cases, following the same reasoning as in Appendix A.1, we have $x_{j+1} - x_j < 1$, which is therefore unconditionally met over the whole spectrum. This is obviously also true for the difference in period.

For the second difference, we consider two solutions x_{j-1} and x_{j+1} such as $x_{j-1} < x^*$ and $x_{j+1} > x^*$. We also consider the solutions of the implicit equation:

$$\bar{x} = \tilde{\mathcal{F}}(n_p, \bar{x}; x_{j-1}), \quad (\text{A.27})$$

where $\tilde{\mathcal{F}}$ is defined in Eqs. A.8. It can be straightforward to see that x_{j-1} is solution of Eq. Eq. (A.27). By considering the consecutive solutions \bar{x}_j and \bar{x}_{j+1} of Eq. Eq. (A.27), we obviously have $\bar{x}_{j+1} - x_{j-1} = 1$ since the $\tilde{\mathcal{F}}$ function has a period of 1. To go further, we then compute from Eq. A.9

$$\frac{\tilde{\theta}_g(x_{j+1}; x_{j-1})}{\pi} - \frac{\theta_g(x_{j+1})}{\pi} = (\mathcal{N}'_j - 1)(x_{j+1} - x_{j-1}), \quad (\text{A.28})$$

with \mathcal{N}'_j defined as in Eq. Eq. (A.25). Therefore, if $\mathcal{N}'_j > 1$, we have $\tilde{\theta}_g(x_{j+1}; x_{j-1}) > \theta_g(x_{j+1})$ according to Eq. Eq. (A.28). This means that the $\tilde{\mathcal{F}}$ function and the identity function intercept at higher values than x_{j+1} . In other words, $x_{j+1} < \bar{x}_{j+1}$, and thus $x_{j+1} - x_{j-1} < 1$. Conversely, if $\mathcal{N}'_j < 1$, we have $\tilde{\theta}_g(x_{j+1}; x_{j-1}) < \theta_g(x_{j+1})$.

This means that the $\tilde{\mathcal{F}}$ function and the identity function can intercept at lower values than x_{j+1} . In other words, $x_{j+1} > \bar{x}_{j+1}$, and thus $x_{j+1} - x_{j-1} > 1$.

Therefore, \mathcal{N}'_j appears to be a relevant proxy of the g-dominated modes density over the whole spectrum. Indeed, we remind that in the previous cases considered in Sects. A.1 and A.2, when $\mathcal{N}(\nu_{j+1}) > 1$, then $\mathcal{N}'_j > 1$ and $\delta\nu_{2,j} < 1$, and when $\mathcal{N}(\nu_{j-1}) < 1$, then $\mathcal{N}'_j < 1$ and $\delta\nu_{2,j} > 1$. Adding in the results of the present section, we thus conclude that over the whole spectrum:

$$0 < \delta\nu_{2,j} < 2 \\ \text{sgn}(\delta\nu_{2,j} - 1) = \text{sgn}(1 - \mathcal{N}'_j), \quad (\text{A.29})$$

where $\text{sgn}()$ denotes the sign function.

Appendix A.4: Illustration

We illustrate in Fig. A.2 the evolution of the second difference (Eq. Eq. (6)) with the reduced period, obtained by solving Eq. Eq. (1). We show this evolution for two choices of the coupling factor $q = 0.1$ and $q = 0.4$ in red and blue, respectively. We also show, as dashed lines, the evolution of the alternate definition for the g-dominated modes density \mathcal{N}' in Eq. Eq. (A.25). We observe that \mathcal{N}' and the second frequency difference cross at a value of 1, as expected from the previous sections. As a consequence, we may locate the transition where $\mathcal{N}_j = 1$ using the second frequency difference.

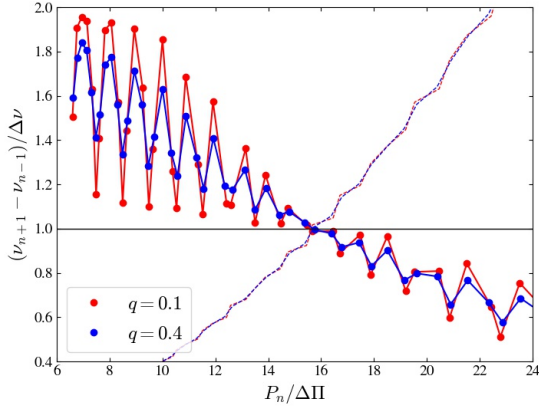


Fig. A.2. Second frequency difference $\delta\nu_2$ as a function of the normalised period of mixed modes (dots). The red and blue colours are for $q = 0.1$ and $q = 0.4$, respectively. It is plotted for a typical value of $\Delta\nu\Delta\pi_1 = 200$. The corresponding dashed curves show the evolution of \mathcal{N}' .

Appendix B: Deriving ζ'

With analogous reasoning as in Mosser et al. (2015), we may express the variation of frequency with the mixed-mode radial order, $n = n_p - n_g$. Assuming the spectrum to be dominated by the pressure modes, $\mathcal{N} \ll 1$, we consider that the frequency of a mixed mode experiences a perturbation from the evenly space frequencies, η . We write:

$$\nu = n\Delta\nu + \eta. \quad (\text{B.1})$$

Because of periodicity, when introducing this relation in the phase of pressure modes, θ_p (Eq. Eq. (2)), $\tan \theta_p$ becomes

$$\tan \left[\pi \left(\frac{\eta}{\Delta\nu} - \epsilon_p \right) \right]. \quad (\text{B.2})$$

The derivation of Eq. Eq. (1) with respect to n , assuming the five mixed-mode parameters to be constant with n , then yields

$$\frac{1}{\Delta\nu \cos^2 \theta_p} \frac{d\eta}{dn} = - \frac{q}{\Delta\pi_1 \nu^2 \cos^2 \theta_g} \frac{d\nu}{dn}. \quad (\text{B.3})$$

Finally, using the relation $\cos^2 \theta_p = \frac{\cos^2 \theta_g}{q^2 \sin^2 \theta_g + \cos^2 \theta_g}$ (obtained from Eq. Eq. (1)), using $\eta = \nu - n\Delta\nu$, and the

definition of the g-dominated modes density evaluated in ν (Eq. Eq. (4)), we retrieve the final expression:

$$\frac{d\nu}{dn} = \Delta\nu \left[1 + \frac{q\mathcal{N}}{\cos^2 \theta_g + q^2 \sin^2 \theta_g} \right]^{-1}. \quad (\text{B.4})$$

We note that θ_g and \mathcal{N} in Eq. Eq. (B.4) are two functions of frequencies provided by Eqs. Eq. (3) and Eq. (4).

Appendix C: Radial order difference between successive modes

Based Eq. Eq. (13), along with the fact that between two g-dominated modes there may exist a p-dominated mode, it is not obvious that Δn_g should be equal to zero or one. By carefully studying the behaviour of first and second frequency differences, Appendix A provides a justification for its value. Nevertheless, to focus only on the Δn_g parameter, we follow a slightly different but equivalent approach in the present section.

From Appendix A, we know that the local value of the period spacing is at most equal to the asymptotic value $\Delta\pi_1$. Furthermore, from the ordering of frequencies, ΔP_i must be positive. We thus have (from Eq. Eq. (13)):

$$0 < \Delta n_g + \Delta\psi_i/\pi \leq 1. \quad (\text{C.1})$$

Also, we have that θ_p is an increasing function of the frequency (see Eq. Eq. (2)), thus $\theta_{p,i} < \theta_{p,i+1}$. As the arctan function is continuous and monotonous and the tan function is continuous and monotonous over a given interval $\theta_p \in [k\pi - \pi/2, k\pi + \pi/2]$, $k \in \mathbb{N}$, the $\psi_i = \arctan(\tan \theta_{p,i}/q)$ is continuous and monotonous over the same interval. In addition, in such an interval, ψ_i increases with $\theta_{p,i}$. Thus, $\Delta\psi_i < 0$. Using the definition of the arctan function, we know that $\psi \in]-\pi/2, \pi/2[$ and $\Delta\psi_i/\pi$ must be greater than -1 . We may thus conclude that:

$$0 < \Delta n_g < 2, \quad (\text{C.2})$$

and, as n_g only takes integer values, $\Delta n_g = 1$. This demonstration does not hold in the case where two successive modes span over different intervals $\theta_p \in [k\pi - \pi/2, k\pi + \pi/2]$, $k \in \mathbb{N}$, the tan function is discontinuous. In that case, $\Delta\psi_i > 0$ and it is necessary to have $\Delta n_g = 0$ to ensure $\Delta P_i/\Delta\pi_1 < 1$. Physically speaking, this corresponds to the case when we alternate between a g-dominated and a p-dominated mode and this is the pressure radial order that changes, keeping a constant n_g value.

Finally, with an analogous reasoning, we may conclude, for the case of p-dominated spectra that Δn_p , appearing in Eq. Eq. (16), must also equal 1 for two successive p-dominated modes. Again, when two successive modes span over different intervals $\theta_g \in [k\pi - \pi/2, k\pi + \pi/2]$, $k \in \mathbb{N}$, we alternate between a p-dominated mode and a g-dominated mode, and the gravity radial order changes, keeping in a constant n_p value.

CHAPTER 6

Conclusion

The objective of the present study was to provide means to seismically and robustly characterise low-mass stars. We considered main-sequence solar-like stars and their evolved counterparts, the subgiant and red giants. To that end, we developed two probing techniques, WhoSGLAd (Farnir et al. 2019) and EGGMiMoSA (Farnir et al. 2021, accepted for publication in A&A). We now summarise our results and discuss a few perspectives of our work.

6.1 Part I: Main-sequence solar-like stars

6.1.1 Summary

The WhoSGLAd method (Chaps. 3 and 4) relies on the Gram-Schmidt orthonormalisation procedure to build an orthonormal basis of functions over which the observed frequencies are projected. This has the essential advantage to be extremely fast, as the procedure corresponds to linear algebra, and to provide completely uncorrelated fitting coefficients (assuming oscillation frequencies to be independent of one another). We paid a close attention to the definition of seismic indicators, inspired by ‘classical’ indicators (e.g. Christensen-Dalsgaard 1988; Roxburgh & Vorontsov 2003), by combining the fitted coefficients, in order to reduce at most their correlations. We demonstrated that these indicators bear relevant structural information (Sect. 3.2.3) and allow us to tightly constraint stellar models (Chap. 4).

In addition, our goal when developing the WhoSGLAd method was to account in a robust way for the acoustic glitches that the oscillation spectra of solar-like stars may present (see Sects. 2.2.5 and 3.1.2). Thanks to the Gram-Schmidt orthonormalisation and a linearised expression for the glitches (Eq. (3.17)), we were able to completely decorrelate the glitches contribution from the smooth part while simultaneously accounting for it. This is in opposition with most of the method previously presented in the literature (e.g. Monteiro et al. 1994; Houdek & Gough 2007; Basu et al. 2004; Verma et al. 2014). Because of the highly non-linear formulation used by these techniques, they tend to discard the contribution of the smooth part to isolate only the glitches and resort to non-linear minimisation techniques, which can introduce unwanted correlations between seismic indicators.

We proceeded to demonstrate the excellent probing potential of our indicators. The large frequency separation, Δ , tightly constrains the mean stellar density. The averaged small separation ratios \hat{r}_{01} and \hat{r}_{02} inform us about the central composition and the evolutionary stage. This is similar to the ‘classical’ small separation ratios (Roxburgh & Vorontsov 2003) but with a greater precision and reduced correlations with the other indicators, as a result of the orthonormalisation. The combination of these three indicators already allows us to constrain the age, mass, radius, and composition of an observed target. We also defined the large frequency separation ratios, between the two spherical degrees 0 and l , Δ_{0l} . We illustrated the ability of Δ_{01} , when combined with \hat{r}_{01} , to probe the amount of central overshooting for main-sequence stars that preserved a convective core (i.e. with $M \gtrsim 1.1 M_{\odot}$). This is not unlike the work of Deheuvels et al. (2016) who demonstrated that the mean frequency ratio between modes of spherical degrees 0 and 1 and the slope of this small separation as a function of the radial order n indeed constrain central overshooting. We also defined the amplitude of the acoustic glitches of both the helium second-ionisation zone, A_{He} , and of the base of the convection zone, A_{CZ} . Both indicators are completely decorrelated from the smooth indicators. While A_{CZ} happens to be barely significant in the main-sequence solar-like pulsators we considered, thus being uninformative, A_{He} allows us to constrain the helium surface abundance, which cannot be retrieved otherwise. We however showed a non-negligible correlation between this indicator and both the metals abundance and the stellar mass. Nevertheless, as the stellar mass and composition are also constrained by the smooth indicators, the possible degeneracy is lifted.

Using these seismic indicators, we applied our technique to several observed targets (Chap. 4). We first considered the 16 Cyg system (Sect. 4.2), which consists of two benchmark stars for which seismic data of unprecedented quality have been gathered. Using four of our seismic indicators (namely Δ , \hat{r}_{01} , \hat{r}_{02} , and A_{He}), we were able to adjust the stellar mass, age, and chemical composition. We did so while testing different hypotheses for the physical ingredients of our models, such as the solar chemical mixture reference, the opacity, and the equation of state tables. Overall, we computed 22 models for each star and observed the necessity to include non-standard processes, such as turbulent diffusion, in order to account for non-seismic constraints. These data

were not explicitly part of the set of constraints. As the stars are binaries, they are expected to have a common origin and we also computed a set of models assuming common formation scenarios for the two stars. This means that we either assumed the stars to have a common age and initial composition or a common age only, as accommodating for all these constraints turned out to be a difficult task. We indeed observed that, with the exception of a few cases, we were not able to adjust all the seismic constraints while requiring common ages and compositions. Allowing different compositions in each star, we managed to improve the results in a few cases. The study of the 16 Cygni system demonstrated the importance of using precise constraints in order to compute precise models. However, it also demonstrated the large impact of the current uncertainties in stellar modelling (as the numerous reference tables testify). Therefore, the use of highly precise data is an essential step to constrain such models and highlight their limitations. Finally, the second part of the study of the system (Buldgen et al. 2021, in prep.) has shown that the use of our method already yields excellent results; structural inversions do not point towards significant differences between our reference models and the real stars, in view of the error bars. This lead them to conclude that we may not assert the necessity of specific non-standard processes to accurately represent the data.

The second application of our method was the characterisation of the Kepler Legacy sample (Lund et al. 2017), the current best solar-like dataset. Our goal was to isolate trends between stellar parameters, specifically between the initial hydrogen and metals content, providing a galactic enrichment ratio $\Delta Y/\Delta Z$, and between the amount of central overshooting and mass. By a linear adjustment, we retrieved a galactic enrichment ratio well within typical literature values while the primordial helium abundance is rather large (e.g. Ribas et al. 2000; Lebreton et al. 2001; Peimbert et al. 2002; Balser 2006; Casagrande et al. 2007; Verma et al. 2019). This could be the result of a different choice of solar-mixture reference. We indeed used the AGSS09 (Asplund et al. 2009) reference and noted, for 16 Cyg, that the use of a more metallic solar mixture, such as GN93 (Grevesse & Noels 1993) or GS98 (Grevesse & Sauval 1998), leads to models which are more metallic and less helium rich. Finally, we also noted, for stars with masses between $\sim 1.1 M_{\odot}$ and $\sim 1.6 M_{\odot}$ that there is a positive correlation between the amount of central overshooting and the stellar mass, very similarly to the conclusions of Claret & Torres (2017, 2018). However, the data presented an important scatter around the linear trend.

6.1.2 Perspectives

The developed method opens numerous perspectives. The first and most obvious one is to pursue the characterisation of the Kepler Legacy sample (Lund et al. 2017). To do so, using a finer grid in the overshooting parameter could be of a great help and significantly increase the number of stars for which acceptable models are retrieved. It would also be especially interesting to select several targets in the sample to take the most advantage of the precise WhoSGLAd indicators and carry a thorough analysis, as we did for the case of 16 Cyg. This would be the occasion to study the impact of different choices of input physics on central overshooting.

Another interesting application would be the study of our Sun. It constitutes a first choice target as a result of the large number of modes that can be detected. Consequently, we would like to put our technique to the test by tackling the Sun as a star problem, that is to use frequencies of degraded quality to meet the quality of typical observed stars. Trying to find models representative of the measured seismic indicators and comparing them with our knowledge of the Sun would be particularly interesting as a performance test of our technique.

Beside applications, we would also like to account for the correlations between individual frequencies in our technique. This would ensure that the adjusted coefficients are decorrelated and therefore that our seismic indicators are as uncorrelated as possible. This is necessary to put the most stringent constraints on stellar models.

6.2 Part II: Subgiant and red-giant stars

6.2.1 Summary

The EGGMiMoSA method (Chap. 5) we developed has been tailor-made to the specific case of the mixed-mode spectra exhibited by low-mass subgiants and red giants. Relying on educated guesses for the mixed-mode parameters (i.e. $\Delta\nu$, $\Delta\pi_1$, ϵ_p , ϵ_g , and q), it efficiently and automatically provides an adjustment to the asymptotic formulation of mixed-modes, even in the most complex cases where the spectra seem irregular. This enables the fast and automated measurement of the mixed-mode parameters in a coherent way for both subgiants and red giants, which can be used as precise seismic indicators.

We then proceeded to demonstrate the ability of the mixed-mode parameters to probe the stellar structure over a grid of stellar models considering different masses and compositions, throughout the subgiant and red-giant phases until the luminosity bump. Overall, we noted that the mixed-mode parameters exhibit different behaviours according to the evolutionary phase. The evolution of these indicators is largely influenced by the stellar mass during the subgiant phase while it becomes nearly insensitive to it on the red-giant phase. This results from the differences in core-envelope density contrasts between these phases. Indeed, as the star evolves through the subgiant and red-giant phases, its core contracts while its envelope expands, increasing the density contrast.

A remarkable result of our study is the ability to combine measurements of $\Delta\nu$ and $\Delta\pi_1$ to determine the age, mass, and radius of subgiant stars. This is also possible for red giants more massive than $\sim 1.8 M_{\odot}$. We have

demonstrated that the degenerate evolution of $\Delta\pi_1$ as a function of $\Delta\nu$ for red-giants less massive than $\sim 1.8 M_\odot$ results from the central electron degeneracy, which is lifted above this threshold.

Following the evolution of the other indicators, we noted a qualitative agreement with both observational and theoretical studies (e.g. Mosser et al. 2014, 2017; Pinçon et al. 2019, 2020). We noted that the mixed-mode coupling factor sharply increases during the subgiant phase, then sharply drops before the red-giant phase and, finally, steadily decreases along this phase, as observed by Mosser et al. (2017). We were also able to present the first evolution of the gravity offset over a grid of models. Our results agree with both the observations from Mosser et al. (2018) and the analytical results of Pinçon et al. (2019). However, as the evolution of ϵ_g remains too unstable, improvements to its determination are necessary for it to serve as a constraint to models.

6.2.2 Perspectives

While we have demonstrated that our method holds great promises for the future of subgiants and red giants seismology, we have not yet used it for the detailed probing of specific targets. For example, applying our technique to several subgiants for which $l = 2$ modes have been detected will be of particular interest. These modes will further help constrain the mixed-mode parameters and increase their precision. Namely, the period spacing of dipolar and quadrupolar modes are proportional and differ by a factor of $\sqrt{3}$ (see Eq. (2.85) for $l = 1$ and $l = 2$). The work of Li et al. (2020) contains several good examples of Kepler subgiants for which quadrupolar modes have been measured. The case of subgiant stars is distinctly relevant as they will be part of the core-science program of the PLATO mission (Rauer et al. 2014). We may therefore expect precise frequencies to be measured for those stars.

In order to apply our technique to observations, a few improvements might be necessary. First of all, the method currently assumes modes to be successive. This does not constitute a critical issue, as we expect several modes identifications to be available (see the works of Mosser et al. 2015; Gehan et al. 2018; Appourchaux 2020, for example) and the expression we use can easily accommodate for such holes in the observed spectra. Nevertheless, the initial parameters estimation may be impacted. Therefore, a revision of this estimation may be necessary.

A second improvement of our method will be the inclusion of higher-order contributions to the phase of pressure modes (e.g. Mosser et al. 2012c), which was shown to have a significant impact in evolved red giants, and to introduce a dependency of the coupling factor with frequency (e.g. Cunha et al. 2019; Pinçon et al. 2020), which is again significant for the late red giants.

Finally, it would be particularly interesting to account for the signature of glitches in the spectra. First of all, we would like to study the acoustic glitches present in radial modes (e.g. Miglio et al. 2010), for which the WhoSGLAd method is already available and of which the efficiency has been proven. Second, we would like to account for buoyancy glitches (e.g. Cunha et al. 2015), which have been demonstrated to hold precise and localised information, and should allow us to tightly constrain stellar properties.

6.3 General perspectives

With the two methods we developed, we have at hand tools that allow us to constrain the structure and evolution of solar-like stars throughout most of the phases they live through during their existence. This constitutes an essential step to their complete understanding. Furthermore, as both methods are fast and automated, they are well suited to the treatment of the already available large catalogues of precise seismic data as well as the abundant data that the future PLATO mission is expected to generate. This will further fuel the many synergies between asteroseismology, even stellar physics, and other astrophysical fields. This could provide substantial amounts of precise stellar parameters determinations, necessary to the precise characterisation of exoplanets and to exoplanetology. This will open the possibility to carry reliable statistical studies of stellar populations, highlighting possible relations between stellar parameters.

Bibliography

- Abt, H. A. & Morrell, N. I. 1995, *ApJS*, 99, 135
- Adelberger, E. G., García, A., Robertson, R. G. H., et al. 2011, *Reviews of Modern Physics*, 83, 195
- Aizenman, M., Smeyers, P., & Weigert, A. 1977, *A&A*, 58, 41
- Appourchaux, T. 2020, *A&A*, 642, A226
- Appourchaux, T., Antia, H. M., Ball, W., et al. 2015, *A&A*, 582, A25
- Appourchaux, T., Chaplin, W. J., García, R. A., et al. 2012, *A&A*, 543, A54
- Asplund, M., Grevesse, N., Sauval, A. J., & Scott, P. 2009, *ARA&A*, 47, 481
- Badnell, N. R., Bautista, M. A., Butler, K., et al. 2005, *MNRAS*, 360, 458
- Baglin, A., Auvergne, M., Barge, P., et al. 2009, in *IAU Symposium*, Vol. 253, *Transiting Planets*, ed. F. Pont, D. Sasselov, & M. J. Holman, 71–81
- Ball, W. H. & Gizon, L. 2014, *A&A*, 568, A123
- Ballot, J., Turck-Chièze, S., & García, R. A. 2004, *A&A*, 423, 1051
- Balser, D. S. 2006, *AJ*, 132, 2326
- Basu, S., Mazumdar, A., Antia, H. M., & Demarque, P. 2004, *MNRAS*, 350, 277
- Bazot, M., Benomar, O., Christensen-Dalsgaard, J., et al. 2019, *A&A*, 623, A125
- Beck, P. G., Montalbán, J., Kallinger, T., et al. 2012, *Nature*, 481, 55
- Bedding, T. R., Huber, D., Stello, D., et al. 2010, *ApJ*, 713, L176
- Bedding, T. R., Mosser, B., Huber, D., et al. 2011, *Nature*, 471, 608
- Belkacem, K., Marques, J. P., Goupil, M. J., et al. 2015a, *A&A*, 579, A31
- Belkacem, K., Marques, J. P., Goupil, M. J., et al. 2015b, *A&A*, 579, A30
- Benomar, O., Bedding, T. R., Stello, D., et al. 2012, *ApJ*, 745, L33
- Borucki, W. J., Koch, D., Basri, G., et al. 2010, in *Bulletin of the American Astronomical Society*, Vol. 42, *American Astronomical Society Meeting Abstracts #215*, 215
- Brent, R. P. 1973, *Algorithms for Minimization without Derivatives* (Prentice-Hall : Engelwood Cliffs, N.J)
- Brewer, J. M., Fischer, D. A., Valenti, J. A., & Piskunov, N. 2016, *ApJS*, 225, 32
- Brillouin, L. 1926, *C. R. Acad. Sci. Paris*, 183, 24
- Brookes, J. R., Isaak, G. R., & van der Raay, H. B. 1978, *MNRAS*, 185, 1
- Broomhall, A. M., Miglio, A., Montalbán, J., et al. 2014, *MNRAS*, 440, 1828
- Brown, T. M. & Morrow, C. A. 1987, *ApJ*, 314, L21
- Bruntt, H., Basu, S., Smalley, B., et al. 2012, *MNRAS*, 423, 122

- Buchhave, L. A. & Latham, D. W. 2015, *ApJ*, 808, 187
- Buldgen, G., Farnir, M., Eggenberger, P. an B  trisey, J., et al. 2021, in prep.
- Buldgen, G., Reese, D. R., & Dupret, M. A. 2015, *A&A*, 583, A62
- Buldgen, G., Reese, D. R., & Dupret, M. A. 2016a, *A&A*, 585, A109
- Buldgen, G., Reese, D. R., & Dupret, M. A. 2018, *A&A*, 609, A95
- Buldgen, G., Salmon, S., & Noels, A. 2019, *Frontiers in Astronomy and Space Sciences*, 6, 42
- Buldgen, G., Salmon, S. J. A. J., Reese, D. R., & Dupret, M. A. 2016b, *A&A*, 596, A73
- Buysschaert, B., Beck, P. G., Corsaro, E., et al. 2016, *A&A*, 588, A82
- Campante, T. L., Barclay, T., Swift, J. J., et al. 2015, *ApJ*, 799, 170
- Cantiello, M., Mankovich, C., Bildsten, L., Christensen-Dalsgaard, J., & Paxton, B. 2014, *ApJ*, 788, 93
- Carlos, M., Nissen, P. E., & Mel  ndez, J. 2016, *A&A*, 587, A100
- Casagrande, L., Flynn, C., Portinari, L., Girardi, L., & Jimenez, R. 2007, *MNRAS*, 382, 1516
- Cassisi, S., Salaris, M., & Irwin, A. W. 2003, *ApJ*, 588, 862
- Chaplin, W. J., Basu, S., Huber, D., et al. 2014, *ApJS*, 210, 1
- Chaplin, W. J. & Miglio, A. 2013, *ARA&A*, 51, 353
- Christensen-Dalsgaard, J. 1988, in *IAU Symposium, Vol. 123, Advances in Helio- and Asteroseismology*, ed. J. Christensen-Dalsgaard & S. Frandsen, 295
- Christensen-Dalsgaard, J. & Daeppen, W. 1992, *A&A Rev.*, 4, 267
- Claret, A. & Torres, G. 2017, *ApJ*, 849, 18
- Claret, A. & Torres, G. 2018, *ApJ*, 859, 100
- Clark, D. H. & Stephenson, F. R. 1975, *The Observatory*, 95, 190
- Cochran, W. D., Hatzes, A. P., Butler, R. P., & Marcy, G. W. 1997, *ApJ*, 483, 457
- Colgan, J., Kilcrease, D. P., Magee, N. H., et al. 2016, *ApJ*, 817, 116
- Cowling, T. G. 1941, *MNRAS*, 101, 367
- Cox, J. P. & Giuli, R. T. 1968, *Principles of stellar structure*
- Cunha, M. S., Avelino, P. P., Christensen-Dalsgaard, J., et al. 2019, *MNRAS*, 490, 909
- Cunha, M. S., Stello, D., Avelino, P. P., Christensen-Dalsgaard, J., & Townsend, R. H. D. 2015, *ApJ*, 805, 127
- Davies, G. R., Chaplin, W. J., Farr, W. M., et al. 2015, *MNRAS*, 446, 2959
- De Ridder, J., Barban, C., Baudin, F., et al. 2009, *Nature*, 459, 398
- Deal, M., Richard, O., & Vauclair, S. 2015, *A&A*, 584, A105
- Deheuvels, S., Ballot, J., Eggenberger, P., et al. 2020, *A&A*, 641, A117
- Deheuvels, S., Brand  o, I., Silva Aguirre, V., et al. 2016, *A&A*, 589, A93
- Deheuvels, S., Doĝan, G., Goupil, M. J., et al. 2014, *A&A*, 564, A27
- Deheuvels, S. & Michel, E. 2011, *A&A*, 535, A91
- Domingo, V., Fleck, B., & Poland, A. I. 1995, *Sol. Phys.*, 162, 1
- Dr  au, G., Cunha, M. S., Vrad, M., & Avelino, P. P. 2020, *MNRAS*, 497, 1008
- Dupret, M. A., Belkacem, K., Samadi, R., et al. 2009, *A&A*, 506, 57
- Dziembowski, W. A. 1971, *Acta Astron.*, 21, 289

- Eggenberger, P., Montalbán, J., & Miglio, A. 2012, *A&A*, 544, L4
- Elliott, J. R. 1996, *MNRAS*, 280, 1244
- Farnir, M., Dupret, M., Pinçon, C., Noels, A., & Scuflaire, R. 2021, accepted for publication in *A&A*
- Farnir, M., Dupret, M. A., Buldgen, G., et al. 2020a, *A&A*, 644, A37
- Farnir, M., Dupret, M. A., Salmon, S. J. A. J., Noels, A., & Buldgen, G. 2019, *Astronomy and Astrophysics*, 622, A98
- Farnir, M., Dupret, M. A., Salmon, S. J. A. J., Noels, A., & Buldgen, G. 2020b, in *Stars and their Variability Observed from Space*, ed. C. Neiner, W. W. Weiss, D. Baade, R. E. Griffin, C. C. Lovekin, & A. F. J. Moffat, 281–286
- Ferguson, J. W., Alexander, D. R., Allard, F., et al. 2005, *ApJ*, 623, 585
- Fossat, E., Boumier, P., Corbard, T., et al. 2017, *A&A*, 604, A40
- Friel, E., Cayrel de Strobel, G., Chmielewski, Y., et al. 1993, *A&A*, 274, 825
- Fröhlich, C., Romero, J., Roth, H., et al. 1995, *Virgo: Experiment for Helioseismology and Solar Irradiance Monitoring*, ed. B. Fleck, V. Domingo, & A. Poland (Dordrecht: Springer Netherlands), 101–128
- Gehan, C., Mosser, B., Michel, E., Samadi, R., & Kallinger, T. 2018, *A&A*, 616, A24
- Goodricke, J. 1783, *Philosophical Transactions of the Royal Society of London Series I*, 73, 474
- Gough, D. O. 1986, *Highlights of Astronomy*, 7, 283
- Gough, D. O. 1990, in *Lecture Notes in Physics*, Berlin Springer Verlag, Vol. 367, *Progress of Seismology of the Sun and Stars*, ed. Y. Osaki & H. Shibahashi, 283
- Goupil, M. J., Mosser, B., Marques, J. P., et al. 2013, *A&A*, 549, A75
- Grec, G., Fossat, E., & Pomerantz, M. A. 1983, *Sol. Phys.*, 82, 55
- Grevesse, N. & Noels, A. 1993, in *Origin and Evolution of the Elements*, ed. N. Prantzos, E. Vangioni-Flam, & M. Casse, 15–25
- Grevesse, N. & Sauval, A. J. 1998, *Space Sci. Rev.*, 85, 161
- Grosjean, M., Dupret, M. A., Belkacem, K., et al. 2014, *A&A*, 572, A11
- Harvey, J., Abdel-Gawad, K., Ball, W., et al. 1988, in *ESA Special Publication*, Vol. 286, *Seismology of the Sun and Sun-Like Stars*, ed. E. J. Rolfe, 203–208
- Hekker, S., Elsworth, Y., & Angelou, G. C. 2018, *A&A*, 610, A80
- Hill, H. A. & Rosenwald, R. D. 1986, *Ap&SS*, 126, 335
- Houdek, G. & Gough, D. O. 2007, *MNRAS*, 375, 861
- Huber, D., Chaplin, W. J., Christensen-Dalsgaard, J., et al. 2013, *ApJ*, 767, 127
- Iglesias, C. A. & Rogers, F. J. 1996, *ApJ*, 464, 943
- Iott, J., Haftka, R. T., Adelman, H. M., & States, U. 1985, *Selecting step sizes in sensitivity analysis by finite differences [microform]* / Jocelyn Iott, Raphael T. Haftka, Howard M. Adelman (National Aeronautics and Space Administration, Scientific and Technical Information Branch ; For sale by the National Technical Information Service) [Washington, D.C.] : [Springfield, Va], 1 v. :
- Jeffreys, H. 1925, *Proceedings of the London Mathematical Society*, s2-23, 428
- Jiang, C. & Christensen-Dalsgaard, J. 2014, *MNRAS*, 444, 3622
- Jiang, C., Cunha, M., Christensen-Dalsgaard, J., & Zhang, Q. 2020, *MNRAS*, 495, 621
- Jørgensen, A. C. S., Montalbán, J., Angelou, G. C., et al. 2021, *MNRAS*, 500, 4277
- Khan, S., Hall, O. J., Miglio, A., et al. 2018, *ApJ*, 859, 156
- King, J. R., Deliyannis, C. P., Hiltgen, D. D., et al. 1997, *AJ*, 113, 1871

- Kippenhahn, R., Weigert, A., & Weiss, A. 2012, *Stellar Structure and Evolution*
- Kjeldsen, H., Bedding, T. R., & Christensen-Dalsgaard, J. 2008, *ApJ*, 683, L175
- Kramers, H. A. 1926, *Zeitschrift fur Physik*, 39, 828
- Lagarde, N., Bossini, D., Miglio, A., Vrad, M., & Mosser, B. 2016, *MNRAS*, 457, L59
- Leavitt, H. S. & Pickering, E. C. 1912, *Harvard College Observatory Circular*, 173, 1
- Lebreton, Y., Fernandes, J., & Lejeune, T. 2001, *A&A*, 374, 540
- Lebreton, Y. & Goupil, M. J. 2014, *A&A*, 569, A21
- Li, Y., Bedding, T. R., Li, T., et al. 2020, *MNRAS*, 495, 2363
- Lund, M. N., Silva Aguirre, V., Davies, G. R., et al. 2017, *ApJ*, 835, 172
- Magic, Z., Weiss, A., & Asplund, M. 2015, *A&A*, 573, A89
- Maia, M. T., Meléndez, J., Lorenzo-Oliveira, D., Spina, L., & Jofré, P. 2019, *A&A*, 628, A126
- Marquardt, D. W. 1963, *SIAM Journal on Applied Mathematics*, 11, 431
- Marques, J. P., Goupil, M. J., Lebreton, Y., et al. 2013, *A&A*, 549, A74
- Mazumdar, A. 2005, *A&A*, 441, 1079
- Mazumdar, A., Monteiro, M. J. P. F. G., Ballot, J., et al. 2014, *ApJ*, 782, 18
- Metcalf, T. S., Chaplin, W. J., Appourchaux, T., et al. 2012, *ApJ*, 748, L10
- Miglio, A., Chiappini, C., Morel, T., et al. 2013, *MNRAS*, 429, 423
- Miglio, A. & Montalbán, J. 2005, *A&A*, 441, 615
- Miglio, A., Montalbán, J., Carrier, F., et al. 2010, *A&A*, 520, L6
- Montalbán, J., Miglio, A., Noels, A., et al. 2013, *ApJ*, 766, 118
- Montalbán, J., Miglio, A., Noels, A., Scuflaire, R., & Ventura, P. 2010, *Astronomische Nachrichten*, 331, 1010
- Montalbán, J. & Rebolo, R. 2002, *A&A*, 386, 1039
- Monteiro, M. J. P. F. G., Christensen-Dalsgaard, J., & Thompson, M. J. 1994, *A&A*, 283, 247
- Monteiro, M. J. P. F. G., Christensen-Dalsgaard, J., & Thompson, M. J. 2000, *MNRAS*, 316, 165
- Monteiro, M. J. P. F. G. & Thompson, M. J. 1998, in *New Eyes to See Inside the Sun and Stars*, ed. F.-L. Deubner, J. Christensen-Dalsgaard, & D. Kurtz, Vol. 185, 317
- Morel, T., Creevey, O. L., Montalbán, J., Miglio, A., & Willett, E. 2021, *A&A*, 646, A78
- Mosser, B., Belkacem, K., Goupil, M. J., et al. 2011, *A&A*, 525, L9
- Mosser, B., Benomar, O., Belkacem, K., et al. 2014, *A&A*, 572, L5
- Mosser, B., Elsworth, Y., Hekker, S., et al. 2012a, *A&A*, 537, A30
- Mosser, B., Gehan, C., Belkacem, K., et al. 2018, *A&A*, 618, A109
- Mosser, B., Goupil, M. J., Belkacem, K., et al. 2012b, *A&A*, 548, A10
- Mosser, B., Goupil, M. J., Belkacem, K., et al. 2012c, *A&A*, 540, A143
- Mosser, B., Michel, E., Belkacem, K., et al. 2013, *A&A*, 550, A126
- Mosser, B., Pinçon, C., Belkacem, K., Takata, M., & Vrad, M. 2017, *A&A*, 600, A1
- Mosser, B., Vrad, M., Belkacem, K., Deheuvels, S., & Goupil, M. J. 2015, *A&A*, 584, A50
- Noels, A., Montalbán, J., & Chiappini, C. 2016, *Astronomische Nachrichten*, 337, 982
- Nsamba, B., Moedas, N., Campante, T. L., et al. 2021, *MNRAS*, 500, 54

- Osaki, Y. 1971, PASJ, 23, 485
- Ouazzani, R. M., Marques, J. P., Goupil, M. J., et al. 2019, A&A, 626, A121
- Paxton, B., Cantiello, M., Arras, P., et al. 2013, ApJS, 208, 4
- Peimbert, A., Peimbert, M., & Luridiana, V. 2002, ApJ, 565, 668
- Perryman, M. A. C., de Boer, K. S., Gilmore, G., et al. 2001, A&A, 369, 339
- Pietrinferni, A., Cassisi, S., Salaris, M., & Castelli, F. 2004, ApJ, 612, 168
- Pinçon, C., Belkacem, K., Goupil, M. J., & Marques, J. P. 2017, A&A, 605, A31
- Pinçon, C., Goupil, M. J., & Belkacem, K. 2020, A&A, 634, A68
- Pinçon, C., Takata, M., & Mosser, B. 2019, A&A, 626, A125
- Pinsonneault, M. H., An, D., Molenda-Żakowicz, J., et al. 2012, ApJS, 199, 30
- Prandtl, L. 1925, Zeitschrift Angewandte Mathematik und Mechanik, 5, 136
- Press, W. H., Flannery, B. P., Teukolsky, S. A., & Vetterling, W. T. 1992, Numerical Recipes in FORTRAN 77: The Art of Scientific Computing, 2nd edn. (Cambridge University Press)
- Proffitt, C. R. & Michaud, G. 1991, ApJ, 380, 238
- Ramírez, I., Meléndez, J., & Asplund, M. 2009, A&A, 508, L17
- Ramírez, I., Meléndez, J., Cornejo, D., Roederer, I. U., & Fish, J. R. 2011, ApJ, 740, 76
- Rauer, H., Catala, C., Aerts, C., et al. 2014, Experimental Astronomy, 38, 249
- Reese, D. R., Marques, J. P., Goupil, M. J., Thompson, M. J., & Deheuvels, S. 2012, A&A, 539, A63
- Refsdal, S. & Weigert, A. 1970, A&A, 6, 426
- Rendle, B. M., Buldgen, G., Miglio, A., et al. 2019, MNRAS, 484, 771
- Ribas, I., Jordi, C., Torra, J., & Giménez, Á. 2000, MNRAS, 313, 99
- Rogers, F. J. & Nayfonov, A. 2002, ApJ, 576, 1064
- Rosu, S., Noels, A., Dupret, M. A., et al. 2020, A&A, 642, A221
- Roxburgh, I. W. & Vorontsov, S. V. 2003, A&A, 411, 215
- Schou, J., Antia, H. M., Basu, S., et al. 1998, ApJ, 505, 390
- Scuflaire, R. 1974, A&A, 36, 107
- Scuflaire, R., Montalbán, J., Théado, S., et al. 2008a, Ap&SS, 316, 149
- Scuflaire, R., Théado, S., Montalbán, J., et al. 2008b, Ap&SS, 316, 83
- Shibahashi, H. 1979, PASJ, 31, 87
- Silva Aguirre, V., Lund, M. N., Antia, H. M., et al. 2017, ApJ, 835, 173
- Sonoi, T., Samadi, R., Belkacem, K., et al. 2015, A&A, 583, A112
- Spada, F., Gellert, M., Arlt, R., & Deheuvels, S. 2016, A&A, 589, A23
- Takata, M. 2016a, PASJ, 68, 109
- Takata, M. 2016b, PASJ, 68, 91
- Tassoul, M. 1980, ApJS, 43, 469
- Thoul, A. A., Bahcall, J. N., & Loeb, A. 1994, ApJ, 421, 828
- Ulrich, R. K. 1986, ApJ, 306, L37
- Unno, W., Osaki, Y., Ando, H., Saio, H., & Shibahashi, H. 1989, Nonradial oscillations of stars

- Verma, K., Faria, J. P., Antia, H. M., et al. 2014, *ApJ*, 790, 138
- Verma, K., Raodeo, K., Antia, H. M., et al. 2017, *ApJ*, 837, 47
- Verma, K., Raodeo, K., Basu, S., et al. 2019, *MNRAS*, 483, 4678
- Vernazza, J. E., Avrett, E. H., & Loeser, R. 1981, *ApJS*, 45, 635
- Vincenzo, F., Miglio, A., Kobayashi, C., Mackereth, J. T., & Montalbán, J. 2019, *A&A*, 630, A125
- Vorontsov, S. V. 1988, in *IAU Symposium, Vol. 123, Advances in Helio- and Asteroseismology*, ed. J. Christensen-Dalsgaard & S. Frandsen, 151
- Vrard, M., Mosser, B., Barban, C., et al. 2015, *A&A*, 579, A84
- Vrard, M., Mosser, B., & Samadi, R. 2016, *A&A*, 588, A87
- Wentzel, G. 1926, *Zeitschrift für Physik*, 38, 518
- White, T. R., Huber, D., Maestro, V., et al. 2013, *MNRAS*, 433, 1262